STUDY OF MORPHOLOGY AND STAR-FORMATION ACTIVITY OF MERGING DWARF GALAXIES IN THE FIELD ENVIRONMENT

A THESIS SUBMITTED TO THE

CENTRAL DEPARTMENT OF PHYSICS

INSTITUTE OF SCIENCE AND TECHNOLOGY

TRIBHUVAN UNIVERSITY

NEPAL

FOR THE AWARD OF

DOCTOR OF PHILOSOPHY

IN PHYSICS

BY

DAYA NIDHI CHHATKULI

FEBRUARY 2023

STUDY OF MORPHOLOGY AND STAR-FORMATION ACTIVITY OF MERGING DWARF GALAXIES IN THE FIELD ENVIRONMENT

A THESIS SUBMITTED TO THE

CENTRAL DEPARTMENT OF PHYSICS

INSTITUTE OF SCIENCE AND TECHNOLOGY

TRIBHUVAN UNIVERSITY

NEPAL

FOR THE AWARD OF

DOCTOR OF PHILOSOPHY

IN PHYSICS

BY

DAYA NIDHI CHHATKULI

FEBRUARY 2023

DECLARATION

Thesis entitled **"Study of morphology and star-formation activity of merging dwarf galaxies in the field environment"** which is being submitted to the Central Department of Physics, Institute of Science and Technology (IOST), Tribhuvan University, Nepal for the award of the degree of Doctor of Philosophy (Ph.D.), is a research work carried out by me under the supervision of Prof. Dr. Binil Aryal of Dean's office (IOST), Tribhuvan University, Nepal and co-supervised by Dr. Sanjaya Paudel of Department of Astronomy, Yonsei University, Seoul, Republic of Korea.

This research is original and has not been submitted earlier in part or full in this or any other form to any university or institute, here or elsewhere, for the award of any degree.

_____

Daya Nidhi Chhatkuli

RECOMMENDATION

This is to recommend that **Daya Nidhi Chhatkuli** has carried out research entitled **"Study of morphology and star-formation activity of merging dwarf galaxies in the field environment"** for the award of Doctor of Philosophy (Ph.D.) in **Physics** under our supervision. To our knowledge, this work has not been submitted for any other degree.

He has fulfilled all the requirements laid down by the Institute of Science and Technology (IOST), Tribhuvan University, Kirtipur for the submission of the thesis for the award of Ph.D. degree.

. . . . . .

Dr. Binil Aryal
Supervisor
(Professor)
Central Department of Physics
Tribhuvan University
Kirtipur, Kathmandu, Nepal

. . . . . .

Dr. Sanjaya Paudel
Co-Supervisor
(Research Professor)
Department of Astronomy
Yonsei University
Seoul, Republic of Korea

FEBRUARY 2023

LETTER OF APPROVAL

[Date: 14/02/2023]

On the recommendation of Prof. Dr. **Binil Aryal** and Dr. **Sanjaya Paudel**, this Ph.D. thesis submitted by **Mr. Daya Nidhi Chhatkuli**, entitled **"Study of morphology and star-formation activity of merging dwarf galaxies in the field environment"** is forwarded by Central Department Research Committee (CDRC) to the Dean, IOST, T.U..

.....

Dr. Om Prakash Niraula
Professor
Head
Central Department of Physics,
Tribhuvan University
Kirtipur, Kathmandu
Nepal

ACKNOWLEDGEMENTS

Whenever we sail in the journey of life, we sail with our companions who help us in every step of the boarding. Similar was my journey of this Ph.D. persuasion. I would like to start acknowledging with the ones who taught me the very fundamentals of my study, my supervisors. They were the ones who allowed me to look at the vast ocean of Physics with my third eye. So, first I would like to express my sincere gratitude to my supervisor Prof. Dr. Binil Aryal, a highly accomplished and respected figure in the field of astronomy for the continuous scientific guidance, supports and parentship throughout my research work. I am indebted to my co-supervisor Dr. Sanjaya Paudel, an exceptional researcher and mentor, for his guidance, patience, and endless support throughout my journey as a Ph.D. student in astronomy.

My sincere gratitude goes to Sloan Digital Sky Survey (SDSS) for providing valuable data through our collaboration. This study is based on the archival images and spectra from the Sloan Digital Sky Survey (the full acknowledgment can be found at `https://www.sdss.org/collaboration/acknowledgements`).

I would like to thank the International Astronomical Union (IAU) and the organizers for providing me grants and allowing me to present my research work in International Astronomical Union General Assembly (IAUGA 2022) held in Republic of Korea and IAUS 379: Dynamical Masses of Local Group Galaxies held in Germany.

I am grateful to the Institute of Science and Technology, Tribhuvan University, Nepal for providing me study leave and the Central Department of Physics (CDP) for providing me with facilities to carry out my research work. It is with great pleasure that I thank University Grants Commission of Nepal for providing Ph.D. fellowship (Ph. D. 75/76-S & T-13). I would also like to thank Tri-Chandra Multiple Campus, T.U. for permitting me to carry out the Ph.D. research.

I am thankful to Mr. Rajesh Kumar Bachchan for his help during the process of data access and processing. He was the backbone for my thesis process, who helped me to compile my works and taught me basics of programming from the very beginning. I would like to express my sincere gratitude to Prof. Dr. Om Prakash Niraula, Prof. Dr. Iswar Koirala, Prof. Dr. Raju Khanal, Prof. Dr. Narayan Prasad Adhikari, Prof. Dr. Narayan Pd. Chapagain, Asso. Prof. Dr. Ajay Kumar Jha, Asso. Prof. Dr. Balram Ghimire, Asso. Prof. Dr. Nurapati Pantha, Asso. Prof. Dr. Tika Ram Lamichhane, Dr. Binod Adhikari and other faculty members of CDP for their constant support and encouragement during the research work. I also would like to remember all the faculties

of department of Physics, Tri-Chandra Multiple Campus.

I am contented towards my family members for their constant support, patience, and encouragement. I would respectfully like to remember my late parents Chuda Mani Chhatkuli and Haripriya Chhatkuli for their sacrifices made for me. I would like to remember my elder brother, Mr. Babu Ram Chhatkuli who encouraged me to excel more since my childhood. I am thankful to my daughter, Ms. Ayushma Chhatkuli and son, Mr. Aryan Chhatkuli who always inspire me to pursue more in life. Lastly, my special thank goes to my wife Mrs. Durga Chhatkuli for her support and encouragement in every step during my research work.

Mr. Daya Nidhi Chhatkuli
FEBRUARY 2023

ABSTRACT

Strong evidence has been found in the past decades that dwarf galaxies have evolved over time. There are a few unanswered questions regarding the role of dwarf-dwarf interaction and merger in the evolution of a galaxy. This thesis focuses mainly on providing a new understanding of the evolution of dwarf galaxies by merger interactions. We studied 25 merging dwarf galaxies of different morphology: 15 compact (labeled Cd-X, $X = 1, ..., 15$) and 10 extended (labeled Ed-X, $X = 1, ..., 10$) morphologies. Out of them, 21 are located in field environment and rest are in group environment. In this work, we extensively utilized photometric and spectroscopic database from the Sloan Digital Sky Survey (SDSS) to measure galaxies' structural and star-formation properties. These compact dwarf galaxies are: LEDA3111971, LEDA3093079, PGC1653806, LEDA4207520, LEDA3461301, PGC0029004, PGC030055, PGC030133, MRK0631, UM454, MRK0750, UGC06850, LEDA2793637, LEDA2214957 and LEDA1129746. Similary, the extended dwarf galaxies are: UGC00993, NGC2604, UGC06433, NGC4765, NGC5058, MRK1481, UGCA375, UGC09588, MRK0689 and PGC057169. The redshift (z) of these candidate dwarf galaxies lies in the range 0.0024 to 0.0197. We performed ellipse fitting in the SDSS g-band images and measured galaxies' size and mean surface brightness by using both parametric and non-parametric methods. For the parametric method, we used Sérsic function modeling of a one-dimensional light profile along the major axis obtained from the ellipse fit. On the other hand, we adopted the Petrosian method to calculate the overall galaxy size, magnitude and mean surface brightness. The SDSS optical spectrum is used to calculate star formation rate (SFR) and metallicity by analyzing emission lines. The SFR is found to vary from 0.0004 $M_{\odot}yr^{-1}$ to 0.4755 $M_{\odot}yr^{-1}$ for the 15 merging compact dwarf galaxies. For the 10 extended merging dwarf galaxies, the values of SFR are found in the range 0.0022 $M_{\odot}yr^{-1}$ to 0.1913 $M_{\odot}yr^{-1}$. It increases from 0.0008 $M_{\odot}yr^{-1}$ to 0.9048 $M_{\odot}yr^{-1}$ for Cd-galaxies and 0.0035 $M_{\odot}yr^{-1}$ to 0.2647 $M_{\odot}yr^{-1}$ for Ed-galaxies when taking into account extinction correction. As expected, the SFR is found to be more (almost 2 times in Cd galaxies and 1.5 times in Ed galaxies) after the extinction correction. The SFR is found to increase with redshift. This reveals the fact that the distant merging dwarf galaxies are gas-rich and metal-rich. Additionally, a weak correlation between redshift and the extinction coefficient is noticed in the merging dwarf galaxies. The abundance of metals is found to be quite different in these two types of dwarf galaxies. From the spectroscopic calculations, the metallicity of the compact merging galaxies is found to be in the range 8.11 dex to 9.19 dex while this value is 8.32 dex to 8.90 dex in the case of extended merging dwarf galaxies. This result

indicates that the merging compact dwarf galaxies show a wider variety of metal-rich environments than that of the extended dwarf field. As a whole, the metallicity is found to increase slowly with the redshift. The effective radius, half-light radius and the Sérsic index of dwarf galaxies are found to lie in the range (1.56 to 81.09) arcsec, (0.47 to 4.39) arcsec and (0.4 to 2.9) respectively. It is noticed that the compact dwarf is located below the main sequence defined by the local star-forming dwarf galaxies on average. The mass-metallicity relation reveals that the compact galaxy shows different behaviors than the extended merging dwarf being significantly metal-rich compared to the comparison sample. On the other hand, extended dwarf galaxies well follow the mass metallicity relation provided by normal star-forming dwarf galaxies with a bit higher scattering. It is found that more evolved merging dwarfs are expected to have low star-formation activity and higher metal contents than less evolved extended merging dwarfs. Additionally, we verified that the merging dwarfs form compact elliptical structures.

LIST OF ACRONYMS AND ABBREVIATIONS

ADS	: Astrophysics Data System
AJ	: Astronomical Journal
ApJ	: Astrophysical Journal
ApJS	: Astrophysical Journal Suppliment
APO	: Apache Point Observatory
APOGEE	: The Apache Point Observatory Galactic Evolution Experiment
arcsec	: arcsecond
CCDs	: Charge Coupled Devices
CDM	: Cold Dark Matter
CGCG	: Catalogue of Galaxies and of Clusters of Galaxies
cm	: centimeter
CMB	: Cosmic Microwave Background
CMBR	: Cosmic Microwave Background Radiation
DAS	: Data Archive Server
DDO	: David Dunlap Observatory
DEC	: Declination
DR	: Data Released
eBoss	: Extended Baryonic Oscillation Spectroscopic Survey
EW(H_α)	: H_α Equivalent Width
FIR	: Far Infrared
FITS	: Flexible Image Transport System
FUV	: Far Ultra Violet
FWHM	: Full Width Half Maxima
GMRT	: Giant Metrewave Radio Telescope
H-R diagram	: Hertzsprung-Russell diagram
HST	: Hubble Space Telescope
ICRS	: International Celestial Reference System
IMF	: Initial Mass Function
IR	: Infra Red
IRAF	: Image Reuction and Analysis Facility
ISM	: Inter Stellar Medium
J2000	: Julian year 2000
JVLA	: Jansky Very Large Array
K	: Kelvin

kpc	: kilo parsec
KUG	: Kiso Ultraviolet Galaxy
LEDA	: Lyon-Meudon Extragalactic Database
LMC	: Large Magellanic Cloud
MCG	: Morphological Catalog of Galaxies
m	: metere
MJD	: Modified Julian Date
Mpc	: Mega persec
NED	: NASA Extragalactic Database
NASA	: National Aeronautical Space Administration
NGC	: New General Catalogue of galaxy
NIR	: Near Infrared
PA	: Position Angle
RA	: Right Ascension
pc	: parsec
RAA	: Research in Astronomy and Astrophysics
s	: second
SAO	: Smithsonian Astrophysical Observatory
SDSS	: Sloan Digital Sky Survey
SFR	: Star Formation Rate
SIMBAD	: Set of Identifications, Measurements and Bibliography for Astronomical Data
SMC	: Small Magellanic Cloud
SNR	: Signal to Noise Ratio
SSPs	: Simple Stellar Populations (SSPs)
TNT	: TiNy Titans
UBV filters	: Ultra Violet, Blue and Visible filters
UGC	: Uppsala General Catalogue
UV	: Ultra Violet
VCC	: Virgo Cluster Center
VLAHI	: Very Large Array Neutral Hydrogen (HI)
yr	: year

LIST OF TABLES

LIST OF FIGURES

TABLE OF CONTENTS

Page No.

CHAPTER 1

1. INTRODUCTION

1.1 Dwarf Galaxy

The universe is full of dwarf galaxies, which are small, low-mass galaxies. Typically, their combined mass is less than 10^{10} $M_{\odot}$, or roughly one-hundredth of the mass of the Milk-Way (Binggeli et al., 1987). Dwarf galaxies, despite their diminutive size, are among the most significant types of celestial objects because they can shed light on the earliest phases of galaxy formation and evolution and are assumed to be the building blocks of the universe.

Dwarf elliptical, spheroidal, and irregular galaxies are only a few of the several forms of dwarf galaxies. These various kinds of dwarf galaxies can display a variety of physical properties, including their form, size, mass, luminosity and chemical composition. An example of dwarf galaxies of the local group is shown in Figure 1. In this figure, we show a typical sample of merging dwarf galaxies. The galaxies are in a decreasing mass order and the first Large Magellanic Cloud (LMC) is our nearest dwarf galaxy. The outskirts of larger galaxies in galaxy clusters and in the field are just a few places where dwarf galaxies can be found (i.e., isolated from other galaxies).

The first dwarf galaxy was discovered in the middle of the 19^{th} century (Binggeli et al., 1985). Since then, astronomers have made enormous strides in their understanding of the features and evolution of these celestial objects. For instance, researches have demonstrated that dwarf galaxies can have complicated star formation histories, with some undergoing intense star formation bursts while others have very moderate star formation rates (e.g., Weisz et al., 2011). Additionally, they can have a variety of chemical properties, some of which have high metallicities and others having low metallicities (Lanfranchi & Matteucci, 2003). Dwarf galaxies are significant and fascinating type of astronomical objects that are still the focus of ongoing investigation.

1.2 Classification

The morphology of a dwarf galaxy refers to its overall shape and structure. Dwarf galaxies are classified into several different types depending on their morphology such as size, shape and other properties. Some of them are discussed briefly:

(a) Dwarf irregular galaxies: These are small, irregularly shaped galaxies that do not

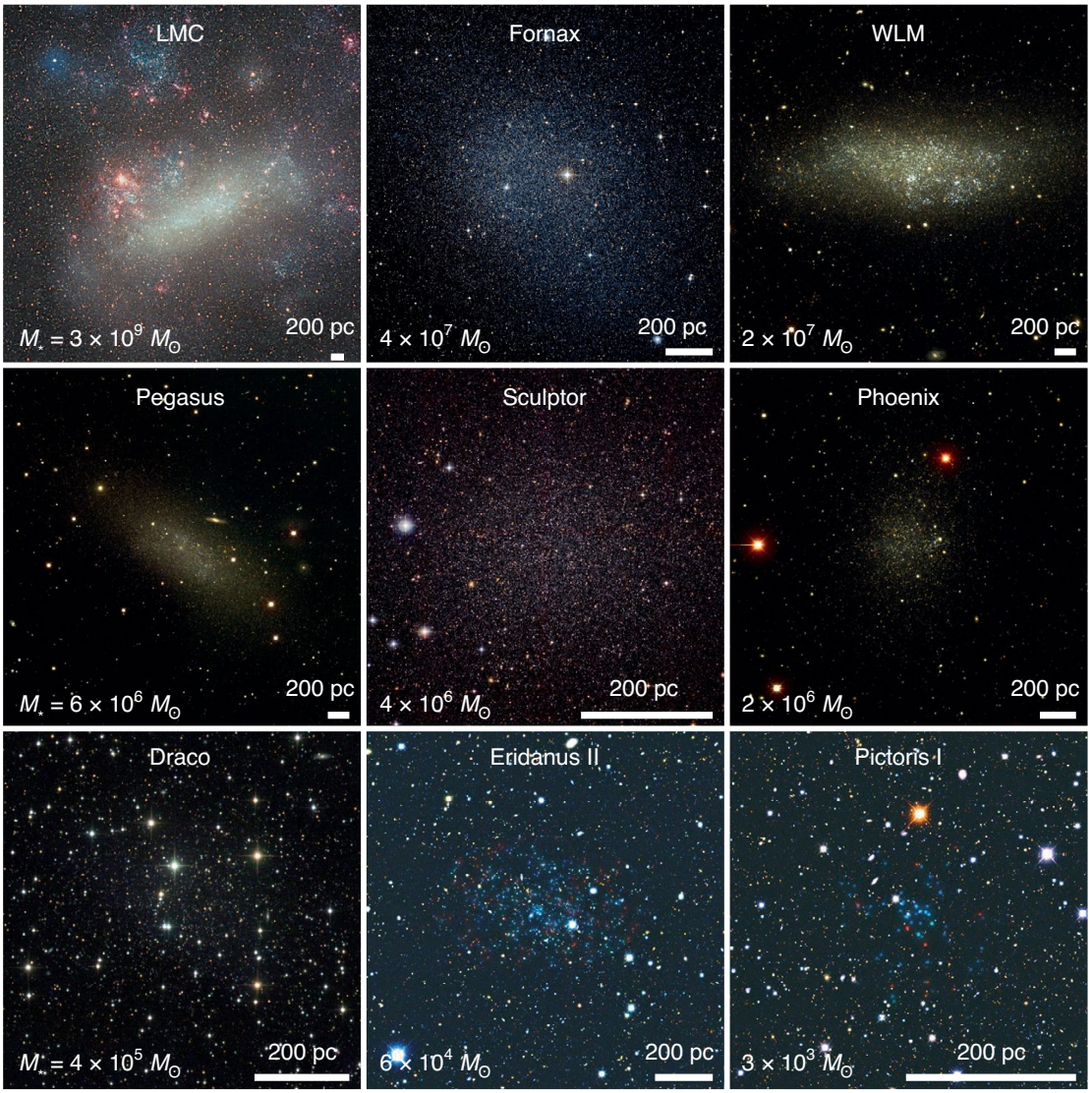

Figure 1: Various examples of dwarf galaxies in local group (Image credit: Crnojević & Mutlu-Pakdil, 2021).

have a lot of structure and tend to have low mass. They often have a lot of gas and dust and are actively forming new stars.

(b) Dwarf elliptical galaxies: These are small galaxies that are shaped like an ellipse. They are similar to dwarf spheroidal galaxies in that they have little gas and dust and are not actively forming new stars.

(c) Spiral dwarf galaxies: These are dwarf galaxies that have a spiral structure, with a central bulge surrounded by a disk of gas, dust and stars. They may have one or more spiral arms and can resemble larger spiral galaxies, but are much smaller in size.

(d) Blue compact dwarf galaxies (BCDs): These are small, irregular galaxies that contain a high concentration of young, hot stars and are actively forming new stars. They are often blue in color due to the presence of these young and hot stars.

(e) Ultra-compact dwarf galaxies (UCDs): These are very small, dense galaxies that have high mass-to-light ratios. They are thought to be the remnants of larger galaxies that have been stripped of their outer layers.

Sandage & Binggeli (1984) classification system highlighted the diversity and complexity within the population of dwarf galaxies. The authors also pointed out that there is no fundamental difference between normal and dwarf galaxies. Due to this lack of distinction, there was no widely accepted definition for dwarf galaxies at the time, and different research groups used their own criteria for defining these systems. Binggeli & Jerjen (1998) attempted to address this issue, but to this day, there is still no widely accepted definition of dwarf galaxies, and different authors continue to use their own definitions.

1.3 Unsolved Issues in Dwarf Galaxy Morphology

There remain a number of unresolved issues in the study of dwarf galaxy morphology, some of which are briefly introduced here.

(a) It is not fully understood how and why dwarf galaxies take on different shapes and structures.

(b) The role of environment in shaping dwarf galaxy morphology: The galaxie's surrounding environment can affect its morphology, but it is not fully understood about its details.

(c) The relationship between dwarf galaxy morphology and other dwarf galaxy properties: It is not clear how the morphology of a dwarf galaxy is related to other properties such as its mass, star formation rate, and central black hole mass.

(d) The role of dwarf galaxies in the evolution of larger galaxies: Dwarf galaxies are believed to be involved in the development of larger galaxies, though the details of this process remain unclear.

(e) The formation and evolution of ultra-compact dwarf galaxies: The process by which the formation of very small and dense UCDs occurs is not well understood.

1.4 Merging Dwarfs

The merging dwarf galaxies are a group of two or more dwarf galaxies that are combining to form a single galaxy. This process can occur when two dwarf galaxies travel close to one another and are pulled together by their gravitational attraction.

Since the merging dwarf galaxies are faint and small in size and less frequently found in dense areas of the universe, the galaxies can be challenging to study. However, the

merging dwarf galaxies are worth researching because they can provide us the knowledge of the early process of formation and evolution of galaxies. A newly identified merging dwarf galaxy NGC 4998 situated at the vicinity of MilkyWay is shown in Figure 2

Figure 2: The first merging dwarf galaxy, NGC4998 was reported by Rich et al. (2012). It has B-band magnitude of -17.83 mag and distance 8.3 Mpc, (Source: *SDSS Legacy Survey*, Accessed: 2019-09-30).

Dwarf galaxies can face a variety of effects as a result of merging. For example, it can trigger bursts of star formation, a in falling gas and other material can be compressed and pushed into the galaxy's center, causing the formation of new stars (Elmegreen et al., 2002). Another effect of galaxy merger is change in the chemical composition of the emerging galaxy. The two merging galaxies, after merger, may have different metallicities and other chemical properties, which can be mixed together during the merger process (Lanfranchi & Matteucci, 2003). During a merger, the gravitational attraction between the two galaxies causes them to accelerate towards each other. As they approach, the differential gravitational forces exerted by each galaxy on the other become significant. These tidal forces lead to the deformation of the galaxies, stretching them along the direction of the gravitational pull called gravitational shearing effect. The gravitational shearing effect plays a crucial role in shaping the morphology and structure of the resulting merged galaxy. It can trigger star formation by compressing gas and dust, leading to the formation of new stars. The tidal force can have severe impact on kinematic and structural properties of affected galaxies where morphologies of these galaxies can be severely disturbed or even completely destroyed. The force of the tidal pull caused by a difference in gravitational shear initially impacts the dynamical

behavior of small satellites as they move around their primary host. The disk galaxies are particularly sensitive to the tidal forces. As a result, gas rich disk of a satellite galaxy gets stretched beyond the tidal radius and forms stellar stream along its orbital path, then finally effected galaxy can lose its entire disk structure. The remain stellar core can become a new low mass early-type dwarf galaxy. On the other hand, a dwarf galaxy can merge with even smaller/similar mass dwarf and, as we have seen in many examples of massive galaxies, such merger process also completely changes the morphological and kinematical properties. Dwarf galaxies are, however, not expected to have experienced any major mergers since their first major star-forming period. Overall, galaxy merger is a crucial event that can impact dwarf galaxy evolution and contribute to the formation of bigger galaxies.

1.5 Star-Formation Rate

The rate at which a galaxy is currently transforming its gases into stars is referred to as the Star Formation Rate (SFR). It measures how much gas and other matter are transformed into stars over a specific period of time and, therefore, is commonly represented in solar masses per year.

The SFR is an important property of a galaxy because it gives an idea about how the galaxy is now forming in terms of star formation and can shed light on its evolution and its future. The SFR can vary greatly amongst galaxies, from extremely low rates in some galaxies to powerful bursts of star formation in others. Within a single galaxy, the SFR can also be changed over time, depending on things like the availability of gas, the presence of an active galactic nucleus (AGN) and the galaxy's environment (Kennicutt & Evans, 2012a).

Among many ways of measuring the SFR of a galaxy, detection of the spectral lines produced by the ionized gas surrounding the young and hot stars and the detection of infrared radiation emitted by the dust that is heated during star formation process are important (Kennicutt & Evans, 2012a).

1.6 SFR in Milky-Way

The SFR of the Milky-Way (MW) is estimated to be in the range of (1 to 3) $M_{\odot}yr^{-1}$. (Chomiuk & Povich, 2011). Compared to the other galaxies, this is relatively low, primarily the ones that undergo extreme bursts of star formation. However, the Milky-Way has not had a constant SFR over time and is thought to have significantly varied over its long history of 13.5 billion years (Calzetti et al., 2010).

Observing the emissions from young and hot stars that are forming actively is one of the

ways to measure the SFR of the Milky-Way. Strong ultraviolet (UV) radiation emitted by these stars can be detected by a telescope. The SFR can be estimated by using the intensity of UV radiation (Robitaille, 2010).

In general, the SFR of the Milk-Way is a significantly important property that can provide some idea about the evolution and future of our galaxy.

1.7 SFR of Dwarf Galaxies

It is estimated that the star-forming dwarf galaxies have an approximate SFR of a few solar masses per year. The SFR of some larger, more actively star-forming galaxies is somehow higher: hundreds or thousands of solar masses per year. The SFR in a dwarf galaxy can vary depending on a number of factors, such as the galaxy's mass, metallicity, gas content, and interactions with neighboring galaxies. Dwarf galaxies are generally characterized by their low masses and small sizes, which can lead to lower SFRs compared to more massive galaxies.

However, some dwarf galaxies have been found to have relatively high SFRs, especially those undergoing a burst of star formation triggered by galaxy interactions and the gas inflow from the intergalactic medium. In general, the SFR in a dwarf galaxy is determined by the availability of gas and the efficiency with which that gas is converted into stars.

1.8 Importance of SFR in Dwarf Galaxies

The SFR is a key property of a galaxy. It provides a clear understanding of the evolution and future of a galaxy. It also shows their role in the larger cosmic context, making it an important asset. Dwarf galaxies are the foundational components of larger galaxies and they can also provide some knowledge about the early stages of galaxy formation as well as evolution. Dwarf galaxies are also assumed to be an important site of chemical enrichment since evolution of the universe through their star formation and supernova activity contribute to the chemical evolution. Because of this, SFR is a very important property in case of dwarf galaxies (Lanfranchi & Matteucci, 2003).

1.9 Role of Metallicity in SFR

The rate of star formation inside a galaxy can be affected by the metallicity of the galaxy, which is a measurement of the quantity of elements heavier than hydrogen and helium in the interstellar medium (ISM). Studies have revealed that a galaxy's metallicity and SFR are frequently connected (Tremonti et al., 2004). Normally, SFRs are typically higher for galaxies with lower metallicities and lower for galaxies with higher metallicities. This is known as "mass-metallicity" relation.

Although the cause of this association is not entirely understood, it is believed that the metallicity of the ISM may have an impact on the star forming efficiency in the galaxies. For example, higher metallicities, for instance, may result in the generation of more dust grains, which can absorb and block the UV light required for the formation of new stars (Dwek, 1998). Additionally, higher metallicities might result in the formation of more complex molecules in the ISM, which could cool the gas and make it harder for it to collapse and generate stars (Omukai et al., 2005). Thus, the metallicity of a galaxy also can affect its SFR and plays a role in its evolution.

1.10 Galaxy Spectroscopy

We can examine the physical properties, kinematics and chemical composition of galaxies by making spectroscopic observations of them. Astronomers can determine the temperatures, densities and velocities of the gas, stars, and other components that make up a galaxy, by analyzing the light emitted by the galaxy and breaking it down into its different wavelengths. From the spectroscopic analysis, we can find the chemical composition of galaxies. By the analysis of emission and absorption lines in the galaxy spectrum, we will be able to determine the abundance of elements heavier than hydrogen and helium such as oxygen, nitrogen and so on. This can shed light on the galaxy's history of star formation as well as the mechanisms that lead to the interstellar medium's enrichment with heavier elements.

1.11 Galaxy Spectrum

A graphical relation between the intensity of a galaxy's light and its wavelength is called a galaxy spectrum, as shown in Figure 3. It is derived by measuring the amount of light at each wavelength after breaking down the spectrum of a galaxy's light into its constituent wavelengths. The resulting spectrum can offer a multitude of details regarding the kinematics, chemical composition and physical properties of the galaxy. We can see the spectral lines in a galaxy spectrum, which are produced due to the absorption and emission of light by atoms or ions. Then we can find the temperature, density and velocity of the gas and other materials inside the galaxy from the analysis of spectral lines (Baldwin et al., 1981).

In addition to the spectral lines, the overall shape of the curve and its slope is also equally important. The slope of the spectrum of a galaxy refers to the rate at which the intensity of the galaxy's emission changes with wavelength. The slope of a galaxy's spectrum can offer useful insights into the physical conditions of the galaxy, such as the temperature of the stars within the galaxy (Baldwin et al., 1981) and composition of the gas and dust, as well as the presence of any dust that may be absorbing and scattering light. In

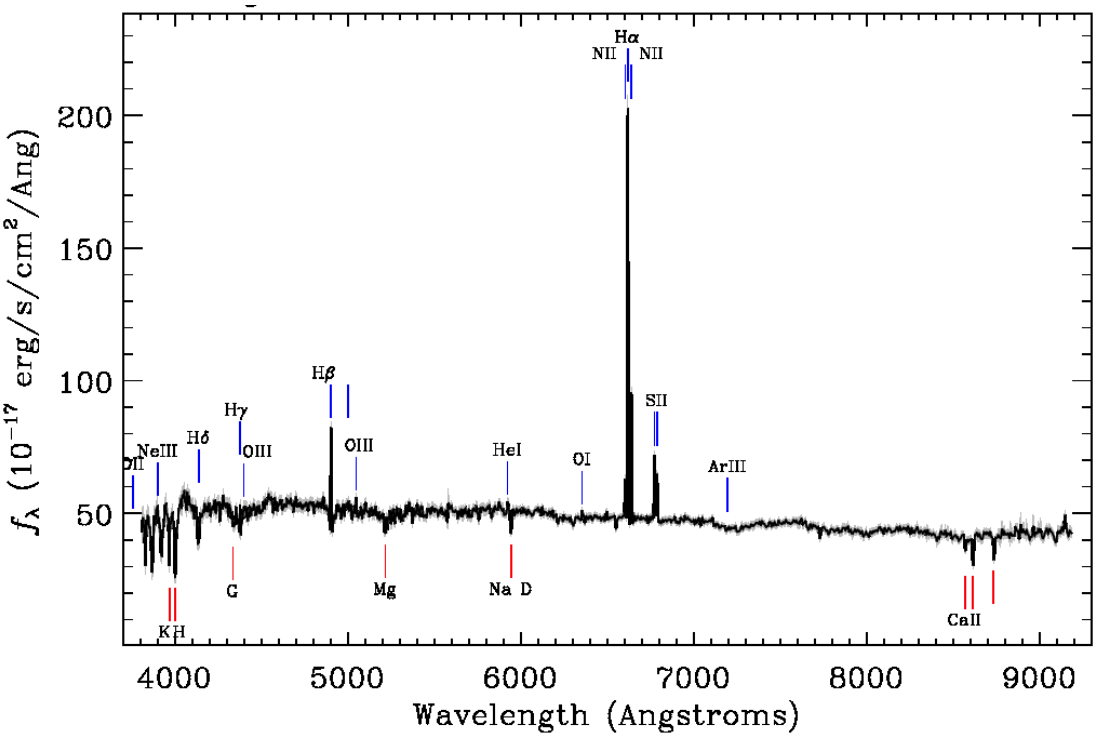

Figure 3: An example spectrum of a star-forming galaxy VCC 145, located at 16.5 Mpc. It has B-band absolute magnitude of -16.4 mag. All prominent emission and absorption lines are marked (Source: (Source: *SDSS Legacy Survey*, Accessed: 2019-09-30).

general, a steep slope may indicate the presence of cool, dense gas, while a shallower slope may suggest a lower density of gas or the presence of hot, diffuse gas. The slope of a galaxy's spectrum can be measured employing multiple methods, such as spectroscopy, which involves analyzing the wavelengths of light emitted by the galaxy to determine its composition and physical properties. However, the existence of features like a "red bump" or a "blue bump" can indicate the presence of specific star types or the rate of star formation inside the galaxy (Kauffmann et al., 2003).

1.12 SFR from the Spectrum

Out of many methods of calculating SFR by using a galaxy spectrum, the emission lines at particular wavelengths produced by the ionized gases in hot and young stars can also be used. The gases in the ISM are ionized by the UV radiations produced by the hot stars. The most popularly used line is H_α line that is produced due to the ionization of hydrogen atoms in ISM by UV radiation and then recombination with electrons. As the intensity of H_α line is directly related with the amount of UV radiation produced, we can measure the rate at which hot and young stars are undergoing formation within the galaxy by measuring the strength of H_α line.

1.13 Problem of SFR Measurement

There are so many issues and problems that may challenge to the calculation of SFR of a galaxy. Some of them found in the literature are included here. To find the SFR in a galaxy, we need to observe the hot and young stars that are being formed in galaxies. It is difficult to observe the stars directly because the stars are deeply engulfed in thick clouds of gas and dust. Between galaxies as well as inside a single galaxy, the SFR can change considerably over time. This can make it challenging to measure the SFR accurately, especially for galaxies that are experiencing bursts of star formation (Calzetti et al., 2010). Utilizing several SFR indicators such as, spectral lines, infrared emission, and radio emission, which can provide complementary information regarding the rate of star formation, is one strategy to address these problems. It might be challenging to interpret the data because these indications can be influenced by other physical phenomena such as the presence of AGN or dust. The SFR can also be affected by the amount of gas, metallicity and density of ISM. The impact of these factors on star formation efficiency and on the properties of the stars makes it challenging to compare the SFRs of different galaxies (Kennicutt & Evans, 2012b).

1.14 Merging Dwarf and SFR

The phenomenon in which two or more interacting dwarf galaxies approach each other and finally coalesce to form a single galaxy is called a galaxy merger. The SFR of the resulting galaxy may be affected by the merger. Elmegreen et al. (2002) studied that merging can trigger bursts of intense star formation in dwarf galaxies because of the compression and funneling of infalling gas and other materials from the merging galaxies into the center of the new galaxy formed. Normally, the SFR of a merging dwarf galaxy is expected to increase as the merger proceeds (Lanfranchi & Matteucci, 2003). However, it is a matter of study to understand better the precise connection between the merging and the SFR of dwarf galaxies. Since the process of merging can also result in the consumption or ejection of gas and other materials required for star formation, several studies have suggested that the SFR may not necessarily increase in all merging dwarf galaxies (Bekki & Couch, 2011).

1.15 Rationale of the Study

Dwarf galaxies are characterized as small, low-mass galaxies believed to be the foundational constituents of larger galaxies. Understanding the process by which dwarf galaxies merge and contribute to the growth of larger galaxies can help us better understand the evolution of the universe and the formation of galaxies.

Merging dwarf galaxies can also provide insight into the dark matter content of the universe. Dwarf galaxies are believed to be some of the most dark matter-dominated objects in the universe and study of the merger of dwarf galaxies can help us better understand the nature of dark matter and its role in galaxy formation and evolution.

Additionally, the study of merging dwarf galaxies can help us understand the role that these small objects play in the overall cosmic ecosystem. For example, dwarf galaxies are believed to be important sites of star formation and the merger of these objects could potentially trigger bursts of star formation that could have significant impacts on their host galaxies.

Overall, research on merging dwarf galaxies can provide important insights into a wide range of fundamental astrophysical questions, including the nature of dark matter contents, the galaxy formation and evolution and the role of small objects in the universe.

1.16 Objectives

1.16.1 General Objective

To examine a selected sample of nearby interacting dwarf galaxies with regards to their star-formation activity and morphological characteristics, and compare their positions in galaxies' fundamental relations such as relationships between star-formation rate and B-band absolute magnitude, as well as metal content and r-band absolute magnitude.

1.16.2 Specific Objectives

1. To analyze optical emission lines (H_β, $OIII_{5008}$, H_α and NII_{6585}) and derive star-formation rate and gas-phase metallicity $(12 + \log(O/H))$ of a sample of merging dwarf galaxies.
2. To fit the ellipse on the optical imaging of a sample of merging dwarf galaxies and analyze a major axis profile of ellipse parameters such as position angle and ellipticity.
3. To construct a one-dimensional light profile model of a sample of merging dwarf galaxies, determine their sizes, and extract structural parameters including Sérsic indices and mean surface brightness.
4. T examine the correlation between SFR and B-band absolute magnitude and determine the trend exhibited by compact and extended merging dwarf galaxies in this correlation.
5. To investigate the correlation between metal content and r-band absolute magnitude and examine positions of compact and extended merging dwarf galaxies in this

relation.

1.17 Organization of the Thesis

this thesis aims to put new and more robust constraints on our understanding of the compact dwarf galaxy formation process, by studying the physical and stellar population properties of a sample of merging dwarf galaxies. We try to search for a connection between the observed stellar population properties and the structural properties and discuss their possible consequences. We study in detail the structural properties of a sample merging dwarf galaxies of both field and group environments. We have used publicly available data sets from various archives, such as the SDSS and Legacy survey. This makes this study broader and aims that it will have a significant contribution to dwarf galaxy research.

The organization of the thesis is as follows:

CHAPTER 1: INTRODUCTION

In Chapter 1, we present a brief introduction on dwarf galaxy, galaxy merger, star formation rate and galaxy morphology. We also present the rationale of the study and the objectives of our work.

CHAPTER 2: LITERATURE REVIEW

In Chapter 2, we briefly introduce the galaxy's environment and physical properties. Furthermore, we detailed the theory of galaxy surface photometry and described how the structural properties of galaxies could be measured.

We then introduce galaxy spectroscopic properties and show the spectra of different morphological galaxies. We then review the theory of star formation and describe how star formation can be measured from H_α flux. We introduce the SDSS survey telescope with its importance and data acquisition technique. Both spectroscopic and imaging surveys are described with a brief overview of technical detail.

We, finally, present a review of dwarf galaxy research at the end of the chapter. We describe the catalog in section 2.8.1 and introduce merging dwarf galaxies in section 2.8.2. A research gap in dwarf galaxy research is presented in section 2.9.

CHAPTER 3: MATERIALS AND METHODS

In Chapter 3, we provide a short description of the sample selection and data acquisition, which is used to study the structural parameter and star-formation properties of merging dwarf galaxies. We introduce our galaxy

sample providing basic physical properties such as sky position, redshift, and magnitude for all. We describe the selection criteria of our sample in section 3.1.1 and list a tabulated value of physical properties in Table 1. The method of analysis is presented in section 3.4. In this section, we describe data acquisition (3.4.1), spectroscopic calculations (3.4.2) and photometric calculations (3.4.3).

CHAPTER 4: RESULTS AND DISCUSSION

The final results obtained from the analysis of imaging and spectroscopic data analysis are presented in Chapter 4. In this chapter, we also discuss our result to make a better interpretation of measured parameters.

CHAPTER 5: CONCLUSION AND RECOMMENDATIONS

In this chapter, we give the conclusion of our work and recommendations for further study.

CHAPTER 6: SUMMARY

In this chapter, we summarize our thesis.

Finally, the references, appendices, published articles and certificates of various conferences/seminars etc. are provided before closing this document.

CHAPTER 2

2. LITERATURE REVIEW

2.1 Dwarf Galaxies in Different Environment

According to the local observable density of galaxy distribution, the immediate environments are defined in three categories: Field, Group and the Cluster.

2.1.1 Field Galaxy

A field galaxy is a galaxy that does not belong to a larger cluster of galaxies and thus is gravitationally isolated (Muldrew et al., 2012). Most of the low-surface brightness galaxies are field galaxies. These are mostly star-forming and most of their baryonic matter consists of neutral gaseous hydrogen. Their stellar population is young compared to other environment galaxies (Gu et al., 2006; Pustilnik & Tepliakova, 2011; Makarov et al., 2013).

Figure 4: NGC 2188, a field dwarf galaxy. It has a B-band absolute magnitude of −18.93 mag and a distance 7.6 Mpc. (Source: *Sloan Digital Sky Survey*, Accessed: 2019-09-30a).

NGC 2188 is a prime example of a field dwarf galaxy (Figure 4). It is a spiral galaxy located in isolation in southern sky. With orientation of 90 degree position angle it is a highly edge-on galaxy.

2.1.2 Group Galaxy

A group of a galaxy is a system of galaxies that have 2 to 100 members galaxies and their total dynamical mass is approximately 10^{13} $M_{\odot}yr^{-1}$ (Makarov & Karachentsev, 2011). The spread of velocities across individual galaxies is approximately 150 km s^{-1}. Groups are the most common structures of galaxies in the universe, comprising at least 50 % of the galaxies in the local universe. Observations have shown that the majority of galaxies in the universe are located in the group environment. Because of high galaxy density and low-velocity dispersion, galaxy-galaxy interaction is also common in a group environment (B. C. Lee et al., 2004). Group member galaxies are both star-forming and non-star-forming but their gas mass fraction is lower compared to the field galaxies (Grützbauch et al., 2005). We show a well known example of a visual group of five galaxies called "Stephan's Quintet" in Figure 5. This is the most studied group of all the compact galaxy groups.

Figure 5: Stephan's Quintet: a visual grouping of five galaxies inside the galaxy group. It is located at 90 Mpc from us. (Source: *Webb Space Telescope*, Accessed: 2019-09-30).

Our home galaxy, Milky-Way, is also a part of the local group. It hosts two giant galaxies: Milky-Way and Andromeda and their satellite dwarf galaxies. Large and small Magellanic clouds are the brightest star-forming dwarf galaxies in the local group. Karachentsev (2005) examined the main features of the Local Group and other closest, most thoroughly studied groups of galaxies. Given their abundance, groups of galaxies make up a significant portion of the average matter density in the universe. Depending on their mass, some groups also emit X-ray, which show the presence of a hot intra-cluster medium. This type of group mainly possesses early-type member galaxies (Mulchaey,

2000).

2.1.3 Cluster Galaxy

Clusters and groups are two distinct categories in astronomy, but there is no precise boundary between them (Bautz & Morgan, 1970). Visually, clusters can be recognized as assemblages of galaxies that are bound together by mutual gravitational attraction (Solanes & Stein, 1998; Struble & Rood, 1999). However, their velocities are too high for them to be held together by gravity alone, suggesting the existence of either an additional unseen mass component or an extra attractive force beyond gravity. The presence of a vast quantity of intergalactic gas known as the intracluster medium has been discovered through X-ray analysis (Seigar et al., 2007; Mihos et al., 2017). This gas is incredibly hot, ranging from 10^7K and 10^8K degrees Kelvin and generates X-rays via bremsstrahlung and atomic line emission (Hashimoto et al., 2007; Jensen & Pimbblet, 2012). Figure 6 depicts the inner core of the Virgo cluster where we can see many bright galaxies both elliptical and spiral grouped together.

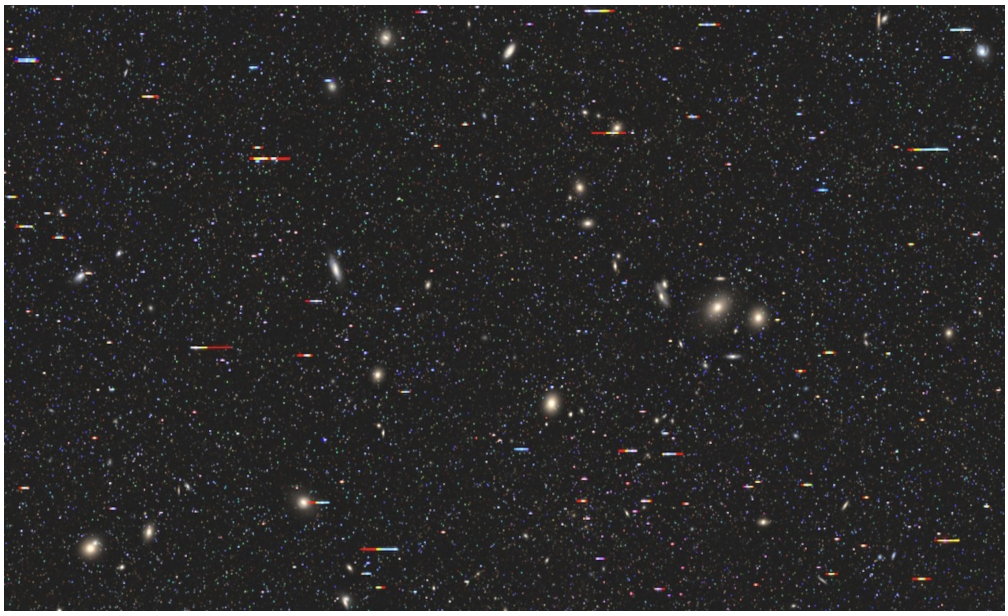

Figure 6: Inner core of Virgo cluster. The Virgo cluster is located 16.5 Mpc from us.(Source: *Sloan Digital Sky Survey*, Accessed: 2019-09-30a)

The overall mass of the gas is nearly two times bigger than the entire mass of the galaxies. The galaxies in the cluster still can't be maintained by this amount of matter, though. Since this gas and the total gravitational field of the cluster are roughly in hydrostatic equilibrium, the distribution of total mass can be calculated (Diaferio, 1999; Geller et al., 1999; Falco et al., 2014). The overall mass that may be deduced from this measurement is about six times greater than the galaxies' mass or hot gas (Buote & Tsai, 1995; Buote et al., 2007). The nature of the missing element, known as dark matter, remains unknown. In a typical cluster, galaxies make up only about 5% of the entire

mass, hot X-ray producing gas makes up about another 10% and the remaining mass is dark matter (Tucker et al., 1998; Hou et al., 2009).

2.2 Galaxy Imaging

Present days galaxy imaging is done with a charge coupled device (CCD) sensor mounted in a telescope. The CCD collects light provided by telescope optics and stores it as a matrix which then computer graphics shows us as a picture. While taking pictures, a monochrome filter of certain bandwidth is also used, which produces specific band images. U-ultraviolet, B-blue and V-visible are classically well-known filters. The color images we see are a combination of three different filter images. Figure 7 shows a difference between mono-color gray image and tri-color combined image reproduced from fits images. In astronomy, these images are typically stored in "Flexible Image Transport System" (FITS) file format (Wells et al., 1981).

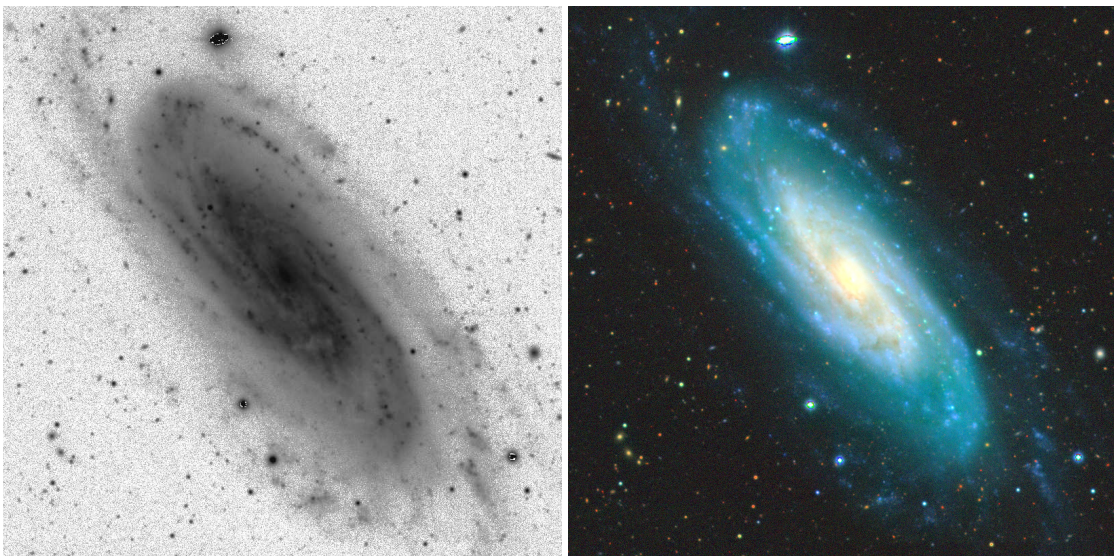

Figure 7: Left: g-band mono-color gray scale image of star-forming galaxy, NGC 3198 taken by the 2.5 m Apache Point telescope. NGC 3198 is located at a distance of 13.75 Mpc from us and it has B-band absolute magnitude of -19.13 mag. Right: $g - r - z$ combined tri-color image of the galaxy (R. Lupton et al., 2004).

2.2.1 Photometry

For the measurement of the surface brightness of a galaxy, we measure its flux density. Flux is defined as the counts in each pixel which is converted to flux density (F) in Janskys by using the calibration: 1 Jy = 10^{-26} W m^{-2} Hz^{-1}. The angle, α subtended by a small patch of a galaxy of side D at some distance d is given by $\alpha = D/d$. The luminosity (L) is the total energy output of a galaxy while the flux is the energy received

by unit area. Therefore,

$$F = \frac{L}{4\pi d^2} \tag{2.1}$$

The amount of light per square arcsecond area in the sky is what we refer to as the surface brightness of the galaxy. It is given by:

$$I(r) = \frac{F}{\alpha^2} \sim \frac{\text{Jy}}{\text{arcsec}^2} \qquad \text{or} \qquad I(r) = \frac{L}{4\pi d^2}\left(\frac{d}{D}\right)^2 = \frac{L}{4\pi D^2} \tag{2.2}$$

It is often measured in solar luminosity per square parsec ($L_\odot$ pc^{-2}). The surface brightness in visual and infrared astronomy is frequently expressed on a magnitude scale, measured in magnitudes per square arcsec in a certain filter band or photometric system. Let us recall the relation that relates the apparent magnitudes m and m_0 of two stars corresponding to the fluxes F and F_0, respectively:

$$m - m_0 = -2.5 \log\left(\frac{F}{F_0}\right) \tag{2.3}$$

So the surface brightness in magnitudes per square arcsec is

$$\mu - \mu_0 = -2.5 \log\left(\frac{F/\alpha^2}{F_0/\alpha^2}\right) = -2.5 \log\left(\frac{I}{I_0}\right) \quad \text{(in mag arcsec}^{-2}\text{)} \tag{2.4}$$

If we take $I_0 = 1\ L_\odot$ pc^{-2} for $\mu_0 = 26.4$ mag arcsec^2, for the Sun in the optical V-band, we get

$$\mu = -2.5 \log(I) + 26.4 \quad \text{(in mag arcsec}^{-2}\text{)}$$

We cannot measure the surface brightness of individual stars of a galaxy. Therefore, the surface brightness is taken as an average of all stars located in a particular region of galaxy. Since we cannot find the sharp edge of a galaxy, we need to model it.

2.2.2 Surface Photometry

From surface photometry, we can describe the distribution of light quantitatively on the surface of extended objects like galaxies. We obtain radial profiles of various quantities and the morphological type of a galaxy from its image.

The Sérsic Profile

The de Vaucouleurs introduced $R^{1/4}$ law to fit surface brightness profile of massive early-type galaxies (de Vaucouleurs, 1948). However, all galaxies do not follow this law.

Later, Sérsic generalized this law with varying exponential terms n (Sersic, 1968), which relatively better fits to different types of galaxies with different n (Schombert, 1986). Sérsic Profile that describes the surface brightness (in intensity unit) at a distance R from the center of a galaxy is given by

$$I(R) = I_{\mathrm{e}} e^{-b_n\left[(R/R_{\mathrm{e}})^{1/n}-1\right]} \tag{2.5}$$

where R_{e} is the effective radius that encloses half of the total light. I_{e} is the intensity in flux per square arcsec at the effective radius R_{e}. n is the Sérsic index which gives the shape of the light profile. b_n is a constant which depends on n and is chosen such that R_{e} encloses half of the total luminosity. It is approximated as $\mathrm{b}_n \approx 2n - 0.327$ (Capaccioli, 1989). If $n = 1$ the Sérsic function reduces to the exponential function, while it reduces to de Vaucouleurs functions if $n = 4$.

The de Vaucouleurs Profile: Substituting for $n = 4$ and $\mathrm{b}_n = 7.67$ in equation 2.5, we get the de Vaucouleurs profile:

$$I_{\mathrm{dev}}(r) = I_{\mathrm{e}}\ \mathrm{e}^{-7.67\left[(R/R_{\mathrm{e}})^{1/4}-1\right]} \tag{2.6}$$

The Expontial Profile: For $n = 1$ in equation and $\mathrm{b}_n = 1.68$

$$I_{\mathrm{exp}} = I_{\mathrm{e}}\ \mathrm{e}^{-1.68[(R/R_{\mathrm{e}})-1]} \tag{2.7}$$

Plotting the total luminosity with radius, in arbitrary units, shows that half of the total luminosity is at R_{e} and 84.8 % of the total luminosity is within $2R_{\mathrm{e}}$.

The Petrosian Profile

The Petrosian ratio used by the SDSS is defined at a radius r from the center of an object (Petrosian, 1976). It is calculated from the integral of the ratio of the local surface brightness average over an annulus at r to the total surface brightness within r. The averaging is just the total surface brightness within the annulus divided by the area of the annulus.

$$\mathcal{R}(r) = \frac{\left(\frac{\text{total surface brightness within annulus}}{\text{area within annulus } (0.8r-1.25r)}\right)}{\left(\frac{\text{total surface brightness within } r}{\text{area within } r}\right)} = \frac{\frac{\int_{0.8r}^{1.25r} 2\pi r' I(r')\ dr'}{\pi(1.25^2-0.8^2)r^2}}{\frac{\int_{0}^{r} 2\pi r' I(r')\ dr'}{\pi r^2}} \tag{2.8}$$

The radius at which this fraction is one is formally defined as the Petrosian Radius. In practice, however, the Petrosian radius turns out to be quite small, we define it as when

the integrated flux is some fraction of the annular flux, η, and take $\eta = 0.2$.

$$I(R_P) = \eta\mathcal{R} \tag{2.9}$$

The total Petrosian flux is defined as the sum of all the flux within k times the Petrosian Radius. The factor k is used to enhance the signal-to-light ratio by including more of the galaxies' light than falls within R_P. The SDSS takes $k = 2$ and defines the other Petrosian Radii as: $R_{P,50}$ = radius containing half the total Petrosian Flux. $R_{P,90}$ = radius containing 90 % of the total Petrosian flux. The Petrosian concentration index is the ratio of these two radii (Graham & Driver, 2005).

$$C_P = \frac{R_{P,90}}{R_{P,50}} \tag{2.10}$$

2.3 Galaxy Spectroscopy

The combined spectrum of all the stars and other radiating matter within a galaxy is known as the galaxy's overall spectrum. The spectra differ from galaxy to galaxy because of their variation in structure and relative composition of stellar type and gas (Veilleux & Osterbrock, 1987; Sodré & Cuevas, 1994; Zaritsky et al., 1995). Figure 8 shows a comparison between spectrum of early-type (red) and late-type (blue) galaxies.

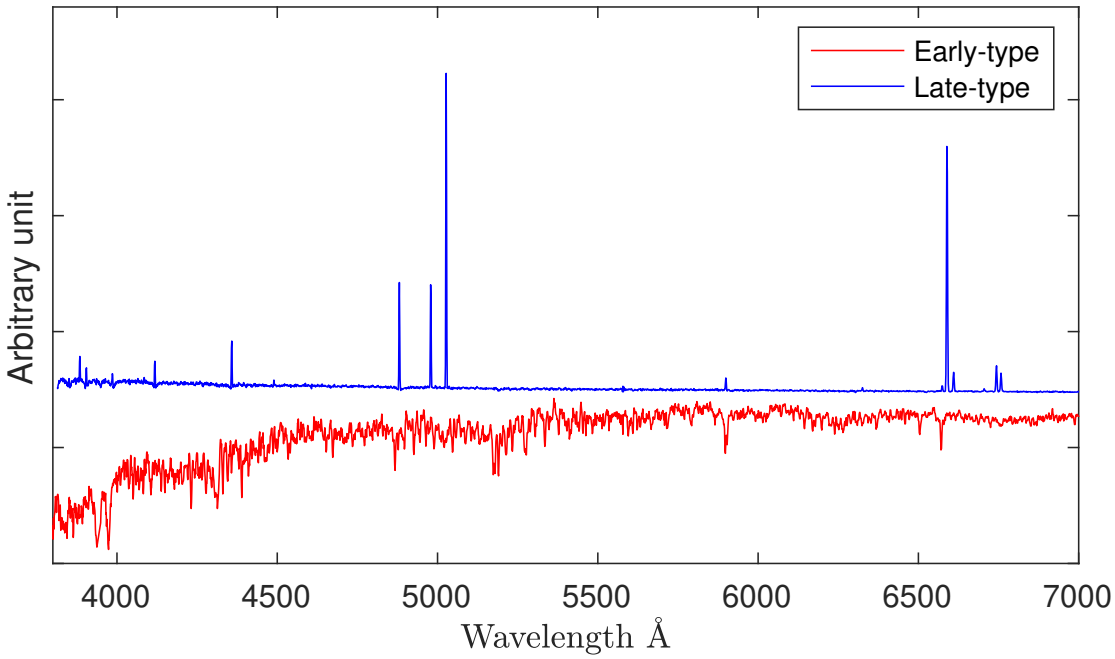

Figure 8: Example spectrum of two different types: early-type (VCC 200) and late-type (NGC 3198) dwarf galaxies. VCC 200 is located at 16.5 Mpc from us and NGC 3198 is located at 13.75 Mpc from us. They have B-band absolute magnitude of −16.4 mag and −19.13 mag respectively.

The combination of a variety of blackbody emitters with a variance in temperature results in galaxy spectra with a high continuous component. This results in a generally flat

spectrum. The strong break at 4000 Å, which results from the blanket absorption of high energy radiation from metals in stellar atmospheres and a lack of bright, blue stars, is one of the main features (Barbaro & Olivi, 1989). It is simple to fit spectra with a smoothly changing function that exhibits a clear break in intensity at 4000 Å. Due to the absence of metal lines and a significant blue/UV component, some stellar type spectra clearly display the 4000 Å break, while others do not (Poggianti & Barbaro, 1997).

2.3.1 Emission Line

When an excited atom, element or molecule returns to lower energy state, it emits a radiation of energy equal to the difference between initial and final energy levels at a particular wavelength called an emission line (Sodré & Stasińska, 1999). HII regions of ionized gas surrounding young star clusters that still include OB stars (spectral categories B and hotter), are characterized by emission lines which are also known as recombination lines in astronomy. If internal extinction is not too high, it is possible to find HII regions in their entirety via narrow-band imaging at H_α (Ho et al., 1997; Alonso-Herrero & Knapen, 2001; Couto da Silva & de Souza, 2006). The line radiation that we observe results from the recombination of the electrons so liberated with a second proton and a cascade toward the ground state.

In a Bohr atom, there is a center comprised of protons and neutrons which is orbited by one or more electrons moving in circular paths. Please refer to Figure 9 for a visual representation. Electrons have wave functions with de Broglie wavelengths. The wavelengths are determined by a specific relation

$$\lambda = \frac{h}{p} = \frac{h}{m_e v} \tag{2.11}$$

where v and p are speed and momentum of the electron. Only those orbits that match an integer number n of wavelengths corresponding to standing waves are allowed. Thus the Bohr radius a_n of the n^{th} permitted electron orbit satisfies the quantization rule

$$2\pi a_n = n\lambda = \frac{nh}{m_e v} \tag{2.12}$$

Here, the number n is principal quantum number. The Bohr's radius is given by

$$a_n = \frac{nh}{2\pi m_e v} = \frac{n\hbar}{m_e v} \tag{2.13}$$

The orbital angular momentum $L = m_e v a_n = n\hbar$, where $\hbar \equiv h/(2\pi)$. Again, for a

hydrogen atom,

$$\frac{e^2}{a_n^2} = \frac{m_e v^2}{a_n} \tag{2.14}$$

The numerical value of the Bohr radius of a hydrogen atom with an electron in the n^{th} energy level is given by,

$$a_n = \frac{\hbar^2}{m_e e^2} n^2 \approx 0.53 \times 10^{-8}\ n^2 \text{ cm}. \tag{2.15}$$

Similarly, in its ground state (n =1), $a_1 \approx 0.53 \times 10^{-8}$ cm = 0.53 Å, but at the highly excited state ($n \approx 100$), the diameter of the atom is very high i.e., $2a_{100} \approx 10^{-4}$ cm = 1 μm. At this state, the hydrogen atom emits radio waves in the ISM.

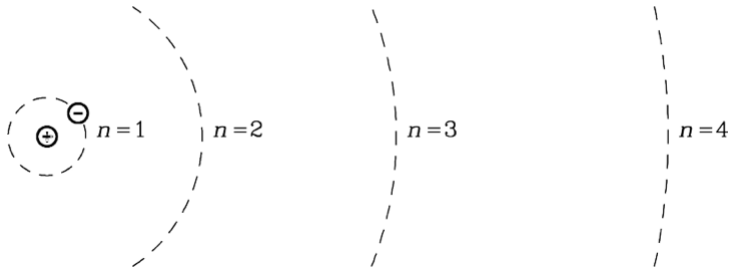

Figure 9: Different orbits of the Bohr atom. As $a_n \propto n^2$, radio-emitting hydrogen atoms ($n \approx 100$) are $\sim 10^4$ times larger than ordinary hydrogen atoms ($n = 1$).

When an electron in an atom falls from the level $(n + \Delta n) \rightarrow n$, where Δn and n are any natural integers, Bohr theorizes that it emits a photon, whose energy is equal to the energy difference ΔE between the initial and final states. Since recombination is the process by which an atom in a high excitation stage absorbs an electron with a lower energy and then descends into a lower excitation stage by emitting photons, these spectral lines are known as recombination lines.

The name of the element, the final level number n and subsequent Greek letters are used by astronomers to identify each recombination line to indicate the level change Δn: α for $\Delta n = 1$, β for $\Delta n = 2$, γ for $\Delta n = 3$, etc. For an example, the recombination line produced by the transition between the $n = 8$ and $n = 7$ levels of a hydrogen atom is called the H7_α line.

From Bohr's theory, the energy of an electron in an energy level n is given by

$$E_n = T + V = -e^2\left(\frac{m_e e^2}{2n^2\hbar^2}\right) = -\left(\frac{m_e e^4}{2\hbar^2}\right)\frac{1}{n^2} \tag{2.16}$$

The change in energy ΔE going from level $(n + \Delta n)$ to level n is

$$\Delta E = \frac{m_e e^4}{2\hbar^2}\left[\frac{1}{n^2} - \frac{1}{(n+\Delta n)^2}\right] = h\nu \tag{2.17}$$

So, the frequency of the emitted photon is

$$\nu = \left(\frac{2\pi^2 m_e e^4}{h^3 c}\right) c\left[\frac{1}{n^2} - \frac{1}{(n+\Delta n)^2}\right] \tag{2.18}$$

Additionally, one will observe emission features as a result of heated gas that then emits energy at particular wavelengths. Within gas clouds, young stars form and ionize them. Four prominent O stars, for instance, produce the majority of the ionizing photons ($E > 13.6$ eV) that energize the nearby HII region and drive the emission from the Orion nebula. Thus, emission characteristics indicate the presence of very hot gas and OB-type stars in the spiral and irregular galaxies' disks. The [OII] doublet (3737 Å), [OIII] (4959 Å and 5007 Å), and the Balmer series (6563 Å, 4861 Å, 4340 Å, 4103 Å) are important features.

2.3.2 Absorption Line

If an absorbent substance is positioned between a source and an observer, an absorption line will be visible in the spectrum (Fan et al., 2016). The outer layers of a star, an interstellar gas cloud or a cloud of dust might all constitute this substance (Worthey et al., 1994). Due to the absorption of radiation by atoms (metals), molecules in stellar atmospheres and interstellar gas clouds, absorption characteristics lines are overlaid on the continuum. This suggests the presence of aging star populations, which are typically observed in spiral and elliptical galaxies' bulges. The Calcium H and K lines (located at 3934 Å and 3969 Å), the G-band (4304 Å), the Magnesium (5175 Å), and the Sodium (5894 Å) lines are important characteristics (Zhu & Ménard, 2013).

2.4 Dust Extinction

In astronomy, the absorption and scattering of electromagnetic radiation by dust and gas between an emitting object and the observer are called extinction. In other words, the dimming of a distant object due to the presence of dust and gas in ISM along the line of sight is called extinction (Duc & Renaud, 2013). It is because the typical size of the dust grain is of the order of blue light wavelength and hence, it is either absorbed or scattered effectively, which disappears from the light approaching us. As a result, the object appears dimmer and redder than the object actually is, called interstellar reddening. The absorption and scattering of light are directly proportional to the amount of dust along the line of sight. Extinction due to dust is not equally effective in all wavelengths. As we

move to red (longer wavelength) light, the photons do not interact with dust strongly and hence some fraction of light reaches the detector. Interstellar reddening is quantified by the extinction coefficient A_λ defined by

$$A_\lambda = -2.5 \log(I_\lambda / I_{0\lambda}) = m - m_0 \tag{2.19}$$

where I_λ and $I_{0\lambda}$ are observed flux and intrinsic flux respectively. Similarly, m and m_0 are observed and intrinsic magnitudes respectively. Let us select two stars a and b of same spectral type and luminosity class. Star a is not reddened (it will be the reference), star b is reddened. One can write

$$m_b(\lambda) = -2.5 \log F_b(\lambda) + c + A(\lambda) \tag{2.20}$$

and

$$\Delta m(\lambda) = m_b(\lambda) - m_a(\lambda) = -2.5 \log F_b(\lambda)/F_a(\lambda) + A(\lambda) \tag{2.21}$$

For two wavelengths λ_1 and λ_2: $\Delta m(\lambda_1) - \Delta m(\lambda_2) = A(\lambda_1) - A(\lambda_2) = E(\lambda_1, \lambda_2)$, defined as the colour excess. The color excess of an object is defined as the difference of the observed color index and intrinsic color excess. i.e., $E(B-V) = (B-V) - (B-V)_0$. The standard color excess is: $E(B,V) = E(B-V)$ which usually measures the amount of dust extinction. It depends on both differences of extinction between B and V band and the total optical depth $E(B-V) = 1.086(\tau_B - \tau_V)$. Where τ is the optical depth. If the extinction curve remains constant between B and V, $E(B-V)$ measures the amount of extinction.

Hydrogen emission (recombination) lines are also affected from extinction. The Balmer decrement is the ratio of the fluxes in H_α and H_β lines. The theoretical value of this ratio is 2.86 (case B of recombination and T = 10^4K) (Osterbrock & Ferland, 2006).

Now, we have

$$A(\mathrm{H}_\alpha) = -2.5 \log \left(\frac{F(\mathrm{H}_\alpha)_{\mathrm{obs}}}{F(\mathrm{H}_\alpha)_{\mathrm{em}}} \right) \tag{2.22}$$

and

$$A(\mathrm{H}_\beta) = -2.5 \log \left(\frac{F(\mathrm{H}_\beta)_{\mathrm{obs}}}{F(\mathrm{H}_\beta)_{\mathrm{em}}} \right) \tag{2.23}$$

From the above two equations, we get

$$A(\mathrm{H}_\beta) - A(\mathrm{H}_\alpha) = E(\beta - \alpha) = 2.5 \log(F(\mathrm{H}_\alpha)_{\mathrm{obs}}/F(\mathrm{H}_\beta)_{\mathrm{obs}}) - 2.5 \log(2.86)$$

where $F(\mathrm{H}_\alpha)_{\mathrm{em}}/F(\mathrm{H}_\beta)_{\mathrm{em}} = 2.86$. $E(\beta-\alpha)$ can be measured from the observed fluxes at H_α and H_β, $A(\mathrm{H}_\beta)/E(B-V)$ and $A(\mathrm{H}_\alpha)/E(B-V)$ are given by the extinction curve: $E(\beta-\alpha)/E(B-V) = 1.07$ for a standard MW extinction curve. Then we can deduce $E(B-V)$ and finally, we get

$$A(H_\alpha) = 2.45E(B-V) \tag{2.24}$$

2.5 Star Formation

Understanding the evolution of galaxies and the cosmos from the earliest moments after the big bang to the current period of cosmic history requires knowledge of the fundamental mechanisms for the production of stars. Stars are formed due to the collapse of dense regions of molecular clouds of gas formed in interstellar space (Stahler & Palla, 2004).

The basic equation that connects the intrinsic luminosity emitted by stars at wavelength λ and time t is given by

$$L(\lambda,t) = \int_0^t \int_{M_{\mathrm{low}}}^{M_{\mathrm{up}}} F_\lambda(m,\theta)\mathrm{SFR}(t-\theta)\psi(m)dm\ d\theta \tag{2.25}$$

where $F_\lambda(m,\theta)$ are the evolutionary stellar tracks, $\psi(m)$ is the initial mass function and SFR(t) is the star formation rate function. There are two approaches to calculate SFRs using this fundamental equation. To fit a huge set of data at multiple wavelengths, one can utilize stellar population synthesis models with different SFR(t); the current SFR is an output parameter of the fit (White & Rees, 1978; Kennicutt, 1989). A different, extremely common method is to create straightforward recipes. When an SFR over a period T is assumed to be constant, it is just proportional to the luminosity integrated over T. To ensure that the luminosity at wavelength λ approaches a steady state, the timescale T is selected:

$$SFR = \left(\int_0^t \int_{M_{\mathrm{low}}}^{M_{\mathrm{up}}} F_\lambda(m,\theta)\mathrm{SFR}(t-\theta)\psi(m)dm\ d\theta\right)^{-1} \times L(\lambda) \tag{2.26}$$

A spectral synthesis code calculates the conversion factor's value, $C = SFR/L(\lambda)$. If the real SFR varies significantly throughout this time, the SFR determined using a conversion factor may diverge from the average of the star formation activity during T. On short timescales, the assumption of a constant SFR is probably true, especially in the UV for recombination lines of ionizing photons. With increasing wavelength, it takes longer to reach a steady state 100 Myr in the UV versus 1Gyr in the optical-near IR. The timescale for ionizing photons is of the order of a few Myr (Kennicutt & Evans, 2012b). At least in

the local universe, there is some evidence for a SFR constant over a few hundred Myr that can be calculated by using Kennicutt (1998).

According to the present paradigm, massive molecular clouds are necessary for star formation. When molecular clouds form, a portion of them quickly becomes stars in comparison to the age of the universe. Gas is the main driver of SFR which is found to depend on neutral gas content. Schmidt (1959) first proposed a power-law relationship between SFR and gas surface densities as shown in Figure 10. In this updated representation of the global Schmidt law in galaxies, the surface density is determined by the total gas mass (molecular and atomic) or SFR normalized to the radius of the primary star-forming disk, as determined from H_α, Paα, or IR maps, and each point is a distinct galaxy. In addition to including individual (IR-based) corrections for dust attenuation and [N_2] contamination, the sample of galaxies analyzed has been expanded from that in Kennicutt (1998).

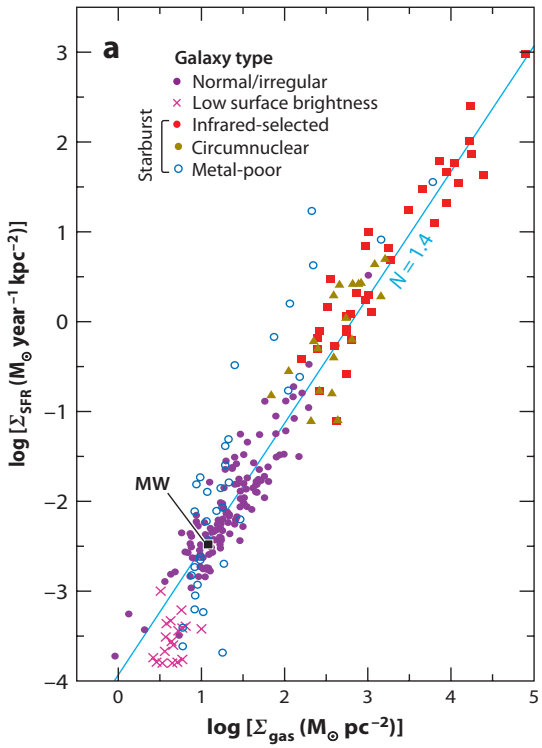

Figure 10: Schmidt-Kennicutt relation between SFR surface density and gas surface density for different classes of star-forming galaxies. Each point represents an individual galaxy, with the SFRs and gas masses normalized to the radius of the main star-forming disk. The light blue line shows a fiducial relation with slope N = 1.4 (not intended as a fit to these data). (Source: Schmidt (1959)).

Assuming that the SFR is proportional to the gas density and inversely proportional to a characteristic period for star formation, one can easily comprehend this relationship.

$$\Sigma_{\rm SFR} \propto (\Sigma_{\rm gas})^n \tag{2.27}$$

Usually, the SFR surface density (Σ_{SFR}) is in the unit ($\mathrm{M}_{\odot}\ \mathrm{yr}^{-1}\mathrm{pc}^{-2}$) and the gas surface density (Σ_{gas}) is in ($\mathrm{g\ pc}^{-2}$). Schmidt proposed a figure of $n = 2$ based on an investigation of gaseous helium and young stars in the solar neighborhood, the local density of white dwarfs and their luminosity function and the local helium density.

2.6 Stellar Population

One way to conceptualize a galaxy is as a collection of stars. A stellar population is a collection of stars in the galaxy that are similar in terms of their spatial distribution, chemical composition or age. Stellar populations exhibit a continuum of attributes rather than discrete ones, representing variations in star formation through time. The Hertzsprung-Russell (HR) diagram can be used to visualize the distribution of stars as shown in Figure 11, (Baade, 1944; Tinsley & Gunn, 1976).

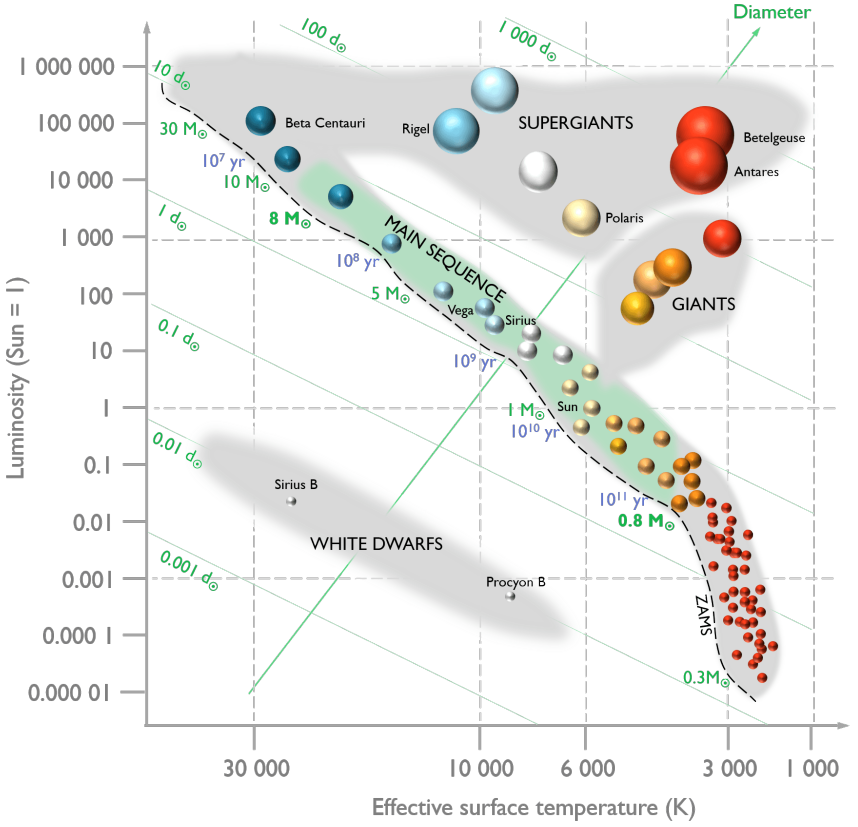

Figure 11: The Hertzsprung-Russell diagram: See text for the description. (Source: *Sciencebydegrees* (Accessed: 2019-09-30))

Every star goes through several developmental stages that are determined by its internal structure and method of energy production depending on its initial mass. The temperature and luminosity of the star fluctuate with each of these stages and as the star develops, it may be seen moving to various locations on the HR diagram. A set of stars are depicted in this HR diagram at various phases of development. The main sequence, which spans the diagram's upper left (hot, brilliant stars) and bottom right (cool, dim stars), is by far

its most noticeable component. Additionally, densely packed and full of white dwarfs is the gigantic branch.

- The HR diagram is dominated by the main sequence, which extends from the upper left (hot, brilliant stars) to the bottom right (cold, dim stars). In their cores, stars spend about 90% of their lives converting hydrogen to helium. Main sequence stars have a Morgan-Keenan luminosity class labeled V.
- Red giant and supergiant stars (luminosity classes I through III) occupy the region above the main sequence. They have low surface temperatures and high luminosities which, according to the Stefan-Boltzmann law, means they also have large radii. Stars enter this evolutionary stage once they have exhausted the hydrogen fuel in their cores and have started to burn helium and other heavier elements.
- White dwarf stars (luminosity class D) are the final evolutionary stage of low to intermediate-mass stars and are found in the bottom left of the HR diagram. These stars are very hot but have low luminosities due to their small size.

The Sun is found on the main sequence with a luminosity of 1 and a temperature of around 5,400 K. HR diagram is used to either summarize the evolution of stars or to investigate the properties of a collection of stars. In particular, by plotting a HR diagram for a stellar system, the stellar population properties like age and metallicities of the system can be calculated(Mould & Kristian, 1986; Soria et al., 1996).

2.7 SDSS Survey

The Sloan Digital Sky Survey (SDSS) has produced the most comprehensive three-dimensional maps of the universe to date, along with the multi-color images of one-third of the sky and spectra of about three million astronomical objects. Measuring the positions and properties of hundreds of millions of objects in the universe is called mapping. From the high-resolution images of the sky obtained in five different SDSS colors u, g, r, i, z, advanced image processing software has measured the brightness, shape and color of millions of the objects detected (Fukugita et al., 1996). SDSS is one of the most successful sky surveys. It was designed and constructed in the 1990s and began its regular survey operations since 2000 only (Gunn et al., 2006; York et al., 2000). The data, both as images and as accurate catalogs of the discovered objects is freely accessible in electronic versions for the general public and scientific communities. The SDSS has an outstanding influence in the study of astronomical objects covering diverse fields such as the origin and evolution of galaxies, the large-scale structure of the universe, the structure of the MW, the relation between dark matter and luminous matter, the formations of stars from the dust. The 2.5 m telescope with imager and spectrographs is placed at Apache Point Observatory (APO) about 9000 feet above sea level in the Sacramento Mountains

of south-central New Mexico (Latitude 32° 46′ 49.30" N, Longitude 105° 49′ 13.50" W, Elevation 2788 m). The telescope used in SDSS is a 2.5 m $f/5$, wide-angle optical telescope. A picture of the SDSS telescope is shown in Figure 12.

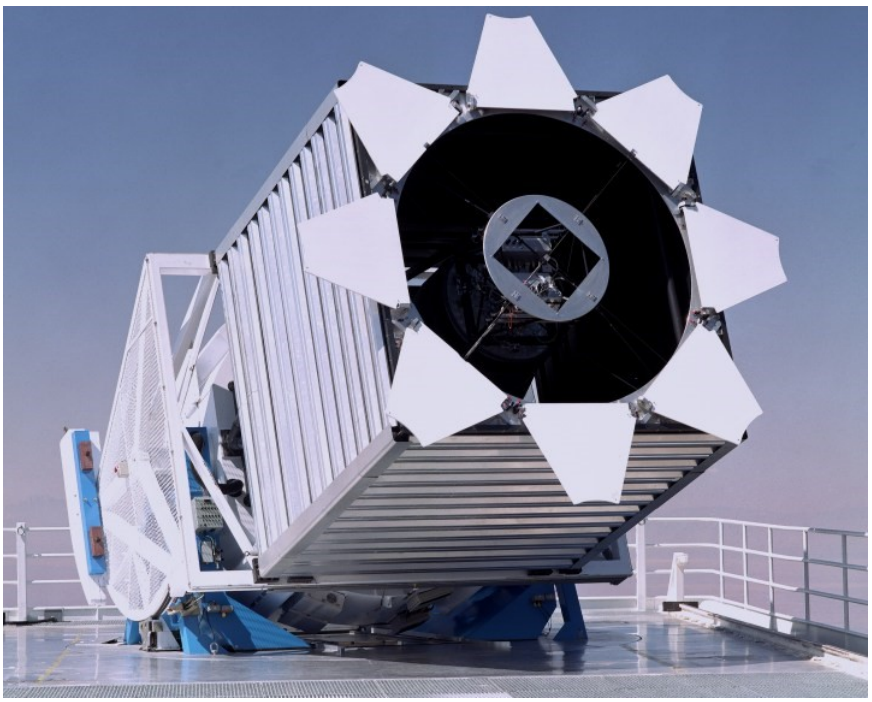

Figure 12: Sloan Foundation 2.5 m SDSS Camera. (Source: *Sloan Digital Sky Survey* (Accessed: 2019-09-30b)

This telescope was used in both imaging and spectroscopic modes from 2000 to 2009 and since then it has been used completely in spectroscopic mode. Two telescopes are employed in SDSS. One is the big telescope of the wide field of view having a big 2.5 m reflector that measures the light from remote galaxies and quasars. The other is the photometric telescope having a small 0.4 m reflector that is used to measure brighter stars in our MW.

2.7.1 SDSS Imaging Survey

The primary job of the SDSS big camera is to map about one-fourth of the sky. So, the big telescope has a wide field of view of 2.5 degree on one side and covers about six square degrees. The SDSS camera instead of using a large photographic plate as a detector in earlier surveys use small electronic devices called charge-coupled device (CCD) to measure light. It is because the CCDs are linear devices (measure photons according to brightness) and are more efficient. The CCDs can reflect its high efficiency by catching even the faint objects in a short exposure time which is crucial for a survey. Similarly, CCDs can measure the brightness and color of the luminous objects more accurately reflecting their linearity. CCD cameras are made up of light-sensitive silicon chips that change the detected photons of light into electronic signals and make the images

of astronomical objects to analyze the amount of light received from the celestial objects. A CCD is electrically divided into a large number of independent pieces called pixels. we use the CCD as a device to measure how much light falls on each pixel. CCDs can detect much fainter objects than those detected by photographs but it requires computers for data reduction (R. H. Lupton et al., 1999; R. Lupton et al., 2001). The arrangement of CCD chips in the SDSS camera is shown in the Figure 13.

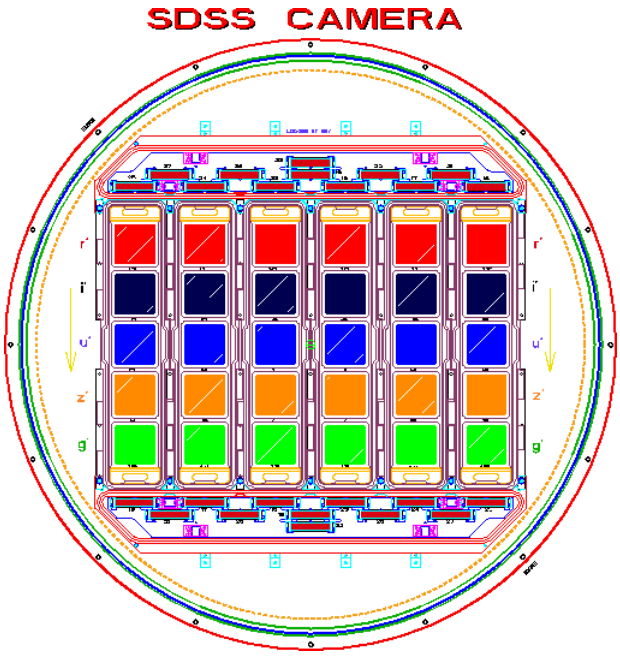

Figure 13: 30 CCD chips arranged in 5 rows and 6 columns in SDSS Camera (Source: *Sloan Digital Sky Survey* (Accessed: 2019-09-30b)

SDSS imaging camera uses an array of 30 CCD chips, each with a resolution of 2048×2048 pixels arranged in 5 rows and 6 columns (Figure 13) to collect photometric images. Each CCD chip in each column is covered by the SDSS filters in the order r, i, u, z, g. This means that each chip in each column is covered by a different filter. r, i, u, z, g represents the magnitudes (light fluxes through UV to IR wavelength range measured in logarithmic units) of the objects in the SDSS. The sky is examined by the telescope such that the stars advance across the camera in straight lines alongside the CCD columns. The CCD chips used in SDSS cameras are operated in drift scan mode (Rabinowitz et al., 2005). In this mode, the shutter is open all the time to gather light and the telescope allows the luminous objects in the sky to drift across the camera. The telescope is moved along great circles in the sky so that the image is continued to read out by moving the image along the CCD columns at the same rate as the object drifts across it. An object drifts from one CCD to the immediate next CCD turn by turn along the column and it takes about one minute (54 seconds) time, called exposure time to drift over one of the CCDs. When the images cross the CCDs in a column, the charges collected in the CCD pixels are shifted along the direction of drifting of the image. In this way, each of the

objects will be exposed through five different SDSS filters and produces five different images of the same object. Finally, combining different filters gives a new color image of the sky. A detailed description of the imager can be found in Gunn et al. (1998).

2.7.2 Spectroscopic Survey

The color image of one quarter of the sky thus produced by SDSS camera will be processed to detect and identify the objects in the sky (Smee et al., 2013). Then the computers at Fermi laboratory execute the calculations of each object in detail to measure and classify the objects as stars galaxies, quasars and so on and the information is stored in a big database on computers. The spectroscopic study of the millions of galaxies detected in the survey region of the sky is more important to get information like the types of stars a galaxy contains, the amount of gas scattered throughout it and the dynamics of the galaxy. Moreover, using redshift, the distance to the galaxy can be estimated from Hubble law,

$$\text{Distance} = \frac{\text{velocity}}{H_0} \tag{2.28}$$

Where H_0 is the Hubble's constant. The spectrograph is used to find the distance of celestial objects because the distance is an important parameter in the study of the origin and the structure of the universe. The spectra of many (about 640) objects are taken simultaneously in SDSS, which would take a very long time. To minimize the time, the spectrographs are connected to an thin aluminum plate in the focal plane of the telescope by optical fiber (Strauss et al., 2002). The plate is drilled with about 500 holes, each of which is plugged with an optical fiber (Figure 14) to carry light from one galaxy to the spectrograph. i.e., each hole corresponds to one object (star or galaxy) in the sky.

The light from each fiber is split up into a spectrum by the spectrograph and all the spectra are measured at a time. Therefore, the telescope can take the spectra of 500 galaxies in one observation. The plates and fibers used also have their unique identification number. So, each spectrum is assigned with a number of the fiber (called fiber ID) with which it was collected. Likewise, the plates used in specific dates are assigned by Modified Julian Date (MJD) of the night when the observation was taken. If a plate is reused more than once, the observations will have different MJD values and the optical fibers will be re-plunged in each use. Therefore, the given fiber ID on various MJDs will correspond to different objects.

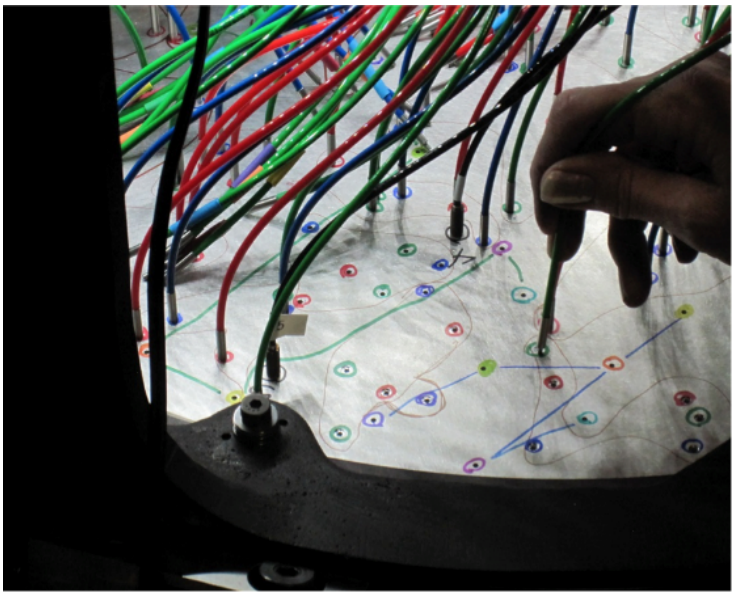

Figure 14: : Fibers plugged into pre-drilled holes in a plate. Different colored fibers represent faint, medium and bright targets (Source: J. Wilson, Accessed: 2020-04-25).

2.8 Review of Dwarf Galaxy Research

2.8.1 Cataloging

Several attempts have been made earlier to prepare a catalog of dwarf galaxies. Some of them are discussed briefly. Deeg et al. (1997) prepared a catalog of dwarf galaxies entitled "A catalog of dwarf galaxy candidates around interacting galaxies". They compiled the potential dwarf galaxies lying very close to the twelve strongly interacting galaxies selected from the Infrared Astronomical Satellite (IRAS) bright galaxy sample (Soifer et al., 1989) and from Condon & Broderick (1991) found inside a field size of $11.4' \times 10.5'$ centered at the main galaxy within which, 100 to 200 non-stellar low brightness, extended objects were found. The number of extended objects varies greatly with the sample. Out of 12 sample interacting galaxies, NGC 1023 has the lowest number of extended objects around it. Only 21 dwarf galaxies are identified. The major physical properties of the galaxies they have listed in the catalog are the central galaxy's name, reference coordinates, morphological type, heliocentric velocity, size field, exposure time, magnitude limits, numbers of expected background galaxies, etc. Karachentsev et al. (2004) prepared a catalog of neighboring galaxies including dwarf galaxies of luminosity 10^4 times less than that of the MW galaxy and other local groups at distance $D \leq 10$ Mpc. Arp (1966) published a catalog of unusual galaxies (interacting and active galactic nuclei) containing a photograph of 338 nearby galaxies, which is now known as a good compilation of interacting and merging galaxies (Chincarini & Rood, 1972). The main goal of the catalog was to compile the galaxies with peculiar structures among all galaxies.

2.8.2 Merging Dwarf Galaxies

Interaction/merging of galaxies is a major process of evolution of galaxy that influences the morphology, growth and star formation activities of the galaxies. Moreover, it leads to the dilution of metallicityand the highest star formation rates are linked incredibly with strong interactions and mergers of the galaxies (Kennicutt, 1998). During the merger of galaxies, stars, planets, dust and gas of the interacting galaxies combine to form a single galaxy. At first, Amorisco et al. (2014) gave concrete confirmation of the dwarf-dwarf merger in the dwarf spheroidal galaxy Andromeda II.

The ability of galaxies to form stars within interstellar gas clouds is influenced by a multitude of factors including gas and dust composition, temperature, gravitational forces, interactions between matter and radiation, hydrodynamics, thermodynamics, and chemical processes. (Krumholz & Dekel, 2012). After the merger, huge gas clouds will be formed that form stars at higher rates. The dwarf galaxies are vulnerable to their surroundings because of their swallow potential well as compared to the massive galaxies. The evolution and growth of dwarf galaxies via merging are to be explored in detail. It has been possible to better detect different features of the galaxies with the advent of low surface brightness imaging techniques and dedicated data reduction procedures (Abraham et al., 2012; Duc et al., 2014; Mihos et al., 2017).

In Stierwalt et al. (2015) work they examined interacting pairs of dwarf galaxies and determined that the star formation rate in gas-rich, isolated pairs with separations < 50 kpc is approximately twice that of unpaired dwarfs with similar gas fractions and stellar masses. This contrasts with findings from studies of large galaxy pairs, such as those conducted by Ellison et al. (2013). Dwarfs, which are typically found in low-density environments, are more gas-rich than giant galaxies and have lower star formation efficiency. While a few recent observational studies have reported on merging features in some dwarf galaxies, little is currently known about their evolution through mergers, as documented by Annibali et al. (2016); Rich et al. (2012); Pearson et al. (2016).

2.9 Research Gap in Dwarf Galaxy Research

Recently, Paudel et al. (2017) discovered a MW twin where they identified Large and Small Magellanic clouds (LMC/SMC) like systems around an isolated spiral galaxy NGC 2718. The common belief is that low-mass dwarf satellites should be more affected by tidal potential of parent halos due to their shallower potential wells, and thus would be less affected by merging events. However, recent evidence indicates that minor galaxy merging may be more common than initially thought. Aside from the now-famous LMC-SMC merger, numerous potential merging dwarfs have been identified in recent studies (Coleman et al., 2004; Sengupta et al., 2012; Amorisco et al., 2014; Chengalur et

al., 2015; Annibali et al., 2016; Privon et al., 2017). It shows that dwarf galaxy enhances the star-formation activity by tidally interacting with another similar or lower mass galaxy (Springel et al., 2005). They are certainly smoking gun examples of not only how dwarf galaxies may evolve in a hierarchical fashion merging with a smaller companion, but also they show how tidal interaction between dwarf galaxies affects their star-formation history. In fact, cosmology is scale-free and there is nothing surprising about these results. But, hierarchical fashion also means that smaller objects are the first to form and grow by merging as time passes (Naab & Burkert, 2003).

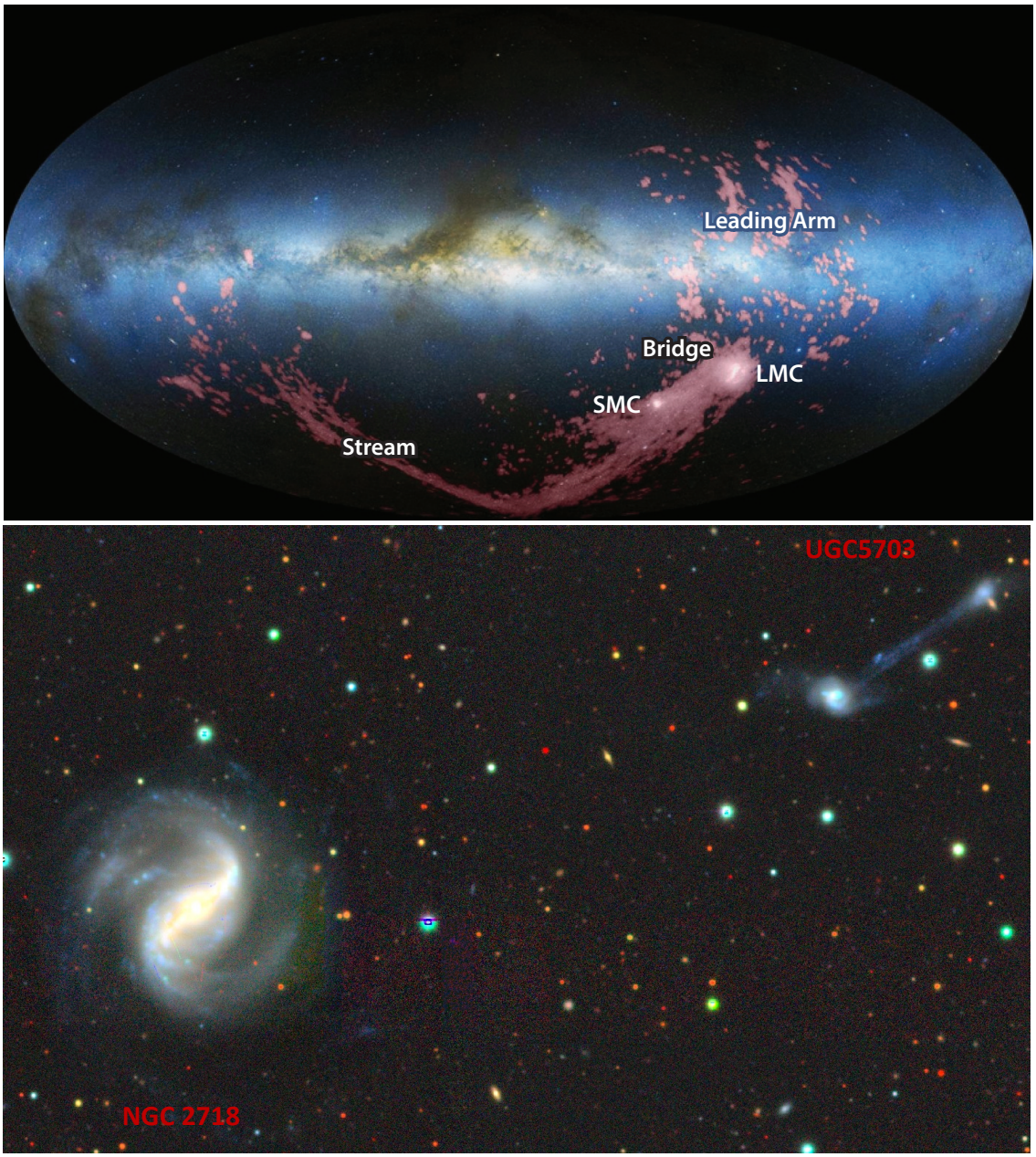

Figure 15: Top: Interaction of dwarf galaxies (LMC and SMC) near to MW (D'Onghia & Fox, 2016). Bottom: Interaction of UGC 5703 near NGC 2718. MW twin (Paudel et al., 2017). Both galaxies are located at a distance of 54.5 Mpc and they have a B-band absolute magnitude of −18.25 and −19.93 mag respectively.

A complex velocity structures are found in the nearby interacting dwarf galaxy NGC 3077 (Walter et al., 2002). This study uses a high-resolution Very Large Array (VLA) H1 observations and it is found that most of the atomic gas (about 90%) around NGC 3077 is situated in a prominent tidal arm with a complex velocity structure. Little is associated with NGC 3077 itself. They found a surprising result for a dwarf galaxy that the CO-to-H_2 conversion factor in NGC 3077 is lower than the galactic value. A large number of work has been ongoing in dwarf galaxies. Sengupta et al. (2015) studied the interactions between pairs of galaxies (NGC 90 and NGC 93) resulting in the displacement of large amounts of gas and stars as debris which then evolves, sometimes forming stars and occasionally forming dwarf galaxies. They conclude that high HI column densities may be a necessary but not sufficient criterion for star formation.

2.9.1 A Chronological Study of Merging Dwarf Galaxy

One of the prime examples of a dwarf-dwarf merger in our vicinity is the interaction between LMC and SMC. There are a plethora of studies in the system explaining the origin of interaction and future evolution of participating galaxies. The system is also particularly important to know how the interacting system affects the evolution of our own galaxy MW. We show the system in Figure 15.

In the early 2000s, Coleman et al. (2004) discovered a shell-like feature in the Fornax dwarf galaxy; this was also interpreted as a merger origin. A major progress in the study of merging dwarf exhaled after the discovery of a small elongated dwarf galaxy in the vicinity of NGC 4449 since then, the candidate of merging dwarf has been growing continuously. A tidally distorted dwarf galaxy near Magellanic irregular starburst NGC 4449 was discovered by Rich et al. (2012). Paudel et al. (2015) studied a system of interacting dwarf galaxies in UGC 6741, where they identified that both the interacting galaxies have similar metallicity and suggest that UGC 6741 appears as a promising system for studying the possible transformation of BCDs into dEs, possibly through a merger episode.

Amorisco et al. (2014) suggested that Andromeda II dwarf galaxy could be a remnant of a merger between two dwarf galaxies. In a study of CGCG 036-042, Paudel et al. (2014) reported the formation of compact elliptical through the merger, where the host galaxy CGCG 036-042 was significantly compact and is located in an isolated environment. Metallicity of CGCG 036-042 was higher than most normal dwarf galaxies. In local volume TiNy Titans (TNT), a survey of merging dwarf galaxies, (Stierwalt et al., 2015) found merging dwarf galaxies likely to have higher SFR than normal dwarf galaxies when their separations are less than a few 100 kpc. Annibali et al. (2016) identified a merging dwarf galaxy in the local void and their radio data shows that these void merging dwarf galaxies are gas-rich and extremely metal-poor.

Pearson et al. (2016) studied a sample of interacting dwarf galaxies from TNT using radio observation and found that the neutral gas was more extended in the interacting pairs when compared to non-paired analogs, providing evidence of tide-driven pre-processing of the gas. The first analog of the Magellanic pair was discovered by Paudel et al. (2017) [Figure 15], where they studied star formation and gas mass distribution using the Giant Metrewave Radio Telescope (GMRT) 21 cm emission line observation. The largest catalog of merging dwarf galaxies in the local universe was published by Paudel et al. (2018a). KUG 0200-096 was studied by Paudel et al. (2018a), where they identified an antennae galaxies like system forming tidal dwarf galaxies at the tip of antennae. Paudel et al. (2020) studied an interacting pair of dwarf galaxies in a group environment using GMRT radio observation, where they compared the system with the previously identified system UGC 6741. Below, we try to summarize these events chronologically. Above description is summarised in the Table 1.

Table 1: Chronological study of merging dwarf galaxies.

Galaxy	**Title**	**Reference**
Fornax Dwarf galaxy	Discovery of Shell feature	(Coleman et al., 2004)
NGC4449	A tidally distorted dwarf galaxy near NGC 4449	(Rich et al., 2012)
Andromeda II	The remnant of a merger between two dwarf galaxies in Andromeda II	(Amorisco et al., 2014)
CGCG 036-042	An isolated, compact early-type galaxy with a diffuse stellar component: merger origin?	(Paudel et al., 2014)
UGC 6741	A Case Study for a Tidal Interaction between Dwarf Galaxies in UGC 6741	(Paudel et al., 2015)
UGC 4722	Study of the Lynx-Cancer void galaxies. - V. The extremely isolated galaxy UGC 4722	(Chengalur et al., 2015)
Local survey	TiNy Titans (TNT) a survey merging dwarf in the nearby universe	(Stierwalt et al., 2015)
DDO 68	Interacting dwarf in Void	(Annibali et al., 2016)
NGC 3448, UGC 6016, NGC 672, IC 1727, UGC 9560 and UGC 9562	Local Volume TiNy Titans: gaseous dwarf–dwarf interactions in the Local Universe	(Pearson et al., 2016)
UGC 4703	UGC 4703 Interacting Pair Near the Isolated Spiral Galaxy NGC 2718: A Milky Way Magellanic Cloud Analog	(Paudel et al., 2017)
Catalog	A Catalog of Merging Dwarf Galaxies in the Local Universe	(Paudel et al., 2018a)
KUG 0200-096	KUG 0200-096: Dwarf Antennae Hosting a Tidal Dwarf Galaxy	(Paudel et al., 2018a)
MCG+07-20-052	MCG+07-20-052: Interacting Dwarf Pair in a Group Environment	(Paudel et al., 2020)

CHAPTER 3

3. MATERIALS AND METHODS

3.1 Dwarf Galaxy

In this work, we aim to understand how merging dwarf galaxies are formed and evolved in a variety of environments. We define a sample of merging dwarfs taken from the catalog prepared by Paudel et al. (2018a). In this chapter, we introduce the basic properties of these galaxies. We explain our selection criteria and statistics used. In addition, we describe the basic data acquisition steps that are used to obtain imaging and spectroscopic data from the SDSS to perform a study of spectroscopic and morphological properties of a representative sample of merging dwarfs of various environments.

3.1.1 Selection Criteria

Compactness and Surrounding Environment

To make a representative sample of merging dwarf galaxies, we selected 25 merging dwarf galaxies of two different morphology: compact and extended. Because, these two different morphology represent two different types of interaction of dwarf galaxies. Compact merging dwarf galaxies represent more evolved final stage of merging whereas, the extended merging dwarf galaxies represent early stage of merging. Their unique physical conditions, enhanced starburst activity, morphological transformations, and relevance to galaxy scaling relations make them valuable targets for investigating the fundamental processes that shape galaxies throughout the universe.This sample list comprises 15 compact and 10 extended merging dwarf galaxies. The visual appearance of compact merging galaxies is of almost solid shape somewhat spherical and elliptical. In most of all galaxies, a halo appears around it while in some other galaxies, the still extended tail-like structure is observed because of ejected matter from the galaxy. In the case of the extended merging galaxies, we can still see the merging galaxies very close to each other connected by a bridge and even appear as a single galaxy but having no regular shape. Some of them appear elongated with their halo around them, whereas, some are forming a tail-like shape.

The galaxy merger plays a major role in the evolution of galaxy (White & Frenk, 1991) and it would increase the size of the galaxy (van Dokkum et al., 2010). The sample galaxies are all blue star-forming dwarf galaxies and have the $g - r$ color of less than 0.46 mag. A significant majority of them are located in an isolated environment as

Paudel et al. (2018a) noted that dwarf-dwarf merger mainly happens in the less dense region. Out of the 25 merging dwarfs, only 4 are located in a group environment and the rest are located in an isolated environment. We adopted a criterion for the search of neighboring giant galaxies of absolute magnitude $M < -20$ mag, with the stellar mass of $< 10^{10}$ $M_\odot$ not outside of 700 kpc radial distance and a relative line of sight radial velocity of $< \pm 700$ km s^{-1}.

Redshift

Redshift is the phenomenon in which the electromagnetic radiation emitted from a source undergoes an increase in its wavelength (decrease in frequency). It is the relative change in observed and emitted wavelength of the radiation from the source. But in the case of blue shift (negative redshift), the wavelength is shortened. The main three types of redshifts are gravitational, cosmological and Doppler's redshifts. An object that has high redshift means that it is receding away with a very high velocity. So, the value of redshift gives an idea of how far and how fast an object is moving. The universe's earliest epochs lie at a redshift of around 100. But these days' people are equally working in low redshift regions. Since dwarf galaxies are of small size having low luminosity, it is hard to detect them. Therefore, only less number of dwarf galaxies have been surveyed to date as compared to normal brighter galaxies and hence we have selected the dwarf galaxies in the low redshift of range 0.0024 to 0.0197. H_α emission-line flux is a very good star formation indicative e.g., Kennicutt (1983) for nearby galaxies.

Figure 16 shows the redshift and stellar mass distribution of the galaxies we have selected. The redshift range of our sample galaxies gives a Hubble flow distance in the range 10 Mpc to 70 Mpc. As we can see, the redshift distribution peak is at the lowest bin. This allows us higher spatial resolution for the majority of our data. The median value of the redshift distribution is 0.007, with a standard deviation of 0.0053. In the next plot, we show the stellar mass distribution of our sample of merging dwarfs. The stellar mass ranges from 10^8 $M_\odot$ to 4×10^9 $M_\odot$ with a median value of 7.2×10^8 $M_\odot$, which means that the faintest galaxy is similar to Fornax dwarf galaxy and the brightest galaxy is of LMC stellar mass.

Morphology

Another criterion of our galaxy selection is their morphology. The main morphology of selection criteria is their tidal feature: interacting, merging, shell, stellar streams, loop, antenna and tidal tail. The morphology of galaxies gives an idea of their development and evolution. According to Hubble's tuning fork model, the major classes of galaxies based on their visual appearance are ellipticals, lenticulars and spirals. Galaxy morphology gives the idea of star formation history, nuclear activity, merger or interaction history and gas accretion from other galaxies (Kormendy & Kennicutt, 2004).

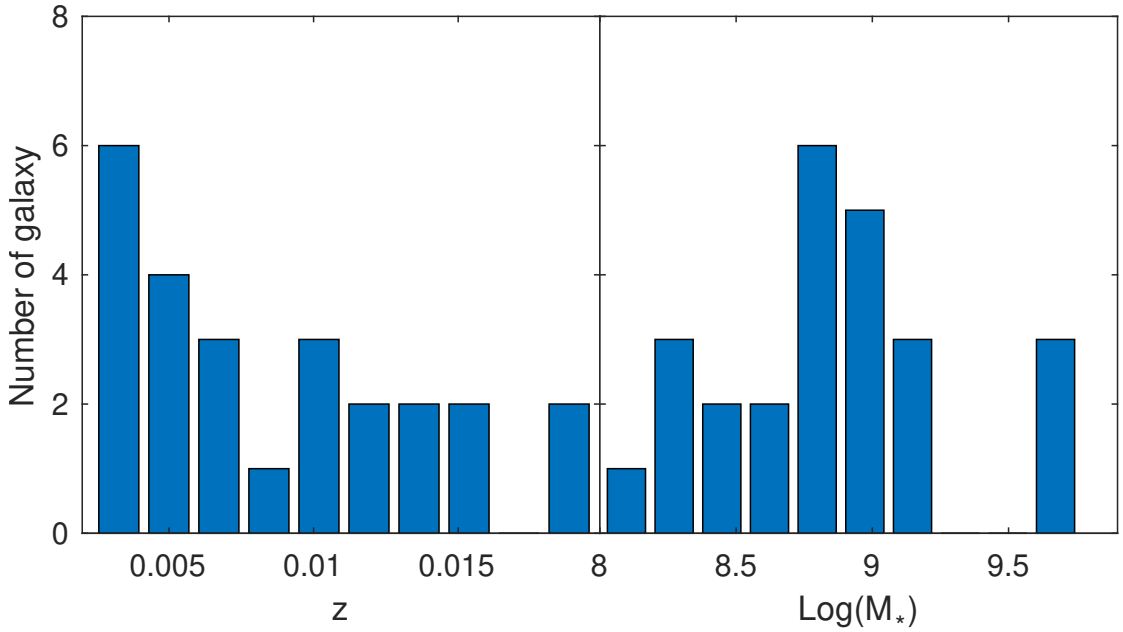

Figure 16: The redshift and stellar-mass distribution of our candidate merging dwarf galaxies.

In Table 3, we list the physical properties of our sample galaxies: both compact merging and extended merging dwarf galaxies. They are taken from Paudel et al. (2018a). In the first and second columns, we provide the catalog number and galaxy id respectively according to the main catalog. The third column represents the galaxy name we assigned (Cd for compact and Ed for extended merging dwarfs) respectively. Columns 4 and 5 list sky-position (RA and Dec.) in h:m:s and d:m:s format respectively. Columns 6, 7, 8 and 9 lists spectroscopic redshift, adopted distance in megaparsec, the SDSS $(g - r)$ color index and stellar mass of the galaxy respectively. Likewise, columns 10, 11, 12 and 13 lists the logarithmic value of SFR derived from the FUV fluxes, the logarithmic value of HI mass, Satellite code (1 for group environment or 0 for field environment) and the feature (morphology) of the galaxy respectively. The morphological class of the galaxies is shown in Table 2.

Table 2: Morphological classification of merging dwarfs.

I	Interacting: two dwarf galaxies visibly distinct
IM	Interacting merged: two dwarf galaxies overlapping or the progenitor is not distinct
IMSh	Interacting merged having Shell
TS	Tidal tail and stellar stream
A	Antenna
Sh	Presence of shell features
T	Tidal tail
S	Stellar stream
SL	stellar stream and Loop
E	Extended tail

Table 3: The Physical Properties of 15 Compact and 10 Extended Merging Dwarf Galaxies Taken from the Catalog by Paudel et al. (2018a)

Catalog No.	Galaxy ID	Galaxy Name	R.A. (h:m:s)	Dec. (d:m:s)	Redshift z	D (Mpc)	$g-r$ (mag)	M^* $\log(M_\odot)$	SFR $\log(M_\odot)$	M_{HI}	Satellite	Feature
Compact Merging Dwarf Galaxies												
004	Id0155-0011	Cd-01	01:55:59.74	−00:11:07.80	0.0121	51.57	0.46	9.09	−0.91	8.43	0	Sh
010	Id0222-0830	Cd-02	02:22:11.95	−08:30:36.36	0.0156	66.66	0.35	9.63	−0.44	NA	0	TS
016	Id08092137	Cd-03	08:09:47.38	+21:37:17.40	0.0111	47.27	0.23	8.86	−0.44	NA	0	T
036	Id09381942	Cd-04	09:38:14.59	+19:42:39.96	0.0144	61.48	0.20	8.56	NA	8.87	1	Sh
040	Id09514419	Cd-05	09:51:39.29	+44:19:08.40	0.0150	64.07	0.19	8.99	−0.42	NA	0	I
047	Id10013704	Cd-06	10:01:14.38	+37:04:15.24	0.0048	20.34	0.14	8.26	−1.29	NA	0	Sh
052	Id10174308	Cd-07	10:17:32.98	+43:08:41.28	0.0037	15.67	0.34	8.01	NA	9.15	0	Sh
053	Id10192117	Cd-08	10:19:01.49	+21:17:00.96	0.0036	24.80	0.22	8.86	−0.92	8.72	0	TS
055	Id10291610	Cd-09	10:29:49.27	+16:10:51.24	0.0108	45.98	0.23	9.18	−0.68	8.19	0	SL
076	Id1148-0138	Cd-10	11:48:18.17	−01:38:23.64	0.0130	55.44	0.22	9.03	−0.51	9.94	0	Sh
077	Id11501501	Cd-11	11:50:02.71	+15:01:23.16	0.0024	11.90	0.09	7.92	−34.95	8.40	1	Sh
079	Id1152-0228	Cd-12	11:52:37.18	−02:28:09.84	0.0034	14.39	0.08	8.33	−0.96	8.52	0	E
111	Id13433644	Cd-13	13:43:13.13	+36:44:57.48	0.0197	84.44	0.36	9.70	−0.07	9.34	0	TS
112	Id13434311	Cd-14	13:43:26.98	+43:11:18.60	0.0083	35.27	0.20	8.49	−1.26	9.41	0	Sh
168	Id2319-0059	Cd-15	23:19:58.01	−00:59:07.80	0.0121	51.57	0.31	9.00	−1.01	9.83	0	TS
Extended Merging Dwarf Galaxies												
002	Id01250759	Ed-01	01:25:34.97	+07:59:26.88	0.0097	41.26	0.04	8.78	−0.35	9.3	0	IM
021	Id08332932	Ed-02	08:33:22.97	+29:32:18.96	0.0069	29.29	0.33	9.76	−0.15	8.9	0	I
067	Id11253803	Ed-03	11:25:31.80	+38:03:37.80	0.0070	29.72	0.23	9.16	−0.60	8.8	0	IMSh
100	Id12530427	Ed-04	12:53:13.99	+04:27:54.00	0.0024	9.68	0.30	8.82	−0.93	NA	1	Sh
104	Id13161232	Ed-05	13:16:52.32	+12:32:53.52	0.0032	13.55	0.30	8.74	−1.13	10.0	0	Sh
110	Id13425241	Ed-06	13:42:59.40	+52:41:17.88	0.0059	25.03	0.31	8.35	NA	NA	0	I
114	Id13516422	Ed-07	13:51:53.57	+64:22:22.08	0.0058	28.40	0.18	8.69	−0.83	NA	1	IM
134	Id14543012	Ed-08	14:54:11.71	+30:12:34.20	0.0094	39.98	0.12	9.06	0.37	NA	0	A
147	Id15363040	Ed-09	15:36:19.34	+30:40:51.96	0.0058	28.50	0.25	8.91	NA	NA	0	I
153	Id16060634	Ed-10	16:06:40.99	+06:34:50.88	0.0058	20.40	0.36	8.84	−1.05	9.2	0	Sh

Now, we introduce each dwarf galaxy of our sample briefly based on the catalog prepared by Paudel et al. (2018a). The galaxies are mainly divided into two groups, i.e., compact merging and extended merging dwarf galaxies. We show the optical image of the galaxy and its spectrum in the wavelength range 4000 Å to 7000 Å in each case.

3.2 Compact Merging Dwarf Galaxies

Below we briefly discuss the compact merging dwarf galaxies used in our study. Figures 17 to 31 show their $(g-r-i)$ combined tri-color optical image and the spectrum obtained from the SDSS sky server. The X-axis is the rest frame wavelength and the Y-axis shows the flux.

3.2.1 Cd-01

Cd-01 has a sky-position of RA (J2000) = $01^{h}\ 55^{m}\ 59.74^{s}$ and Dec. (J2000) = $-00^{\circ}\ 11'\ 07.80''$ with a line-of-sight radial velocity 3642 km s^{-1}. It is a shell-featured galaxy located in a field environment, surrounded by 3 neighboring galaxies around it. The $(g-r)$ color of the galaxy is 0.46 mag and is located at a distance of 51.57 Mpc from us. It has a stellar mass of 1×10^{9} $M_{\odot}$ and HI gas mass 2.6×10^{9} $M_{\odot}$. The $(g-r-i)$ combined tri-color image of the galaxy Cd-01 is shown in the left panel of Figure 17. The galaxy has compact morphology with a bright center compared to the outer part. A reddish, extended tail-like structure can be seen along its major axis. The optical spectrum of the galaxy Cd-01 is shown in the right panel of Figure 17. We can see both the emission and the absorption lines in the spectrum but most of the lines are prominent emission lines. There is strong emission in H_{α} and OIII lines and we can also see strong absorption features in the higher order Balmer lines.

3.2.2 Cd-02

Cd-02 has sky-position of RA (J2000) = $02^{h}\ 22^{m}\ 11.95^{s}$ and Dec. (J2000) = $-08^{\circ}\ 30'\ 36.36''$ with a line-of-sight radial velocity of 4695 km s^{-1}. It is a stellar stream feature merging dwarf located in the field environment and there are three neighboring galaxies within a sky-projected distance of 700 kpc. It is a blue star-forming galaxy with a $(g-r)$ color of 0.35 mag. The g, r and b-band absolute magnitudes of the galaxy are 15.25 mag, 14.90 mag and −18.53 mag respectively. The distance to the galaxy taken from Nasa Extragalactic Database (NED) is 66.66 Mpc. The optical image and the spectrum of the galaxy Cd-02 are shown in Figure 18. The central region of the galaxy is brighter as compared to the outer region. A reddish, extended tail-like structure can be seen along its major axis. The spectrum shows strong emission in H_{α} and OIII lines and we can also see strong absorption features in higher-order Balmer lines.

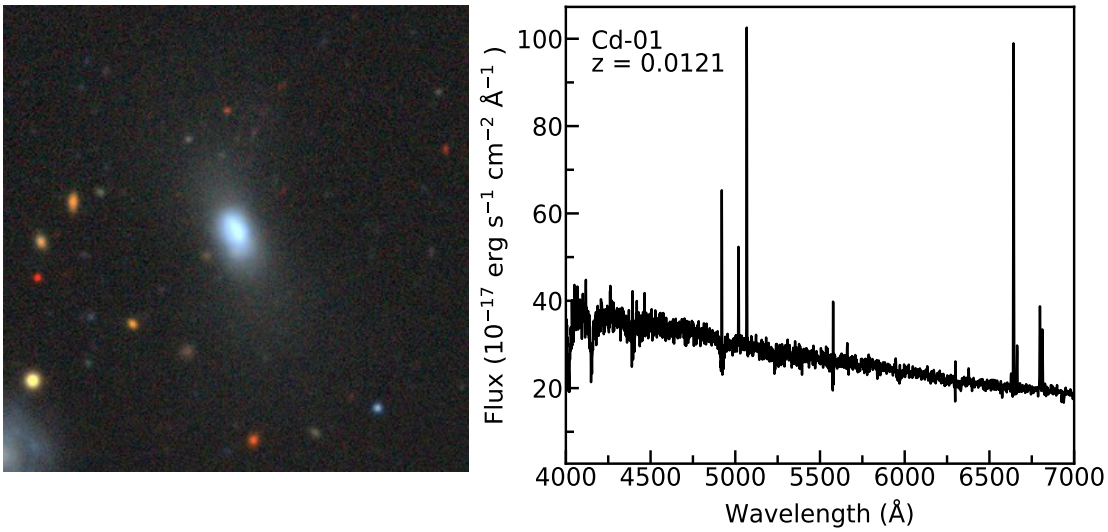

Figure 17: Optical image and spectrum of compact merging dwarf galaxy Cd-01. Both the image and spectrum are obtained from the SDSS skyServer. The X-axis is rest-frame wavelength and Y-axis shows the flux.

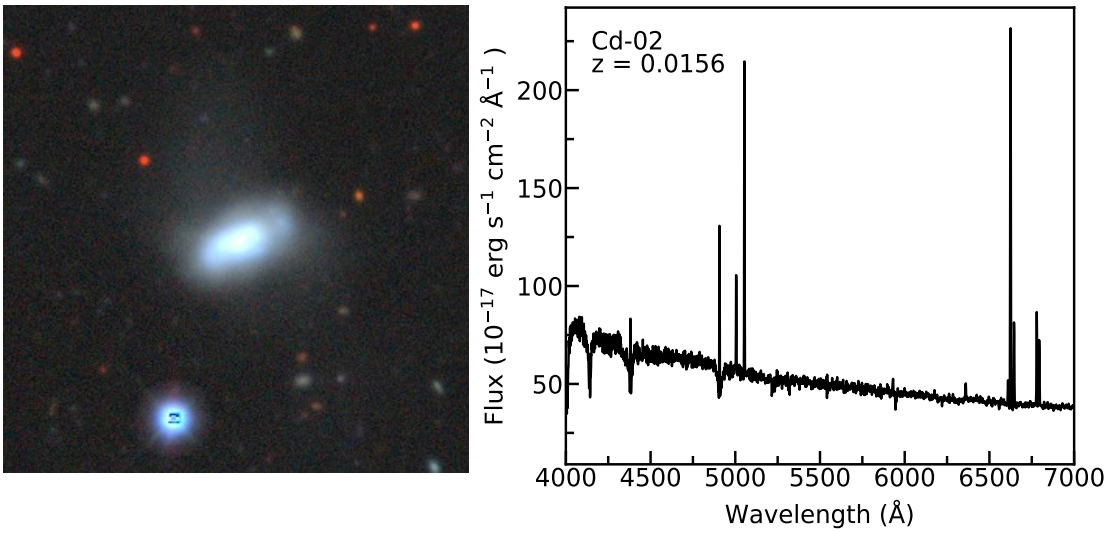

Figure 18: Optical image and spectrum of Cd-02

3.2.3 Cd-03

Cd-03 has sky-position: RA (J2000) = $08^{h}\,09^{m}\,47.38^{s}$ and Dec. (J2000) = $+21^{\circ}\,37'\,17.40''$. It is a field galaxy having only one neighboring galaxy around it. It is a blue star-forming galaxy with a $(g-r)$ color of 0.23 mag. The g, r and b-band absolute magnitudes of the galaxy are 15.98 mag, 15.75 mag and −17.09 mag respectively. The galaxy lies at a distance of 47.27 Mpc. The line-of-sight radial velocity of the galaxy is 3330.6 km s^{-1}. The $(g-r-i)$ combined tri-color optical image of the galaxy and its optical spectrum is shown in Figure 19. We can see the tidal tail and boxy morphology of the galaxy. The central region of the galaxy is brighter as compared to the outer region. The galaxy seems to be almost merged with each other. We can distinctly see two blue regions inside the galaxy in which star-forming activities are going on. A reddish, extended tail-like

structure can be seen in its southeast direction and appears as a tadpole galaxy. This galaxy has a stellar mass of 3.6×10^8 $M_\odot$ and the main catalog does not list the total HI mass of the system. The spectrum shows strong emission in H_α and OIII lines.

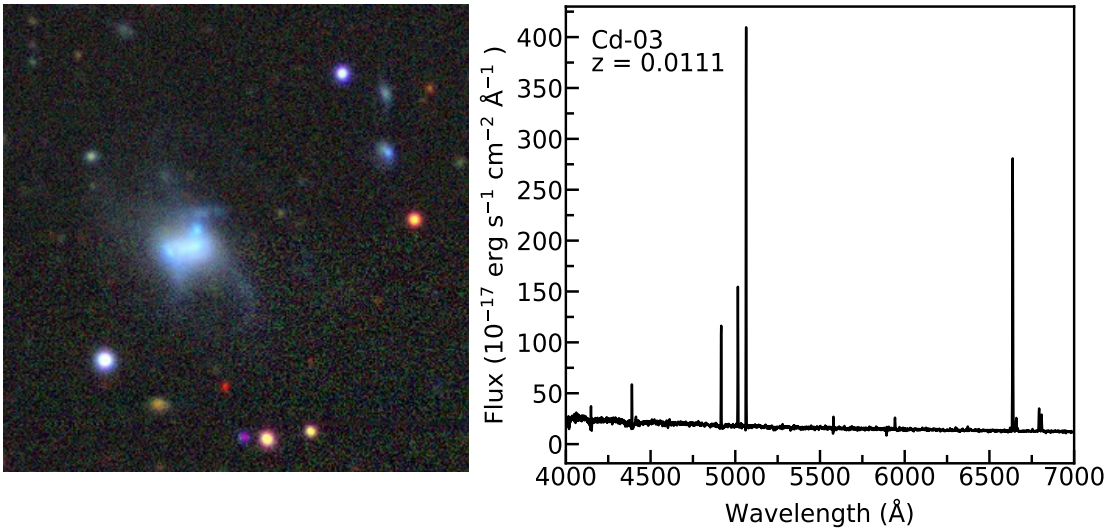

Figure 19: Optical image and spectrum of Cd-03.

3.2.4 Cd-04

Cd-04 has sky-position: RA (J2000) = $09^h\ 38^m\ 14.59^s$ and Dec. (J2000) = $+19°\ 42'\ 39.96''$ and redshift $z = 0.0144$. Figure 20 shows the optical image and the spectrum of the galaxy Cd-04. Although the galaxy is very compact, it has a small tidal tail elongated toward the north direction. It is a shell-featured galaxy located in a group environment and the nearest giant galaxy is NGC 4283. It is a blue star-forming galaxy with a $(g - r)$ color of 0.20 mag. The g, r and b-band absolute magnitudes of the galaxy are 17.19 mag, 16.99 mag and −17.19 mag respectively. The galaxy is situated at a distance of 61.48 Mpc and has 26 neighboring objects within a sky-projected distance of less than 700 kpc. The mass ratio of the interacting galaxies is 1. The line-of-sight radial velocity of the galaxy is 4329 km s^{-1}. The spectrum has a bit low signal-to-noise ratio but shows strong emission in H_α and OIII lines.

3.2.5 Cd-05

Cd-05 has sky-position RA (J2000) = $09^h\ 51^m\ 39.29^s$ and Dec. (J2000) = $+44°\ 19'\ 08.40''$ with a spectroscopic redshift of 0.0151. Figure 21 shows the optical image and spectrum of the galaxy Cd-05. We can see that a long elongated tidal tail is coming out of the host galaxy. The galaxy is compact in nature whose central region seems to be bluish in color and brighter than the outer region indicating that star-forming activities are going on. An extended tail-like structure can be seen along the semi-major axis which indicates that the

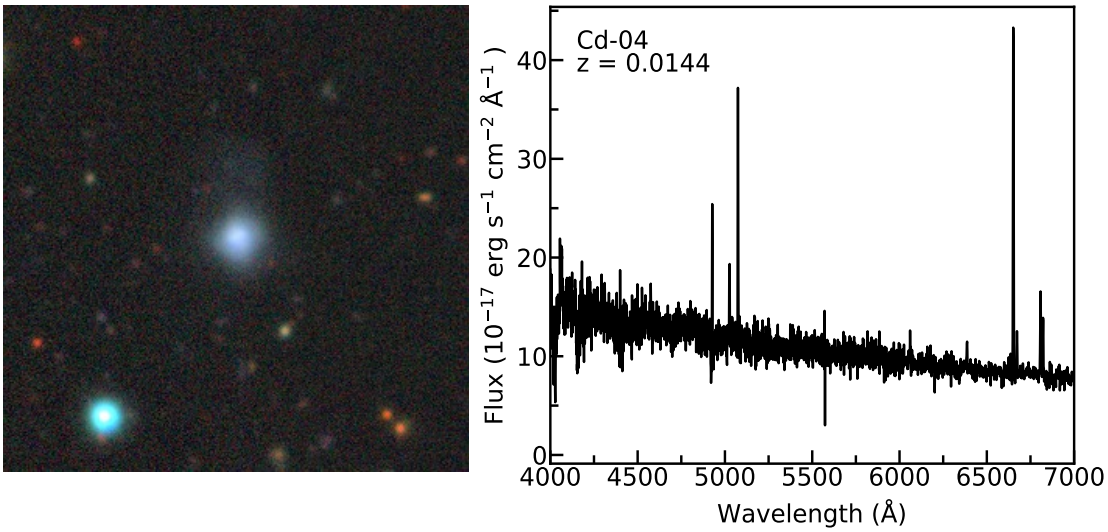

Figure 20: Optical image and spectrum of Cd-04.

galaxy is formed by the merger. The tidal tail is somewhat redder in color compared to the compact host galaxy color. The g, r and b-band absolute magnitudes of the galaxy are 16.18 mag, 15.99 mag and −17.56 mag respectively. This galaxy is a field galaxy lying at a distance of 64.07 Mpc. It has 3 neighboring objects within a sky-projected distance of less than 700 kpc and a relative line-of-sight radial velocity of less than ± 700 km s^{-1}. The line-of-sight radial velocity of the galaxy is 4519 km s^{-1}. This galaxy has a stellar mass of 9.7×10^8 M$_\odot$. The spectrum shows strong emission in H$_\alpha$ and OIII lines. we can also see strong absorption features in higher-order Balmer lines.

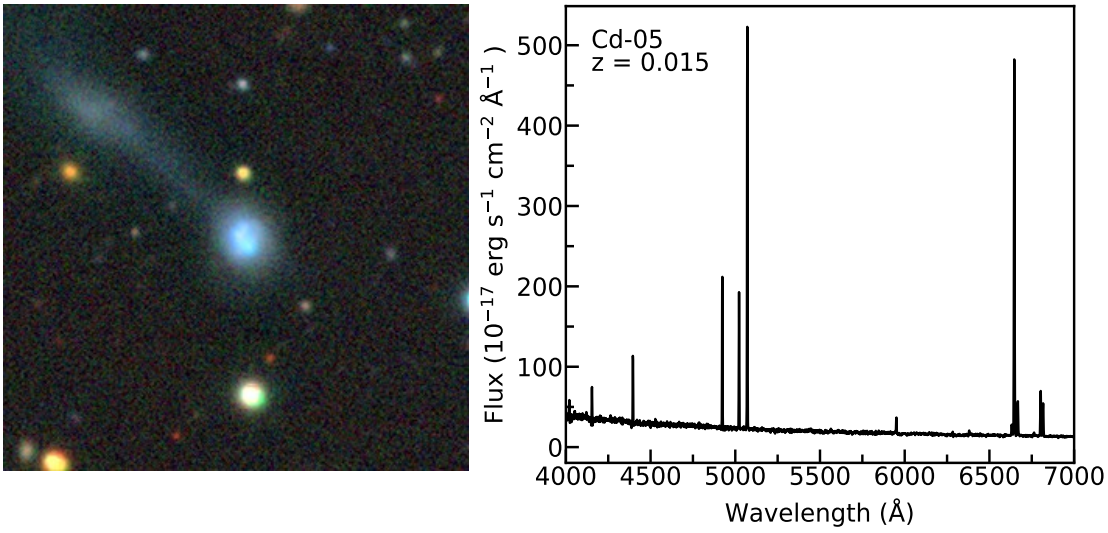

Figure 21: Optical image and spectrum of compact dwarf galaxy Cd-05.

3.2.6 Cd-06

Cd-06 has sky-position: RA (J2000) = $10^h\,01^m\,14.38^s$ and Dec. (J2000) = $+37°\,04'\,15.24''$ and redshift $z = 0.0048$. The g, r and b-band absolute magnitudes of the galaxy are

15.33 mag, 15.19 mag and −15.94 mag respectively. The galaxy lying at an adopted distance of 20.34 Mpc has 3 neighboring objects within a sky-projected distance of less than 700 kpc. The line-of-sight radial velocity of the galaxy is 1467 km s^{-1}. The optical image and spectrum of the galaxy are shown in Figure 22. It is an elongated shell feature merging compact dwarf galaxies. The whole body of the galaxy seems to be bluish in color and a low surface brightness blue color halo is seen in the outer surrounding. It is located in a field environment. It is a blue star-forming galaxy with a $(g - r)$ color of 0.14 mag. The spectrum shows a strong emission line with absorption in higher-order Balmer lines.

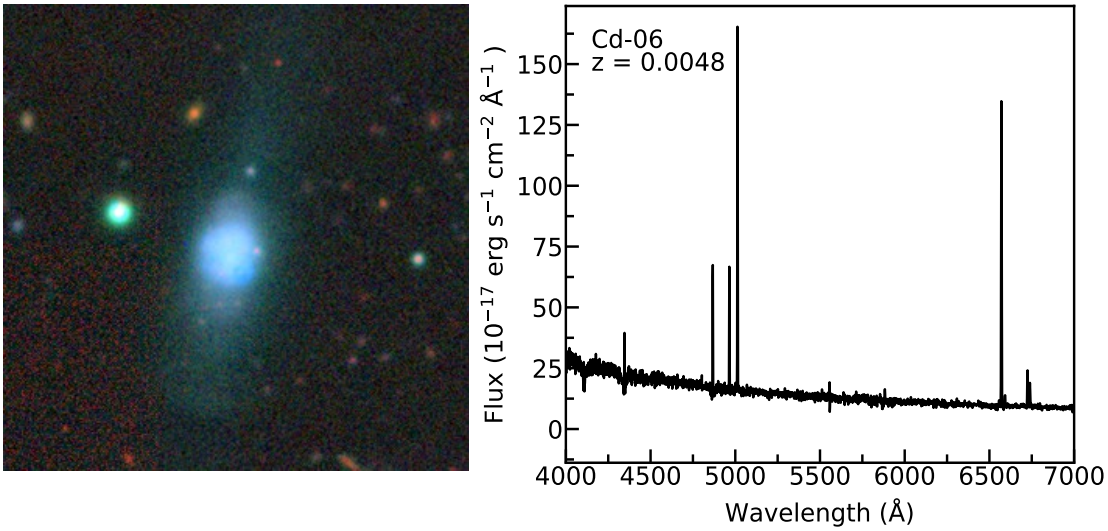

Figure 22: Optical image and the spectrum of compact dwarf galaxy Cd-06.

3.2.7 Cd-07

Cd-07 has sky-position RA (J2000) = 10^h 17^m 32.98^s and Dec. (J2000) = +43° 08′ 41.28″ with a spectroscopic redshift of 0.0038. Figure 23 shows the image and the spectrum of this galaxy. It is a star-forming galaxy having a compact shell feature with tidal tail morphology. The central core is bluish in color and an extended tail-like structure is observed along its semi-major axis. The outer region is reddish as compared to its core. It is located in a field environment surrounded by 3 neighboring galaxies. The g, r and b-band absolute magnitudes of the galaxy are 16.14 mag, 15.80 mag and −14.51 mag respectively. The line-of-sight radial velocity of the galaxy is 1132 km s^{-1}. This galaxy has a stellar mass of 1.0×10^8 $M_\odot$ and total HI mass of the system is 1.4×10^9 $M_\odot$. The spectrum shows strong emission in H_α and OIII lines, but the spectrum has low signal-to-noise ratio (SNR).

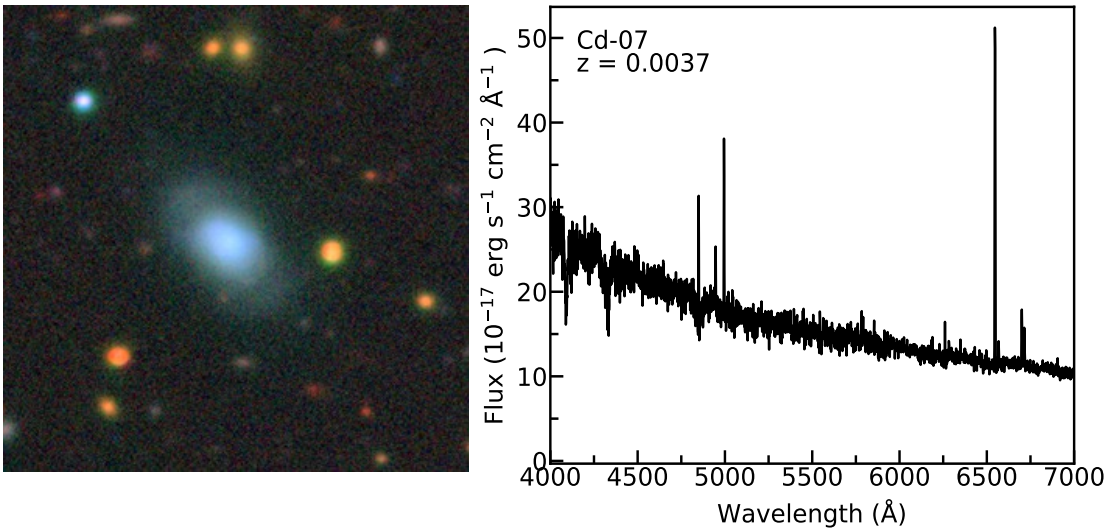

Figure 23: Optical image and the spectrum of compact merging dwarf galaxy Cd-07.

3.2.8 Cd-08

Cd-08 has sky-position RA (J2000) = $10^h\ 19^m\ 01.49^s$ and Dec. (J2000) = $+21°\ 17'\ 00.96''$ and redshift $z = 0.0036$. The g, r and b-band absolute magnitudes of the galaxy are 14.56 mag, 14.34 mag and −17.11 mag, respectively. The galaxy lying at a distance of 24.80 Mpc is a star-forming field galaxy having 2 neighboring objects within the search criteria. Morphologically, it is a galaxy having a tidal tail and stellar stream (TS). The line-of-sight radial velocity of the galaxy is 1083 km s^{-1}. The optical image and spectrum of the galaxy are shown in Figure 24. It has a strong tidal tail extended toward a north direction and we can also see a faint low-surface brightness blue tail extension diametrically opposite to the first one. The overall color of the galaxy is $g - r = 0.22$ mag. It has stellar mass and gass mass 7.2×10^8 M$_\odot$ and 5.2×10^8 M$_\odot$ respectively. It is located in a field environment. The spectrum shows a strong emission line with absorption in higher-order Balmer lines.

3.2.9 Cd-09

Cd-09 has sky-position RA (J2000) = $10^h\ 29^m\ 49.27^s$ and Dec. (J2000) = $+16°\ 10'\ 51.24''$. The g, r and b-band absolute magnitudes of the galaxy are 15.12 mag, 14.89 mag and −17.89 mag respectively. The galaxy is located at a distance of 45.98 Mpc. The optical image and spectrum of Cd-07 are displayed in Figure 25. The central region of the galaxy is spherical and blue in color whose outer region is reddish. It is a starburst compact galaxy having stellar stream and loop (SL) features as its morphology. This galaxy has no neighbors within a sky-projected distance of less than 700 kpc. The radial velocity of the galaxy is 3265 km s^{-1}. This galaxy has a stellar mass of 1.5×10^9 M$_\odot$ and total HI mass of 1.5×10^8 M$_\odot$. The SDSS spectrum shows strong emission in H$_\alpha$ and OIII lines.

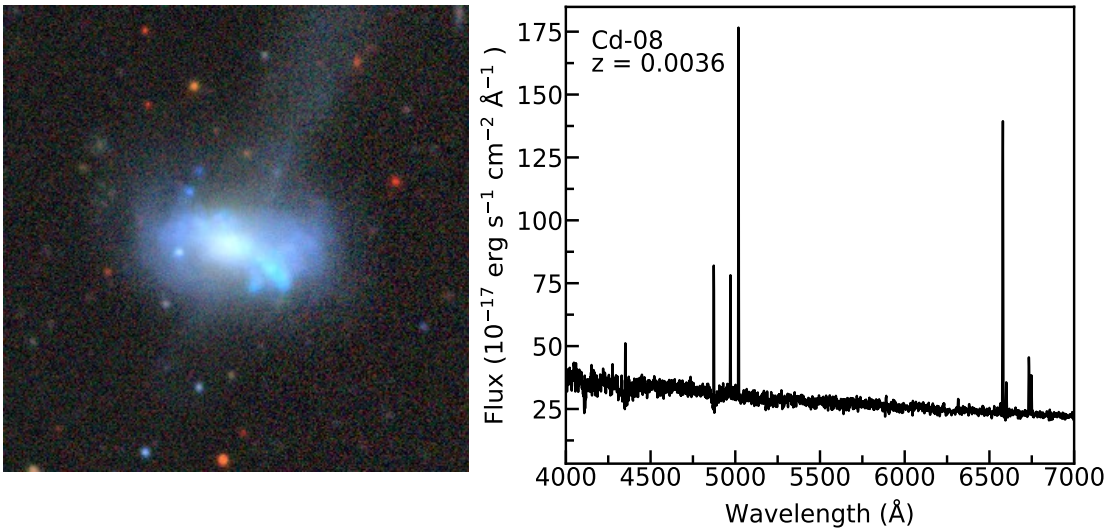

Figure 24: Optical image and the spectrum of compact dwarf galaxy Cd-08.

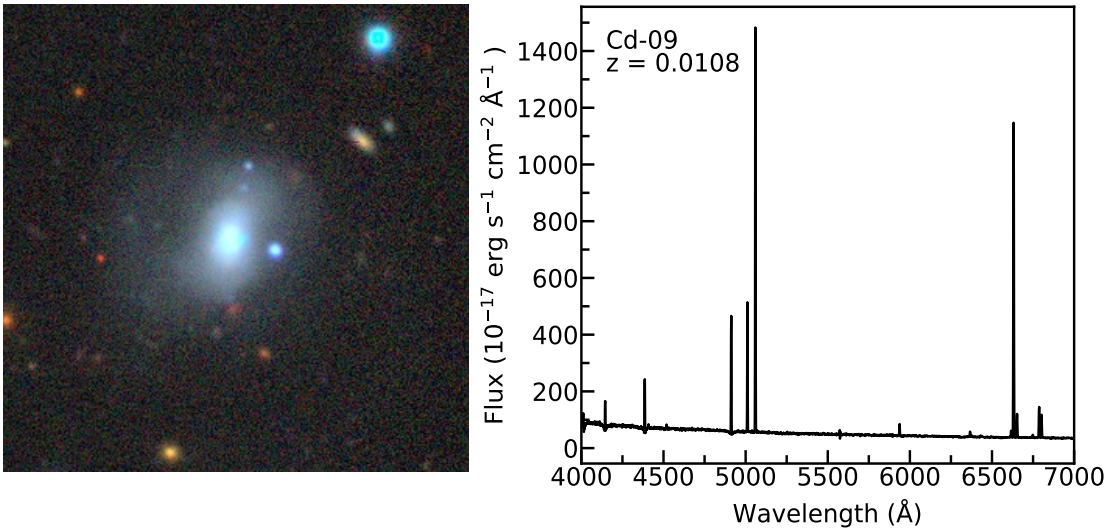

Figure 25: Optical image and the spectrum of Cd-09.

3.2.10 Cd-10

Cd-10 is a starburst compact dwarf galaxy having RA (J2000) = $11^{h}\ 48^{m}\ 18.19^{s}$ and Dec. (J2000) = $-01^{\circ}\ 38'\ 23.64''$ with a spectroscopic redshift of 0.0130. The g, r and b-band absolute magnitudes of the galaxy are 15.88 mag, 15.66 mag and −17.54 mag respectively. It is a starburst field galaxy located at a distance of 55.44 Mpc and has 5 neighboring objects within the search criteria. Figure 26 shows the optical image and the spectrum of Cd-10. The central region of the galaxy is spherical and blue in color. It has a strong tidal tail extended toward a north direction and we can also see a faint low-surface brightness blue tail extended diametrically opposite to the first one. Morphologically, it is a shell-featured (Sh) galaxy. The line-of-sight radial velocity of the galaxy is 3907 km s^{-1}. The overall color of the galaxy is $(g - r) = 0.22$ mag. It has stellar mass and gass-mass of 1.0×10^{9} $M_{\odot}$ and 8.7×10^{9} $M_{\odot}$ respectively. The SDSS

spectrum shows a strong emission line with absorption in higher-order Balmer lines.

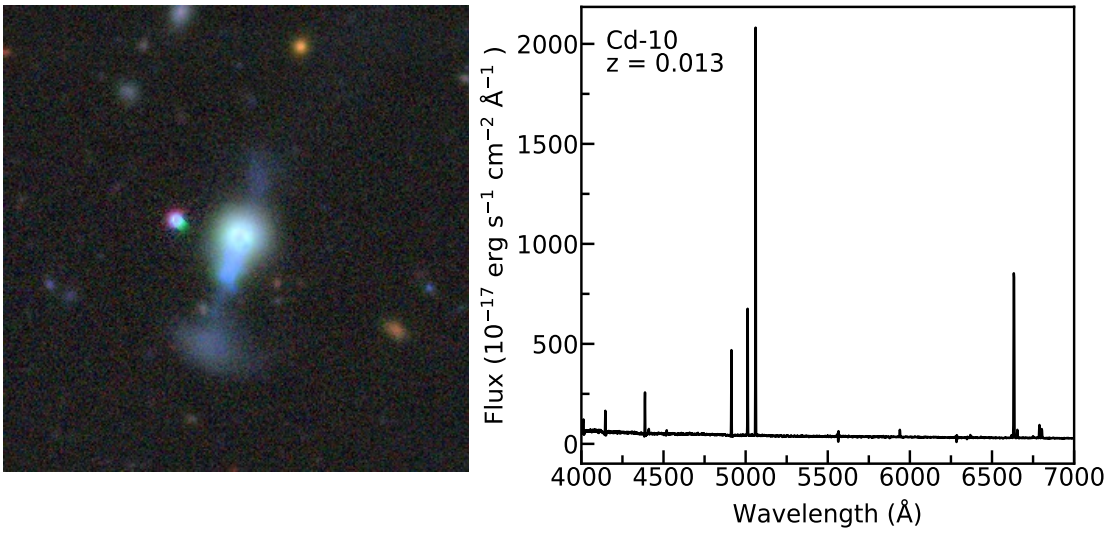

Figure 26: Optical image and the spectrum of Cd-10.

3.2.11 Cd-11

Cd-11 is a compact dwarf galaxy having RA (J2000) = 11^{h} 50^{m} 02.72^{s} and Dec. (J2000) = $+15°\,01'\,23.16''$ with a spectroscopic redshift of 0.0024. The g, r and b-band absolute magnitudes of the galaxy are 14.81 mag, 14.72 mag and −15.29 mag respectively. The galaxy is located at a distance of 11.90 Mpc and has 52 neighboring objects within a sky-projected distance of less than 700 kpc. Figure 27 shows the optical image and the spectrum of the galaxy Cd-11. The central region of the galaxy is tadpole-like in shape and blue in color. The outer shell is relatively reddish in color. Morphologically, it is a shell-featured (Sh) galaxy. The line-of-sight radial velocity of the galaxy obtained from the Extragalactic Database (NED) is 751 km s^{-1}. This galaxy has a stellar mass of 8.3×10^{7} $M_{\odot}$ and total HI of the system is 2.5×10^{8} $M_{\odot}$. The SDSS spectrum shows strong emission in H_{α} and OIII lines.

3.2.12 Cd-12

Cd-12 is a starburst compact dwarf galaxy having sky position RA (J2000) = 11^{h} 52^{m} 37.18^{s} and Dec. (J2000) = $-02°\,28'\,09.84''$ at a redshift of 0.0034. The g, r, and b-band absolute magnitudes of the galaxy are 14.18 mag, 14.10 mag and −16.36 mag respectively. The galaxy is located a distance of 14.39 Mpc and has 6 neighboring objects within the search criteria. The line-of-sight radial velocity of the galaxy is 1040 km s^{-1}. Figure 28 shows the optical image and the spectrum of the galaxy Cd-12 which is taken from the Legacy survey. The elongated central region is deep blue in color. It has a strong tidal tail extended toward a north direction and we can also see a faint low-surface brightness blue

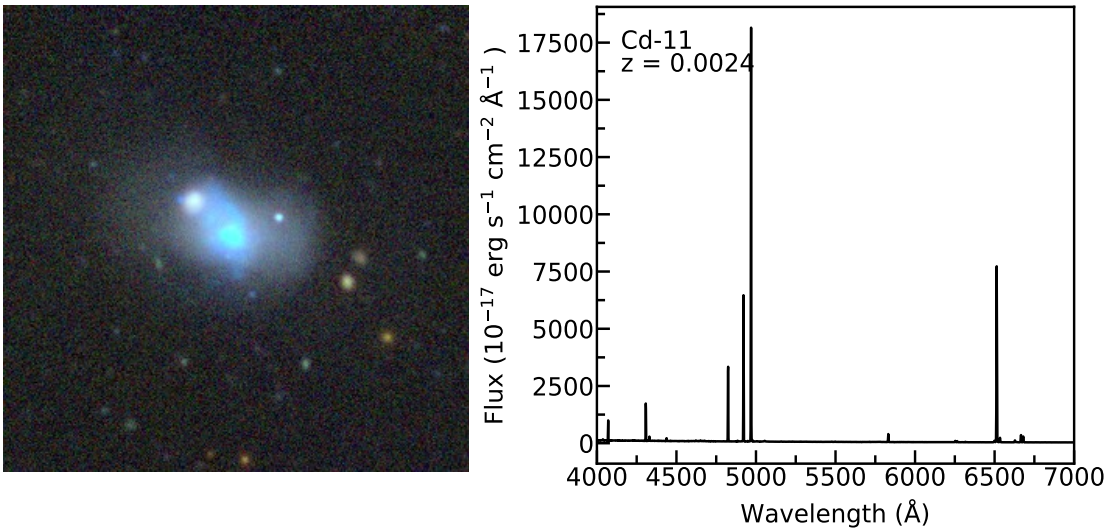

Figure 27: Optical image and the spectrum of compact dwarf galaxy Cd-11.

tail extension diametrically opposite to the first one. Morphologically, it is an extended tail-featured galaxy. The overall color of the galaxy is $(g - r) = 0.08$ mag. It has stellar mass and gass-mass of 2.1×10^8 $M_\odot$ and 3.3×10^8 $M_\odot$ respectively. It is located in a field environment. The spectrum shows strong emission lines.

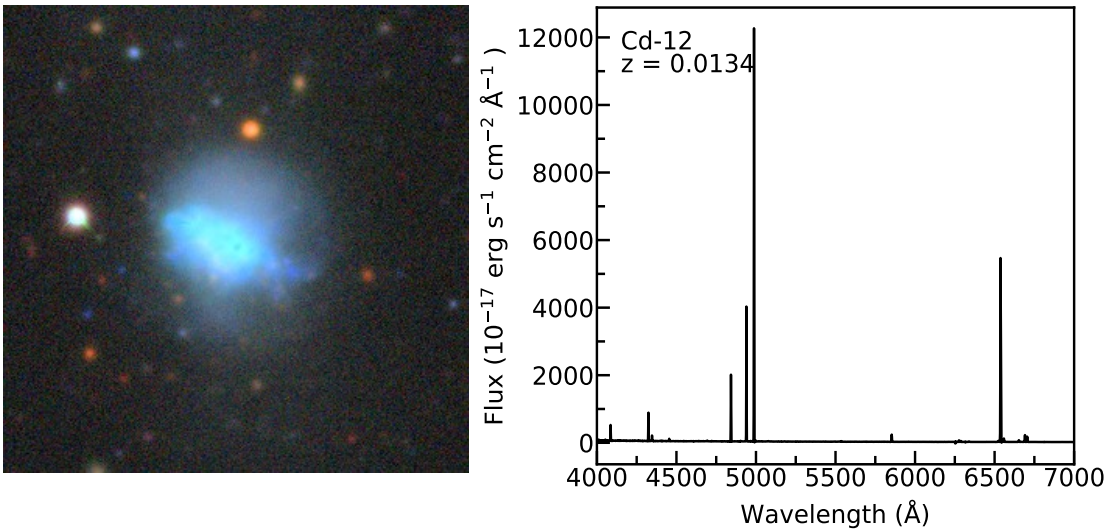

Figure 28: Optical image and the spectrum of Cd-12.

3.2.13 Cd-13

Figure 29 shows the image and spectrum of the starburst compact merging dwarf galaxy Cd-13 having RA (J2000) = $13^{\rm h}$ $43^{\rm m}$ $13.13^{\rm s}$ and Dec. (J2000) = $+36^\circ\,44'\,57.48''$ with a spectroscopic redshift of 0.0197. The g, r and b-band absolute magnitudes of the galaxy are 15.64 mag, 15.28 mag and −18.65 mag respectively. Cd-13 is a field galaxy located at a distance of 84.44 Mpc and has 6 neighboring objects. The line-of-sight radial velocity

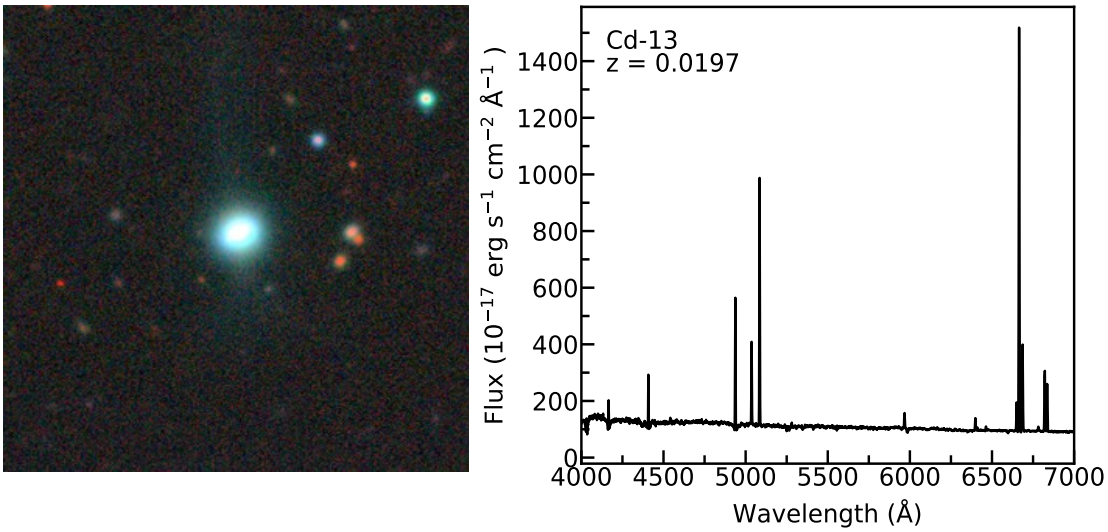

Figure 29: Optical image and the spectrum of Cd-13.

of the galaxy is 5930 km s^{-1}. The galaxy is spherical in shape, with a tidal tail and stellar stream (TS) along its major axis. The central region of the galaxy is saturated and the outer region is blue in color. There are 6 neighboring galaxies around it. This galaxy has a stellar mass of 5.0×10^9 M$_\odot$ and total HI mass of 2.1×10^9 M$_\odot$. The spectrum shows strong emission in H$_\alpha$ and OIII lines as well as strong absorption lines in the Balmer region.

3.2.14 Cd-14

Cd-14 is a starburst compact dwarf galaxy having RA (J2000) = $13^h\ 43^m\ 26.98^s$ and Dec. (J2000) = $+43°\ 11'\ 18.60''$ with a spectroscopic redshift of 0.0083. The g, r and b-band absolute magnitudes of the galaxy are 16.18 mag, 15.98 mag and −16.27 mag respectively. The galaxy is located at a distance of 35.27 Mpc and has 5 neighboring objects within a sky-projected distance of less than 700 kpc. The line-of-sight radial velocity of the galaxy is 2510 km s^{-1}. Figure 30 displays the optical image and the spectrum of Cd-14. The galaxy is elongated in shape having a shell feature. It has a strong tidal tail extended toward a north direction and we can also see a faint low-surface brightness blue tail extension diametrically opposite to the first one. The overall color of the galaxy is $(g - r) = 0.20$ mag. It has stellar mass and gass-mass of 3.1×10^8 M$_\odot$ and 2.5×10^9 M$_\odot$ respectively. It is located in a field environment. Its spectrum shows a strong emission line.

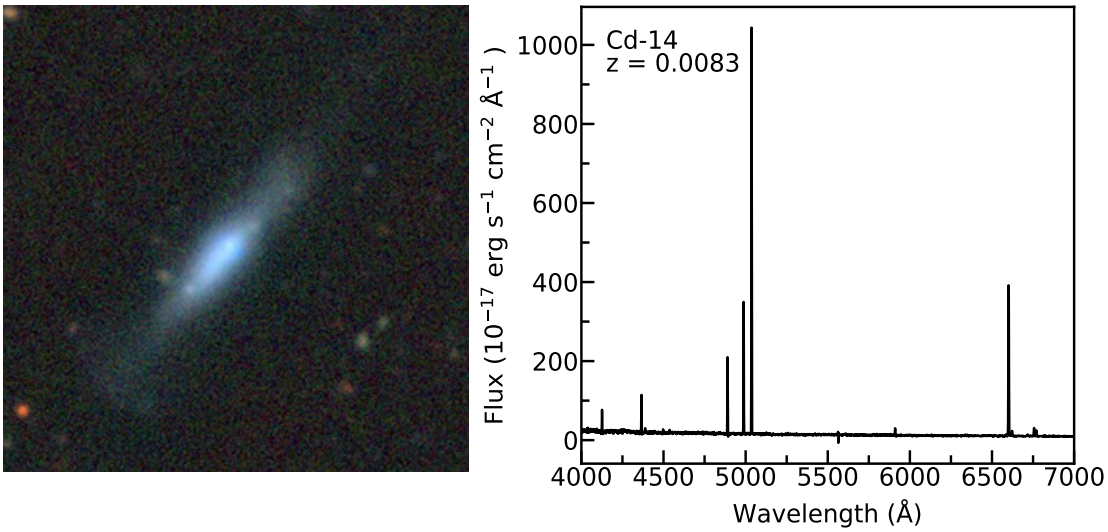

Figure 30: Optical image and the spectrum of Cd-14.

3.2.15 Cd-15

Cd-15 is a star-forming compact dwarf galaxy having RA (J2000) = 23^{h} 19^{m} 58.01^{s} and Dec. (J2000) = $-00°\ 59'\ 07.80''$ with a redshift of 0.0121. The g, r and b-band absolute magnitudes of the galaxy are 16.12 mag, 15.81 mag and −17.12 mag respectively. The galaxy is located at a distance of 51.57 Mpc in a field environment and has 3 neighboring objects within a sky-projected distance of less than 700 kpc and a relative line-of-sight radial velocity of less than ±700 km s^{-1}. The line-of-sight radial velocity of the galaxy is 3634 km s^{-1}. Figure 31 shows the optical image and the spectrum of the galaxy Cd-15. The central region is blue and the outer region is reddish in color. Morphologically, the galaxy has a tidal tail and stellar stream along a north direction. This galaxy has a stellar mass of 1.0×10^{9} $M_{\odot}$ and total HI mass of 6.7×10^{9} $M_{\odot}$. The spectrum shows strong emission in H_{α} and OIII lines and strong absorption in Balmer lines.

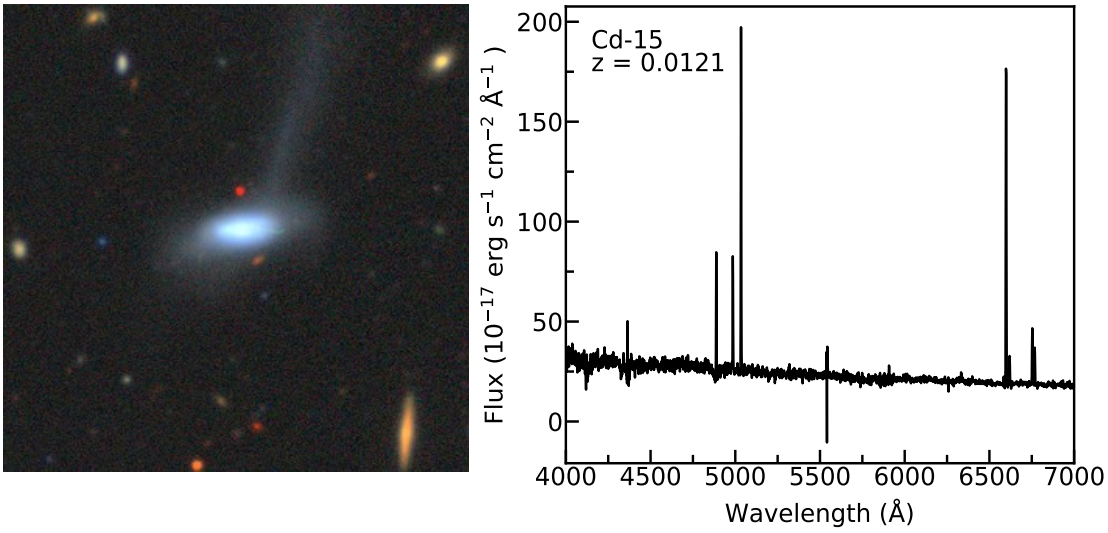

Figure 31: Optical image and the spectrum of Cd-15.

3.3 Extended Merging Dwarf Galaxies

Below we briefly discuss the extended merging dwarf galaxies in our study. Figures 32 to 41 show their $(g-r-i)$ combined tri-color optical image and the spectrum obtained from the SDSS sky server. The X-axis is the rest frame wavelength and the Y-axis shows the flux.

3.3.1 Ed-01

Ed-01 is an extended merging dwarf galaxy of starburst subclass having sky position RA (J2000) = $01^{h}\ 25^{m}\ 34.97^{s}$ and Dec. (J2000) = $+07^{\circ}\ 59'\ 26.88''$ and redshift of 0.0097. The g, r and b-band absolute magnitudes of the galaxy are 15.18 mag, 15.14 mag and -17.66 mag respectively. The $(g-r)$ color of Ed-01 is 0.04 mag. The galaxy is located at a distance of 41.26 Mpc and has 9 neighboring objects within the search criteria. Figure 32 shows the optical image and the spectrum of the galaxy Ed-01. As we can see, it is not a fully merged system and the two prominently disturbed dwarf galaxies are also visible. Both interacting galaxies are blue and star-forming. Morphologically, the galaxy is interacting and merged (IM). It has stellar mass and gass-mass of 6.0×10^{8} $M_{\odot}$ and 1.9×10^{9} $M_{\odot}$, respectively. It is located in a field environment. The spectrum in the right panel of Figure 32 shows that the galaxy is pure of emission type and OIII and H_{α} lines are the strong emission lines.

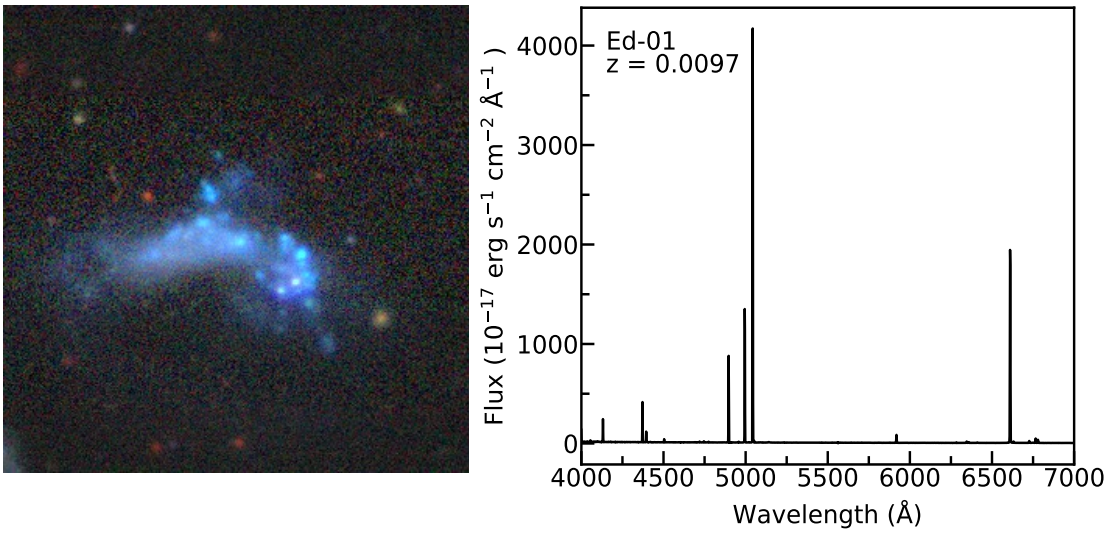

Figure 32: Optical image and the spectrum of Ed-01.

3.3.2 Ed-02

Ed-02 is an extended merging dwarf galaxy of starburst subclass with RA (J2000) = 08^{h} $33^{m}\ 22.97^{s}$ and Dec. (J2000) = $+29^{\circ}\ 32'\ 18.96''$ at a spectroscopic redshift of 0.0069. The g, r and b-band absolute magnitudes of the galaxy are 13.06 mag, 12.73 mag and $-$

18.94 mag respectively. The SDSS $(g - r)$ color of Ed-02 is 0.33 mag. The galaxy is located at a distance of 29.29 Mpc in a field environment and has 3 neighboring objects. The line-of-sight radial velocity of the galaxy is 2082 km s^{-1}. Figure 33 shows the optical image and the spectrum of the galaxy Ed-02. It is not a fully merged system and the bar-like structure is also visible. The interacting galaxies are blue and star-forming. It has stellar mass and gass-mass of 5.7×10^9 $M_\odot$ and 8.1×10^8 $M_\odot$ respectively.

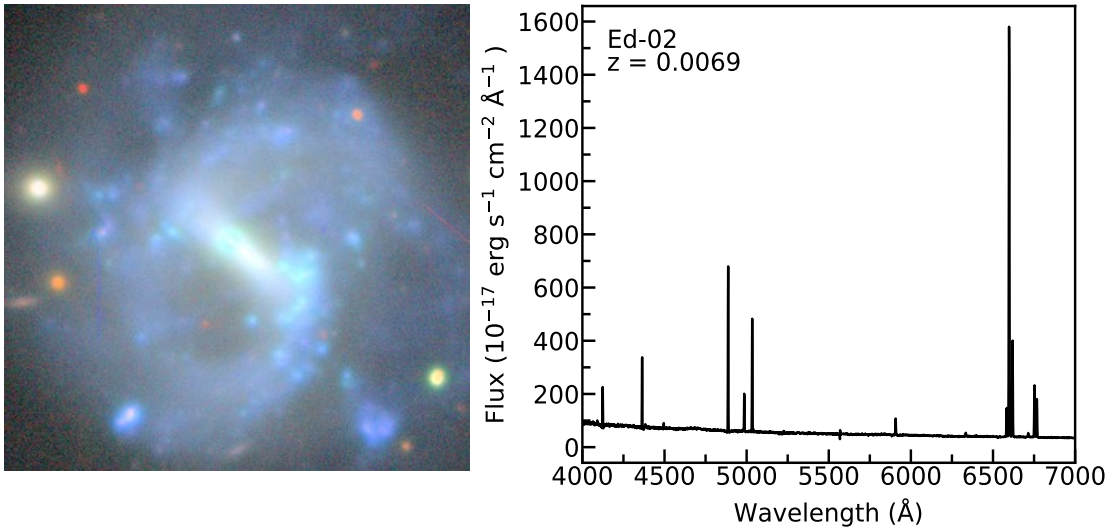

Figure 33: The $(g - r - i)$ tricolor optical image and the spectrum of extended merging dwarf galaxy Ed-02.

3.3.3 Ed-03

Ed-03 is a starburst galaxy located at RA (J2000) = 11^h 25^m 31.80^s and Dec. (J2000) = $+38°$ $03'$ $37.80''$ with a spectroscopic redshift of 0.0070 (Figure 34). The g, r and b-band absolute magnitudes of the galaxy are 14.24 mag, 14.01 mag and −17.83 mag respectively. It is a field galaxy located at a distance of 29.72 Mpc and has 12 neighboring objects within the search criteria. The line-of-sight radial velocity of the galaxy obtained from NED is 2110 km s^{-1}. It is not a fully merged system and the two prominently disturbed dwarf galaxies connected by a bridge are also visible. Both the interacting galaxies are blue and star-forming. Morphologically, the galaxy is interacting merged and shell featured (IMSh) in which progenitor is visibly distinct. The shell is reddish in color as compared to its blue colored elongated main body. The overall color of the galaxy is $(g - r) = 0.23$ mag. It has stellar mass and gass-mass of 1.4×10^9 $M_\odot$ and 6.1×10^8 $M_\odot$ respectively. The spectrum shows that the galaxy is purely emission type.

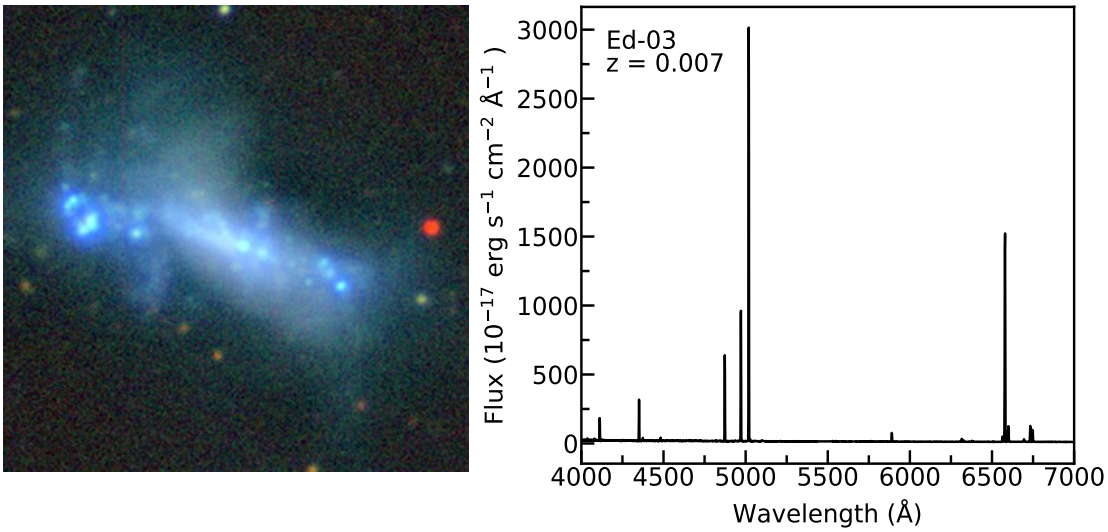

Figure 34: Optical image and the spectrum of extended merging dwarf galaxy Ed-03.

3.3.4 Ed-04

Ed-04 is a starburst galaxy. It has sky-position RA (J2000) = 12^{h} 53^{m} 14.00^{s} and Dec. (J2000) = $+04°\,27'\,54.00''$ and has redshift of 0.0024. The galaxy is at a distance of 9.68 Mpc surrounded by 26 neighboring objects within the search criteria. The line-of-sight radial velocity of the galaxy is 716 km s^{-1}. As we can see in Figure 35, the galaxy is a shell featured (Sh) in which a reddish color shell can be seen outside the blue color main body. It is not a fully merged system. The overall color of the galaxy is 0.30 mag. It has stellar mass of 6.6×10^{8} $M_{\odot}$. It is located in a dense environment. The spectrum shows a strong emission line with absorption in higher-order Balmer lines.

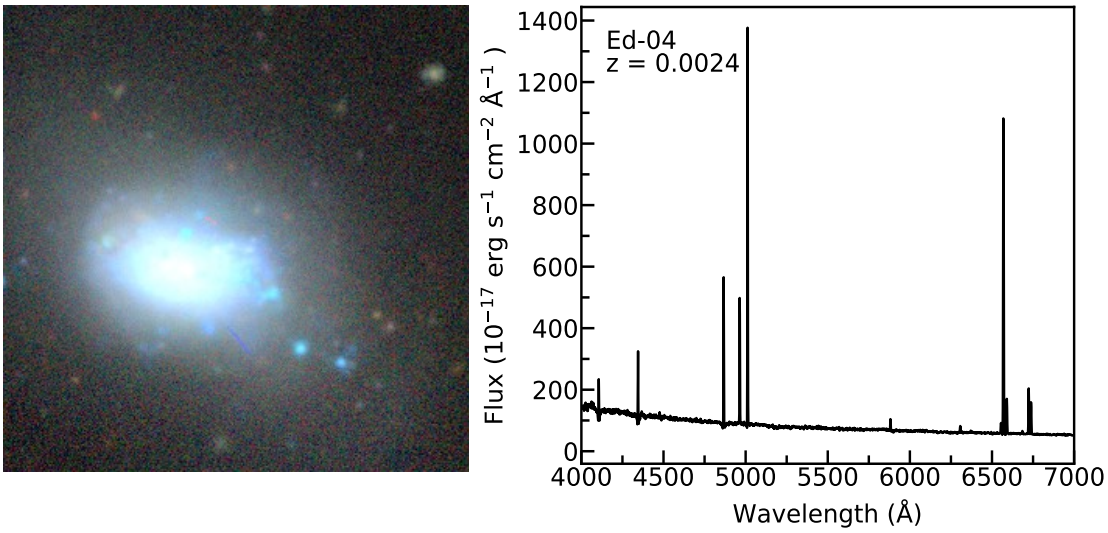

Figure 35: Optical image and the spectrum of extended merging dwarf galaxy Ed-04.

3.3.5 Ed-05

Ed-05 is a star-forming extended merging dwarf galaxy with sky-position RA (J2000) = $13^{h}\ 16^{m}\ 52.32^{s}$ and Dec. (J2000) = $+12^{\circ}\ 32'\ 53.52''$ at a spectroscopic redshift of $z = 0.0032$. The g, r and b-band absolute magnitudes of the galaxy are 13.85 mag, 13.55 mag and −16.49 mag respectively. The $(g - r)$ color of Ed-05 is 0.30 mag. It is located at a distance of 13.55 Mpc and has 9 neighboring objects within a sky-projected distance of less than 700 kpc. The line-of-sight radial velocity of the galaxy is 958 km s^{-1}. Figure 36 shows the $(g - r - i)$ combined tri-color optical image of the galaxy and its spectrum. Morphologically, the galaxy is a shell featured (Sh) whose central region is bright. It has stellar mass and gass-mass of 5.4×10^{8} $M_{\odot}$ and 9.1×10^{9} $M_{\odot}$, respectively. It is located in a field environment. The SDSS spectrum shows a strong emission line with absorption in higher-order Balmer lines.

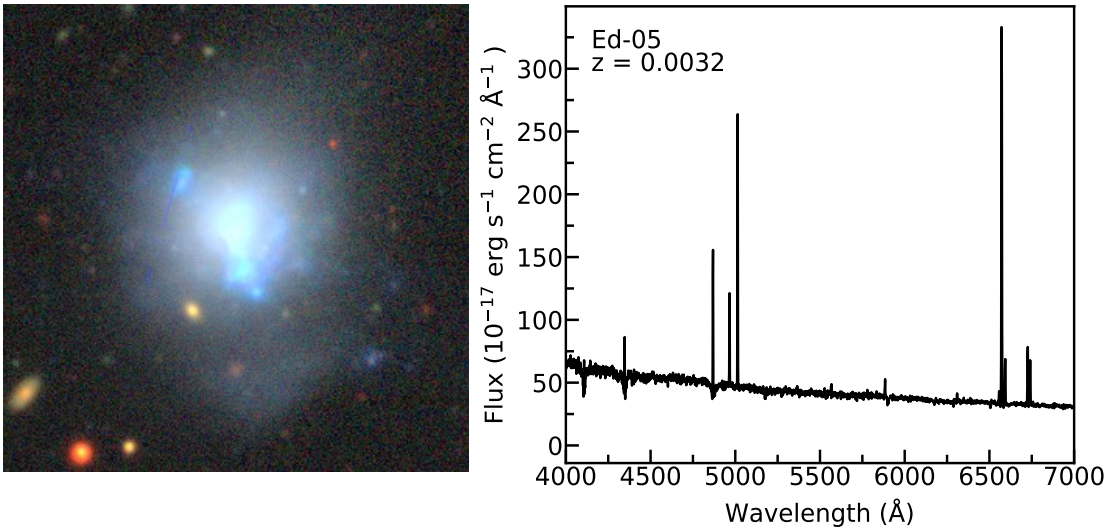

Figure 36: Optical image and the spectrum of extended merging dwarf galaxy Ed-05.

3.3.6 Ed-06

Ed-06 is a starburst extended merging dwarf galaxy having sky position of RA (J2000) = $13^{h}\ 42^{m}\ 59.40^{s}$ and Dec. (J2000) = $+52^{\circ}\ 41'\ 17.88''$ and redshift $z = 0.0059$. The g, r and b-band absolute magnitudes of the galaxy are 16.18 mag, 15.87 mag and −15.49 mag respectively. The $(g - r)$ color of Ed-06 is 0.31 mag. The galaxy is located at a distance of 25.03 Mpc and has 9 neighboring objects within a sky-projected distance of less than 700 kpc. The line-of-sight radial velocity of the galaxy is 1803 km s^{-1}. Figure 37 shows the optical image of the galaxy Ed-06 and its spectrum. The galaxy is interacting (I) whose central region is blue. Its body is elongated to the N-S direction. It has stellar mass of 2.2×10^{8} $M_{\odot}$ and is located in a field environment. The spectrum shows a strong emission line with absorption in higher-order Balmer lines.

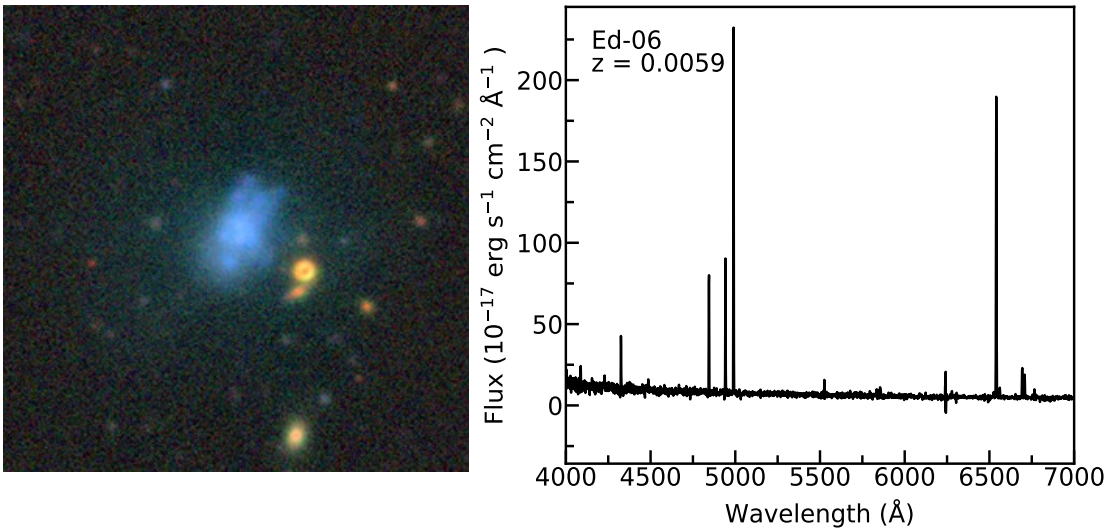

Figure 37: Optical image and the spectrum of extended merging dwarf galaxy Ed-06.

3.3.7 Ed-07

Ed-07 is a starburst galaxy with RA (J2000) = 13^{h} 51^{m} 53.57^{s} and Dec. (J2000) = $+64°\ 22'\ 22.08''$ and redshift $z = 0.0058$. The g, r and b-band absolute magnitudes of

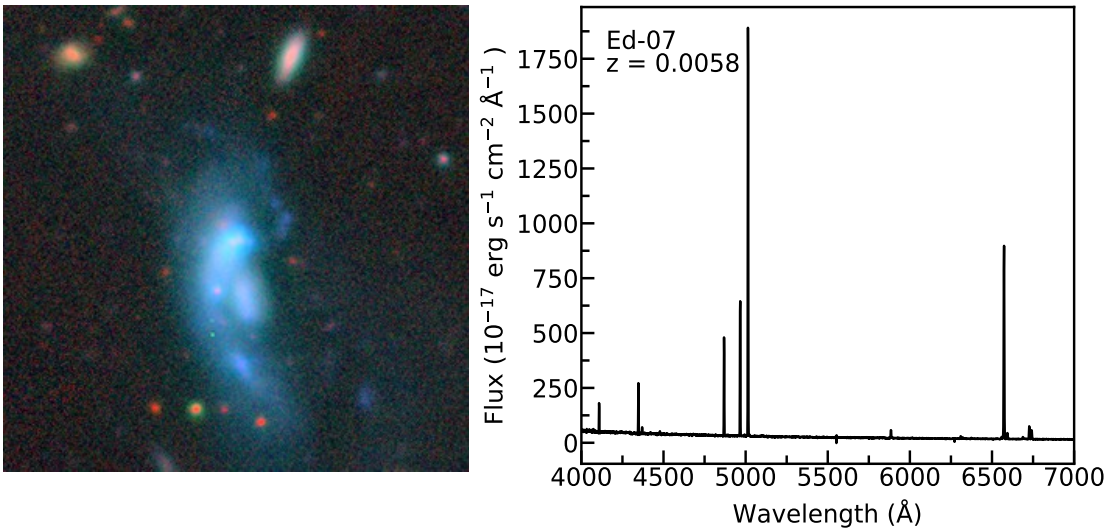

Figure 38: Optical image and the spectrum of extended merging dwarf galaxy Ed-07.

the galaxy are 15.11 mag, 14.93 mag and − 16.87 mag respectively. The SDSS $(g - r)$ color of Ed-07 is 0.18 mag. The galaxy is located at a distance of 28.40 Mpc and has 5 neighboring objects within the search criteria. The line-of-sight radial velocity of the galaxy is 1763 km s^{-1}. Figure 38 shows the optical image of the galaxy Ed-07 and its spectrum. Morphologically, the galaxy is interacting merged (IM) which is blue in color and is elongated in shape in the N-S direction. it is not a fully merged system. A stellar tail-like structure is observed along its length. It has stellar mass of 4.9×10^{9} $M_{\odot}$ and is located in a dense environment. The spectrum shows that the galaxy is an emission type.

3.3.8 Ed-08

Ed-08 is a starburst subclass of galaxy having RA (J2000) = 14^{h} 54^{m} 11.71^{s}, Dec. (J2000) = $+30^{\circ}$ $12'$ $34.20''$ and redshift z = 0.0094. The g, r and b-band absolute magnitudes of the galaxy are 14.72 mag, 14.60 mag and − 18.03 mag respectively. The $(g - r)$ color of Ed-08 is 0.12 mag. The galaxy is located at a distance of 39.98 Mpc and has 3 neighboring objects. The line-of-sight radial velocity of the galaxy is 2809 km s^{-1}. Figure 39 shows the optical image of the galaxy Ed-08 and its spectrum. It is also not a fully merged system. The galaxy is a guitar galaxy having an antenna (A) along the N-E direction. The main body of the galaxy is blue in color but the antenna is reddish as compared to its main body. It has a stellar mass of 1.1×10^{9} $M_{\odot}$. It is located in a field environment. The spectrum shows a strong emitting feature of the galaxy.

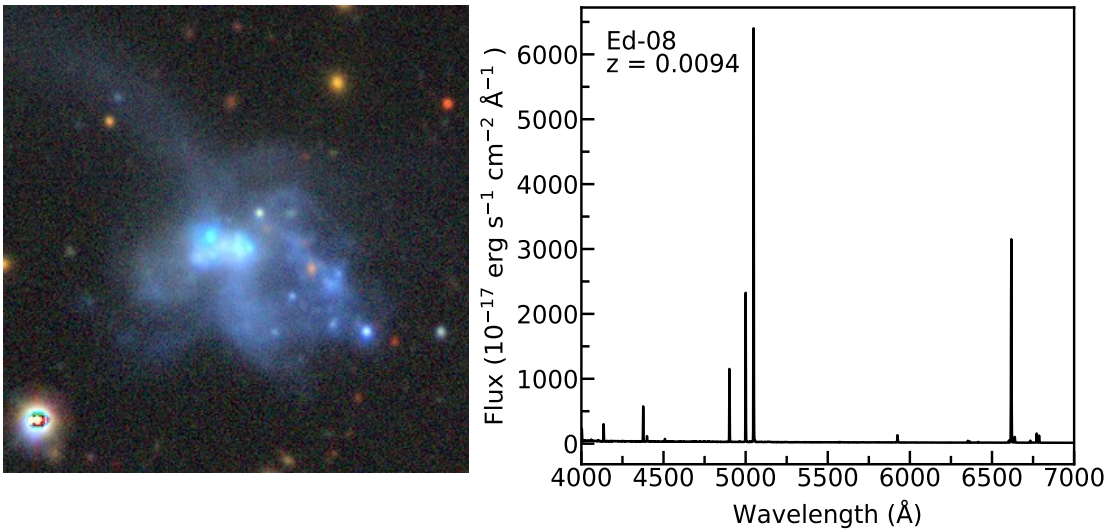

Figure 39: Optical image and the spectrum of extended merging dwarf galaxy Ed-08.

3.3.9 Ed-09

Ed-09 is a starburst extended merging dwarf galaxy having RA (J2000) = 15^{h} 36^{m} 19.34^{s} and Dec. (J2000) = $+30^{\circ}$ $40'$ $51.96''$ at a spectroscopic redshift of 0.0058. The g, r and b-band absolute magnitudes of the galaxy are 14.84 mag, 14.59 mag and − 17.12 mag respectively. The $(g - r)$ color of Ed-09 is 0.25 mag. The distance of the galaxy is 28.50 Mpc. The line-of-sight radial velocity of the galaxy is 1756 km s^{-1}. Figure 40 shows the $(g - r - i)$ combined tri-color optical image of the galaxy Ed-09 and its spectrum. The galaxy is an interacting galaxy having an elongated shape with a stellar tail-like structure along its major axis (N-S direction). The stellar mass of the galaxy is 8.1×10^{8} $M_{\odot}$. It is located in a field environment and has 2 neighboring galaxies. The SDSS spectrum shows that the galaxy is purely emission type.

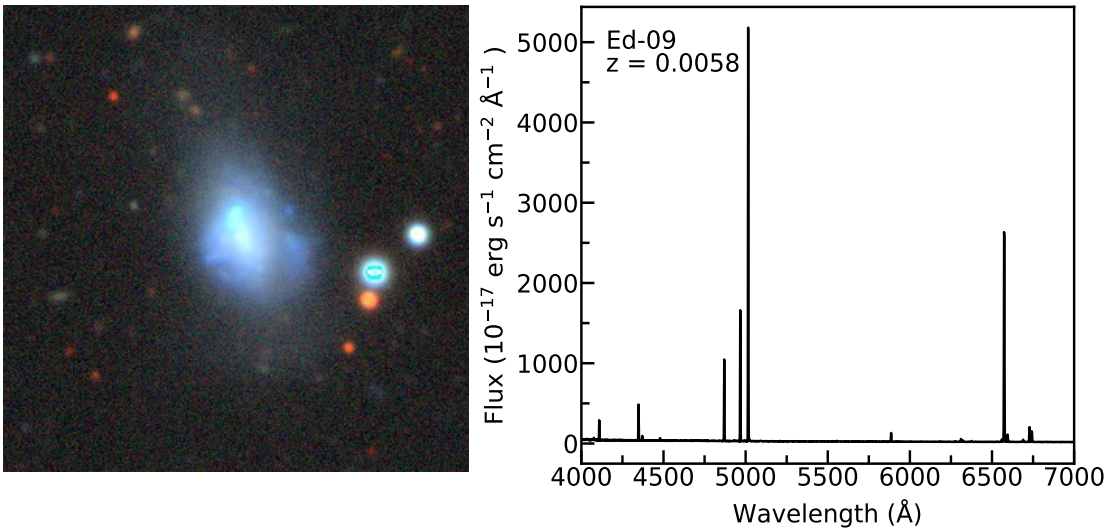

Figure 40: Optical image and the spectrum of extended merging dwarf galaxy Ed-09.

3.3.10 Ed-10

Ed-10 is galaxy located at the sky position of RA (J2000) = 16^{h} 06^{m} 40.99^{s}, Dec.(J2000) = $+6°$ $34'$ $50.88''$ and redshift $z = 0.0058$. It is a star-forming shell-featured galaxy with g and r band absolute magnitudes of 14.69 mag and 14.33 mag respectively. The SDSS $(g - r)$ color of E-10 is 0.36 mag and its b-band absolute magnitude is $-$ 16.52 mag. It is a field galaxy situated at a distance of 20.40 Mpc. The line-of-sight radial velocity of the galaxy obtained from NED is 1749 km s^{-1}. The optical image of the galaxy and its optical spectrum is shown in Figure 41. In this image, we see that the central region is blue and dense as compared to the outer region of the galaxy. There is an extended tail-like structure along the major axis of the galaxy that is reddish in color. It has stellar mass and gass-mass of 6.9×10^{8} $M_{\odot}$ and 1.4×10^{9} $M_{\odot}$ respectively. The spectrum shows a strong emission line with absorption in higher-order Balmer lines.

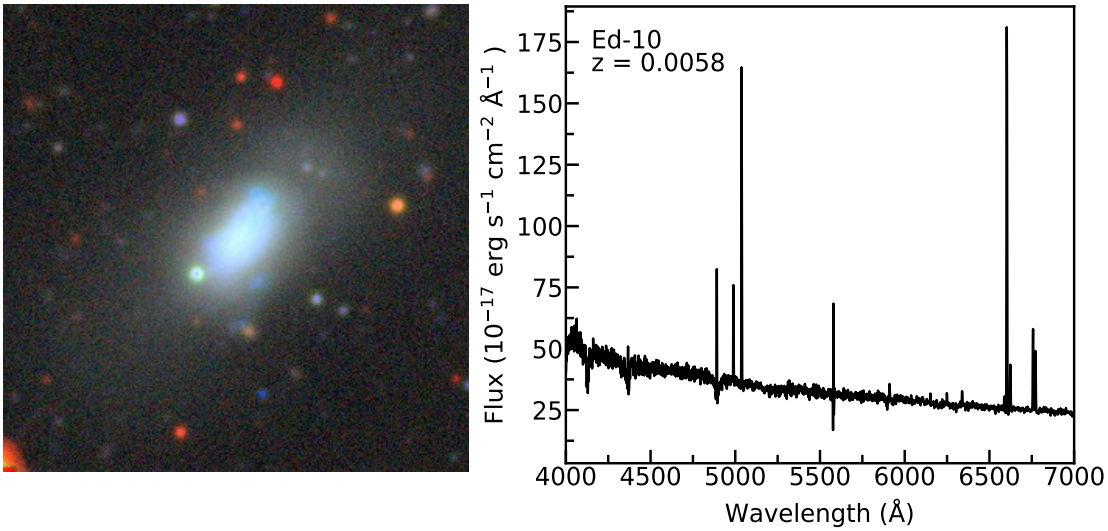

Figure 41: Optical image and the spectrum of extended merging dwarf galaxy Ed-10.

3.4 Method

3.4.1 Data Acquisition

In this work, we extensively use the SDSS DR12 archival data to measure the morphological and chemical parameters of the galaxy (Aihara et al., 2011). We obtained the SDSS $g-$ and $r-$band images and optical fiber spectrum from the SDSS Data Archive Server (DAS). The images and spectrum are already well-calibrated and we do not perform any operation in this regard. Both the image and the spectrum data are in the FITS file format. FITS stands for Flexible Image Transport System and is a digital file format used in astronomy for long-term storage, transmission and processing of astronomical data such as 2-D images, 2-D tables, spectra, data cubes, etc. FITS files contain both the images and the binary data in a specific format and many programming languages can read and write such files. Moreover, such files store other information like time and date of observation, place of the telescope and weather at observation time. The SDSS fiber has a diameter of 3 arcsecs. Hence, the observed spectrum only covers a small portion of the galaxy area (Abazaj ian et al., 2003). In Figure 42, we show the data acquisition process from the SDSS data server. For a given coordinate of the galaxy, we first use the SDSS navigate tool to identify the galaxy's position. Once the object is identified, we then use explore tool. The Explore tab provides a link to the FITS file of both spectrum and imaging data which we download for our analysis.

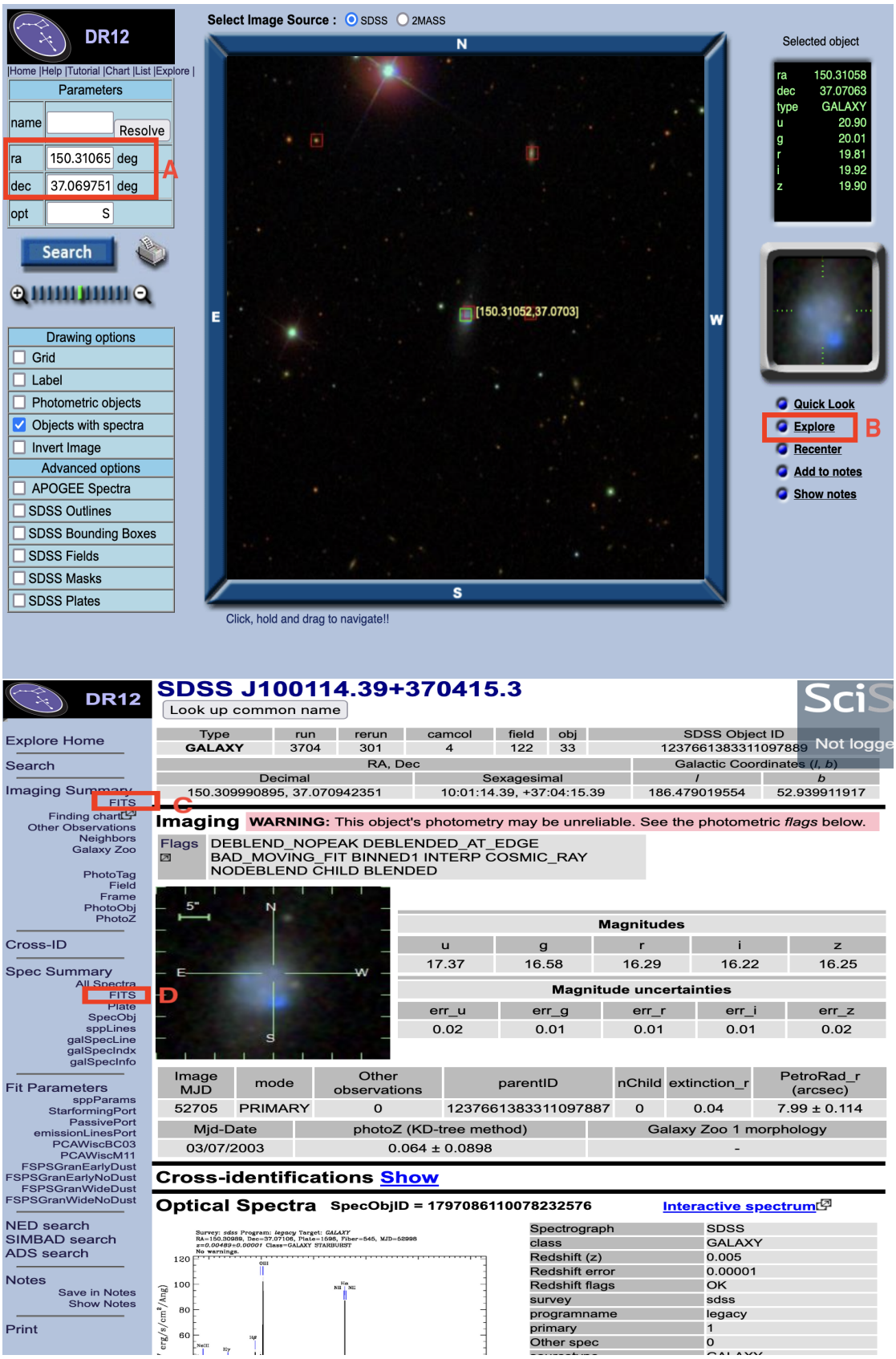

Figure 42: Process of data acquisition using the SDSS graphical interface. The four positions A, B, C, and D are highlighted, where RA and Dec. are interred in A and click the search button. When the object of interest appears in the main navigation window, we use explore button (B) to go to explore tab. From the explore tab, we can download fits files of imaging and spectroscopic data by clicking at C and D respectively.

3.4.2 Spectroscopic Calculations

For the spectroscopic analysis of the galaxies, their FITS files are downloaded and the SDSS DR12 spectral data is extracted with the help of a software called ALADIN of version 11. Then we obtain the flux of the galaxy in erg s^{-1} $cm^{-2}Å^{-1}$ corresponding to the logarithmic value of the wavelength in the extracted data. The wavelength is now expressed on a linear scale. The data were plotted by using the software ORIGIN 8.0 to obtain the spectra of the galaxies. We show an example spectrum of LEDA 2793637 plotted from the extracted data in Figure 43. The spectrum ranges from wavelength 4000 Å to 9000 Å. It shows a strong signature of the star-forming galaxies with prominent emission lines produced by different elements like OI, OII, NII, SII, H_α, H_β, H_γ, H_δ as shown in the Table 4.

Table 4: Emission line list that is widely found in galaxy spectrum. The first and second columns represent the wavelength and name of the emission lines respectively. The third column represents orbital transition configurations and the fourth column represents the elements responsible for emission lines. (source Sharpee et al. (2003)).

Wavelength Å	Line name	Transition	Element
4102.89	H_δ	$n_2 - n_6$	Hydrogen
4341.68	H_γ	$n_2 - n_5$	Hydrogen
4364.43	OIII	1D $2s^2 2p^2$ – 1S $2s^2 2p^2$	Oxygen
4862.68	H_β	$n_2 - n_4$	Hydrogen
4960.29	OIII	3P $2s^2 2p^2$ – 1D $2s^2 2p^2$	Oxygen
5008.24	OIII	3P $2s^2.2p^2$ – 1D $2s^2.2p^2$	Oxygen
6549.86	NII	3P $2s^2 2p^2$ – 1D $2s^2 2p^2$	Nitrogen
6564.61	H_α	$n_2 - n_3$	Hydrogen
6585.27	NII	3P $2s^2 2p^2$ – 1D $2s^2 2p^2$	Nitrogen
6718.29	SII	4S $3s^2 3p^3$ – 2D $3s^2 3p^3$	Sulphur
6732.67	SII	4S $3s^2 3p^3$ – 2D $3s^2 3p^3$	Sulphur

If we magnify the spectrum, the small lines which are barely seen or even not seen in the spectrum will be seen in the broadened form (Figure 43). The magnified form of a small portion around H_α line of the spectrum of LEDA 2793637 is also shown in the inset in which broad NII lines can be seen on either side of H_α line.

Once the emission lines were identified, we fit a Gaussian profile to them. For the redshift correction, the wavelength of all data is divided by $(1 + z)$, z being the redshift of the galaxy. This is applied in the x-axis (wavelength) for each Gaussian fit. On the other hand, the continuum correction of the flux has been done by subtracting the median of two separate regions on either side of the emission line. As we have shown in Figure 44, we calculate the median value from the flat regions in the tails of wavelength range from X_1 *to* X_2 and from X_3 *to* X_4 respectively.

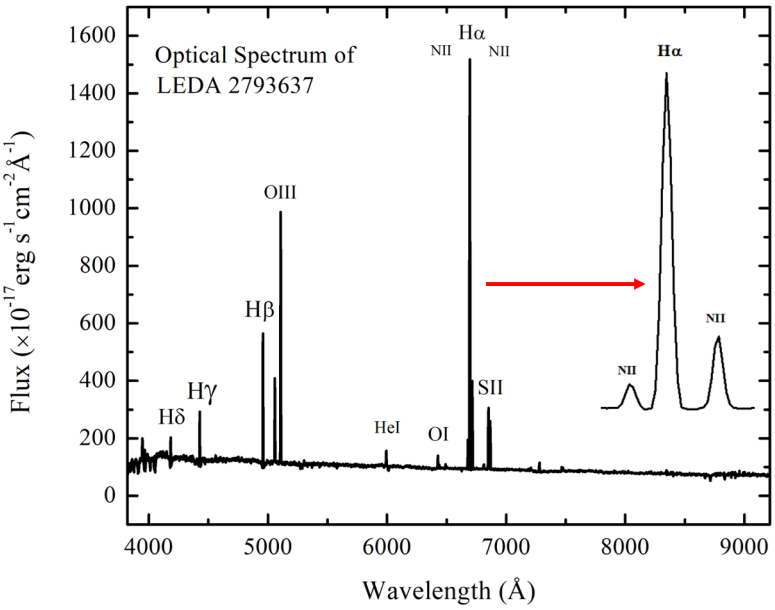

Figure 43: A detailed view of SDSS DR 12 Optical Spectrum of LEDA 2793637, a star-forming galaxy. The emission lines above the continuum are due to different elements Hydrogen, Oxygen, Sulphur and Helium. In the inset, we have a zoom-in version of H_α and NII-doublet emission lines.

The redshift-corrected data of flux and wavelength is plotted and the Gaussian fit of the emission line is obtained. The sample Gaussian fit of the H_α line of an example spectrum is shown in Figure 44, where the red-colored solid line curve is the best-fitted Gaussian curve and black dots represent the observed data. The error bars are also shown.

The emission line profile of the extragalactic object is dominated by Doppler broadening. The atoms/molecules in a gas, which emit the radiation, will have a distribution of velocities. The photon emitted by transition will be either red or blue-shifted by the Doppler effect, depending on the atom's velocity relative to the observer. Since the spectral line is a combination of all of the emitted radiation, the line profile is considered Gaussian in nature. The center is zero shift or an average shift of the system. It was assumed that the characteristic lines get broadened because of Doppler broadening, permitted line cooling and fine structure cooling. These are natural processes; therefore, the Gaussian distribution was expected. Mathematically, a Gaussian distribution is defined as (Squires, 2001);

$$f_G(x) = \frac{1}{\sqrt{2\pi\sigma^2}} e^{\frac{-(x-\mu)^2}{2\sigma^2}} \tag{3.1}$$

where x is a normal random variable, μ is the mean and σ is the standard deviation of the distribution. If the number of events is very large, then the Gaussian distribution function may be used to describe physical events. The Gaussian distribution is a continuous function that approximates the exact binomial distribution of events.

Once we fit the Gaussian curve, we obtain Gaussian parameters such as the height of the

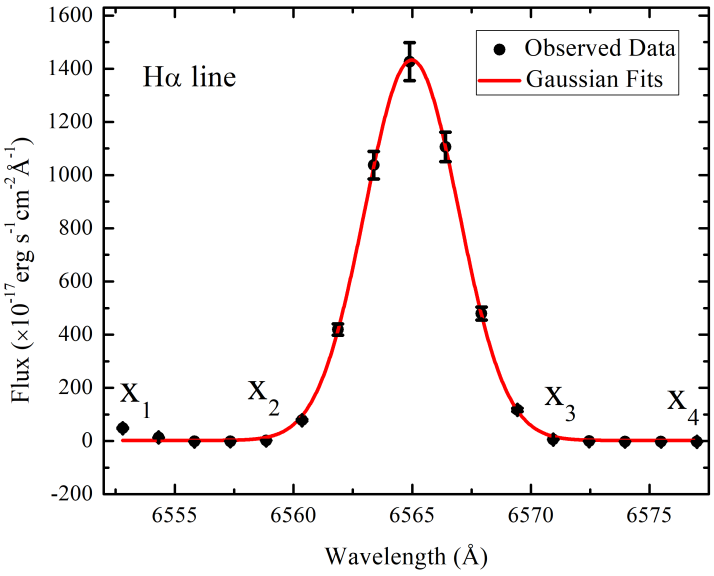

Figure 44: An example of Gaussian fit in H_α emission line. We also marked the two flat regions of the tails by X_1, X_2, X_3 and X_4, where we sample the continuum flux to make continuum correction. The black dots represent observed data points and the red solid line represents the best-fitted Gaussian profile.

Gaussian curve, its area, peak intensity, the wavelength corresponding to peak intensity and Full Width Half Maximum (FWHM). The Gaussian parameters will be enlisted in a separate table and the corresponding elements will be identified. For our analysis, we have fitted four well-known emission lines, H_α, H_β, OIII and NII to get their emission line parameters, such as flux, FWHM and peak intensity.

3.4.2.1 Star Formation Rate (SFR)

The H_α luminosity is the main estimator of the galaxies' instantaneous SFR in this study. When the ionized hydrogen present in the gas and dust clouds surrounding the recently formed stars undergo into the recombination process, H_α line is produced. Massive stars of type O and B generate a powerful radiation field that has the power to ionize hydrogen atoms. At equilibrium condition, the free electrons combine with the ionized hydrogen atoms and produce several emission lines like HeI_{3890}, H_δ, H_γ, $OIII_{4363}$, H_β, $OIII_{4960}$, $OIII_{5008}$, HeI_{5877}, OI_{6366}, NII_{6550}, H_α, NII_{6585}, SII_{6720}, SII_{6732} and $NeIII_{3869}$. The star formation rate is calculated by adopting the empirical formula proposed by Kennicutt (1998) as follows:

$$\mathrm{SFR}(\mathrm{M}_\odot\ \mathrm{yr}^{-1}) = 7.9 \times 10^{-42} \sum L(H_\alpha)(\mathrm{erg\ s}^{-1}). \tag{3.2}$$

Here, $\sum L(H_\alpha)$ is the total luminosity of H_α line calculated by using Gaussian fits. H_α makes out SFR directly and depends very little on the metallicity or the ionization levels

of the gas cloud. Extinction plays a significant effect to SFR among many other factors which is common to optical indicators. Here, we calculate extinction coefficient and calculate SFR after extinction correction. However, SFR can be calculated by using fluxes of X-rays, UV, forbidden recombination lines (OII_{3727}), far infrared, radio etc. which lie in a broad scale of electromagnetic spectrum.

3.4.2.2 Metallicity Measurement

Our understanding of the formation and development of galaxies depends on measuring the chemical histories of galaxies. Metals accumulate over time via each generation of star formation in a simple closed-box model of chemical evolution. Typically, the evolution of a galaxy's metallicity is described in terms of star mass. The stellar mass and galaxy bolometric luminosity both exhibit high correlations with the metallicity of the gas-phase stars. If low mass galaxies contain higher gas fractions than higher mass galaxies, as seen in nearby galaxies, then there will naturally be a correlation between mass and metallicity (McGaugh & de Blok, 1997; Bell & de Jong, 2000; Boselli & Gavazzi, 2006). For measuring metallicities in HII regions without auroral lines, metallicity calibrations based on optical strong-line ratios were originally created. These calibrations, often referred to as empirical methods, are obtained by fitting the observed relationship between Auroral metallicities and strong-line ratios. From the calibration provided by Marino et al. (2013), the emission line metallicity using a line ratio between NII and H_α is calculated as

$$12 + \log(O/H) = 8.743 + 0.462 \times \log(NII/H_\alpha) \tag{3.3}$$

The gas-phase metallicity should be expressed in terms of log(O/H) + 12 rather than units of solar abundance because solar abundances are not a good indicator of the local present-day galactic abundances. The current solar value of oxygen abundance, log(O/H) + 12 is 8.69 (Allende Prieto et al., 2001; Asplund et al., 2009).

3.4.3 Photometric Calculations

We use the SDSS *r*-band optical image to perform surface photometry because this band has higher signal-to-noise ratio as compared to other bands. The signal-to-noise ratio (SNR) is a measure of the quality of an image and is defined as the ratio of the signal level (i.e., the brightness of the object) to the noise level (i.e., the random fluctuations in the image). A high SNR image has a strong signal with relatively low noise. In surface photometry, accurate measurements of the brightness distribution of an object require high SNR images because they enable the detection of faint structures and small intensity variations in the object. Moreover, high SNR images also allow for better removal of the background sky brightness and other sources of noise, which is crucial for accurate

surface photometry. Additionally, high SNR images provide better spatial resolution, allowing for the detection of finer structures in the object's light distribution.

The variation of intensity, surface brightness, position angle and ellipticity with radius can be studied by using the quantities derived from surface photometry. Structural parameters like size, concentration and ellipticity are important tools to study galaxy formation and evolution. A curve connecting the points of equal brightness in the image is called an isophote and it determines the smoothness of the surface brightness on the image. The colors of the galaxies derived from surface photometry provide the knowledge of ages and the metallicity of the galaxies. On the other hand, the galaxy morphology is found out by the visual examination of the optical image. As we cannot measure the magnitude of an individual star in a galaxy, we use the integrated light profile of the galaxy along the major axis to quantify its structure. First of all, we take the optical image of the galaxy. Before doing surface photometry, both foreground and background unrelated objects in the image of the galaxy like other galaxies, stars and cosmic ray events are visually identified and are masked manually. In the optical image, the centre of the galaxy is derived by using "imcentric task centroid" in Image Reduction and Analysis Facility (IRAF) for the calculation of the centroid of the image. Centroid is the geometric centre of a plane image; it is the arithmetic mean position of all points in the image. To extract the integrated light profile along the semi-major axis, the IRAF task ellipse is used (Tody, 1986). IRAF is a freely available software. It is a collection of softwares used in the images that read two-dimensional optical image of a galaxy and reduces the isophots into one-dimensional digital output in tabulated form.

The "ellipse task" in IRAF is used to fit elliptical isophotes (as shown in the first panel of Figure 45) at discrete radii in the optical image by using an iterative method described in (Jedrzejewski, 1987). The discrete radii of ellipses are specified by the rule that the different semimajor axis lengths are spaced by a factor of 1.1. For each pre-defined length of the semimajor axis, an isophote is fitted with an initial guess for the isophote's center (X, Y), ellipticity and the position angle. While fitting the ellipses, the center and the shape (ellipticity and position angle) of the ellipse are set as free parameters and the semi-major axis is increased logarithmically. The optical image of the galaxy can be reduced to surface photometry by approximating isophotes closely by ellipses and these elliptical isophotes reflect the condition of Keplerian steller orbits in galaxies. The fitting produces different ellipse parameters like radial distance from the center, ellipticity, position angle, intensity and so on. It is assumed that the isophotes are represented by the ellipses but practically, it is departed from the pure ellipse shape. Therefore, the intensity changes along the elliptical path. For each length of the semimajor axis of the ellipse, the intensity $I(\phi)$ is averaged azimuthally along the ellipse. Intensity is expanded to quantify the deviation of intensity from being constant along the fitted elliptical path. Therefore,

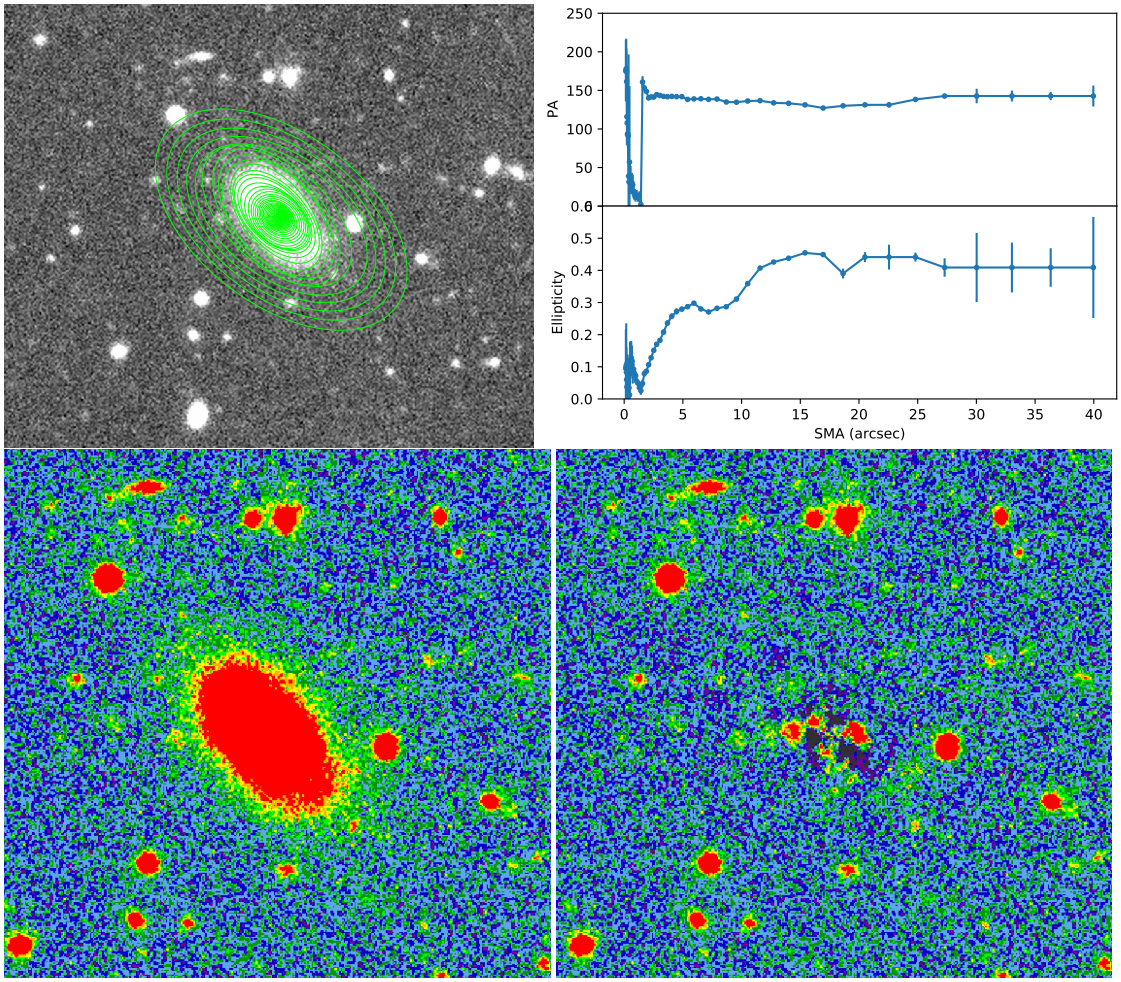

Figure 45: Ellipse fits on the SDSS g-band images of the compact merging dwarf galaxy, Cd-07. (a) best-fitted ellipse overlaid on g-band image. (b) variation of ellipse parameters (ellipticity and position angle) along the major axis (c) g-band image and (d) the residual after subtracting the model produced from the best-fitted ellipse.

the intensity is expanded in the following Fourier series (Milvang-Jensen & Jørgensen, 1999).

$$I(\phi) = I_0 + \sum_k [A_k \sin(k\phi) + B_k \cos(k\phi)] \tag{3.4}$$

where I_0 is the intensity averaged over the ellipses and ϕ is the azimuthal angle. A_k and B_k are the Fourier coefficients which will be small for correct fitting of the ellipses. If an isophot is a perfect ellipse, A_k and B_k will be exactly zero. The ellipse can be described by the Fourier coefficients. We have used a pre-built program in python program called "ellipse fit" in "photutils" package of Astropy, which is a part of IRAF integrated in python. From the ellipse fitting, the radial profiles of a number of quantities such as intensity, surface brightness, position angle and ellipticity can be obtained. An example of the radial profiles of position angle (PA) and ellipticity along the major axis is shown

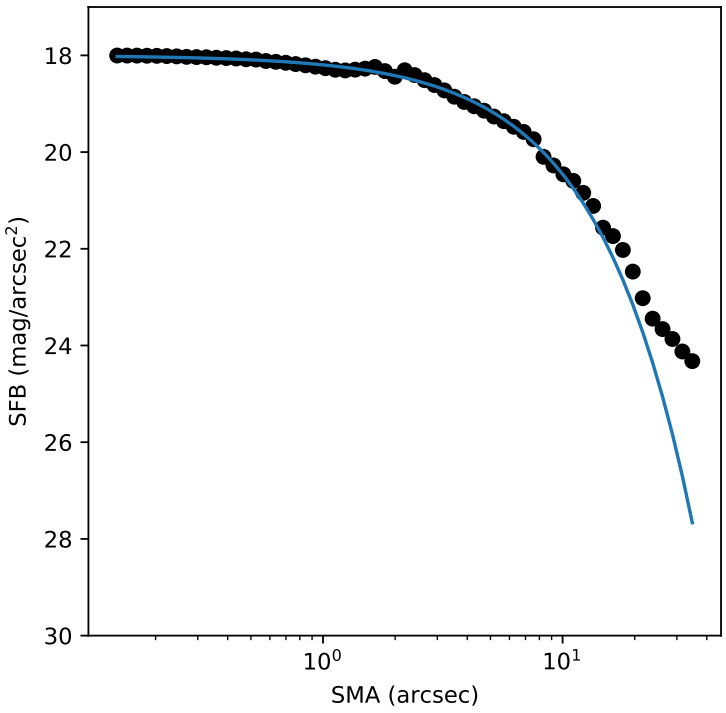

Figure 46: An example of Sérsic fitting of surface brightness profile. The black dot represents observed data points and the blue line represents best fitted line.

in the second panel of Figure 45. The third panel shows the original image and fourth panel shows the residual image of the galaxy in the same figure. The residual image is the difference of original image and the fitted image.

3.4.3.1 Measurement of Galaxy Size

Galaxies never have an endpoint; therefore, a measurement of galaxy size is not a trivial task. In general, we use two different approaches to derive galaxy size, i.e., parametric and non-parametric. In the parametric approach, we first approximate the galaxy light profile into a parametric function such as exponential or de Vaucouleurs. In general, both the exponential and the de Vaucouleurs are special cases of the Sérsic function defined by equation 2.5.

In general, as special case of Sérsic model, we use $n = 4$ for the early-type galaxy called de Vaucouleursand for late type galaxy, we use $n = 1$, which is exponential. The higher value of n indicates that there is higher concentration of light in the central region of the galaxy. These analytic functions have free parameters such as effective radius R_e, Sérsic index and effective brightness μ_e. We finally model the observed light profile with these functions and find the best-fit parameters, see Figure 46. We do not need to know where the galaxy ends in this approach and we simply use the best fit effective radius as a galaxy

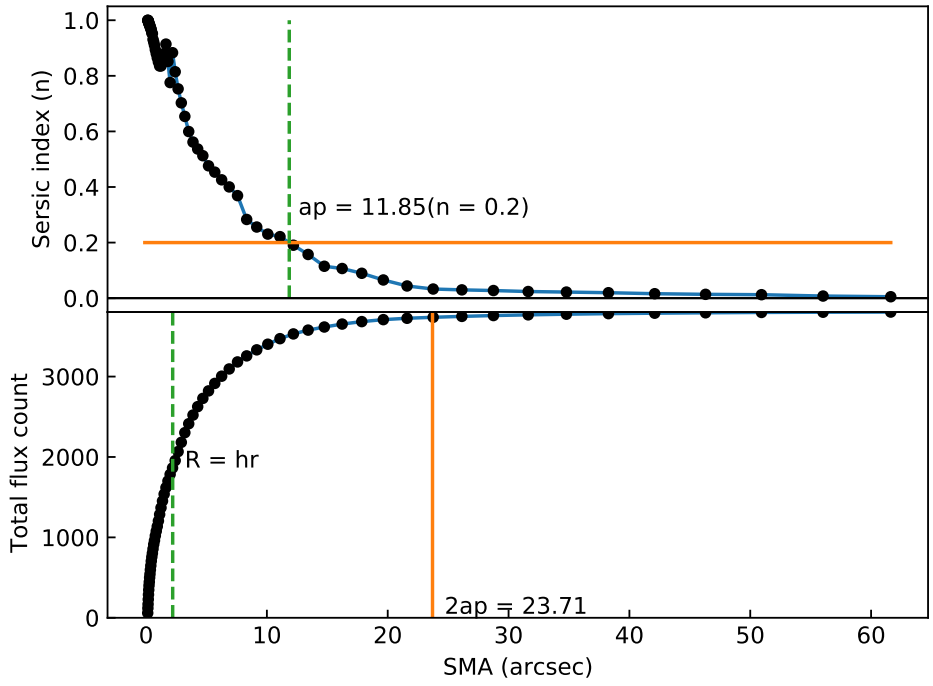

Figure 47: Galaxy photometry using a non-parametric method where we utilize Petrosian method to calculate total flux of the galaxy and hence measure the half-light radius. Upper panel: variation of the Petrosian index along the major axis of the galaxy. The Petortian radius (a_P) is marked at the position $n = 0.2$. Upper panel: Cumulative flux along the major axis and we marked the positions of $2a_P$ and half-flux radius, which covers 99% of the flux and half of that respectively.

size.

On the other hand, non-parametric methods measure the galaxy size without the use of any analytic function. One simple method is called the Petrosian method; we first define an empirical radius from the observed intensity profile, called Petrosian radius a_P (Blanton et al., 2001). To calculate this, we first derive the Petrosian index, which is the ratio of the surface brightness at R ($\mu(R)$) to the mean surface brightness within R ($\langle\mu(R)\rangle$) i.e.,

$$n(R) = \frac{\mu(R)}{\langle\mu(R)\rangle} \tag{3.5}$$

Petrosian radius is defined at $n = 0.2$. The Petrosian radius a_P is defined as radius where the local surface brightness in an annulus equals to 20 percent of the mean surface brightness interior to this annulus. Then it is assumed that the galaxy extension is at most out to $2a_P$ and the total flux in it is measured within a $2a_P$ aperture. Once we know the total flux, we can measure the distance where the flux becomes half and this galactocentric distance is called half-light radius (h_r). A schematic diagram is shown in Figure 47.

CHAPTER 4

4. RESULTS AND DISCUSSION

4.1 Results

If the gravitational fields of the galaxies produce disturbances to each other, they are said to be interacting galaxies. During the course of interaction, the galaxies come closer to each other due to their gravitational attraction and ultimately, they coalesce to each other to form a single galaxy after billions of billion years. The galaxies which are just at the verge of merging and are connected by the tidal tail like structure, are called extended merging galaxies. The morphology of such galaxies is not stable, rather, it keeps on changing. On the other hand, the galaxies after merging, settle down and form a single galaxy having compact, fixed shape is called a compact merging galaxy. In this section, 15 compact merging galaxies (Cd) and 10 extended merging galaxies (Ed) are discussed individually based on their spectroscopic and photometric calculations and are compared them in different perspectives.

Table 5 enlists the Gaussian parameters of 15 compact merging and 10 extended merging dwarf galaxies. First column represents the galaxy name. The flux of H_{β}, $OIII_{4960}$, $OIII_{5008}$ and NII_{6550} emission lines along with their systematic (measurement) error are listed in columns 2, 3, 4 and 5 respectively. Columns 6, 7 and 8 register the H_{α} flux, full width half maxima (FWHM) of H_{α} line and coefficient of determination respectively. The last column records the NII_{6585} line flux. We have noticed the maximum flux in case of H_{α} and $OIII_{5008}$ lines. The value of H_{α} FWHM is around the standard value 3.9 Å and even more than that. The FWHM of the sample compact galaxies like Cd-04, Cd-05, Cd-07, Cd-11, Cd-12, Cd-13 and extended galaxies like Ed-02, Ed-04, Ed-07 is more than 3.9 Å. It signifies that the galaxies could have turbulence or overflow, as the molecules and atoms have high speed. There will be abrupt change in SFR. In other galaxies, there is no or less turbulence and going on normal (smooth) star forming activities. Thus, FWHM is related to gas velocity. Many workers use EW(H_{α}) as a measure of starburst in the galaxies which undergoing an exceptionally high rate of star formation and have EW(H_{α}) equivalent width larger than 100 Å. More than 99% coefficient of determination of H_{α} line except in case of Cd-12 (96%) signifies that the observed data resembles with the Gaussian distribution.

Table 5: Gaussian parameters of compact merging dwarf galaxies (abbreviated by Cd-X, X = 1, ..., 15) and extended merging dwarf galaxies (abbreviated by Ed-X, X = 1, ..., 10) obtained after performing Gaussian fitting procedure on the selected prominent emission lines. The values of flux are a multiple of 10^{-17} in erg s^{-1} cm^{-2} $Å^{-1}$. The $\pm\sigma$ error of respective parameters is also shown. Zero value is shown in some cases where we obtained insignificant errors after round-figuring it. The absence of NII_{6550} line in Ed-01, Ed-05, Ed-06 and Ed-07 galaxies is indicated by NA.

Galaxy Name	H_β flux (erg s^{-1} cm^{-2} $Å^{-1}$)	$OIII_{4960}$ flux (erg s^{-1} cm^{-2} $Å^{-1}$)	$OIII_{5008}$ flux (erg s^{-1} cm^{-2} $Å^{-1}$)	NII_{6550} flux (erg s^{-1} cm^{-2} $Å^{-1}$)	H_α flux (erg s^{-1} cm^{-2} $Å^{-1}$)	H_α FWHM Å	H_α R^2	NII_{6585} flux (ergs^{-1}cm^{-2}Å^{-1})
Comapct Merging Dwarf Galaxies (Cd-X)								
Cd-01	117 ± 4	71 ± 4	224 ± 6	18 ± 2	359 ± 3	3.8 ± 0.0	0.999	45 ± 4
Cd-02	253 ± 6	152 ± 5	514 ± 4	53 ± 4	879 ± 9	3.9 ± 0.0	0.999	189 ± 5
Cd-03	306 ± 4	408 ± 6	1218 ± 20	18 ± 2	1142 ± 15	3.9 ± 0.0	0.999	60 ± 5
Cd-04	50 ± 4	27 ± 3	87 ± 6	21 ± 2	166 ± 3	4.1 ± 0.0	0.996	21 ± 2
Cd-05	640 ± 6	543 ± 4	1638 ± 9	61 ± 4	2066 ± 15	4.1 ± 0.0	1.000	201 ± 6
Cd-06	168 ± 7	149 ± 4	439 ± 11	27 ± 4	550 ± 11	3.9 ± 0.0	0.997	27 ± 4
Cd-07	49 ± 3	5 ± 1	64 ± 2	5 ± 1	188 ± 4	4.0 ± 0.1	0.997	9 ± 2
Cd-08	163 ± 6	154 ± 8	457 ± 11	19 ± 6	502 ± 9	3.9 ± 0.1	0.998	63 ± 6
Cd-09	1354 ± 9	1507 ± 30	4524 ± 47	113 ± 7	4820 ± 64	3.9 ± 0.1	0.999	380 ± 5
Cd-10	1261 ± 29	1928 ± 37	6028 ± 116	180 ± 5	3757 ± 75	3.9 ± 0.1	0.998	180 ± 5
Cd-11	10811 ± 162	19116 ± 365	56954 ± 1174	259 ± 19	35342 ± 1450	4.3 ± 0.2	0.991	834 ± 19
Cd-12	5964 ± 141	11346 ± 97	34880 ± 947	422 ± 11	24552 ± 2466	4.5 ± 0.4	0.957	422 ± 11
Cd-13	1774 ± 17	1123 ± 16	3497 ± 38	518 ± 15	7081 ± 78	4.7 ± 0.1	0.999	1535 ± 13
Cd-14	602 ± 18	998 ± 23	2958 ± 46	17 ± 5	1647 ± 18	3.8 ± 0.0	0.999	53 ± 2
Cd-15	197 ± 5	176 ± 9	547 ± 9	19 ± 5	721 ± 9	3.8 ± 0.1	0.999	66 ± 4
Extended Merging Dwarf Galaxies (Ed-X)								
Ed-01	2524 ± 45	3930 ± 35	13963 ± 758	NA	8234 ± 122	3.7 ± 0.1	0.999	54 ± 3
Ed-02	1921 ± 18	4397 ± 6	1350 ± 10	492 ± 10	7048 ± 94	4.1 ± 0.1	0.999	492 ± 10
Ed-03	1843 ± 20	3008 ± 13	8811 ± 48	153 ± 6	6454 ± 84	3.7 ± 0.1	0.999	153 ± 6
Ed-04	1545 ± 26	1376 ± 23	4231 ± 92	160 ± 9	4981 ± 101	4.2 ± 0.1	0.998	160 ± 9
Ed-05	352 ± 9	227 ± 7	669 ± 14	NA	1278 ± 27	3.8 ± 0.1	0.997	162 ± 8
Ed-06	247 ± 7	240 ± 5	712 ± 15	NA	775 ± 20	3.8 ± 0.1	0.997	27 ± 3
Ed-07	1440 ± 21	2017 ± 20	6095 ± 62	NA	4007 ± 59	4.1 ± 0.1	0.999	133 ± 9
Ed-08	3756± 57	7277 ± 72	21263 ± 331	126 ± 8	12710 ± 58	3.8 ± 0.1	1.000	126 ± 8
Ed-09	3241 ± 43	5422 ± 55	15979 ± 230	122 ± 6	11574 ± 104	3.8 ± 0.0	1.000	122 ± 6
Ed-10	151 ± 6	119 ± 7	376 ± 5	21 ± 4	686 ± 15	3.9 ± 0.1	0.997	21 ± 4

We calculated the SFR of the galaxies by using H_α emission line flux and line metallicity by using the line ratio of NII_{6550} and H_α fluxes from Table 5. We have used NII_{6585} line flux to calculate metallicity in some cases where NII_{6550} line is absent. The calculated values of SFR, metallicity, Balmer decrement and extinction coefficient are recorded in Table 6. The first column represents the name of the galaxy. The second column enlists the star formation rate of the galaxy. Columns 3, 4, 5 and 6 represent Balmer decrement, line metallicity, the color excess between B and V bands, and extinction coefficient respectively. The last column represents the SFR calculated after extinction correction. We can see that the SFR after extinction correction is almost double of that before extinction correction. The SFR varies from galaxy to galaxy because the formation of stars in the interstellar gas clouds are influenced by various factors like gravity, matter-radiation interaction, hydrodynamics, thermodynamics, and chemical processes (Krumholz & Dekel, 2012). The star-forming dwarf galaxies are characterized by low mass, low metallicity, high gas and high dark matter content. The SFR in low mass galaxies can be determined by using different methods: the ultraviolet (UV) flux, the far infrared (FIR) dust emission, the radio continuum or the H_α luminosity, (Kennicutt, 1998). But, we used H_α flux because Hydrogen is the most abundant element in the galaxies. Moreover, H_α line lies in the Balmer series and Balmer series radiations are less affected by the dust extinction as it lies in red color in visible light. The value of Balmer decrement is more than the solar value (2.86) in all galaxies except for Cd-14 and Ed-07.

The ratio of oxygen to hydrogen atoms in a galaxy's gas component is normalized to the dimensionless quantity Z = 12 + log(O/H) to measure metallicity. Z = 8.69 is the current estimate of the solar oxygen abundance in these units (Allende Prieto et al., 2001; Asplund et al., 2009). The calculated value of metallicity of our sample galaxies is around solar value. Interestingly, the oxygen abundance of both Cd and Ed dwarfs are found to lie in the range of (8.11 to 9.19) dex and (8.32 to 8.90) dex respectively. Therefore, the evolution scheme of the chemical composition in these dwarf galaxies might be similar. The extinction coefficient quantifies the amount of extinction or attenuation experienced by light at a specific wavelength, such as the H-alpha emission line. It is commonly used to estimate the amount of interstellar dust or other intervening material along the line of sight, which reduces the observed intensity of the light. Positive values of the extinction coefficient indicate that the light is being attenuated or absorbed as it passes through the medium. Higher positive values correspond to stronger attenuation meaning that the galaxy is fainter. A value of zero for the extinction coefficient implies that there is no attenuation or extinction of light at that wavelength. The value of extinction coefficient can't be negative. But the galaxies Cd 14 and Ed 07 have negative values of extinction coefficient. Despite a few instances where the calculated Balmer decrement falls slightly below the expected value of 2.88, these variations remain within the data's margin of

error. However, as a consequence of these cases yielding unphysically negative values for the extinction correction coefficient, we have chosen to exclude them and refrain from implementing any correction for extinction.

The range of SFR in the Cd galaxies is found to be 0.0008 $M_{\odot}yr^{-1}$ to 0.9048 $M_{\odot}yr^{-1}$, whereas this range is 0.0035 $M_{\odot}yr^{-1}$ to 0.2647 $M_{\odot}yr^{-1}$ in the Ed galaxies. Similarly, the ratio of H_{α} to H_{β} is found to lie in the range of 2.74 to 4.12 for Cd and 2.78 to 4.54 for Ed galaxies. Therefore, the flux values of H_{α} are found to be at least 2.5 times larger than that of the H_{β}. This might be because of the presence of interstellar dust in the region, which absorbs the emission from fine-structure cooling. This indicates the fact that the Cd and Ed dwarfs are emission-type.

Table 6: Star formation rate and metallicity of the compact merging dwarf galaxies (abbreviated by Cd-X, $X = 01, ..., 15$) and extended merging dwarf galaxies (abbreviated by Ed-X, $X = 01, ..., 10$) obtained from spectroscopic calculations. The first column lists the name of the galaxy. The descriptions of the second to last columns are given in the text.

Galaxy Name	SFR $M_{\odot}$ yr^{-1}	$c = H_{\alpha}/H_{\beta}$	Metallicity (dex)	$E(B-V)$ (mag)	Ext. Coefficient $A(H_{\alpha})$ (mag)	SFR_{ext} $M_{\odot}$ yr^{-1}
Cd-01	0.0090	3.08	9.03	0.4103	0.1534	0.0104
Cd-02	0.0368	3.47	8.85	0.1654	0.4061	0.0534
Cd-03	0.0240	3.73	8.80	0.2272	0.5553	0.0401
Cd-04	0.0059	3.34	9.19	0.1327	0.3277	0.0080
Cd-05	0.0799	3.23	8.68	0.1041	0.2554	0.1010
Cd-06	0.0021	3.27	8.95	0.1146	0.2804	0.0028
Cd-07	0.0004	3.83	9.16	0.2499	0.6108	0.0008
Cd-08	0.0029	3.07	8.97	0.0610	0.1510	0.0033
Cd-09	0.0960	3.56	8.51	0.1870	0.4582	0.1463
Cd-10	0.1087	2.98	8.56	0.0352	0.0854	0.1176
Cd-11	0.0471	3.27	8.11	0.1120	0.2801	0.0610
Cd-12	0.0479	4.12	8.19	0.3123	0.7635	0.0967
Cd-13	0.4755	3.99	8.44	0.2850	0.6985	0.9048
Cd-14	0.0193	2.74	8.73	-0.0367	-0.0923	0.0193
Cd-15	0.0180	3.66	8.89	0.2110	0.5150	0.0290
Ed-01	0.1320	3.26	8.41	0.1120	0.2757	0.1702
Ed-02	0.0569	3.67	8.44	0.2134	0.5222	0.0921
Ed-03	0.0537	3.50	8.45	0.1728	0.4250	0.0794
Ed-04	0.0044	3.23	8.51	0.1040	0.2512	0.0055
Ed-05	0.0022	3.63	8.78	0.2040	0.5002	0.0035
Ed-06	0.0046	3.15	8.88	0.0826	0.1997	0.0055
Ed-07	0.0304	2.78	8.55	-0.0242	-0.0593	0.0308
Ed-08	0.1913	3.38	8.32	0.1430	0.3526	0.2647
Ed-09	0.0885	3.57	8.34	0.1900	0.4653	0.1359
Ed-10	0.0027	4.54	8.90	0.3950	0.9695	0.0066

Table 7 enlists the morphological parameters of 15 Cd galaxies and 10 Ed galaxies which are obtained from photometric calculations. We have used Sérsic approach (Chapter 2, Equation 2.5) and Petrosian approach (Chapter 3, Equation 3.5) for this calculation. The first column represents the name of galaxies. The second and third columns enlist the Right Ascension (RA) and Declination (Dec.) in J2000 coordinates respectively. J2000 stands for "Julian year 2000" and is a reference system used to define celestial

coordinates based on the International Celestial Reference System (ICRS), which defines the positions of celestial objects with respect to a fixed frame of reference. Columns 4, 5 and 6 show the mean surface brightness measured in mag arcsec^{-2}, effective radius (R_e) measured in arcsec and Sérsic index (n) respectively. Finally, the columns 7 and 8 give g-band magnitude measured in mag and half-light radius (h_e) measured in arcsec respectively. We can see that the value of effective radius (R_e), half-light radius (h_r) and Sérsic index (n) vary in the range of (1.56 to 11.52) arcsec, (0.47 to 3.38) arcsec and (0.4 to 2.2) respectively for Cd galaxies in our sample. Likewise, the respective variables change in the range of (3.21 to 81.09) arcsec, (1.41 to 4.39) arcsec, and (0.7 to 2.9) correspondingly for Ed galaxies. In the majority of the galaxies, the value of n is nearly equal to 1 which signifies that the surface brightness profile is exponential type.

Table 7: Structural parameters of compact merging dwarf galaxies (abbreviated by Cd-X, $X = 1, ..., 15$) and extended merging dwarf galaxies (abbreviated by Ed-X, $X = 1, ..., 10$) obtained from Sérsic and Petrosian methods. These methods are described in Chapter 3, Section 3.4.3.1 First three columns list the name and positions of dwarf galaxies. Columns 4th to 8th are described in the text.

Galaxy Name	RA (degree)	Dec. (degree)	MS Brightness (mag. arcsec^{-2})	E Radius (R_e) (arcsec)	Sérsic Index (n)	g-band Mag. (mag.)	HL Radius (h_r) (arcsec)
Cd-01	028.999	-00.186	20.87	02.20	0.7	16.08	0.82
Cd-02	035.550	-08.510	20.04	03.41	0.4	15.24	1.53
Cd-03	122.445	21.622	21.33	03.72	0.5	16.39	1.52
Cd-04	144.561	19.711	22.08	02.42	0.7	17.13	1.16
Cd-05	147.914	44.319	21.14	02.44	0.7	16.17	0.97
Cd-06	150.310	37.071	22.93	11.52	2.2	15.55	1.09
Cd-07	154.387	43.145	22.00	04.39	0.8	16.21	1.61
Cd-08	154.756	21.284	21.89	09.56	1.0	15.55	3.38
Cd-09	157.455	16.181	21.22	05.02	1.2	15.20	1.08
Cd-10	177.076	-01.640	20.32	01.88	0.9	15.48	0.59
Cd-11	177.511	15.023	19.08	01.56	0.9	14.35	0.47
Cd-12	178.155	-02.469	20.96	07.52	1.0	14.68	2.03
Cd-13	205.805	36.749	19.34	01.79	0.6	14.77	0.63
Cd-14	205.862	43.189	22.78	08.21	1.3	16.41	1.57
Cd-15	349.992	-00.986	21.21	03.82	0.6	16.04	1.40
Ed-01	021.396	07.991	25.14	29.03	2.9	16.37	1.55
Ed-02	128.346	29.539	22.27	11.07	2.1	14.63	2.37
Ed-03	171.383	38.061	24.62	81.09	2.3	15.56	4.39
Ed-04	193.308	04.465	19.63	06.88	0.9	13.57	2.21
Ed-05	199.218	12.548	20.99	06.56	0.9	14.89	2.84
Ed-06	205.748	52.688	22.84	06.62	0.8	16.84	2.73
Ed-07	207.973	64.373	21.34	03.92	0.9	15.60	1.49
Ed-08	223.549	30.210	21.27	03.21	0.7	15.81	1.91
Ed-09	234.081	30.681	21.14	05.57	1.1	15.18	1.41
Ed-10	241.671	06.581	21.29	06.42	0.8	15.52	2.75

In the following, we first present the results of photometric and spectroscopic data analysis of each dwarf galaxy and finally discuss and interpret the findings.

4.1.1 Merging Compact Dwarf Galaxies

4.1.1.1 Cd-01

By using the ELLIPSE task in IRAF, the best-fitted ellipses are drawn at a number of discrete radii to the isophotes in the optical image as shown in Figure 48 (a). The radial profiles of position angle (PA) and ellipticity along the major axis of dwarf galaxy Cd-01

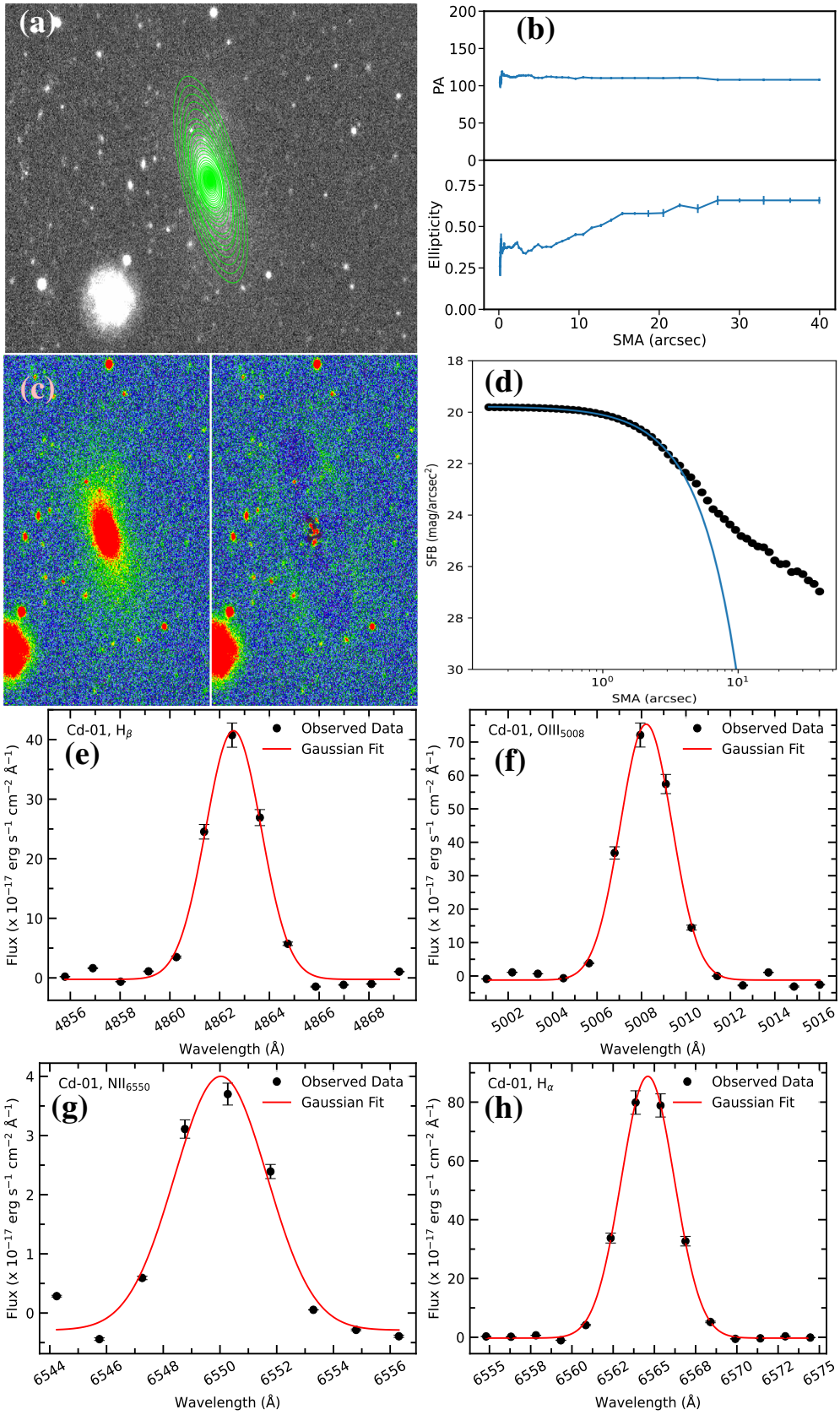

Figure 48: (a) Dwarf Galaxy Cd-01 with best fitted ellipse. (b) Radial profiles of position angle and ellipticity. Error bar is the observational error. (c) Residual image of galaxy. (d) Sérsic modeling of the observed light profile. The solid circle represents the observed data and the solid line represents the Sérsic model fitting. (e, f, g and h) Four major emission lines: H_β, $OIII_{5008}$, NII_{6550} and H_α fitted with Gaussian profile. The statistical error bars ($\pm\sigma$) are shown.

are shown in the upper panel and lower panel of Figure 48 (b). We can see that the position angle and ellipticity seem to be free parameters and vary randomly along the major axis in the inner regions and become almost flat at the outer region. It signifies that the galaxy has an elongated tidal tail. The g-band image and residual image of the galaxy are shown in the left and right panel of Figure 48 (c) respectively. There is almost no sign of the galaxy in the residual image suggesting that our ellipse-fitting model is appropriate. Figure 48 (d) shows the observed light profile modeled with the Sérsic function. It shows that the observed light profile is almost well fitted with Sérsic function with Sérsic index of 0.7 (Table 7). The mean surface brightness of the galaxy is obtained to be 20.87 mag arcsec^{-2} and the effective radius of the galaxy is obtained to be 2.20 arcsec as free parameters. The half-life radius (h_r) obtained from the Petrosian method is 0.82 arcsec which better represents the overall size of the galaxy.

The fits of the four prominent emission lines, H_β, $OIII_{5008}$, NII_{6550} and H_α in the wavelength range 4856 Å to 6575 Å are shown in Figure 48 (e, f, g and h). From Table 5, it is clear that the value of the coefficient determination of H_α line is more than 99%, which suggests the agreement of the observed data with the Gaussian distribution. We calculated the SFR of the galaxy Cd-01 by using H_α flux in Equation 3.2 which is found to be 0.0090 $M_\odot yr^{-1}$ and 0.0104 $M_\odot yr^{-1}$ before and after extinction correction respectively. Moreover, this value of SFR is low as compared to its catalog value (0.1230 $M_\odot yr^{-1}$). It is because of the large area coverage of Far Ultraviolet (FUV) flux as compared to H_α flux taken in our calculations. It shows that only a small fraction of star formation takes place in the middle region of the galaxy. The line ratio, c = 3.08, which is greater than its normal value of 2.86 (Osterbrock & Ferland, 2006). It is, therefore, the intensity of the first Balmer line is found to be three times stronger than that of the second line in the middle region of the galaxy. The line metallicity calculated from Equation 3.3 is 9.03 dex. We will discuss the variations of oxygen abundance in the Cd galaxies in the general discussion section.

4.1.1.2 Cd-02

The isophotes drawn on the grayscale image and the radial profiles of position angle (PA) and ellipticity of the galaxy are shown in Figure 49 (a) and (b) respectively. The PA is almost constant in the inner region, which indicates that the galaxy is face-on. It flips by about 180° from about 15 arcsec distance that can be realized from the ellipse orientation as well. The galaxy has a bar-like feature at center. The ellipticity of the galaxy varies quite randomly in the inner region. The g-band image and its residual image are shown in Figure 49 (c). The residual image suggests that our model is appropriate. The observed light profile of the galaxy modeled with the Sérsic function is shown in Figure 49 (d). The observed data points are shown by dotted points, and the best-fitted Sérsic modeled

line is shown by the blue solid line. This model is found to be perfect up to 4 arcsecs from the center of the galaxy. The surface brightness of the galaxies is maximum and constant around the central region and then it goes on decreasing in the outer region. The observed light profile is best fitted with Sérsic function with Sérsic index of 0.4. The mean surface brightness of the galaxy is obtained to be 20.04 mag arcsec^{-2} and the effective radius of the galaxy is 3.41 arcsec. The half-life radius (h_r) obtained from the Petrosian method is 1.53 arcsec which represents the size of the galaxy.

Among of many observed emission lines, only four strong lines, H_β, $OIII_{5008}$, NII_{6550} and H_α are shown in Figure 49 (e, f, g, and h) respectively. The solid line represents the Gaussian fits and the dots represent the observed data points. The Balmer lines H_β and H_α are sensitive to the galaxies' gas mass and star-formation rate. The H_α line flux is used to calculate the star-formation rate of the gas-rich galaxies while, NII_{6550} and H_α line fluxes are used to calculate line metallicity. We can see from Table 5 that the maximum flux is $(879 \pm 9) \times 10^{-17}$ erg s^{-1} cm^{-2} Å^{-1}, for the H_α line corresponding to the central wavelength 6564 Å. The second maximum flux is $OIII_{5008}$ line is $(514 \pm 4) \times 10^{-17}$ erg s^{-1} cm^{-2} Å^{-1} corresponding to wavelength 5008 Å. The coefficient determination for H_α line 99.9 %. This suggests an almost perfect agreement of the observed data with the Gaussian distribution. The positive offset of NII_{6550} and H_α lines means that the right-hand tail is longer than the left-hand tail. The negative value of the offset of the Gaussian distribution of H_β and $OIII_{5008}$ shows that the left-hand tail of the Gaussian profile is longer than the right-hand tail. The SFR calculated by using H_α flux in Equation 3.2 is found to be 0.0368 $M_\odot yr^{-1}$ and 0.0534 $M_\odot yr^{-1}$ before and after extinction correction respectively. The extinction coefficient is calculated to be 0.4061. The SFR after extinction correction is more than before correction. Moreover, this value of SFR is low as compared to its catalog value (0.3631 $M_\odot yr^{-1}$). The line ratio, $c = 3.47$ is greater than its normal value of 2.86 (Osterbrock & Ferland, 2006). The oxygen abundance calculated from Equation 3.3 is 8.85 dex which is less than the Cd-1 dwarf galaxy.

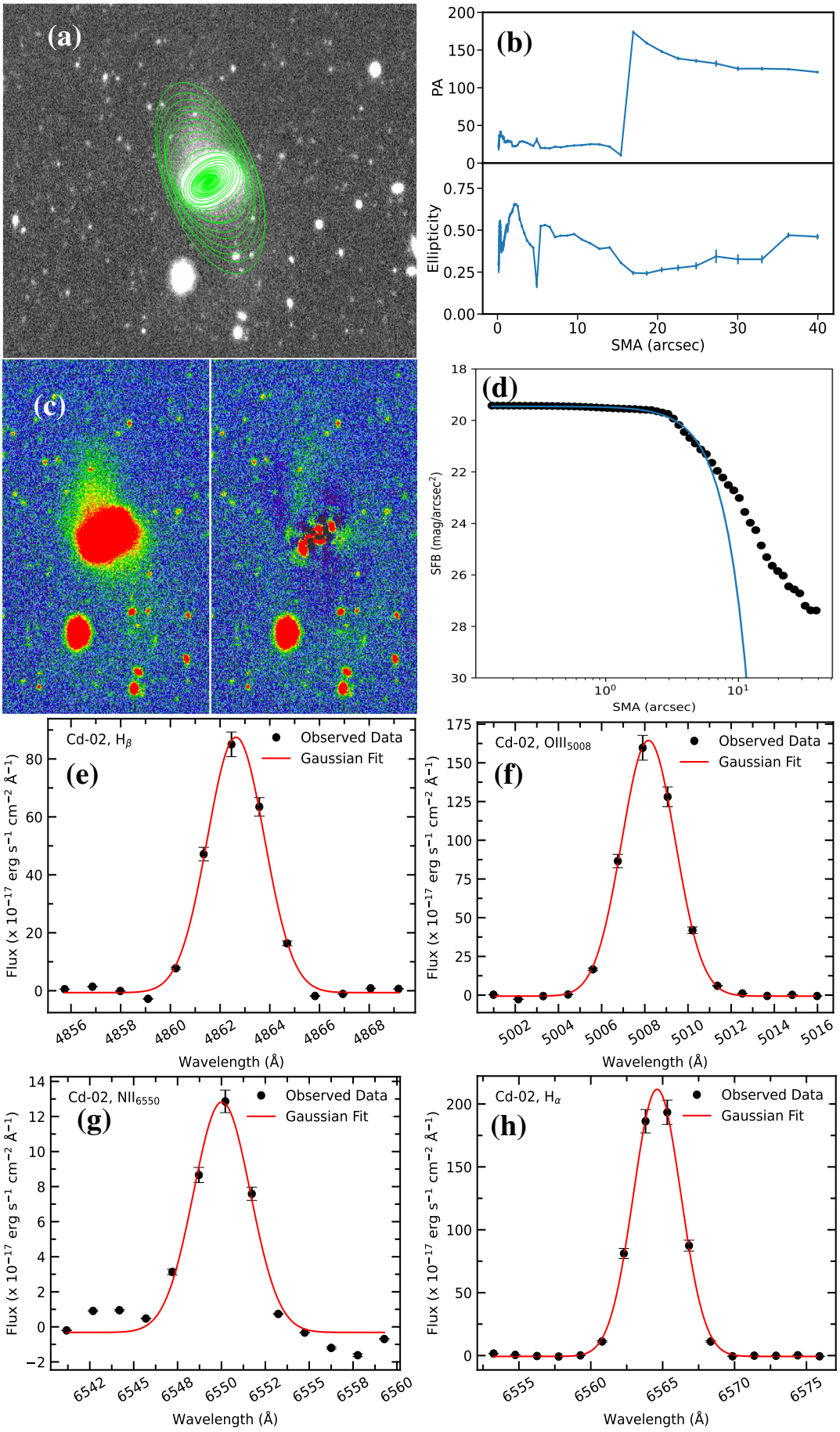

Figure 49: Results of Cd-2 galaxy. We show surface photometry in sub-figures (a) to (d) and spectroscopy in (e) to (h). For a detailed description of each sub-figure and symbol identification, see Figure 48.

4.1.1.3 Cd-03

The best-fitted ellipses at different radii on the g-band optical image and the radial profiles of PA and ellipticity of the dwarf galaxy Cd-03 are shown in Figure 50 (a and b) respectively. We can see different orientations of the ellipses extended outside and they are almost constant in the outer region of the galaxy, which indicates that the galaxy is almost stable in that region. There is multiple flips of PA and increasing and decreasing ellipticity. This is the signature of spiral arms in the galaxy. The g-band image and its residual image after modeling are shown in Figure 50 (c). As in the previous galaxies, the residual image is clean, except for the central region, which means the derived ellipse model well represents the observed galaxy. Figure 50 (d) shows the brightness profile of the galaxy modeled with the Sérsic function. The surface brightness of the galaxy is optimum and constant around the central region and then gradually decrement in the outer area. Thus the observed light profile is best fitted with Sérsic function with Sérsic index of 0.5. The mean surface brightness of the galaxy is obtained to be 21.33 mag arcsec^{-2} and the effective radius of the galaxy is 3.72 arcsec. The half-life radius (h_r) obtained from the Petrosian method is 1.52 arcsec which represents the size of the galaxy.

From the spectrum, HeI, SII, H_δ, H_γ, $OIII_{4365}$, H_β, $OIII_{4950}$, $OIII_{5008}$, HeI, OI_{6302}, NII_{6550}, H_α, NII_{6585}, SII_{6720}, and SII_{6732} lines were detected. Among of them, we analyzed H_α , H_β, $OIII_{5008}$ and NII_{6550} emission lines in the wavelength range 4855 Å to 6575 Å. They are presented in Figure 50 (e, f, g, and h) respectively. The dots in the curve represent observed points and the solid red line represents Gaussian fits. The probable error is shown by the error bars. The H_β and $OIII_{5008}$ lines have positive offsets, which indicates that the right-hand tail is longer than the left-hand tail. Likewise, the negative offsets of NII_{6550} and H_α lines mean their longer left-hand tail than the right-hand tail. In addition, more than 99.9% coefficient determination and less than 4 Å FWHM of the lines means that the observed data act in accordance with Gaussian distribution almost accurately. We used H_α line optical flux in Equation 3.2 to calculate SFR which is found to be 0.0240 $M_\odot yr^{-1}$ and 0.0401 $M_\odot yr^{-1}$ before and after extinction correction respectively. The latter is almost double because of extinction correction which obviously means a higher value of actual flux than the observed flux. The catalog value of SFR is 0.3631 $M_\odot yr^{-1}$ which is equal to that of the galaxy Cd-02. The Balmer decrement, $c = 3.73$. The higher value of c suggests the presence of dust at the center which effectively absorbs lower wavelength light. The presence of dust advocates the higher values of oxygen abundance. The oxygen abundance calculated from Equation 3.3 is 8.80 dex.

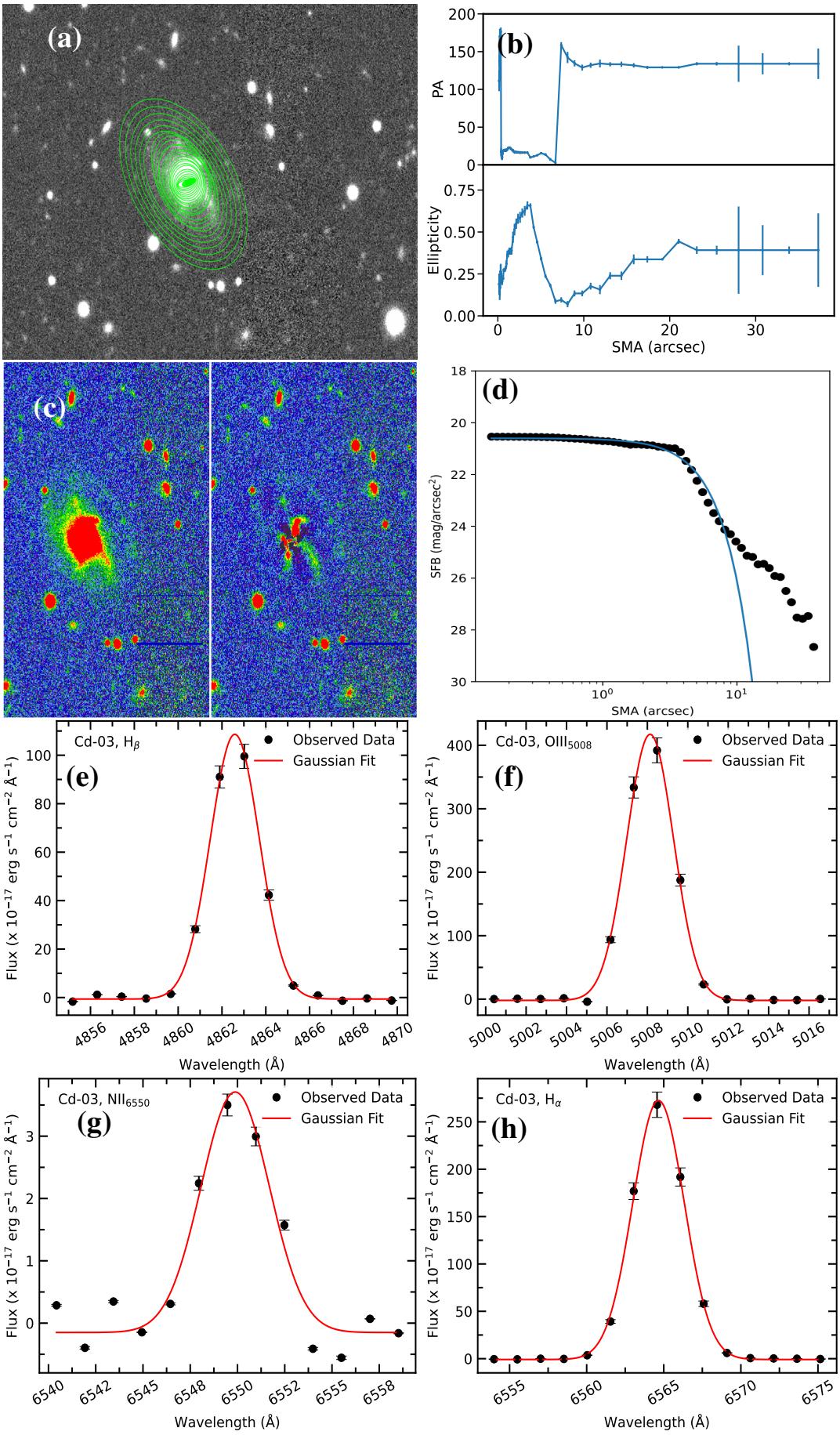

Figure 50: Results of Cd-3 galaxy. We show surface photometry in sub-figures (a) to (d) and spectroscopy in (e) to (h). For a detailed description of each sub-figure and symbol identification, see Figure 48.

4.1.1.4 Cd-04

The best-fitted ellipses drawn on the optical image of the dwarf galaxy Cd-04 by using the ELLIPSE task in IRAF are shown in Figure 51 (a). We can see different orientations of the ellipses and large areas covered by them outside the observed galaxy size. The radial profiles of position angle (PA) and ellipticity of the galaxy Cd-04 are shown in Figure 51 (b). Both PA and ellipticity vary randomly in the central region and are constant in the outer area of the galaxy, indicating a rather complicated core region. The g-band image and its residual image are shown in Figure 51 (c). The image of the galaxy completely disappeared in the residual image. The modeling of the observed light profile of the galaxy with the Sérsic function shown in Figure 51 (d) suggests that the observed data points (shown by dotted points) agree well with the best-fitted Sérsic model (blue color solid line). The maximum value of surface brightness of the galaxy observed in the central region goes on decreasing exponentially in the outer region. In this way, the observed light profile is best fitted with Sérsic function with Sérsic index of 0.7 (Table 7). The larger the value of Sérsic index, the slower the merger. The mean surface brightness and half-life radius ($h_{\rm r}$) of the galaxy are obtained to be 22.08 mag arcsec^{-2} and 1.16 arcsec respectively.

From the spectrum of the compact dwarf galaxy Cd-04, H_δ, H_γ, $OIII_{4365}$, H_β, $OIII_{4950}$, $OIII_{5008}$, OI_{6302}, NII_{6585}, H_α, NII_{6585}, SII_{6720}, and SII_{6732} lines were detected. We analyzed H_γ, $OIII_{5008}$, NII_{6550} and H_α lines in the wavelength range 4855 Å to 6575 Å and are presented in the Figure (e, f, g, h) respectively. In the Gaussian curve, the observed points are shown along with probable errors (error bars). The H_β and $OIII_{5008}$ lines have positive offsets and hence they have longer right-hand tail. Likewise, the negative offsets of NII_{6550} and H_α lines means their longer left-hand tail. In addition, more than 99.9% coefficient determination and FWHM of 4.1 Å of the H_α line means that the observed points follow Gaussian distribution almost accurately. The calculated value of SFR before extinction correction 0.0059 $M_\odot yr^{-1}$ and after doing that is 0.0080 $M_\odot yr^{-1}$ respectively. The latter is slightly less than its double value because of the higher value of the actual flux than the observed flux. The higher value of line ratio, $(c) = H_\alpha/H_\beta = 3.34$ suggests the presence of dust at the center, which effectively absorbs lower wavelength light. The oxygen abundance calculated from Equation 3.3 is $12 + \log(O/H) = 9.19$ dex, which is the relatively highest value of all sample dwarf galaxies.

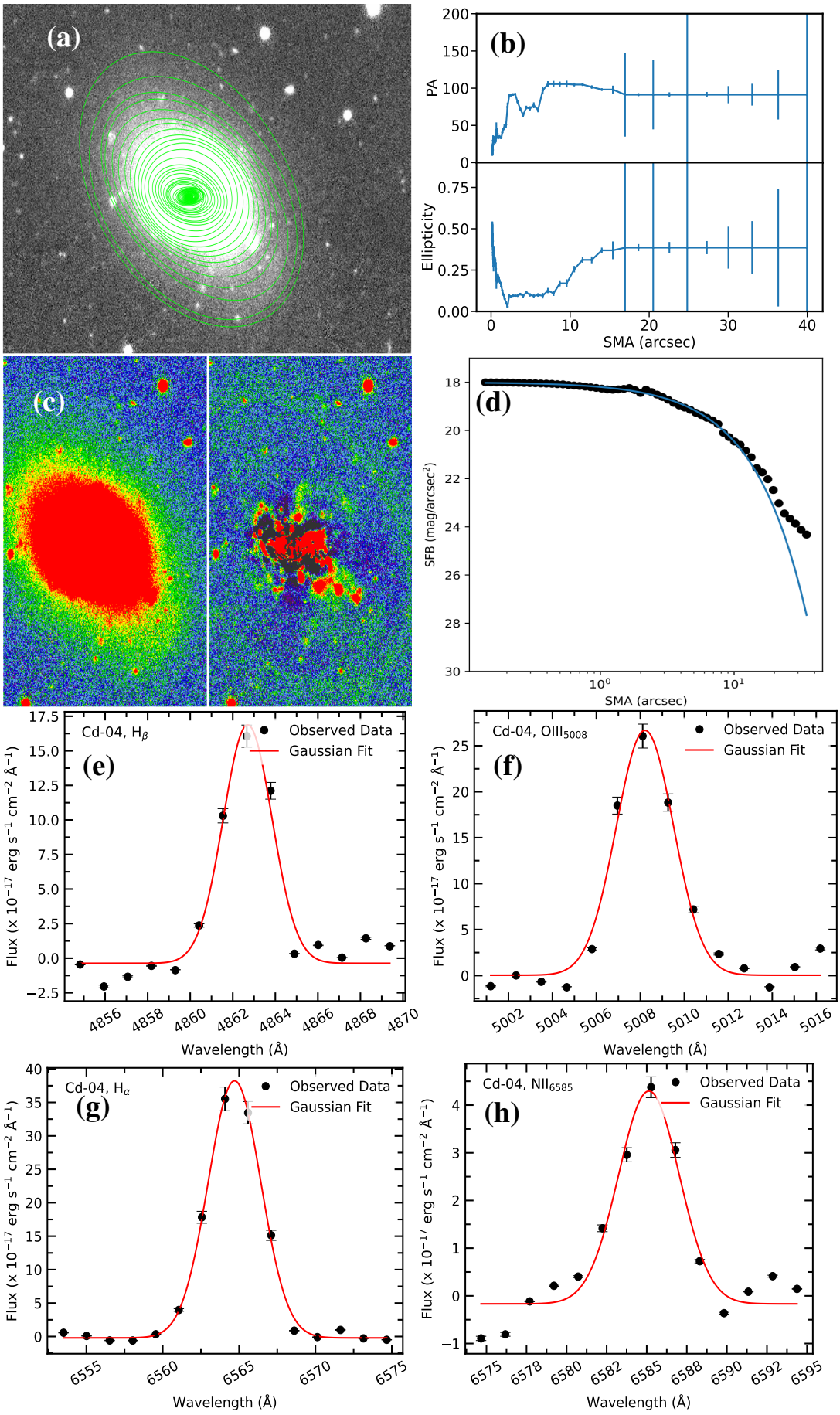

Figure 51: Results of Cd-4. We show surface photometry in sub-figures (a) to (d) and spectroscopy in (e) to (h). For a detailed description of each sub-figure and symbol identification, see Figure 48.

4.1.1.5 Cd-05

The best fitted ellipses drawn on the optical image of the dwarf galaxy Cd-05 by using ELLIPSE task in IRAF, after masking both foreground and background objects, are shown in Figure 52 (a). We can see different orientations of the ellipses and large areas covered by them outside the observed galaxy size. The radial profiles of the position angle (PA) and ellipticity of Cd-05 are shown in Figure 52 (b). Both quantities vary rapidly in the central region and they remain constant in the outer part of the galaxy indicating a rather complicated core area. The g-band image and its residual image are shown in Figure 52 (c). The image of the galaxy completely disappeared in the residual image. The modeling of the observed light profile of the galaxy with Sérsic function is shown in Figure 52 (d). It shows that the observed data points (shown by dotted points) agree well with the best-fitted Sérsic modeled line (blue color solid line). The maximum value of surface brightness of the galaxy observed in the central region goes on decreasing exponentially in the outer region. We find that the observed light profile is best fitted with Sérsic function with Sérsic index of 0.7 (Table 7). The mean surface brightness and half-life radius ($h_{\rm r}$) of the galaxy are obtained to be 21.14 mag arcsec^{-2} and 0.97 arcsecs respectively.

We fit Gaussian line profiles with H_β, $OIII_{5008}$, NII_{6550}, and H_α lines in the wavelength range 4855 Å to 6575 Å. They are presented in Figures (e, f, g and h) respectively. In the Gaussian curve, the observed points are shown by the dots and the probable error is shown by the error bars. The positive offset of H_β and $OIII_{5008}$ lines reveals a longer right-hand tail than their left-hand tail. Likewise, the negative offsets of NII_{6550} and H_α lines mean their longer left-hand tail than the right-hand tail. In addition, 100 % coefficient determination of the Gaussian fit of H_α line manifests to go along with the Gaussian distribution exactly. The calculated values of SFR are 0.0799 $M_\odot yr^{-1}$ and 0.1010 $M_\odot yr^{-1}$ before and after extinction correction ($A(H_\alpha) = 0.2554$ mag) respectively. The latter is almost double because of extinction correction. This means there is radiation losses on the way because of the foreground field. The catalog value of SFR derived from the FUV fluxes after foreground extinction correction is 0.3802 $M_\odot yr^{-1}$. The higher value of SFR is because of the large area coverage of FUV flux as compared to H_α flux taken in our calculations. It shows that only a small fraction of star formation takes place in the middle region of the galaxy. The line ratio, $(c) = H_\alpha/H_\beta = 3.23$ which is greater than its normal value of 2.86 (Osterbrock & Ferland, 2006). The ratio of oxygen to hydrogen atoms in a galaxy's gas component is used to measure oxygen abundance. This ratio is normalized to a quantity $12 + \log(O/H) = 8.68$ dex which is nearly equal to the solar value $Z_\odot = 8.69$ (Allende Prieto et al., 2001; Asplund et al., 2009).

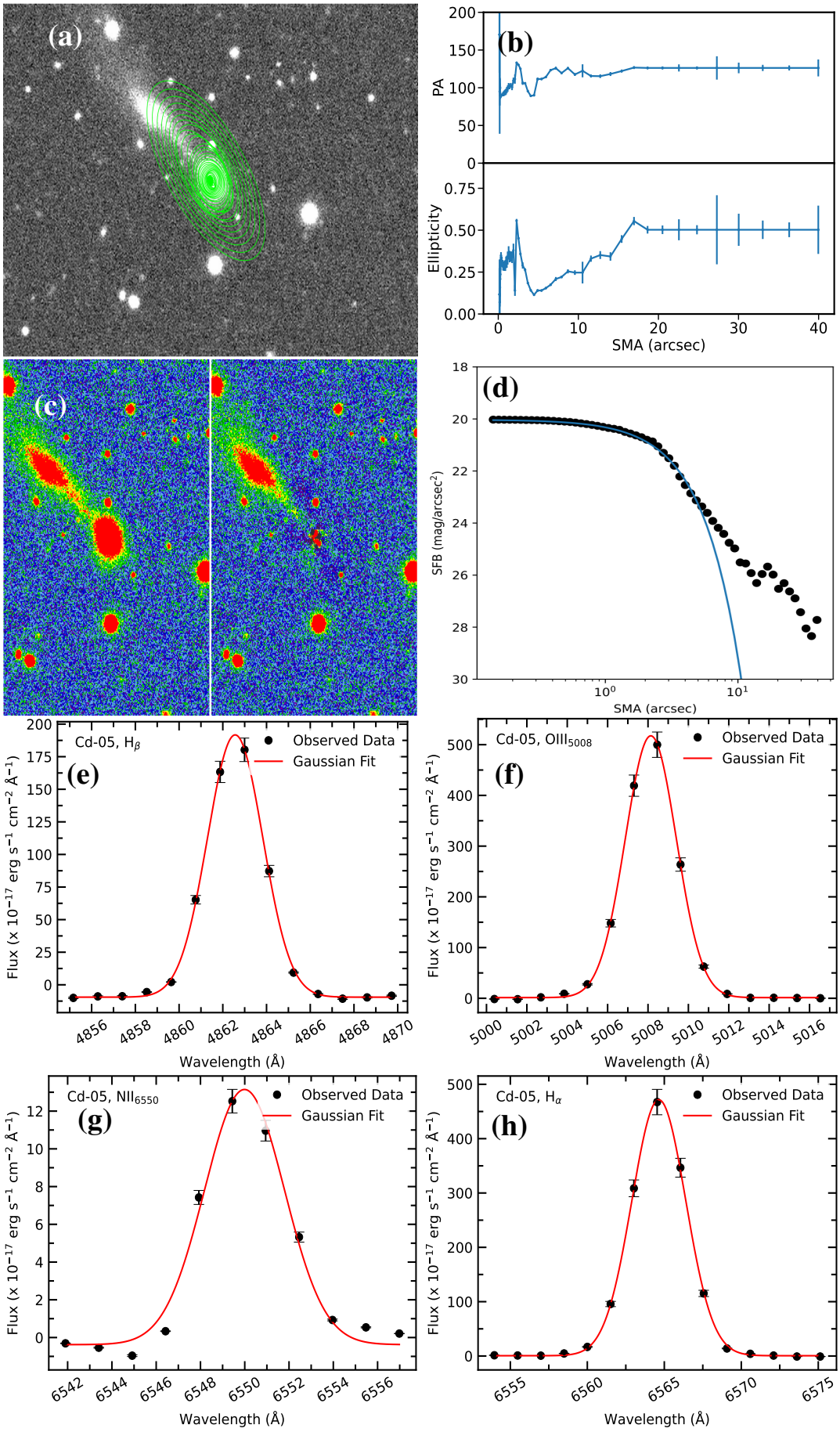

Figure 52: Results of Cd-5. We show surface photometry in sub-figures (a) to (d) and spectroscopy in (e) to (h). For a detailed description of each sub-figure and symbol identification, see Figure 48.

4.1.1.6 Cd-06

The best-fitted ellipses drawn on the optical image of the compact dwarf galaxy Cd-06 are as shown in Figure 53 (a). The ellipses are oriented in different directions. The ellipses at the center of the galaxy vary rapidly, which signifies that the flux is not smoothly distributed. The radial profiles of PA and ellipticity are shown in the upper panel and lower panel of Figure 53 (b) respectively. Both quantities are fairly constant in the outer region. It signifies that the light profile of the galaxy is regular in the outer region. The g-band image and its residual image of the galaxy Cd-06 are shown in Figure 53 (c). The residual image suggests that our ellipse-fitting model is appropriate. The observed light profile of the galaxy modeled with the Sérsic function is shown in Figure 53 (d). The observed data (dotted poits) is close to the modelled best-fitted Sérsic line which is shown by the blue color solid line. This reveals that the observed light profile is best fitted with Sérsic function with Sérsic index of 2.2 which is the maximum value of all compact group galaxies in our sample. The mean surface brightness of the galaxy is obtained to be 22.93 mag arcsec^{-2} which is also the maximum value of the compact group. This means this galaxy is the brightest of all. From the Petrosian method, the half-life radius ($h_{\rm r}$) obtained is 1.09 arcsec.

From the spectrum, H_δ, H_γ, $OIII_{4365}$, H_β, $OIII_{4932}$, $OIII_{4960}$, $OIII_{5008}$, H_α, NII_{6585}, SII_{6720} and SII_{6732} lines were detected. We selected only (H_β, $OIII_{5008}$, H_α and $OIII_{6585}$ lines in the wavelength range 4855 Å to 6594 Å which are shown in Figure (e, f, g and h) respectively. These lines are important to calculate SFR and emission line metallicity. The Gaussian curve points represent the observed points, whereas the continuous red line represents the Gaussian adjustments. The probable error appears on the error bars. The H_β and $OIII_{5008}$ lines have positive offsets, which indicate the right tail is longer than the left tail. Likewise, the negative offsets of H_α and NII_{6585} lines mean their longer left-hand tail than the right-hand tail. In addition, more than 99.7% coefficient determination and less than 3.90 Å FWHM of the lines means that the observed points follow Gaussian distribution almost accurately. From Table 6, we can see that the calculated values of SFR of the galaxy Cd-06 are 0.0021 $M_\odot yr^{-1}$ and 0.0028 $M_\odot yr^{-1}$ before and after extinction correction ($A(H_\alpha)$ = 0.2804 mag) respectively. The catalog value of SFR derived from the FUV fluxes after foreground extinction correction is 0.0513 $M_\odot yr^{-1}$. The line ratio, (c) = 3.27 is greater than its normal value of 2.86 (Osterbrock & Ferland, 2006). The higher value of the Balmer decrement suggests the presence of dust at the center which effectively absorbs lower wavelength light. The oxygen abundance calculated from equation (3) is 12 + log(O/H) = 8.95 dex which is nearly equal to the solar value $Z_\odot$ = 8.69 Allende Prieto et al. (2001); Asplund et al. (2009).

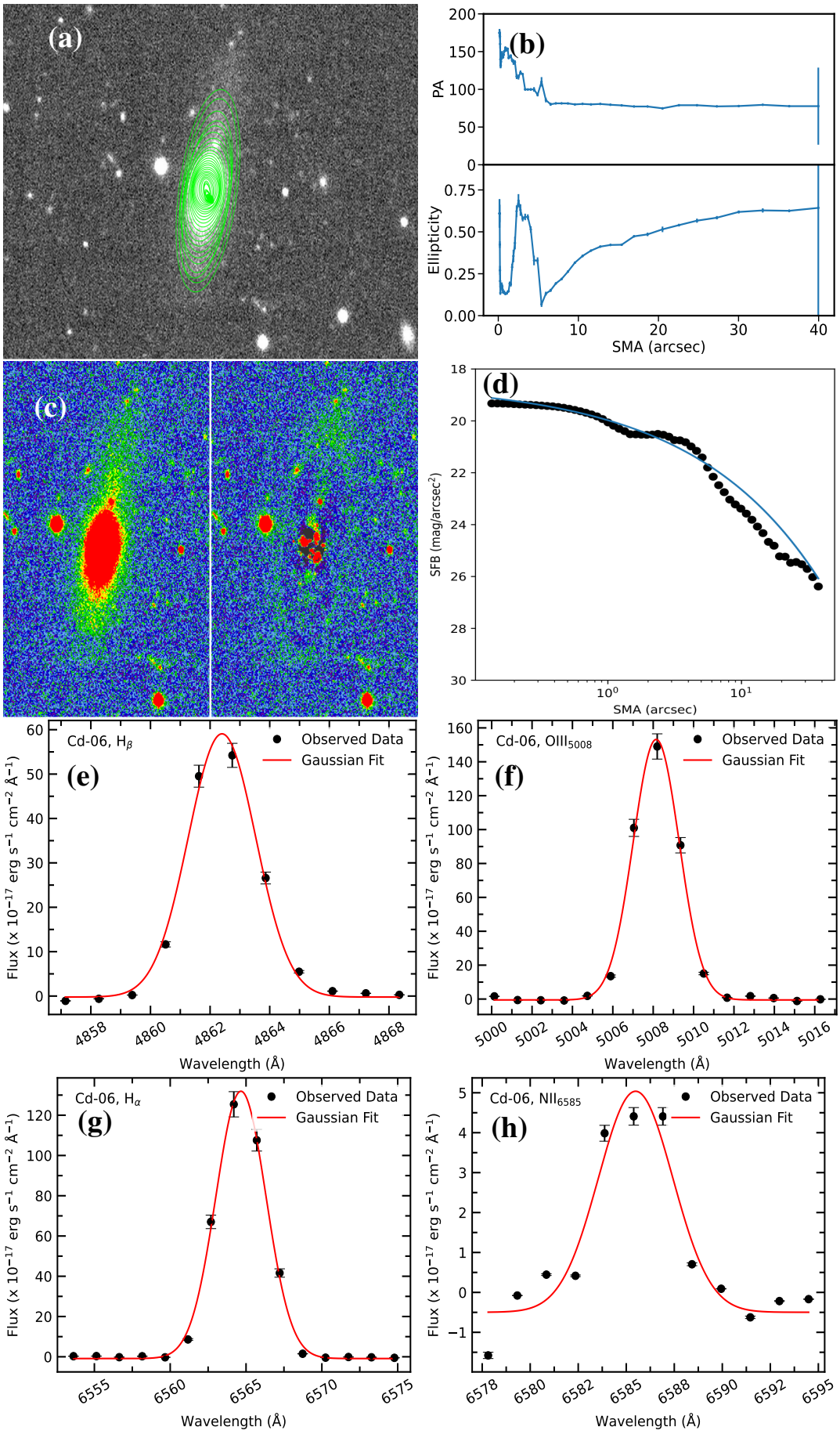

Figure 53: Results of Cd-6. We show surface photometry in sub-figures (a) to (d) and spectroscopy in (e) to (h). For a detailed description of each sub-figure and symbol identification, see Figure 48.

4.1.1.7 Cd-07

The appearance of the compact dwarf galaxy Cd-07's best-fitting ellipses on its optical image is depicted in Figure 54 (a). The ellipses are oriented almost in the same direction in the outside area of the central core. The radial profiles of PA and ellipticity are shown in Figure 54 (b). The PA flips by more than 150 ° at about 3 arcsec distance and then it remains constant. It signifies that the light profile of the galaxy is not regular in the inner region and the galaxy is stable in the outer region. This is, indeed, a sign of star-formation activity. The g-band image and its residual image of the galaxy Cd-07 are shown in Figure 54 (c). The absence of the galaxy in the residual image suggests that our model is suitable. Figure 54 (d) displays the galaxy's observed light profile that was modeled using the Sérsic function. The blue solid line indicates how closely the observed data (dotted points) resembles the model's best-fit Sérsic line. This demonstrates that the observed light profile resembles with Sérsic function with a Sérsic index of 0.8. The galaxy's average surface brightness is calculated to be 22.00 mag arcsec^{-2} as recorded in Table 7. The Petrosian approach yielded a half-life radius ($h_{\rm r}$) of 1.61 arcsec.

From the optical spectrum of Cd-07, H_{δ},H_{γ}, H_{β}, $OIII_{4932}$, $OIII_{4960}$, $OIII_{5008}$, NII_{6550}, H_{α} ,NII_{6585}, SII_{6720} and NII_{6732} lines were detected but Figure 54 (e, f, g and h) respectively displays H_{β}, $OIII_{5008}$, NII_{6550} and H_{α} lines only covering the wavelength range 4858 Å to 6574 Å. The solid red line depicts the Gaussian fits, the dots show the observed data and the error bars display the probable error. In H_{β}, $OIII_{5008}$, $NIII_{6550}$ and H_{α} lines with negative offset, the left tail is longer than the right tail. In addition, more than 99.9% coefficient of determination and less than (4.0 ± 0.1) Å FWHM of the lines means that the observed points follow the Gaussian distribution in an almost exact manner. The calculated value of SFR by using H_{α} line flux is found to be 0.0004 $M_{\odot}yr^{-1}$ and 0.0008 $M_{\odot}yr^{-1}$ before and when extinction correction ($A(H_{\alpha})$ = 0.6108 mag) respectively. The latter is simply double attributable to extinction correction and it implies that the actual flux of the galaxy is over the perceived flux. Moreover, this value of SFR is least of all 25 galaxies in the sample. The Balmer decrement, (c) = 3.83 which is greater than its normal value of 2.86 (Osterbrock & Ferland, 2006). The oxygen abundance calculated from Equation 3.3 is 12 + log(O/H) = 9.16 dex which is nearly equal to the solar value $Z_{\odot}$ = 8.69 Allende Prieto et al. (2001); Asplund et al. (2009).

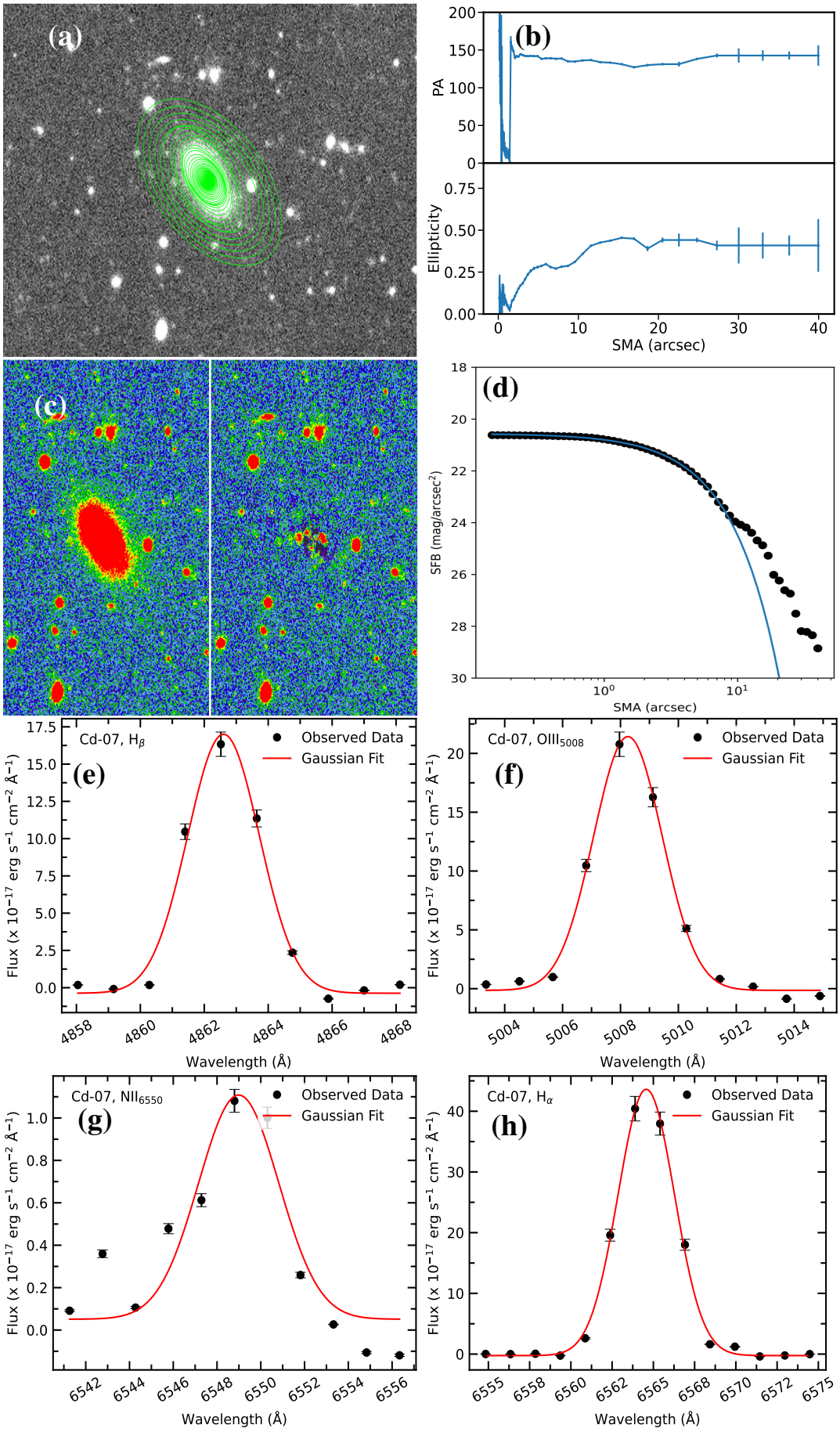

Figure 54: Results of Cd-7. We show surface photometry in sub-figures (a) to (d) and spectroscopy in (e) to (h). For a detailed description of each sub-figure and symbol identification, see Figure 48.

4.1.1.8 Cd-08

Figure 55 (a) depicts the best-fitted ellipses on the grayscale optical image of merging compact dwarf galaxy Cd-08. The elliptical isophotes are aligned arbitrarily. The radial profiles of position angle (PA) and ellipticity are shown in Figure 55 (b). The trend of variation of PA and ellipticity seems to be similar: quite irregular at the center, almost constant and finally increasing in the exterior part. This suggests that the galaxy has a tidal tail along its semi-major axis. The g-band image and its residual image of the galaxy Cd-08 are shown in Figure 55 (c). Only a small residual part of the galaxy suggests that our model is almost appropriate. Figure 55 (d) displays the galaxy's observed surface brightness profile modeled using the Sérsic function. The solid circles represent the observed data while the solid line represents the best-fitted line for surface brightness obtained after modeling the observed surface brightness with Sérsic function. The values of some photometric parameters obtained from Sérsic and Petrosian methods are listed in Table 7. The best fit Sérsic function has index of 1.0. There is a very good agreement between the observed value and the model. The average surface brightness and effective radius are 21.89 mag arcsec^{-2} and 9.56 arcsec respectively. The half-life radius ($h_{\rm r}$) measured by the Petrosian approach is 3.38 arcsec which is the brightest of all Cd galaxies.

The analyzed emission lines H_β, $OIII_{5008}$, NII_{6550} and H_α are shown in the Figure 55 (e, f, g and h) respectively. The red color solid lines represent Gaussian fits and the solid circles represent the observed data. From Table 5, we see H_α line has the maximum flux of value, $(502 \pm 9) \times 10^{-17}$ erg s^{-1} cm^{-2} Å^{-1}. The coefficient determination of H_α line is 99.8 %. Similarly, from Table 6, we have the calculated values of SFR are 0.0029 $M_\odot yr^{-1}$ and 0.0033 $M_\odot yr^{-1}$ before and after extinction correction ($A(H_\alpha) = 0.1510$ mag) respectively. The higher value of SFR after extinction correction signifies that the actual flux of the galaxy is more than the observed flux. The Balmer decrement is 3.07 and the line metallicity calculated from Equation 3.3 is $12 + \log(O/H) = 8.97$ dex.

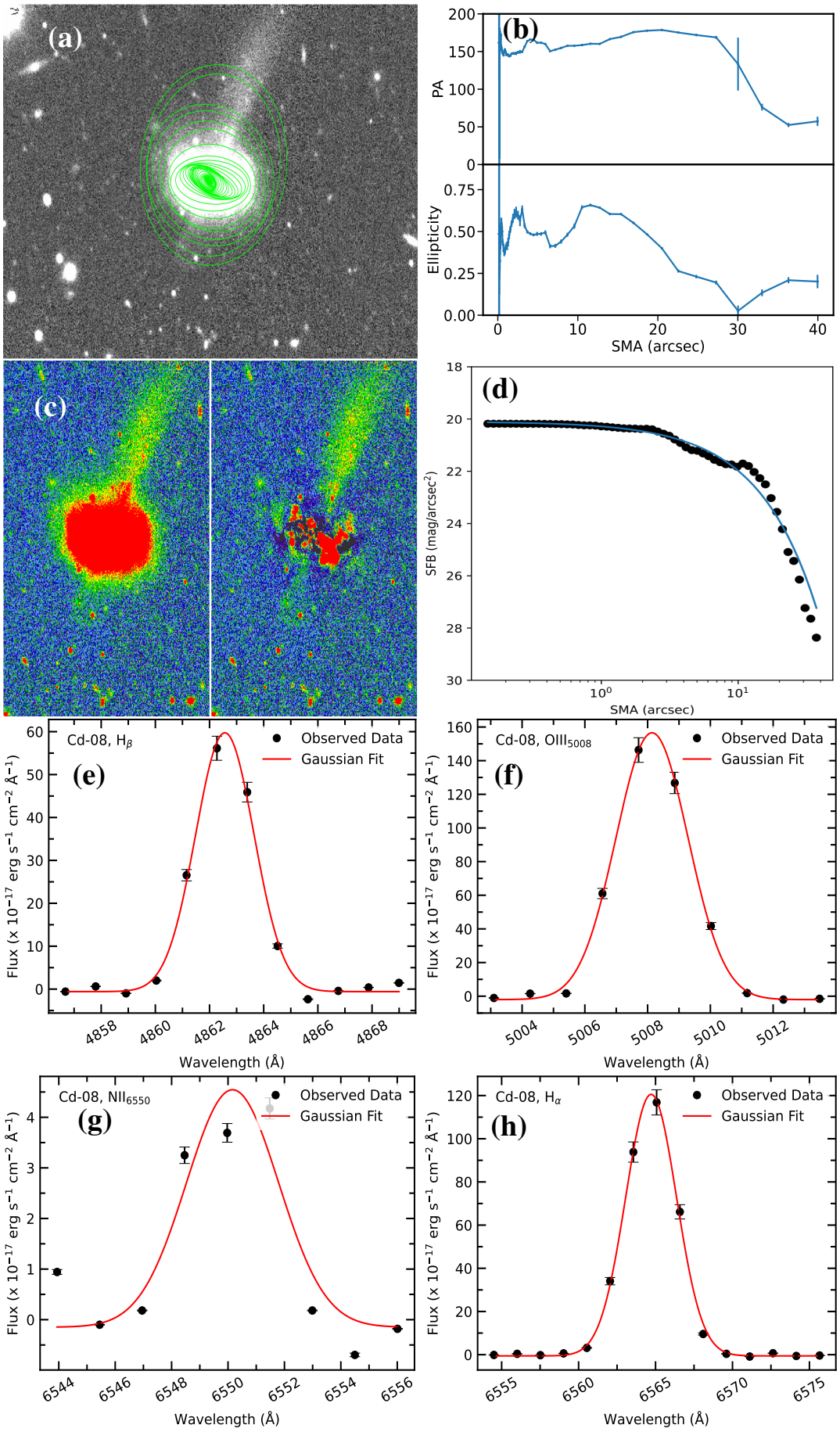

Figure 55: Results of Cd-8. We show surface photometry in sub-figures (a) to (d) and spectroscopy in (e) to (h). For a detailed description of each sub-figure and symbol identification, see Figure 48.

4.1.1.9 Cd-09

Using ELLIPSE task in IRAF, the ellipses fitted to the intensities in the image of merging compact dwarf galaxy Cd-09, are shown in Figure 56 (a). The ellipses are oriented in different directions. The inner ellipses are varying rapidly and are densely packed. The radial profiles of PA and ellipticity are shown in Figure 56 (b). The PA and ellipticity vary in the same manner. Another type of output of ellipse fit is the residual image, which is the difference between the original image and the model image connected with the best-fitting ellipses. The g-band optical image and its residual image of the galaxy Cd-09 are shown in Figure 56 (c). A very small structure of the galaxy is seen in the residual image suggesting that our model is almost appropriate. Figure 56 (d) displays the galaxy's observed surface brightness profile modeled using the Sérsic function. The blue solid line indicates how closely the observed data (dotted points) resembles the model's best-fit Sérsic line. This demonstrates that the observed light profile best fits with Sérsic function with a Sérsic index of 1.2 (Table 7). The galaxy's average surface brightness is calculated to be 21.22 mag arcsec^{-2}. The Petrosian approach yielded a half-life radius ($h_{\rm r}$) of 1.08 arcsec.

From the spectrum, H_{δ}, H_{γ}, $OIII_{4364}$, H_{β}, $OIII_{4960}$, $OIII_{5008}$, NII_{6550}, H_{α}, NII_{6585}, SII_{6720} and NII_{6732} lines were detected but only H_{β}, $OIII_{5008}$, NII_{6550} and H_{α} lines in the wavelength range 4856 Å to 6573 Å are shown in the Figure 56 (e, f, g and h) respectively. The dotted points, solid red line and error bars represent the observed points, Gaussian fits, and the probable error respectively. The positive offset of the lines H_{β} and $OIII_{5008}$ means that their right-hand tail is longer than the left-hand tail and the negative offset of NII_{6550} and H_{α} lines means that their left-hand tail is longer than the right-hand tail. In addition, referring to Table 5, more than 99.9 % coefficient determination and less than (3.9 ± 0.1) Å FWHM of the lines means that the observed points follow Gaussian distribution significantly. We calculated SFR which are 0.0960 $M_{\odot}yr^{-1}$ and 0.1463 $M_{\odot}yr^{-1}$ before and after extinction correction respectively. The catalog value of SFR derived from the FUV fluxes after foreground extinction correction is 0.2089 $M_{\odot}yr^{-1}$. The Balmer decrement is 3.56 which is greater than its normal value of 2.86 (Osterbrock & Ferland, 2006). The oxygen abundance calculated from Equation 3.3 is Z = 8.51 dex which is more than the solar value $Z_{\odot}$ = 8.69 (Allende Prieto et al., 2001; Asplund et al., 2009).

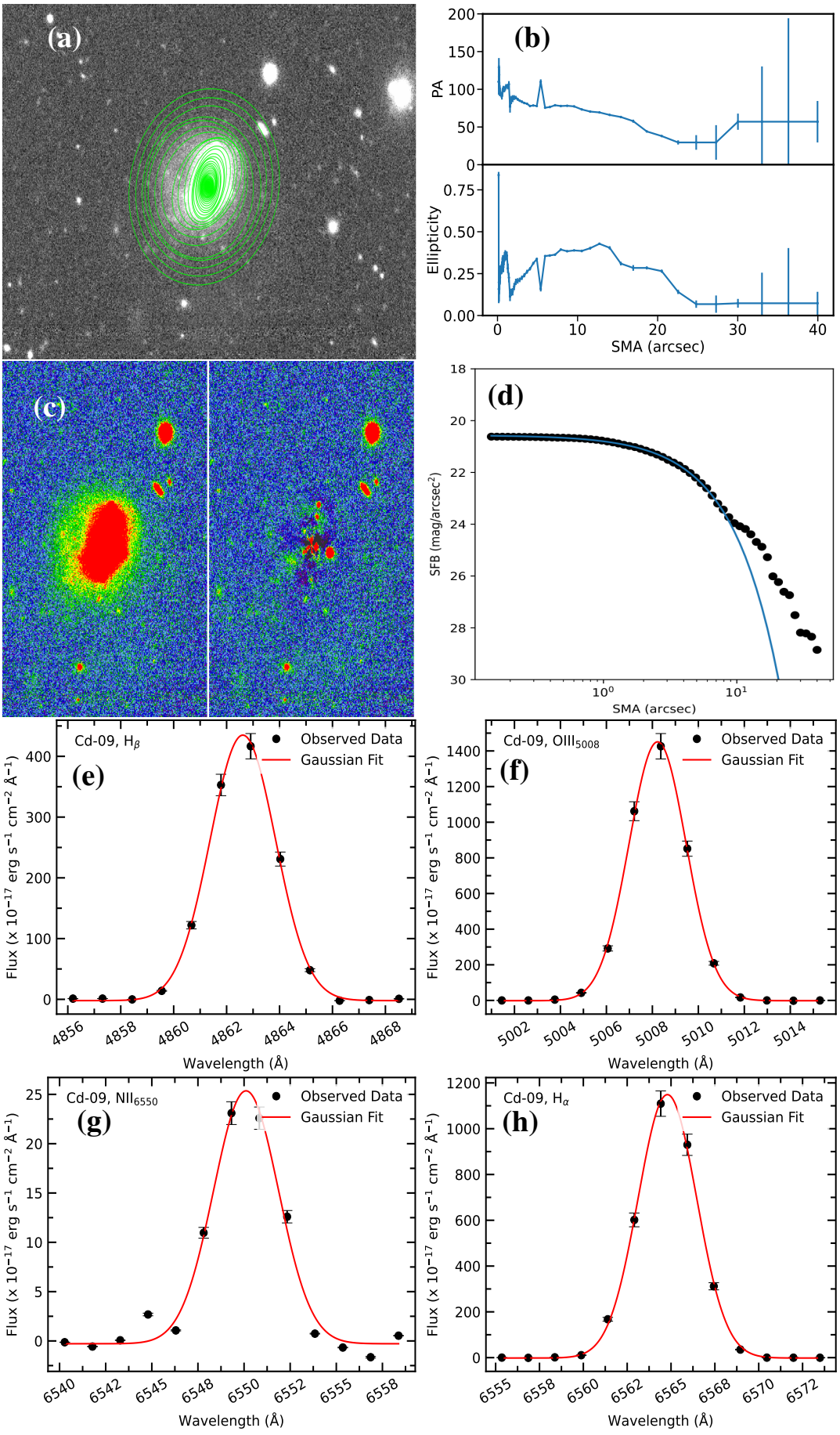

Figure 56: Results of Cd-9. We show surface photometry in sub-figures (a) to (d) and spectroscopy in (e) to (h). For a detailed description of each sub-figure and symbol identification, see Figure 48.

4.1.1.10 Cd-10

Figure 57 (a) displays the ellipses that were created by fitting the intensities in the image of merging compact dwarf galaxy Cd-10 using the IRAF ELLIPSE task. The ellipses are oriented in different directions. The ellipses are regular and densely packed in the central region. Figure 57 (b) displays the radial profiles of position angle (PA) and ellipticity. The PA and ellipticity vary quite randomly within 14 arcsec and then are constant. The residual picture, which is the difference between the original image and the model image is shown in Figure 57 (c). A small part of the galaxy seen in the residual image suggests that our model is proper. Figure 57 (d) displays the galaxy's observed surface brightness profile modeled using the Sérsic function. The blue solid line indicates how closely the observed data (dotted points) resembles the model's best-fit Sérsic line. This demonstrates that the observed light profile best fits with Sérsic function with a Sérsic index of 0.9. The galaxy's average surface brightness is calculated to be 20.32 mag arcsec^{-2}. The Petrosian approach yielded a half-life radius ($h_{\rm r}$) of 0.59 arcsec.

From the optical spectrum of merging compact dwarf galaxy Cd-10, HeI_{3889}, H_{δ}, H_{γ}, H_{β}, $OIII_{4960}$, $OIII_{5008}$, OI_{6366}, H_{α}, NII_{6585}, and SII_{6718} lines were detected but only H_{β}, $OIII_{5008}$, H_{α}, and NII_{6585} lines in the wavelength range 4855 Å to 6596 Å are shown in the Figure 57 (e, f, g and h) respectively. The positive offset of the line H_{β} means that its right-hand tail is longer than left-hand tail and the negative offset of $OIII_{5008}$, H_{α} and NII_{6585} lines means that their left-hand tail is longer than right-hand tail. In addition, more than 99.8% coefficient determination and less than (3.9 ± 0.1) Å FWHM of the lines means that the observed points follow Gaussian distribution almost accurately. We used H_{α} line flux in Equation (3.2) to calculate SFR which is found to be 0.1087 $M_{\odot}yr^{-1}$ and 0.1176 $M_{\odot}yr^{-1}$ before and after extinction correction ($A(H_{\alpha}) = 0.0854$ mag) respectively. The catalog value of SFR derived from the FUV fluxes after foreground extinction correction is 0.3090 $M_{\odot}yr^{-1}$. The line ratio is calculated to be 2.98 which is slightly greater than its normal value of 2.86 (Osterbrock & Ferland, 2006). The oxygen abundance is calculated to be 8.56 dex which is more than the solar value of 8.69 dex (Allende Prieto et al., 2001; Asplund et al., 2009).

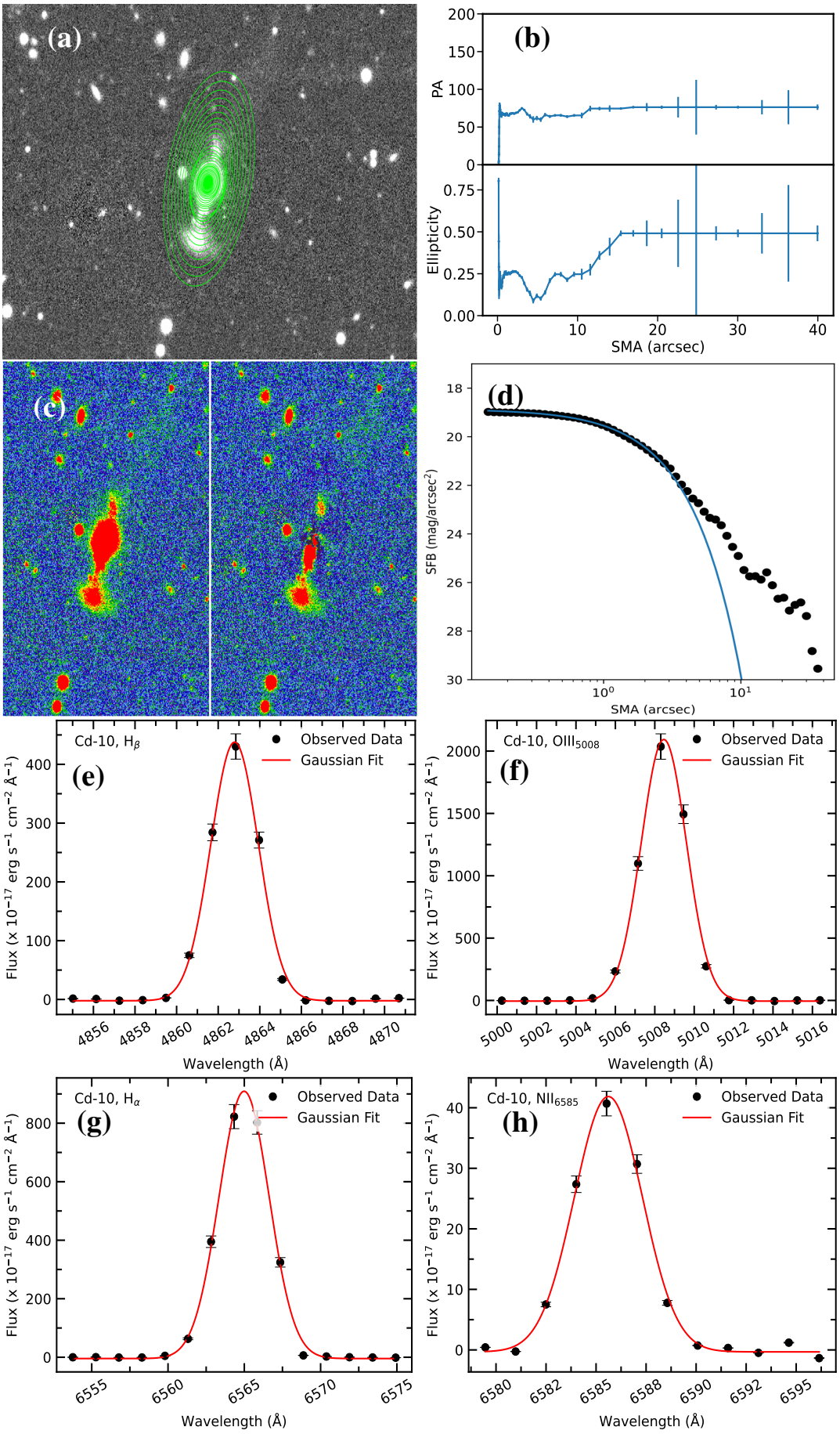

Figure 57: Results of Cd-10. We show surface photometry in sub-figures (a) to (d) and spectroscopy in (e) to (h). For a detailed description of each sub-figure and symbol identification, see Figure 48.

4.1.1.11 Cd-11

Figure 58 (a) shows the green contour map on the grayscale SDSS original image of the merging compact dwarf galaxy Cd-11. The ellipses are oriented in different directions. The ellipses are random and closely packed at the central region. The radial profiles of PA and ellipticity are shown in Figure 58 (b). The PA and ellipticity are varying in the same manner: random in central part and almost constant in the outer area of the galaxy. More or less constant value of PA beyond 6 arcsec indicates that the galaxy has the tidal feature. The error bars in PA and ellipticity are the observational error bars of data that show the uncertainty in the measurement of these quantities. Another type of output of ellipse fit is the residual image, which is the difference between the original image and the model image connected with the best-fitting ellipses. The g-band optical image and its residual image of the galaxy are shown in Figure 58 (c). Only a small residue of the galaxy seen in the image suggests that Sérsic model is appropriate. Figure 58 (d) displays the galaxy's observed surface brightness profile modeled using the Sérsic function. We find that the best fit Sérsic function in the inner region with a Sérsic index of 0.9. The break takes place at about 10 arcsec which is about 21 times of half-light radius of the galaxy. The main body of the galaxy ends at this point and the tidal feature starts beyond this. The effective radius and half-life radius of the galaxy is calculated to be 1.56 arcsec and 0.47 arcsec respectively Which are the minimum values of all compact galaxies in the sample. The mean surface brightness of the galaxy is 19.08 mag arcsec^{-2}.

Analyzed H_α, H_β, $OIII_{5008}$ and NII_{6550} lines in the wavelength range 4856 Å to 6573 Å are shown in the Figure 58 (e, f, g and h) respectively. They are all fitted with a Gaussian profile. The dots represent the observed points and the solid red lines represent the Gaussian fits. The probable error is shown by the error bars. The lines H_β and $OIII_{5008}$ have positive offsets means that their right-hand tail is longer than the left-hand tail. Similarly, the negative offsets of NII_{6550} and H_α lines means that their left-hand tail is longer than the right-hand tail. In addition, more than 98% coefficient determination and less than (4.3 ± 0.2) Å FWHM of the lines means that the observed points follow Gaussian distribution. We used H_α line flux in Equation 3.2 to calculate SFR which is found to be 0.0471 $M_\odot yr^{-1}$ and 0.0610 $M_\odot yr^{-1}$ before and after extinction correction ($A(H_\alpha)$ = 0.2801 mag) respectively. The line ratio c is calculated to be 3.27 which is greater than its normal value of 2.86 (Osterbrock & Ferland, 2006). The higher value of the Balmer decrement suggests the presence of dust at the center which effectively absorbs lower wavelength light. The abundance of oxygen is calculated to be 8.11 dex which is minimum of all our sample galaxies.

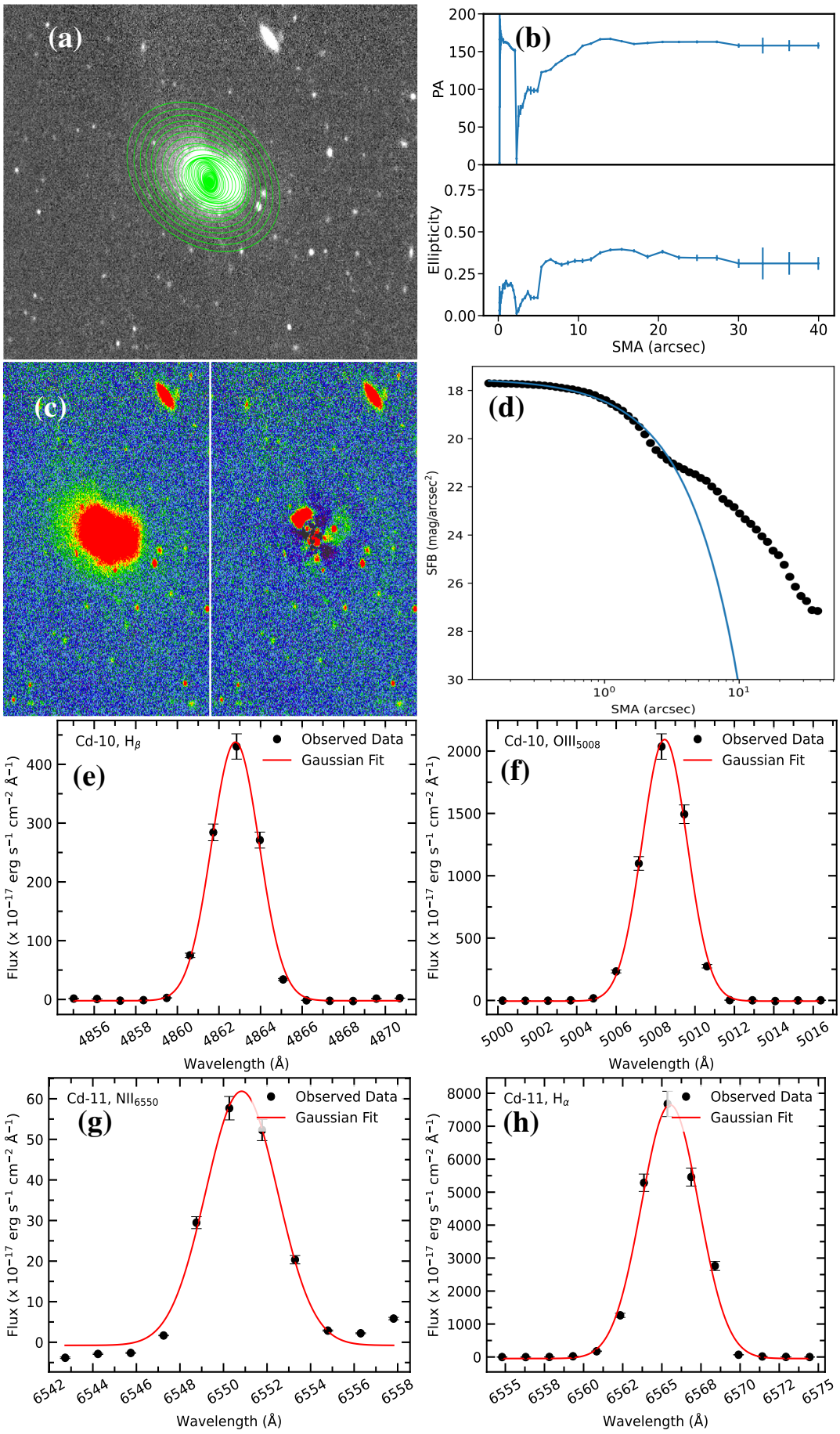

Figure 58: Results of Cd-11. We show surface photometry in sub-figures (a) to (d) and spectroscopy in (e) to (h). For a detailed description of each sub-figure and symbol identification, see Figure 48.

4.1.1.12 Cd-12

The green color ellipses are drawn on the grayscale image of the galaxy Cd-12 is shown in Figure 59 (a). The ellipses cover the main body of the galaxy and are oriented randomly. Variation of PA and ellipticity is shown in Figure 59 (b). The PA is rapidly changing and it flips by 180° in the central region and then remains constant beyond 14 arcsec suggesting the tidal feature in the outer region of the galaxy. A residual image ellipse modeling is shown in Figure 59 (c). Figure 59 (d) displays the Sérsic modeling of the surface brightness profile of the galaxy. This shows that the observed data (dotted points) resembles the model's best-fit Sérsic line (blue color). The best fit with Sérsic function has a Sérsic index of 1.0. The bumps observed in the observed light profile suggest that the galaxy has shells that have higher surface brightness. The galaxy's average surface brightness is calculated to be 20.96 mag arcsec^{-2}. The Petrosian approach yielded a half-life radius ($h_{\rm r}$) of 2.03 arcsec which is the maximum value in a compact group. The effective radius of the galaxy is 7.52 arcsec which is about three times of its half-light radius.

In a spectroscopic analysis of the compact galaxy Cd-12, we fitted four selected emission lines H_β, $OIII_{5008}$, H_α and NII_{6585} in the wavelength range 4857 Å to 6591 Å with Gaussian profiles which are shown in the Figure 59 (e, f, g and h) respectively. The dots represent the observed points and the solid red line represents the Gaussian fits. The probable error is shown by the error bars. The line H_β has a positive offset means that its right-hand tail is longer than the left-hand tail. Similarly, the negative offset of $OIII_{5008}$, H_α, and NII_{6585} lines means that their left-hand tail is longer than the right-hand tail. We find a relatively higher value of FWHM (4.5 ± 0.4) Å than the instrumental value (3.9 Å) which suggests the higher dispersion velocity of the galaxy. The SFR calculated without extinction correction is 0.0479 $M_\odot yr^{-1}$ and that after correction is 0.0967 $M_\odot yr^{-1}$. The value of SFR after extinction correction is more than double its value before extinction correction. It means that the actual flux of the galaxy is more (almost double) than the observed flux. The value of the extinction coefficient is obtained to be 0.7635 mag. The line ratio is 4.12 which is the highest value of all compact galaxies and is also higher than its normal value of 2.86 (Osterbrock & Ferland, 2006). The abundance of oxygen is calculated to be 8.97 dex.

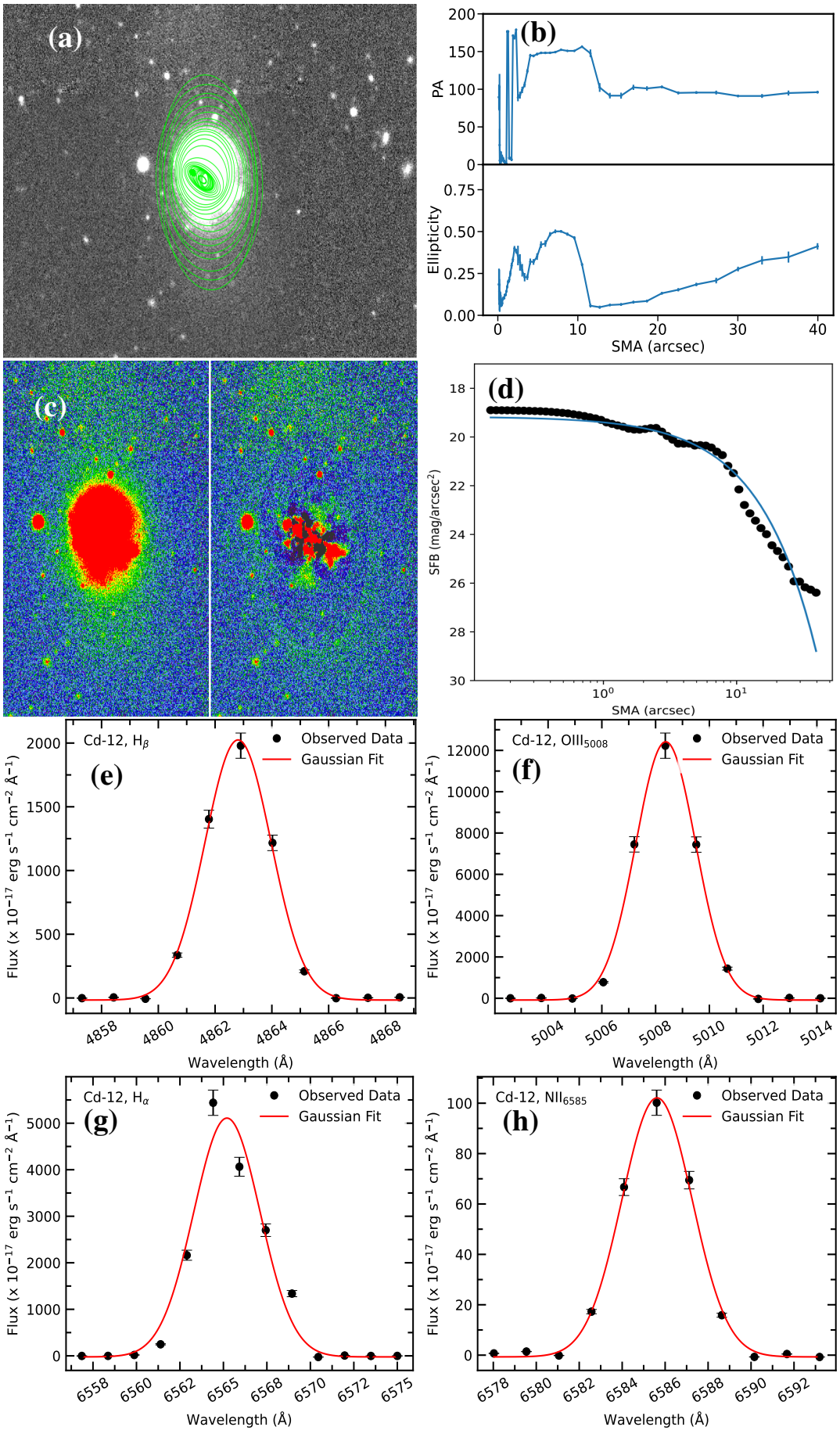

Figure 59: Results of Cd-12. We show surface photometry in sub-figures (a) to (d) and spectroscopy in (e) to (h). For a detailed description of each sub-figure and symbol identification, please refer to Figure 48.

4.1.1.13 Cd-13

For the study of imaging part of merging compact dwarf galaxy Cd-13, we draw green color ellipses on the grayscale image by using IRAF ELLIPSE task as shown in Figure 60 (a). The ellipse density is highest and random at the inner core and it seems almost uniform in the outer region covering the main body of the galaxy. We can see a similar trend of the radial profiles of PA and ellipticity in Figure 60 (b) as in previous cases, in which, both parameters vary rapidly within around 17 arcsecs. They are unchanged at the outer distance. The constancy of PA in the outer region suggests the presence of elongated tidal features. The observational error bars in PA and ellipticity that measures the uncertainty in the measurement of these quantities are also shown in the figure. The error bars are longer due to the noise of the foreground and background objects. The g-band optical image of the galaxy and its residual image are shown in the left and right panels of 60 (c) respectively. Only a very small residue of the galaxy is seen in the image and some signature of tidal features remained, suggesting that the Sérsic model is best fitted for the main body of the galaxy. The observed surface brightness is modeled with Sérsic function, as shown in Figure 60 (d). This shows that the observed data (dotted points) resembles the model's best-fit Sérsic line (blue color) in the main body of the galaxy but there is an outer break at about 10 arcsecs. The humps in observed data also resemble the shell feature of the galaxy. Thus the galaxy has both a tidal tail and shell. The observed data is best fitted with a Sérsic function and the Sérsic index is 0.6. The galaxy's average surface brightness is calculated to be 19.34 mag arcsec^{-2}. The Petrosian approach yielded a half-life radius ($h_{\rm r}$) of 0.63 arcsecs. An effective radius of the galaxy of 1.79 arcsecs is three times its half-light radius.

For the spectroscopic analysis, only H_β, $OIII_{5008}$, NII_{6550}, and H_α lines are used and they are shown in Figure 60 (e, f, g and h) respectively. The dots are observed values plotted against the Gaussian fitting curve and quoted so as to make the point plain and the line of fit obvious. The probable error is shown by the error bars. The lines H_β, $OIII_{5008}$, NII_{6550}, and H_α have positive offsets means that its right-hand tail is longer than the left-hand tail. In addition, more than 99.9% coefficient determination of Gaussian fits of H_α means that the observed points follow Gaussian distribution accurately. The FWHM of the curve is (4.7 ± 0.1) Å which is more than the instrumental value (3.9 Å). This suggests the higher dispersion velocity of the galaxy. The estimated values of SFR form the H_α emission line flux are 0.4755 $M_\odot yr^{-1}$ and 0.9048 $M_\odot yr^{-1}$ before and after extinction correction respectively. This galaxy has the highest value of SFR of all 25 sample galaxies. The line ratio, (c) = 3.99, which is greater than its theoretical value of 2.86 (Osterbrock & Ferland, 2006). The abundance of oxygen calculated from equation (3) is $12 + \log(O/H) = 8.44$ dex.

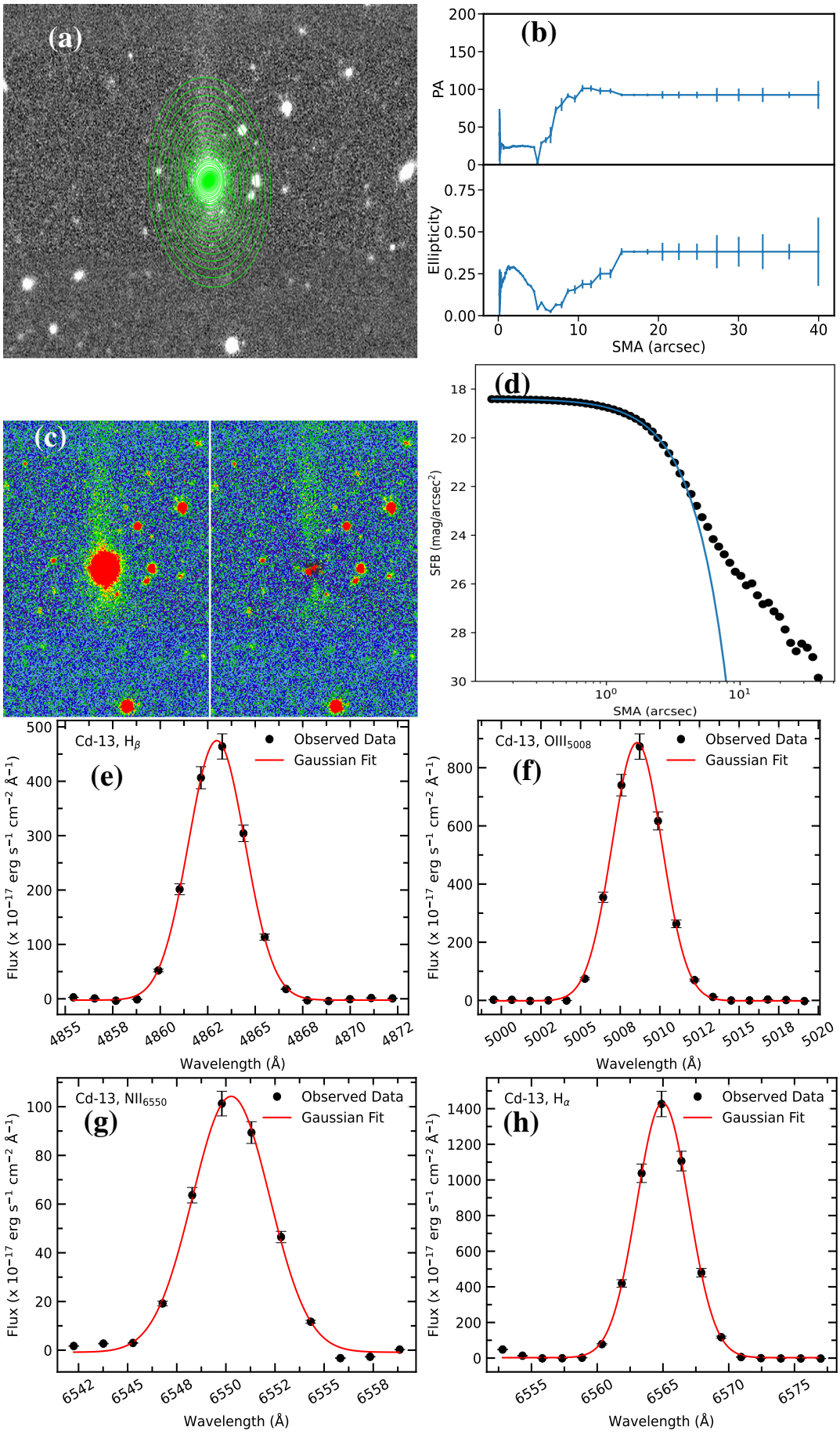

Figure 60: Results of Cd-13. We show surface photometry in sub-figures (a) to (d) and spectroscopy in (e) to (h). For a detailed description of each sub-figure and symbol identification, refer to Figure 48.

4.1.1.14 Cd-14

As explained in other galaxies earlier, the green color ellipses drawn on the grayscale image of merging compact dwarf galaxy Cd-14 are as shown in Figure 61 (a). The bundle of ellipses appears such that we are looking at the galaxy laterally. In Figure 61 (b), we can see the radial profiles of PA and ellipticity in which both quantities go randomly within around 7 arcsec distance and are almost constant in the outer region. The constancy of PA in the outer region suggests that the galaxy has a tidal feature. The observational error bars in PA and ellipticity are also shown in the figure. In the right panel of Figure 61 (c), we can see only a small fraction of the image of the galaxy is the residue after ellipse fitting. It suggests that our model of ellipse fitting is appropriate. Figure 61 (d) shows the best-fitted Sérsic line on the observed surface brightness data. This shows that the observed data (dotted points) resembles the model's best-fitted Sérsic line (blue solid line) in the main body but there is an outer break at above 10 arcsecs. The humps in observed data signify that the galaxy has a shell feature. So, the observed data best fits with Sérsic's function with an index of 1.3. The galaxy's average surface brightness is calculated to be 22.78 mag arcsec^{-2}. The Petrosian approach yielded a half-life radius (h_r) of 1.57 arcsec. The effective radius of the galaxy obtained from the Sérsic method is 8.21 arcsec which is more than five times of its half-light radius.

From the optical spectrum of compact galaxy Cd-14, HeI_{3890}, H_{δ}, H_{γ}, $OIII_{4363}$, H_{β}, $OIII_{4960}$, $OIII_{5008}$, HeI_{5877}, OI_{6366}, NII_{6550}, H_{α}, NII_{6585}, SII_{6720}, SII_{6732} and $NeIII_{3869}$ lines were detected but only H_{β}, $OIII_{5008}$, NII_{6550}, and H_{α} lines in the wavelength range 4857 Å to 6573 Å are shown in the Figure 61(e, f, g and h) respectively. The best-fitted Gaussian curve is shown in red color with probable error bars. The positive offsets of H_{β} and NII_{6550} lines signify their longer right-hand tail than the left-hand tail. On the other hand, the negative offset of the lines $OIII_{5008}$ and H_{α} indicates the longer left-hand tail than the right-hand tail of the Gaussian curve. The resemblance of observed points with the Gaussian distribution is indicated by more than 99.9% coefficient determination. FWHM of H_{α} line is (3.8 ± 0.0) Å . SFR computed by utilizing H_{α} line flux in Equation 3.2 came out to be 0.0193 $M_{\odot}yr^{-1}$ and 0.0193 $M_{\odot}yr^{-1}$ before and after extinction correction respectively. The SFR is found to be unchanged as there is no extinction. The catalog value of SFR derived from the FUV fluxes after foreground extinction correction is 0.0550 $M_{\odot}yr^{-1}$. The line ratio, (c) = 2.74 which is slightly less than its normal value of 2.86 (Osterbrock & Ferland, 2006). This value of c is the lowest value of all 25 galaxies. The abundance of oxygen is calculated to be 8.73 dex.

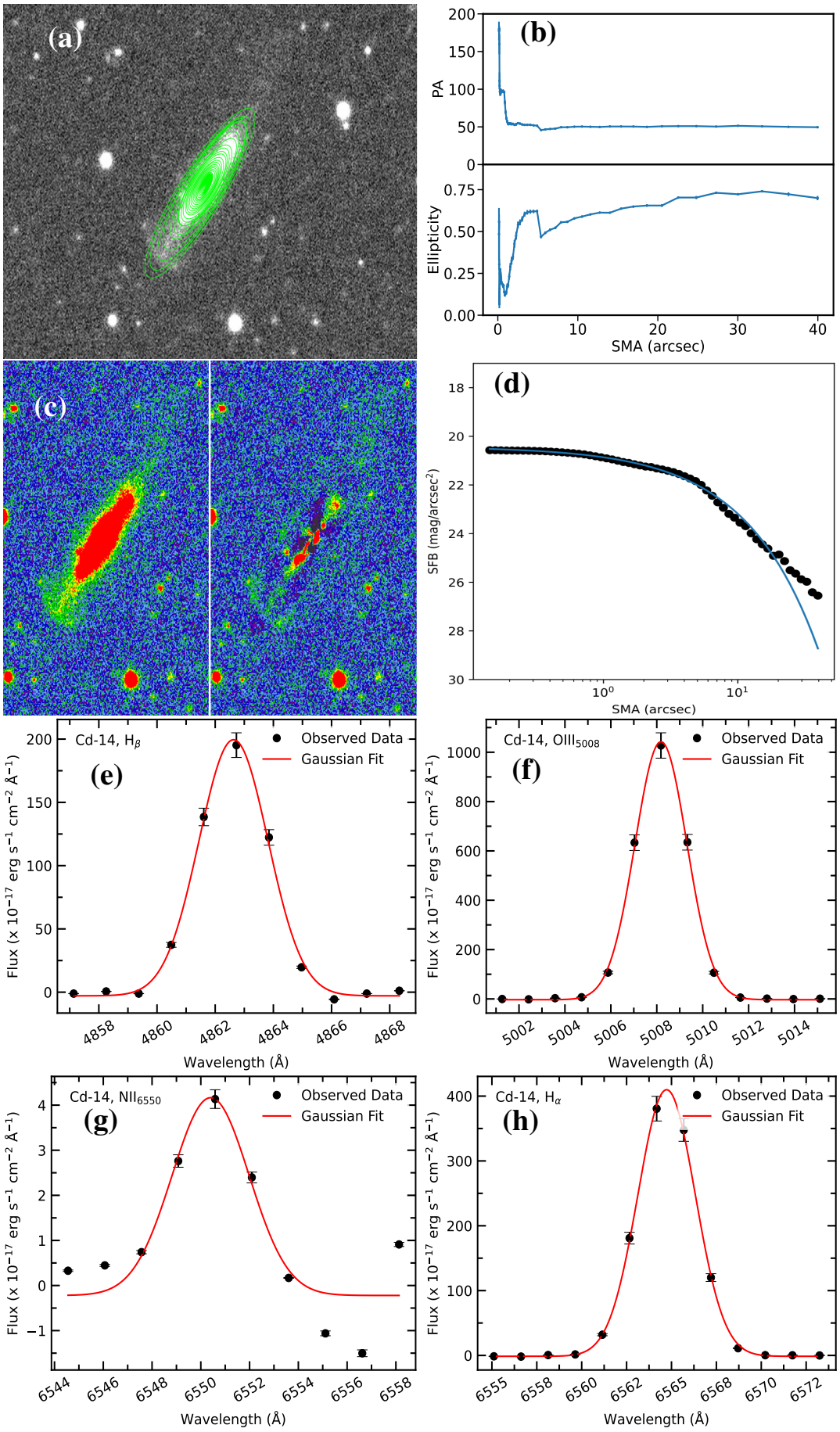

Figure 61: Results of Cd-14. surface photometry is shown in sub-figures (a) to (d) and spectroscopy is shown in (e) to (h). For a detailed description of each sub-figure and symbol identification, refer to Figure 48.

4.1.1.15 Cd-15

To analyze the imaging part of the merging compact dwarf galaxy Cd-15, the green color ellipses drawn on the grayscale image are as shown in Figure 62 (a). The ellipses cover the main body of the galaxy, but it doesn't cover the tidal tail. In Figure 62 (b), the radial profiles of PA and ellipticity are presented in which both quantities go randomly within around 4 arcsec distance, then are almost constant and finally remain constant beyond 23 arcsecs in the outer region. The constancy of PA in the outer region suggests the tidal feature. The PA flips by about 180° at the central core of the galaxy. The long observational error bars in PA and ellipticity are due to noise coming from the foreground and background objects. In Figure 62 (c), we can see only a small fraction of the original image of the galaxy after subtraction of the modeled image. It suggests that our model of ellipse fitting is suitable, but the tidal feature is clearly seen. Figure 62 (d) shows the best-fitted model of the Sérsic function on the observed surface brightness profile. This shows that the observed data (dotted points) resembles the model's best-fitted Sérsic line (blue solid line) within 10 arcsecs and then the break occurs above 10 arcsecs. This signifies that the main body of the galaxy ends at about 10 arcsecs and then its tidal feature starts. The hump in observed data beyond 10 arcsec signifies the shell feature as well. The Sérsic index and effective radius of the galaxy obtained after modeling the observed surface brightness with the Sérsic function are 0.6 and 3.82 arcsecs respectively. Likewise, the half-life radius (h_r) and average surface brightness of the galaxy obtained by the Petrosian approach are 1.40 arcsec and 21.21 mag arcsec^{-2} respectively. The effective radius is almost three times its half-light radius.

For the spectroscopic study of the merging compact dwarf galaxy Cd-15, we have displayed only four important emission lines: H_α, H_β, $OIII_{5008}$ and NII_{6550}in the wavelength range 4856 Å to 6576 Å among the observed lines, H_δ, H_γ, $OIII_{4363}$, H_β, $OIII_{4960}$, $OIII_{5008}$, NII_{6550}, H_α, NII_{6585}, SII_{6720}, and SII_{6732} obtained after Gaussian fitting procedure, as shown in the Figure 62 (e, f, g and h) respectively. We can see that the observed points perfectly fit with the Gaussian distribution along with the coefficient determination of 99.9% and FWHM of (3.8 ± 0.1) Å for H_α line. The probable error is shown by the error bars. The positive offsets of H_β and NII_{6550} lines signifies that their right-hand tail is longer than the left-hand tail. On the other hand, the negative offset of the lines $OIII_{5008}$ and H_α indicates the longer left-hand tail than the right-hand tail of the Gaussian curve. We used H_α line flux to calculate SFR which is found to be 0.0180 $M_\odot yr^{-1}$ and 0.0290 $M_\odot yr^{-1}$ before and after extinction correction respectively. The value of SFR after extinction correction is higher than that before extinction correction. The line ratio is calculated to be 3.66. The abundance of oxygen is calculated to be 8.89 dex.

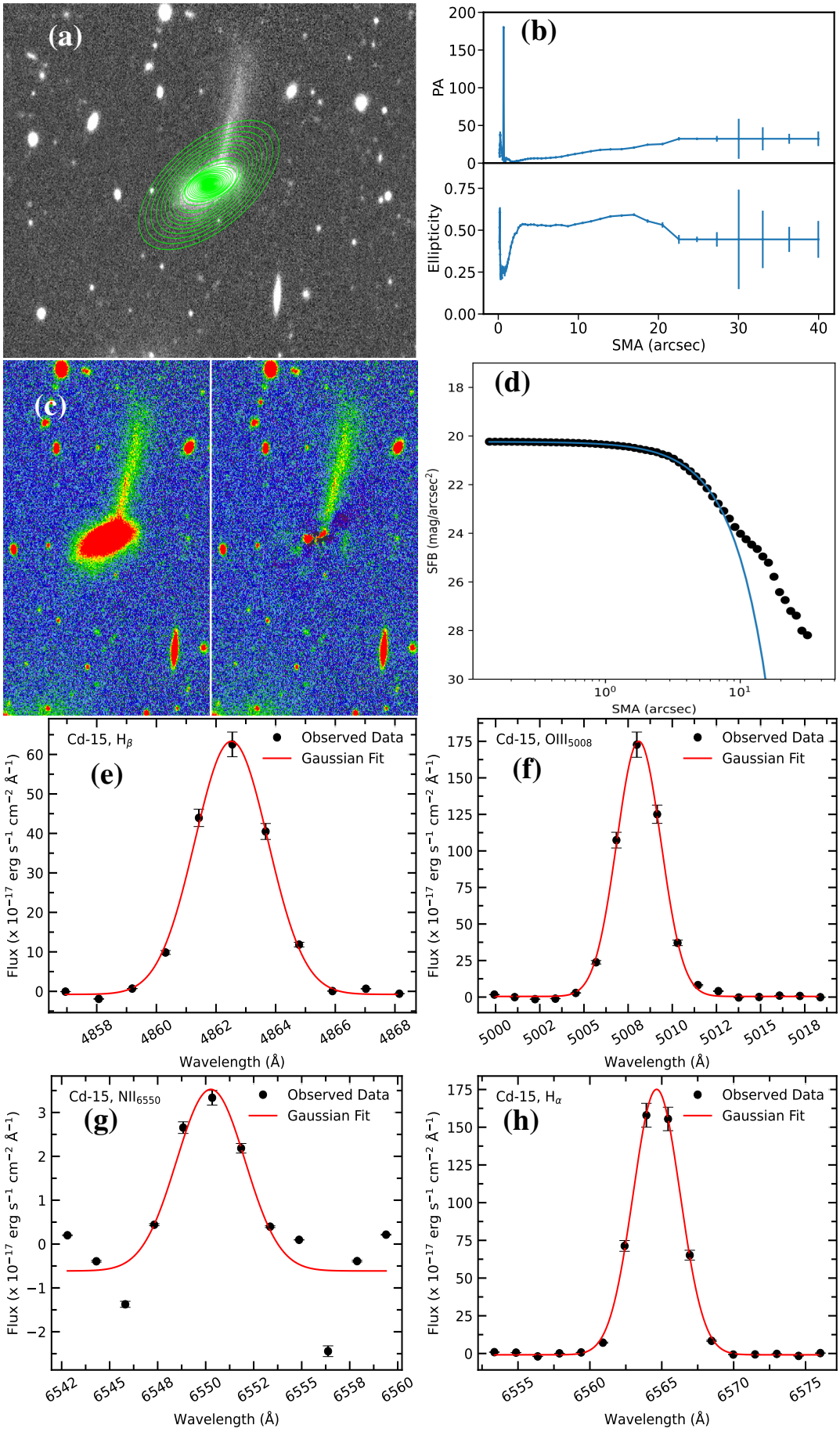

Figure 62: Results of Cd-15. We show surface photometry in sub-figures (a) to (d) and spectroscopy in (e) to (h). For a detailed description of each sub-figure and symbol identification, please refer to the Figure 48.

4.1.2 Extended Merging Dwarf Galaxy

4.1.2.1 Ed-01

To analyze the photometric database of the extended merging dwarf galaxy Ed-01, the green color ellipses are drawn on the grayscale image, which is shown in Figure 63 (a). The ellipses cover the main galaxy but it doesn't cover another galaxy. The ellipses in the central area are very much randomly oriented. In Figure 63 (b), the radial profiles of PA and ellipticity are presented. PA flips by more than 180°, goes randomly within around 3 arcsec distance, then is almost constant and finally flips by around 180°, remains constant beyond around 10 arcsecs in the outer region. The sudden change of PA signifies that a new structure is forming and its random variation signifies the non-uniform density profile. The ellipticity initially decreases then increases randomly and finally goes constant beyond around 12 arcsec. The region of constancy in both quantities signifies the smooth galaxy surface. The uncertainty in the measurement of PA and ellipticity is shown by error bars. In Figure 63 (c), we see the g-band optical image (left panel) and its residual image (right panel). In the residual image, we can see a significant area of the original image that was not covered by the ellipses. It suggests that our model of ellipse fitting may not be so appropriate in this galaxy. The observed light profile modeled with Sérsic function is shown in Figure 63 (d). This plot shows that the observed data (dotted points) resembles the model's best-fitted Sérsic line for the main galaxy. The hump in the outside region signifies the shell feature. The Sérsic index and effective radius of the galaxy obtained as free parameters after modeling the observed surface brightness with the Sérsic function are 2.9 and 29.03 arcsecs respectively. Besides, the half-life radius (h_r) and average surface brightness of the galaxy obtained by the Petrosian method are 1.55 arcsec and 25.14 mag arcsec^{-2} respectively. This galaxy has the highest mean surface brightness of all 25 sample galaxies.

Out of many, only H_β, $OIII_{5008}$, H_α and NII_{6585} lines in the wavelength range 4857 Å to 6595 Å appear in the Figure 63 (e, f, g and h) respectively after Gaussian fitting procedure. The observed fluxes are shown by black dots and the solid red lines represent the Gaussian fits. This shows that the observed data perfectly resemble in the company of Gaussian distribution with coefficient determination of 99.9% and FWHM (3.7 ± 0.1) Å for H_α line. The probable error is shown by the error bars on Gaussian curve. The positive values of offset in lines H_β and $OIII_{5008}$ signifies their longer right-hand tail than left-hand tail. Similarly, the negative offset of H_α and NII_{6585} lines signifies their longer left-hand tail. The value of SFR calculated without extinction correction is 0.1320 $M_\odot yr^{-1}$ and after correction is 0.1702 $M_\odot yr^{-1}$. The catalog value of SFR derived from the FUV fluxes after foreground extinction correction is 0.4467 $M_\odot yr^{-1}$. The Balmer decrement and the abundance of oxygen are calculated to be 3.26 and 8.41 dex respectively.

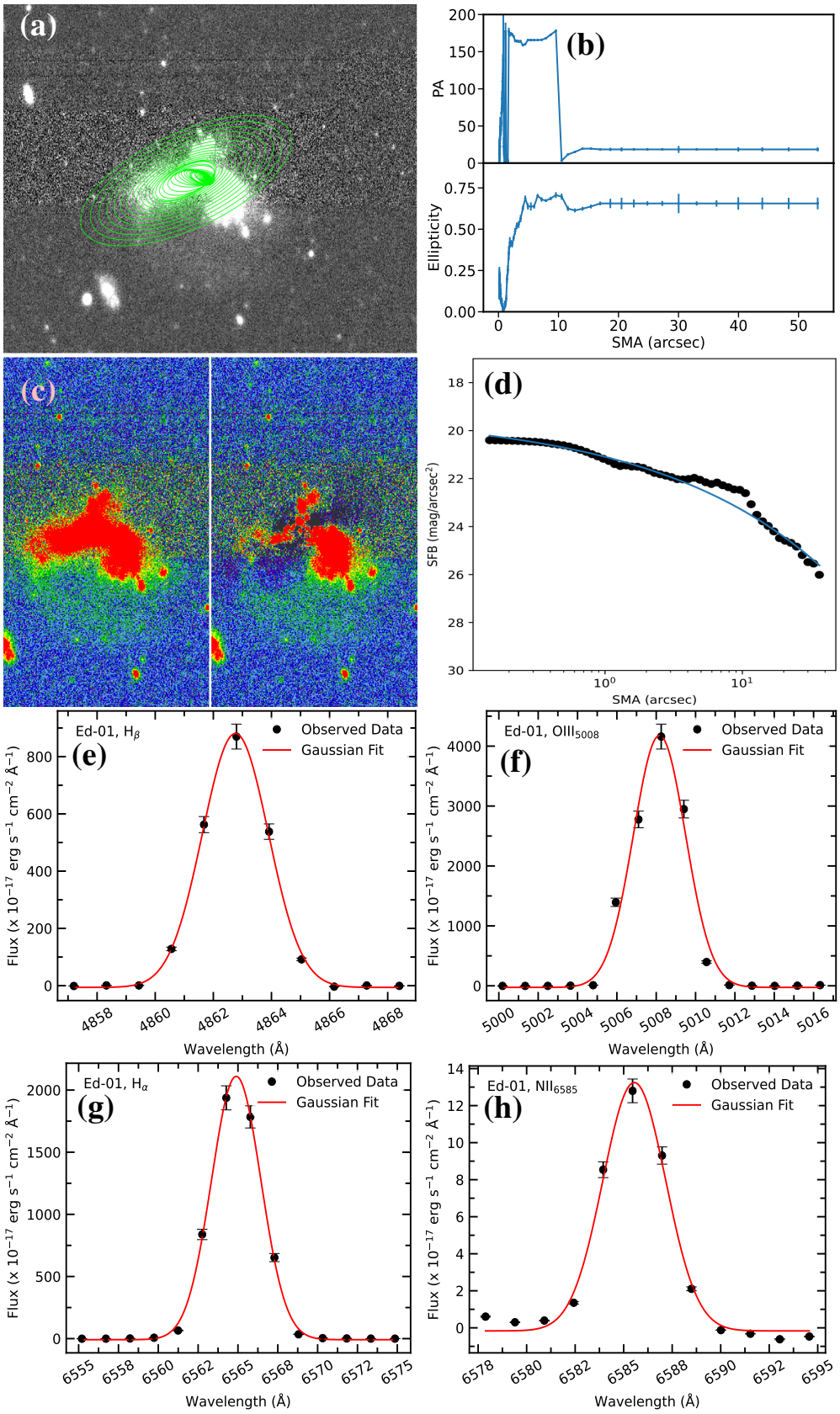

Figure 63: Result of surface photometry and spectroscopy of Ed-01. (a) Best fitted ellipse. (b) Radial profiles of position angle and ellipticity. The error bar is the observational error. (c) Residual image of the galaxy. (d) Sérsic modeling of the observed light profile. The solid circle represents the observed data and the solid line represents the Sérsic model fitting. (e, f, g and h) Four major emission lines fitted with Gaussian profile. The statistical error bars ($\pm\sigma$) are shown.

4.1.2.2 Ed-02

We model the grayscale image of the extended merging dwarf galaxy Ed-02, with the green color ellipse fitting on the isophotes as shown in Figure 64 (a). The ellipses cover up to the outer region but it doesn't cover all body parts of the galaxy. The ellipses in the central area are very much randomly oriented and densely packed, but another bundle of ellipses appears in very few numbers in the perpendicular direction. In Figure 64 (b), the radial profiles of PA and ellipticity are presented. PA seems to be varying randomly, indicating that the galaxy is not uniform and is changing its shape in different regions. The ellipticity is also changing randomly. After modeling with ellipse fitting, we can see the g-band optical image (left panel) and its residual image (right panel) in Figure 64 (c). In the residual image, we can see a remarkable part of the original image. It shows that in this galaxy, our elliptical fitting model may not be as accurate. The observed light profile modeled with the Sérsic function is shown in Figure 64 (d). The blue color solid line is the best-fitted line modeled with Sérsic function. We can see two breaks on the surface brightness profile of the observed light: one at around 10 arcsec and the other above that. This reveals that there are different components of the galaxy. The hump in outside region signifies the shell feature. The Sérsic index and effective radius of the galaxy obtained from the Sérsic method are 2.1 and 11.07 arcsec respectively. Apart from this, the half-life radius (h_r) and average surface brightness of the galaxy obtained from the Petrosian method are 2.37 arcsec and 22.27 mag arcsec^{-2} respectively. The effective radius is almost 9 times of its half-light radius.

From the spectrum of extended merging dwarf galaxy Ed-02, HeI_{3890}, H_δ, H_γ, H_β, $OIII_{4960}$, $OIII_{5008}$, NII_{6550}, H_α, NII_{6585}, SII_{6720}, and SII_{6732} lines were detected. Among them, H_β, $OIII_{5008}$, NII_{6550} and H_α lines in the wavelength range 4855 Å to 6574 Å are shown in Figure 64 (e, f, g and h) respectively. The dots, solid red lines, and error bars have the usual meaning. The H_α line has more than 99.9% coefficient determination and FWHM of (4.1 ± 0.1) Å , showing that the observed points follow Gaussian distribution almost appropriately. The lines H_β, $OIII_{5008}$ and NII_{6550}, have positive offset signifies that their right-hand tail is longer than the left-hand tail. Likewise, the negative offset of the H_α line signifies its longer left-hand tail. After utilizing the value of H_α line flux, the computed value of SFR came out to be 0.0569 $M_\odot yr^{-1}$ and 0.0921 $M_\odot yr^{-1}$ before and after extinction correction respectively. The catalog value of SFR derived from the FUV fluxes after foreground extinction correction is 0.7079 $M_\odot yr^{-1}$. The flux ratio of two Balmer lines is calculated as (c) = 3.67, which is greater than its normal value of 2.86 (Osterbrock & Ferland, 2006). This value helps to determine dust extinction. The abundance of oxygen calculated from Equation 3.3 is $12 + \log(O/H) = 8.41$.

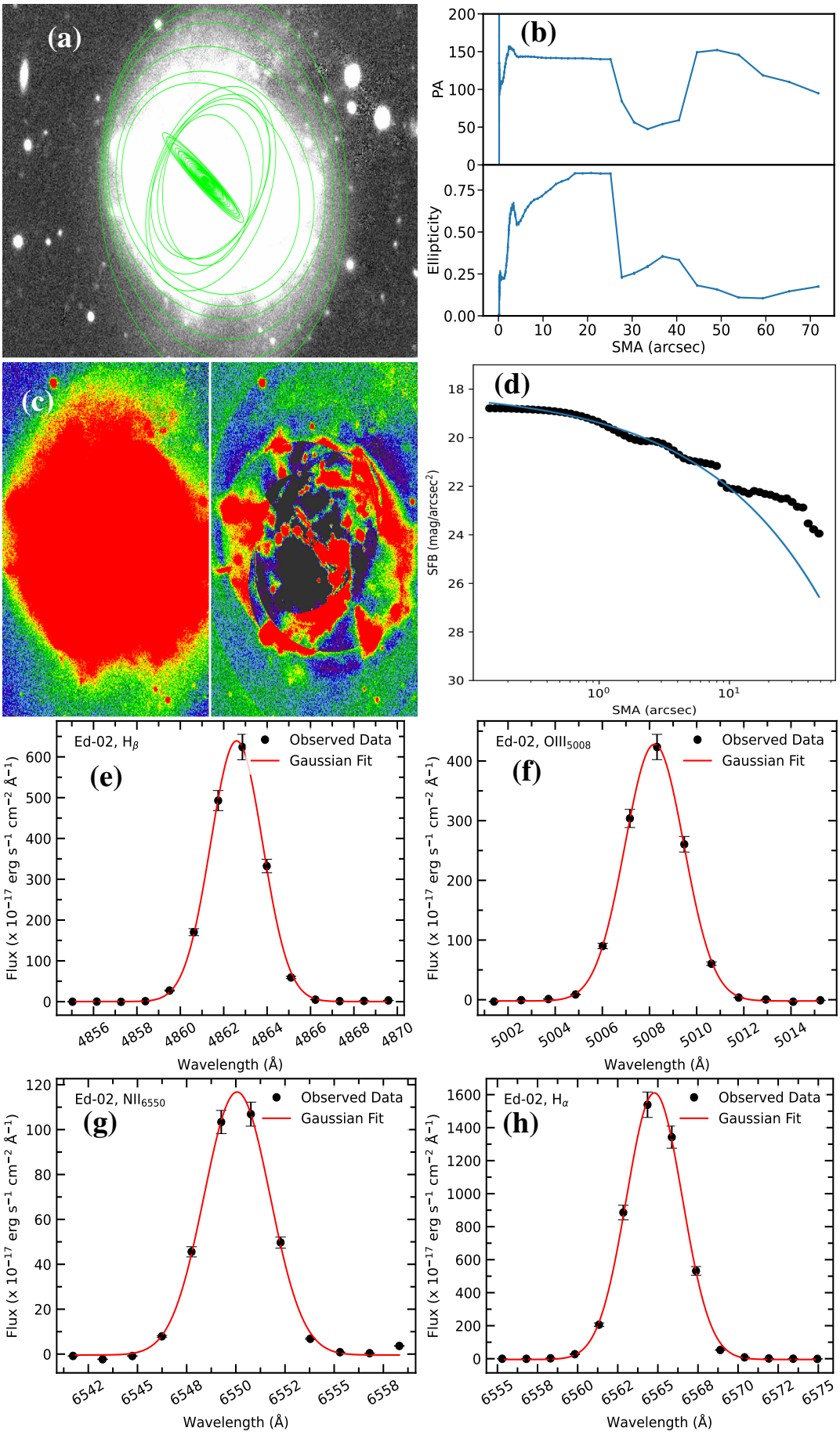

Figure 64: Results of Ed-02. We show surface photometry in sub-figures (a) to (d) and spectroscopy in (e) to (h). For a detailed description of each sub-figure and symbol identification, see Figure 63.

4.1.2.3 Ed-03

The gray scale image of the galaxy is shown in Figure 65 (a), in which the isophotes are closely approximated by green color best-fitted ellipses. We can see two bundles of ellipses: one is a dense inner bundle and the other is countable outer bundle. A gap can be clearly seen between them. The variation of PA and ellipticity with galactocentric distance is shown in Figure 65 (b). PA flips by more than 150° at the center and then it seems almost constant. The ellipticity decreases sharply first, then increases, becomes constant, again decreases and finally rises slowly. In Figure 65 (c), the left panel shows the g-band image of the galaxy, and the right panel shows the residual image obtained after subtraction of the ellipse-fitted model image from the original image. A notable residue of the image suggests that our elliptical fitting model may not be appropriate in this galaxy. The observed light profile modeled with the Sérsic function is shown in Figure 65 (d). The blue color solid line is the best-fitted line modeled with the Sérsic function. A break is seen above 10 arcsec on the surface brightness profile, indicating the different components in the galaxy. The bump in outside region signifies the shell feature. The Sérsic index and effective radius of the galaxy obtained from the Sérsic method are 2.3 and 81.09 arcsec respectively. Apart from this, the half-life radius (h_r) and average surface brightness of the galaxy obtained from the Petrosian method are 4.39 arcsec and 24.62 mag arcsec^{-2} respectively. The effective radius is almost 5 times its half-light radius. The values of effective radius and the half-light radius of this galaxy are the highest of all 25 galaxies in the sample.

From the spectrum, HeI_{3890}, H_δ, H_γ, $OIII_{4365}$, H_β, $OIII_{4960}$,$OIII_{5008}$, OI_{6302}, NII_{6550}, H_α, NII_{6585}, SII_{6720}, and SII_{6732} lines were detected. However only H_β, $OIII_{5008}$, NII_{6550}, and H_α lines in the wavelength range 4854 Å to 6575 Å are shown in the Figure 65 (e, f, g and h) respectively. The lines H_β and $OIII_{5008}$ have positive offset means that their right-hand tail is longer. Similarly, the negative offset of NII_{6550} and H_α lines means that their left-hand tail is longer. In addition, more than 99.9% coefficient determination and less than (3.7 ± 0.1) Å FWHM of the lines suggests that the observed points follow Gaussian distribution almost accurately. We used H_α line flux in Equation 3.2 to calculate SFR which is found to be 0.0537 $M_\odot yr^{-1}$ and 0.0794 $M_\odot yr^{-1}$ before and after extinction correction ($A(H_\alpha)$ = 0.4250 mag) respectively. The value of SFR after extinction correction is more than before extinction correction. The catalog value of SFR derived from the FUV fluxes after foreground extinction correction is 0.2512 $M_\odot yr^{-1}$. The line ratio, $(c) = H_\alpha/H_\beta = 3.50$, which is greater than its normal value of 2.86 (Osterbrock & Ferland, 2006). The abundance of oxygen calculated from Equation 3.3 is $12 + \log(O/H) = 8.45$ dex.

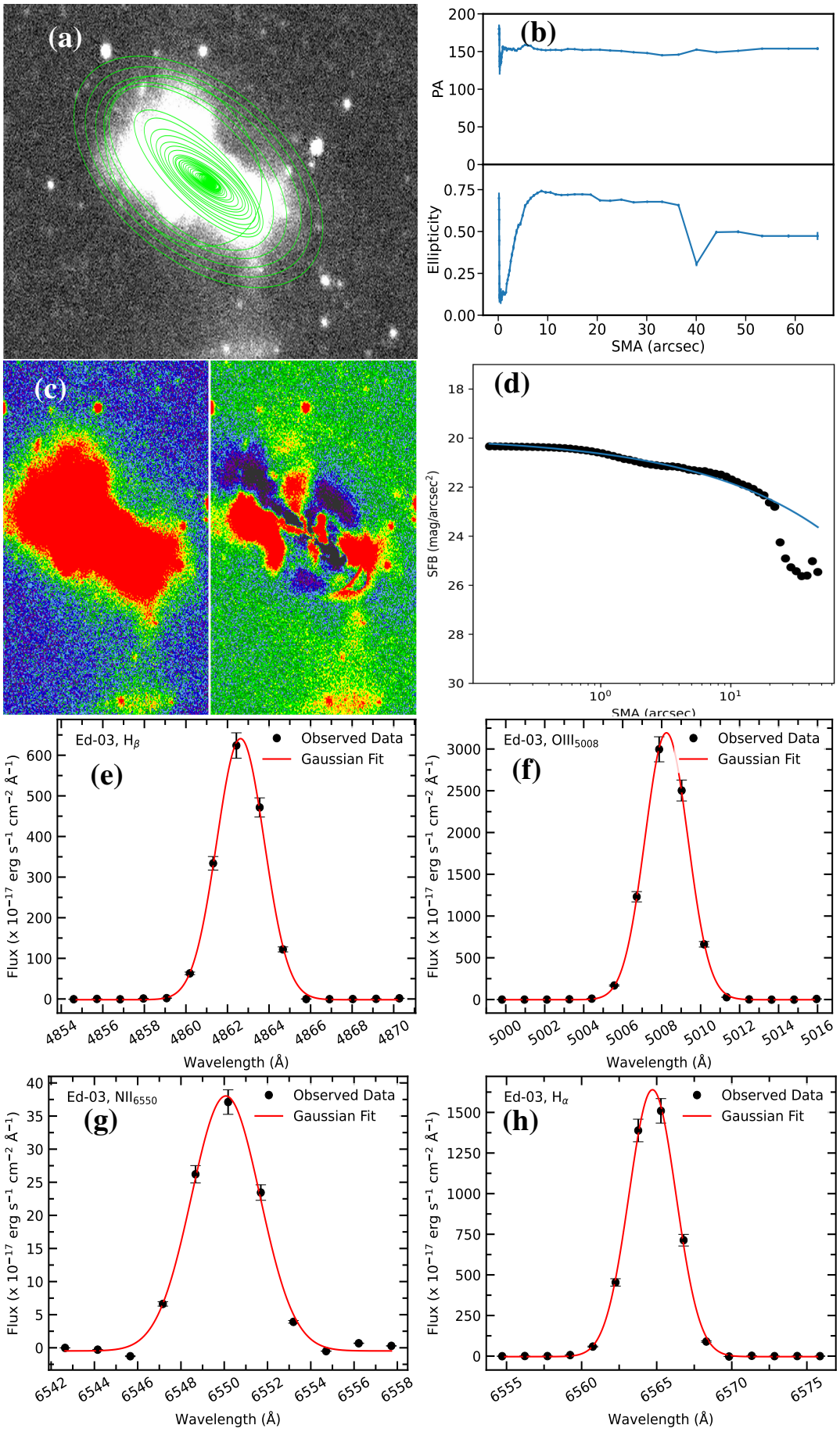

Figure 65: Results of Ed-03. We show surface photometry in sub-figures (a) to (d) and spectroscopy in (e) to (h). For a detailed description of each sub-figure and symbol identification, please refer to Figure 63.

4.1.2.4 Ed-04

The galaxy's grayscale image can be seen in Figure 66 (a), where the green color ellipses are drawn. Figure (b) illustrates the variation of PA and ellipticity with galactocentric distance. PA flips by about 180° at the center many times, then is constant at a very small angle and it seems almost unchanged after increasing by more than 150° beyond around 6 arcsecs. The small values of ellipticity in the outer region mean that the galaxy is less elliptical in this region. The g-band image and model subtracted residual image are displayed in Figure 66 (c). The small residue of the galaxy signifies that the best-fitting model may be appropriate. The observed surface brightness profile modeled with a Sérsic function is presented in Figure 66 (d). The bump and break in the observed data signify that the galaxy is shell featured and has changed its structure. The best-fitted Sérsic index and effective radius of the galaxy are 0.9 and 6.88 arcsec respectively. Apart from this, the half-life radius ($h_{\rm r}$) and average surface brightness of the galaxy obtained from the non-parametric (Petrosian) method are 2.21 arcsec and 19.63 mag arcsec^{-2} respectively.

Out of many, analyzed emission lines in the spectrum, H_β, $OIII_{5008}$, NII_{6550}, and H_α are presented in the Figure 66 (e, f, g and h) respectively. The dots represent the observed points and the solid red line represents the Gaussian fits. The probable error is shown by the error bars. The lines H_β and NII_{6550} have positive offset means that their right-hand tail is longer than left-hand tail. Similarly, the negative offset of $OIII_{5008}$ and H_α lines means that their left-hand tail is longer than right-hand tail. Fitting with Gaussian profile, we find FWHM of H_α line is (4.2 ± 0.1) Å. The SFR calculated by using H_α flux is found to be 0.0044 $M_\odot yr^{-1}$ and 0.0055 $M_\odot yr^{-1}$ before and after extinction correction, respectively. The line ratio, (c) = 3.23 is greater than its normal value of 2.86 (Osterbrock & Ferland, 2006). The abundance of oxygen is $12 + \log(O/H) = 8.51$ dex.

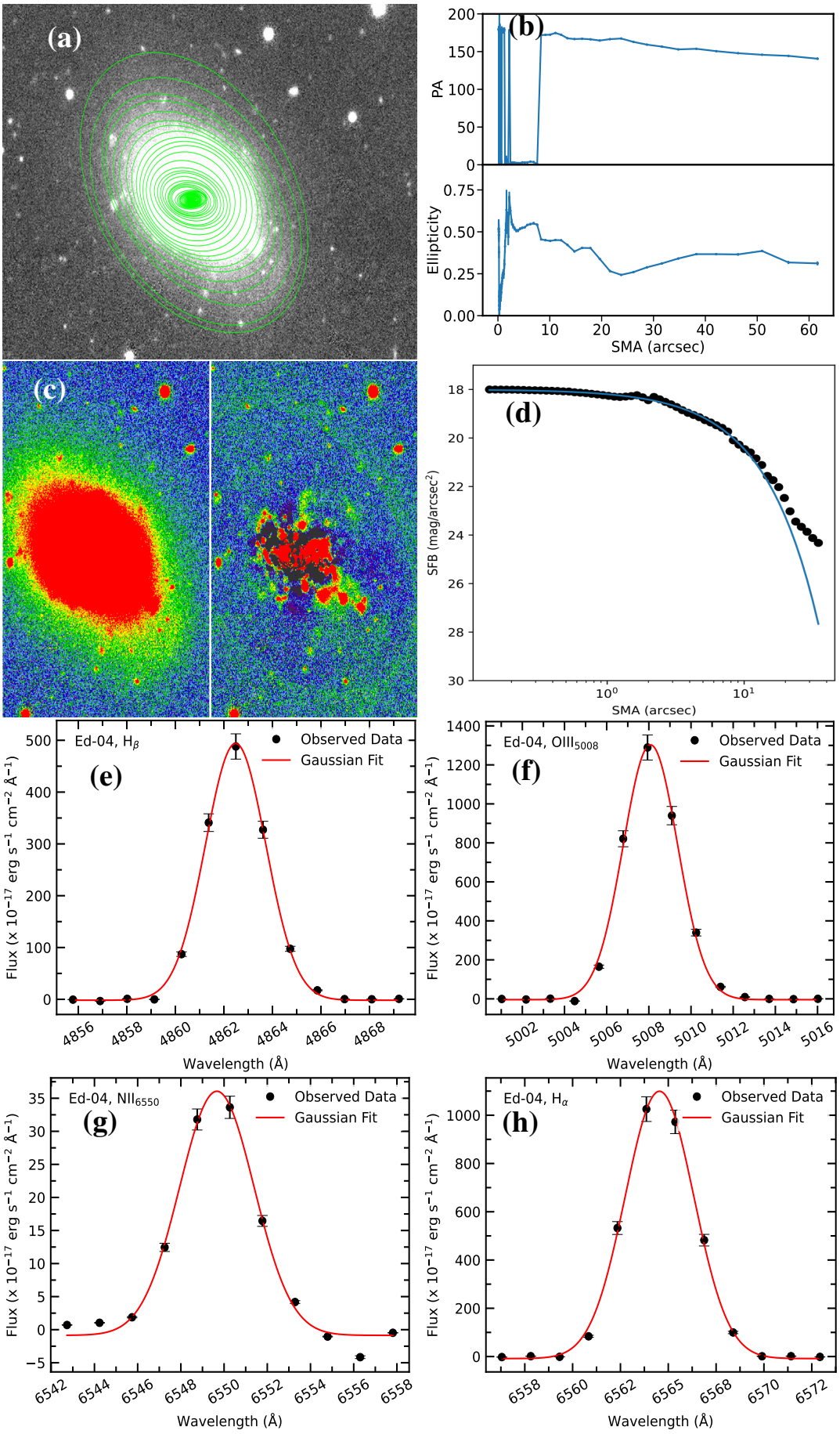

Figure 66: Results of Ed-04. We show surface photometry in sub-figures (a) to (d) and spectroscopy in (e) to (h). For a detailed description of each sub-figure and symbol identification, refer to Figure 63.

4.1.2.5 Ed-05

We drew the best-fitted ellipses of the isophotes over the grayscale image, which is shown in Figure 67 (a). The ellipses appear virtually homogeneous in the outer area but are crowded and erratic in the center. Figure 67 (b) illustrates the radial profile of PA and ellipticity. PA and ellipticity change randomly within 16 arcsecs and then both quantities are almost constant in the outer region of the galaxy. Figure 67 (c) shows the galaxy's g-band picture in the left panel and its residual image in the right panel after the model image has been subtracted from the original image. A small residue of the image left over signifies that our ellipse-fitting model is nearly appropriate. The surface brightness profile modeled with the Sérsic function is presented in Figure 67 (d). A clear deviation of the observed data points from the model line implies the tidal feature. The bumps on the observed light profile signify the shell feature of the galaxy. The Sérsic index and effective radius of the galaxy obtained from the parametric (Sérsic) method are 0.9 and 6.56 arcsec respectively. Apart from this, the half-life radius ($h_{\rm r}$) and average surface brightness of the galaxy obtained from the non-parametric (Petrosian) method are 2.84 arcsec and 20.99 mag arcsec^{-2} respectively. This value of surface brightness is the minimum of all extended groups of galaxies.

For the spectroscopic study of the extended merging dwarf galaxy Ed-05, the emission lines H_β, $OIII_{5008}$, H_α and NII_{6585} are analyzed and their Gaussin profile fitting are shown in the Figure 67 (e, f, g and h) respectively. The lines H_β, $OIII_{5008}$ and NII_{6585} have positive offset indicating their longer right-hand tail. Similarly, the negative offset of H_α line indicates their left-hand tail. We used H_α line flux to calculate SFR which is found to be 0.0022 $M_\odot yr^{-1}$ and 0.0035 $M_\odot yr^{-1}$ before and after extinction correction respectively. The SFR of this galaxy is least of all members of our sample extended group. The value of SFR after extinction correction is more than before extinction correction. The catalog value of SFR derived from the FUV fluxes after foreground extinction correction is 0.0741 $M_\odot yr^{-1}$. The line ratio, (c) = 3.63 which is greater than its normal value of 2.86 (Osterbrock & Ferland, 2006). The abundance of oxygen is $12 + \log(O/H) = 8.78$ dex.

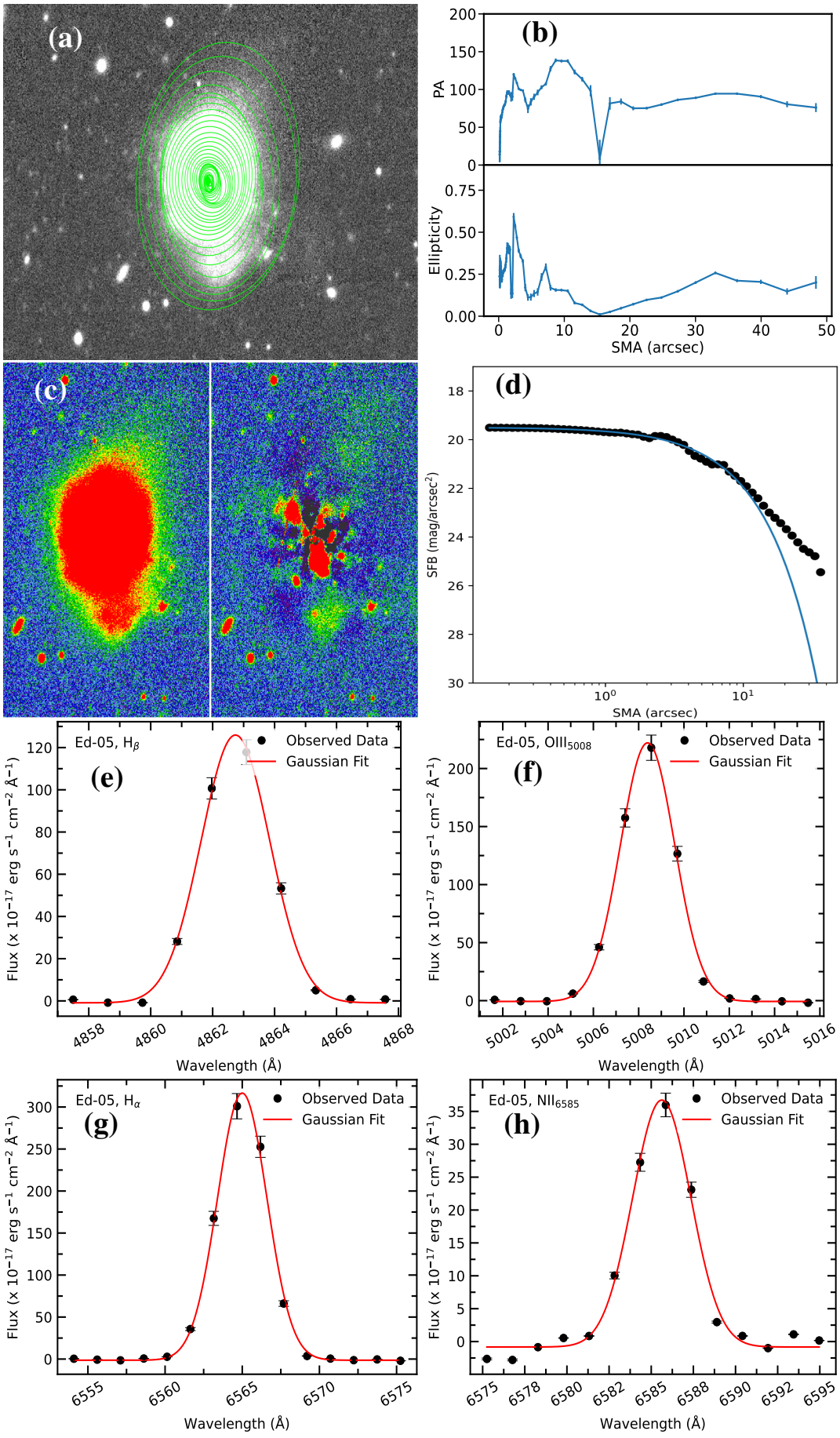

Figure 67: Results of Ed-05. We show surface photometry in sub-figures (a) to (d) and spectroscopy in (e) to (h). For a detailed description of each sub-figure and symbol identification, see Figure 63.

4.1.2.6 Ed-06

To study the surface photometry of the extended merging dwarf galaxy Ed-06, we run the IRAF ELLIPSE task to fit elliptical isophotes. We show the resultant ellipse overlaying on the gray-scale image in Figure 68 (a) and measure the light profiles. The ellipses cover almost all areas on the image of the galaxy and are randomly oriented. In Figure 68 (b), the radial profiles of PA and ellipticity are presented. The PA seems to vary randomly in the range 0 to 180°, but it is almost constant at the region of about 23-31 arcsec. After removing the modeled image from the original image, we can only make out a tiny portion of the galaxy's original image as shown in Figure 68 (c). It suggests that our model of ellipse fitting is applicable. Figure 68 (d) shows the observed surface brightness profile modeled with the Sérsic function. The best fitting is performed at the central region as the focused main galaxy is in that area. We can see that the observed data (dotted points) resembles mostly the model's best-fitted Sérsic line (blue solid line) in the inner region and then the break occurs above 10 arcsec which is above three times the half-light radius of the galaxy. At this distance, the main body of the galaxy ends and then its tidal feature starts. We can see many bumps in observed data that identify the shell feature. The Sérsic index and effective radius of the galaxy obtained after modeling the observed surface brightness with the Sérsic function are 0.8 and 6.62 arcsec respectively. Likewise, the half-life radius ($h_{\rm r}$) and average surface brightness of the galaxy obtained by the Petrosian approach are 2.73 arcsecs and 22.84 mag arcsec^{-2} respectively. The effective radius is almost three times of its half-light radius.

From the spectrum, HeI$_{3870}$, H$_{\delta}$, H$_{\gamma}$, H$_{\beta}$, OIII$_{4960}$, OIII$_{5008}$, H$_{\alpha}$, NII$_{6585}$, SII$_{6720}$ and SII$_{6732}$ lines were detected. We used H$_{\beta}$, OIII$_{5008}$, H$_{\alpha}$ and NII$_{6585}$ lines for spectroscopic analysis and they are shown in Figure 68 (e, f, g and h) respectively. The dots represent observed points and the solid red lines represent the Gaussian fits. The probable error is shown by the error bars. FWHM of H$_{\alpha}$ line is (3.8 ± 0.1) Å and its 99.7 % coefficient determination signifies that the observed data follows Gaussian distribution. Other lines also follow normal distribution except for slight deviation of the observed points in the case of NII$_{6585}$ line. The positive offset of lines H$_{\beta}$, OIII$_{5008}$ and NII$_{6585}$ means their longer right-hand tail and the negative offset of H$_{\alpha}$ line means its longer left-hand tail in the Gaussian curve. SFR calculated before extinction correction is 0.0046 M$_{\odot}$yr^{-1} and that after rectification is 0.0055 M$_{\odot}$yr^{-1}. The Balmer decrement (c) = 3.15 which is higher than its normal value of 2.86 (Osterbrock & Ferland, 2006). The abundance of oxygen is 12 + log(O/H) = 8.88 dex that is higher than the solar value $Z_{\odot}$ = 8.44 Allende Prieto et al. (2001); Asplund et al. (2009).

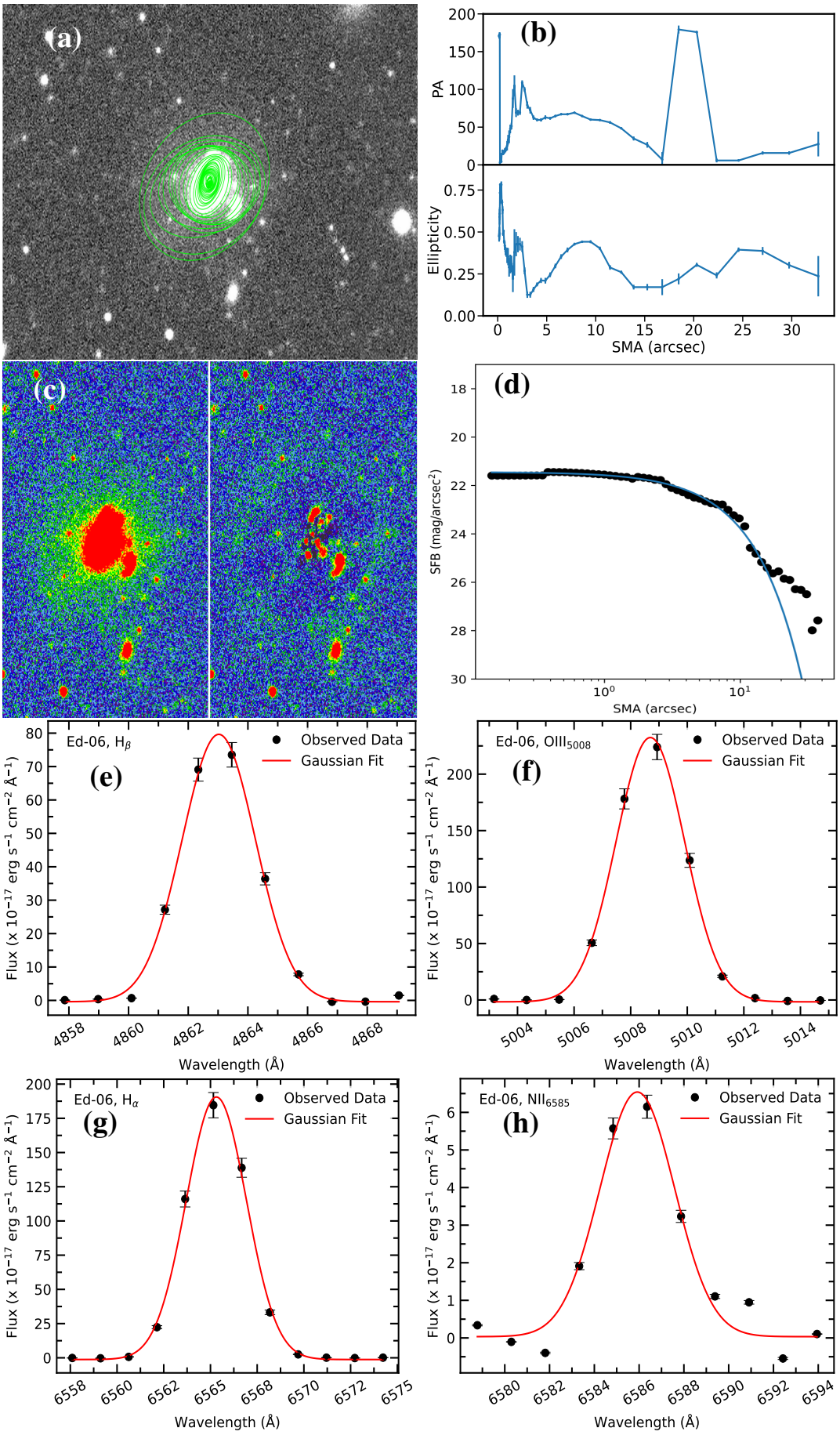

Figure 68: Results of Ed-06. We show surface photometry in sub-figures (a) to (d) and spectroscopy in (e) to (h). For a detailed description of each sub-figure and symbol identification, refer to Figure 63.

4.1.2.7 Ed-07

The best-fit ellipse overlaying in a grayscale image is shown in Figure 69 (a). Figure 69 (b) shows the variation of PA and ellipticity as a function of distance from the galaxy center. The PA starts to increase from 150 °, reaches more than 125 °, decreases slightly and remains constant beyond around 14 arcsec distance. It means there is a tidal feature in the outer region of the galaxy. The ellipticity seems to change rapidly around 7 arcsec but increases gradually outward. This means the galaxy is elongated in the outer region. In Figure 69 (c), we can see the g-band image of the galaxy in the left panel and the residual image in the right panel. Only a small section of the image is seen, which signifies the ellipse-fitting model is proper. Figure 69 (d) shows the observed surface brightness profile modeled with the Sérsic function. The main galaxy is located in the central region, where the best fitting is done. We can see that in the inner region, the observed data (dotted points) resembles the best-fitted Sérsic line (blue solid line) and the break occurs above 10 arcsec, which is more than eight times the galaxy's half-light radius. At this distance, the galaxy's main body ends and its tidal feature begins. We can see a break in the observed data at around 9 arcsec distance indicating the change in structure of the galaxy. The Sérsic index and effective radius of the galaxy from the Sérsic method are obtained to be 0.9 and 3.92 arcsec respectively. Likewise, the half-life radius (h_r) and average surface brightness of the galaxy acquired by the Petrosian approach are 1.49 arcsec and 21.34 mag arcsec^{-2} respectively. The effective radius is almost three times its half-light radius.

In the visual inspection of the optical spectrum of the compact merging dwarf galaxy Ed-07, we detected HeI_{3870}, H_δ, H_γ, H_β, $OIII_{4960}$, $OIII_{5008}$, OI_{6302}, H_α, NII_{6585}, SII_{6720} and SII_{6732} emission lines. For our work, we use H_β, $OIII_{5008}$, H_α and NII_{6585} lines in the wavelength range 4854 Å to 6592 Å that are shown in Figure 69 (e, f, g and h) respectively. Gaussian fitting is performed on the emission lines. The dots represent observed points and the solid red lines represent the Gaussian fits. The probable error is shown by the error bars. 99.9% coefficient determination and less than (4.1 ± 0.1) Å FWHM of the H_α line means that the observed points follow Gaussian distribution almost accurately. The lines H_β and H_α have positive offset means that their right-hand tail is longer than the left-hand tail. Similarly, the negative offset of lines $OIII_{5008}$ and NII_{6585} means that their left-hand tail is longer than the right-hand tail. We used H_α line flux in equation 3.2 to calculate SFR which is found to be 0.0304 $M_\odot yr^{-1}$ and 0.0308 $M_\odot yr^{-1}$ before and after extinction correction respectively. The value of SFR before and after extinction correction is almost same because there is no extinction. The catalog value of SFR derived from the FUV fluxes after foreground extinction correction is 0.0741 $M_\odot yr^{-1}$. The line ratio $(c) = 2.78$ which is less than its normal value of 2.86 (Osterbrock & Ferland, 2006). The abundance of oxygen of the galaxy is calculated to be 8.55 dex.

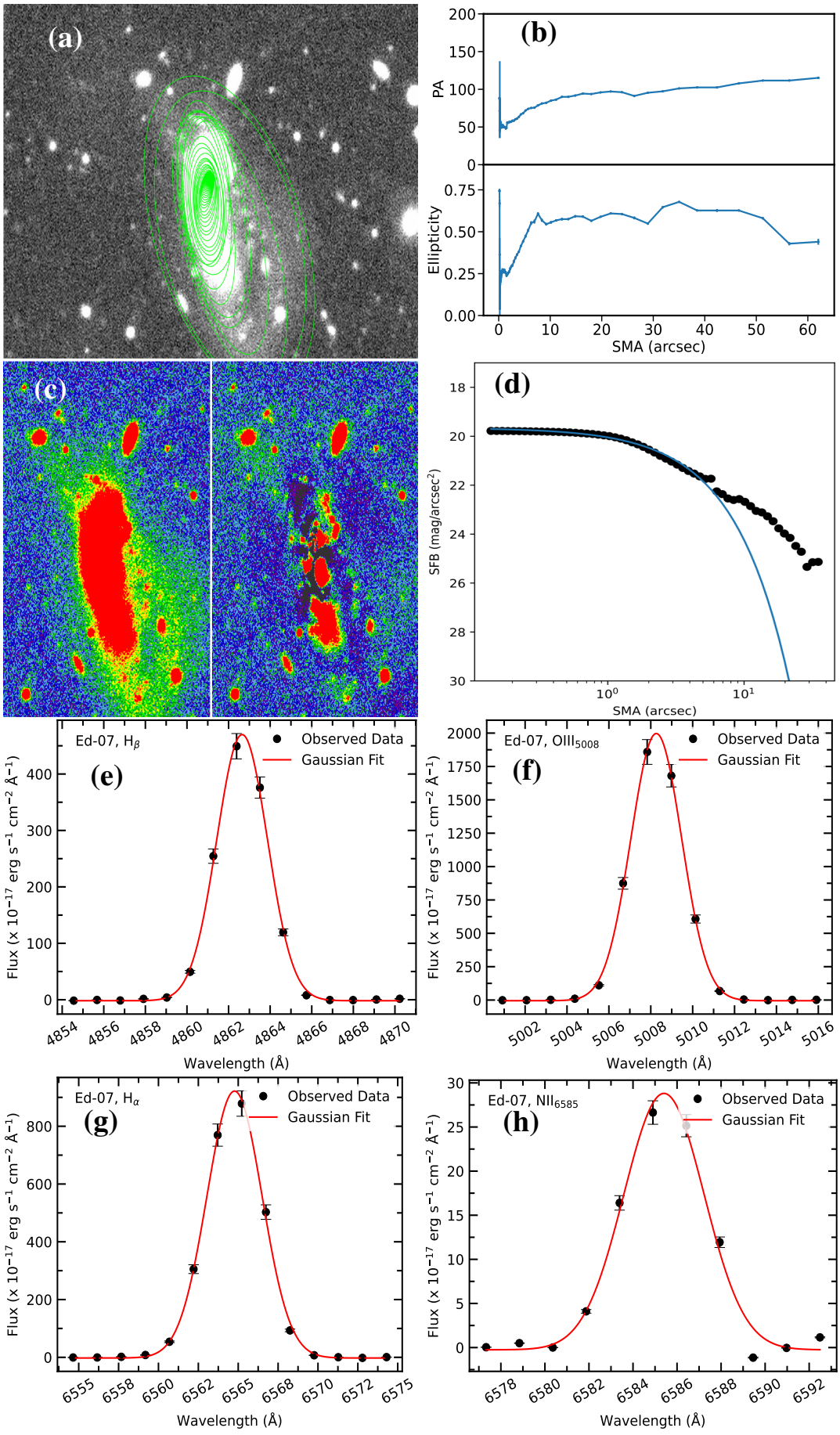

Figure 69: Results of Ed-07. We show surface photometry in sub-figures (a) to (d) and spectroscopy in (e) to (h). For a detailed description of each sub-figure and symbol identification, see Figure 63.

4.1.2.8 Ed-08

To study the surface photometry of the extended merging dwarf galaxy Ed-08, we run the IRAF ELLIPSE task on the SDSS g-band image because of its higher SNR. We show the resultant ellipse overlaying in the g-band image in Figure 70 (a). The image seems like a guitar galaxy in which a clear stellar stream forms tail like structure oriented along the N-E direction. The ellipses are regular and uniform but are more concentrated at the center. The variation of PA and ellipticity as a function of galactocentric distance from the galaxy center is shown in Figure 70 (b). The PA starts to increase randomly from the center, then flips by about 140 °, and remains constant beyond around 5 arcsec distance, signifying that there is a significant antenna outside the galaxy. The ellipticity decreases randomly and remains constant beyond 3 arcsec distance. This means the ellipses are almost circular and the galaxy body is nearly uniform i.e., there is no change in structure. The long error bars are due to light coming from background and foreground objects. In Figure 70 (c), we show the g-band image of the galaxy in the left panel and the residual image in the right panel. A significant section of the image is seen as residue which implies that the ellipse fitting model is not so fitted correctly. It might be because the galaxy is still interacting. We can see a clear antenna structure. Figure 70 (d) shows the observed surface brightness profile modeled with the Sérsic function. Unlike other galaxies, the observed data (dotted points) resembles the best-fitted Sérsic line (blue solid line) and the outer break occurs just above 10 arcsec which is more than five times the galaxy's half-light radius. At this distance, the galaxy's main body ends and its tidal feature begins. The Sérsic index and effective radius of the galaxy from the Sérsic method are obtained to be 0.7 and 3.21 arcsec respectively. This value of Sérsic index is the least in the extended galaxy group. Likewise, the half-life radius ($h_{\rm r}$) and average surface brightness of the galaxy acquired by the Petrosian approach are 1.91 arcsec and 21.27 mag arcsec^{-2}, respectively. The effective radius is almost two times of its half-light radius.

Out of many emission lines in the spectrum, only four lines H_β, $OIII_{5008}$, NII_{6550}, and H_α are utilized and they are shown in the Figure 70 (e, f, g and h) respectively. The black dots, solid red lines, and error bars have the usual meanings as in previous cases. The positive ofsect of $OIII_{5008}$ and H_α lines and the negative offset of H_β and NII_{6550} lines means the same as in Ed-07. In addition, the 100% coefficient determination and less than (3.8 ± 0.1) Å FWHM of H_α line means that the observed points follow Gaussian distribution perfectly. We used H_α line flux in Equation 3.2 to calculate SFR which is found to be 0.1913 $M_\odot yr^{-1}$ and 0.2647 $M_\odot yr^{-1}$ before and after extinction correction respectively. This SFR is the highest value in the extended group. The catalog value of SFR is 0.4266 $M_\odot yr^{-1}$. The abundance of oxygen is calculated to be 8.32 dex.

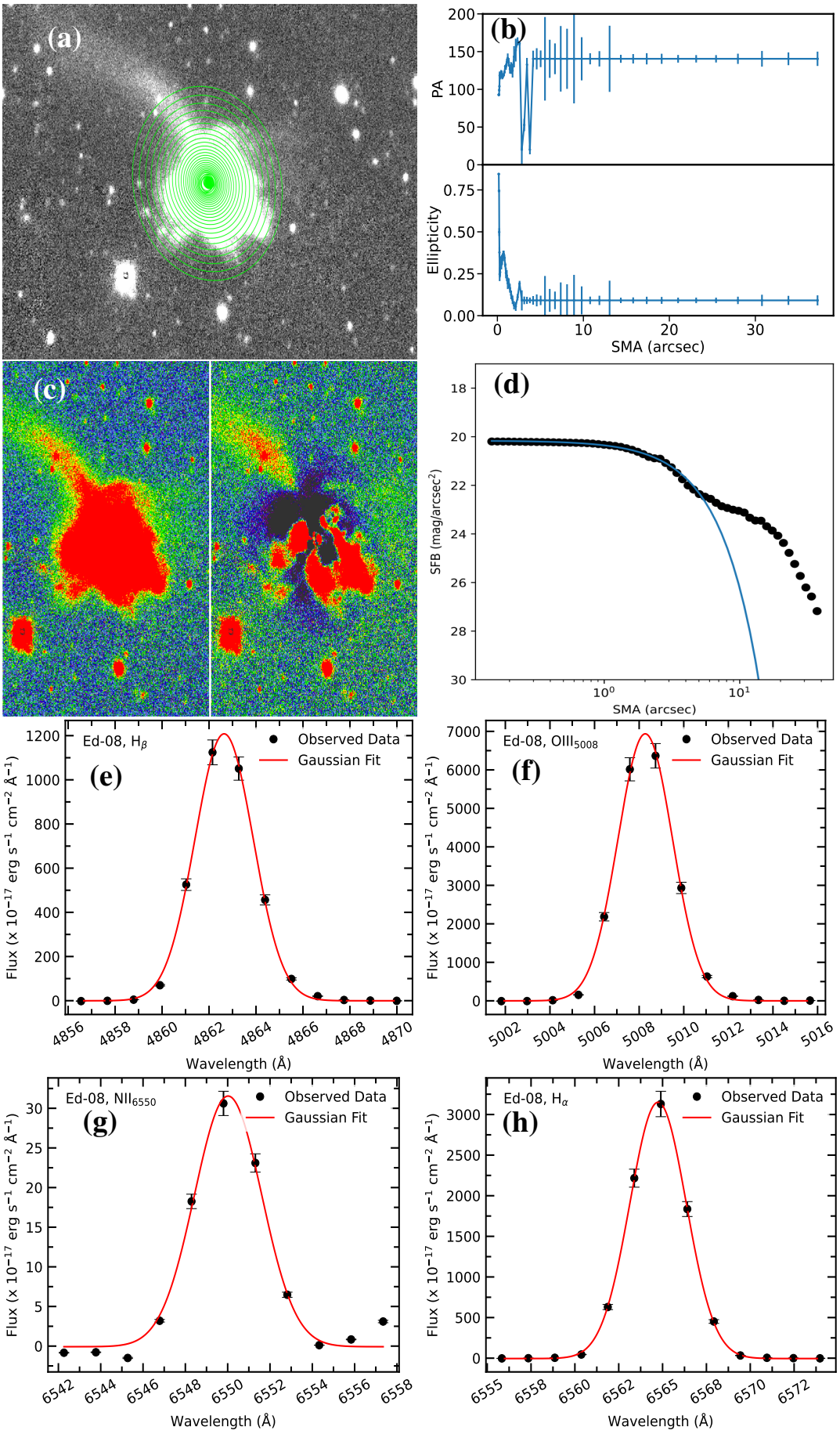

Figure 70: Results of Ed-08. We show surface photometry in sub-figures (a) to (d) and spectroscopy in (e) to (h). For a detailed description of each sub-figure and symbol identification, see Figure 63.

4.1.2.9 Ed-09

We show the best-fitted ellipse overlay on the grayscale SDSS image of the extended merging dwarf galaxy Ed-09 as shown in Figure 71 (a) for the study of the photometric database. The variation of PA and ellipticity as a function of galactocentric distance from the galaxy center is shown in Figure 71 (b). Both PA and ellipticity change randomly in the inner region and are roughly constant beyond around 8 arcsec radial distance from the center. In Figure 71 (c), we show a g-band image of the galaxy Ed-09 and its residual image. Only a small fraction of the image has remained as a residue after ellipse fitting. It signifies that the ellipse-fitting model is appropriate. Figure 71 (d) shows the modeling of the observed light profile with a Sérsic function. Unlike other galaxies, the observed data (dotted points) resembles the best-fitted Sérsic line (blue solid line) and the outer break occurs just above 10 arcsec. The break seen in the observed data resembles the change in structure of the galaxy. Similarly, the hump signifies the shell feature. The Sérsic index and effective radius of the galaxy from Sérsic method are obtained to be 1.1 and 5.57 arcsec respectively. Likewise, the half-life radius (h_r) and average surface brightness of the galaxy acquired by the Petrosian approach are 1.41 arcsec and 21.14 mag arcsec^{-2} respectively. The half-light radius of this galaxy is the minimum of all galaxies in the extended group.

We detected several emission lines in the spectrum of extended merging dwarf galaxy Ed-9. Out of them, the Gaussin fitting on H_β, $OIII_{5008}$, NII_{6550}, and H_α lines in the wavelength range 4855 Å to 6574 Å are shown in the Figure 71 (e, f, g and h) respectively. The dots represent observed data and the solid red lines represent the Gaussian fits. The probable error is shown by the error bars. We find 100 % coefficient determination of the H_α line which signifies that the observed points follow Gaussian distribution. The FWHM is (3.8 ± 0.0) Å. NII_{6550} line has positive offset means that its right-hand tail is longer than left-hand tail. Similarly, the negative offset of H_β, $OIII_{5008}$ and H_α lines means that their left-hand tail is longer than right-hand tail. SFRs derived from H_α line flux are 0.0885 $M_\odot yr^{-1}$ and 0.1359 $M_\odot yr^{-1}$ before and after extinction correction. The calculated values of abundance of oxygen and Balmer decrement are 8.34 dex and 3.57 respectively.

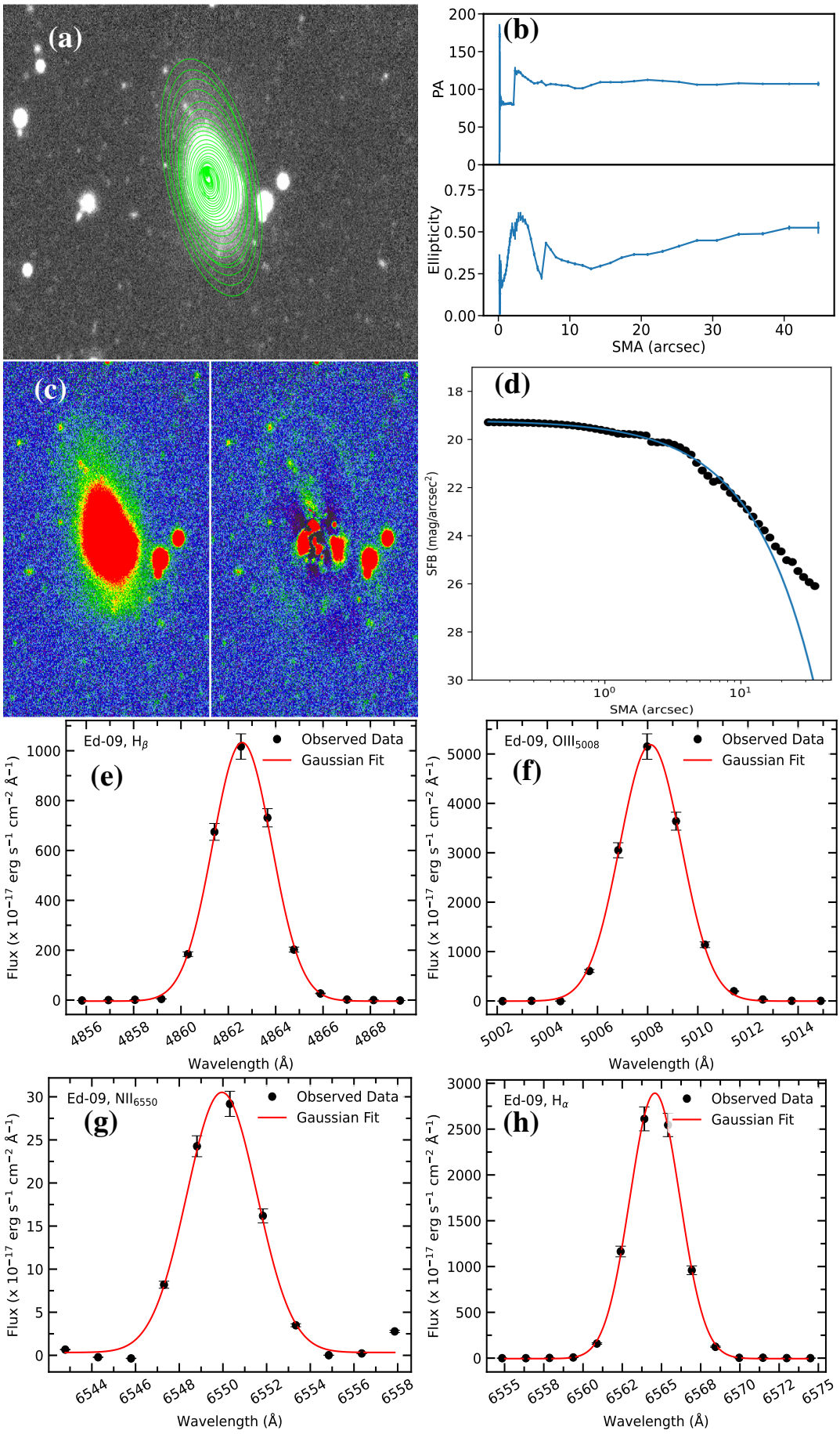

Figure 71: Results of Ed-09. We show surface photometry in sub-figures (a) to (d) and spectroscopy in (e) to (h). For a detailed description of each sub-figure and symbol identification, refer to Figure 63.

4.1.2.10 Ed-10

As done in previous cases, we show the best-fitted ellipse of the Ed-10 overlay on the grayscale image as shown in Figure 72 (a). The ellipses are dense and random at the center but seem almost uniform in the outer region. Both variation of PA and ellipticity as a function of radial distance from galaxy center is shown in Figure 72 (b). Beyond around 8 arcsec radial distance from the center, both PA and ellipticity are essentially constant. In Figure 72 (c), the g-band image and its residual image are shown. The minimum leftover residue signifies that the fitting model is appropriate. The modeling of the observed light profile using a Sérsic function is shown in Figure 72 (d). The outer break occurs just over 10 arcsec, which is almost four times the galaxy's half-light radius and the main body separates at this distance. The observed curve has diverged after the break and it means the shell feature of the galaxy. From the Sérsic fit, we obtained Sérsic index and effective radius of the galaxy to be 0.8 and 6.42 arcsec respectively. Likewise, the half-life radius (h_r) and average surface brightness of the galaxy acquired by the Petrosian approach are 2.75 arcsec and 21.29 mag arcsec^{-2} respectively. Nearly eight times as large as the half-light radius is the effective radius.

From the spectrum of extended galaxy Ed-10, H_γ, $OIII_{4365}$, H_β, $OIII_{4960}$, $OIII_{5008}$, OI_{6302}, NII_{6550}, H_α, NII_{6585}, SII_{6720} and SII_{6732} lines were detected but performed Gaussian fitting on H_β, $OIII_{5008}$, NII_{6550}, and H_α lines only in the wavelength range 4857 Å to 6576 Å as shown in the Figure 72 (e, f, g and h) respectively. The solid red line depicts the Gaussian fits and the dots show the observed positions. The error bars display the probable error. The positive offset of the H_β and NII_{6550} lines indicates their longer right-hand tails than their left-hand tails. Similar to this, $OIII_{5008}$ and H_α lines' negative offset indicates that their longer left-hand tails than their right-hand tails. More than 99% coefficient determination for the H_α line signifies the perfect agreement of the observed points with normal distribution. The value of FWHM is (3.9 ± 0.1) Å. By using H_α line flux, SFR of the galaxy Ed-10 is calculated to be 0.0027 $M_\odot yr^{-1}$ and 0.0066 $M_\odot yr^{-1}$ before and after extinction correction, respectively. The Balmer decrement is calculated to be 4.54 and the metallicity is, $Z = 12 + \log(O/H) = 8.90$ dex. This value of abundance of oxygen is the highest of all members of the extended group and the value of the Balmer decrement of this galaxy is the highest of all 25 sample galaxies.

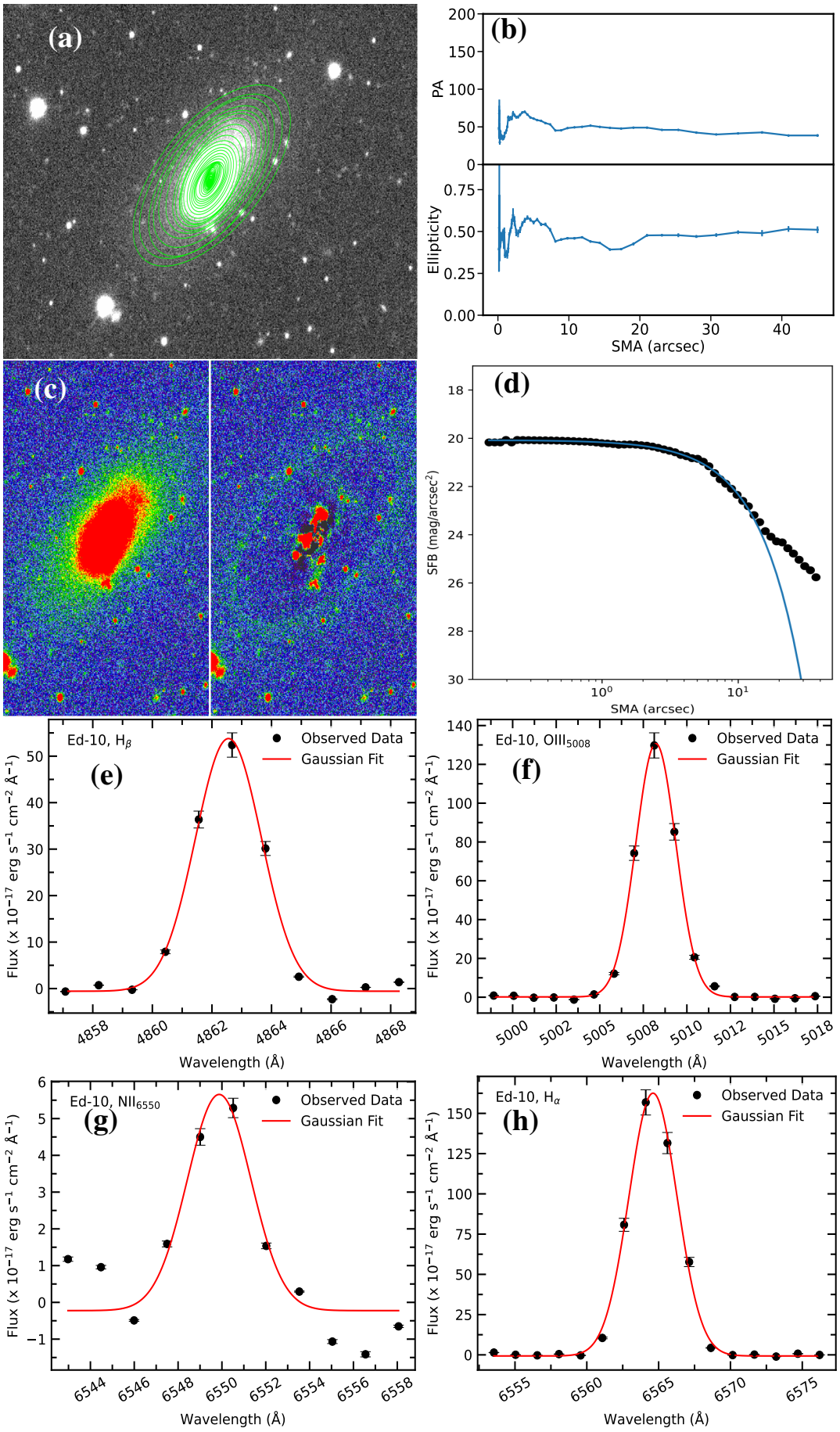

Figure 72: Results of Ed-10. We show surface photometry in sub-figures (a) to (d) and spectroscopy in (e) to (h). For a detailed description of each sub-figure and symbol identification, refer to Figure 63.

4.2 General Discussion

In this chapter, we discuss the general trends shown by different parameters (redhift, star formation rate, surface brightness, line ratios, extinction and metallicity) of 15 Compact merging dwarf and 10 Extended merging dwarf galaxies. In all cases, the catalog value of SFR is found to be greater than the calculated value by using H_α line flux. The catalog value of SFR is calculated by using FUV flux in the equation SFR ($M_\odot$ yr^{-1}) = 1.4×10^{-28} L_ν(UV) (erg s^{-1} Hz^{-1}). The higher value is because of many reasons. One of them is due to the large area coverage of FUV flux in the galaxy as compared to H_α line flux. This shows that only a small fraction of star formation takes place in the middle region of the galaxy. Moreover, the SFR calculated after extinction correction is more (double or even more than double in some cases) than before extinction correction in all cases. it means that the actual flux of the galaxy is more than the observed flux.

Likewise, the higher value of the Balmer decrement than its normal value i.e., 2.86 (Osterbrock & Ferland, 2006) in all galaxies except for Cd-14 and Ed-07, suggests the presence of micron-sized dust particles at the center which effectively absorbs shorter wavelength bluer light more than the longer wavelength redder light. More dust particles produce more disparity between the theoretical and observed values of Balmer decrement. On the other hand, the low abundance of oxygen of Cd-14 and Ed-07 galaxies could be due to several reasons. The galaxies may be older than the Sun. The galaxies may have formed from gas that had a lower metallicity, to begin with, such as primordial gas left over from the Big Bang. The galaxy may have undergone a period of gas expulsion or gas stripping, which removed some of its metal-rich gas.

Figure 73 shows the all-sky distribution of compact and extended merging dwarf galaxies. Red Solid circles represent 15 Cd galaxies and black triangles represent 10 Ed galaxies. It shows that most of the galaxies lie in RA (J2000) = (120° to 260°) and Dec.(J2000) = (-15° to $+75^\circ$).

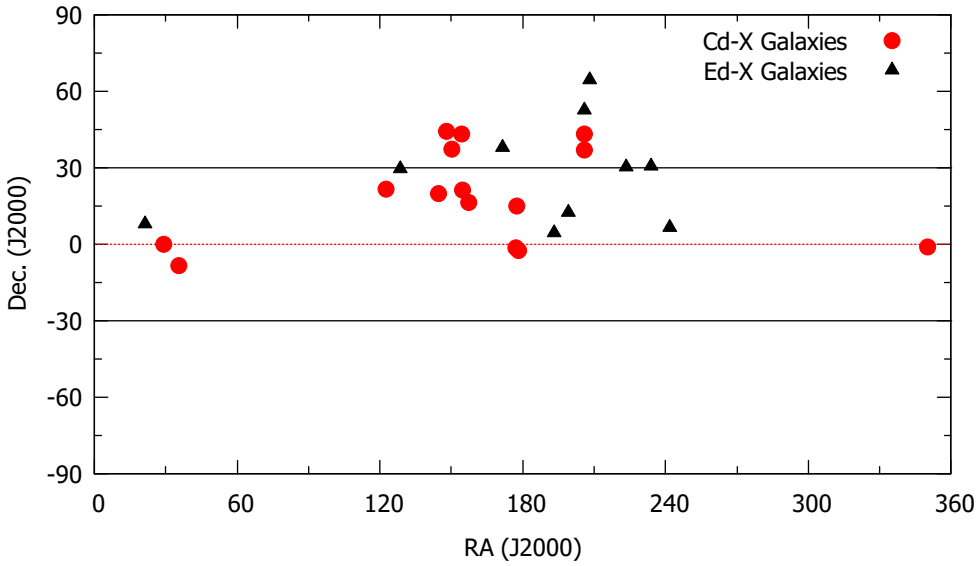

Figure 73: All sky distribution of Cd-X galaxies and Ed-X galaxies.

Figure 74 shows the extinction distribution of dwarf galaxies. The black solid triangles represent Ed galaxies while the red solid circles represent the Cd galaxies. The empirical relation between extinction coefficient $A(\mathrm{H}_\alpha)$ and redshift (z) of 15 dwarf galaxies is found to be

$$A(\mathrm{H}_\alpha) = 2.8z + 0.3 \tag{4.1}$$

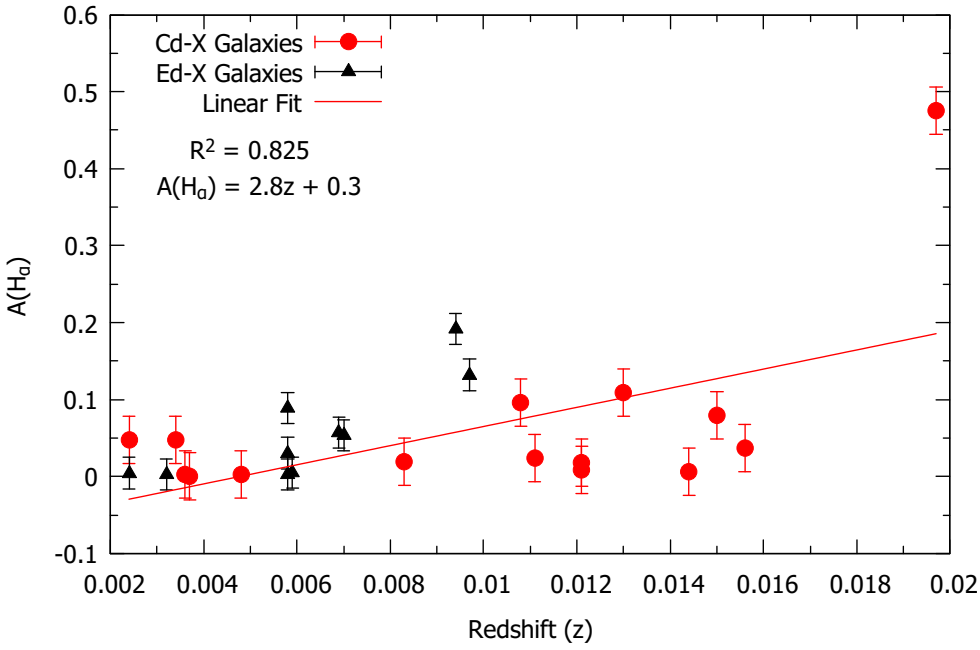

Figure 74: Redshift-extinction relation of Cd-X and Ed-X galaxies. The solid line shows the best fit line whose equation is also shown. The error bars represent the standard error.

Extinction is found to increase with redshift. The extended dwarf galaxies are confined within the redshift of 0.010 while most of the compact dwarf galaxies are confined within the redshift of 0.008 to 0.020. Therefore, extended dwarf galaxies are closer than compact dwarf galaxies. The straight line represents the best-fitted linear line of all galaxies. The value of the extinction varies with the line-of-sight. The general trend showed that the extinction or radiation losses increase with the radial velocity (or distance to the galaxy).

Figure 75 shows the relationship between H_α flux and surface brightness of Ed galaxies. The error bars represent standard errors. We notice that the H_α flux of extended dwarf galaxies increases with the surface brightness of the galaxies according to the relation:

$$\text{Flux}(H_\alpha) = 2.98 \times 10^{-15}\mu - 7.99 \times 10^{-15} \tag{4.2}$$

Because of low R^2 value, the relation 4.2 cannot be accepted as empirical relation. This relation needs to be verified and improved by adding more data. The best-fitted line has a positive slope of 2.9 $\times 10^{-15}$ with a poor value of the coefficient of determination.

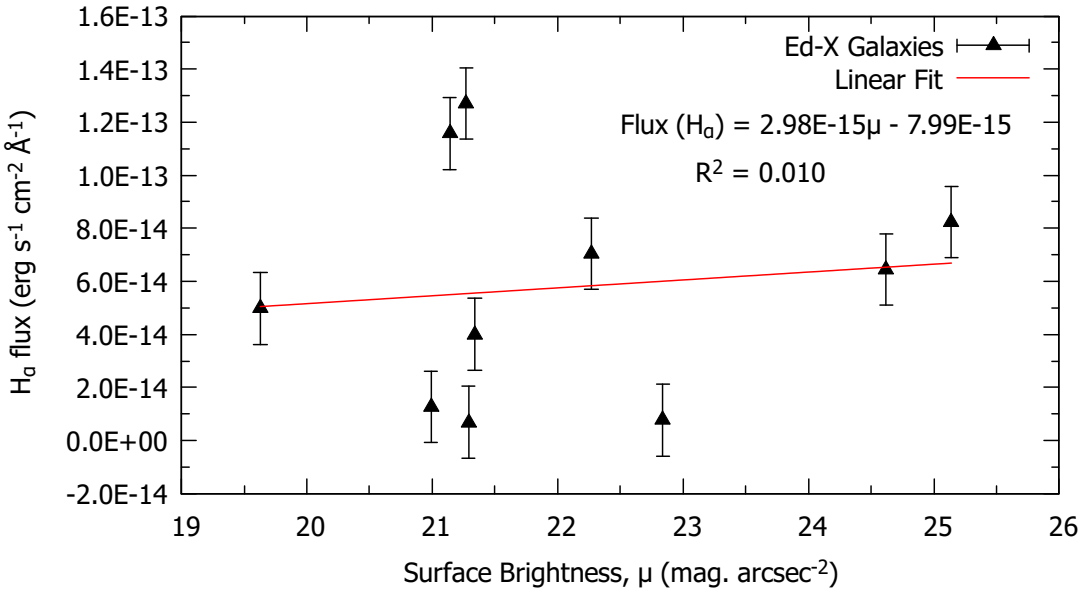

Figure 75: Variation of H_α flux with a surface brightness of Ed-X galaxies. The solid red line represents the linear fit of the data. The red solid circle represents Cd galaxies and the black solid triangle represents Ed galaxies. The standard error of the deviation ($\pm\ 1\sigma$) is represented by the error bars.

Figure 76 shows H_α line flux versus redshift distribution for 10 extended merging dwarf galaxies. Interestingly, H_α flux is found to increase with the redshift according to the empirical relation

$$\text{Flux}(H_\alpha) = 1.0 \times 10^{-11} z - 8.0 \times 10^{-15} \tag{4.3}$$

Here, coefficient of determination is 32.7%.

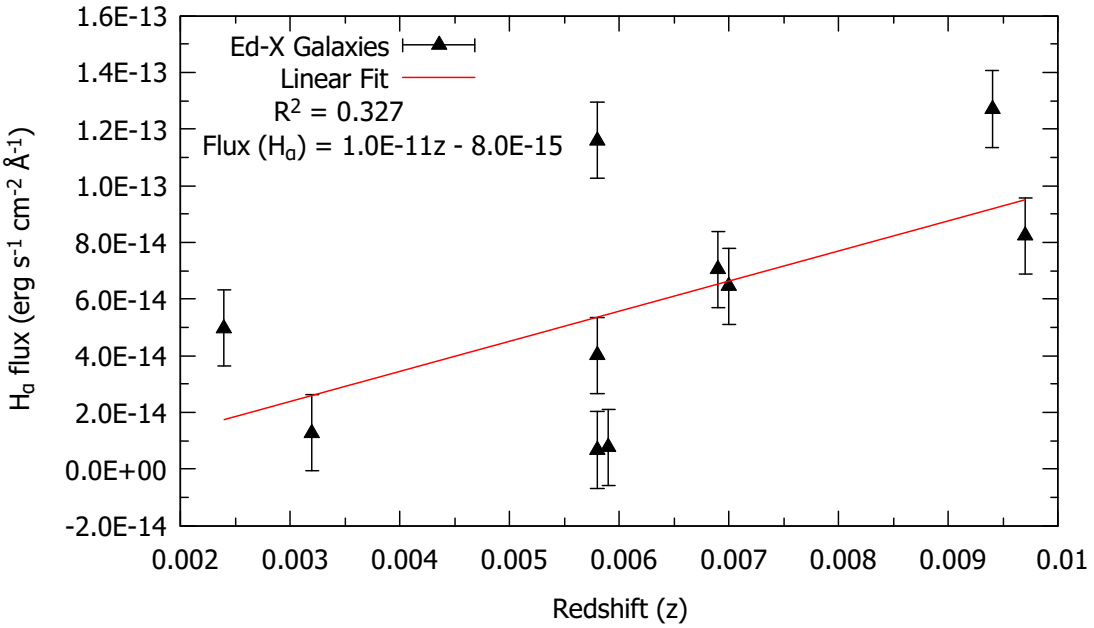

Figure 76: H_α versus redshift (z) distribution of Ed-*X* galaxies. The best-fit line and the equation are shown. The symbols signify same meaning as the Figure 75. The error bars represent the standard error.

The distribution of SFR (before extinction correction) of 15 Cd and 10 Ed galaxies is shown in Figure 77.

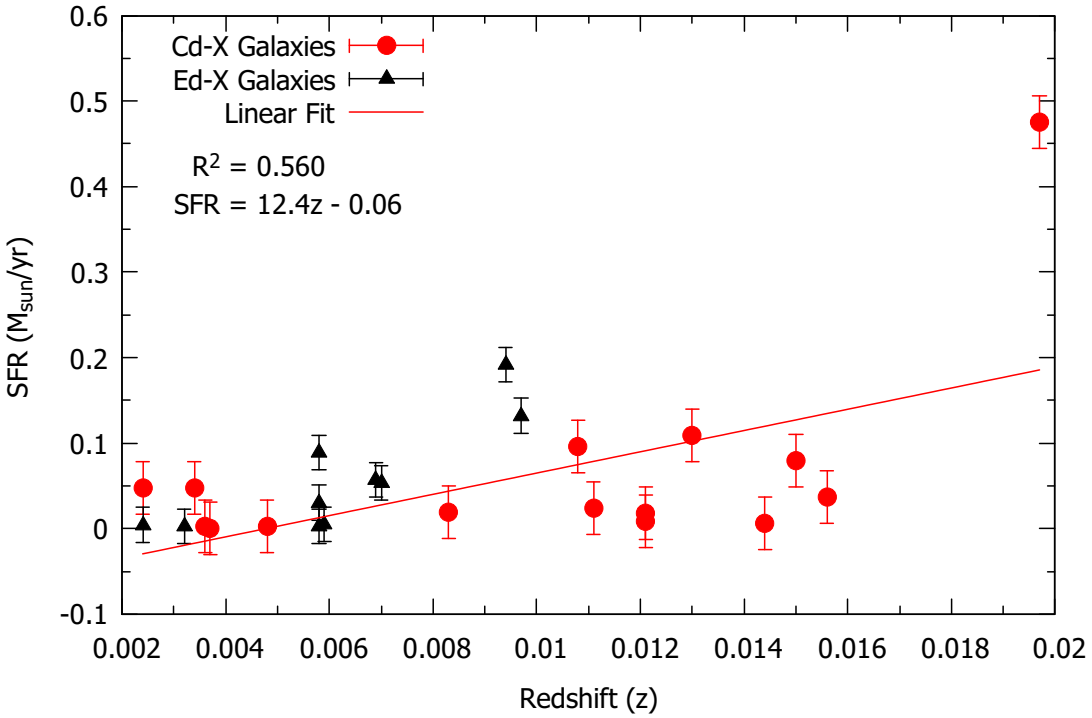

Figure 77: SFR of Cd-X galaxies and Ed-X galaxies (before extinction correction) versus redshift. The best-fit line and equation are shown. The symbols have the same meaning as in previous figures. The error bars represent the standard error.

SFR is found to increase with respect to the redshift of the galaxies which is governed by

the relation,

$$SFR = 12.4z - 0.06 \tag{4.4}$$

The SFR of the Cd and Ed galaxies is found to increase with the redshift. Moreover, the SFR of Ed galaxies is more than that of Cd galaxies. This is an interesting result.

In Figure 78, redshift versus SFR after extinction correction for both Cd and Ed galaxies is shown. These are found to be related as

$$SFR_{\text{extin}} = 22.5z - 0.1 \tag{4.5}$$

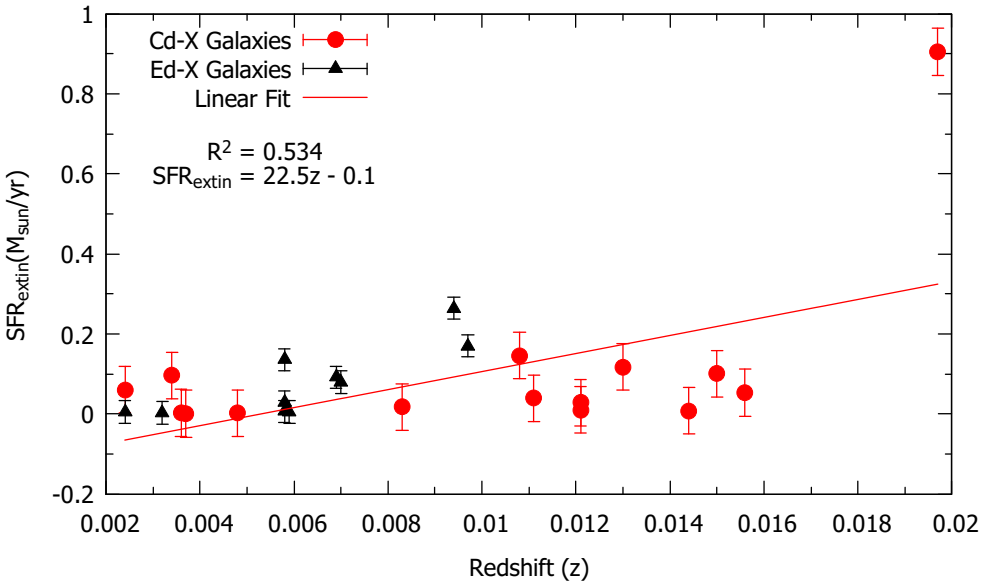

Figure 78: SFR versus Redshift of Cd-X galaxies and Ed-X galaxies after extinction correction.The red color solid circles represent Cd galaxies and black color solid triangles represent Ed galaxies. The best-fitted solid red line and its equation are shown. The error bars represent the standard error.

The SFR (after extinction correction) is found to increase with the redshift. At higher redshifts, we are observing the galaxies that existed when the universe was younger. During the early stages of the universe, there was a higher abundance of gas and dust, which are the raw materials for star formation. As a result, galaxies in the early universe had more material available for star formation, leading to higher SFRs. Moreover, in the early universe, galaxies being closer to each other, got merged thereby triggering intense bursts of star formation as the gravitational forces disrupt gas clouds and drive their collapse, leading to increased SFRs. Therefore, we conclude that the SFR of dwarf galaxies generally increases with the increase of redshift. It means that distant dwarf galaxies show higher rate of star formation.

Figure 79 shows the Balmer decrement-redshift relation of 15 compacts (red solid circles)

and 10 extended (black triangles) dwarf galaxies, which is given by

$$c = H_\alpha/H_\beta = 3.4\,z + 3.8 \tag{4.6}$$

This relation suggests that the Balmer decrement is almost independent of redshift.

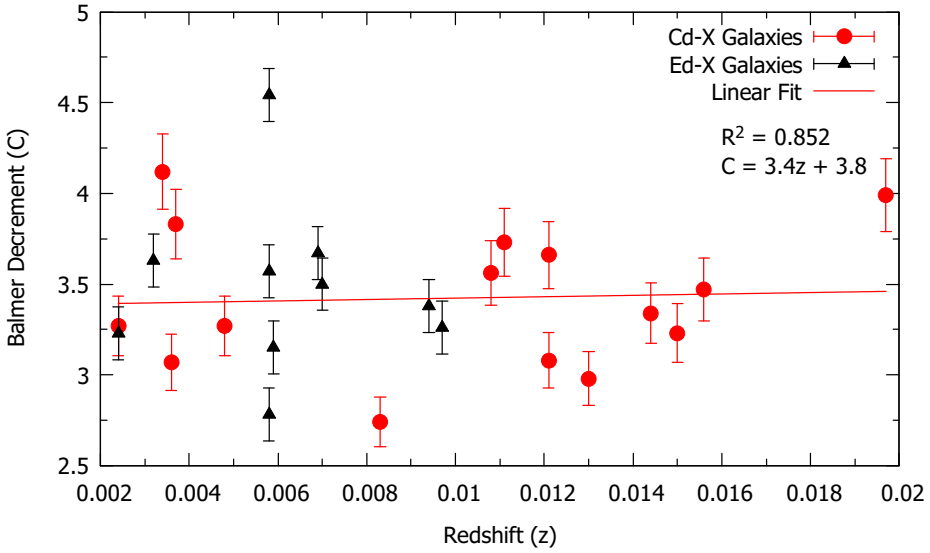

Figure 79: Balmer decrement (C) versus redshift distribution of all 25 merging dwarf galaxies. The symbols and line have the same meaning as in Figure 78. The error bars represent the standard error.

.

Figure 80 shows the change in the redenning of compact and extended merging dwarf galaxies with the redshift.

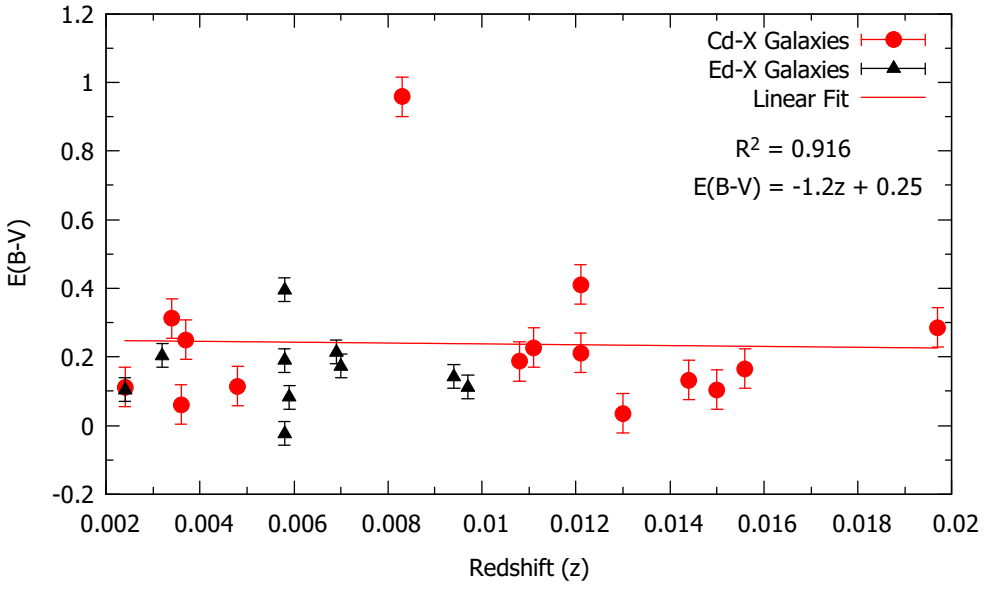

Figure 80: Reddening-Redshift plot of compact and extended merging galaxies. The symbols and error bars have same meaning as in Figure 78

This change is found to be governed by the equation,

$$E(B-V) = -1.2\,z + 0.25 \tag{4.7}$$

Here, the negative slope is insignificant. Therefore, the color index of dwarf galaxies are found to be almost independent of redshift.

The variation of the abundance of oxygen of compact and extended dwarf galaxies with redshift is shown in Figure 81. The linear fit gives the relation of oxygen abundance,

$$12 + \log(\mathrm{O/H}) = 7.2\,z + 8.7 \tag{4.8}$$

Their relation suggests that the the abundance of oxygen increases with the redshift. In principle, this is true. But the coefficient of determination is not very good. Therefore, more data is needed to verify the relation 4.8 and to use it as empirical relation for dwarf galaxies.

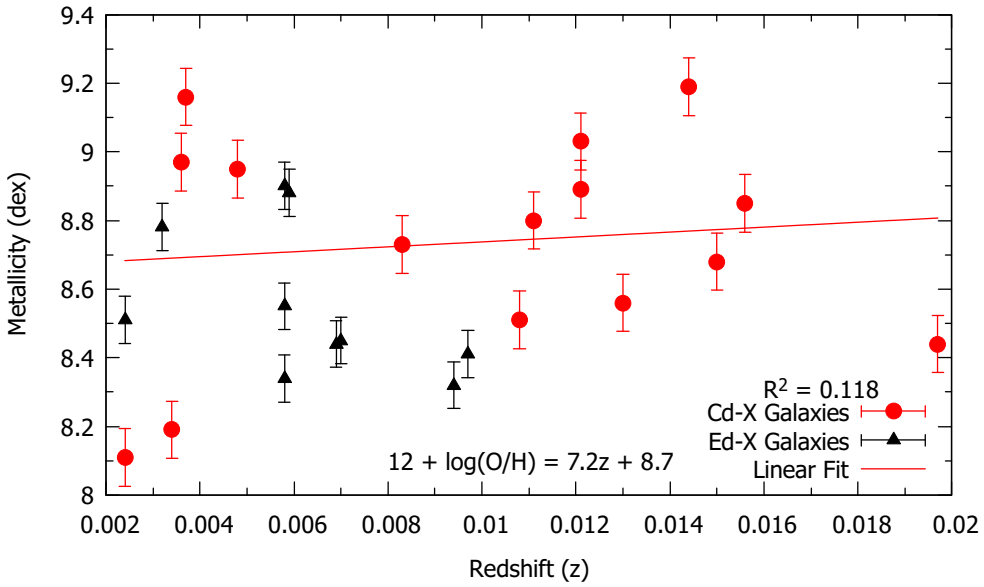

Figure 81: The abundance of oxygen versus redshift relation of all 25 merging dwarf galaxies. The symbols and error bars have the same meaning as in Figure 78

Star Formation Law and Galaxy Main Sequence

Star-forming galaxies follow a relation between their B-band absolute magnitude and log(SFR) and this relation is called the main sequence of galaxies. A relation between the B-band absolute magnitude and log(SFR) of star-forming galaxies is shown in Figure 82. The star-formation rate of our galaxies is derived from the H_α flux of the SDSS spectrum. The B-band magnitude of our sample galaxies is calculated from the SDSS $g-$band magnitude using the color transformation equation provided by the SDSS webpage [B = g + 0.39 $\times$ $(g-r)$ + 0.21]. The comparison sample in gray dots is taken from J. C. Lee et al. (2009), which provides a statistical study of star-formation activity in local volume star-forming galaxies using a volume-limited sample. Interestingly, the compact dwarf (shown in blue color solid circle) are located below the main sequence defined by the local star-forming dwarf galaxies on average. On the other hand, extended merging dwarf seems to follow the trend. However, the scattering is large and because of poor statistics, we can not confirm the observed trend. The SFR in galaxies is influenced by a range of internal and external factors, including the availability of gas, gravitational interactions, and environmental effects.

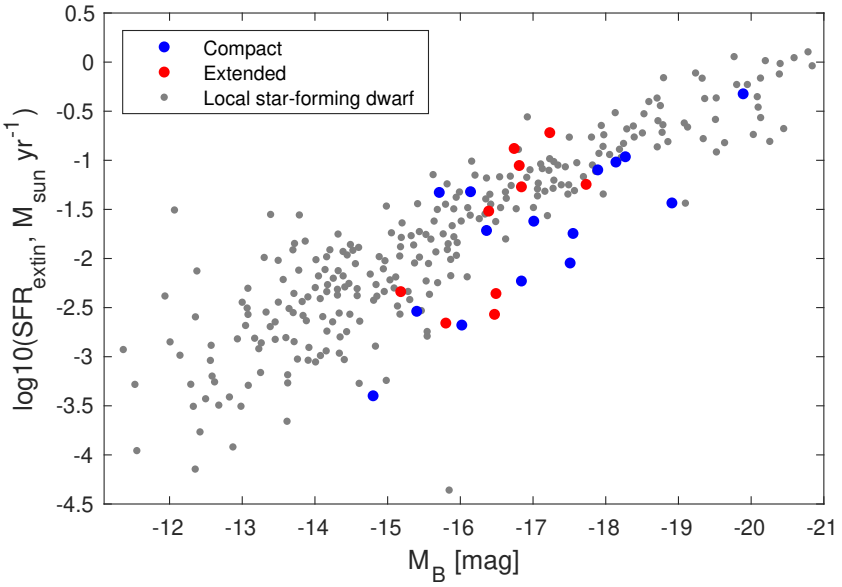

Figure 82: The main sequence relation of star-forming galaxies. Cd galaxies are shown in blue and Ed galaxies are shown in red solid circles. We have taken a comparison sample from (J. C. Lee et al., 2009), shown in the gray symbol.

The Kennicutt-Schmidt law is an empirical relationship that describes the relationship between the galaxy's star formation rate and galaxy's physical properties such as gas mass or B-band absolute magnitude. It states that the star formation rate is logarithmically proportional to the surface density of the gas. This relationship has been observed in a variety of galaxies and holds over a wide range of scales: from individual molecular clouds to entire galaxies.

The validity of the Kennicutt-Schmidt law has been supported by numerous studies, although there is some scatter in the data and the relationship may not hold perfectly in all cases. It is generally considered to be a useful tool for comprehending the correlation between gas and star formation in galaxies, although more work is needed to fully understand the physical processes that underlie this relationship.

Mass-Metallicity Relation

The mass-metallicity relation (also known as the "mass-metallicity" or "MZ" relation) is a correlation observed in galaxies between the mass (also presented with magnitude) of a galaxy and the metallicity of its stars. In Figure 83, we show a relation between B-band absolute magnitude and emission line metallicities. We show Cd galaxies in blue and Ed galaxies in red color solid circles. A comparison sample from (Paudel et al., 2017) is also used where they compiled data from the SDSS database.

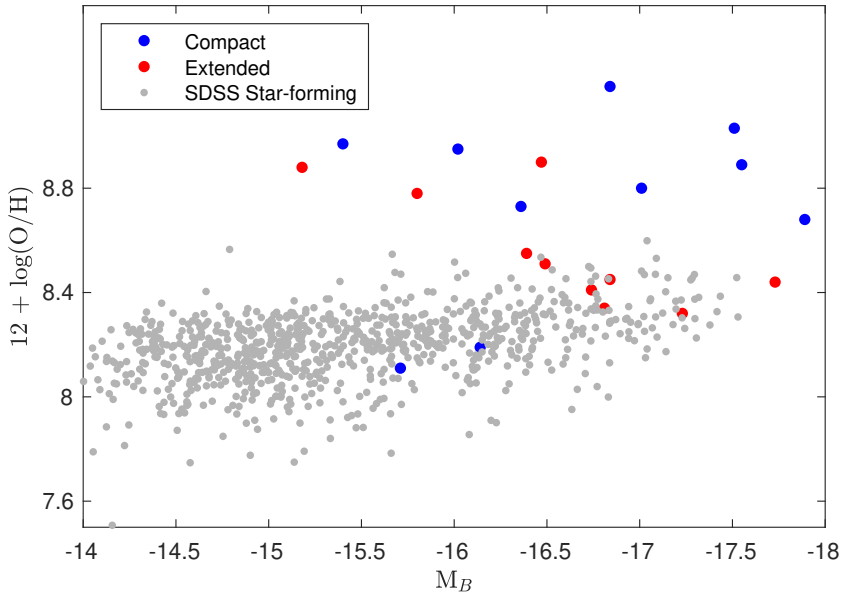

Figure 83: Mass-metallicity relation of star-forming galaxies. Cd galaxies are shown in blue and Ed galaxies are shown in blue solid circles. We have taken a comparison sample from (Paudel et al., 2017), shown in the gray symbol.

Interestingly, the Cd galaxies show different behaviors than the Ed galaxies being significantly metal-rich compared to the comparison sample. On the other hand, Ed galaxies well follow the mass-metallicity relation provided by normal star-forming dwarf galaxies, with a bit higher scattering. The difference can be well explained by comparing with the previous star formation law relation, where the compact galaxies also show a different trend. As the galaxy's merger progress, the star-formation activity decreases because of the depletion of star-forming gas. In the interaction progress in time, the leftover gas will have sufficient time to intermix with metal-rich outflow, which intern increases the metallicity content. It is also true that the gas depletion reduces the gas-mass

fraction which also helps to increase the value of emission line metallicity in relatively evolved galaxies, like compact galaxies in our sample.

4.3 Limitations

We have derived emission line metallicity and SFR of 25 compact and extended merging dwarf galaxies in this work. Below we discuss the limitations of the method we have used and what are the other alternatives.

In this work, we calculated metallicity using N_2 method which uses a flux ratio between N_2 and Hα. Although this method is widely used in practice but this is not entirely error free. N_2 method assumes a direct correlation between Nitrogen abundance and Oxygen abundance. Traditionally, the emission line metallicity is derived from Oxygen line abundance because Oxygen 4383 emission line better corelates with gas temperature than Nitrogen emission line. But the Oxygen line is extremely weak and is difficult to measure. Therefore, we used N_2 flux. This method has a systematic uncertainty of 0.2 dex which mainly comes from the scattering of data while calculating a correlation coefficient between the parameters.

To measure the star-formation rate, we have used H_α emission line flux. Although this is most accurate and widely used diagnostic but there are a few limitations on this method too. First, H_α SFR do not trace long term star-formation activity with a typical SFR period of a few hundred Mega years. H_α is also highly prone to absorption and extinction. Indeed, there are other methods to derive SFR, such as use of Infra-red flux or FUV flux. The infra-red flux has less chance to get absorbed and it also traces significantly larger SFR period, near a giga years. On the other hand, FUV fluxes is highly extinct and traces very short period of SFR, a few Mega years.

This study is not designed to characterize the dark matter distribution of dwarf galaxies. Indeed, the gravitational tidal force affects the dark matter as much as baryons. However, to study the characteristics of dark matter in the galaxy, we need to explore internal kinematics. For this, we need radio 21 cm observation data which we do not have now. We plan to do in future. Dwarf galaxies are, however, not expected to have experienced any major mergers since their first major star-forming period. They are instead expected to have gained their shape in their early formation or through tidal interaction in high-density environments.

Significant effort has been expended to comprehend the physical mechanisms that govern galaxy evolution during the coalescence of massive galaxies. Many observational and theoretical studies have demonstrated that during the intermediate phases of interactions, large-scale tidal interactions can trigger the emergence of distinctive features such as shells, streams, bridges, and tails including enhancement in star-formation rate. Formation

of compact galaxies by central burst of star-formation after collision is also commonly discussed in literatures. However, in the low mass regime, the mechanism that triggers the burst of star formation in dwarf galaxies, particularly in BCDs, also remains a mystery. Mergers, fly-by encounters, or gas turbulence have been proposed. But observations have shown that interacting tidal forces acting on the gaseous disk could displace beyond the optical discs. A little is known observationally and theoretically about interactions between the gas-rich dwarf galaxies and consequences on the star-formation activities.

4.4 Comparison to the Previous Studies

Research on the merging of dwarf galaxies is a relatively recent area of study. In this section, we will compare our findings with those of previous studies on merging dwarf galaxies. In the local volume, the Tiny Titans (TNT) survey discovered that merging dwarf galaxies tend to have a higher star formation rate than non-merging dwarf galaxies when they are located within a few hundred kiloparsecs of each other (Stierwalt et al., 2015) . Additionally, Annibali et al. (2016) identified a merging dwarf galaxy in a local void and found that these void merging dwarf galaxies are particularly rich in gas and extremely low in metal content through their radio data analysis.

Pearson et al. (2016) examined 12 interacting dwarf galaxy pairs (LMC/SMC, IC 2058/PGC 75125, NGC 4532/DDO 132, NGC 4618/NGC 4625, ESO 435-IG 16/IG 20, NGC 4490/NGC 4485, NGC 3448/UGC 6016, UGC 9560/62, NGC 672/IC 1727 and NGC 4449/DDO 125) from the Tiny Titans survey using radio observations and found that the neutral gas in these interacting pairs is more extended than in non-interacting analogs, suggesting that the gas is being tidally pre-processed. The first analog of the Magellanic pair (UGC 6241) was discovered through a study of star formation and gas-mass distribution using the Giant Metrewave Radio Telescope (GMRT) 21 cm emission line observation.

Compared to these previous studies, our study reveals that more evolved merging dwarfs are expected to have low star-formation activity and higher metal content than less evolved extended merging dwarfs. Similar to a study in CGCG 036-042, by Paudel et al. (2014), we find some of the merging dwarfs could form compact elliptical, which is the evidence of a high star-formation rate and low gas mass fraction. On the other hand, Paudel et al. (2015) found in UGC 6741 that the metallicity of compact and extended merging dwarfs is significantly different.

Zhang et al. (2020) shows that a merger event between two dwarf galaxies and increased star formation in a Virgo cluster BCD known as VCC 848. The researchers utilized both optical imaging and a JVLA HI emission line map to investigate the effects of the merger on both the gaseous and stellar distributions. The study found that although VCC 848

experienced a burst of star formation in its center, the concentration of gas in the center was less than 30%. The researchers compared the morphology of VCC 848 to the results of N-body hydrodynamical simulations and suggested that the merger likely occurred around one billion years ago. It should be noted that our merging BCDs are situated in an environment with low density, unlike the environment of VCC 848.

CHAPTER 5

5. CONCLUSION AND RECOMMENDATIONS

5.1 Conclusion

In this work, we extensively studied a group of merging dwarf galaxies of low redshift (0.0024 – 0.0197) selected from the catalogue of Paudel et al. (2018b). We selected 25 merging dwarf galaxies on the basis of selection criteria discussed in Chapter 3. Our database includes 15 compact and 10 extended dwarf galaxies. We used a photometric and spectroscopic database from the Sloan Digital Sky Survey (SDSS DR12) to study structural and star-formation properties of the galaxies. We performed ellipse fitting on the SDSS g-band images to measure galaxy size and mean surface brightness, using both parametric and non-parametric methods. The parametric method employed Sérsic function modeling (Sersic (1968)) of a one-dimensional light profile along the major axis obtained from the ellipse fit, while the non-parametric method used the Petrosian method (Petrosian (1976)). Additionally, SDSS optical spectrum has been used to determine the star formation rate (SFR) and metallicity by analysing emission lines. From photometric calculations, we found the morphological properties of the galaxies: the effective radius, half-light radius and sersic index. We conclude our results as follows:

- The value of SFR is found to vary in the range of (0.0004 to 0.0960) $M_{\odot}yr^{-1}$ for 15 merging compact dwarf galaxies before extinction correction. As expected, SFR is found to be more (almost two-times) after the correction of extinction: (0.0008 to 0.9048) $M_{\odot}yr^{-1}$. The maximum value of SFR in our 25 sample galaxies is found to be 0.9048 $M_{\odot}yr^{-1}$ in the compact dwarf galaxy Cd-13 (LEDA 2793637) and the minimum value is 0.0008 $M_{\odot}yr^{-1}$ for Cd-07 (PGC 030055) after extinction correction.

- Among 10 extended merging galaxies, the values of SFR are found to range from (0.0022 to 0.1913) $M_{\odot}yr^{-1}$ before extinction correction. It increases from 0.0035 $M_{\odot}yr^{-1}$ to 0.2647 $M_{\odot}yr^{-1}$ when taking into account extinction correction. Here, the values of SFR are found to increase by $\sim 50\%$.

- The star formation rate is found to increase with redshift (z) according to this relation:

$$SFR = Az - B \tag{5.1}$$

where A, B = 12.4, 0.06 (without extinction correction) and 22.5, 0.1 (with extinction correction). This reveals the fact that the distant merging dwarf galaxies are gas-rich and metal-rich galaxies. Additionally, a weak correlation between redshift and the extinction coefficient is noticed in merging dwarf galaxies.

- The abundance of metals is found to be quite different in two types of dwarf galaxies. From the spectroscopic calculations, the metallicity of the compact merging galaxies is found to be in the range of (8.11 to 9.19) dex while it is found in the range of (8.32 to 8.90) dex in the case of extended merging galaxies. It suggests that the merging compact dwarf galaxies showed a wider variety of metal-rich environments than that of the extended dwarf field. As a whole, metallicity is found to increase with the redshift, though the rate of increase is very low.

- Different quantities are found for compact and extended merging dwarf galaxies respectively in the following range.

  Balmer decrement: (2.74 to 4.12) and (2.78 to 4.54) from spectroscopic calculation. Effective radius: (1.56 to 11.52) arcsec and (3.21 to 81.09) arcsec from photometric calculation. Half-light radius: (0.47 to 2.03) arcsec and (1.41 to 4.39) arcsec from photometric calculation. Sérsic index: (0.4 to 2.2) and (0.7 to 2.9) from photometric calculation. Mean surface brightness: (20.04 to 22.93) mag arcsec^{-2} and (20.99 to 25.14) mag arcsec^{-2} from potometric calculation. This calculation improves the existing catalog of dwarf galaxies. These values are already reported through our publications.

- We find that the compact dwarf is located below the main sequence defined by the local star-forming dwarf galaxies on average. On the other hand, extended merging dwarfs seem to follow the trend. The result has been published in Chhatkuli, Paudel, Gautam, & Aryal (2021); Chhatkuli, Paudel, & Aryal (2021) .

- The mass-metallicity relation reveals that the Cd galaxies show different behaviors than the Ed galaxies being significantly metal-rich compared to the comparison sample. On the other hand, extended dwarf galaxies well follow the mass metallicity relation provided by normal star-forming dwarf galaxies with a bit higher scattering (Chhatkuli et al. (2022)).

- We noticed that more evolved merging dwarfs are expected to have low star-formation activity and higher metal contents than less evolved extended merging dwarfs. Additionally, we find some of the merging dwarfs could form compact elliptical.

5.2 Recommendations

Scientists do not fully understand the processes that shape the evolution of baryons, which play a role in the formation of galaxies within dark matter halos. There are two main theories about how galaxies gain mass over time: through violent merging events when galaxies collide, or through the gradual inflow of gas. Determining the relative importance of these two mechanisms is crucial for understanding galaxy evolution. One way to study the role of galaxy mergers is to count the number of pairs of close galaxies. However, it has been difficult to accurately detect such pairs, so the rate and prevalence of major mergers (involving two galaxies of similar mass) has only been studied up to a redshift of 3 using this method. The rate of minor mergers (involving two galaxies with significantly different masses) has largely remained unconstrained.

There are several logical next steps that could be taken to extend our understanding further about the properties of dwarf galaxies. One immediate extension would be to incorporate radio data sets into the analysis as they provide more accurate estimates of kinematic properties. With this information, we can calculate the total mass (including both light and dark matter) of a galaxy. The mass of a galaxy plays a significant role in its evolution and appearance.

It is clear that not all dwarf galaxies are alike, either in terms of appearance or kinematics. Some exhibit kinematically decoupled cores, misaligned rotation axes and anisotropic velocity distributions, which makes a detailed study of their kinematics essential for understanding the formation and evolution of early-type galaxies.

This thesis has analyzed structural and star-formation properties under the assumption that all stars are formed in a single event. However, recent research has demonstrated that galaxies often have more complex star-formation histories, consisting of multiple episodes or a continuous process. In light of this, it may be more useful to derive evolutionary time scales using the Kennicutt-Schmidt law rather than relying on a single age and metallicity. Deriving the star-formation history of a galaxy from its integrated light is challenging, but an alternative approach has been proposed: decomposing the integrated spectra of early-type galaxies into multiple simple stellar populations (SSPs).

The formation of dwarf galaxies is expected to be strongly linked to the environment in which these objects reside. However, we found dwarfs in isolation, which must have formed in the absence of any environmental transformation process. Therefore, to put constraints over the various formation channels that followed by the merging dwarfs, We further aim make study of dwarf galaxies using radio 21 cm observation data.

There are several theories that have been proposed to explain the origin of the mass-metallicity relation. One possibility is that it arises due to the way in which galaxies form

and evolve. More massive galaxies may be more efficient at retaining their gas and forming new stars, which can lead to the production of more heavy elements. Alternatively, the relation may be due to the way in which gas is removed from galaxies over time, with more massive systems being better able to retain their gas and lower mass systems losing gas more easily.

Other factors that may contribute to the mass-metallicity relation include the initial conditions of the galaxy, such as its density and the amount of dark matter it contains and its environment, including the presence of nearby galaxies or the impact of cosmic gas flows. More research is needed to fully understand the origin of this relationship.

CHAPTER 6

6. SUMMARY

Our goal in this thesis is to strengthen our understanding of the process of forming dwarf galaxies through the merger. The universe is full of dwarf galaxies, which are small, low-mass galaxies. Dwarf galaxies are a significant and fascinating type of astronomical objects that are still the focus of ongoing investigation. To do this, we will examine the physical and stellar characteristics of a group of merging dwarf galaxies. We will investigate whether there is a connection between the observed stellar properties and the structural properties and consider the potential implications of this relationship. Our study is focused specifically on the structural properties of merging dwarf galaxies in both field and group environments. We utilized data from various public sources, such as the SDSS and Legacy survey, to ensure the broadest possible scope for our research and maximize its contribution to the field of dwarf galaxy studies.

In Chapter 2, we provided an overview of the environments and physical properties of galaxies. A galaxy that does not belong to a larger cluster of galaxies and hence is gravitationally alone is called a field galaxy and a group of a galaxy is a system of galaxies that have 2 to 100 members of galaxies. We also discussed the theory of galaxy surface photometry and explained how to measure the structural properties of galaxies. We presented details of CCD photometry and described how we obtain radial profiles of various quantities and the morphological type of a galaxy from its image. In addition, we described the spectroscopic properties of galaxies and presented spectra for different morphological types. We also reviewed the theory of star formation and described how it could be measured using H_{α} flux.

We introduced the SDSS survey telescope, highlighting its importance and the techniques used to acquire data. We also gave a brief overview of both spectroscopic and imaging surveys, including technical details. The SDSS uses a 2.5-meter telescope located at Apache point observatory, New Mexico, USA. It takes images of the sky in five different bands u, g, r, i and z, and using advanced image processing software will measure the brightness, shape and color of millions of the objects detected.

We, finally, present a review of dwarf galaxy research at the end of the chapter. We describe the catalog in section 2.8.1 and introduce merging dwarf galaxies in section 2.8.2. A research gap in dwarf galaxy research is presented in section 2.9.

In Chapter 3, we provided a short description of the sample selection and data acquisition,

which is used to study the structural parameter and star-formation properties of merging dwarf galaxies. We introduced our galaxy sample, providing basic physical properties such as sky position, redshift and magnitude for all. These parameters are all obtained from previous studies, mainly from a catalog of merging dwarf galaxies (Paudel et al., 2018a). The method of analysis is presented in section 3.4. In this section, we described how imaging and spectroscopic data are obtained from the SDSS archive server Data Acquisition (3.4.1). For each galaxy, we have downloaded the fits file of imaging and spectroscopic data from the SDSS archive server. For this, we use the SDSS explorer tool to identify the galaxy in the SDSS data base which redirects to the source-specific database.

The final results from the analysis of imaging and spectroscopic data analysis are presented in Chapter 4. For each galaxy, we provided a detailed plot of ellipse fit and radial profile of PA and ellipticity. In addition, we also provided a plot of Sérsic fit to measure structural properties. Galaxy photometry using a non-parametric method utilizing the Petrosian method to calculate the total flux of the galaxy and hence measure the half-light radius is also discussed.

We, finally, presented statistics of measured structural and spectroscopic parameters and how they are related to the redshift and sky position. We analyze the relationship between extinction and galaxy redshift. We find a weak correlation between redshift and the extinction coefficient, as our data shows that the extinction coefficient appears to be more in low redshift galaxies. This is somewhat in agreement with the previous study (Vladilo et al., 2006).

Our analysis of the flux-brightness relation for compact dwarfs shows that H_α emission line flux strongly correlates with the surface brightness of the galaxy. We also discussed how star formation varies with the environment and sky position. The flux-redshift relation of extended dwarfs shows that H_α emission line flux strongly correlates with redshift.

REFERENCES

Abazaj ian, K., Adelman-McCarthy, J. K., Agüeros, M. A., Allam, S. S., Anderson, S. F., Annis, J., . . . Zucker, D. B. (2003, October). The First Data Release of the Sloan Digital Sky Survey. *Astronomical Journal*, *126*(4), 2081-2086. doi: 10.1086/378165

Abraham, S., Philip, N. S., Kembhavi, A., Wadadekar, Y. G., & Sinha, R. (2012, January). A photometric catalogue of quasars and other point sources in the Sloan Digital Sky Survey. *Monthly Notices of the Royal Astronomical Society*, *419*(1), 80-94. doi: 10.1111/j.1365-2966.2011.19674.x

Aihara, H., Allende Prieto, C., An, D., Anderson, S. F., Aubourg, É., Balbinot, E., . . . Zehavi, I. (2011, April). The Eighth Data Release of the Sloan Digital Sky Survey: First Data from SDSS-III. *The Astrophysical Journal Supplement*, *193*, 29. doi: 10.1088/0067-0049/193/2/29

Allende Prieto, C., Lambert, D. L., & Asplund, M. (2001, July). The Forbidden Abundance of Oxygen in the Sun. *The Astrophysical Journal Letters*, *556*(1), L63-L66. doi: 10.1086/322874

Alonso-Herrero, A., & Knapen, J. H. (2001, September). Statistical Properties of Circumnuclear H II Regions in Nearby Galaxies. *Astronomical Journal*, *122*(3), 1350-1364. doi: 10.1086/322130

Amorisco, N. C., Evans, N. W., & van de Ven, G. (2014, March). The remnant of a merger between two dwarf galaxies in Andromeda II. *Nature*, *507*, 335-337. doi: 10.1038/nature12995

Annibali, F., Nipoti, C., Ciotti, L., Tosi, M., Aloisi, A., Bellazzini, M., . . . Sacchi, E. (2016, August). DDO 68: A Flea with Smaller Fleas that on Him Prey. *The Astrophysical Journal Letters*, *826*, L27. doi: 10.3847/2041-8205/826/2/L27

Arp, H. (1966, November). Atlas of Peculiar Galaxies. *The Astrophysical Journal Supplement*, *14*, 1. doi: 10.1086/190147

Asplund, M., Grevesse, N., Sauval, A. J., & Scott, P. (2009, September). The Chemical Composition of the Sun. *Annual Review of Astron and Astrophys*, *47*(1), 481-522. doi: 10.1146/annurev.astro.46.060407.145222

Baade, W. (1944, September). The Resolution of Messier 32, NGC 205, and the Central Region of the Andromeda Nebula. *Astrophysical Journal*, *100*, 137. doi: 10.1086/144650

Baldwin, J. A., Phillips, M. M., & Terlevich, R. (1981, February). Classification parameters for the emission-line spectra of extragalactic objects. *Publications of the Astronomical Society of the Pacific*, *93*, 5-19. doi: 10.1086/130766

Barbaro, G., & Olivi, F. M. (1989, February). Models of Spectral Energy Distributions of Elliptical Galaxies. *Astrophysical Journal*, *337*, 125. doi: 10.1086/167093

Bautz, L. P., & Morgan, W. W. (1970, December). On the Classification of the Forms of Clusters of Galaxies. *The Astrophysical Journal Letters*, *162*, L149. doi: 10.1086/180643

Bekki, K., & Couch, W. J. (2011, August). Transformation from spirals into S0s with bulge growth in groups of galaxies. *Monthly Notices of the Royal Astronomical Society*, *415*(2), 1783-1796. doi: 10.1111/j.1365-2966.2011.18821.x

Bell, E. F., & de Jong, R. S. (2000, March). The stellar populations of spiral galaxies. *Monthly Notices of the Royal Astronomical Society*, *312*(3), 497-520. doi: 10.1046/j.1365-8711.2000.03138.x

Binggeli, B., & Jerjen, H. (1998, May). Is the shape of the luminosity profile of dwarf elliptical galaxies an useful distance indicator? *Astronomy and Astrophysics*, *333*, 17-26. doi: 10.48550/arXiv.astro-ph/9704027

Binggeli, B., Sandage, A., & Tammann, G. A. (1985, September). Studies of the Virgo Cluster. II - A catalog of 2096 galaxies in the Virgo Cluster area. *Astronomical Journal*, *90*, 1681-1759. doi: 10.1086/113874

Binggeli, B., Tammann, G. A., & Sandage, A. (1987, August). Studies of the Virgo cluster. VI - Morphological and kinematical structure of the Virgo cluster. *Astronomical Journal*, *94*, 251-277. doi: 10.1086/114467

Blanton, M. R., Dalcanton, J., Eisenstein, D., Loveday, J., Strauss, M. A., SubbaRao, M., ... York, D. G. (2001, May). The Luminosity Function of Galaxies in SDSS Commissioning Data. *Astronomical Journal*, *121*(5), 2358-2380. doi: 10.1086/320405

Boselli, A., & Gavazzi, G. (2006, April). Environmental Effects on Late-Type Galaxies in Nearby Clusters. *Publications of the Astronomical Society of the Pacific*, *118*(842), 517-559. doi: 10.1086/500691

Buote, D. A., Gastaldello, F., Humphrey, P. J., Zappacosta, L., Bullock, J. S., Brighenti, F., & Mathews, W. G. (2007, July). The X-Ray Concentration-Virial Mass Relation. *Astrophysical Journal*, *664*(1), 123-134. doi: 10.1086/518684

Buote, D. A., & Tsai, J. C. (1995, January). The Reliability of X-Ray Constraints of Intrinsic Cluster Shapes. *Astrophysical Journal*, *439*, 29. doi: 10.1086/175148

Calzetti, D., Wu, S. Y., Hong, S., Kennicutt, R. C., Lee, J. C., Dale, D. A., ... Wu, Y. (2010, May). The Calibration of Monochromatic Far-Infrared Star Formation Rate Indicators. *Astrophysical Journal*, *714*(2), 1256-1279. doi: 10.1088/0004-637X/714/2/1256

Capaccioli, M. (1989). Galaxy Photometry. In M. Capaccioli & H. G. Corwin (Eds.), *Gerard and antoinette de vaucouleurs: A life for astronomy* (Vol. 4, p. 173).

Chengalur, J. N., Pustilnik, S. A., Makarov, D. I., Perepelitsyna, Y. A., Safonova, E. S., & Karachentsev, I. D. (2015, April). Study of the Lynx-Cancer void galaxies. - V. The extremely isolated galaxy UGC 4722. *Monthly Notices of the Royal Astronomical Society*, *448*, 1634-1643. doi: 10.1093/mnras/stv086

Chhatkuli, D. N., Paudel, S., & Aryal, B. (2021, Dec.). A detailed morphological and spectroscopic study of merging dwarf galaxy pgc 030133. *Journal of Nepal Physical Society*, *7*(4), 28–35. doi: 10.3126/jnphyssoc.v7i4.42928

Chhatkuli, D. N., Paudel, S., Bachchan, R. K., Aryal, B., & Yoo, J. (2022, December). Forming blue compact dwarf galaxy (BCD) through mergers. *Monthly Notices of the Royal Astronomical Society*. doi: 10.1093/mnras/stac3700

Chhatkuli, D. N., Paudel, S., Gautam, A. K., & Aryal, B. (2021, Aug.). SDSS J114818.18-013823.7: Forming Compact Dwarf Galaxy through the Dwarf-Dwarf Merger. *Journal of Nepal Physical Society*, *7*(2), 49–57. doi: 10.3126/jnphyssoc.v7i2.38622

Chincarini, G., & Rood, H. J. (1972, February). Radial velocities of galaxies. *Astronomical Journal*, *77*, 4-8. doi: 10.1086/111236

Chomiuk, L., & Povich, M. S. (2011, December). Toward a Unification of Star Formation Rate Determinations in the Milky Way and Other Galaxies. *Astronomical Journal*, *142*(6), 197. doi: 10.1088/0004-6256/142/6/197

Coleman, M., Da Costa, G. S., Bland-Hawthorn, J., Martínez-Delgado, D., Freeman, K. C., & Malin, D. (2004, February). Shell Structure in the Fornax Dwarf Spheroidal Galaxy. *Astronomical Journal*, *127*, 832-839. doi: 10.1086/381298

Condon, J. J., & Broderick, J. J. (1991, November). Radio Properties of Extragaglctic IRAS Sources. *Astronomical Journal*, *102*, 1663. doi: 10.1086/115986

Couto da Silva, T. C., & de Souza, R. E. (2006, October). Optical spectroscopy for a sample of southern binary galaxies. *Astronomy and Astrophysics*, *457*(2), 425-435. doi: 10.1051/0004-6361:20054444

Crnojević, D., & Mutlu-Pakdil, B. (2021, December). Dwarf galaxies yesterday, now and tomorrow. *Nature Astronomy*, *5*, 1191-1194. doi: 10.1038/s41550-021-01563-1

de Vaucouleurs, G. (1948, January). Recherches sur les Nebuleuses Extragalactiques. *Annales d'Astrophysique*, *11*, 247-+.

Deeg, H. J., Duric, N., & Brinks, E. (1997, July). Star formation histories in H II galaxies. I. Optical and radio observations. *Astronomy and Astrophysics*, *323*, 323-336.

Diaferio, A. (1999, November). Mass estimation in the outer regions of galaxy clusters. *Monthly Notices of the Royal Astronomical Society*, *309*(3), 610-622. doi: 10.1046/j.1365-8711.1999.02864.x

D'Onghia, E., & Fox, A. J. (2016, September). The Magellanic Stream: Circumnavigating the Galaxy. *Annual Review of Astron and Astrophys*, *54*, 363-400. doi: 10.1146/annurev-astro-081915-023251

Duc, P.-A., Paudel, S., McDermid, R. M., Cuillandre, J.-C., Serra, P., Bournaud, F., ... Emsellem, E. (2014, May). Identification of old tidal dwarfs near early-type galaxies from deep imaging and H I observations. *Monthly Notices of the Royal Astronomical Society*, *440*(2), 1458-1469. doi: 10.1093/mnras/stu330

Duc, P.-A., & Renaud, F. (2013). Tides in Colliding Galaxies. In J. Souchay, S. Mathis, & T. Tokieda (Eds.), *Lecture notes in physics, berlin springer verlag* (Vol. 861, p. 327). doi: 10.1007/978-3-642-32961-6_9

Dwek, E. (1998, July). The Evolution of the Elemental Abundances in the Gas and Dust Phases of the Galaxy. *Astrophysical Journal*, *501*, 643. doi: 10.1086/305829

Ellison, S. L., Mendel, J. T., Patton, D. R., & Scudder, J. M. (2013, November). Galaxy pairs in the Sloan Digital Sky Survey - VIII. The observational properties of post-merger galaxies. *Monthly Notices of the Royal Astronomical Society*, *435*(4), 3627-3638. doi: 10.1093/mnras/stt1562

Elmegreen, B. G., Palouš, J., & Ehlerová, S. (2002, August). Environmental dependences for star formation triggered by expanding shell collapse. *Monthly Notices of the Royal Astronomical Society*, *334*(3), 693-698. doi: 10.1046/j.1365-8711.2002.05559.x

Falco, M., Hansen, S. H., Wojtak, R., Brinckmann, T., Lindholmer, M., & Pandolfi, S. (2014, August). A new method to measure the mass of galaxy clusters.

Monthly Notices of the Royal Astronomical Society, *442*(2), 1887-1896. doi: 10.1093/mnras/stu971

Fan, Z., de Grijs, R., Chen, B., Jiang, L., Bian, F., & Li, Z. (2016, December). Lick Indices and Spectral Energy Distribution Analysis Based on an M31 Star Cluster Sample: Comparisons of Methods and Models. *Astronomical Journal*, *152*(6), 208. doi: 10.3847/0004-6256/152/6/208

Fukugita, M., Ichikawa, T., Gunn, J. E., Doi, M., Shimasaku, K., & Schneider, D. P. (1996, April). The Sloan Digital Sky Survey Photometric System. *Astronomical Journal*, *111*, 1748. doi: 10.1086/117915

Geller, M. J., Diaferio, A., & Kurtz, M. J. (1999, May). The Mass Profile of the Coma Galaxy Cluster. *The Astrophysical Journal Letters*, *517*(1), L23-L26. doi: 10.1086/312024

Graham, A. W., & Driver, S. P. (2005). A Concise Reference to (Projected) Sérsic $R^{1/n}$ Quantities, Including Concentration, Profile Slopes, Petrosian Indices, and Kron Magnitudes. *Publications of the Astronomical Society of Australia*, *22*, 118-127. doi: 10.1071/AS05001

Grützbauch, R., Kelm, B., Focardi, P., Trinchieri, G., Rampazzo, R., & Zeilinger, W. W. (2005, April). Small-Scale Systems of Galaxies. II. Properties of the NGC 4756 Group of Galaxies. *Astronomical Journal*, *129*(4), 1832-1848. doi: 10.1086/428368

Gu, Q., Zhao, Y., Shi, L., Peng, Z., & Luo, X. (2006, February). IC 225: A Dwarf Elliptical Galaxy with a Peculiar Blue Core. *Astronomical Journal*, *131*, 806-813. doi: 10.1086/498891

Gunn, J. E., Carr, M., Rockosi, C., Sekiguchi, M., Berry, K., Elms, B., ... Brinkman, J. (1998, December). The Sloan Digital Sky Survey Photometric Camera. *Astronomical Journal*, *116*(6), 3040-3081. doi: 10.1086/300645

Gunn, J. E., Siegmund, W. A., Mannery, E. J., Owen, R. E., Hull, C. L., Leger, R. F., ... Wang, S.-i. (2006, April). The 2.5 m Telescope of the Sloan Digital Sky Survey. *Astronomical Journal*, *131*(4), 2332-2359. doi: 10.1086/500975

Hashimoto, Y., Böhringer, H., Henry, J. P., Hasinger, G., & Szokoly, G. (2007, May). Robust quantitative measures of cluster X-ray morphology, and comparisons between cluster characteristics. *Astronomy and Astrophysics*, *467*(2), 485-499. doi: 10.1051/0004-6361:20065125

Ho, L. C., Filippenko, A. V., & Sargent, W. L. W. (1997, October). Properties of H II Regions in the Centers of Nearby Galaxies. *Astrophysical Journal*, *487*(2), 579-590. doi: 10.1086/304642

Hou, A., Parker, L. C., Harris, W. E., & Wilman, D. J. (2009, September). Statistical Tools for Classifying Galaxy Group Dynamics. *Astrophysical Journal*, *702*(2), 1199-1210. doi: 10.1088/0004-637X/702/2/1199

J. Wilson. (Accessed: 2020-04-25). *Apogee plate.* Retrieved from https://www.sdss4.org/instruments/apogeen-plugging/

Jedrzejewski, R. I. (1987, June). CCD surface photometry of elliptical galaxies - I. Observations, reduction and results. *Monthly Notices of the Royal Astronomical Society*, *226*, 747-768. doi: 10.1093/mnras/226.4.747

Jensen, P. C., & Pimbblet, K. A. (2012, June). Red sequence modal colour gradients across intermediate X-ray luminosity galaxy clusters. *Monthly Notices of the Royal Astronomical Society*, *422*(4), 2841-2853. doi: 10.1111/j.1365-2966.2012.20564.x

Karachentsev, I. D. (2005, January). The Local Group and Other Neighboring Galaxy Groups. *Astronomical Journal*, *129*(1), 178-188. doi: 10.1086/426368

Karachentsev, I. D., Karachentseva, V. E., Huchtmeier, W. K., & Makarov, D. I. (2004, April). A Catalog of Neighboring Galaxies. *Astronomical Journal*, *127*(4), 2031-2068. doi: 10.1086/382905

Kauffmann, G., Heckman, T. M., White, S. D. M., Charlot, S., Tremonti, C., Peng, E. W., ... York, D. (2003, May). The dependence of star formation history and internal structure on stellar mass for 10^5 low-redshift galaxies. *Monthly Notices of the Royal Astronomical Society*, *341*(1), 54-69. doi: 10.1046/j.1365-8711.2003.06292.x

Kennicutt, R. C. (1983, September). The rate of star formation in normal disk galaxies. *Astrophysical Journal*, *272*, 54-67. doi: 10.1086/161261

Kennicutt, R. C. (1989, September). The Star Formation Law in Galactic Disks. *Astrophysical Journal*, *344*, 685. doi: 10.1086/167834

Kennicutt, R. C. (1998). Star Formation in Galaxies Along the Hubble Sequence. *Annual Review of Astron and Astrophys*, *36*, 189-232. doi: 10.1146/annurev.astro.36.1.189

Kennicutt, R. C., & Evans, N. J. (2012a, September). Star Formation in the Milky Way and Nearby Galaxies. *Annual Review of Astron and Astrophys*, *50*, 531-608. doi: 10.1146/annurev-astro-081811-125610

Kennicutt, R. C., & Evans, N. J. (2012b, September). Star Formation in the Milky Way and Nearby Galaxies. *Annual Review of Astron and Astrophys*, *50*, 531-608. doi: 10.1146/annurev-astro-081811-125610

Kormendy, J., & Kennicutt, R. C. (2004, September). Secular Evolution and the Formation of Pseudobulges in Disk Galaxies. *Annual Review of Astron and Astrophys*, *42*(1), 603-683. doi: 10.1146/annurev.astro.42.053102.134024

Krumholz, M. R., & Dekel, A. (2012, July). Metallicity-dependent Quenching of Star Formation at High Redshift in Small Galaxies. *Astrophysical Journal*, *753*(1), 16. doi: 10.1088/0004-637X/753/1/16

Lanfranchi, G. A., & Matteucci, F. (2003, October). Chemical evolution of dwarf spheroidal and blue compact galaxies. *Monthly Notices of the Royal Astronomical Society*, *345*(1), 71-85. doi: 10.1046/j.1365-8711.2003.06919.x

Lee, B. C., Allam, S. S., Tucker, D. L., Annis, J., Johnston, D. E., Scranton, R., ... Yanny, B. (2004, April). A Catalog of Compact Groups of Galaxies in the SDSS Commissioning Data. *Astronomical Journal*, *127*(4), 1811-1859. doi: 10.1086/382236

Lee, J. C., Gil de Paz, A., Tremonti, C., Kennicutt, R. C., Salim, S., Bothwell, M., ... Weisz, D. (2009, November). Comparison of Hα and UV Star Formation Rates in the Local Volume: Systematic Discrepancies for Dwarf Galaxies. *Astrophysical Journal*, *706*, 599-613. doi: 10.1088/0004-637X/706/1/599

Lupton, R., Blanton, M. R., Fekete, G., Hogg, D. W., O'Mullane, W., Szalay, A., & Wherry, N. (2004, February). Preparing Red-Green-Blue Images from CCD Data. *Publications of the Astronomical Society of the Pacific*, *116*(816), 133-137. doi: 10.1086/382245

Lupton, R., Gunn, J. E., Ivezić, Z., Knapp, G. R., & Kent, S. (2001, January). The SDSS Imaging Pipelines. In J. Harnden F. R., F. A. Primini, & H. E. Payne (Eds.), *Astronomical data analysis software and systems x* (Vol. 238, p. 269).

Lupton, R. H., Gunn, J. E., & Szalay, A. S. (1999, September). A Modified Magnitude System that Produces Well-Behaved Magnitudes, Colors, and Errors Even for Low Signal-to-Noise Ratio Measurements. *Astronomical Journal*, *118*(3), 1406-1410. doi: 10.1086/301004

Makarov, D., & Karachentsev, I. (2011, April). Galaxy groups and clouds in the local (z$\sim$ 0.01) Universe. *Monthly Notices of the Royal Astronomical Society*, *412*(4), 2498-2520. doi: 10.1111/j.1365-2966.2010.18071.x

Makarov, D., Karachentsev, I. D., Chengalur, J. N., Uklein, R., & Marchuk, A. (2013, March). A coupling pair of dwarfs in Lynx. *arXiv e-prints*, arXiv:1303.2477. doi: 10.48550/arXiv.1303.2477

Marino, R. A., Rosales-Ortega, F. F., Sánchez, S. F., Gil de Paz, A., Vílchez, J., Miralles-Caballero, D., ... CALIFA Team (2013, November). The O3N2 and N2 abundance indicators revisited: improved calibrations based on CALIFA and T_e-based literature data. *Astronomy and Astrophysics*, *559*, A114. doi: 10.1051/0004-6361/201321956

McGaugh, S. S., & de Blok, W. J. G. (1997, May). Gas Mass Fractions and the Evolution of Spiral Galaxies. *Astrophysical Journal*, *481*(2), 689-702. doi: 10.1086/304100

Mihos, J. C., Harding, P., Feldmeier, J. J., Rudick, C., Janowiecki, S., Morrison, H., ... Watkins, A. (2017, January). The Burrell Schmidt Deep Virgo Survey: Tidal Debris, Galaxy Halos, and Diffuse Intracluster Light in the Virgo Cluster. *Astrophysical Journal*, *834*, 16. doi: 10.3847/1538-4357/834/1/16

Milvang-Jensen, B., & Jørgensen, I. (1999, January). Galaxy Surface Photometry. *Baltic Astronomy*, *8*, 535-574. doi: 10.1515/astro-1999-0408

Mould, J., & Kristian, J. (1986, June). The Stellar Population in the Halos of M31 and M33. *Astrophysical Journal*, *305*, 591. doi: 10.1086/164273

Mulchaey, J. S. (2000, January). X-ray Properties of Groups of Galaxies. *Annual Review of Astron and Astrophys*, *38*, 289-335. doi: 10.1146/annurev.astro.38.1.289

Muldrew, S. I., Croton, D. J., Skibba, R. A., Pearce, F. R., Ann, H. B., Baldry, I. K., ... Zibetti, S. (2012, January). Measures of galaxy environment - I. What is 'environment'? *Monthly Notices of the Royal Astronomical Society*, *419*(3), 2670-2682. doi: 10.1111/j.1365-2966.2011.19922.x

Naab, T., & Burkert, A. (2003, November). Statistical Properties of Collisionless Equal- and Unequal-Mass Merger Remnants of Disk Galaxies. *Astrophysical Journal*, *597*, 893-906. doi: 10.1086/378581

Omukai, K., Tsuribe, T., Schneider, R., & Ferrara, A. (2005, June). Thermal and Fragmentation Properties of Star-forming Clouds in Low-Metallicity Environments. *Astrophysical Journal*, *626*(2), 627-643. doi: 10.1086/429955

Osterbrock, D. E., & Ferland, G. J. (2006). *Astrophysics of gas nebulae and active galactic nuclei*. University science books.

Paudel, S., Duc, P. A., & Ree, C. H. (2015, March). A Case Study for a Tidal Interaction between Dwarf Galaxies in UGC 6741. *Astronomical Journal*, *149*, 114. doi: 10.1088/0004-6256/149/3/114

Paudel, S., Lisker, T., Hansson, K. S. A., & Huxor, A. P. (2014, September). An isolated, compact early-type galaxy with a diffuse stellar component: merger origin? *Monthly Notices of the Royal Astronomical Society*, *443*, 446-453. doi: 10.1093/mnras/stu1171

Paudel, S., Sengupta, C., Yoon, S.-J., & Chhatkuli, D. N. (2020, April). MCG+07-20-052: Interacting Dwarf Pair in a Group Environment. *Astronomical Journal*, *159*(4), 141. doi: 10.3847/1538-3881/ab722f

Paudel, S., Smith, R., Duc, P.-A., Côté, P., Cuillandre, J.-C., Ferrarese, L., . . . Zhang, H. (2017, January). The Next Generation Virgo Cluster Survey. XXII. Shell Feature Early-type Dwarf Galaxies in the Virgo Cluster. *Astrophysical Journal*, *834*, 66. doi: 10.3847/1538-4357/834/1/66

Paudel, S., Smith, R., Yoon, S. J., Calderón-Castillo, P., & Duc, P.-A. (2018a, August). A Catalog of Merging Dwarf Galaxies in the Local Universe. *The Astrophysical Journal Supplement*, *237*(2), 36. doi: 10.3847/1538-4365/aad555

Paudel, S., Smith, R., Yoon, S. J., Calderón-Castillo, P., & Duc, P.-A. (2018b, August). A Catalog of Merging Dwarf Galaxies in the Local Universe. *The Astrophysical Journal Supplement*, *237*(2), 36. doi: 10.3847/1538-4365/aad555

Pearson, S., Besla, G., Putman, M. E., Lutz, K. A., Fernández, X., Stierwalt, S., . . . Sung, E.-C. (2016, June). Local Volume TiNy Titans: gaseous dwarf-dwarf interactions in the Local Universe. *Monthly Notices of the Royal Astronomical Society*, *459*, 1827-1846. doi: 10.1093/mnras/stw757

Petrosian, V. (1976, October). Surface brightness and evolution of galaxies. *The Astrophysical Journal Letters*, *209*, L1-L5. doi: 10.1086/182253

Poggianti, B. M., & Barbaro, G. (1997, September). Indicators of star formation: 4000 Å break and Balmer lines. *Astronomy and Astrophysics*, *325*, 1025-1030. doi: 10.48550/arXiv.astro-ph/9703067

Privon, G. C., Stierwalt, S., Patton, D. R., Besla, G., Pearson, S., Putman, M., . . . Titans, T. (2017, September). A Widespread, Clumpy Starburst in the Isolated Ongoing Dwarf Galaxy Merger dm1647+21. *Astrophysical Journal*, *846*, 74. doi: 10.3847/1538-4357/aa8560

Pustilnik, S. A., & Tepliakova, A. L. (2011, August). Study of galaxies in the Lynx-Cancer void - I. Sample description. *Monthly Notices of the Royal Astronomical Society*, *415*, 1188-1201. doi: 10.1111/j.1365-2966.2011.18733.x

Rabinowitz, D., Tourtellotte, S., Brown, M., & Trujillo, C. (2005, August). Photometric observations of a very bright TNO with an extraordinary lightcurve. In *Aas/division for planetary sciences meeting abstracts #37* (Vol. 37, p. 56.12).

Rich, R. M., Collins, M. L. M., Black, C. M., Longstaff, F. A., Koch, A., Benson, A., & Reitzel, D. B. (2012, February). A tidally distorted dwarf galaxy near NGC 4449. *Nature*, *482*, 192-194. doi: 10.1038/nature10837

Robitaille, T. P. (2010, September). On the modified random walk algorithm for Monte-Carlo radiation transfer. *Astronomy and Astrophysics*, *520*, A70. doi: 10.1051/0004-6361/201015025

Sandage, A., & Binggeli, B. (1984, July). Studies of the Virgo cluster. III. A classification system and an illustrated Atlas of Virgo cluster dwarf galaxies. *Astronomical Journal*, *89*, 919-931. doi: 10.1086/113588

Schmidt, M. (1959, March). The Rate of Star Formation. *Astrophysical Journal*, *129*, 243. doi: 10.1086/146614

Schombert, J. M. (1986, March). The Structure of Brightest Cluster Members. I. Surface Photometry. *The Astrophysical Journal Supplement*, *60*, 603. doi: 10.1086/191100

Sciencebydegrees. (Accessed: 2019-09-30). https://sciencebydegrees.com.

SDSS Legacy Survey. (Accessed: 2019-09-30). https://www.legacysurvey.org/.

Seigar, M. S., Graham, A. W., & Jerjen, H. (2007, July). Intracluster light and the extended stellar envelopes of cD galaxies: an analytical description. *Monthly Notices of the Royal Astronomical Society*, *378*(4), 1575-1588. doi: 10.1111/j.1365-2966.2007.11899.x

Sengupta, C., Scott, T. C., Paudel, S., Saikia, D. J., Dwarakanath, K. S., & Sohn, B. W. (2015, December). Arp 65 interaction debris: massive H I displacement and star formation. *Astronomy and Astrophysics*, *584*, A114. doi: 10.1051/0004-6361/201425149

Sengupta, C., Scott, T. C., Verdes Montenegro, L., Bosma, A., Verley, S., Vilchez, J. M., ... Portas, A. (2012, October). H I asymmetry in the isolated galaxy CIG 85 (UGC 1547). *Astronomy and Astrophysics*, *546*, A95. doi: 10.1051/0004-6361/201219948

Sersic, J. L. (1968). *Atlas de galaxias australes* (Sersic, J. L., Ed.). Univ. Nac. Cordoba, Argentina: Observatorio Astronomico, 1968.

Sharpee, B., Williams, R., Baldwin, J. A., & van Hoof, P. A. M. (2003, November). Introducing EMILI: Computer-aided Emission Line Identification. *The Astrophysical Journal Supplement*, *149*(1), 157-187. doi: 10.1086/378321

Sloan Digital Sky Survey. (Accessed: 2019-09-30a). https://www.sdss.org.

Sloan Digital Sky Survey. (Accessed: 2019-09-30b). https://www.sdss.org.

Smee, S. A., Gunn, J. E., Uomoto, A., Roe, N., Schlegel, D., Rockosi, C. M., ... York, D. G. (2013, August). The Multi-object, Fiber-fed Spectrographs for the Sloan Digital Sky Survey and the Baryon Oscillation Spectroscopic Survey. *Astronomical Journal*, *146*(2), 32. doi: 10.1088/0004-6256/146/2/32

Sodré, J., L., & Cuevas, H. (1994, January). Spectral classification of galaxies. *Vistas in Astronomy*, *38*(3), 287-291. doi: 10.1016/0083-6656(94)90039-6

Sodré, J., L., & Stasińska, G. (1999, May). The emission line sequence of normal spiral galaxies. *Astronomy and Astrophysics*, *345*, 391-402. doi: 10.48550/arXiv.astro-ph/9903130

Soifer, B. T., Boehmer, L., Neugebauer, G., & Sanders, D. B. (1989, September). The IRAS Bright Galaxy Sample. IV. Complete IRAS Observations. *Astronomical Journal*, *98*, 766. doi: 10.1086/115178

Solanes, J. M., & Stein, P. (1998, August). Kinematics of the southern galaxy cluster Abell 3733. *Astronomy and Astrophysics, Supplement*, *131*, 221-227. doi: 10.1051/aas:1998263

Soria, R., Mould, J. R., Watson, A. M., Gallagher, I., John S., Ballester, G. E., Burrows, C. J., ... Westphal, J. A. (1996, July). Detection of the Tip of the Red Giant Branch in NGC 5128. *Astrophysical Journal*, *465*, 79. doi: 10.1086/177403

Springel, V., Di Matteo, T., & Hernquist, L. (2005, February). Black Holes in Galaxy Mergers: The Formation of Red Elliptical Galaxies. *The Astrophysical Journal Letters*, *620*, L79-L82. doi: 10.1086/428772

Squires, G. L. (2001). *Practical Physics*. Wiley, New York.

Stahler, S. W., & Palla, F. (2004). *The Formation of Stars*. Wiley, New York.

Stierwalt, S., Besla, G., Patton, D., Johnson, K., Kallivayalil, N., Putman, M., ... Ross, G. (2015, May). TiNy Titans: The Role of Dwarf-Dwarf Interactions in Low-mass Galaxy Evolution. *Astrophysical Journal*, *805*, 2. doi: 10.1088/0004-637X/805/1/2

Strauss, M. A., Weinberg, D. H., Lupton, R. H., Narayanan, V. K., Annis, J., Bernardi, M., . . . Zehavi, I. (2002, September). Spectroscopic Target Selection in the Sloan Digital Sky Survey: The Main Galaxy Sample. *Astronomical Journal*, *124*(3), 1810-1824. doi: 10.1086/342343

Struble, M. F., & Rood, H. J. (1999, November). A Compilation of Redshifts and Velocity Dispersions for ACO Clusters. *The Astrophysical Journal Supplement*, *125*(1), 35-71. doi: 10.1086/313274

Tinsley, B. M., & Gunn, J. E. (1976, January). Evolutionary synthesis of the stellar population in elliptical galaxies. I. Ingredients, broad-band colors, and infrared features. *Astrophysical Journal*, *203*, 52-62. doi: 10.1086/154046

Tody, D. (1986, January). The IRAF Data Reduction and Analysis System. In D. L. Crawford (Ed.), *Instrumentation in astronomy vi* (Vol. 627, p. 733). doi: 10.1117/12.968154

Tremonti, C. A., Heckman, T. M., Kauffmann, G., Brinchmann, J., Charlot, S., White, S. D. M., . . . Brinkmann, J. (2004, October). The Origin of the Mass-Metallicity Relation: Insights from 53,000 Star-forming Galaxies in the Sloan Digital Sky Survey. *Astrophysical Journal*, *613*(2), 898-913. doi: 10.1086/423264

Tucker, W., Blanco, P., Rappoport, S., David, L., Fabricant, D., Falco, E. E., . . . Ramella, M. (1998, March). 1E 0657-56: A Contender for the Hottest Known Cluster of Galaxies. *The Astrophysical Journal Letters*, *496*(1), L5-L8. doi: 10.1086/311234

van Dokkum, P. G., Whitaker, K. E., Brammer, G., Franx, M., Kriek, M., Labbé, I., . . . Wake, D. (2010, February). The Growth of Massive Galaxies Since z = 2. *Astrophysical Journal*, *709*(2), 1018-1041. doi: 10.1088/0004-637X/709/2/1018

Veilleux, S., & Osterbrock, D. E. (1987, February). Spectral Classification of Emission-Line Galaxies. *The Astrophysical Journal Supplement*, *63*, 295. doi: 10.1086/191166

Vladilo, G., Centurión, M., Levshakov, S. A., Péroux, C., Khare, P., Kulkarni, V. P., & York, D. G. (2006, July). Extinction and metal column density of HI regions up to redshift $z = 2$. *Astronomy and Astrophysics*, *454*(1), 151-164. doi: 10.1051/0004-6361:20054742

Walter, F., Weiss, A., Martin, C., & Scoville, N. (2002, January). The Interacting Dwarf Galaxy NGC 3077: The Interplay of Atomic and Molecular Gas with Violent Star Formation. *Astronomical Journal*, *123*(1), 225-237. doi: 10.1086/324633

Webb Space Telescope. (Accessed: 2019-09-30). https://webbtelescope.org/news/first-images/gallery.

Weisz, D. R., Dolphin, A. E., Dalcanton, J. J., Skillman, E. D., Holtzman, J., Williams, B. F., . . . Zaritsky, D. (2011, December). How Typical Are the Local Group Dwarf Galaxies? *Astrophysical Journal*, *743*(1), 8. doi: 10.1088/0004-637X/743/1/8

Wells, D. C., Greisen, E. W., & Harten, R. H. (1981, June). FITS - a Flexible Image Transport System. *Astronomy and Astrophysics, Supplement*, *44*, 363.

White, S. D. M., & Frenk, C. S. (1991, September). Galaxy Formation through Hierarchical Clustering. *Astrophysical Journal*, *379*, 52. doi: 10.1086/170483

White, S. D. M., & Rees, M. J. (1978, May). Core condensation in heavy halos: a two-stage theory for galaxy formation and clustering. *Monthly Notices of the Royal Astronomical Society*, *183*, 341-358. doi: 10.1093/mnras/183.3.341

Worthey, G., Faber, S. M., Gonzalez, J. J., & Burstein, D. (1994, October). Old stellar populations. 5: Absorption feature indices for the complete LICK/IDS sample of stars. *The Astrophysical Journal Supplement*, *94*, 687-722. doi: 10.1086/192087

York, D. G., Adelman, J., Anderson, J., John E., Anderson, S. F., Annis, J., Bahcall, N. A., . . . SDSS Collaboration (2000, September). The Sloan Digital Sky Survey: Technical Summary. *Astronomical Journal*, *120*(3), 1579-1587. doi: 10.1086/301513

Zaritsky, D., Zabludoff, A. I., & Willick, J. A. (1995, October). Spectral Classification of Galaxies Along the Hubble Sequence. *Astronomical Journal*, *110*, 1602. doi: 10.1086/117634

Zhang, H.-X., Smith, R., Oh, S.-H., Paudel, S., Duc, P.-A., Boselli, A., . . . Zhao, Y. (2020, September). The Blue Compact Dwarf Galaxy VCC 848 Formed by Dwarf-Dwarf Merging: H I Gas, Star Formation, and Numerical Simulations. *Astrophysical Journal*, *900*(2), 152. doi: 10.3847/1538-4357/abab96

Zhu, G., & Ménard, B. (2013, August). Calcium H & K Induced by Galaxy Halos. *Astrophysical Journal*, *773*(1), 16. doi: 10.1088/0004-637X/773/1/16

APPENDIX

A. Papers published in international journals

Chhatkuli, D. N., Paudel, S., Bachchan, R. K., Aryal, B., & Yoo, J. (2022, 12). Forming blue compact dwarf galaxy through mergers. *Monthly Notices of the Royal Astronomical Society*, *520*(4), 4953-4960. doi: 10.1093/mnras/stac3700

Paudel, S., Sengupta, C., Yoon, S.-J., & Chhatkuli, D. N. (2020, April). MCG+07-20-052: Interacting Dwarf Pair in a Group Environment. *Astronomical Journal*, *159*(4), 141. doi: 10.3847/1538-3881/ab722f

Paudel, S., Yoon, S.-J., Moon, J.-S., & Chhatkuli, D. N. (2023, March). Early-type dwarf galaxies in the local universe. Evidence of ex situ growth. *Monthly Notices of the Royal Astronomical Society*, *520*(1), L5-L10. doi: 10.1093/mnrasl/slac159

Paudel, S., Yoon, S.-J., Yoo, J., Smith, R., Chhatkuli, D. N., Bachchan, R. K., . . . Baral, R. (2023, April). An Extensive Catalog of Early-type Dwarf Galaxies in the Local Universe: Morphology and Environment. *The Astrophysical Journal Supplement*, *265*(2), 57. doi: 10.3847/1538-4365/acbfa7

B. Papers published in national journals

Chhatkuli, D. N., Paudel, S., & Aryal, B. (2020). Study of star formation rate and metallicity of an interacting dwarf galaxy NGC 2604. *Journal of Institute of Science and Technology*, *25*(2), 55–60. doi: 10.3126/jist.v25i2.33736

Chhatkuli, D. N., Paudel, S., & Aryal, B. (2021a). A Detailed Morphological and Spectroscopic Study of Merging Dwarf Galaxy PGC 030133. *Journal of Nepal Physical Society*, *7*(4), 28–35. doi: 10.3126/jnphyssoc.v7i4.42928

Chhatkuli, D. N., Paudel, S., & Aryal, B. (2021b). A spectroscopic study of the low redshift dwarf galaxy SDSS J134326. 99+ 431118.7 to calculate star formation rate. *BIBECHANA*, *18*(1), 100–107. doi: 10.3126/bibechana.v18i1.29466

Chhatkuli, D. N., Paudel, S., Gautam, A. K., & Aryal, B. (2021). SDSS J114818. 18-013823.7: Forming Compact Dwarf Galaxy through the Dwarf-Dwarf Merger. *Journal of Nepal Physical Society*, *7*(2), 49–57. doi: 10.3126/jnphyssoc.v7i2 .38622

Chhatkuli, D. N., Paudel, S., Sedhain, A., & Aryal, B. (2022, December). Structural Parameter of a Merging Compact Dwarf Galaxy CG 0315. *Journal of Institute of Science and Technology*, *27*(2), 85–89. doi: 10.3126/jist.v27i2.35312

C. Participation in conferences, seminars, workshops and lecture series

- Presented a Poster entitled "Forming Blue Compact Dwarf Galaxies (BCD) through Mergers" in IAU S379: Dynamical Masses of Local Group Galaxies held in Telegrafenberg, Potsdam, Germany, organized by International Astronomical Union and Local Organizing Committee of Germany, March 20-24, 2023.
- "Workshop on Southampton IUCAA Training for Astronomical Research and Education (SITARE) Workshop" jointly organized by University of Southampton UK, Inter-University Centre for Astronomy and Astrophysics (IUCAA) and Central Department of Physics, Tribhuvan University, Nepal, June 13-15, 2018.
- "16th International Symposium on Bio-cosmology (16ISBC)" organized by Research Centre for Applied Science and Technology (RECAST), Tribhuvan University, Kathmandu, Nepal, April 16-18, 2018.
- "Scientific secession of NPS 36th Annual Convention" organized by Nepal Physical Society at Central Department of Physics, Kirtipur, Nepal, November 8-9, 2019.
  Oral presentation: "A study of Star Formation Rate in the Low Redshift Dwarf Galaxy NGC 2604"
- "National Symposium on Research, Development, and Innovation in Physics (NSRDIP-2019)" organized by St. Xavier's College, Kathmandu, Nepal, September 3-4, 2019
- "Three Days Online School on Space and Atmospheric Physics" organized by Department of Physics, St. Xavier's College, Kathmandu, Nepal, August 5-7, 2020.
- "Scientific secession of NPS 37th Annual Convention" organized by Nepal Physical Society at Central Department of Physics, Kirtipur, Nepal, February 6, 2021.
  Oral presentation: "Structural Parameter of a Merging Compact Dwarf Galaxy CG 0315"
- "Six month NPS School of Computing-2022" conducted by Nepal Physical Society, Kathmandu, Nepal, July 4, 2020 - January 31, 2021.
- "International Conference on Nano sciences and High Energy Physics (ICNHEP-2019)" organized by Central Department of Physics, Kirtipur, Kathmandu, Nepal, February 4 - 6, 2019.

Poster presentation: "Star-Forming Regions in Interacting Dwarf Galaxies"

- "Workshop on SITARE-Advanced workshop on Astrophysics" held at IUCAA, Pune, India, jointly organized by University of Southampton UK and IUCAA, January 10-16, 2019.
- "Best oral presentation on, 1st International e-Conference on Recent Advances in Physics & Materials Science-2020 (IC-RAPMS-2020)" organized by Kurseong College, & St. Joseph's College, Darjeeling, West Bengal, India and Condensed Matter Physics Research Center, Nepal, July 9 - 10, 2020.
  Oral presentation: "A Spectroscopic Study of the Low Redshift Dwarf Galaxy SDSS J134326.99+431118.7 to Calculate Star Formation Rate"
- "XXXIst General Assembly of International Astronomical Union (IAUGA 2022)" organized by International Astronomical Union and the National Organizing Committee of Korea, held in BEXCO, Busan, the Republic of Korea, August 2-11, 2022.
  Poster presentation: "A Detailed Morphological and Spectroscopic Study of Merging Blue Compact Dwarf Galaxies"
- "ANPA Conference" organized by Association of Nepali Physicists in America (ANPA), USA, July 17-19, 2020.
- "Online Interaction Session on Astronomy & Astrophysics" organized by Kurseong College, Darjeeling, September 30, 2020.
- "Participation in online talks by IUCAA scientists on astronomy and Astrophysics", organized by Inter University Centre for Astronomy and Astrophysics (IUCAA), Pune, India on February 28, 2021.
- "4th ANPA Conference" organized by Association of Nepali Physicists in America (ANPA) (July 16 -18, 2021).
  Oral presentation: "Structural Parameter of a Merging Compact Dwarf Galaxy CG 0315"
- "ANPA Conference 2022" organized by Association of Nepali Physicists in America (ANPA) (July 15-17, 2022).
  Oral presentation: "Forming Blue Compact Dwarf Galaxy (BCD) through the Merger"
- "International Conference on Frontier of Physics (ICFP)-2022" organized by Nepal Physical Society (January 22-24, 2022).
  Oral presentation: "Forming Blue Compact Dwarf Galaxy (BCD) through the Merger"

D. Courses taken in first and second semester

First semester

- PHS 911: Philosophy of science (3 CH)
- PHS 912: Research methodology (3 CH)
- PHS 913: Seminar (3 CH)

Second semester

- PHS 951: Advanced research methodology (3 CH)
- PHS 957: Advanced astrophysics (3 CH)
- PHS 952: Seminar (3 CH)

The Astrophysical Journal Supplement Series, 265:57 (14pp), 2023 April https://doi.org/10.3847/1538-4365/acbfa7

An Extensive Catalog of Early-type Dwarf Galaxies in the Local Universe: Morphology and Environment

Sanjaya Paudel[1], Suk-Jin Yoon[1], Jaewon Yoo[2], Rory Smith[2], Daya Nidhi Chhatkuli[3], Rajesh Kumar Bachchan[4], Binil Aryal[3], Binod Adhikari[4,5], Namuna Adhikari[3], Amrit Sedain[3], Sharup Sheikh[3], Sarashwati Dhital[3], Ashutosh Giri[5], and Rabin Baral[5]

[1] Department of Astronomy, Yonsei University, Seoul 03722, Republic of Korea; sjyoon0691@yonsei.ac.kr
[2] Korea Astronomy and Space Science Institute (KASI), 776 Daedeokdae-ro, Yuseong-gu, Daejeon 34055, Republic of Korea
[3] Central Department of Physics, Tribhuvan University, Kirtipur, Kathmandu, Nepal
[4] Department of Physics, Patan Multiple College, Tribhuvan University, Nepal
[5] Department of Physics, St. Xavier's College, Tribhuvan University, Kathmandu, Nepal
Received 2022 April 5; revised 2023 February 6; accepted 2023 February 20; published 2023 April 11

Abstract

We present an extensive catalog of 5405 early-type dwarf (dE) galaxies located in the various environments, i.e., clusters, groups, and fields, of the local universe ($z < 0.01$). The dEs are selected through visual inspection of the Legacy survey's g–r–z combined tricolor images. The inspected area, covering a total sky area of 7643 deg^2, encompasses two local clusters (Virgo and Fornax), 265 groups, and the regions around 586 field galaxies of $M_K < -21$ mag. The catalog aims to be one of the most extensive and publicly accessible collections of data on dEs, despite its complex completeness limits, which may not accurately represent its statistical completeness. The strength of the catalog lies in the morphological characteristics, including nucleated, tidal, and ultradiffuse dEs. The two clusters contribute nearly half (2437 out of 5405) of the dEs, and the 265 groups contribute 2103 dEs. There are 864 dEs in 586 fields, i.e., ∼1.47 dEs per field. Using a standard definition commonly used in literature, we identify 100 ultradiffuse galaxies (UDGs), which compose ∼2% of the dE population. We find that 40% of our sample dEs harbor a central nucleus, and among the UDG population, a majority (79%) are nonnucleated. About 1.3% of dEs suffer from ongoing tidal disturbance by nearby massive galaxies, and only 0.03% show a sign of recent dwarf–dwarf mergers. The association between dEs and their nearest bright neighbor galaxies suggests that dEs are more likely created where their neighbors are non-star-forming ones.

Unified Astronomy Thesaurus concepts: Dwarf galaxies (416); Early-type galaxies (429); Low surface brightness galaxies (940); Galaxy nuclei (609); Galaxy groups (597); Galaxy clusters (584); Field galaxies (533)

Supporting material: machine-readable table

1. Introduction

Stated as a morphology–density relation, galaxy population depends on the local environment (e.g., Dressler 1980; Whitmore et al. 1993). Massive galaxy clusters are dominated by red and dead early-type morphology galaxies, and low-density groups and fields host a larger fraction of star-forming late-type galaxies (Oemler 1974). In the dwarf galaxy regime (commonly defined as less massive than the Large Magellanic Cloud (LMC)), we can see an extreme form of the morphology–density relation, with the nonexistence of early-type dwarf galaxies (dEs) outside the group and cluster environments (Binggeli et al. 1987; Geha et al. 2012).

A natural explanation for the existence of an extreme form of the morphology–density relation in the dwarf galaxy population is that the environment-related mechanisms mainly cause the quenching of dwarf galaxies and there are varieties of candidates (Boselli et al. 2008; Kormendy et al. 2009). Ram pressure stripping (RPS; a high-speed interaction between hot cluster gas and the reservoir of star-forming gas of an infalling galaxy introduces a viscous drag, which eventually removes the star-forming gas; Gunn et al. 1972), tidal harassment/stripping (removal of gas through tidal deformations; Moore et al. 1996; Mayer et al. 2001; Smith et al. 2010), and starvation (a short supply of star-forming gas in the cluster environment; Larson et al. 1980) are the prime candidates that are frequently discussed in the literature. Since the environments themselves vary from the cluster and group to the field, a long-standing and critical issue is which particular mechanism is more efficient in which particular environment. The RPS is expected to be more efficient in the cluster environment. Evidence of ongoing RPS in the cluster environment, explicitly in the Virgo Cluster, has been frequently presented in the recent literature (Kenney et al. 2004, 2014; Vollmer et al. 2001). The tidal stirring or harassment is more frequent in the small group environments (Mayer et al. 2001; Paudel & Ree 2014). It is also important to note that the combination of time spent while undergoing a given mechanism and its strength should be considered. It has been suggested that only a combination of several different processes can explain the diverse morphological properties of cluster dEs (see, e.g., Lisker 2009, for an overview). On the other hand, the importance of the environment relative to a small-scale merger in the evolution of dwarf galaxies remains poorly understood.

By definition, dEs are non-star-forming and gas-poor objects, somewhat lower mass cousins of elliptical galaxies (Ferguson & Binggeli 1994). Therefore, a smooth appearance and red and dead (aka old stellar populations) are the prime characteristics of these galaxies, but more notably, their low

surface brightness nature makes them an outstanding class of object compared with massive early-type galaxies. Due to their low surface brightness and scarcity in the nearby universe, particularly in low-dense environments like the field, a detailed study of environmental effects on their observational properties using a large sample of dEs has been lacking.

On the other hand, detailed studies on the morphological properties of cluster dEs have revealed that dEs are not a homogeneous class of objects. With the help of sophisticated image analysis techniques, a great deal of complexity in dE structure has been discovered. Fine structures such as tidal tails, blue cores, spiral arms, or bars are frequent in the brighter dE population (Jerjen et al. 2000; Lisker et al. 2007; Paudel & Ree 2014), and, in general, cluster dE light profiles are not well fitted by a single Sérsic function (Janz et al. 2014; Su et al. 2021). A careful analysis of these fine structures has shown that they could contribute up to 10% of the total light of the dE main body (Smith et al. 2021; Paudel & Ree 2014).

Very recent deep-imaging surveys have also revealed that dEs of stellar mass as low as the Fornax dwarf galaxy are hosting tidal features that are likely to have originated through mergers (Crnojević et al. 2014; Paudel et al. 2017). In addition, a compact star cluster is also found in the center of many dEs, called the nucleus. Many detailed observational studies have shown that the central nucleus is almost universal in the brighter dE population of the cluster environment (Côté et al. 2006) and that the nucleated fraction declines to as low as 30% among the fainter ($M_g > -12$ mag) dEs (Sánchez-Janssen et al. 2019). Interestingly, a few dedicated studies on these substructural properties of dEs beyond the cluster environment, particularly outside of the Virgo and Fornax Clusters, are available to date, and it is not well understood that the cluster environment is necessary for forming these substructural properties.

There is a recent upsurge in the exploration of diffuse and extended dEs called ultradiffuse galaxies (UDGs; van Dokkum et al. 2015; Marleau et al. 2021), although their examples have been known for decades (Thompson & Gregory 1993; Caldwell & Bothun 1987; Impey et al. 1988; Jerjen et al. 2000; Conselice et al. 2002, 2003; Penny et al. 2011). A multitude of recent literature has presented the UDGs as if they were a newly discovered class of dwarf galaxies (Mihos et al. 2015; Martínez-Delgado et al. 2016; Merritt et al. 2016; Román & Trujillo 2017; Zaritsky et al. 2021), and there are reports of discovering them in all environments—cluster, group, and field, with a diverse color, morphology, and globular cluster population (Beasley & Trujillo 2016; Lim et al. 2020; Müller et al. 2020). The diverse and complex UDG properties essentially suggest that UGDs could also form a mixed bag of populations, and there is no single origin for them, with multiple possible evolutionary tracks at play (Duc et al. 2014; Amorisco & Loeb 2016; Bennet et al. 2018; Chan et al. 2018; Carleton et al. 2019; Jones et al. 2021).

With the advent of sophisticated observing techniques and wide-aperture telescopes, there has been a growing interest in low surface brightness galaxies like dEs. Some groups have focused on building catalogs of dwarf galaxies with different morphology, and others have focused on a more specific type, like dEs or UDGs in the cluster or group environment. For example, Habas et al. (2020) investigated the overall dwarf galaxy population of different morphologies around massive early-type galaxies, while Ferrarese et al. (2012), Venhola et al. (2017), Eigenthaler et al. (2018), Ferrarese et al. (2020), and La Marca et al. (2022) are more focused on the cluster environment. As a part of the Satellites Around Galactic Analogs (SAGA) survey Geha et al. (2012) searched dwarf galaxy populations around Milky Way analogs and Carlsten et al. (2022) explored satellite populations in Local Volume ($D < 12$ Mpc) host galaxies. In addition, Chiboucas et al. (2013), Crnojević et al. (2016), Müller et al. (2017), and Bennet et al. (2019) searched member dwarf satellite galaxies in nearby groups.

In this paper, we investigate the morphological properties of dEs sampled from diverse environments in an attempt to understand their relationship with the environment where they are located and provide statistically homogeneous data sets of a large sample of dEs and their morphological properties. This paper is organized as follows: Section 2 briefly describes the dE candidate identification procedure. In Section 3, we present a measurement of photometric properties. Section 4 presents the analysis of results of photometric and morphological properties. Finally, How our dEs are distributed in the cluster and group environment and their association with massive galaxies are described in Section 5. Our main findings are given in Section 6.

2. Identification

A primary motivation of this work is to create a large sample of dEs located in various environments, i.e., cluster, group, and field, of the local universe $z < 0.01$. We first used the publicly available imaging and spectroscopic data of the Sloan Digital Sky Survey (SDSS; Aihara et al. 2011) to identify pure red and dead dwarf galaxies, selecting all dwarf galaxies of $M_g > -18$ mag and visually classifying them as dE. We classify a galaxy as dE if the SDSS color image shows a red (color index $g - r > 0.5$ mag; Lisker et al. 2006) and smooth appearance and the presence of no significant Hα emission in the SDSS optical spectrum. It is customary to use the first criteria to classify galaxies as dE in case the optical spectrum is not available. Since the SDSS also provides the optical spectrum, we have added the second constraint to confirm that we are selecting purely non-star-forming galaxies.

Within the area covered by the SDSS, there are 786 dEs in the redshift range of less than 0.01. These spectroscopically selected dEs served as a training sample to further extend the dE sample from a wider sky coverage imaging database provided by the Legacy survey (Dey et al. 2019). This training is crucial, particularly for students who are starting to learn galaxy evolution research. Since the Legacy survey does not have spectroscopic observation, we only used visual inspection to identify the dEs using g–r–z tricolor images provided by the Legacy survey visual tool. Contrary to the common practices, which first determine the sources/objects from a prebuilt catalog that is primarily produced by an algorithm and then select the object of interest using specific criteria, we identified the dEs directly in the field, taking advantage of experienced knowledge of visual analysis of dEs selected from the SDSS. Our method avoids the preselection of the sources detected by some automated software like Source Extractor (Bertin & Arnouts 1996). Given the heterogeneous morphology of dEs, including extremely diffuse UDGs, the automated source detection may miss the faint low surface brightness objects owing to their low signal. Even when detected, specific criteria may not cover all dE-like objects.

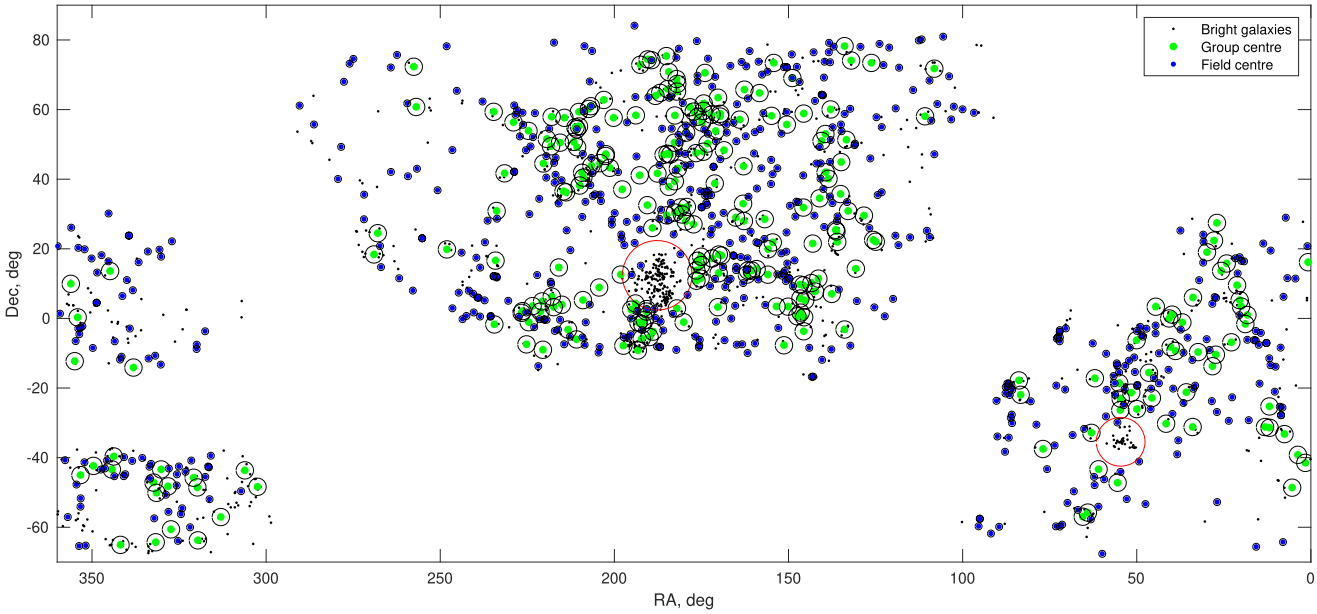

Figure 1. All-sky map of our visually inspected area. We show the visually inspected areas of groups (shown in green) and fields (shown in blue) with circles of radius $2\overset{\circ}{.}5$ and $1\overset{\circ}{.}0$, respectively. We also mark the Virgo and Fornax regions by the red circles of radius 15° and 10°, respectively. The small black circles represent bright ($M_K < -21$ mag) galaxies at $z < 0.01$.

To minimize the contamination from the compact, high surface brightness interlopers (such as foreground stars, globular clusters, and high-redshift galaxies), we explicitly select low surface brightness and extended galaxies, the prime characteristics of dE. This selection may be biased against the compact early-type dwarf galaxies, such as M32. Nevertheless, there are a handful of cE-like compact non-star-forming dwarf galaxies, while there are more than 500 normal dEs in the Virgo Cluster Catalog (VCC) of the Virgo Cluster (Janz & Lisker 2008; Chilingarian et al. 2009).

To select a variety of environments that host dE, we have chosen all three essential aspects, i.e., cluster, group, and field. For the cluster, we have chosen two local clusters, Virgo and Fornax, and for the group, we have selected groups from a group catalog provided by Makarov & Karachentsev (2011). For the field, we define an area around bright galaxies of magnitude $M_k < -21$ mag that are not members of any cluster or group according to the Makarov & Karachentsev (2011) group catalog. We select the host environment to avoid the distance uncertainty of newly detected dEs. Since, by design, most newly identified dEs will not have radial velocity information, we assume that they are located at line-of-sight distances of the hosts. Note that the definition used here for the field dE could be inconsistent with that commonly used in the literature. Since we deliberately searched dEs around giant galaxies, they are indeed members of the satellite system of that host galaxy, assuming that their distances are similar to the host. The selected environment represents the environment of host galaxies, not those detected dEs. However, we use the terminology "field dE" for those detected around the field host to simplify environment classification. In total, we selected two clusters, 265 groups, and 586 fields within a redshift range between -0.0013 and <0.01.

Indeed, there is a large body of dE surveys in cluster environments, particularly for Virgo and Fornax (Binggeli et al. 1985; Venhola et al. 2017; Ordenes-Briceño et al. 2018; Ferrarese et al. 2020), which can be found in the literature. However, this study aims to provide a more homogeneous sampling of dEs in diverse environments ranging from cluster to field.

Finally, we visually inspected a 1 Mpc area around the group center, typically a $2\overset{\circ}{.}5$ sky-projected radius for a group located at a distance of 25 Mpc. This distance corresponds to the median distance of our selected groups. We inspected a 15° radius around the Virgo and a 10° radius around the Fornax Cluster. We inspected a 450 kpc area from the host center for the field; this corresponds to a 1° angular radius for the field located at 25 Mpc, which is the median distance of our field sample.

The motivation for selecting areas around the cluster, group, and area around bright field galaxies is the finding of Geha et al. (2012) that it is uncommon to find non-star-forming dwarf galaxies outside of group or cluster environments, or they may not exist at all. In addition, from our spectroscopy sample, we noticed that very few dEs were located beyond 500 kpc of giant galaxies with a relative velocity larger than 500 km s^{-1}.

We show an all-sky view of the inspected area covered by the Legacy survey DR9[6] in Figure 1, where each circle represents a group area with a $2\overset{\circ}{.}5$ radius. The two nearby clusters, Virgo and Fornax, are defined by the red circles of 10° and 7° radii, respectively. As we can see, the inspected areas frequently overlap with one another; in total, we have inspected 7643 deg^2 of the Legacy survey images.

For visual inspection purposes, we extensively use tricolor cutout images provided by the sky-viewer of the Legacy survey.[7] By design, we will not have radial velocity information for our dEs. Instead, based on their morphology and surface brightness, we assessed their heliocentric distance, less than 40 Mpc for $z = 0.01$. The basic idea is that our dEs have lower surface brightness than background sources for a given apparent magnitude. Furthermore, morphologically our

[6] https://www.legacysurvey.org/dr9
[7] https://www.legacysurvey.org/viewer

Table 1
Recovery Fraction as a Function of Magnitude and Mean Surface Brightness

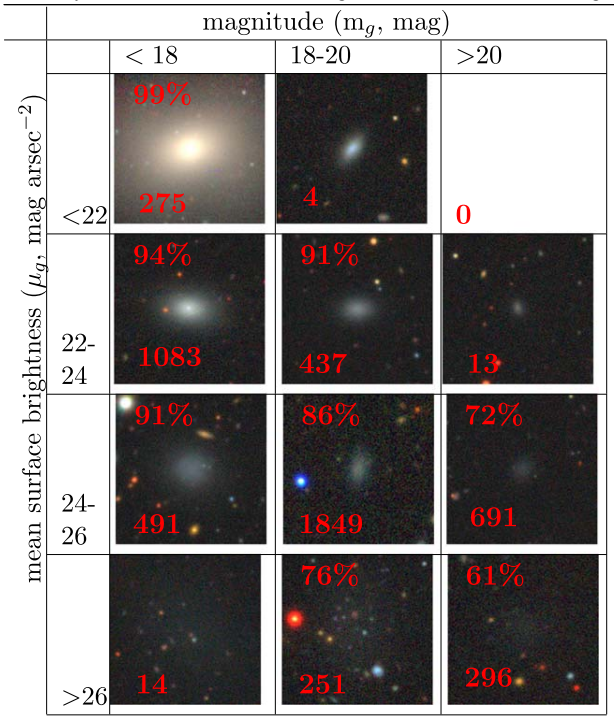

Note. Rows represent the $\langle \mu_g \rangle$ bins, and columns represent g-band magnitude bins. We show an example dE of each particular bin, randomly drawn from the sample. At each bin, the recovery fraction and the total number of dEs are denoted at the top and bottom, respectively. This analysis provides a representative sample of the recovery fraction but does not fully reflect the statistical completeness of the study.

dEs are smooth and regular, and they follow a well-defined relation between absolute magnitude versus radius and surface brightness, which can also be used to constrain their heliocentric distances.

The visual catalog is created by a simple visual inspection of tricolor cutout images provided by the sky-viewer. At least two persons visually check each field, and we find that there are quite good agreements between them (>85%). Indeed, such a visual scanning procedure is not 100% complete, and there remains the possibility that some dEs in the field of view (FOV) have been missed. In an effort to quantify the missing frequency, we rescanned the field after placing the previously identified dE in a randomly chosen position. The mock dEs were selected based on binning of magnitude and mean surface brightness, and we repeated this exercise 100 times for each designated bin. In Table 1, we list the recovery fraction of dEs in our identification method, where the results are binned with the width of 2 mag in both surface brightness (y-axis) and magnitude (x-axis). We also list the total number of dEs in each bin and note that we ran our experiment only for those bins that have more than 100 dEs. As we expected, the recovery fraction depends on the magnitude and the mean surface brightness. We find that the recovery fraction is 99% for the brightest dE sample and decreases to 61% for the faintest sample. The median g-band magnitude of our sample dE is 19 mag, and the magnitude range 18–20 covers two-thirds of our dE sample (see Section 3); thus, we can consider that our recovery fraction is over 80% on average. Our detection might also be influenced by the fact that we have used the SDSS-confirmed dE (mostly brighter one) for training purposes, and that may lead to a memory bias toward these bright dEs compared to the faint dEs, which is seen for the first time by the inspector.

An all-sky distribution of our dE sample is shown in Figure 2. To assign a host for a dE, we used the minimum radial separation between the host center and the dE; this is particularly important for the overlapping groups. For the Virgo Cluster member dEs we used a circle with a 10° radius centering on M87, and for the Fornax Cluster we used a circle with a 7° radius centering on NGC 3407. As we can see clearly, a large majority of dEs are concentrated around the clusters and large groups. The two clusters alone contribute nearly half (2437 out of 5405) of the total dE sample, and 265 groups contribute 2103 dEs. We have found 864 dEs in 586 fields.

We have identified a total of 5405 dEs in the clusters, groups, and fields; among them, 1324 dEs have radial velocity information (hereafter spectroscopic sample) obtained from the NED and the SDSS. We show the redshift distribution of the spectroscopic sample in Figure 3, and the peak of the distribution matched with the mean radial velocity of the Fornax and Virgo Clusters, and indeed, they dominate the spectroscopic sample dEs. The two clusters constitute more than two-thirds of spectroscopy sample dEs.

We list this main sample of dEs in Table 2. We consider the distance to the dE similar to their host cluster, group, or field. We consider 16.5 and 17.5 Mpc distance for the Virgo and Fornax Clusters, and for the group we obtained it from Makarov & Karachentsev (2011). For the field galaxies that do not belong to any group or cluster we use Hubble flow distance, using a standard cosmology with $H_0 = 71$ km s^{-1} Mpc^{-1}, $\Omega_m = 0.3$, and $\Omega_\Lambda = 0.7$.

3. Image Analysis

Once we finalized the source catalog, we performed the image analysis and measured the photometric and structural parameters. For this purpose, we exclusively used the g-band stacked images provided by the Legacy survey. We retrieved stacked images from the Legacy survey archive. While the Legacy image processing pipeline is optimized for relatively small objects, the photometric measurement of the large extended object is often inaccurate owing to imperfect sky subtraction and deblending of multiple sources. Galaxies with large angular sizes and irregular morphologies are often shredded into multiple separate objects, and thus the total derived fluxes for these galaxies are often unreliable. Furthermore, the Legacy survey photometric pipeline systematically underestimates the luminosities of galaxies of large sizes owing to the overestimation of the sky background. In order to overcome these problems, we performed photometric measurements for all dE. We retrieved $3' \times 3'$ fits image cutout. We subtracted the sky background preparing a background map for each object. The background maps were constructed after masking out all identified sources in the image, which were defined by Source Extractor segmentation maps, and the segmentation images were filled by the median values calculated from surrounding all pixels. This method allows us to eliminate any contribution of light from stars and background galaxies. Finally, the background map was subtracted from the original fits file to remove the sky background contribution to the observed flux.

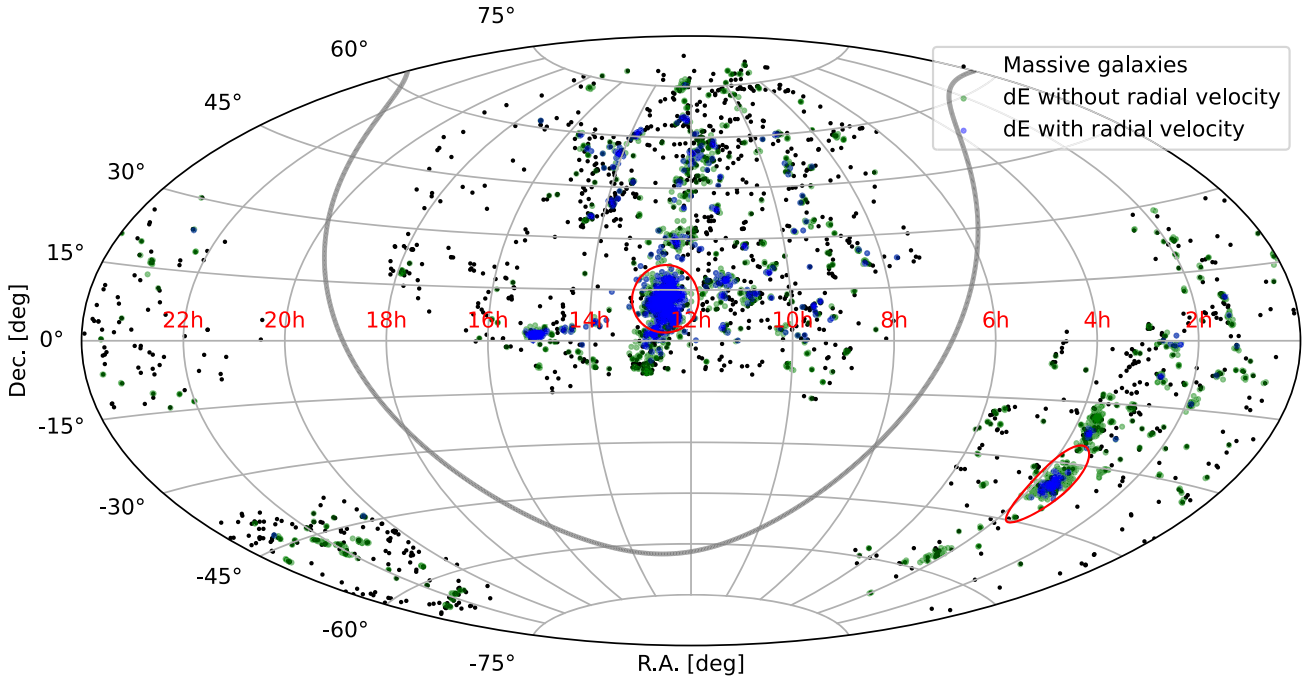

Figure 2. All-sky distribution of identified dEs in our sample. The sky coordinate is in the Aitoff projection. The blue and green circles represent the sky position of dEs with and without radial velocity information, respectively. The black circles represent the sky positions of giant galaxies. We also highlight two cluster regions, Virgo and Fornax, using the red circles of 10° and 7° radii, respectively.

Further image analysis was done largely in the same way as in Paudel et al. (2015). All unrelated foreground and background objects were masked, and the centers of galaxies were calculated as the centroid of the flux distribution in the masked image. The total magnitudes were calculated using the Petrosian method (Petrosian 1976); for this, we derived an azimuthally averaged light profile using a circular aperture. The Petrosian radius is defined as the galactocentric radial position where the ratio of surface brightness at the radius R to the average surface brightness within the R reaches a certain value, denoted by n, i.e.,

$$n(R) = \frac{\mu(R)}{\langle \mu(R) \rangle}, \quad (1)$$

where $\mu(R)$ is surface brightness at radius R and $\langle \mu(R) \rangle$ is the average surface brightness. We determine the Petrosian radii, $R_{p,n=2}$, and corresponding magnitudes, $m_{p,n=0.2}$, by adopting the most commonly used parameter $n_R = 0.2$.

We finally calculated the total brightness (m_g), summing up all pixel flux within the two a_p. The half-light radius is then calculated where the total flux becomes half, and uncommon to the usual practice, our derived half-light radius is circularized, and it is not necessary to correct it by multiplying a scaling factor $(b/a)^{0.5}$.

If the Petrosian radius did not converge, due to the fact that these galaxies sit within the light of nearby bright sources, or they are highly deblended/overlapped with the nearby foreground/background bright object, we performed manual aperture photometry in g-band images only, after manually masking those unrelated objects. In that case, we will not have structural parameters derived for these galaxies.

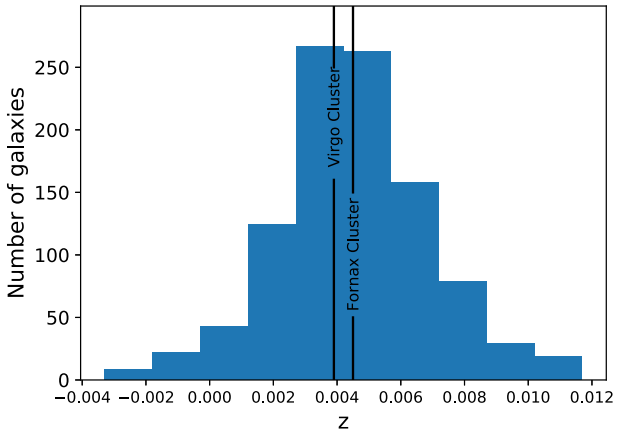

Figure 3. Redshift distribution of dEs, for which radial velocity information is available. We also highlight the position of two clusters, Virgo and Fornax, by the vertical lines.

The mean surface brightness ($\langle \mu_g \rangle$) was calculated using the equation

$$\langle \mu \rangle_{1/2} = m + 2.5 \log(2\pi R_{1/2}^2). \quad (2)$$

The derived magnitudes were corrected for Galactic extinction using Schlafly & Finkbeiner (2011), but not K-correction. As expected, however, the K-correction factors are negligible for the distance range of our target galaxies. Therefore, no K-correction has been performed in the derived magnitudes. Using the g band as a reference, we followed the same procedure to measure photometric parameters in the r-band images.

We show the distribution of g-band magnitude of our dE sample in Figure 4, which has a peak of around 19 mag. The median magnitude of our sample is 18.68 mag, immediately reflecting that the majority of our dE sample galaxies are fainter

Table 2
Catalog Table (a Representative Sample)

ID (hhmmssddmmss) (1)	R.A. (deg) (2)	Decl. (deg) (3)	m_g (mag) (4)	M_g (mag) (5)	$\langle\mu_g\rangle$ (mag arcsec^{-2}) (6)	R_h (kpc) (7)	z (8)	Nuc. (9)	Class (10)	Env. Type (11)	Host Name (12)
000033+165423	000.1392	16.9065	18.58	−12.75	24.58	0.52(06.33)	⋯	0	ND	2	218
000044+152725	000.1855	15.4572	19.52	−11.81	26.10	0.68(08.25)	⋯	0	ND	2	218
000222+160140	000.5929	16.0279	19.56	−11.77	24.16	0.27(03.31)	⋯	0	ND	2	218
000248+163546	000.7041	16.5962	19.21	−12.12	25.41	0.57(06.94)	⋯	1	ND	2	218
000250+163742	000.7105	16.6284	19.38	−11.94	26.52	0.88(10.67)	⋯	1	ND	2	218
000306+161829	000.7791	16.3083	18.27	−13.06	26.30	1.34(16.13)	⋯	0	ND	2	218
000324+161111	000.8508	16.1865	18.54	−12.79	25.79	0.93(11.23)	⋯	0	ND	2	218
000417+204430	001.0715	20.7419	18.48	−14.50	24.24	0.99(05.66)	⋯	1	ND	3	279
000844+143529	002.1856	14.5916	16.65	−14.68	24.04	0.99(11.97)	⋯	1	ND	2	218
001746+113147	004.4420	11.5299	20.37	−11.45	26.57	0.65(06.95)	⋯	0	ND	3	1160
002922−332302	007.3456	−33.3839	21.22	−10.07	26.47	0.38(04.48)	⋯	0	ND	2	1851
003102−331613	007.7622	−33.2705	15.97	−15.32	23.68	1.18(13.95)	⋯	1	SP	2	1851
003155−331600	007.9815	−33.2668	16.65	−14.64	24.28	1.14(13.41)	⋯	0	TS	2	1851
003258−324548	008.2426	−32.7636	18.15	−13.14	24.61	0.66(07.82)	⋯	1	ND	2	1851
003351−275024	008.4651	−27.8401	17.33	−14.52	25.77	2.16(19.46)	⋯	0	UD	3	2052
003414−081008	008.5585	−8.1691	16.66	−15.52	23.29	1.04(08.48)	⋯	0	ND	3	2081
003506−280306	008.7789	−28.0518	17.53	−14.31	25.11	1.45(13.09)	⋯	0	ND	3	2052
003637−082457	009.1542	−8.4160	20.12	−12.06	25.94	0.71(05.82)	⋯	0	ND	3	2081
004103−210808	010.2636	−21.1356	19.49	−12.38	24.17	0.38(03.44)	⋯	1	ND	3	2478
004434−314204	011.1453	−31.7013	21.12	−10.51	24.98	0.23(02.36)	⋯	0	ND	2	2778
004643−313058	011.6808	−31.5163	19.20	−12.44	25.14	0.61(06.15)	⋯	0	ND	2	2778
005124−065818	012.8526	−6.9719	20.90	−11.38	25.65	0.45(03.55)	⋯	0	ND	3	2980
005236−310921	013.1524	−31.1561	16.15	−15.22	22.68	0.71(08.09)	⋯	0	BC	2	3089
005249−305753	013.2051	−30.9648	20.11	−11.25	24.95	0.32(03.70)	⋯	0	ND	2	3089
005733−040804	014.3901	−4.1345	19.64	−13.43	25.23	0.97(05.25)	⋯	0	ND	3	3429
005914−075715	014.8103	−7.9544	19.73	−12.63	25.49	0.68(05.67)	⋯	0	ND	3	3572
005916−073511	014.8192	−7.5867	19.92	−12.44	24.77	0.45(03.72)	⋯	1	ND	3	3572
005949−071341	014.9559	−7.2281	20.37	−11.99	25.37	0.48(03.99)	⋯	1	ND	3	3572
010149−073750	015.4583	−7.6308	18.69	−13.67	25.45	1.08(08.95)	⋯	1	ND	3	3572
010339−061053	015.9145	−6.1814	18.81	−14.35	24.99	1.18(06.85)	⋯	1	ND	3	3768

Note. Column (1): ID in *hhmmssddmmss* format. Column (2): R.A. Column (3): decl. Column (4): g-band magnitude. Column (5): g-band absolute magnitude. Column (6): mean surface brightness. Column (7): half-light radius in kiloparsecs (in arcseconds). Column (8): z. Column (9): nucleated or not; −1 for yes and 0 for no. Column (10): dE morphological subclass (see Section 4.4). Column (11): environment (1 for cluster, 2 for group, and 3 for field). Column (12): host environment name given in PGC number.

(This table is available in its entirety in machine-readable form.)

than the spectroscopic target selection limit of the SDSS, i.e., 18 mag, as shown by a vertical line. We also overlay the distribution of our spectroscopic sample dE (the blue histogram), and as expected, it mainly overlaps in the brightest part.

In Figure 5, we show the $g-r$ color distribution of our dE sample, and all three subsample dEs show a single peak Gaussian distribution, with a peak around 0.6 mag. The overall median value of the $g-r$ color of our sample dE is 0.58 mag, with a standard deviation of 0.14 mag.

To compare our measured g-band magnitudes with that of the Legacy survey pipeline values, we obtained the Legacy survey magnitudes using the SQL queries within a 6″ radius of the dE center. We used the primary source catalog provided by the tractor. In Figure 6, we compare our g-band magnitudes and the Legacy survey catalog values. We find that these two magnitudes agree well with each other for the bright galaxies, and for the fainter galaxies, it seems that the Legacy tractor pipeline underestimates the flux.

We show the distribution of $\langle\mu_g\rangle$ in Figure 7. It is very clear that most dEs have mean surface brightness higher than 24.5 mag arcsec^{-2}, which has been frequently used as a cutoff magnitude to define UDGs; see Section 4.2. Our dE sample has a median value of $\langle\mu_g\rangle = 25.97$ mag arcsec^{-2}. Although we do not use any magnitude or surface brightness limit for the visual selection while preparing the final catalog, we select dEs brighter than $m_g = 22.5$ mag and $\langle\mu_g\rangle < 28$ mag arcsec^{-2}. We introduced these limits based on the measurement error.

4. Morphology

4.1. Color–Magnitude Relation

Early-type galaxies follow a well-defined color–magnitude relation (CMR), and it has been shown that they are astonishingly similar for various environments (Visvanathan & Sandage 1977; Sandage & Visvanathan 1978). However, as noted by Janz & Lisker (2009), this relation is not linear in going from higher-mass elliptical galaxies to lower-mass dEs. In Figure 8, we show the CMR of our dE, and for comparison we overplot an average CMR sequence of Virgo dEs derived by Janz & Lisker (2009); see the black dashed line. Although our dEs are located in diverse environments, they generally follow

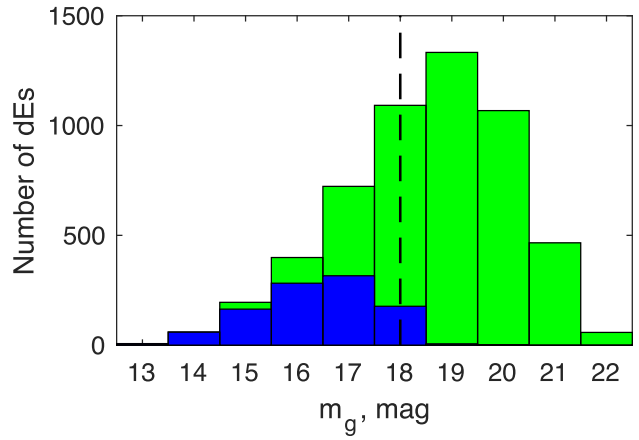

Figure 4. The g-band magnitude distributions of our dE sample (green) and a subset having radial velocity information (blue). The vertical dashed line represents the magnitude limit of the spectroscopic target selection of the SDSS.

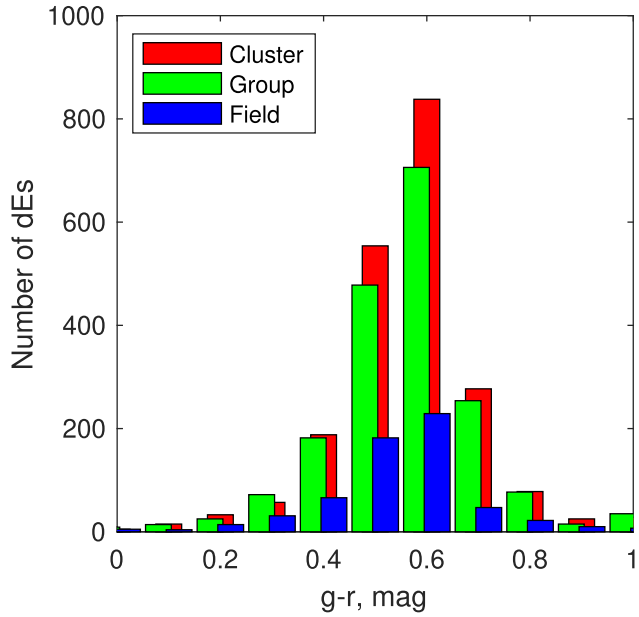

Figure 5. The $g - r$ color distribution of our sample dEs. The bin positions of the group and field samples are shifted by $+0.01$ and -0.01 mag, respectively.

the CMR defined by Virgo dEs on average. As expected, the scatter at fainter magnitude is larger; in the brighter magnitude ($M_g < -14$ mag) regime, however, the CMR is well constrained within the $g - r$ color scattering of 0.2 mag.

4.2. Scaling Relation and UDG

Early-type galaxies obey a scaling relation between their structural parameters (such as R_h and $\langle\mu_g\rangle$) and the total luminosities (Kormendy 1977; Guzman et al. 1993). In Figure 9, we show the relation between $\log(R_h)$ and the magnitudes for the early-type galaxies. For comparison, we used a sample of early-type galaxies studied in JL08 (Janz & Lisker 2008), shown by gray symbols. Our sample dEs are shown in red, green, and blue for the cluster, group, and field members, respectively. At first glance, our dE sequence is well matched with the dE sequence of JL08, and as was discussed in

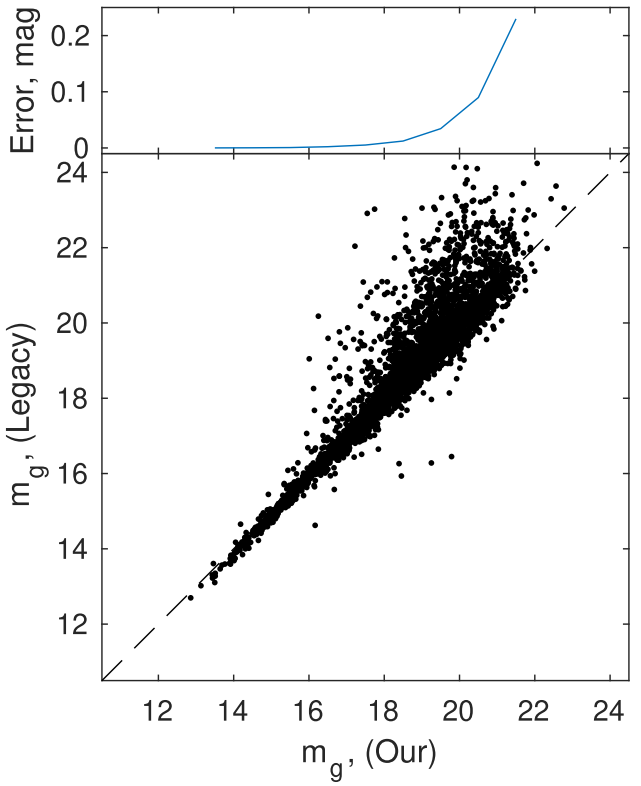

Figure 6. Comparison between our g-band magnitude and the Legacy survey's pipeline-based g-band magnitude. In the top panel, we show a median error in our g-band photometry.

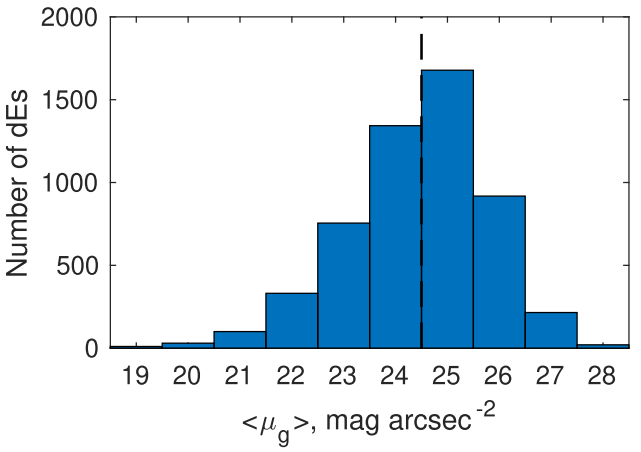

Figure 7. The g-band mean surface brightness distribution of our sample dEs. The vertical dashed line represents the surface brightness limit that is customarily used to define UDGs.

JL08, the dE follows a less steep scaling relation of magnitude and $\log(R_h)$ compared to the scaling relation for Es.

Our sample includes many extended, low surface brightness galaxies, which satisfy the definition of UDGs, i.e., dEs with $\langle\mu_g\rangle > 24.5$ mag arcsec^{-2} and $R_h > 1.5$ kpc (Marleau et al. 2021). However, to select UDGs, there is no standard cutoff limit on $\langle\mu_g\rangle$. In the literature, we find a range of $\langle\mu_g\rangle$ from 24 to 25 mag arcsec^{-2} that has been used to select UDG candidates (Habas et al. 2020; Lim et al. 2020). For this work, we used 24.5 mag arcsec^{-2} in the g band. In our sample, we find 100 dEs that can be classified as UDGs. Among them,

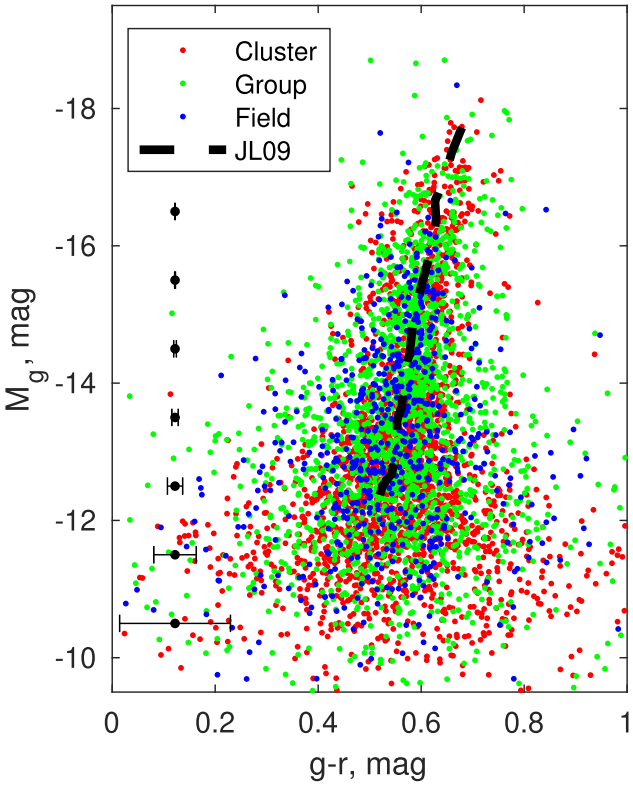

Figure 8. The CMR of our sample dEs. We show cluster, group, and field dEs with red, green, and blue circles, respectively. The dashed line represents an average CMR measured by Janz & Lisker (2009) for the Virgo Cluster dEs using the SDSS data. The SDSS magnitudes are converted to the Legacy DECaLS filter system according to the transformation formula provided by the Legacy web page. We show a typical error bar for each magnitude bin in black.

12 are in the cluster (10 in Virgo and 2 in Fornax), 59 in groups, and 29 in the field environment. On average, we find six UDGs per cluster and 0.22 per group, agreeing with the trend found by van der Burg et al. (2017).

In Figure 10, we show the interdependence of the structural parameters (R_h, $\langle\mu_g\rangle$, and M_g) of our sample of dEs and try to explore whether the UDG occupies a special position within it. In the middle panel, we show the scaling relation between $\log(R_h)$ and M_g, where the red symbol represents the median value of $\log(R_h)$ in each magnitude bin, with a standard deviation shown as an error bar. In the top panel we show the relation between $\langle\mu_g\rangle$ and M_g, and in the right panel we show the relation between $\langle\mu_g\rangle$ and $\log(R_h)$. The UDGs are shown in black, and the green points represent dEs.

As per the definition, UDGs occupy the upper left corner of the $\langle\mu_g\rangle$ and $\log(R_h)$ relation defined by the crossing demarcation lines. Given the large scatter of the data points, we find no special clustering of UDGs distinct from the overall dE population. They are, however, a 1σ outlier in the size −magnitude relation. The middle panel reveals that the limit of $R_h > 1.5$ kpc may well separate UDGs from dEs in the fainter regime but not in the brighter regime, as we can see that all dEs fainter than −15.96 mag with R_h larger than 1.5 kpc can be classified as UDGs. On the other hand, the top panel reveals that the demarcation line of $\langle\mu_g\rangle = 24.5$ mag arcsec^{-2} cannot uniquely separate UDGs from dEs, and many dEs have mean surface brightness higher than $\langle\mu_g\rangle = 24.5$ mag arcsec^{-2}; in fact, the majority our sample dEs have $\langle\mu_g\rangle > 24.5$ mag arcsec^{-2}.

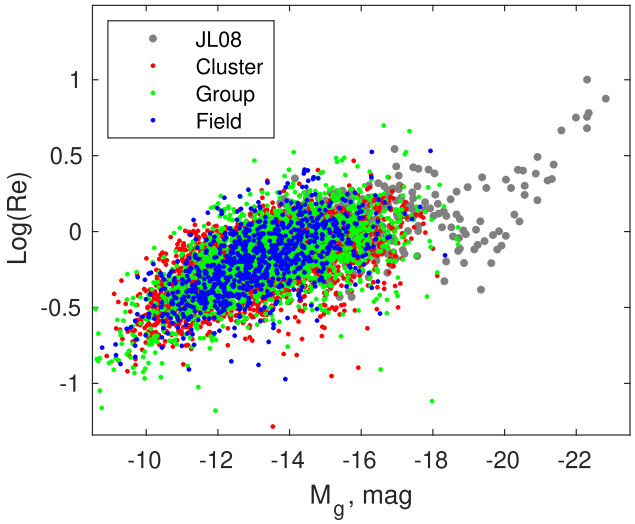

Figure 9. The luminosity−size relation of early-type galaxies. Data for Es/dEs (gray circles) are from Janz & Lisker (2008). The symbol color represents cluster, group, and field dEs according to Figure 8.

Our analysis reinforces the conclusion noted by Conselice (2018) and Danieli & van Dokkum (2019) that UDGs do not occupy a special position in the parameter space of early-type galaxies, defining them as a special class of objects, nor are their structural parameters uniquely different from the overall dE population, being only a 1σ outlier on the $\log(R_h)$ and M_g relation. We show that the UDGs and dEs have a significant overlap in parameter space that supports a conclusion that the dEs and UDGs are essentially the same objects, where the latter represents an extended subpopulation of the former.

4.3. Presence of Nucleus

There are a plethora of works on nuclei of dEs in the cluster environments, particularly Virgo, Fornax, and Coma (Côté et al. 2006; Paudel et al. 2011; den Brok et al. 2014; Ordenes-Briceño et al. 2018; Wittmann et al. 2019; Sánchez-Janssen et al. 2019; Poulain et al. 2021). In this work, we homogeneously investigate the presence of nuclei in dEs located in diverse environments, i.e., cluster, field, and group. Although there is no standard definition of the nucleus in dEs, the nucleus is usually defined as the existence of a luminosity excess over the main stellar distribution in the core region (Sánchez-Janssen et al. 2019; Paudel & Yoon 2020). In this work, we consider the presence of a compact point source of point-spread function (PSF) size at the core region as a nucleus. To identify a nucleus at the center of a dE, we carefully examine the color image cutout of every dE with an FOV of $1' \times 1'$. We excluded certain dEs with central star formation and high central surface brightness during the visual examination. This was due to the irregular blue core of the central star-forming dEs, which created confusion in identifying the nucleus (Lisker et al. 2006; Urich et al. 2017; Paudel & Yoon 2020). High central surface brightness dEs are primarily compact objects. It is impossible to visually identify the presence of a separate PSF component at the center of these compact galaxies. In any case, cEs, M32-like galaxies, rarely host a central nucleus.

We can classify 4767 dEs as nucleated or nonnucleated, and among them, 2065 dEs are nucleated. A few randomly selected

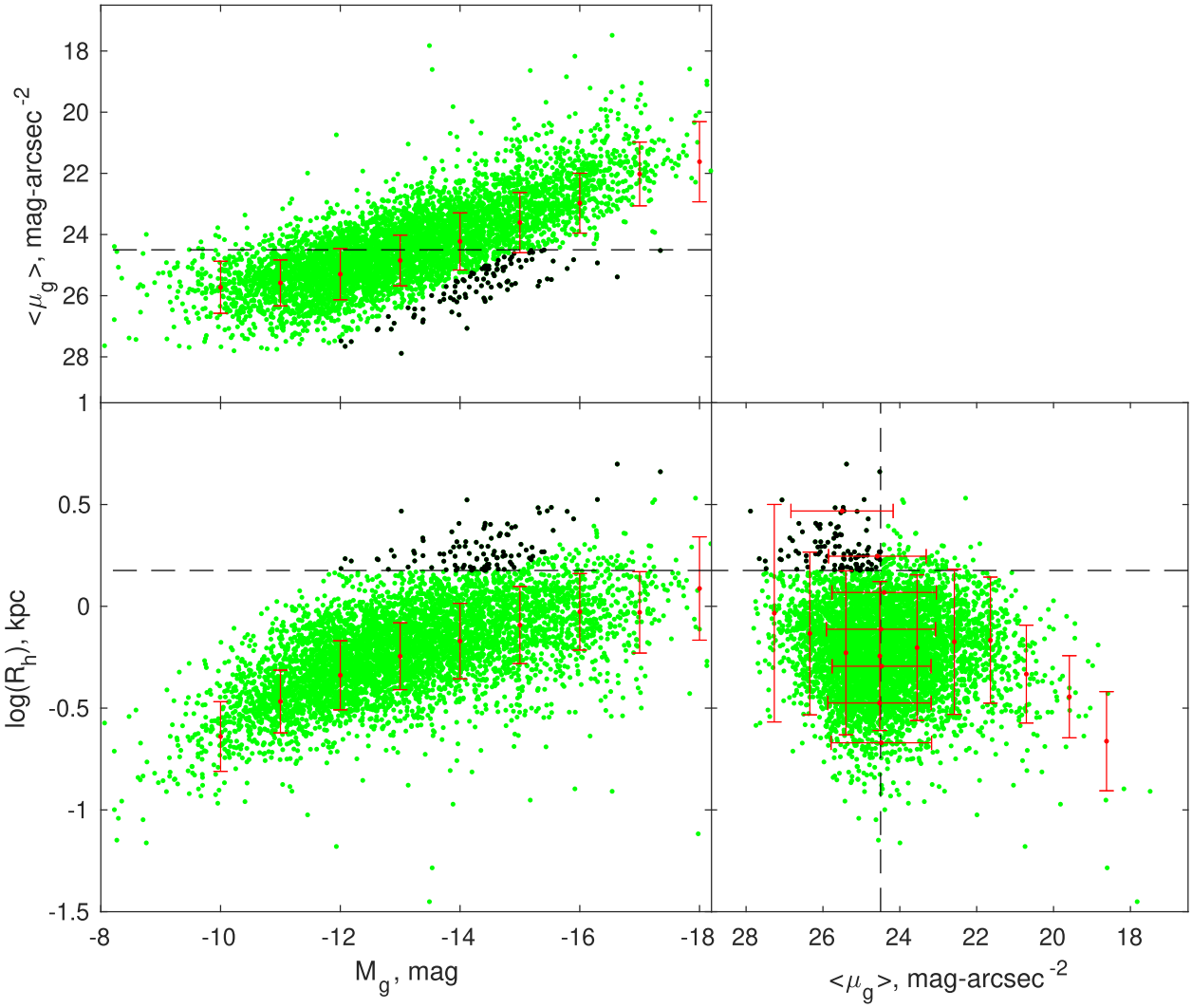

Figure 10. The scaling relations between the structural parameters (R_h and $\langle\mu_g\rangle$) and M_g of our sample dEs. Green and black circles represent dEs and UDGs, respectively. The thresholds on $\langle\mu_g\rangle$ and R_h that are used to define UDGs are shown by the dashed lines. The red circles with a 1σ standard deviation represent the median values of the distribution.

example dEs of both nucleated and nonnucleated classes are shown in Figure 11, where the top panel represents nonnucleated dEs and the bottom panel represents nucleated dEs. In Figure 12, we show the magnitude distribution of nucleated and nonnucleated dEs. The magnitude distribution shows that the nuclei are common in bright dEs, and they become rare in the least luminous dEs, as we can see that the red histogram dominates the brighter part while the blue histogram dominates the faint end. We show the relation between nucleated fraction and magnitude in the top panel. The red line represents the nucleated fraction of the overall dE population, and magenta, green, and blue lines represent the nucleated fraction of cluster, group, and field subsample dEs, respectively. The error bar denotes the fraction of dEs that we were not able to classify into nucleated and nonnucleated. For comparison, we also show the measurement of the nucleated fraction by Sánchez-Janssen et al. (2019) for the Virgo Cluster core region of 4 deg^2 ($2^\circ \times 2^\circ$). Our overall nucleated fraction reasonably agrees with the Sánchez-Janssen et al. (2019) result. A careful inspection of these results shows that the cluster environment is likely to have a higher nucleated fraction than the group. The field environment hosts a comparatively lower nucleated fraction than both clusters and groups. However, these differences are well within the measurement uncertainty.

We study a radial dependence of nucleated fractions inside the Virgo and Fornax Clusters, where the nucleated fractions are binned in the annular aperture of 1° width; see the bottom panel of Figure 13. We show the result in the top panel and find that the nucleated fraction mildly anticorrelates with cluster-centric distance. Comparatively, the Fornax Cluster shows slightly steeper anticorrelation than the Virgo Cluster. Within the central 1° radius area, Virgo and Fornax host nucleated fractions of 43% and 52%, respectively. At the outer region, beyond a 5° cluster-centric distance, the nucleated fraction reaches down to 30% for both clusters.

4.4. Morphological Feature

We carefully examine dE images and classify them according to their low surface brightness and color characteristics. The primary purpose of this classification scheme is to recognize some unique dEs that are not frequent in observation. Indeed, we excluded most of the normal dEs in this

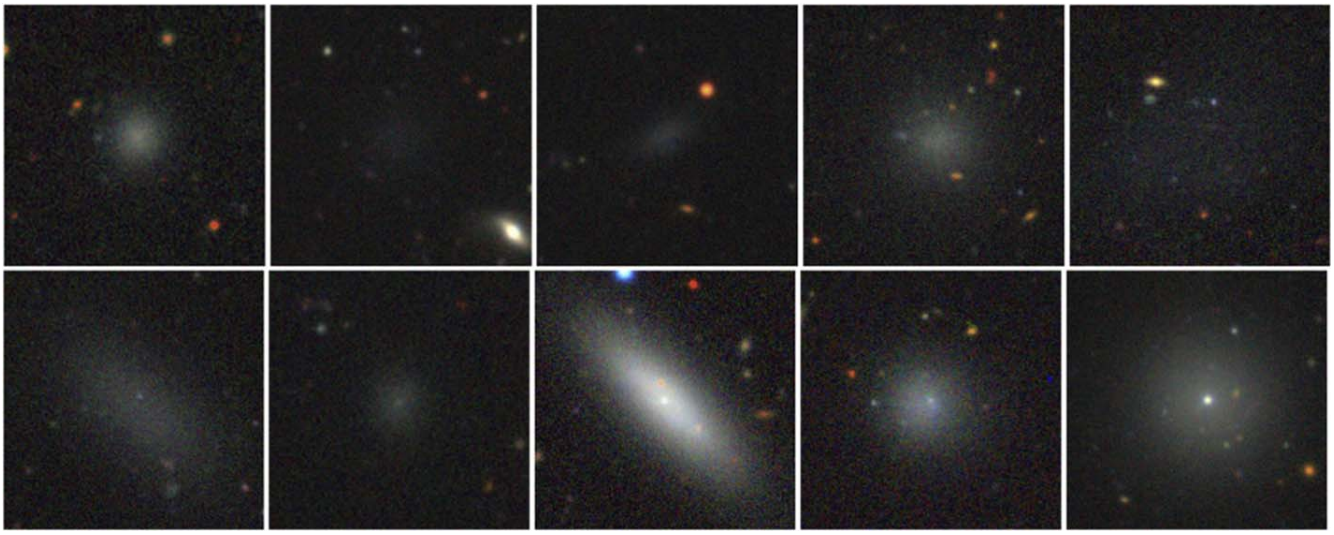

Figure 11. Examples of nonnucleated (top row) and nucleated (bottom row) dEs. All stamp images have an FOV of $1' \times 1'$.

classification, which host no special feature. Using a broad scheme of classifiers, we try to identify six distinctive morphological features present in dEs. Indeed, these features are already well investigated in some individual cases of dEs, particularly in the cluster environment. For example, the presence of a spiral arm and blue center in dEs were studied by Lisker et al. (2006, 2007), and tidal features, like a shell or the stellar streams, were studied in Paudel & Ree (2014) and Paudel et al. (2017). This sample aims to provide homogeneous statistics of these features' presence in dEs in various environments. Below, we itemize these six general categories.

1. Blue core (BC): the presence of a blue core region as a sign of recent star-forming activity (Lisker et al. 2006).
2. Spiral arm (SP): the presence of a spiral arm or bar commonly called disk feature dEs (Lisker et al. 2007; Smith et al. 2021).
3. Tidal stream (TS): tidally stretched dE due to interaction with a nearby massive galaxy (Paudel & Ree 2014).
4. Merging dwarf (MD): the low surface brightness features that are most likely to originate through the dwarf–dwarf merger, e.g., shell or tidal tail (Paudel et al. 2014, 2017, 2018).
5. UDG: ultradiffuse galaxies; see Section 4.2.
6. Disk–halo (DH): we identify some dEs that possess a prominent edge-on disk with a rounder and diffuse stellar halo.
7. Normal dEs (ND): rest of dEs, which are not classified by any of the above classifiers.

We show examples of these subclasses in Figure 14. We find that 288 dEs possess a central blue core that may reveal recent star-forming activity at the center (Urich et al. 2017). These blue core dEs are mostly located at the outskirts of cluster or group environments. They could instead represent transition-type dwarf galaxies that are in the process of being transformed into the dEs after cessation of star formation activity (Koleva et al. 2013).

We find that 17 dEs possess prominent spiral arms. However, we note that this number could be higher because we only selected them based on visual assessment, without using unsharp masking to identify these features as done in Lisker et al. (2007). As Michea et al. (2021) have shown, we may need to use a more sophisticated image analysis procedure to reveal the disk feature hidden inside the smooth stellar halo of dEs.

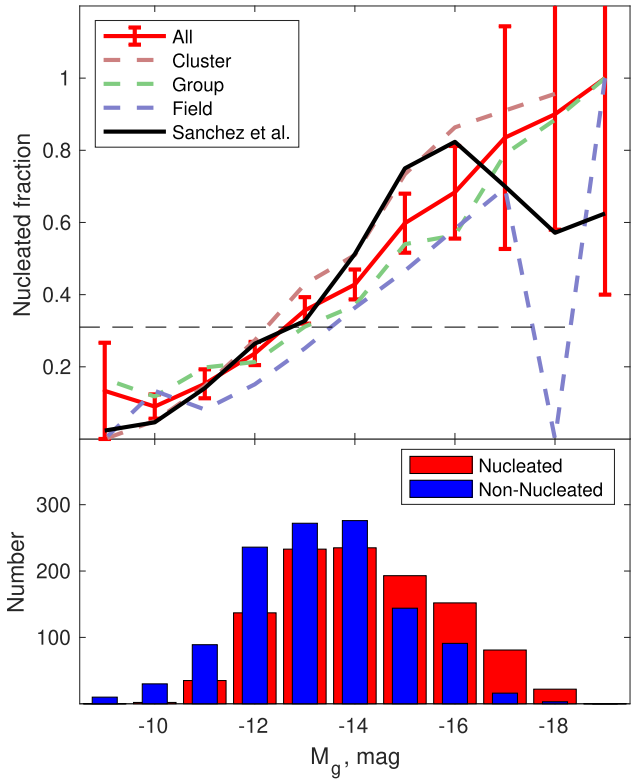

Figure 12. Top: the nucleated dwarf fraction with respect to magnitude. The black line represents the nucleated dE fraction measured by Sánchez-Janssen et al. (2019) for the Virgo Cluster, and the red line represents a nucleated fraction of our entire dE population. The nucleated fractions of dEs for clusters, groups, and fields are shown with magenta, green, and blue lines, respectively. Bottom: magnitude distribution of nucleated (red histogram) and nonnucleated (blue) dEs.

Approximately 1.3% (71 out of 5405) of dEs are experiencing tidal distortion due to the effect of the tidal

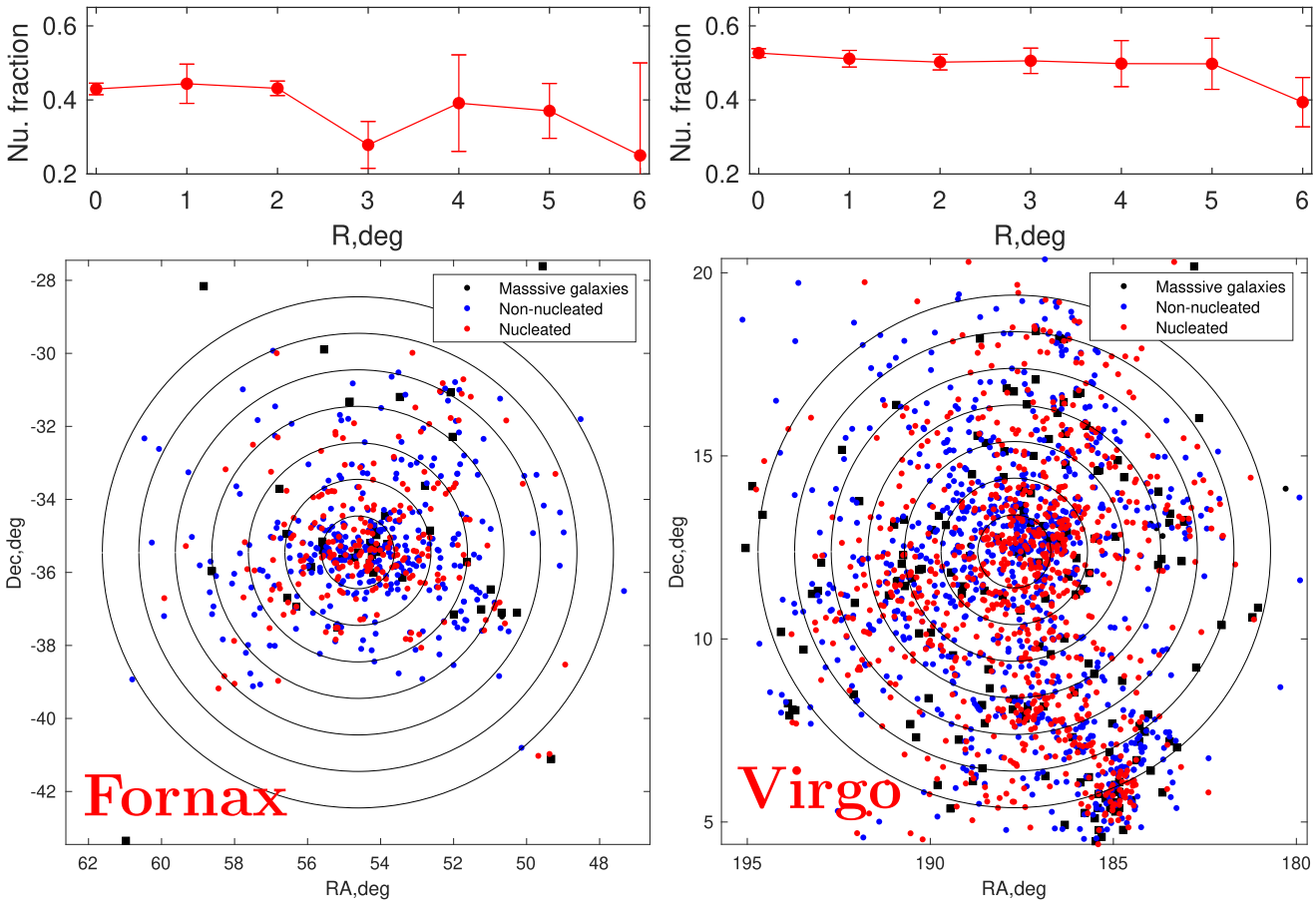

Figure 13. Distribution of nucleated dEs (red circles) and nonnucleated dEs (blue circles) inside the Virgo and Fornax Clusters. Fornax is shown on the left, centering at NGC 1407, and Virgo is shown on the right, centering at M87. The positions of bright member galaxies of clusters are shown by black squares. The black concentric rings represent the annular aperture of 1° width, where we measure the nucleated fraction. The results are shown in the top panels.

potential of nearby massive galaxies. Out of 71 tidally disturbed dEs, only 13 are located inside the cluster environment, and an overwhelming majority (58 out of 71) of them are located in the group or field environment. This result, in fact, agrees with the Paudel & Ree (2014) study, which shows that the tidal harassment process is more frequent in a low-density environment like a group and field compared to a dense cluster. Only 0.3% of dEs show tidal features that may have originated from merging even smaller dwarf galaxies.

In this work, we introduce, for the first time, a unique class of dE that possesses two distinct morphological features: an edge-on disk and a round stellar halo. These two-component systems may be a scaled-down version of the disk–halo system (DH) of our Galaxy. These DH dEs could be an edge-on view of spiral arm dEs viewed on the higher inclination angle of the disk, where the diffuse halo remains hidden behind the prominent spiral arm (Smith et al. 2021). In that case, dE (SP) and dE (DH) could represent the same class but are different in viewing angle. Nevertheless, we do not see the underlying spiral arm owing to high inclination, and we keep them in a separate class. To get a statistical estimate, we calculate the probability of an edge-on view of a spiral arm galaxy at a random viewing angle. Using an assumption of a thin disk (intrinsic thickness $q_0 = 0.2$; Sánchez-Janssen et al. 2010), we find that there isa ≈30% chance that the thin disk can be viewed edge-on ($b/a < 0.5$). We have found only five DH dEs, which is 29% of SP dEs.

5. Environment

As per our selection procedure, our dEs are either inside the cluster/group or near bright field galaxies (hereafter the host). In this subsection, we explore the dE positions with respect to the host and morphology types of their companion bright galaxies (BGs, $M_k < -21$ mag).

In the bottom panel of Figure 15, we show a phase-space position of our dEs within their respective host environment. In the top panel, we show the distribution of sky-projected separation of the dEs from the host center, where the host-centric distance is normalized by viral radii of their respective cluster, group, and field. We used 1.7 and 1.2 Mpc for the Virgo and Fornax Clusters, respectively. For the group we used 800 pc, and for the field we used 300 pc.

Almost all dEs are located well within the 1.5 virial radii; however, a few field dEs are significantly away from the host. Although they are few, we noticed that these field outliers are a spectroscopically selected sample of dEs from the SDSS. We have used an all-sky catalog from the SDSS rather than searching around predefined areas of the cluster, group, or field.

In terms of number count, the two clusters contribute nearly half, 2437 (1837 and 864 in Virgo and Fornax, respectively) out of 5405. We find that there are 7.9 dEs per group and 1.5

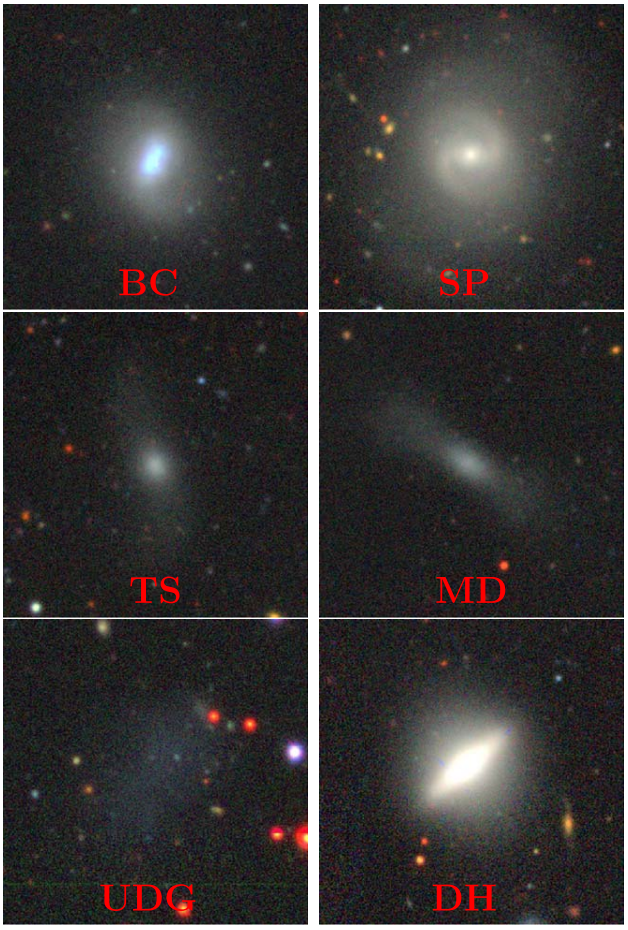

Figure 14. Exemplary dEs of the different classes of dEs according to their morphological feature and color (see text for detail).

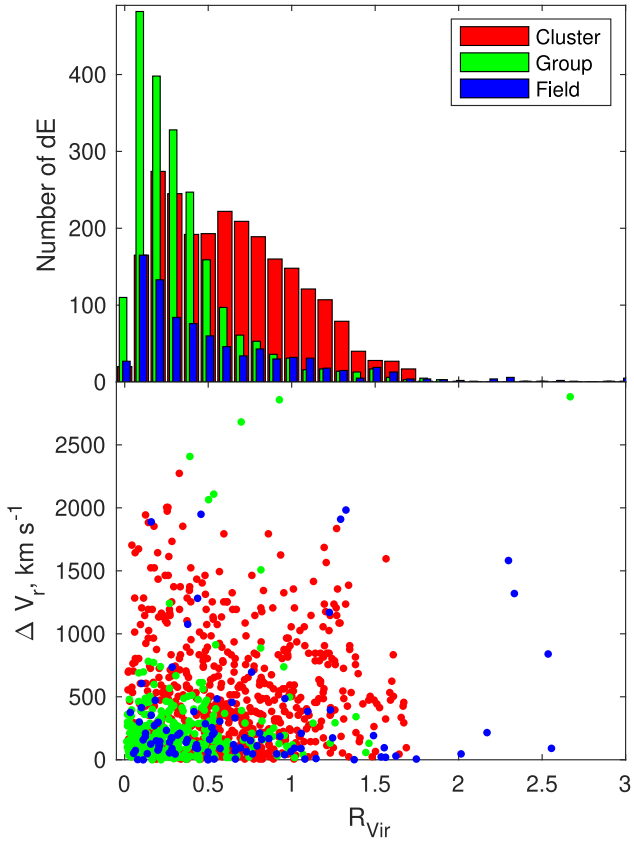

Figure 15. Top: the distribution of sky-projected separation of dEs from the host center. The x-axis is normalized by the assumed viral radius of each cluster, group, and field. Red, blue, and green histograms are for clusters, groups, and fields, respectively. Bottom: phase-space distribution of our spectroscopic dE sample. Red, blue, and green circles are for clusters, groups, and fields, respectively.

dEs per field, on average. We noticed that there are many fields that contain no dEs. Out of total of 586 fields we have inspected, only 233 fields host one or more dEs. We further classify the field host as an early-type (E) and star-forming (Sf) and find that there are 437 Sps and 153 Es field hosts. We find that out of 437 fields with a Sfs host, only 154 have one or more dEs, and out of 153 field with an Es host, only 79 have one or more dEs, which indicates a higher chance of hosting a dE by an Es than Sfs. On average, we find that early-type fields host a significantly higher number (2.8) of dEs per field compared to star-forming field hosts, which have 1.0 dE per field, on average.

Further, we explore the relationship between the location of dEs and morphological types of neighbor BGs, regardless of their environment. We counted BG frequency of each type around each dE within a 300 kpc radius. The result of this exercise is shown in Figure 16. We find a higher frequency of dEs around Es than Sfs. On average dEs have a 2.5 times higher chance to have an Es as a neighbor than Sfs.

Indeed, this result might have been heavily influenced by the cluster environment, where E dominates by number. We performed this exercise again, separating the cluster, group, and field. We find a similar trend in the cluster and group dEs, but in the field environment, where Sf dominates, we find an equal chance to have both E and Sf as a neighbor of dE on average. The results are listed in Figure 16.

6. Conclusion and Discussions

We have identified 5405 dEs located in the various environments, i.e., cluster, group, and field, spanning the luminosity range $-18 < M_g < -8$ mag. They are selected via visual inspection of the 7643 deg^2 area of the Legacy survey g–r–z combined tricolor images, which include two clusters (Virgo and Fornax), 265 groups, and around 586 field galaxies. Our dE catalog provides several different metrics by which we quantify morphological and environmental properties. The salient feature of this catalog lies in their morphological properties, as we identified morphological characters such as nucleated, tidal, and UDGs.

Given the nature of the selection procedure, it is not trivial to calculate the completeness limit of our sample. Although we aim to search dEs of up to $z = 0.01$, we should emphasize that this is not a volume-limited sample in many regards. Indeed, we have not explored all sky areas of this volume. In addition, one of the main caveats of this work is the distance of candidate dEs, and in most cases we do not have that information. There may be a faction of dEs that are foreground or background galaxies or at least not directly related to the host. To confirm their distance and association with the host environment, we need radial velocity information, which we do not have in most cases.

This work is explicitly designed to find dEs in an extensive database, and there are not many surveys of this kind for which

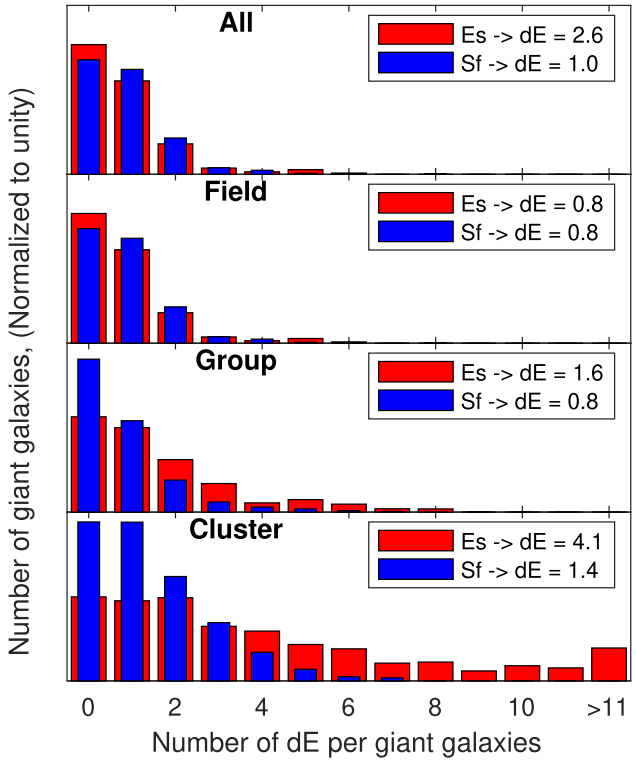

Figure 16. Frequency of bright galaxies around different types of dEs. The first to last rows are for all, field, group, and cluster dEs. The blue (red) histograms represent the number of Sfs (Es) around dEs within the 300 kpc sky-projected radius.

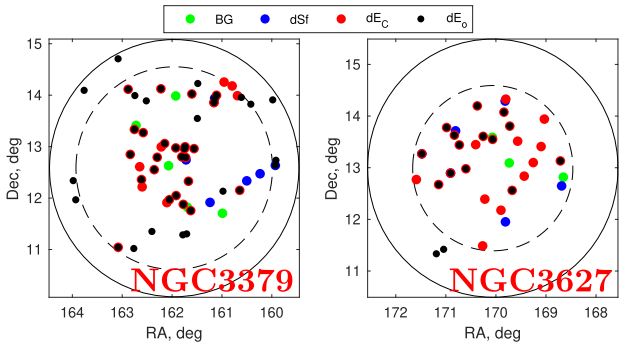

Figure 17. We compare dE detection in two groups, NGC 3379 and NGC 3627, with detection of C22, where the circle represents our search area. Giant galaxies are shown in green. C22-identified star-forming (dSf) and non-star-forming (dE$_C$) dwarf galaxies are shown in blue and red, respectively. Our identified dEs (dE$_o$) are shown in black. The solid and dashed circles represent our and C22 search areas, respectively.

we can make a direct comparison. We found that Carlsten et al. (2022, hereafter C22) searched satellite dwarf galaxies (of all types) in the Local Volume ($D < 12$ Mpc) in the Legacy survey imaging.

Unfortunately, we found that only two areas around the NGC 3379 group and NGC 3627 group broadly overlap with our searched sky regions. In the case of NGC 3379, they have found 36 dwarf galaxies, and among them, 33 can be classified as dE from our visual inspection; see Figure 17. Our catalog recovers 26 (78%) out of 33. Similarly, we recovered 16 (64%) out of 25 dEs in the case of NGC 3627. We noticed that those unrecovered 16 ($9 + 7$) dEs are mostly fainter dEs of $m_g \gtrsim 20$ mag. In the C22 search area, we identified 8 additional dEs, bringing the total number of identified dEs in two systems to 50. Calculating the recovery fraction of the C22 dE sample, we have recovered 42 (72%) dEs, which is smaller compared to the overall recovery fraction for $m_g < 20$ mag (i.e., 87%). Multiple factors may have contributed to this discrepancy, including environmental differences. The cluster environment plays a crucial role in shaping the brightness distribution of dEs, where brighter dEs are more likely to be formed (Geha et al. 2012) and they have higher recovery fractions. In this sample, a substantial portion of dEs are found within the cluster environment. In addition, a potential memory bias in our calculation may have contributed to the high recovery fraction.

Based on this extensive data set, our results are summarized as follows:

1. Systematic analysis of the derived structure parameters of dEs reveals that the dEs generally follow a universal relation between magnitude, size, and mean surface brightness regardless of their host environment.
2. Using a standard definition, we identify 100 dEs in our sample that can be classified as UDGs. However, we find that UDGs do not occupy a special position in the parameter space of dEs to define them as a special class of objects. In addition, their structural parameters are not uniquely different from the overall dE population, being only 1σ outlying from the $\log(R_h)$ and M_g relationship.
3. We identify that only 40% of our sample dEs host a central nucleus, and among the UDG population, the vast majority, 79 out of 100, are nonnucleated. We find a mild radial dependence of nucleated fraction in both the Virgo and Fornax Clusters, and overall, the nucleated fraction declines as we go from the higher-density environment cluster to the low-density environment.
4. We find that about 1.3% of dEs suffer a tidal disturbance from nearby massive galaxies and only 0.03% suffer recent dwarf–dwarf merging.
5. We find that dEs are found more frequently in environments where massive galaxies are already quenched.

We hope that this catalog will serve as a valuable resource for follow-up studies on dEs. In particular, considering the laborious nature of visual inspection and classification, this data set will be useful for training and testing machine-learning approaches. In future work, we plan to test the ability of convolutional neural networks to detect and characterize dEs with a view to applying them to a larger set of imaging data.

S.P. and S.-J.Y., respectively, acknowledge support from the New Researcher Program (Shinjin grant No. 2019R1C1 C1009600) and the Midcareer Researcher Program (No. 2019R1A2C3006242) through the National Research Foundation of Korea. S.-J.Y. and S.P. acknowledge support from the Basic Science Research Program (2022R1A6A1A03053472) through the National Research Foundation (NRF) of Korea. D. N.C. acknowledges the University Grants Commission of Nepal for financial support (Ph. D. -75/76-S & T-13).

This study is based on archival images and spectra from the Sloan Digital Sky Survey and images of the Legacy survey. The full acknowledgment for the SDSS can be found at http://www.sdss.org/collaboration/credits.html. Funding for the SDSS has been provided by the Alfred P. Sloan Foundation,

the Participating Institutions, the National Science Foundation, the U.S. Department of Energy, the National Aeronautics and Space Administration, the Japanese Monbukagakusho, the Max Planck Society, and the Higher Education Funding Council for England. The SDSS website is http://www.sdss.org/.

The Legacy Surveys consist of three individual and complementary projects: the Dark Energy Camera Legacy Survey (DECaLS; NOAO Proposal ID No. 2014B-0404; PIs: David Schlegel and Arjun Dey), the Beijing-Arizona Sky Survey (BASS; NOAO Proposal ID No. 2015A-0801; PIs: Zhou Xu and Xiaohui Fan), and the Mayall z-band Legacy Survey (MzLS; NOAO Proposal ID No. 2016A-0453; PI: Arjun Dey). DECaLS, BASS, and MzLS together include data obtained, respectively, at the Blanco telescope, Cerro Tololo Inter-American Observatory, National Optical Astronomy Observatory (NOAO); the Bok telescope, Steward Observatory, University of Arizona; and the Mayall telescope, Kitt Peak National Observatory, NOAO. The Legacy Surveys project is honored to be permitted to conduct astronomical research on Iolkam Du'ag (Kitt Peak), a mountain with particular significance to the Tohono O'odham Nation. The full acknowledgment for the Legacy Surveys can be found at https://www.legacysurvey.org/acknowledgment.

ORCID iDs

Sanjaya Paudel https://orcid.org/0000-0003-2922-6866
Suk-Jin Yoon https://orcid.org/0000-0002-1842-4325
Jaewon Yoo https://orcid.org/0000-0002-6841-8329
Rory Smith https://orcid.org/0000-0001-5303-6830

References

Aihara, H., Allende Prieto, C., An, D., et al. 2011, ApJS, 193, 29
Amorisco, N. C., & Loeb, A. 2016, MNRAS, 459, L51
Beasley, M. A., & Trujillo, I. 2016, ApJ, 830, 23
Bennet, P., Sand, D. J., Crnojević, D., et al. 2019, ApJ, 885, 153
Bennet, P., Sand, D. J., Zaritsky, D., et al. 2018, ApJL, 866, L11
Bertin, E., & Arnouts, S. 1996, A&AS, 117, 393
Binggeli, B., Sandage, A., & Tammann, G. A. 1985, AJ, 90, 1681
Binggeli, B., Tammann, G. A., & Sandage, A. 1987, AJ, 94, 251
Boselli, A., Boissier, S., Cortese, L., & Gavazzi, G. 2008, ApJ, 674, 742
Caldwell, N., & Bothun, G. D. 1987, AJ, 94, 1126
Carleton, T., Errani, R., Cooper, M., et al. 2019, MNRAS, 485, 382
Carlsten, S. G., Greene, J. E., Beaton, R. L., Danieli, S., & Greco, J. P. 2022, ApJ, 933, 47
Chan, T. K., Kereš, D., Wetzel, A., et al. 2018, MNRAS, 478, 906
Chiboucas, K., Jacobs, B. A., Tully, R. B., & Karachentsev, I. D. 2013, AJ, 146, 126
Chilingarian, I., Cayatte, V., Revaz, Y., et al. 2009, Sci, 326, 1379
Conselice, C. J. 2018, RNAAS, 2, 43
Conselice, C. J., Gallagher, J. S. I., & Wyse, R. F. G. 2002, AJ, 123, 2246
Conselice, C. J., Gallagher, J. S. I., & Wyse, R. F. G. 2003, AJ, 125, 66
Côté, P., Piatek, S., Ferrarese, L., et al. 2006, ApJS, 165, 57
Crnojević, D., Sand, D. J., Caldwell, N., et al. 2014, ApJL, 795, L35
Crnojević, D., Sand, D. J., Spekkens, K., et al. 2016, ApJ, 823, 19
Danieli, S., & van Dokkum, P. 2019, ApJ, 875, 155
den Brok, M., Peletier, R. F., Seth, A., et al. 2014, MNRAS, 445, 2385
Dey, A., Schlegel, D. J., Lang, D., et al. 2019, AJ, 157, 168
Dressler, A. 1980, ApJ, 236, 351
Duc, P.-A., Paudel, S., McDermid, R. M., et al. 2014, MNRAS, 440, 1458
Eigenthaler, P., Puzia, T. H., Taylor, M. A., et al. 2018, ApJ, 855, 142
Ferguson, H. C., & Binggeli, B. 1994, A&ARv, 6, 67
Ferrarese, L., Côté, P., Cuillandre, J.-C., et al. 2012, ApJS, 200, 4
Ferrarese, L., Côté, P., MacArthur, L. A., et al. 2020, ApJ, 890, 128
Geha, M., Blanton, M. R., Yan, R., & Tinker, J. L. 2012, ApJ, 757, 85
Gunn, J. E., Gott, J., & Richard, I. 1972, ApJ, 176, 1
Guzman, R., Lucey, J. R., & Bower, R. G. 1993, MNRAS, 265, 731
Habas, R., Marleau, F. R., Duc, P.-A., et al. 2020, MNRAS, 491, 1901
Impey, C., Bothun, G., & Malin, D. 1988, ApJ, 330, 634
Janz, J., Laurikainen, E., Lisker, T., et al. 2014, ApJ, 786, 105
Janz, J., & Lisker, T. 2008, ApJL, 689, L25
Janz, J., & Lisker, T. 2009, ApJL, 696, L102
Jerjen, H., Binggeli, B., & Freeman, K. C. 2000, AJ, 119, 593
Jones, M. G., Bennet, P., Mutlu-Pakdil, B., et al. 2021, ApJ, 919, 72
Kenney, J. D. P., Geha, M., Jáchym, P., et al. 2014, ApJ, 780, 119
Kenney, J. D. P., van Gorkom, J. H., & Vollmer, B. 2004, AJ, 127, 3361
Koleva, M., Bouchard, A., Prugniel, P., De Rijcke, S., & Vauglin, I. 2013, MNRAS, 428, 2949
Kormendy, J. 1977, ApJ, 218, 333
Kormendy, J., Fisher, D. B., Cornell, M. E., & Bender, R. 2009, ApJS, 182, 216
La Marca, A., Peletier, R., Iodice, E., et al. 2022, A&A, 659, A92
Larson, R. B., Tinsley, B. M., & Caldwell, C. N. 1980, ApJ, 237, 692
Lim, S., Côté, P., Peng, E. W., et al. 2020, ApJ, 899, 69
Lisker, T. 2009, AN, 330, 1043
Lisker, T., Glatt, K., Westera, P., & Grebel, E. K. 2006, AJ, 132, 2432
Lisker, T., Grebel, E. K., Binggeli, B., & Glatt, K. 2007, ApJ , 660, 1186
Makarov, D., & Karachentsev, I. 2011, MNRAS, 412, 2498
Marleau, F. R., Habas, R., Poulain, M., et al. 2021, A&A, 654, A105
Martínez-Delgado, D., Läsker, R., Sharina, M., et al. 2016, AJ, 151, 96
Mayer, L., Governato, F., Colpi, M., et al. 2001, ApJ, 559, 754
Merritt, A., van Dokkum, P., Danieli, S., et al. 2016, ApJ, 833, 168
Michea, J., Pasquali, A., Smith, R., et al. 2021, AJ, 161, 268
Mihos, J. C., Durrell, P. R., Ferrarese, L., et al. 2015, ApJL, 809, L21
Moore, B., Katz, N., Lake, G., Dressler, A., & Oemler, A. 1996, Natur, 379, 613
Müller, O., Jerjen, H., & Binggeli, B. 2017, A&A, 597, A7
Müller, O., Marleau, F. R., Duc, P.-A., et al. 2020, A&A, 640, A106
Oemler, A. J. 1974, ApJ, 194, 1
Ordenes-Briceño, Y., Puzia, T. H., Eigenthaler, P., et al. 2018, ApJ, 860, 4
Paudel, S., Duc, P. A., & Ree, C. H. 2015, AJ, 149, 114
Paudel, S., Lisker, T., Hansson, K. S. A., & Huxor, A. P. 2014, MNRAS, 443, 446
Paudel, S., Lisker, T., & Kuntschner, H. 2011, MNRAS, 413, 1764
Paudel, S., & Ree, C. H. 2014, ApJL, 796, L14
Paudel, S., Smith, R., Duc, P.-A., et al. 2017, ApJ, 834, 66
Paudel, S., Smith, R., Yoon, S. J., Calderón-Castillo, P., & Duc, P.-A. 2018, ApJS, 237, 36
Paudel, S., & Yoon, S.-J. 2020, ApJL, 898, L47
Penny, S. J., Conselice, C. J., de Rijcke, S., et al. 2011, MNRAS, 410, 1076
Petrosian, V. 1976, ApJL, 210, L53
Poulain, M., Marleau, F. R., Habas, R., et al. 2021, MNRAS, 506, 5494
Román, J., & Trujillo, I. 2017, MNRAS, 468, 4039
Sánchez-Janssen, R., Côté, P., Ferrarese, L., et al. 2019, ApJ, 878, 18
Sánchez-Janssen, R., Méndez-Abreu, J., & Aguerri, J. A. L. 2010, MNRAS, 406, L65
Sandage, A., & Visvanathan, N. 1978, ApJ, 223, 707
Schlafly, E. F., & Finkbeiner, D. P. 2011, ApJ, 737, 103
Smith, R., Davies, J. I., & Nelson, A. H. 2010, MNRAS, 405, 1723
Smith, R., Michea, J., Pasquali, A., et al. 2021, ApJ, 912, 149
Su, A. H., Salo, H., Janz, J., et al. 2021, A&A, 647, A100
Thompson, L. A., & Gregory, S. A. 1993, AJ, 106, 2197
Urich, L., Lisker, T., Janz, J., et al. 2017, A&A, 606, A135
van der Burg, R. F. J., Hoekstra, H., Muzzin, A., et al. 2017, A&A, 607, A79
van Dokkum, P. G., Abraham, R., Merritt, A., et al. 2015, ApJL, 798, L45
Venhola, A., Peletier, R., Laurikainen, E., et al. 2017, A&A, 608, A142
Visvanathan, N., & Sandage, A. 1977, ApJ, 216, 214
Vollmer, B., Cayatte, V., Balkowski, C., & Duschl, W. J. 2001, ApJ, 561, 708
Whitmore, B. C., Gilmore, D. M., & Jones, C. 1993, ApJ, 407, 489
Wittmann, C., Kotulla, R., Lisker, T., et al. 2019, ApJS, 245, 10
Zaritsky, D., Donnerstein, R., Karunakaran, A., et al. 2021, ApJS, 257, 60

Monthly Notices of the ROYAL ASTRONOMICAL SOCIETY

MNRAS **520,** 4953–4960 (2023) https://doi.org/10.1093/mnras/stac3700
Advance Access publication 2022 December 20

Forming blue compact dwarf galaxy through mergers

Daya Nidhi Chhatkuli,[1] Sanjaya Paudel ,[2]★ Rajesh Kumar Bachchan,[3] Binil Aryal[1] and Jaewon Yoo[4,5]

[1]*Central Department of Physics, Institute of Science and Technology, Tribhuvan University, Kirtipur, Kathmandu, Nepal*
[2]*Department of Astronomy, Yonsei University, Seoul 03722, Republic of Korea*
[3]*Patan Multiple Campus, Tribhuvan University, Patandhoka, Lalitpur, Nepal*
[4]*Quantum Universe Center, Korea Institute for Advanced Study (KIAS), 85 Hoegiro, Dongdaemum-gu, Seoul 02455, Korea*
[5]*Korea Astronomy and Space Science Institute (KASI), 776 Daedeokdae-ro, Yuseong-gu, Daejeon 34055, Republic of Korea*

Accepted 2022 December 12. Received 2022 December 4; in original form 2022 June 28

ABSTRACT

It has long been speculated that blue compact dwarf galaxies (BCDs) are formed through the interaction between low-mass gas-rich galaxies, but a few candidates of such systems have been studied in detail. We study a sample of compact star-forming dwarf galaxies that are selected from a merging dwarf galaxy catalog. We present a detailed study of their spectroscopic and structural properties. We find that these BCDs looking galaxies host extended stellar shells and thus are confirmed to be a dwarf–dwarf merger. Their stellar masses range between 8×10^7 M$_\odot$ and 2×10^9 M$_\odot$. Although the extended tail and shell are prominent in the deep optical images, the overall major axis light profile is well modeled with a two-component Sérsic function of inner compact and extended outer radii. We calculate the inner and outer component stellar-mass ratio using the two-component modeling. We find an average ratio of 4:1 (with a range of 10:1 to 2:1) for our sample, indicating that the central component dominates the stellar mass with an ongoing burst of star formation. From the measurement of H_α equivalent width, we derived the star-formation ages of these galaxies. The derived star-formation ages of these galaxies turn out to be in the order of a few 10 Myr, suggesting the recent ignition of star formation due to events of satellite interaction.

Key words: galaxies: evolution – galaxies: irregular – galaxies: dwarf – galaxies: starburst – galaxies: interactions.

1 INTRODUCTION

A significant effort has been made to study the interaction of massive galaxies, whereas mergers between dwarf galaxies ($M_\star < 10^9$) received little attention until very recently. Because dwarf galaxies have shallow potential-well, their evolution is expected to be more driven by the large-scale environment than by merging events (Boselli & Gavazzi 2006; Kormendy et al. 2009; Lisker 2009). Indeed, both observations and numerical simulations have extensively concluded that massive elliptical galaxies were likely to be originated first major mergers, building a dense inner core at high redshift, and grow through minor mergers, contributing to the formation of extended outer stellar halos (Khochfar & Silk 2006; Oser et al. 2010; Duc et al. 2011).

In contrast to their massive counterparts, star-forming dwarf galaxies, and hence their merger, are often gas dominated.

Recent observations have revealed that sub-structures like a stellar shell, kinematically decoupled core, or even tidal stream around dwarf galaxies are common, which can be considered as the signatures of past merger events (Geha, Guhathakurta & van der Marel 2005; Rich et al. 2012; Penny et al. 2012; Toloba et al. 2014). Stierwalt et al. (2015) carried out the first systematic study of gas-rich dwarf–dwarf interacting pairs and found that the star formation rate (SFR) of relatively close pair is enhanced by a factor of ∼2 on average. Pearson et al. (2016) further showed that gas-rich dwarf pairs have more extended atomic gas distribution than unpaired analogs. In addition, case studies of several star-forming dwarf pairs have been carried out recently (Annibali et al. 2016; Privon et al. 2017; Paudel & Sengupta 2017; Paudel, Sengupta & Yoon 2018a).

Structural parameters, such as size, concentration, and ellipticity are important tools to study galaxy formation and evolution. Galaxies follow a scaling relation between size and magnitude that is continuous over the whole range of luminosities (Graham & Guzmán 2003; Ferrarese et al. 2006; Janz & Lisker 2008). The universality of this relation has been a subject of considerable debate because of the presence of outliers and non-linearity of the relation (Kormendy et al. 2009; Chen et al. 2010). In particular, early formed galaxies are compact compared to the later formed galaxies, as we see that the high redshift galaxies are significantly compact compared to the local ($z < 0.1$) galaxies. The size, evolution, and formation of compact galaxies in the early universe are some of the mysteries of current cosmology. Compact dwarf galaxies are prominent outliers of galaxies in the conventional size-magnitude relation (Paudel et al. 2014). Their formation and evolution have been poorly understood. Compact early-type galaxies, like M32, are mainly found in the vicinity of large galaxies, e.g. M31, and such proximity to the nearby giant has led to an argument that the galaxies like M32 might have formed through the tidal stripping (Faber & Lin 1983). On contrary, recent discoveries are evidence that all compact dwarf galaxies are not located nearby of giant galaxies. Huxor, Phillipps & Price (2013) found that a

★ E-mail: sanjpaudel@gmail.com

Table 1. Basic physical parameters of six BCDs.

Galaxy	RA (°)	DEC (°)	z	D (Mpc)	$g-r$ (mag)	M_r [log(M$_\odot$)]	M_* [log(M$_\odot$)]	SFR [log(M$_\odot$/yr)]	$M_{\rm gas}$ [log(M$_\odot$)]	Feature
D004	028.9989	−0.1855	0.0121	51.57	0.46	−16.72	9.09	−0.91	8.43	Sh
D036	144.5608	19.7111	0.0144	61.48	0.20	−16.46	8.56	–	8.87	Sh
D047	150.3099	37.0709	0.0048	20.34	0.14	−15.94	8.26	−1.29	–	Sh
D055	157.4553	16.1809	0.0108	45.98	0.23	−17.89	9.18	−0.68	8.19	SL
D075	177.0757	−1.6399	0.0130	55.44	0.22	−17.54	9.03	−0.51	9.94	Sh
D076	177.5113	15.0231	0.0024	11.90	0.09	−15.29	7.92	–	8.40	Sh

Note. The first column is the name according to the Paudel et al. (2018b) catalog. Columns 2–10 represent RA, DEC, redshift, Hubble flow distance of the galaxies, $g-r$ colour, r-band magnitude, stellar mass, star-formation rate, HI gas mass, respectively. In last column we list the tidal feature of the galaxies as noted in Paudel et al.

compact dwarf galaxy is located in an isolated environment. Such discovery of isolated compact dwarf galaxies has put forward another hypothesis that compact dwarf galaxies might have formed through the merging of even smaller dwarfs. Indeed, Paudel & Ree (2014) discovered a nearly isolated compact dwarf galaxy, CGCG 036-042, with prominent evidence of merging features.

Blue compact dwarf galaxies (BCDs) are low-luminosity galaxies ($M_B > -18$ mag) with a compact optical appearance and are blue in colour (Papaderos et al. 1996). In particular, supercompact BCDs are considered young objects which have accumulated most of their stellar mass at late cosmic epochs (Drinkwater & Hardy 1991). Various lines of thought have been presented for their origin and future evolution. The mechanism that triggers the burst of star formation in these compact dwarf galaxies remains a mystery. Mergers, fly-by encounters, or gas turbulence have been proposed to explain the recent burst star-formation activity in BCDs (Noeske et al. 2001; Pustilnik et al. 2001; Bekki 2008).

Here, we present a study of a unique sample of BCDs that recently underwent merging activity and hosts clear stellar shells and streams as a signature of a recent merger.

2 SAMPLE AND DATA ANALYSIS

To study the formation and evolution of BCD-type galaxies, we preferentially selected six compact merging dwarf candidates with a clear tidal feature. Our sample galaxies are taken from the catalog of merging dwarf galaxies prepared by Paudel et al. (2018a). The basic properties of our sample galaxies are listed in Table 1 that we have fetched from the parent catalog. These dwarf galaxies have a stellar-mass range of 8×10^7 M$_\odot$ to 2×10^9 M$_\odot$, which are comparable to the large magellanic and small magellanic clouds of the local group. By chance, we found a substantial amount of multiwavelength data of these galaxies in public archives, which allowed us to thoroughly analyse their morphology, chemical properties, and stellar populations. Fig. 1 reveals the optical view of our galaxies, where we can see an elongated low surface brightness tidal tail along the major axis. The colour image is a cutout of the legacy sky-survey imaging database (Dey et al. 2019), which is prepared by combining $g-$, $r-$, and $z-$band images. The field-of-view of the image is 2 arcmin × 2 arcmin. We can see that the inner part is quite round and bluish, and the outer low surface-brightness extended tidal tail is relatively reddish. We also show the size of the measured half-light radius with a red circle and a blue circle representing the SDSS fibre position. Given their compact nature, D036 and D075 are visually similar to tadpole galaxies identified by Straughn et al. (2015) in Hubble Deep Field. D036 has a short faint tail-like structure that shows one-side elongation. On the contrary, D076 seems to have a tail on both sides, with one side's low-surface brightness tail quite prominent compared to the other.

All, except D047, are located in a nearly isolated environment. The D036 is located at the edge of small group CGCG 092-005 at a 445 kpc sky-projected distance from the group center.

2.1 Imaging and Photometry

We used the SDSS image to perform image analysis (Ahn et al. 2012). For this purpose, the SDSS $r-$band images have been used extensively because they have a higher signal-to-noise ratio than the other bands and we mainly used this band image to perform surface photometry. The surface photometry of very low surface brightness objects is notoriously difficult. There are several factors that are crucial in making an accurate estimation of photometric parameters. Sky background is among the most important ones. Although the sky background subtraction in the latest version of the SDSS pipeline processed images is relatively good, we additionally process the SDSS images. We retrieved stacked images (3 arcmin × 3 arcmin fits-image cutout) from the SDSS data archival service. We subtracted the sky background preparing a background map for each object. The background maps were constructed after masking out all identified sources in the image, which were defined by source-extractor segmentation maps, and the segmentation images were filled by the median values calculated from all the surrounding pixels. This method allows us to eliminate any contribution of light from stars and background galaxies. Finally, the background map was subtracted from the original fits file to remove the sky background contribution to the observed flux.

To perform surface photometry, we exploit the image reduction and analysis facility (IRAF) *ellipse* task, which outputs the major-axis profile of average intensity and ellipse parameters, such as position angle and ellipticity. The *ellipse* uses the methodology presented in Jedrzejewski (1987), where for each semimajor axis length, an azimuthally averaged intensity $I(\phi)$ is calculated within the concentric ellipse area. The ellipse is defined with an initial guess for the isophote's centre (X, Y), ellipticity (ϵ), and semimajor axis position angle (θ). The best fit ellipse is obtained by minimizing the sum of the squares deviation between the data while expanding the $I(\phi)$ into a Fourier series as:

$$I(\phi) = I_0 + \sum_k [A_k \sin(k\phi) + B_k \cos(k\phi)]. \quad (1)$$

and for a good approximation of the ellipse, the expansion should be truncated to the first two terms.

All foreground and background unrelated objects were masked. The masking was performed manually, where we visually identified the unrelated objects. The centre of galaxies was derived by using

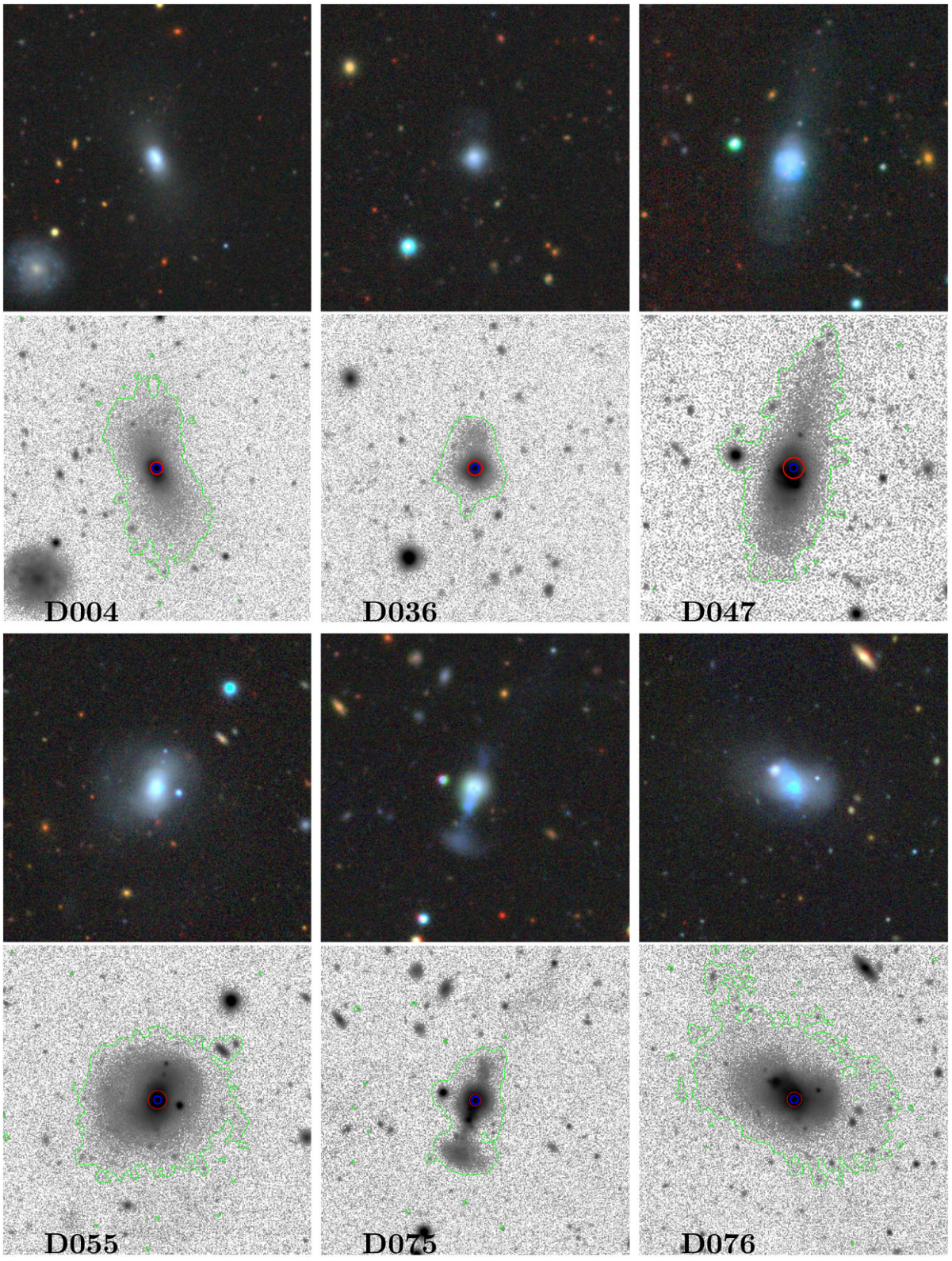

Figure 1. Legacy survey colour images of our sample galaxies. The second and fourth rows represent grey-scale g-band images with a field of view of 2 inch $\times$ 2 inch. In the second and fourth rows, we show tri-colour images of the respective galaxies, produced from a combination of $g - r - z$ band images. We also show the size of the measured half-light radius with a red circle and a blue circle representing the SDSS fibre position. In each grey scale image, we draw a green contour representing a surface brightness level of 27 mag-arcsec^{-2} at the g −band.

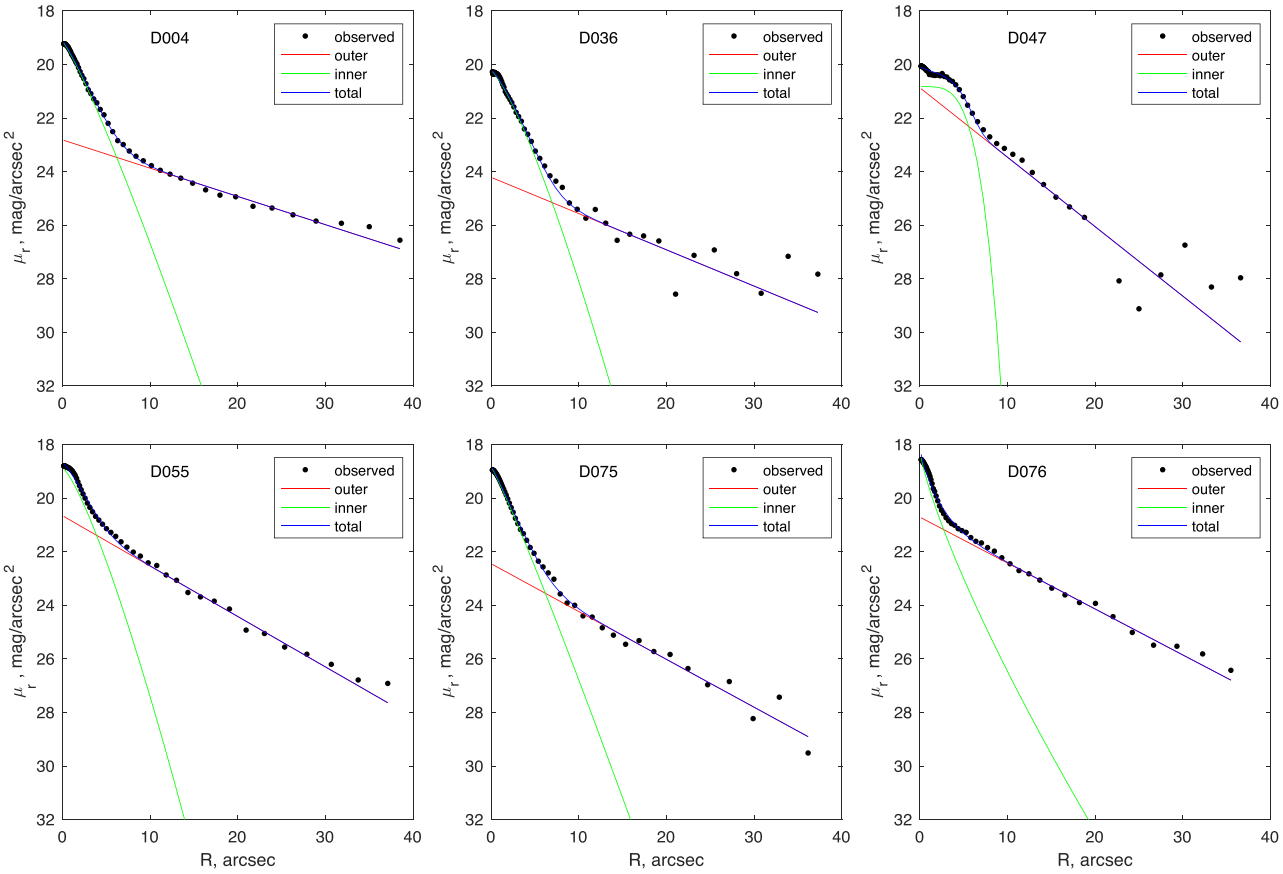

Figure 2. Multicomponent Sérsic modelling of observed one-dimensional light profile. The black dots represent the observed data points. We show the inner and outer best fit Sérsic function in green and red lines, respectively. The blue line represents a combination of both the inner and outer best-fit model.

imcentre task in the IRAF, which calculates a centroid of the provided image section. While fitting the ellipse, the position angle and the ellipticity were allowed to vary freely, and the semimajor axis was increased logarithmically. The ellipse centre was not allowed to move by more than 3 pixels between the successive isophotes.

The derived r −band major axis light profiles of our sample galaxies are shown in Fig. 2. The light profile generally shows a break which shows an abrupt change in gradient. We see that the inner component's light profile rises steeply compared to the outer component. However, in the case of D047, we see a somewhat irregular profile in the inner region. We then approximate the observed galaxy light profile into a multicomponent Sérsic function, namely, $I_{\rm overall} = I_{\rm In} + I_{\rm Out}$, where the Sérsic (Sersic 1968) function is defined as

$$I(R) = I_{\rm e} \exp\left\{-b_n\left[\left(\frac{R}{R_{\rm e}}\right)^{1/n} - 1\right]\right\}, \quad (2)$$

where $I_{\rm e}$ is the intensity of the light–profile at the effective radius $R_{\rm e}$, and n defines the 'shape' of the profile. The term b_n is simply a function of n and chosen to ensure that the radius $R_{\rm e}$ encloses half of the profile's total luminosity Graham et al. (2005).

In Fig. 2, we show the modeled inner and outer components in green and red solid lines, respectively. The overall model two-component function is shown in the blue line. To obtain the best fit model, we used χ^2-minimization scheme. In doing so, we found that the outer components generally have a near exponential ($n = 1$) Sérsic index, and we decided to fix $n = 1$ for the outer component in the final fitting.

The two-component modeling is used to decompose merger remanent in its progenitor, assuming that each component roughly represents the individual progenitor. Finally, we performed integrated photometry in each component model to calculate each component's total flux and magnitude. We estimated the stellar masses by multiplying the SDSS-r-band fluxes with a mass-to-light ratio obtained from Zhang, Puzia & Weisz (2017) for the observed $g - r$ colour. These values are most likely upper limits.

The stellar mass ratio between the two components of our sample BCDs varies between 0.1 and 0.5, where we calculate stellar mass from their r-band flux and $g - r$ colour. However, we warn that there is a reasonable chance that both components' stellar populations are well mixed and therefore, the calculation may have a large uncertainty.

Because of the complexity in the observed light profile of the merging galaxies, no overall structural parameters can be derived using a simple Sérsic function modeling. To measure the overall photometric properties, we used a non-parametric approach, i.e. the Petrosian method (Janz & Lisker 2008).

Using the Petrosian method, we estimated the value of total luminosities and half-light radii. The global half-light radii of our sample galaxies range from 0.23 kpc to 0.56 kpc which, indeed, proves that our selected sample dwarf galaxies are compact dwarfs in general.

Table 2. Derived properties of the sample galaxies.

ID	c	Z (dex)	SFR log($M_\odot$/yr)	R_a ($''$)	R_i ($''$)	n_i	R_o ($''$)
D004	4.62	8.33	0.022	2.841	2.490	0.8	17.1
D036	3.34	8.33	0.022	2.101	2.751	0.8	19.4
D047	3.27	8.14	0.002	4.234	1.212	0.3	06.1
D055	3.56	8.23	0.148	3.162	2.481	0.7	10.0
D075	2.98	8.13	0.118	2.659	2.358	0.9	10.4
D076	3.26	7.99	0.061	1.998	2.067	1.2	10.5

Note. The first column is ID of the galaxies. The Balmer decrement, emission line metallicity, and SFR derived from spectroscopic data are listed in columns 2, 3, and 4, respectively. In the columns 5, 6, 7, and 8, we list the overall galaxy size (R_a), inner size (R_i), inner Sérsic index (n_i), and the outer size (R_o), respectively.

2.2 Spectroscopy

All of our sample galaxies are targeted by the SDSS fibre spectroscopy observation. We retrieved the optical spectra of these galaxies from the SDSS data archive. These optical spectra have a reasonable signal-to-noise ratio. They are observed with the fibres spectrograph of 3 arcsec diameter. The sample galaxies have a broad range of distances; the central 3 arcsec represents a 50 pc to 100 pc core region depending on their distance from us.

The SDSS spectra show strong emission lines, particularly Balmer lines, and resemble a typical spectrum of a star-forming H II region. The emission line fluxes were measured after subtracting the stellar absorptions, which are particularly strong in the case of H_β. For this, we used a publicly available code, the GANDLF (Sarzi et al. 2006) of a version particularly designed for the SDSS spectra, which uses a combination of stellar templet from Tremonti et al. (2004). The emission line fluxes are measured by fitting a Gaussian profile which allows us to measure total flux, full width at half maximum (FWHM), and equivalent width simultaneously. For this purpose, we use IRAF *splot* task.

We derived Oxygen abundances ($12 + \log[\mathrm{O/H}]$) using these emission line fluxes. The extinction coefficient, $E(B-V)$, was derived from H_α/H_β emission-line ratios using a calibration provided by Cardelli, Clayton & Mathis (1989). The derived value of the extinction coefficient varies between 0.12 mag to 0.21 mag. D004 shows the largest extinction and D075 shows the least extinction (Table 2). We finally derived the SFR from the extinction corrected emission line H_α flux using the calibration of Kennicutt (1998).

3 RESULTS

3.1 Imaging

We have performed the surface photometry and the emission line analysis on a sample of merger remanent dwarf galaxies that are selected from a merging dwarf galaxy catalog. We used a publicly available optical imaging and spectroscopic data from the SDSS data server. The derived structural and spectroscopic parameters are listed in Table 2. As expected, the inner component is in general five times smaller than the outer component and has a smaller Sérsic index. The measured photometric parameters show that the outer component is significantly redder than the inner component. The difference in $g-r$ colour index of two-components is ≈0.2 on average.

In Fig. 3, we show the relation between log (size) and r-band absolute magnitude for our galaxies, and for the reference, we used a sample of early-type dwarf galaxies from Janz & Lisker (2008).

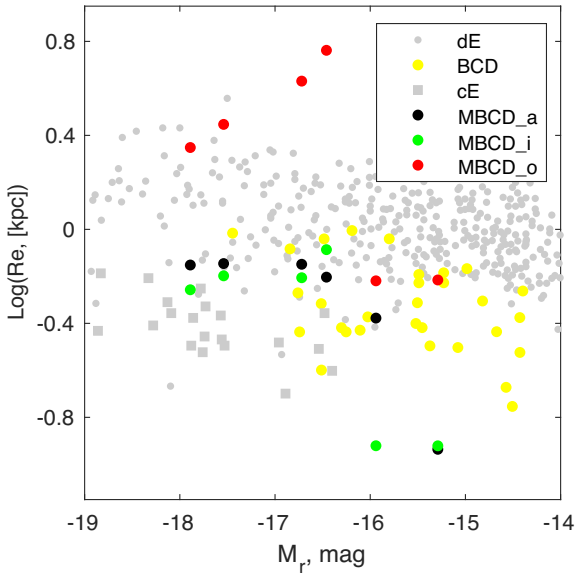

Figure 3. Scaling relation between log (R_e) and magnitude. The merging BCDs (MBCD) data points are shown in green, red, and black colours representing inner, outer, and overall sizes, respectively. For the reference, we have used a sample of early-type dwarf galaxies (shown in grey dots) from Janz & Lisker (2008). The yellow dots represent Virgo cluster BCD studied by Meyer et al. (2014), and we show compact elliptical in a grey square sample taken from Chilingarian et al. (2009).

In addition, we show a sample of BCDs of Virgo cluster in yellow colour dot, they are taken from the study of Meyer et al. (2014) and we show compact ellipticals in a grey square sample taken from Chilingarian et al. (2009). Our sample merging BCDs are shown in three different colours: green, red, and black for the inner, outer, and overall components, respectively. As expected, the BCDs fall well below the relation defined by the reference sample dE. They are slightly larger than cE but significantly smaller in size than dEs. We also notice that the inner component sizes are comparable to the overall size of merging BCDs compared to their outer component size implying that the inner component largely dominates the light distribution. On the contrary, the cE population is the most compact class of object in this diagram.

3.2 Spectroscopy

The $\mathrm{SFR}_{H\alpha}$ is lower compared to the cataloged SFR that is derived from far-ultra-violet (FUV) flux. There are many reasons for this discrepancy. The H_α and FUV fluxes trace different time domains of star formation, the former being significantly shorter than the latter. However, they generally follow the relation between log (SFR) and B-band absolute magnitude (Fig. 4 top panel). In addition, while measuring the FUV flux, we considered the entire galaxy using a larger aperture, and the H_α fluxes were measured from a central 3 arcsec fibre spectroscopy. The B-band magnitude of our sample galaxies is calculated from the SDSS g −band magnitude using the colour transformation equation provided by the SDSS webpage.[1] The comparison sample in grey dots is taken from Lee et al. (2009), which provides a statistical study of star-formation activity in local volume star-forming galaxies using volume-limited sample.

[1] http://www.sdss3.org/dr8/algorithms/sdssUBVRITransform.php

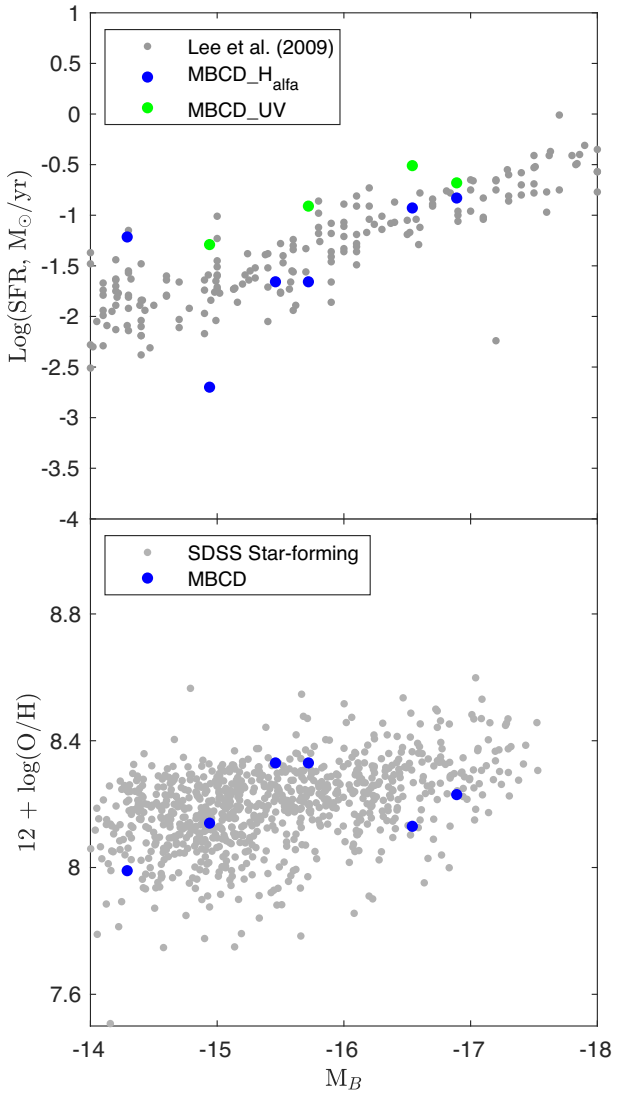

Figure 4. **Top**: Relation between B-band absolute magnitude and log (SFR). The merging BCDs (MBCD) are shown in green and blue symbols, representing SFR derived from UV and H_α emission line flux, respectively. We can see only four galaxies for ultraviolet (UV) because there are no UV data for galaxies D036 and D076. The comparison sample, shown in grey dots, are taken from Lee et al. (2009). **Bottom**: Relation between emission line metallicity and B-band absolute magnitude. MBCDs are shown in blue dots. In this plot, we used a reference sample of star-forming dwarf galaxies that are taken from (Paudel et al. 2014).

To derive oxygen abundances, we employed a method suggested by Marino et al. (2013), where a line ratio between H_α and [NII] is used. Our sample galaxies have a range of 12 + log (O/H) between 7.99 dex and 8.33 dex. Being slightly sub-solar, these values are typical of BCDs. In this sample, D076 is the most metal-poor galaxy, and also has the highest gas mass fraction.

In the bottom panel of Fig. 4, we show a relation between B-band absolute magnitude and emission line metallicities. Our BCDs well follow the relation defined by a sample of star-forming dwarf galaxies drawn from the SDSS, which we have taken from Paudel et al. (2017).

To get a rough estimate of the star formation age, we used H_α equivalent width ($EW_{H\alpha}$). For the majority of our sample, the measured values of $EW_{H\alpha}$ is larger than 100Å , and using the Starburst99 model (Leitherer et al. 1999) assuming an instantaneous burst of star formation and a half of solar metallicity, these values indicate that the ages of star formation are estimated to be in the order of a few 10 Myr.

3.3 Gas Content

Queering the CDS catalog service, we find neutral hydrogen (HI) 21-cm radio data for five of our merging BCDs (except D047). They are mainly observed by a single dish telescope (Arecibo observations) with a typical beam size of 3 arcmin and we expect that the HI flux measurement is for the overall galaxy. Using equation $M_{\rm HI} = 2.356 \times 10^5\, d^2 \int S_c(v)\, dv\, M_\odot$,[2] we derived HI mass from the 21-cm radio emission flux and we find that our merging BCDs possess an $M_{\rm HI}$ in the range 2.5×10^8 M $_\odot$ to 8.7×10^9 M $_\odot$. The calculated $M_{\rm HI}$ to blue band luminosity ratio varies between 0.5 M $_\odot$/L $_\odot$ to 0.8 M $_\odot$/L $_\odot$ for our sample galaxies. This number is similar to an average value of $M_{\rm HI}/L_{\rm B}$ for a typical sample of BCDs studied in Huchtmeier, Gopal-Krishna & Petrosian (2005) but significantly lower than an average value of low-surface brightness dwarf galaxies found in the isolated environments (Pustilnik & Tepliakova 2011). Note, however, the estimated stellar mass using a single optical colour has uncertainty as large as 0.3 dex (Zhang et al. 2017). To make a more accurate estimation of stellar mass, a detailed analysis of spectral energy distribution with a longer baseline wavelength is required.

4 DISCUSSION AND CONCLUSIONS

This work studies a sample of compact merging dwarf galaxies and performs a detailed analysis of morphological parameters. These compact star-forming dwarf galaxies are selected from a catalog of merging dwarf galaxies prepared by Paudel et al. (2018b). Our detailed image analysis shows that, although they are compact systems, these dwarf galaxies' light profiles are no better modeled with one component Sérsic function. They are better represented with two components: (i) inner compact and (ii) outer extended low-surface brightness component. However, the overall sizes of these galaxies are also significantly smaller compared to the normal dwarf galaxies and the size of the inner component is comparable to the compact early-type galaxies. On the contrary, the relation between B-band magnitude and emission line metallicity and SFR show no anomaly, being consistent with the relation defined by normal star-forming dwarf galaxies. However, a typical 0.3 dex scatter is seen in the relation between SFR and B-band magnitude, even for normal galaxy samples.

4.1 Comparison to the Previous Study

It is well known that BCDs have two components – inner compact star-forming core and outer low-surface brightness extended halo (Sung et al. 1998; Loose & Thuan 1986). A detailed morphological property of a complete sample of BCDs of the Virgo cluster was done by Meyer et al. (2014). They decomposed these two components' light profiles and studied their similarity with various morphology dwarf galaxies, such as dwarf elliptical or dwarf irregular. The work, however, makes no comment on the origin of starburst activity

[2]where d is the distance in Mpc and $\int S_c(v)$ is expressed in Jy and v in km/s (Roberts 1978)

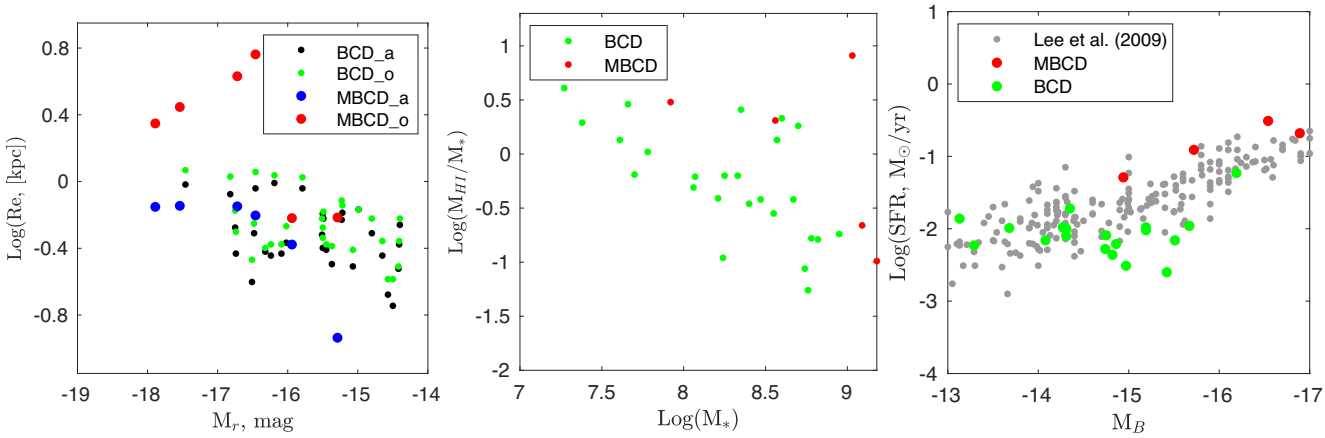

Figure 5. Comparison of physical and star-formation parameters between merging BCDs and Virgo cluster BCDs. For the Virgo cluster BCDs, we used Meyer et al. (2014) photometric measurement.

and mainly focuses on the future evolution of BCDs in the cluster environment.

In Fig. 5, we compare the physical properties of normal BCDs of the Virgo cluster with that of merging BCDs of this study. For the Virgo cluster, we used Meyer et al. (2014) photometric measurement. In the leftmost panel, we show the size magnitude relation of BCDs, and particularly we noticed that although the overall sizes of both sample BCDs are similar, the outer component sizes of merging BCDs are significantly larger than that of normal Virgo BCDs. Such extended outer component, indeed, mainly shows the presence of tidal components that may have built up by merging/accreting other galaxies.

The middle panel of Fig. 5 displays a scaling relation between gas mass fraction and stellar mass. The Virgo BCDs gas masses are estimated from 21 cm neutral hydrogen emission line flux provided by ALPHA–ALPHA survey (Haynes et al. 2018) and stellar masses are derived similarly to that derived for merging BCDs from $r-$band magnitude and $g-r$ colour. It reveals that merging BCDs tends to have a higher gas mass fraction than BCDs of the Virgo cluster. The discrepancy in gas mass fraction can also be attributed to their environmental differences. Our merging BCDs are primarily located in field environments where galaxies are dominantly gas rich and star forming. In the rightmost panel, we show a relation between B-band absolute magnitude and Log(SFR), and similar to Fig. 4, we added Lee et al. (2009) data for the reference. The star-formation rates of Virgo BCDs are estimated from FUV flux provided by the GALEX UV survey of Virgo cluster (Boselli et al. 2011). As we have already noticed in Fig. 4, merging BCDs clearly shows enhanced star-formation activity compared to the reference star-formation sequence provided by Lee et al. (2009), and Virgo BCDs are located below the sequence.

4.2 Formation of Blue Compact Dwarf Galaxies through the Merger

Various observational and theoretical lines of evidence suggest that the evolutionary pathways of BCDs have to be diverse, and multitudes of starburst mechanisms are discussed. Particularly, dwarf–dwarf mergers, interactions, or gas inflow may trigger the gas collapse or strong dissipation, which ignites the burst of star formation in these low-mass galaxies (Papaderos et al. 1996; Nusser 2005; Bournaud & Elmegreen 2009; Elmegreen, Zhang & Hunter 2012; Zhang et al. 2020b; Nusser & Silk 2022).

Zhang et al. (2020b), Zhang et al. (2020a) studied a link between a dwarf–dwarf merger event and enhanced star formation in a Virgo cluster BCD, VCC 848. Using a combination of JVLA HI emission line map and optical imaging, they examined the effect of the merger on the stellar and the gaseous distributions and concluded that although VCC 848 possesses a central burst of star-formation, it has less than 30 per cent of gas concentration in the centre. Comparing the general morphological feature with N-body hydrodynamical simulations results, they suggested the timing of the merger about a Giga year ago. On contrary to VCC 848 environments, our merging BCDs are located in a low, dense environment.

While studying the HI morphology of a sample of starburst dwarfs (selected from BCD-like galaxies), Lelli, Verheijen & Fraternali (2014) found that the outer extended HI part was more asymmetric in starburst dwarfs than normal star-forming galaxies, and the age of starburst is correlated with the strength of asymmetric feature, suggesting that some external mechanism triggered the starburst. In a similar line, Ramya, Kantharia & Prabhu (2011) suggests that some of the BCDs they studied might have a tidal origin.

Several physical properties of our sample merging dwarf galaxies, i.e. colour, metal content, and star-formation rate are fairly similar to a typical BCD and there is little doubt that the star formation activity is affected by the interaction. The star-formation ages derived from H_α equivalent width reveal that the burst of star-formation is a recent activity and the event is very likely triggered by the interaction. Galaxy merger efficiently supplies the gas towards the centre helping to ignite a central starburst (Bekki 2008) and such merger-induced central starburst builds a central blue core that dominates the optical light.

How would these compact BCDs evolve after ceasing the star-formation activity? The sizes of star-forming galaxies are likely to increase as the dynamic and stellar population evolution proceeds, which leads to a decrease in the surface brightness (Wellons et al. 2015). These galaxies are significantly compact compared to the normal galaxy. The current star-formation rate is not significantly high and the SDSS spectrum reveals strong higher-order Balmer absorption feature, indicating that the star-formation activity is a temporal feature and it hosts a significant amount of old stellar population. The presence of old stellar population could be due to the effect of the accretion of a smaller satellite by these galaxies and the event eventually perturbed the gaseous disk of the primary, which leads to a burst of star formation at the centre.

A general prediction of early simulations is that galaxies mergers develop substantial gas inflows and induce intense starbursts at the

centre producing core-like structure (Mihos & Hernquist 1994). The intense starburst at the centre of our merging compact dwarf galaxies appears to align with these simulations' results. It has also been proposed that a pre-existing compact core, i.e. a dense central bulge, may help to maintain an intense starburst activity (Mihos & Hernquist 1996).

ACKNOWLEDGEMENTS

DNC acknowledges the University Grants Commission of Nepal for financial support (Ph. D. -75/76-S & T-13). SP acknowledges support from the New Researcher Program (Shinjin grant No. 2019R1C1C1009600) through the National Research Foundation of Korea. JY was supported by a KIAS Individual Grant (QP089901) via the Quantum Universe Center at Korea Institute for Advanced Study. This study is based on the archival images and spectra from the Sloan Digital Sky Survey (the full acknowledgment can be found at https://www.sdss.org/collaboration/acknowledgements).

DATA AVAILABILITY

Most of the data underlying this article are publicly available. The derived data generated in this research will also be shared on reasonable request to the corresponding author.

REFERENCES

Ahn C. P. et al., 2012, ApJS, 203, 21
Annibali F. et al., 2016, ApJ, 826, L27
Bekki K., 2008, MNRAS, 388, L10
Boselli A., Gavazzi G., 2006, PASP, 118, 517
Boselli A. et al., 2011, A&A, 528, A107
Bournaud F., Elmegreen B. G., 2009, ApJ, 694, L158
Cardelli J. A., Clayton G. C., Mathis J. S., 1989, ApJ, 345, 245
Chen C.-W., Côté P., West A. A., Peng E. W., Ferrarese L., 2010, ApJS, 191, 1
Chilingarian I., Cayatte V., Revaz Y., Dodonov S., Durand D., Durret F., Micol A., Slezak E., 2009, Science, 326, 1379
Dey A. et al., 2019, AJ, 157, 168
Drinkwater M., Hardy E., 1991, AJ, 101, 94
Duc P.-A. et al., 2011, MNRAS, 417, 863
Elmegreen B. G., Zhang H.-X., Hunter D. A., 2012, ApJ, 747, 105
Faber S. M., Lin D. N. C., 1983, ApJ, 266, L17
Ferrarese L. et al., 2006, ApJS, 164, 334
Geha M., Guhathakurta P., van der Marel R. P., 2005, AJ, 129, 2617
Graham A. W., Guzmán R., 2003, AJ, 125, 2936
Graham A. W., Driver S. P., Petrosian V., Conselice C. J., Bershady M. A., Crawford S. M., Goto T., 2005, AJ, 130, 1535
Haynes M. P. et al., 2018, ApJ, 861, 49
Huchtmeier W. K., Gopal-Krishna, Petrosian A., 2005, A&A, 434, 887
Huxor A. P., Phillipps S., Price J., 2013, MNRAS, 430, 1956
Janz J., Lisker T., 2008, ApJ, 689, L25
Jedrzejewski R. I., 1987, MNRAS, 226, 747
Kennicutt R. C. Jr, 1998, ARA&A, 36, 189
Khochfar S., Silk J., 2006, ApJ, 648, L21
Kormendy J., Fisher D. B., Cornell M. E., Bender R., 2009, ApJS, 182, 216
Lee J. C. et al., 2009, ApJ, 706, 599
Leitherer C. et al., 1999, ApJS, 123, 3
Lelli F., Verheijen M., Fraternali F., 2014, MNRAS, 445, 1694
Lisker T., 2009, Astronomische Nachrichten, 330, 1043
Loose H. H., Thuan T. X., 1986, in Kunth D., Thuan T. X., Van J. T. T., eds, Star-forming Dwarf Galaxies and Related Objects, Editions Frontie`res in Gif sur Yvette. France, p. 73
Marino R. A. et al., 2013, A&A, 559, A114
Meyer H. T., Lisker T., Janz J., Papaderos P., 2014, A&A, 562, A49
Mihos J. C., Hernquist L., 1994, ApJ, 437, L47
Mihos J. C., Hernquist L., 1996, ApJ, 464, 641
Noeske K. G., Iglesias-Páramo J., Vílchez J. M., Papaderos P., Fricke K. J., 2001, A&A, 371, 806
Nusser A., 2005, MNRAS, 361, 977
Nusser A., Silk J., 2022, MNRAS, 509, 2979
Oser L., Ostriker J. P., Naab T., Johansson P. H., Burkert A., 2010, ApJ, 725, 2312
Papaderos P., Loose H.-H., Thuan T. X., Fricke K. J., 1996, A&AS, 120, 207
Paudel S., Ree C., 2014, ApJ, 796, L14
Paudel S., Sengupta C., 2017, ApJ, 849, L28
Paudel S., Lisker T., Hansson K. S. A., Huxor A. P., 2014, MNRAS, 443, 446
Paudel S. et al., 2017, ApJ, 834, 66
Paudel S., Sengupta C., Yoon S.-J., 2018a, AJ, 156, 166
Paudel S., Smith R., Yoon S. J., Calderón-Castillo P., Duc P.-A., 2018b, ApJS, 237, 36
Pearson S. et al., 2016, MNRAS, 459, 1827
Penny S. J., Pimbblet K. A., Conselice C. J., Brown M. J. I., Grützbauch R., Floyd D. J. E., 2012, ApJ, 758, L32
Privon G. C. et al., 2017, ApJ, 846, 74
Pustilnik S. A., Tepliakova A. L., 2011, MNRAS, 415, 1188
Pustilnik S. A., Kniazev A. Y., Lipovetsky V. A., Ugryumov A. V., 2001, A&A, 373, 24
Ramya S., Kantharia N. G., Prabhu T. P., 2011, ApJ, 728, 124
Rich R. M., Collins M. L. M., Black C. M., Longstaff F. A., Koch A., Benson A., Reitzel D. B., 2012, Nature, 482, 192
Roberts M. S., 1978, AJ, 83, 1026
Sarzi M. et al., 2006, MNRAS, 366, 1151
Sersic J. L., 1968, Atlas de Galaxias Australes, Observatorio Astronomico, Cordoba, Argentina
Stierwalt S., Besla G., Patton D., Johnson K., Kallivayalil N., Putman M., Privon G., Ross G., 2015, ApJ, 805, 2
Straughn A. N. et al., 2015, ApJ, 814, 97
Sung E.-C., Han C., Ryden B. S., Chun M.-S., Kim H.-I., 1998, ApJ, 499, 140
Toloba E. et al., 2014, ApJ, 783, 120
Tremonti C. A. et al., 2004, ApJ, 613, 898
Wellons S. et al., 2015, MNRAS, 449, 361
Zhang H.-X., Puzia T. H., Weisz D. R., 2017, ApJS, 233, 13
Zhang H.-X. et al., 2020a, ApJ, 891, L23
Zhang H.-X. et al., 2020b, ApJ, 900, 152

This paper has been typeset from a TEX/LATEX file prepared by the author.

Monthly Notices of the ROYAL ASTRONOMICAL SOCIETY

MNRAS **520,** L5–L10 (2023) https://doi.org/10.1093/mnrasl/slac159
Advance Access publication 2022 December 12

Early-type dwarf galaxies in the local universe. Evidence of *ex situ* growth

Sanjaya Paudel [1,2]★ Suk-Jin Yoon,[1,2] Jun-Sung Moon [1,3] and Daya Nidhi Chhatkuli[4]

[1]*Department of Astronomy, Yonsei University, Seoul 03722, Republic of Korea*
[2]*Center for Galaxy Evolution Research, Yonsei University, Seoul 03722, Republic of Korea*
[3]*Astronomy Program, Department of Physics and Astronomy, Seoul National University, Seoul 08826, Republic of Korea*
[4]*Central Department of Physics, Tribhuvan University, Kirtipur 44618, Kathmandu, Nepal*

Accepted 2022 December 4. Received 2022 November 8; in original form 2022 July 3

ABSTRACT

We report the discovery of a rare early-type dwarf galaxy (dE), SDSS J125651.47+163024.2 (hereafter, dE1256), possessing a tidal feature that was likely built up by accretion of an even smaller dwarf galaxy. dE1256 is located in a nearly isolated environment, at the outskirt of the Virgo cluster. A detailed morphological examination reveals that the accreted stellar population is mainly deposited in the outer part of dE1256, where the tidal tail is most prominent. The inner part of dE1256 is perfectly modelled with a simple Sérsic function of index n = 0.63 and half-light radius R_h = 0.6 kpc, but in contrast, the entire galaxy has a size of R_h = 1.2 kpc. The mass ratio between the host and the putative accreted dwarf galaxy is calculated to be 5:1, assuming that the observed two components, inner Sérsic and outer tidal tail residual, represent the host's and accreted galaxy's stellar populations, respectively. We suggest that while the accretion contributes only 20 per cent of the overall stellar population, the size of dE1256 grew by a factor of two via the accretion event. Our results provide, for the first time, strong observational evidence that a dE is undergoing a two-phase growth, a common phenomenon for massive galaxies.

Key words: galaxies: dwarf – galaxies: evolution – galaxies: interactions – galaxies: irregular – galaxies: starburst.

1 INTRODUCTION

The size of massive early-type galaxies (Es) has grown up dramatically since z = 3 (Daddi et al. 2005; Trujillo et al. 2007). Detailed theoretical studies have shown that Es have undergone a two-phase formation process (Oser et al. 2010). In the first phase, an initial rapid dissipative gas collapse produces a compact E which primarily hosts *in situ* stars (Khochfar & Silk 2006; Barro et al. 2013; Wellons et al. 2016). In the second, the growth mainly occurs through the accretion of satellite galaxies and the accreted satellite galaxies deposit their stellar population in the outskirt of the primary host, eventually making the host larger in overall size (Naab, Johansson & Ostriker 2009). The fraction of *ex situ* stars is as high as 80 per cent in the case of high-mass Es. It is well established that Es are the products of merged disc galaxies (Springel et al. 2005; Naab et al. 2007; Duc et al. 2015), and galaxy mergers and accretions are fundamental to shape the observable properties of massive galaxies. On the other hand, the lower mass systems, a.k.a., dwarf galaxies, are predominantly made up of *in situ* stars (Cooper et al. 2013; Pillepich et al. 2018; Davison et al. 2020). Thus, the evolution of dwarf galaxies is expected to be influenced by the environment-related mechanism more than the merger or accretion (Boselli & Gavazzi 2006; Kormendy et al. 2009; Lisker 2009; Paudel & Ree 2014).

Large-scale observational studies reported that early-type dwarf galaxies (dEs) are primarily found in cluster and group environments, supporting their origin as the product of the environment (Binggeli, Tammann & Sandage 1987; Geha et al. 2012). However, several recent deep-imaging surveys revealed that some dEs might have experienced recent merger or accretion (Paudel et al. (2017, 2018).

This work presents a detailed morphological study on a dE, SDSS J125651.47+163024.2 (hereafter, dE1256), located in an almost isolated environment. dE1256 possesses a signature of ongoing interaction with an even smaller satellite galaxy whose stellar mass was once five times lower than that of dE1256. dE1256 has a luminosity M_g = −14.88 mag, which is similar to the luminosity of previously discovered shell-feature merging dwarfs (VCC 1361 and VCC 1668) in the Virgo cluster (Paudel et al. 2017, hereafter, P17).

2 ENVIRONMENT AND IDENTIFICATION

We have conducted a systematic search of low-mass early-type galaxies in diverse environments (clusters, groups, and fields) of the local volume (z < 0.01). For this purpose, we visually inspected a large-sky area observed by the SDSS and Legacy imaging surveys (Aihara et al. 2011; Dey et al. 2019), and identified 5054 dEs which are located in clusters, groups, and fields. The resultant main catalogue will be published in Paudel et al. (2022, *submitted*). The strength of the catalogue lies in detailing the morphological characteristics like tidal, merger, diffuse, and nucleated or non-nucleated features. We found that a very small fraction (∼0.3 per cent) of dEs possess the morphological features that could possibly originate from a merger. Among them, dE1256 is unique, in that, it shows signs of ongoing accretion of a smaller dwarf galaxy (Fig. 1).

dE1256 is located at z = 0.004 in the north-east of the Virgo cluster at an angular distance of ∼8° from M87, and has no significant massive neighbour (Fig. 3). Based on the NED, the nearest companion galaxy is NGC 4758, which is located at a sky-

★ E-mail: sjyoon0691@yonsei.ac.kr

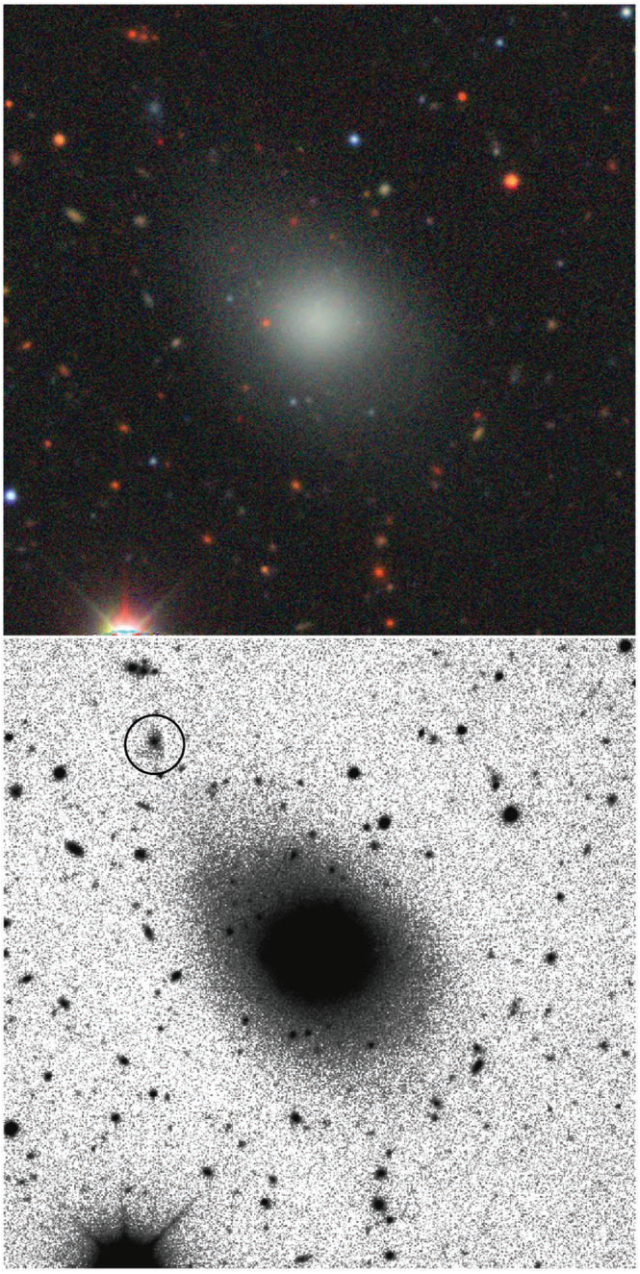

Figure 1. dE1256 seen from the Legacy survey images. We show a *g*–*r*–*z* combined colour image in the top panel, which we obtained from the Legacy survey viewer tool. The bottom panel gray scale image is produced from coadding *g*–*r*–*z* band images which have a field of view of 2.5 arcmin × 2.5 arcmin. The colour stretching is arbitrarily chosen to make the best view of low-surface brightness features. We identify a possible disrupted companion by a black circle of 7 arcsec radius.

projected distance of 370 kpc from the centre of dE1256 in the south-west direction. NGC 4758 is a star-forming low-mass galaxy of $M_B = -17.64$ mag and has a radial velocity similar to that of dE1256, i.e. 1245 km s^{-1}. According to the main catalogue, dE1256 is a member of the Virgo cluster and has an assigned distance of 16.5 Mpc. It is a non-nucleated galaxy with a mean surface brightness of 22.3 mag arcsec^{-2}.

3 DATA ANALYSIS

A view of dE1256 in the optical band images is shown in Fig. 1. We show a *g*–*r*–*z* combined colour image in the top panel, which we obtained from the Legacy survey viewer tool. To get a higher signal of the low-surface brightness component, we coadded the legacy *g*-, *r*-, and *z*- band images, and show the resulting image in the lower panel. The extension of low-surface brightness component toward upper north-east direction is clear. After a careful inspection of the asymmetric tidal feature, we spot a possible disrupted companion located at an angular distance of 1 arcmin (black circle) from the centre of dE1256.

In Fig. 2, we show the comparative picture of the Legacy (middle) and SDSS (right) images. To make a quantitate comparison, we also show a coadded high-S/N image as a reference in left-most panel, where we overlaid colour (green, red, magenta, blue, and cyan) contours representing surface brightness levels of 28, 27, 26, 25, and 24 mag arcsec^{-2}, respectively. It is clear that the low-surface brightness component can be detected as low as 27 mag arcsec^{-2} level in the coadded image. While looking single filter *g*-band image in the middle and right-hand panels, the legacy image is comparatively deeper than the SDSS and indeed, the extended tidal feature is much more evident in the Legacy image. However, the similar appearance of the low-surface brightness feature around dE1256 in the two images taken by two independent surveys, i.e. the SDSS and the Legacy, confirms that the observed low-surface brightness asymmetric tidal tail is not an artefact of image processing or instrumental defect.

In order to perform a detailed analysis of the morphology and structure of dE1256, we used the SDSS-III images (Aihara et al. 2011). Although the Legacy images are deeper than the SDSS, we noticed that the sky-background subtraction is not as perfect as the SDSS. In the stacked and mosaiced Legacy images, the sky background seems over-subtracted, which creates an artificial decrease of the count at the outer parts of galaxies. The effect is severe for extended low-surface brightness objects. Therefore, we only used the SDSS images for the surface photometry and derived structural parameters.

With help of the IRAF *ellipse* task (Jedrzejewski 1987), we performed surface photometry on the *r*-band image of dE1256. Before running the ellipse task, we subtracted the sky-background as described in Paudel, Duc & Ree (2015) and manually masked background and foreground unrelated objects. Fitting ellipses to the isophotes of the surface brightnesses, we extracted azimuthally averaged radial surface brightness profiles along the major axis. In doing so, the centre and position angle of the ellipse were held fixed. The ellipticity was allowed to vary. The galaxy centre was calculated using the task *imcntr*, and input ellipse parameters were determined applying several iterative runs of the *ellipse* task.

In the lower panel of Fig. 4, we present the *r*-band major axis light profile of dE1256, which clearly shows a break at ∼15 arcsec (or $\mu_r = 24.7$ mag arcsec^{-2}) attributing to the presence of a dominant tidal tail at that region. We modelled the observed *r*-band major axis light profile with a Sérsic function (Sérsic 1963). Since the asymmetrical tidal feature dominates the outer part of dE1256, we skipped this region during the modelling. We only used the inner part (before the break) using a surface brightness cut of $\mu_r < 23.7$ mag arcsec^{-2}. With the help of χ^2-minimization scheme, we obtained a best-fitting Sérsic function with an index $n = 0.63$ and a half-light radius $R_h = 0.6$ kpc. These values are typically representative of normal dE of luminosity $M_g \simeq -13.5$ mag (Janz et al. 2014).

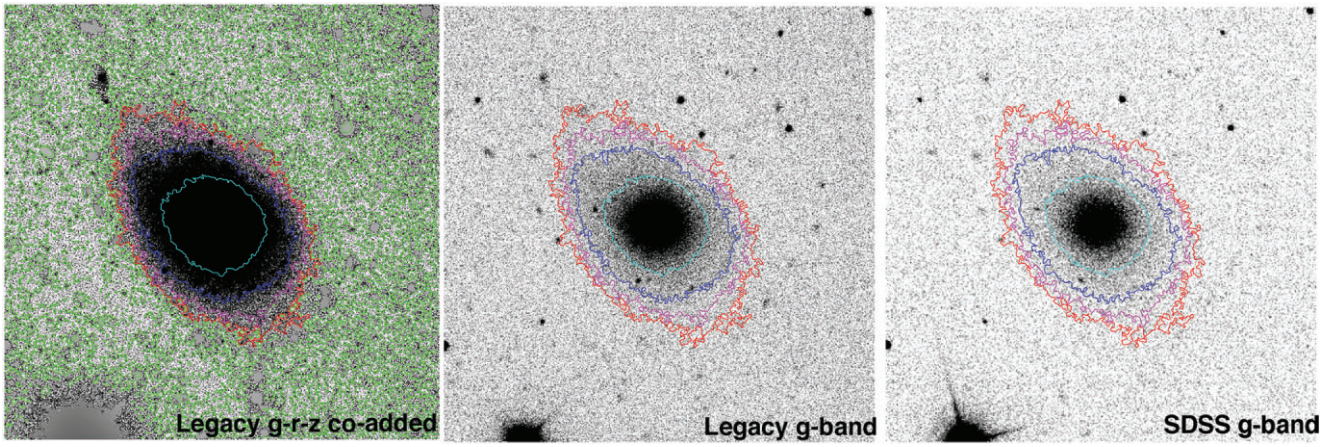

Figure 2. We show a coadded *g*–*r*–*z* high S/N image in the left-hand panel, where the colour (green, red, magenta, blue, and cyan) contours represent surface brightness levels of 28, 27, 26, 25, and 24 mag arcsec^{-2}, respectively. In this image, all unrelated foreground and background sources are masked. To make a comparison between Legacy and SDSS image, we show their *g*-band image in the middle and right-hand panel, respectively. We also show a colour contour as a visual guidance, which was prepared in coadded image in the leftmost panel. It is clear that the Legacy survey image is deeper than the SDSS where the low-surface brightness component is prominent.

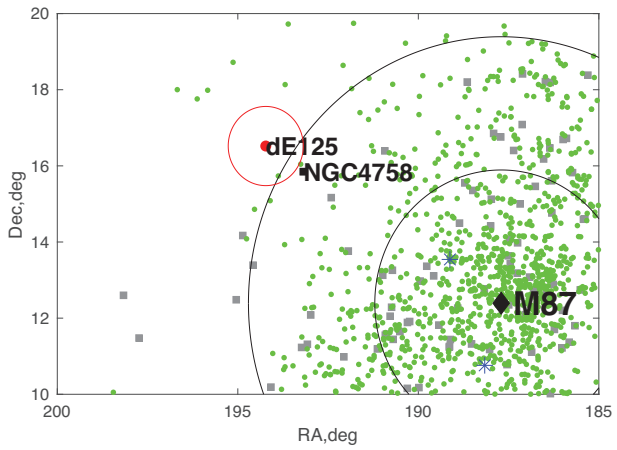

Figure 3. Location of dE1256, next to the Virgo cluster. Green dots and gray squares represent dEs and bright galaxies, respectively. The centre of the Virgo cluster, position of M87, is marked with a large diamond symbol and the two black concentric rings represent sky-projected radii of 1 and 2 Mpc from M87. We highlight an area of 300 kpc radius around dE1256 with a red circle. The position of NGC 4758 is marked by a black-square symbol. With two blue asterisks, we also mark the positions of the Virgo cluster's shell-featured dEs which were studied in P17.

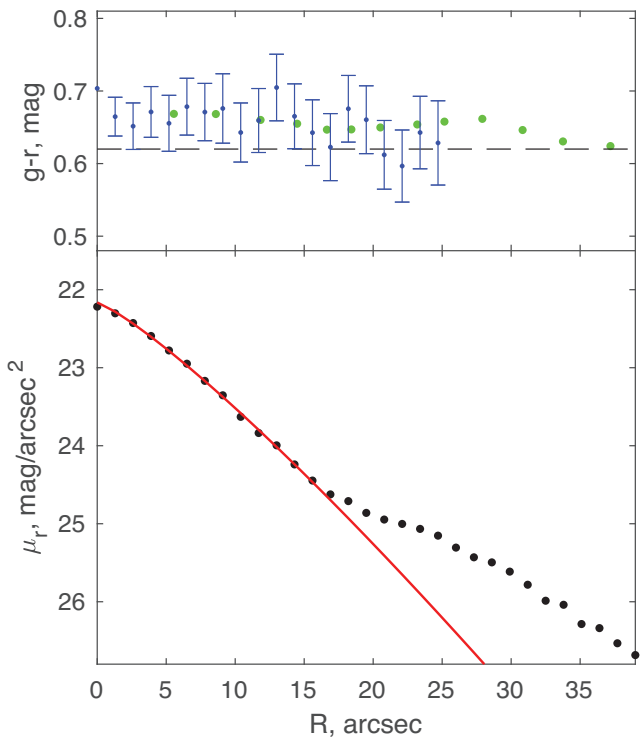

Figure 4. (Top panel) The *g*–*r* colour profile of dE1256 along its major axis (blue dots with error bars). We also derived the colour profile (green dots) by selecting 5 arcsec × 5 arcsec box region along the major axis. The estimated error bar on these green points is in order of 0.02 mag which is significantly low compared to that of the blue dots. The black dash horizontal line represents the overall *g*–*r* colour of the putative disrupted companion. (Bottom) The SDSS *r*-band surface brightness profile of dE1256 along its major axis. We show best-fitting Sérsic profile for R ≤ 15 arcsec in red (n = 0.63 and R_h = 0.6 kpc).

We show the $g - r$ colour profile along the major axis in the upper panel of Fig. 4. The colour profile was derived from the azimuthally averaged light profiles obtained from ellipse fitting in the *g* and *r* bands. To increase the signal-to-noise ratio in derived colour indices, we also calculated the colour profile along the major axis by selecting the 5 arcsec × 5 arcsec box region along the major axis shown by green dots. The horizontal dash line represents the colour index of the putative disrupted companion. We find that *g*–*r* of dE1256, in general, declines at large galactocentric radii, and it matches fairly well with the colour of the disruptive companion.

From a morphological perspective, dE1256 is likely undergoing a minor merger event. Although it is not trivial to calculate the merger ratio from the remnant, we used a two-component model – one is an undisturbed host at the centre and the other is a destroyed tidal tail – to calculate the approximate stellar mass in each component. The supposed primary galaxy, which has an undisturbed inner component, is modelled with a Sérsic function, and thus the best-fitting inner component model represents the host galaxy. And then the leftover tidal feature (residual) is assumed to

be entirely built up by an accreted minor galaxy. The flux ratio between the two components is 0.2, and considering their similar stellar population properties suggested by their similar *g–r* colour, the flux ratio directly corresponds to stellar mass ratio. However, there is a reasonable chance that both components' stellar populations mix at any galactocentric distance. We might have underestimated the contribution of dE1256's stellar population as we used only its inner part to calculate the mass.

Because of the complexity in the observed light profile of dE1256, no overall structural parameters can be derived using a simple Sérsic function modelling. To measure overall photometric properties, we used a non-parametric approach, i.e. the Petrosian method (J08; Janz & Lisker 2008). Using the Petrosian method, the estimated value of total luminosity and half-light radius are $M_g = -14.88$ mag and $R_h = 1.2$ kpc, respectively. It has *g–r* colour index of 0.66 mag, a typical colour index of dEs of $M_g \simeq -14.88$ mag (Lisker, Grebel & Binggeli 2008; Janz & Lisker 2009). The survived part of the possible companion has a total luminosity of $M_g = -8.94$ mag, and it has a *g–r* colour of 0.61 mag. We calculate the stellar masses using a calibration provided by Zhang, Puzia & Weisz (2017) for the *g–r* colour. The calculated stellar masses of dE1256 and the companion are 1.3×10^8 and 4.8×10^5 $M_\odot$, respectively.

We find that the SDSS targeted the host galaxy dE1256 for spectroscopic observation. As expected, the SDSS fiber spectrum shows no emission in the Balmer lines. We derived simple stellar population (SSP) properties by fitting the SDSS spectrum with an SSP model. To estimate the SSP parameters, we followed a similar procedure that we employed in Paudel et al. (2014). The procedure uses a publicly available full-spectrum fitting tool ULySS (Koleva et al. 2009), which compares the observed spectrum with the SSP models of Vazdekis et al. (2010). The SSP age and metallicity of dE1256, derived based on the SDSS fiber spectroscopy, is 6.2 ± 1.2 Gyr and $\log(Z/Z_\odot) = -0.26 \pm 0.07$ dex, respectively.

Indeed, the SDSS fiber spectroscopy observes only the central 3 arcsec region of a galaxy, and therefore the derived stellar population properties pertain to the inner component. The typical survival time of a tidal tail is at most a couple of Giga years (Mancillas et al. 2019), and a significantly larger SSP age than the tidal tail survival time suggests that dE1256 was already quenched before the interaction.

4 SUMMARY AND DISCUSSION

We have presented a case of an interacting dwarf galaxy system in a nearly isolated environment. From our primary catalogue of 5405 dEs, there are only 13 dEs that are classified as merger remnants, and among them, only dE1256 exhibits a feature other than the shell. Paudel et al. (2017) have shown that symmetric shell features are more likely a product of an equal mass merger with a head-on collision, where the stellar populations of both interacting galaxies can redistribute homogeneously at any galactocentric radii. Indeed, the tidal tail in dE1256 tells a different story presenting a unique perspective on growth of a low-mass galaxy with the minor merger, which mainly deposits the stellar populations at the outer parts. The growth of galaxies through hierarchical merging is a natural phenomenon of our well-known ΛCDM cosmology (e.g. Springel et al. 2005). However, at the lower mass scale, it has been shown through observation and theory, that the galaxy–galaxy merger is a rare phenomenon (e.g. De Lucia et al. 2006).

Paudel et al. (2018) presented an extensive survey of merging dwarf galaxies in the local universe and showed that the dry merger between dwarf galaxies is a rare phenomenon. There are only three early-type merging dwarfs out of 177, and dE1256 is one of them. On the other hand, there are three shell feature dEs in the Virgo cluster and dE1256 is the fourth dE that possesses the tidal feature originating from the dwarf–dwarf merger.

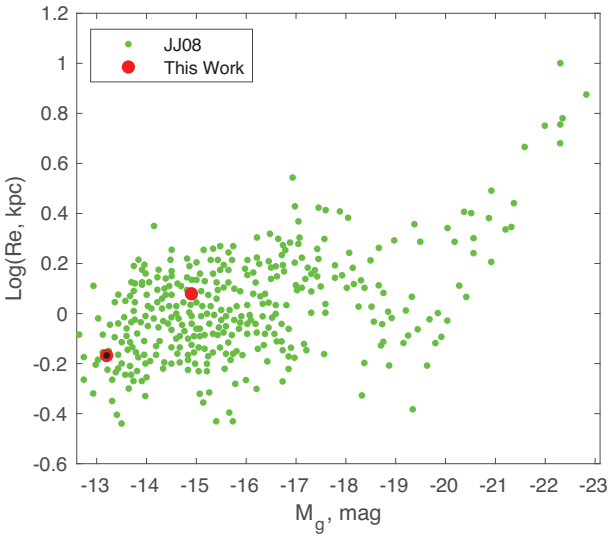

Figure 5. The size–magnitude relation of early-type galaxies. The large red symbol represents the entire body of dE1256 and the same symbol with a black dot is for its inner Sérsic-profiled component. The comparison sample (small green symbols) is taken from J08.

To quantify the merger parameter – namely merger ratio, we have used a simple approach fitting the galaxy light profile into two components model – one inner primary and another outer secondary. We assume that the outer secondary component is entirely built up by the accretion of another dwarf. We know that dEs possess multicomponent surface brightness profile (Jerjen, Kalnajs & Binggeli 2000; Janz et al. 2014; Lee et al. 2018), and there are as high as 60 per cent dEs which have such multicomponent features at the brighter end of their population (Lisker et al. 2007). The origin of such a multicomponent light profile, in general, is attributed to the presence of a disc feature, like a bar or a spiral arm, an indication of the environmental transformation of a late-type galaxy to dE through the mechanism such as ram-pressure stripping or tidal harassment (Boselli & Gavazzi 2006; Smith et al. 2021). dE1256 inner core looks rather regular and non-nucleated, and the outer extended tidal tail is asymmetric. Therefore, we have interpreted that the observed multicomponent light profile with outer tidal features originated from the tidal disruption of a smaller dwarf galaxy.

In Fig. 5, we show the size–magnitude relation of dEs, where the comparison sample is taken from Janz & Lisker (2008). We see two different regimes of the relation; in the bright part, the relation is steep, and in the faint part, the relation is nearly constant. As identified by the red circle, dE1256 falls in the faint regime, where the data point shows a large scatter. The red circle with a black dot represents an inner component that is significantly smaller than the overall size of dE1256 (shown as the red circle). We find that while the accretion contributes only 20 per cent of the overall stellar population, the size of dE1256 increases by a factor of two after the accretion.

Fig. 6 displays the derived *ex situ* stellar mass fraction of dE1256 as a function of galactocentric radius. For the comparison, we overplot the radial *ex situ* fraction derived from the TNG50 simulation of the ILLUSTRISTNG project (Nelson et al. 2019a, b; Pillepich et al. 2019). For this, we produced stacked profiles of the *ex situ* mass

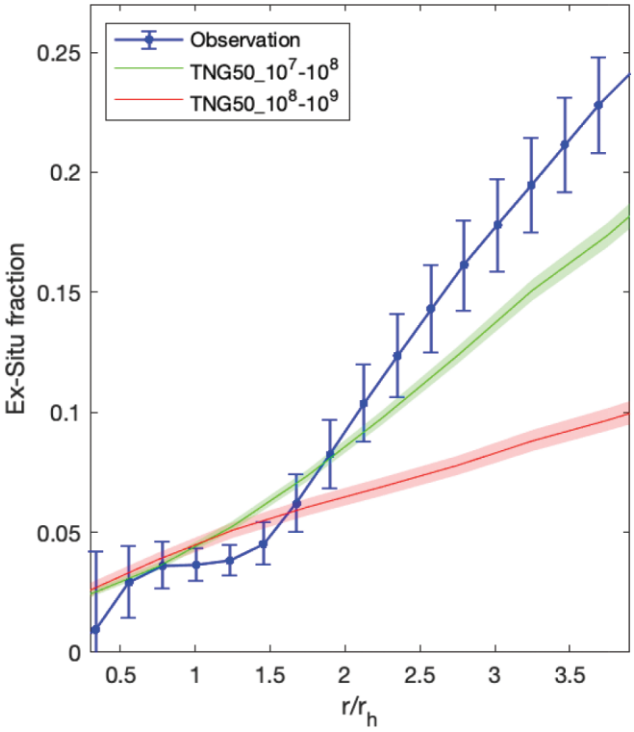

Figure 6. The radial profile of the *ex situ* stellar mass fraction for early-type galaxies. The blue line represents dE1256. The error bar represents uncertainty in photometric measurement which does not include the uncertainty in the Sérsic modelling. We show the result of TNG50 simulation in red and green, which represent binned sample of $M_{stellar} = 10^7 \sim 10^8\,M_\odot$ (7047 galaxies) and $M_{stellar} = 10^8 \sim 10^9\,M_\odot$ (2546 galaxies), respectively. The shade regions show the 95 per cent confidence intervals estimated by 1000 bootstrap resamplings of the simulated galaxies. See Section 4 for the detail.

fraction of all early-type subhaloes in stellar mass bins of $M_{stellar} = 10^7 \sim 10^8\,M_\odot$ and $M_{stellar} = 10^8 \sim 10^9\,M_\odot$, respectively. The subhaloes are classified as early-type subhaloes when their specific star-formation rate (sSFR) is as low as $\log(\mathrm{sSFR\,yr^{-1}}) < -10$. *Ex situ* stars were defined as those formed outside the main progenitor, following the method of Rodriguez-Gomez et al. (2016) and Davison et al. (2020). We discarded a small fraction of stellar particles formed at very early times when the main progenitor has not yet been detected. We find that our estimated *ex situ* stellar-mass profile for dE1256 agrees, in general, with the simulated galaxy *ex situ* stellar mass profiles. Compared to the TNG50 result, it seems that we have slightly underestimated the *ex situ* stellar mass fractions at the inner region and overestimated at the outer region. Such deviation can be a consequence of our simple assumption that the host dominates the inner component and the disrupted dwarf satellite primarily deposits its stellar population at the outer radii. Moreover, the simulation estimates the *ex situ* fraction based on the actual merging history, yet in observation, we use a simple assumption that the observed dual component light profile is due to the different stellar populations of the host and satellite. Compared to the simulation result, the high *ex situ* fraction at the outer region of dE1256 is atypical, pointing to an ongoing tidal accretion of a satellite.

ACKNOWLEDGEMENTS

SP and S-JY, respectively, acknowledge support from the New Researcher Program (Shinjin grant no. 2019R1C1C1009600) and the Midcareer Researcher Program (no. 2019R1A2C3006242) through the National Research Foundation of Korea.

This study is based on archival images and spectra from the Sloan Digital Sky Survey and images from the Legacy survey. The full acknowledgment for the SDSS can be found at http://www.sdss.org/collaboration/credits.html. Funding for the SDSS has been provided by the Alfred P. Sloan Foundation, the Participating Institutions, the National Science Foundation, the U.S. Department of Energy, the National Aeronautics and Space Administration, the Japanese Monbukagakusho, the Max Planck Society, and the Higher Education Funding Council for England. The SDSS website is http://www.sdss.org/.

The Legacy Surveys consist of three individual and complementary projects: the Dark Energy Camera Legacy Survey (DECaLS; NOAO Proposal ID # 2014B-0404; PIs: David Schlegel and Arjun Dey), the Beijing-Arizona Sky Survey (BASS; NOAO Proposal ID # 2015A-0801; PIs: Zhou Xu and Xiaohui Fan), and the Mayall *z*-band Legacy Survey (MzLS; NOAO Proposal ID # 2016A-0453; PI: Arjun Dey). DECaLS, BASS, and MzLS together include data obtained, respectively, at the Blanco telescope, Cerro Tololo Inter-American Observatory, National Optical Astronomy Observatory (NOAO); the Bok telescope, Steward Observatory, University of Arizona; and the Mayall telescope, Kitt Peak National Observatory, NOAO. The Legacy Surveys project is honoured to be permitted to conduct astronomical research on Iolkam Du'ag (Kitt Peak), a mountain with particular significance to the Tohono O'odham Nation. The full acknowledgement for the Legacy Surveys can be found at https://www.legacysurvey.org/acknowledgment.

The ILLUSTRISTNG simulations were undertaken with compute time awarded by the Gauss Centre for Supercomputing (GCS) under GCS Large-Scale Projects GCS-ILLU and GCS-DWAR on the GCS share of the supercomputer Hazel Hen at the High Performance Computing Center Stuttgart (HLRS), as well as on the machines of the Max Planck Computing and Data Facility (MPCDF) in Garching, Germany

5 DATA AVAILABILITY

Most of the data underlying this article are publicly available. The derived data generated in this research will also be shared on reasonable request to the corresponding author.

REFERENCES

Aihara H. et al., 2011, ApJS, 193, 29
Barro G. et al., 2013, ApJ, 765, 104
Binggeli B., Tammann G. A., Sandage A., 1987, AJ, 94, 251
Boselli A., Gavazzi G., 2006, PASP, 118, 517
Cooper A. P., D'Souza R., Kauffmann G., Wang J., Boylan-Kolchin M., Guo Q., Frenk C. S., White S. D. M., 2013, MNRAS, 434, 3348
Daddi E. et al., 2005, ApJ, 626, 680
Davison T. A., Norris M. A., Pfeffer J. L., Davies J. J., Crain R. A., 2020, MNRAS, 497, 81
De Lucia G., Springel V., White S. D. M., Croton D., Kauffmann G., 2006, MNRAS, 366, 499
Dey A. et al., 2019, AJ, 157, 168
Duc P.-A. et al., 2015, MNRAS, 446, 120
Geha M., Blanton M. R., Yan R., Tinker J. L., 2012, ApJ, 757, 85
Janz J., Lisker T., 2008, ApJ, 689, L25
Janz J., Lisker T., 2009, ApJ, 696, L102
Janz J. et al., 2014, ApJ, 786, 105
Jedrzejewski R. I., 1987, MNRAS, 226, 747
Jerjen H., Kalnajs A., Binggeli B., 2000, A&A, 358, 845
Khochfar S., Silk J., 2006, ApJ, 648, L21
Koleva M., Prugniel P., Bouchard A., Wu Y., 2009, A&A, 501, 1269

Kormendy J., Fisher D. B., Cornell M. E., Bender R., 2009, ApJS, 182, 216
Lee Y., Park H. S., Kim S. C., Moon D.-S., Lee J.-J., Kim D.-J., Cha S.-M., 2018, ApJ, 859, 5
Lisker T., 2009, Astron. Nachr., 330, 1043
Lisker T., Grebel E. K., Binggeli B., Glatt K., 2007, ApJ, 660, 1186
Lisker T., Grebel E. K., Binggeli B., 2008, AJ, 135, 380
Mancillas B., Duc P.-A., Combes F., Bournaud F., Emsellem E., Martig M., Michel-Dansac L., 2019, A&A, 632, A122
Naab T., Johansson P. H., Ostriker J. P., Efstathiou G., 2007, ApJ, 658, 710
Naab T., Johansson P. H., Ostriker J. P., 2009, ApJ, 699, L178
Nelson D. et al., 2019a, Comput. Astrophys. Cosmology, 6, 2
Nelson D. et al., 2019b, MNRAS, 490, 3234
Oser L., Ostriker J. P., Naab T., Johansson P. H., Burkert A., 2010, ApJ, 725, 2312
Paudel S., Ree C. H., 2014, ApJ, 796, L14
Paudel S., Lisker T., Hansson K. S. A., Huxor A. P., 2014, MNRAS, 443, 446
Paudel S., Duc P. A., Ree C. H., 2015, AJ, 149, 114
Paudel S. et al., 2017, ApJ, 834, 66 (P17)
Paudel S., Smith R., Yoon S. J., Calderón-Castillo P., Duc P.-A., 2018, ApJS, 237, 36
Pillepich A. et al., 2018, MNRAS, 475, 648
Pillepich A. et al., 2019, MNRAS, 490, 3196
Rodriguez-Gomez V. et al., 2016, MNRAS, 458, 2371
Sérsic J. L., 1963, Bol. Asociacion Argentina Astron. La Plata Argentina, 6, 41
Smith R. et al., 2021, ApJ, 912, 149
Springel V. et al., 2005, Nature, 435, 629
Trujillo I., Conselice C. J., Bundy K., Cooper M. C., Eisenhardt P., Ellis R. S., 2007, MNRAS, 382, 109
Vazdekis A., Sánchez-Blázquez P., Falcón-Barroso J., Cenarro A. J., Beasley M. A., Cardiel N., Gorgas J., Peletier R. F., 2010, MNRAS, 404, 1639
Wellons S. et al., 2016, MNRAS, 456, 1030
Zhang H.-X., Puzia T. H., Weisz D. R., 2017, ApJS, 233, 13

This paper has been typeset from a TEX/LATEX file prepared by the author.

The Astronomical Journal, 159:141 (9pp), 2020 April https://doi.org/10.3847/1538-3881/ab722f

MCG+07-20-052: Interacting Dwarf Pair in a Group Environment

Sanjaya Paudel[1], Chandreyee Sengupta[2], Suk-Jin Yoon[1], and Daya Nidhi Chhatkuli[3]
[1] Department of Astronomy and Center for Galaxy Evolution Research, Yonsei University, Seoul 03722, Republic of Korea; sjyoon0691@yonsei.ac.kr
[2] Purple Mountain Observatory, Chinese Academy of Sciences, Nanjing, 210034, People's Republic of China
[3] Central Department of Physics, Tribhuvan University, Kirtipur, Kathmandu, Nepal
Received 2019 September 17; revised 2020 January 29; accepted 2020 January 30; published 2020 March 3

Abstract

We present an observational study of the interacting pair of dwarf galaxies, MCG+07-20-052, in the vicinity of Milky Way mass spiral galaxy NGC 2998. MCG+07-20-052 is located at a sky-projected distance of 105 kpc from NGC 2998 and the two have a relative line-of-sight velocity of 60 km s^{-1}. We observed tidal tail-like extensions on both members (D1 and D2) of the interacting pair MCG+07-20-052. The interacting dwarf galaxies, D1 and D2, have *B*-band absolute magnitudes of −17.17 and −17.14 mag, respectively, and D2 is significantly bluer than D1. We obtained H I 21 cm line data of the NGC 2998 system using the Giant Metrewave Radio Telescope to get a more detailed view of the neutral hydrogen (H I) emission in the interacting dwarf galaxies and in the galaxy members of the NGC 2998 group. Evidence of a merger between the dwarf galaxies in the MCG+07-20-052 is also present in the H I kinematics and morphology where we find that H I is mostly concentrated around D2, which also shows a higher level of star-forming activity and a bluer *g*–*r* color index compared to D1. In addition, we detect extended tenuous H I emission around another member galaxy, NGC 3006, located close to the MCG+07-20-052 pair at a sky-projected distance of 41 kpc. We compare here our results from the MCG+07-20-052 pair NGC 2998 system with other known Large Magellanic Cloud/Small Magellanic Cloud/Milky Way-type systems and discuss the possible origin of the dwarf–dwarf interaction.

Unified Astronomy Thesaurus concepts: Draco dwarf galaxy (408); Interacting galaxies (802); Star formation (1569); H I line emission (690)

1. Introduction

The theory of large-scale structure formation with Λ cold dark matter cosmology predicts that a major mass assembly of galaxies happens in a hierarchical way and in this hierarchy low-mass galaxies play a crucial role. They are, indeed, the dominant population at all redshifts and simulations predict that dwarf galaxies experience on average three major mergers in their lifetime (Fakhouri et al. 2010). While dwarf–dwarf mergers were expected to be more common in the early universe (Klimentowski et al. 2010; Fitts et al. 2018), recent observations have shown that they are also present in current epoch. The interaction between dwarf galaxies in isolated environments are frequently reported, however they are rare around a massive host (Stierwalt et al. 2015; Paudel et al. 2018a; Kado-Fong et al. 2020).

Massive galaxy mergers have been studied in great detail in both observation and numerical simulations (Barnes 1992; Naab & Ostriker 2009; Duc et al. 2011). The dwarf–dwarf interactions, on the other hand, are only starting to be explored as a population (Stierwalt et al. 2015; Pearson et al. 2016; Besla et al. 2018; Paudel et al. 2018a). This is partly because such systems are possibly not common in the local universe or they are fainter, which makes them harder to detect. The presence of tidal tails, shells, and streams have been studied in great detail around massive galaxies, which provides an unequivocal proof of merger origin of these galaxies (Duc et al. 2015). However for dwarf galaxies, such observations are few. The small shell-like feature at the Fornax dwarf galaxy detected by Coleman et al. (2004) indicated merger and recently Paudel et al. (2017) presented a detailed analysis of shell feature early-type dwarf galaxies in the Virgo cluster suggesting merger origin.

Gas-rich mergers of massive galaxies leading to the bursts of star formation play an important role in the stellar mass growth and morphological evolution (Mihos & Hernquist 1994; Wilman et al. 2013). However, the physical processes that trigger enhanced star formation activity in the low-mass galaxies are still not well understood. Often to explain starburst activity in blue compact dwarf galaxies (BCDs), similar processes of massive galaxies, e.g., the mergers and interactions, have been proposed (Noeske et al. 2001; Bekki 2008; Lee et al. 2009; Privon et al. 2017). For the Large and Small Magellanic clouds (LMC and SMC), interaction is a frequently mentioned reason in the literature to explain the enhanced star formation activity (Harris & Zaritsky 2009; Glatt et al. 2010). The LMC–SMC system is located in the group environment in vicinity of the Milky Way (MW). A number of studies have shown that such interaction in the group environment is not common and the pair can be quickly disrupted by the host tidal potential (Robotham et al. 2012; Deason et al. 2014). In this paper, we present yet another dwarf–dwarf interacting system (MCG+07-20-052), located in the vicinity of NGC 2998.

2. Interacting Dwarf

As our primary interest is to find low-mass interacting galaxies in the nearby universe, we carried out a systematic search for such objects in the local volume ($z < 0.02$). We published the most extended catalog of interacting dwarf galaxies (Paudel et al. 2018b), which comprises 177 interacting dwarf galaxies. These galaxies are selected by the visual inspection of color images of the two wide-field optical surveys (SDSS-III and the Legacy Survey). We select them according to their observed low surface brightness features that are likely the result of an interaction between dwarf galaxies. The parent sample of the dwarf galaxies is selected from NASA Extragalactic Database (NED) with a magnitude cut of $M_r > -19$ mag. We found that a significant majority of

interacting dwarfs are located in the isolated environment and less then 10% of them are located in the vicinity of giant, MW mass, or more massive galaxies. Recently, Kado-Fong et al. (2020) also published a sample of interacting dwarf galaxies where they study the star formation and host properties. They also found that dwarf galaxies that host tidal debris are systematically blue, indicating merger-induced star formation, which agrees with the findings of Paudel et al. (2018b) where an overwhelming majority of interacting dwarf galaxies are star forming and blue.

To maximize the number of systems where the interacting galaxies are in spatial and kinematic proximity similar to the LMC–SMC–MW, we defined an LMC–SMC–MW analog as the interacting dwarf located within a 300 kpc sky-projected distance from the MW mass galaxy with a relative line-of-sight velocity less than 300 km s^{-1}. Indeed this simple criteria does not entirely reflect the actual LMC–SMC orbital and spatial properties. LMC and SMC are located relatively close, <60 kpc, to the MW compared to our 300 kpc projected distance of an interacting dwarf from the host. One of the main motivations for using this criteria is that we do not have three-dimensional information of our system whereas in the case of LMC and SMC, we know their detailed spatial and orbital information in six dimensions.

Among the LMC–SMC–MW analogs found using our criteria, we selected a few systems to study further in detail with H I 21 cm observations. MCG+07-20-052 is the second object in this series. Previously, we studied the UGC 4703 interacting pair near the isolated spiral NGC 2718 (Paudel & Sengupta 2017), where we discussed the similarity of UGC 4703 pair galaxies to the LMC–SMC system.

2.1. MCG+07-20-052

MCG+07-20 is located at the sky position of R.A. = 09:49:06.46, decl. = +44:02:54.35 and a redshift of z = 0.01575. It is an interacting pair of star-forming dwarf galaxies located in a group environment. The most massive galaxy in the group, NGC 2998, is an MW mass spiral. The NGC 2998 group is a relatively dense group that has at least seven member galaxies of stellar mass larger than 10^8 $M_\odot$ within the 300 kpc sky-projected radius and relative line-of-sight radial velocity ±300 km s^{-1} from the central galaxy. NGC 2998. MCG+07-20-052 is the nearest neighbor to the spiral galaxy NGC2998 at a sky-projected distance of 105 kpc[4] and they have a relative line-of-sight radial velocity of 60 km s^{-1}.

3. Data Analysis

3.1. Analysis of Archival Data

Optical band photometric measurements were done in the archival images available at the Sloan Digital Sky Survey (SDSS)-III Data Archive Server (Abazajian et al. 2009). Although deeper optical images are also available from the Legacy survey (Blum et al. 2016), we did not use them for the photometric measurement because their flux calibration and sky-background subtraction are not as good as the SDSS images. In this paper, we used the Legacy survey images only for display purpose. The SDSS images were already bias-subtracted, flat-field-corrected, sky-subtracted, and flux-calibrated. We used a tool provided by the SDSS-III to create a mosaic image with a large field of view and no further effort has been made on the image reduction part. However, we used a simple and similar approach to subtract the sky-background count as in our previous publications (Paudel et al. 2018b, 2018a).

In Figure 1, we show the Legacy $g-r-z$ combined tri-color image with a field of view of $14' \times 15'$ around NGC 2998 that covers all member galaxies of the group. MCG+07-20-052 is located in between the NGC 3006 and NGC 2998 and two tidal tail-like extensions can be seen emanating from the interacting dwarf pair along the direction of NGC 2998. The sky-projected separation between NGC 3006 and MCG+07-20-052 is 41 kpc and the relative line-of-sight velocity between the two is 100 km s^{-1}. The relative line-of-sight velocities of D1 and D2 from NGC 2998 are 18 and 59 km s^{-1}, respectively.

In Figure 2, we show a zoomed-in region around MCG+07-20-052 and NGC 3006. We named the two interacting dwarf galaxies in MCG+07-20-052 pair as D1 and D2 located to the east and west respectively. Their sky-projected separation is 7.5 kpc, which we measured calculating the centroid of each individual, see the cross marks at Figure 2. Although both galaxies look like typical blue star-forming galaxies, the observed color distribution shows that the main body of D1 is slightly redder and smooth. On the other hand, the main body of D2 is clumpy and its morphology mimics a typical tadpole galaxy with a prominently blue star-forming head and a low surface brightness tail (Elmegreen et al. 2012). A careful look at NGC 3006 reveals a low surface brightness (slightly above the detection limit) extension toward MCG+07-20-052, which is significantly blue compared to the main body of the galaxy. The region has been marked with a dashed line in Figure 2.

To measure the photometric parameters of each individual galaxy, we performed aperture photometry in the SDSS g- and $r-$band filter images. We chose different aperture sizes for each individual galaxy depending on their extension, but kept them fixed for different filters. The sizes of apertures were selected visually and they were wide enough to secure all the flux in the region of interest. Before the doing aperture photometry, we masked all unrelated foreground and background objects manually. Foreground Galactic extinction correction was done by applying an extinction map of Schlafly & Finkbeiner (2011) and no correction has been made for internal extinction and cosmological deeming, the later being actually insignificant.

The result of the photometric measurements are listed in Table 1. We converted the SDSS g-band magnitudes to B-band magnitudes using an equation, $B = g + 0.227 \times (g - r) - 0.337$, provided by the SDSS color transformation tool.[5] To derive the stellar mass, we used the r–band magnitude with an appropriate mass-to-light ratio (M/L). The M/L is obtained using $\log(M/L) = -0.306 + 1.097 \times (g - r)$. This assumes a simple stellar population with a single burst of star formation to derive a relation between the mass-to-light ratio and galaxy color. Indeed, galaxy star formation histories are complex. However, it is shown that scatter in the mass-to-light ratio derived from different star formation history for a given color is ∼0.2 dex, see Section 4.3 of Zhang et al. (2017). Therefore, we consider ±0.2 dex as a typical conservative error on our stellar mass estimates.

[4] We use an NED quoted distance of 60 Mpc for the NGC 2998 group. The distance is derived from the Tully–Fisher relation (Tully et al. 2016).

[5] http://www.sdss3.org/dr8/algorithms/sdssUBVRITransform.php

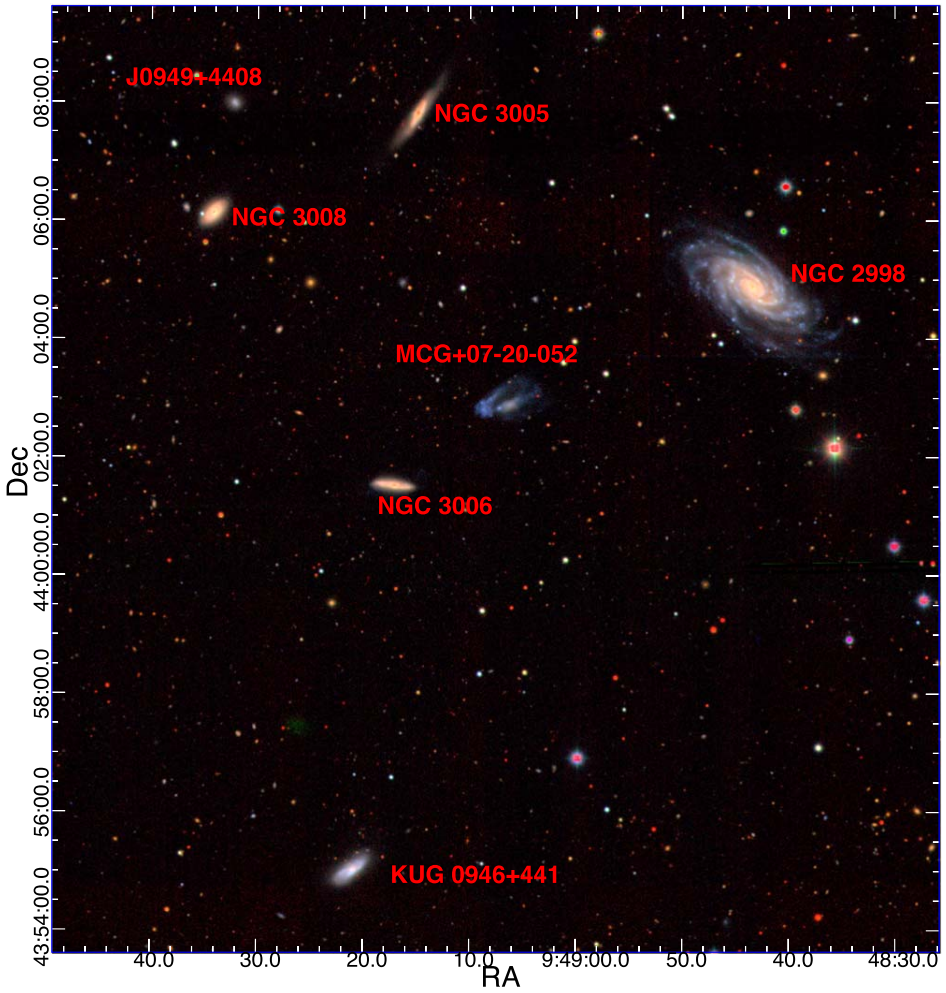

Figure 1. Optical view NGC 2998 seen from the SDSS $g-r-z$ combined tri-color image. The field of view is $14' \times 15'$. The center is adjusted to include all galaxies in the field of view and they are marked.

The interacting dwarfs, D1 and D2, have a similar brightness with B-band absolute magnitudes of -17.17 and -17.14 mag, respectively, but D2 is significantly bluer. Their $g-r$ color indexes are 0.23 and 0.05 mag, respectively. Overall, a combined (D1+D2, a.k.a, MCG+07-20-052) photometry, with a large aperture that covers both, yields a B-band absolute magnitude of -17.94 mag. NGC 3006 has a B-band absolute magnitude of -18.28 mag and it turns out much redder than an interacting dwarf pair with a $g-r$ color index of 0.66 mag. The estimated stellar mass of D1, D2, and NGC 3006 are 5.37×10^8, 2.63×10^8, and 8.12×10^9 $M_\odot$, respectively. That gives a stellar mass ratio between the interacting dwarfs pair of $\sim$2:1.

We measured the $g-r$ color index of the tidal tail-like extensions of D1 and D2, marked with the dashed line in Figure 2. We found the tidal tails of both the dwarfs to have a similar $g-r$ color index of 0.22 mag. And for NGC 3006, we found the low surface brightness eastern extension, also marked with a dashed line in Figure 2, to be significantly bluer compared to its main body, with a $g-r$ color index of 0.14 mag.

To calculate ongoing star formation rates we used the *Galaxy Evolutionary Explorer* (*GALEX*) images. The area around NGC 2998 is covered by the *GALEX* all-sky survey (Martin et al. 2005) and we downloaded the intensity map from the archive. Although the all-sky survey images are not of deep exposure, we still find a reasonable detection in far-UV (FUV) band images for all galaxies in the NGC 2998 system. We performed aperture photometry as done in the SDSS images in both FUV images. We derived the star formation rates from the FUV flux using a calibration provided by Kennicutt (1998). The values are listed in Table 1.

The SDSS fiber spectroscopy has targeted the brighter galaxy, D1, of the interacting pair and its measured optical redshift is $z = 0.0156$. We obtain the optical spectrum from the SDSS archives. The SDSS $3''$ diameter fiber is placed at a relatively red part of central body and the spectrum continuum does not have a high S/N. However, the emissions from early Balmer lines (Hα, Hδ, Hγ, and Hβ) are clear. The Hα equivalent width measured in the SDSS fiber spectrum is 15 Å and this value is not high enough to consider the galaxy as a starburst, which is typical for local blue compact dwarf galaxies (BCDs; Meyer et al. 2014). Emission line metallicity derived

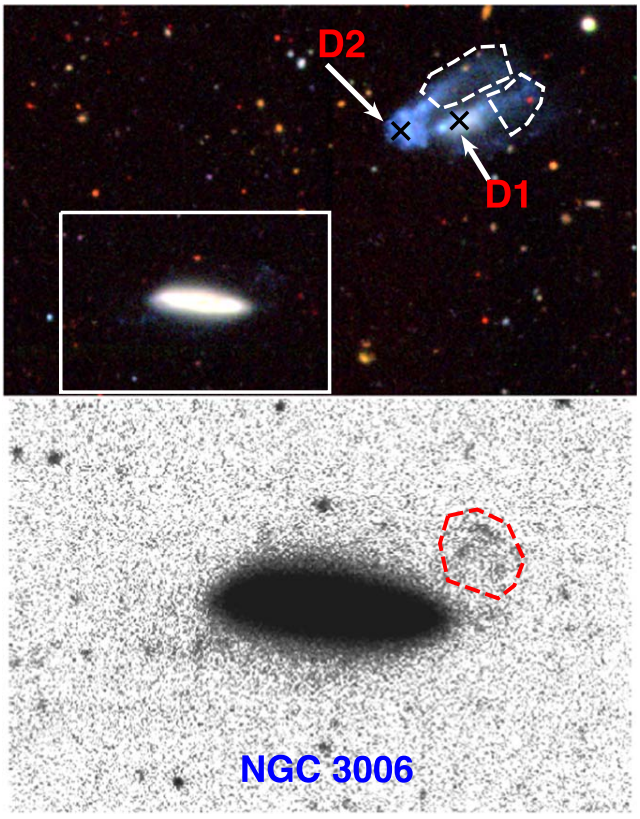

Figure 2. Zoomed-in view of the region around MCG+07-20-052 and NGC 3006. The upper panel image is reproduced same way as Figure 1, which has a field of view of 4.′5 × 3′. Here we marked the two interacting dwarf galaxies (D1 and D2) in MCG+07-20-052. The supposed center, calculated as the centroid, of D1 and D2 are also marked by black crosses and their separation is 25.″77. In lower panel image, we show further zoom-in of NGC 3006 and this image is reproduced by co-adding legacy $g-r-z$ band images to gain signal at the low surface regions. The polygons, white in top panel and red in the lower panel, represent the regions of stellar stream we have chosen for the photometric measurement, see the text.

from a ration of Hα/[N II] is 8.2 (Marino et al. 2013) and the star formation rate derived from the Hα emission line flux is 0.001 $M_{\odot}\,\mathrm{yr}^{-1}$, which is significantly lower than the star formation rate derived from the FUV flux. However we note that 3″ diameter fiber spectroscopy only represents the central part of the galaxy and the star formation rate derived from the FUV flux is summed over the entire galaxy.

3.2. H I 21 cm Observations

H I observations of MCG+07-20-052 were carried out using the Giant Metrewave Radio Telescope (GMRT[6]) located at Pune, India. The system was observed between 2019 January 30 and February 1 as a part of our observing proposal "GMRT H I mapping of LMC–SMC–MW analog." A 16 MHz bandwidth was used yielding a velocity resolution of $\sim$7 km s^{-1}. The GMRT primary beam at the L band is 24′ and the synthesized beams of the images presented in the paper are 37.″0 × 32.″9 (low resolution) and 15.″3 × 11.″9 (high resolution). At the adopted distance of MCG+07-20-052, 60 Mpc, 37″, and 15″ sample 11 kpc and 4 kpc respectively. The data was analyzed using the software AIPS.[7] After flagging bad data for radio frequency interference or from malfunctioning antennas, the UV data was calibrated and continuum subtracted. Image cubes of various resolutions were then made using the AIPS task IMAGR. Finally the integrated H I, velocity field, and velocity dispersion maps were made from the H I cubes using the AIPS task MOMNT. Further details of the observations are given in Table 2.

Figure 3 shows a low-resolution integrated H I map overlaid on the SDSS $g-r-z$ co-added image. Significant H I emission is detected in four galaxies NGC 2998, MCG+07-20-052, NGC 3006, and KUG 0946+441. NGC 3005 and NGC 3008 show marginal detections. The H I masses of the interacting dwarf pair MCG+07-20-052 and its two significant neighbors, NGC 3006 and NGC 2998, were estimated from our observations and are listed in Table 1. Lack of spatial resolution limited us from estimating individual masses of D1 and D2. The H I disk in NGC 2998 seem quite regular and unperturbed while both MCG+07-20-052 and NGC 3006 show extended and irregular H I morphologies. The high-resolution (15.″3 × 11.″9) image of a part of the field, with NGC 3006 and MCG+07-20-052, is presented in the inbox. The outermost contour here is $\sim$2.5 × 10^{20} cm^{-2} compared to the outermost contour of 0.4 × 10^{20} cm^{-2} tracing the diffuse gas in the low-resolution image. In MCG+07-20-052, the high-resolution image reveals that the H I peaks in the merger system coincide mostly with D2. While it was not possible to resolve emission from individual galaxies, two H I peaks were detected. The stronger peak coincides with the head of the tadpole D2, and the other one is seen in the region between D1 and D2, see the inset of Figure 3. The H I distribution in NGC 3006 is extended significantly beyond the optical size of the galaxy. The H I disk of NGC 3006 is almost U-shaped and extends toward MCG+07-20-052, though no H I bridge was detected between NGC 3006 and MCG+07-20-052.

Figure 4 shows the H I velocity field of NGC 2998, the MCG +07-20-052 pair, and NGC 3006. In top panel, we show the velocity field obtained from the low-resolution H I cube. In bottom panel, we show a zoomed-in view of the region highlighted by a green box in the top panel and it shows the high-resolution velocity field. As seen in the low-resolution image, NGC 2998 does not seem to be kinematically affected by any of the other galaxies. H I in the MCG+07-20-052 seem to be merged with the bulk of the gas shifted toward D2. We see no signs of rotation or clear velocity gradient in D1 and D2 and they are indistinguishable even in the high-resolution image. The velocity field of NGC 3006 seems to be preserving its rotation while showing an extended U-shaped morphology, an asymmetry possibly caused by some past interactions. The gas kinematic center seems to be coincident with the optical center. The H I spectrum of NGC 3006 shows a regular rotating feature as we can see the classic double-horn profile and its center perfectly matches with the optical velocity of the galaxy center, Figure 5 blue line. SDSS spectroscopy exists for two pointings in NGC 3006: one at the center and another to its west, which have been marked by the black crosses. We find that the gradient in the optical velocity of NGC 3006 matches with that of the H I velocity, suggesting that the gas and stellar masses share the same sense of rotation. However, we note that the spatial resolution of our observations, specially the H I data, is not sufficient to make strong claims about the matching gradient, nonetheless the matching spectral line width combined with the velocity gradient information from the optical and H I maps suggest an alignment of gas and stellar kinematics in NGC 3006.

[6] http://www.ncra.tifr.res.in/ncra/gmrt
[7] http://www.aips.nrao.edu

Table 1
Physical Properties Galaxies in the NGC 2998 System

Galaxy	R.A. (deg)	Decl. (deg)	z	M_B (mag)	$g-r$ (mag)	D (kpc)	SFR $\log(M_\odot\ \mathrm{yr}^{-1})$	M_* $\log(M_\odot)$	$M_{\mathrm{H\,I}}$ $\log(M_\odot)$
NGC 2998	147.1825	44.0815	0.01595	−20.94	0.43	000	0.39	10.58	10.67
NGC 3006	147.3221	44.0259	0.01600	−18.28	0.66	152	−1.03	9.91	9.43
NGC 3005	147.3125	44.1313	0.01515	−17.99	0.75	141	−1.49	9.95	
NGC 3008	147.3927	44.1026	0.01579	−18.65	0.75	214	−1.66	10.21	
KUG 0946+441	147.3383	43.9179	0.01585	−18.68	0.33	228	−0.86	9.51	
J0949+4408	147.3849	44.1338	0.01512	−16.18	0.37	212	−1.29	8.58	
D1	147.2771	44.0483	0.01575	−17.17	0.23	101	−0.78	8.73	
D2	147.2870	44.0470		−17.14	0.05	111	−0.66	8.42	
MCG+07-20-052				−17.94	0.18	105	−0.40	8.96	9.18

Note. We list the galaxies names and their position in sky (RA & Dec) in columns 1–3, respectively. In the last row MCG+07-20-052 represents a combined value of D1 and D2. The listed redshifts, in the fourth column, are obtained from the SDSS spectroscopy. The *B*-band magnitudes, in the fifth column, are converted from the *g*-band magnitudes and corrected for foreground Galactic extinction. A typical error on the magnitudes is 0.01 mag in all optical band photometry. The star formation rates are derived from FUV flux measured in the *GALEX* all-sky survey images. The stellar mass, listed in column 8, is derived from the SDSS *r*–band magnitudes in which we expect a systematic uncertainty of 0.2 dex, see the text.

Table 2
GMRT Observation Details

Frequency	1398.3949 MHz
Observation date	2019, 30 Jan–1 Feb
Phase calibrator (flux density)	0834+555
Observation time	15.0 hr
Primary beam	24′ at 1420 MHz
Low-resolution beam	$37\farcs0 \times 32\farcs9$ (PA = −12.°3)
High-resolution beam	$15\farcs3 \times 11\farcs9$ (PA = 20.°3)
rms for low-resolution map	1.1 mJy beam^{-1}
rms for high-resolution map	0.9 mJy beam^{-1}
R.A. (pointing center)	$09^{\mathrm{h}}\ 49^{\mathrm{m}}\ 07\fs6$
decl. (pointing center)	$44^{\mathrm{d}}\ 02^{\mathrm{m}}\ 52\farcs0$

This probably indicates that NGC 3006 has not undergone a strong interaction with any of its neighbors. Being in the group, interactions with its neighbors may have affected the outer edges of its H I disk, but they were never strong enough to disrupt its gas disk or disturb its rotation pattern. Additionally, while the H I in NGC 3006 is asymmetric and somewhat shows an extension toward MCG+07-20-052, in the velocity space they seem to be separated by $\sim$100 km s^{-1}, suggesting that they might have suffered a fast and weak interaction in the recent past.

4. Discussion

4.1. Comparison with the LMC–SMC–MW System and Interaction

The ongoing interaction between the LMC and SMC, indeed, is happening in a group environment in the vicinity of the MW, although a satellite pair of LMC–SMC mass around the MW mass host is not commonly seen (Robotham et al. 2012). Cosmological volume numerical simulations predict that there is less than a 10% chance that the MW mass halo would host two subhalos of the mass of the Magellanic clouds (Boylan-Kolchin et al. 2010; Tollerud et al. 2011). Similarly, analyzing the Galaxy And Mass Assembly Catalog of Galaxies, Robotham et al. (2012) estimated the probability of such systems is less than 5%. Following these statistics, the merger probability of LMC–SMC morphology dwarf galaxy satellites around the MW mass host maybe even smaller. While analyzing the statistics, we have found ≈10% (19 out of 177) of interacting dwarfs are located within the 700 kpc sky-projected radius from the MW mass halo and among them only four are qualified as LMC–SMC–MW analogs located within the 300 kpc radius. Different authors have used different criteria to search the LMC–SMC analog. Robotham et al. (2012) selected a pair of dwarf galaxies located within the spatial and velocity radius of 100 kpc ± 400 km s^{-1}, respectively, from the host and Liu et al. (2011) selected a pair of dwarf galaxies located within the spatial and velocity radius of 100 kpc ± 300 km s^{-1}, respectively, from the host. Whereas, we selected the interacting dwarfs, not simply a pair, located within the 300 kpc sky-projected radius and ±300 km s^{-1} line-of-sight radial velocity from the host. Given different selection criteria for LMC–SMC analogs in the literature and this study, we refrain from making any strong claims and only present a qualitative comparison.

MCG+07-20-052 is located at a sky-projected distance of 105 kpc from NGC 2998, which has a stellar mass similar to the MW. We list a direct comparison of physical parameters between the LMC–SMC–MW system and the NGC 2998-MCG+07-20-052 in Table 3. In comparison to the MW and NGC 2718, NGC 2998 is located in a relatively dense environment where we find several bright (brighter than SMC) galaxies around it. There are at least seven galaxies with confirmed redshift information within a sky-projected radius of 300 kpc around NGC 2998. In addition to the galaxies presented in Figure 1, we find that NGC 3009 is located at a sky-projected distance of 442 kpc, which is a magnitude fainter than NGC 2998.

In Figure 6, we show the immediate environment of NGC 2998 within an area of ±500 kpc in the sky. The position and radial velocities of the galaxies are obtained from NED. We can see many galaxies within our selected sky area and this certainly makes the immediate environment of NGC 3009 significantly different from the MW and NGC 2718. There are only two bright star-forming galaxies located around the MW (LMC and SMC) and NGC 2718 (UGC 4703 and UGC 4703B). This, indeed, shows that NGC 2998 is located in a significantly denser environment than the MW and NGC 2718.

In NGC 2718, the interacting satellites were connected through a stellar stream where we identified a blue star-forming region, a possible candidate of the tidal dwarf galaxy

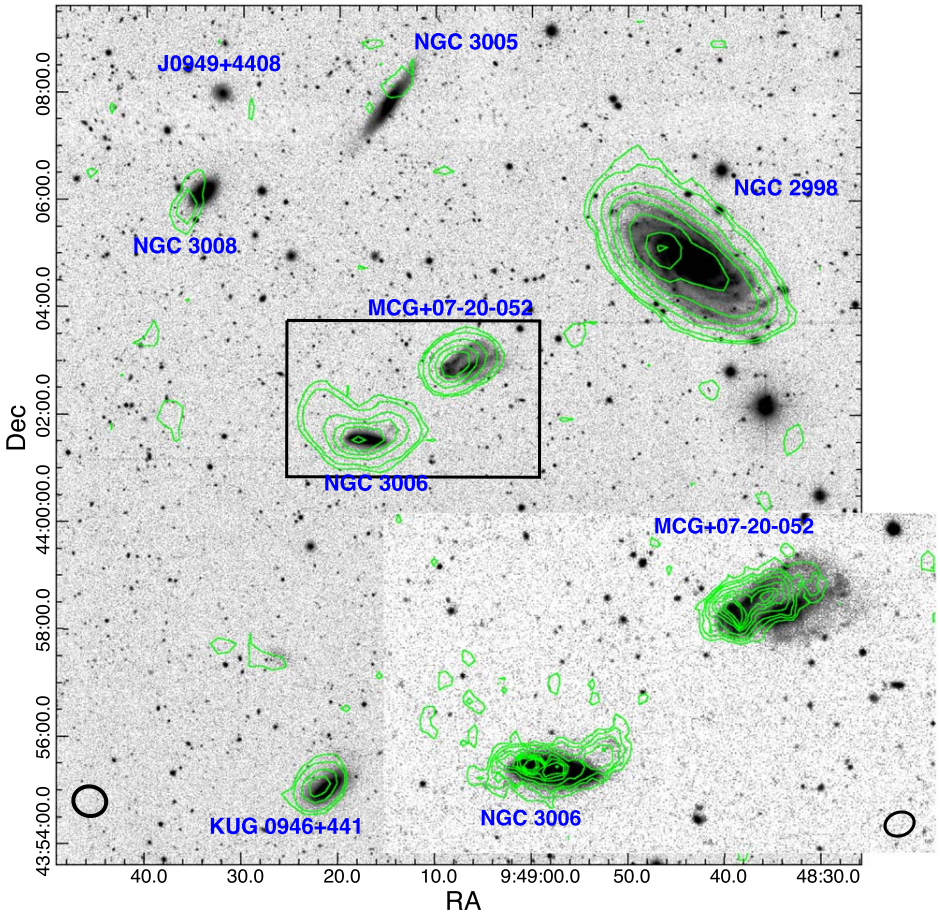

Figure 3. Integrated H I contours from the GMRT low-resolution map overlaid on the Legacy co-added *g*–*r*–*z* band images. The field of view of the image is similar to that in Figure 1. The H I column density levels are $N(\mathrm{H\,I}) = 10^{20} \times (0.4, 0.9, 2.7, 4.5, 6.3, 9.0, 11.7, 13.5)$ cm^{-2}. A black ellipse at the bottom left corner represents beam size of the GMRT observation. In the inset we show a zoomed-in view of a region highlighted by black box with a field of view similar to Figure 2. The overlaid H I contour is obtained from a high-resolution map that has a beam size of $15\farcs3 \times 11\farcs9$, see the bottom right corner. The H I column density levels are $N(\mathrm{H\,I}) = 10^{20} \times (2.5, 4.3, 6.1, 9.0, 12.0, 13.9, 15.1, 16.3, 18.1)$ cm^{-2}.

and their sky-projected separation was 20 kpc. However in MCG+07-20-052 we do not find such a stellar stream connecting the interacting dwarfs D1 and D2, and also their separation is quite small, almost overlapping each other. The lack of spatial resolution prevented us from estimating the gas loss in terms of individual H I deficiencies for D1 or D2, but we do notice a hint of an H I shift toward D2. So we tried to estimate the average gas content of the MCG pair, although we acknowledge the uncertainties are large in such an estimate. Assuming that the net H I content of $1.6 \times 10^9\ M_\odot$ is shared equally by D1 and D2, and the average optical diameter of the galaxies is 0.′5 (8.8 kpc), the H I surface density ($M_{\mathrm{H\,I}}/\mathrm{D}_l^2$) value turns out to be ∼7.0. Comparing this with the average H I surface density value of an unperturbed field galaxy of similar morphological type and taking into account the uncertainty on that number (Haynes & Giovanelli 1984), we conclude that the MCG pair shows no significant H I deficiency. Compared to the reported cases of gas transfer to the outskirts in forms of extended tails in dwarf–dwarf pairs (Pearson et al. 2016), the MCG pair shows no major gas loss and seems to retain the majority of its gas close to its optical extent. The two dwarfs D1 and D2 seem to be interacting, leading to gas transfer or a projected shift of the bulk of the gas from D1 to D2, but there seems to be no massive gas loss from the pair into the intergalactic medium.

Our H I data is fairly deep, with the lowest H I contour tracing $\sim 4 \times 10^{19}$ cm^{-2}. But unlike the Magellanic Stream (MS) we do not detect any H I extension/emission connecting NGC 2998 and the MCG+07-20-052. Instead, we find that the H I distribution around NGC 3006, another LMC mass dwarf galaxy, to be asymmetric and stretched toward MCG+07-20-052. The warped but unperturbed rotation pattern of NGC 3006, as observed in the H I as well as optical data, suggests it may be undergoing or may have undergone a flyby interaction with its neighbor galaxy MCG+07-20-052. We derive a tidal index, Θ,[8] on the MCG+07-20-052 pair from the NGC 2998 and NGC 3006, i.e., $\Theta_{\mathrm{NGC\ 2998}} \sim 2.4$ and $\Theta_{\mathrm{NGC\ 3006}} \sim 3.07$. Which, indeed, shows that the tidal influence of NGC 3006 is significantly larger than that of NGC 2998. The LMC/SMC tidal index is significantly larger than these values, which is 3.7 (Pearson et al. 2016).

The head–tail elongation seen in the optical in D1 and D2 as well as the pushed U-shaped H I morphology seen in

[8] $\Theta = \log\left(\frac{M_*[\times 10^{11}]}{D^3_{\mathrm{proj}}}\right)$ where M_* is the stellar mass of host and D_{proj} is the projected distance from the dwarf (Karachentsev et al. 2013).

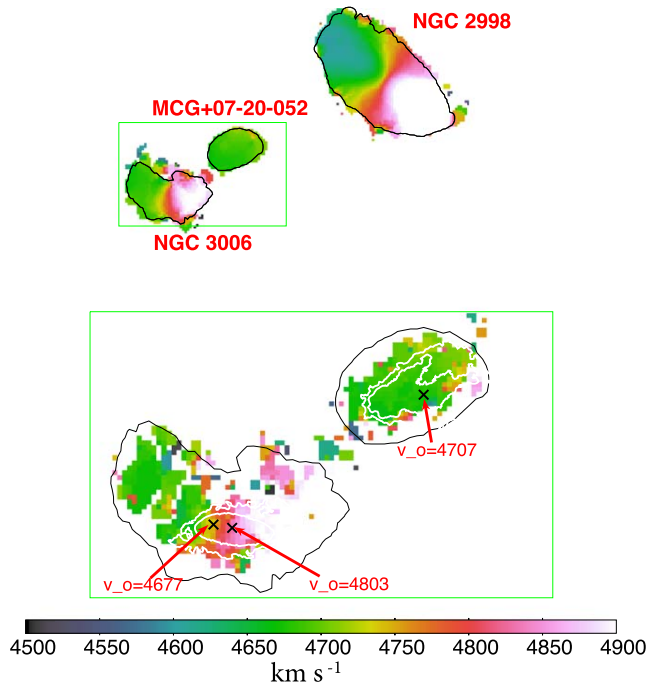

Figure 4. Top: the H I velocity field from the GMRT low-resolution cube. The black contour traces the lowest column density contour of the low-resolution integrated H I image (N(H I) = 0.4 × 10^{20} cm^{-2}). Bottom: we show a zoomed-in view of the region highlighted by a green box. This shows the high-resolution velocity field. The white contours trace the optical g-band light at the surface brightness levels of 25 and 26.5 mag arsec^{-2} for the inner and outer, respectively. The black contour traces the lowest column density contour of the low-resolution integrated H I image, same as the top panel. The black crosses represent the SDSS fiber spectroscopy targeted position, where optical velocities are available.

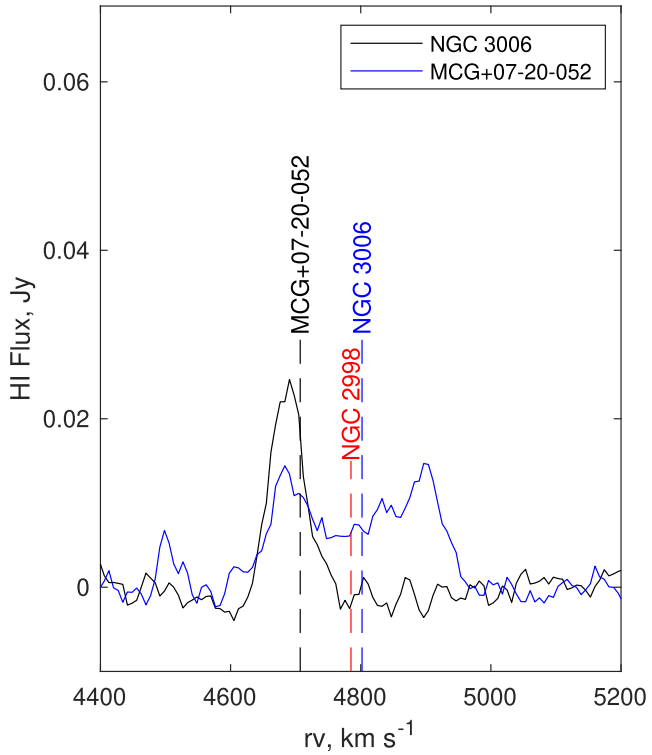

Figure 5. Integrated H I spectrum of MCG+07-20-052 and NGC 3006. To show the optical velocities, we draw a vertical dashed line for each galaxy.

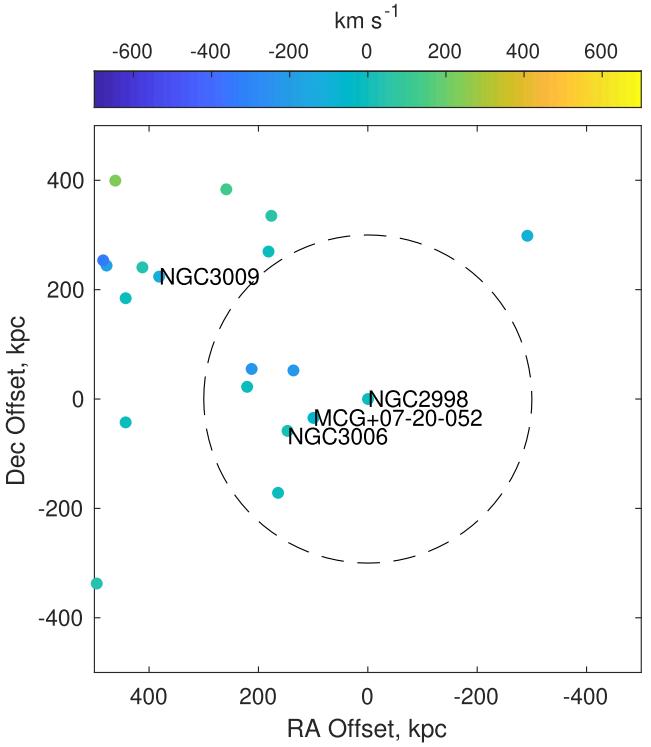

Figure 6. Distribution of galaxies around NGC 2998 where we sampled all galaxies available at the NED within the velocity range of ±700 km s^{-1} with respect to the line-of-sight velocity of NGC 2998. The x-axis and y-axis are offsets in R.A. and decl. from NGC 2998, respectively, and both are in units of kiloparsecs. The symbol color represents their relative line-of-sight velocities with respect to NGC 2998, according to the color bar at the top of the plot. We highlight the immediate, 300 kpc sky-projected radius region around the NGC 2998 by a dotted red circle.

Table 3
Comparison with LMC–SMC, UGC470, and MCG+07-20-052

Galaxy	M_B (mag)	D (kpc)	M_* $M_\odot$	SFR $M_\odot$ yr^{-1}	H I$_{mass}$ $M_\odot$
			MW		
MW	−21.17	0	5 × 10^{10}	0.68–1.45	8 × 10^9
LMC	−18.60	50	2.3 × 10^9	0.2	4.4 × 10^8
SMC	−17.20	60	5.3 × 10^8	0.04	4 × 10^8
			NGC 2718		
NGC 2718	−21.01	0	7 × 10^{10}	0.97	1.12 × 10^{10}
UGC 4703	−18.0	81	1.8 × 10^9	0.2	1.4 × 10^{9a}
UGC 4703B	−16.5	104	5.4 × 10^8	0.03	
			NGC 2998		
NGC 2998	−20.94	0	3.8 × 10^{10}	2.45	8.7 × 10^9
D1	−17.17	105	5.3 × 10^8	0.16	1.5 × 10^{9a}
D2	−17.14	112	2.6 × 10^8	0.21	
NGC 3006	−18.28	157	8.1 × 10^9	0.09	2.6 × 10^9

Notes. The H I masses of the NGC 2998 system have been estimated from the GMRT spectra. The table is reproduced from our previous study on UGC470 in the NGC 2718 group (Paudel et al. 2018b).
[a] Combined H I mass of the interacting pair.

NGC 3006 could usually be seen as signs of ongoing ram pressure stripping (RPS; Abramson et al. 2011) in the group. Commonly known as jelly-fish galaxies, ongoing RPS galaxies

also show compression of H I on the opposite side of an elongated tail and depending on the strength of the ram pressure, the H I distribution show signs of outer edge gas stripping, e.g., JO206 (see Ramatsoku et al. 2019). Also RPS mainly affects the gas distribution before it affects the stellar disk. In MCG +07-20-052, while the tadpole-like feature is visible in the optical, we find no hint of compression or shrinking of the H I disk and the H I distribution is more extended than the galaxy's stellar distribution in both NGC 3006 and MCG+07-20-052 (see the white contour in Figure 4). Therefore this extended, merged, and asymmetric H I distribution in MCG +07-20-052 suggests that the observed tidal features on both H I gas and stellar population, including the tadpole-like appearance of the dwarfs, may have originated mainly from tidal interaction and not from RPS. Ram pressure alone could not be responsible for the optical features of D1 and D2, rather it could be tidal assisted ram pressure which is more commonly found to influence galaxy evolution in group environments (Davis et al. 1997; Sengupta et al. 2007; Besla et al. 2012; Pearson et al. 2018). In contrast, in the LMC the presence of stars well beyond the H I distribution in the leading edge suggests that RPS played a strong role and Salem et al. (2015) concludes that the disk of the LMC was truncated by the peak ram pressure at pericentric passage.

5. Conclusions

We present GMRT H I images and optical photometry data of the galaxies in the NGC 2998 group. From the data analysis and their discussion in the broader context, we draw the following conclusions.

(1) We identify MCG+07-20-052, a pair of dwarf galaxies of LMC–SMC mass, located in the vicinity of MW mass spiral galaxy NGC 2998.
(2) H I is mostly concentrated around only one member of the interacting pair, i.e., D2, which also shows a higher level of star-forming activity and bluer $g-r$ color index compared to the other member of interacting pair, i.e., D1.
(3) We detect extended tenuous emission of H I around another member galaxy, NGC 3006, located close to the MCG+07-20-052 at a sky-projected distance of 41 kpc.
(4) We present a comparative analysis between LMC–SMC–MW, NGC 2718-UGC 4703, and NGC 2998 -MCG+07-20-052. We found that NGC 2998 is located in a relatively denser environment compared to the MW and NGC 2718. In addition, unlike the MS we do not detect any H I extension connecting MCG+07-20-052 and the host NGC 2998.

We thank the staff of the GMRT who have made these observations possible. GMRT is run by the National Centre for Radio Astrophysics of the Tata Institute of Fundamental Research. S.P. acknowledges support from the New Researcher Program (Shinjin grant No. 2019R1C1C1009600) through the National Research Foundation of Korea and by the Yonsei University Research Fund (Post-doctoral Researcher Supporting Program) of 2019 (No. 2019-12-0005). S.-J.Y. acknowledges support from the Mid-career Researcher Program (No. 2019R1A2C3006242) and the SRC Program (Center for Galaxy Evolution Research; No. 2017R1A5A1070354) through the National Research Foundation of Korea. This study is based on the archival images and spectra from the Sloan Digital Sky Survey (the full acknowledgment can be found at http://www.sdss.org/collaboration/credits.html). The Legacy Surveys imaging of the DESI footprint is supported by the Director, Office of Science, Office of High Energy Physics of the U.S. Department of Energy under Contract No. DE-AC02-05CH1123, by the National Energy Research Scientific Computing Center, a DOE Office of Science User Facility under the same contract, and by the U.S. National Science Foundation, Division of Astronomical Sciences under Contract No. AST-0950945 to NOAO. We also made use of the *GALEX* all-sky survey imaging data. *GALEX* is operated for NASA by the California Institute of Technology under NASA contract NAS5-98034.

ORCID iDs

Sanjaya Paudel https://orcid.org/0000-0003-2922-6866
Suk-Jin Yoon https://orcid.org/0000-0002-1842-4325

References

Abazajian, K. N., Adelman-McCarthy, J. K., Agüeros, M. A., et al. 2009, ApJS, 182, 543
Abramson, A., Kenney, J. D. P., Crowl, H. H., et al. 2011, AJ, 141, 164
Barnes, J. E. 1992, ApJ, 393, 484
Bekki, K. 2008, MNRAS, 388, L10
Besla, G., Kallivayalil, N., Hernquist, L., et al. 2012, MNRAS, 421, 2109
Besla, G., Patton, D. R., Stierwalt, S., et al. 2018, MNRAS, 480, 3376
Blum, R. D., Burleigh, K., Dey, A., et al. 2016, AAS Meeting, 228, 317.01
Boylan-Kolchin, M., Springel, V., White, S. D. M., & Jenkins, A. 2010, MNRAS, 406, 896
Coleman, M., Da Costa, G. S., Bland-Hawthorn, J., et al. 2004, AJ, 127, 832
Davis, D. S., Keel, W. C., Mulchaey, J. S., & Henning, P. A. 1997, AJ, 114, 613
Deason, A., Wetzel, A., & Garrison-Kimmel, S. 2014, ApJ, 794, 115
Duc, P.-A., Cuillandre, J.-C., Karabal, E., et al. 2015, MNRAS, 446, 120
Duc, P.-A., Cuillandre, J.-C., Serra, P., et al. 2011, MNRAS, 417, 863
Elmegreen, D. M., Elmegreen, B. G., Sánchez Almeida, J., et al. 2012, ApJ, 750, 95
Fakhouri, O., Ma, C.-P., & Boylan-Kolchin, M. 2010, MNRAS, 406, 2267
Fitts, A., Boylan-Kolchin, M., Bullock, J. S., et al. 2018, MNRAS, 479, 319
Glatt, K., Grebel, E. K., & Koch, A. 2010, A&A, 517, A50
Harris, J., & Zaritsky, D. 2009, AJ, 138, 1243
Haynes, M. P., & Giovanelli, R. 1984, AJ, 89, 758
Kado-Fong, E., Greene, J. E., Greco, J. P., et al. 2020, AJ, 159, 103
Karachentsev, I. D., Makarov, D. I., & Kaisina, E. I. 2013, AJ, 145, 101
Kennicutt, R. C., Jr. 1998, ARA&A, 36, 189
Klimentowski, J., Łokas, E. L., Knebe, A., et al. 2010, MNRAS, 402, 1899
Lee, J. C., Kennicutt, R. C., Jr., Funes, S. J. J. G., Sakai, S., & Akiyama, S. 2009, ApJ, 692, 1305
Liu, L., Gerke, B. F., Wechsler, R. H., Behroozi, P. S., & Busha, M. T. 2011, ApJ, 733, 62
Marino, R. A., Rosales-Ortega, F. F., Sánchez, S. F., et al. 2013, A&A, 559, A114
Martin, D. C., Fanson, J., Schiminovich, D., et al. 2005, ApJL, 619, L1
Meyer, H. T., Lisker, T., Janz, J., & Papaderos, P. 2014, A&A, 562, A49
Mihos, J. C., & Hernquist, L. 1994, ApJL, 425, L13
Naab, T., & Ostriker, J. P. 2009, ApJ, 690, 1452
Noeske, K. G., Iglesias-Páramo, J., Vílchez, J. M., Papaderos, P., & Fricke, K. J. 2001, A&A, 371, 806
Paudel, S., & Sengupta, C. 2017, ApJL, 849, L28
Paudel, S., Sengupta, C., & Yoon, S.-J. 2018a, AJ, 156, 166
Paudel, S., Smith, R., Duc, P.-A., et al. 2017, ApJ, 834, 66
Paudel, S., Smith, R., Yoon, S. J., Calderón-Castillo, P., & Duc, P.-A. 2018b, ApJS, 237, 36
Pearson, S., Besla, G., Putman, M. E., et al. 2016, MNRAS, 459, 1827
Pearson, S., Privon, G. C., Besla, G., et al. 2018, MNRAS, 480, 3069
Privon, G. C., Stierwalt, S., Patton, D. R., et al. 2017, ApJ, 846, 74
Ramatsoku, M., Serra, P., Poggianti, B. M., et al. 2019, MNRAS, 487, 4580
Robotham, A. S. G., Baldry, I. K., Bland-Hawthorn, J., et al. 2012, MNRAS, 424, 1448
Salem, M., Besla, G., Bryan, G., et al. 2015, ApJ, 815, 77
Schlafly, E. F., & Finkbeiner, D. P. 2011, ApJ, 737, 103

Sengupta, C., Balasubramanyam, R., & Dwarakanath, K. S. 2007, MNRAS, 378, 137
Stierwalt, S., Besla, G., Patton, D., et al. 2015, ApJ, 805, 2
Tollerud, E. J., Boylan-Kolchin, M., Barton, E. J., Bullock, J. S., & Trinh, C. Q. 2011, ApJ, 738, 102
Tully, R. B., Courtois, H. M., & Sorce, J. G. 2016, AJ, 152, 50
Wilman, D. J., Fontanot, F., De Lucia, G., Erwin, P., & Monaco, P. 2013, MNRAS, 433, 2986
Zhang, H.-X., Puzia, T. H., & Weisz, D. R. 2017, ApJS, 233, 13

Journal of Institute of Science and Technology, 27(2), 85-89 (2022)
ISSN: 2467-9062 (print), e-ISSN: 2467-9240
https://doi.org/10.3126/jist.v27i2.35312

Research Article

STRUCTURAL PARAMETER OF A MERGING COMPACT DWARF GALAXY CG 0315

Daya Nidhi Chhatkuli[1]*, Sanjaya Paudel[2], Amrit Sedhain[3], Binil Aryal[1]
[1]Central Department of Physics, Tribhuvan University, Nepal,
[2]Department of Astronomy, Yonsei University, Seoul, 03722, Republic of Korea
[3]University of potsdam, Am Neuen Palais 10, 14469 Potsdam, Germany
**Correspondence: chhatkulidn@gmail.com*
(Received:** February 28, 2021; **Final Revision:** December 30, 2022; **Accepted:** December 31, 2022**)

ABSTRACT
Structural parameters like size, Sersic index, total luminosity and ellipticity are important tools to study galaxy formation and evolution. This work studies a compact dwarf galaxy CG 0315, originated from a merger, and performs a detailed analysis of morphological parameters. The galaxy size is derived by using two different methods, i.e., parametric and non-parametric. The parametric uses the Sersic modeling, but it is found that the observed light profile of CG 0315 cannot be modeled with a simple Sersic function. This is, however, common in merging feature galaxies. Therefore, for further analysis, the half-light radius derived from the non-parametric method can be used as the size of the galaxy. CG 0315 is far more compact than a typical galaxy. We measured its effective radius of 4.05 arcseconds and half-light radius of 2.60 arcseconds that corresponds to a physical value of 221 parsec. Its ratio between the minor and major axis is 0.82, and the position angle is 179 degrees to the North. The star formation rate of the galaxy is $0.051 M_{\odot}$ year^{-1}. We conclude from these observational data that CG 0315 will continue to be a compact dwarf galaxy when star formation stops and transforms into a well-known compact elliptical galaxy. Therefore, CG 0315 might be a progenitor of an elliptical galaxy.

Keywords: Compact dwarf galaxy, Galaxy merger, Sersic index, half-light radius

INTRODUCTION
Structural parameters; size, concentration, and ellipticity are important tools for studying galaxy formation and evolution. Galaxies follow a scaling relation between size and magnitudes that is continuous over the whole range of luminosities (Graham & Guzmán, 2003; Ferrarese *et al.,* 2006; Janz & Lisker 2008). The universality of this relation has been a subject of considerable debate because of the presence of outliers and the non-linearity of the relation (Kormendy 1985; Kormendy *et al.,* 2009; Chen *et al.,* 2010). The high redshift galaxies are noticeably more compact than the local ($z < 0.1$) galaxies, indicating that early formed galaxies are more compact than later produced galaxies. One of the enigmas of modern cosmology is the size, history, and formation of compact galaxies in the early universe.

Galaxies are three-dimensional objects, and we observe them in a projected plane of the sky. Their structures, in general, are quantified through the use of integrated light profiles along the major axis. These profiles are measured by averaging the observed intensity of a galaxy at a given radius in a concentric ellipse and then determining how this intensity varies as a function of radius. It was first formulated by de Vaucouleurs in 1948 (Buta, 1996), who used light measurements for elliptical galaxies. Surface photometry is a process of quantifying galaxy morphology. The colors of the galaxies derived from surface photometry through different passbands provide information about the ages and metallic contents of the stellar population of the galaxies. The measured light profile is called the surface brightness profile, which reduces observed two-dimensional isophotes to a 1D set of parameters. Galaxies' isophotes are closely approximated by ellipses which simply reflect the condition that underlying stellar orbits in galaxies are Keplerian. From the surface photometry, we can find the variation of intensity and ellipticity with a radius of the ellipses.

In this work, we present an analysis of the structural parameter of a compact merging dwarf galaxy CG 0315. We derive its size, Sersic index and position angle. We make comparative study between morphological and star-formation properties.

MATERIALS AND METHODS
Sample Selection
CG 0315 is taken from a catalog (Paudel *et al.*, 2018) of merging dwarf galaxies which shows compact visual morphology. It has a sky position R.A. = $10^{h}\ 01^{m}\ 14.38^{s}$, Dec. = + 37° 04'15.24", and a redshift of $z = 0.0048$. In the catalog, it is listed as a shell feature merging dwarf galaxy. It is located in an isolated environment where we identify no nearby companion within the 500 kiloparsec (kpc) sky projected radius with a line-of-sight relative radial velocity range of ± 500 km s^{-1}.

Figure 1 reveals the optical view of CG 0315, where we can see elongated low surface brightness tidal tail along the galaxy's major axis. The color image is a cutout of the Legacy sky-server images (Dey *et al.,* 2019), which is prepared by combining *g*-, *r*-, and *z*-band images. The field of view of the image is 1'×2'. For the distance of

CG 0315, it corresponds to a physical value of 28 × 56 kpc. We can see that the inner part is quite round and bluish, and the outer low surface brightness extended tidal tail is relatively reddish.

Figure 1. Optical image of CG 0315. Field of view of image is 1 × 2 arcmin, where the north is top and the east is left. The image is obtained from Legacy sky viewer which is prepared by combining the mono-color *g-r-z* filter images.

The basic photometric properties; R. A., Dec., red shift, *b*-band absolute magnitude, difference of *g* and *r* band magnitudes and star formation rate of CG 0315 are listed in Table 1. Located at 20.34 Megaparsec distance from us, it has an *b*-band absolute magnitude $M_B = -15.94$ magnitude (mag) and an overall $g - r$ color index of 0.14 mag, with a star-formation rate of 0.051 $M_\odot$ year^{-1}. This value of the star formation rate (SFR) is slightly less than the star formation rate of a newly formed, less metallic interacting dwarf galaxy NGC 2604 of value 0.057 $M_\odot$ year^{-1} obtained from the spectroscopic calculation using Hα emission line flux (Chhatkuli *et al.,* 2020). The line-of-sight radial velocity of the galaxy obtained from NED is 1467 km s^{-1}.

Imaging Analysis

To perform image analysis, the Sloan Digital Sky Survey (SDSS) images are used which we obtained from the SDSS archive database (Ahn *et al.,* 2012). We primarily employed the *r*-band image from the SDSS to carry out surface photometry because of its higher signal-to-noise ratio. The Image Reduction and Analysis Facility (IRAF) task ellipse was used to extract the galaxy's major-axis light profile. IRAF is a collection of software, which is used to fit elliptical isophotes in an optical image of galaxies, and we can obtain several parameters like intensity, radial distance, ellipticity, etc. The IRAF reads the 2D image section and produces output in tabular form. The ellipse uses the methodology described in Jedrzejewski (1987), where for each semi-major axis length, the intensity I(ϕ) is azimuthally averaged along an elliptical path described by an initial guess for the isophote's center (X, Y), ellipticity (e), and semi-major axis position angle (θ). The intensity I(ϕ) is expanded into the following Fourier series to quantify how the intensity deviates from being constant along the fitted ellipse.

Table 1. Basic Physical Parameters of CG 0315

Parameters	R. A. (deg.)	Dec. (deg.)	z	M_B (mag)	g-r (mag)	SFR ($M_\odot$year^{-1})
Value	150.309990	37.0709423	0.0048	-15.94	0.14	0.051

$$I(\phi) = I_o + \sum_k [A_k \sin(k\phi) + B_k \cos(k\phi)] \quad (1)$$

Where I_0 is the intensity averaged over the ellipse and ϕ is azimuthal angle. A_k and B_k are the Fourier coefficients. If an isophote is a perfect ellipse, A_k and B_k will be exactly zero.

All foreground and background unrelated objects were masked. The masking was performed manually, where we visually identified the unrelated objects. The center of galaxies was derived using the imcentre task in the IRAF, which calculates a centroid of the provided image section. The centroid of the image is the arithmetic mean position of all points in the image. The upper panel of Figure 2 shows the *r*−band grayscale image where the green circled regions were masked before the fitting. While fitting the ellipse, position angle and ellipticity were allowed to vary freely, and the semi-major axis was increased logarithmically. The discrete radii of ellipses are specified by the rule that the different semi-major axis lengths are spaced by a factor of 1.1. The ellipse center was not allowed to wander by more than 3 pixels between consecutive isophotes.We show the derived surface brightness profile along the major axis in the bottom panel of Figure 2. It is clear that the surface brightness profile is not smooth, and we can see a steep rise in the middle and nearly constant at the outer radius. Figure 3 shows a variation of position (PA) angle and ellipticity (e) along the major axis. The position angle varies rapidly at the inner part, and it remains nearly constant beyond a five arcsecond radius. The ellipticity shows the same behavior in the central region. It continuously increases at the outer radius, which we also see in the overlay blue ellipse of Figure 2 at the top right panel.

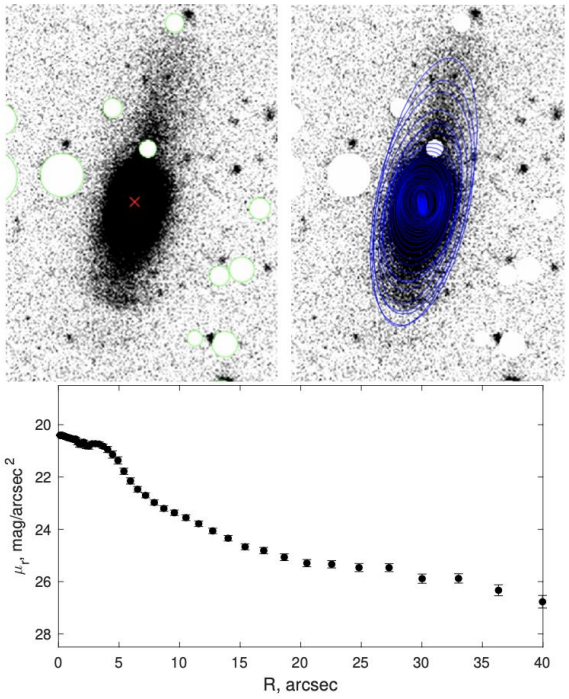

Figure 2. In the top left panel, we show SDSS r-band image, where we masked foreground and background unrelated objects, see green circle. The center of the galaxy is marked by a red cross. In top right, we overlay best fitted ellipse obtained from IRAF ellipse task. In the bottom panel, we show derived light profile along the major axis. The y-axis is the surface brightness in the unit of mag per arcsec^2.

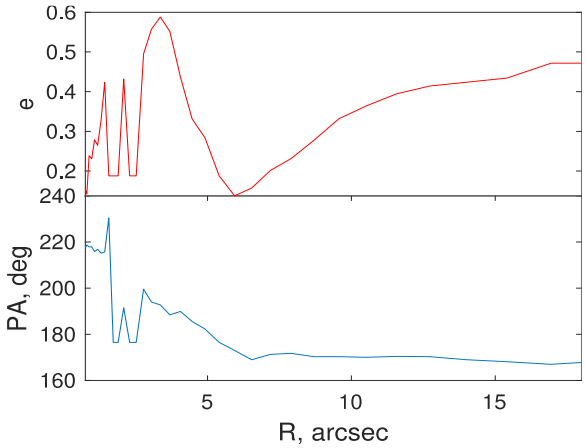

Figure 3. Variation of ellipticity and Position angle along the major axis in upper and lower panels respectively

Measurement of Galaxy Size

Galaxies never have an endpoint; therefore, a measurement of galaxy size is not a trivial task. In general, we use two different approaches to derive galaxy size, i.e., parametric and non-parametric. In the parametric approach, we first approximate the galaxy light profile into a parametric function such as exponential or de Vaucouleurs. In general, both exponential and de Vaucouleurs are the special cases of Sersic function (Sersic 1968) defined as

$$I(R) = I_e \exp\left\{-b_n\left[\left(\frac{R}{R_e}\right)^{1/n} - 1\right]\right\} \qquad (2)$$

Where I_e is the intensity of the light–profile at the effective radius R_e and n is called Sersic index, which defines the 'shape' of the profile. The term b_n is simply a function of n and is chosen to ensure the radius R_e encloses half of the profile's total luminosity. In general, as a special case of the Sersic model, we use $n = 4$ for the early-type galaxy called de Vaucouleurs, and for the late-type galaxy, we use $n = 1$, which is exponential.

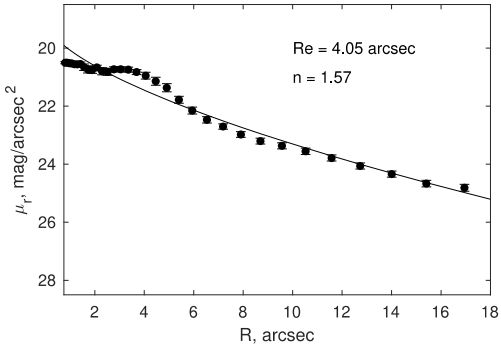

Figure 4. Modeling of observed light profile with a Sersic function. The black line represents a best fitted Sersic function to the data

The exponential function is generally used for late-type galaxies, and de Vaucouleurs functions are typically used for early-type galaxies. These analytic functions have free parameters such as effective radius R_e and effective surface brightness μ_e. We finally modeled the observed light profile with these functions and found the best-fit parameters. We do not need to know where the galaxy ends in this approach, and we simply use the best fit effective radius as a galaxy size.

On the other hand, non-parametric methods measure the galaxy size without the use of any analytic function. One simple method is called the Petrosian method; we first define an empirical radius from the observed intensity profile, called Petrosian radius a_p, (Blanton *et al.,* 2001; Petrosian 1976). To calculate this, we first derive the Petrosian index, which is the ratio of the surface brightness at R to the mean surface brightness within R, i.e.,

$$n(R) = \frac{\mu(R)}{\langle \mu(R) \rangle} \qquad (3)$$

Where $\mu(R)$ is surface brightness at radius R, and $\langle \mu(R) \rangle$ is the average surface brightness within that radius, and Petrosian radius is defined where $n = 0.2$. Then it is assumed that the galaxy extension is at most out to $2a_p$, and the total flux in it is measured within a $2a_p$ aperture. Once we know the total flux, we can measure the distance where the flux becomes half and this galactocentric distance is called half-light radius (R_h).

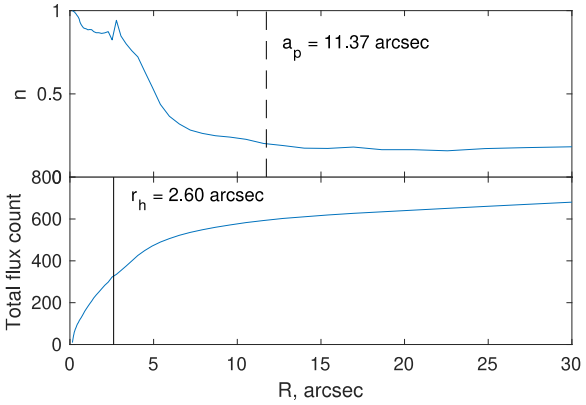

Figure 5. Top: we show variation of Petrosian index n along the major axis and the position of a_p, where n = 0.2, is marked by dashed line. Bottom: we show cumulative intensity profile along the major axis, and at r_h = 2.60 arcsec marked by the black line represents the radius at which the flux is half of its total value

We calculate the galaxy size using the non-parametric approach, i.e., the Petrosian method, as shown in Figure 5. We derive a half-light radius for the CG 0315 is 2.60 arcsec. We calculate the global value of PA and ellipticity of galaxy by averaging these values beyond the 5 arcsecond radius, which is well beyond the spatial resolution of the SDSS imaging data. The calculated values of position angle, ellipticity, effective radius, half-light radius and Sersic index are listed in second, third, fourth, fifth and sixth columns respectively in Table 2. The position angle and ellipticity are 179° and 0.18 respectively.

In Figure 4, we have tried to model the galaxy light profile with a Sersic function. It is clear that the modeled black line does not fit well with the data points. The derived Sersic index and effective radius are 1.57 and 4.05 arcsec, respectively. However, it is normal for galaxies like CG 0315, which possess tidal features like long extended tails.

Table 2. Global Structural Parameters of CG 0315

Parameter Name	Position Angle (deg.)	Ellipticity	Effective Radius (arcsec)	Half-light Radius (arcsec)	Sersic Index
Value	179	0.18	4.05	2.60	1.57

CONCLUSIONS

In this work, we perform a detailed morphological study of a compact dwarf galaxy, CG 0315. CG 0315 hosts a prominent shell feature and is listed in a merging dwarf galaxy catalog of Paudel *et al.,* (2018). We measured its half-light radius of 2.60 arcseconds using the Petrosian method that corresponds to a physical value 221 parsec and *b*-band absolute brightness M_B = −15.94 mag. However, the parametric modeling galaxy's light profile with a Sersic function gives an effective radius of 4.05 arcsecond. Its ratio between the minor and major axis is 0.82, and the position angle is 179 degrees to the North. Current star-formation rate derived using H_a emission line flux is 0.051 $M_\odot$/yr. This value of SFR is normal as compared to the normal star-forming galaxies. From these observational evidence, we conclude that CG 0315 will still be a compact dwarf galaxy once its star-formation ceases, and become well known compact elliptical galaxy. CG 0315 could therefore be a progenitor of elliptical galaxy.

ACKNOWLEDGEMENTS

D. N. Chhatkuli gratefully acknowledges the University Grants Commission of Nepal, for financial support by providing Ph. D. Fellowship and Research Support Grant (Award No.: PhD-75/76-S & T-13) to carry out this research.

AUTHORS CONTRIBUTION STATEMENT

DNC conceptualized the research project, led the data processing and prepared the manuscript. SP performed the candidate selection and contributed to the analysis and interpretation. AS contributed to proof reading of the manuscript. BA contributed to the interpretation.

CONFLICT OF INTEREST

The authors do not have any conflict of interest pertinent to this work.

DATA AVAILABILITY STATEMENT

The data that support the findings of this study are available from the corresponding author, upon reasonable request.

REFERENCES

Ahn, C.P., Alexandroff, R., Prieto, C.A., Anderson, S.F., Anderton, T., Andrews, B.H., ... & Pattarakijwanich, P. (2012). The ninth data release of the Sloan Digital Sky Survey: first spectroscopic data from the SDSS-III Baryon Oscillation Spectroscopic Survey. *The Astrophysical Journal Supplement Series, 203*(2), 21.

Blanton, M.R., Dalcanton, J., Eisenstein, D., Loveday, J., Strauss, M.A., SubbaRao, M., ... & York, D.G. (2001). The Luminosity function of galaxies in SDSS commissioning data. *The Astronomical Journal, 121*(5), 2358-2380.

Buta, R. (1996). Obituary: Gerard Henri De Vaucouleurs, 1918-1995. *Bulletin of the American Astronomical Society, 28*(4), 1449-1450.

Chen, C.W., Cote, P., West, A.A., Peng, E.W., & Ferrarese, L. (2010). Homogeneous UGRIZ photometry for ACS Virgo Cluster Survey Galaxies: A non-parametric analysis from SDSS imaging. *The Astrophysical Journal Supplement Series, 191*(1), 1-31.

Chhatkuli, D., Paudel, S., & Aryal, B. (2020). Study of star formation rate and metallicity of an interacting

dwarf Galaxy NGC 2604. *Journal of Institute of Science and Technology, 25*(2), 55-60.

Dey, A., Schlegel, D.J., Lang, D., Blum, R., Burleigh, K., Fan, X., ... & Vivas, A.K. (2019). Overview of the DESI legacy imaging surveys. *The Astronomical Journal, 157*(5), 168.

Ferrarese, L., Côté, P., Jordán, A., Peng, E.W., Blakeslee, J.P., Piatek, S., Mei, S., Merritt, D., Milosavljević. M., Tonry. J.L., & West, M.J. (2006). The ACS Virgo cluster survey. VI. Isophotal analysis and the structure of early-type galaxies. *The Astrophysical Journal Supplement Series, 164*(2), 334-434.

Graham, A.W., & Guzmán, R. (2003). HST photometry of dwarf elliptical galaxies in coma, and an explanation for the alleged structural dichotomy between dwarf and bright elliptical galaxies. *The Astronomical Journal, 125*(6), 2936-2950.

Janz, J., & Lisker, T. (2008). The sizes of early-type Galaxies. *The Astrophysical Journal, 689*(1), L25.

Jedrzejewski, R.I. (1987). CCD surface photometry of elliptical galaxies–I. Observations, reduction and results. *Monthly Notices of the Royal Astronomical Society, 226*(4), 747-768.

Kormendy, J. (1985). Families of ellipsoidal stellar systems and the formation of dwarf elliptical galaxies. *The Astrophysical Journal, 295*, 73-79.

Kormendy, J., Fisher, D.B., Cornell, M.E., & Bender, R. (2009). Structure and formation of elliptical and spheroidal galaxies. *The Astrophysical Journal Supplement Series, 182*(1), 216-309.

Paudel, S., Smith, R., Yoon, S.J., Calderón-Castillo, P., & Duc, P.A. (2018). A catalog of merging dwarf galaxies in the local universe. *The Astrophysical Journal Supplement Series, 237*(2), 36.

Petrosian, V. (1976). Surface brightness and evolution of galaxies. *The Astrophysical Journal, 209,* L1-L5.

Sersic, J.L. (1968). Atlas de Galaxias Australes – English translation of the chapter "Photometric Analysis". https://doi.org/10.5281/zenodo.2562394.

.

JNPS 7 (4): 28-35 (2022)
ISSN: 2392-473X (Print), 2738-9537 (Online)

Research Article *© Nepal Physical Society*
DOI: http://doi.org/10.3126/jnphyssoc.v7i4.42928

A Detailed Morphological and Spectroscopic Study of Merging Dwarf Galaxy PGC 030133

D. N. Chhatkuli[1, *], S. Paudel[2] and B. Aryal[1]
[1]Central Department of Physics, Tribhuvan University, Nepal
[2]Centre for Galaxy Evolution Research, Department of Astronomy, Yonsei University, Seoul, South Korea
[*]Corresponding Email: chhatkulidn@gmail.com

Received: *20th November, 2021;* ***Revised:*** *19th December, 2021;* ***Accepted:*** *29th December, 2021*

ABSTRACT

We present a detailed morphology and spectroscopic study of a merging dwarf galaxy PGC 030133. Using the publicly available fiber spectroscopic data from the Sloan Digital Sky Survey (SDSS), we analyzed nine-strong emission lines of wavelength range 4336 Å to 6739 Å. We find that the strongest emission line is $OIII_{5007}$, with an intensity of 146.32×10^{-17} erg/s/cm^2/Å. The observed emission lines are well fitted with a Gaussian profile with a coefficient of regression greater than 96%, and the derived full-width half maximum (FWHM) is less than 4.2 Å. The Balmer decrement, characterized by the line ratio between H_α and H_β is 3.07, suggesting a presence of dust at the center of PGC 030133. Using extinction corrected emission line fluxes, we derived the star-formation rate and emission line metallicity of PGC 030133. SFR derived from H_α emission line flux is 0.0033 $M_\odot$year^{-1} and emission line metallicity derived from flux ratio between NII and H_α is 8.13 dex. We derived morphological parameters using the SDSS, g, and z-band imaging data. PGC 030133 has a half-light radius of 3.38 arc second and 3.05 arc second in g-band and z-band respectively and observed one-dimensional light profile is well fitted with a Sersic function with near exponential Sersic index ~ 0.9.

Keywords: Compact dwarf galaxy, Galaxy merger, Half-light radius, H_α line, Star Formation Rate.

1. INTRODUCTION

In a galaxy merger, the interacting galaxies combine into a single galaxy that contains stars, planets, dust, and gas. In the gas clouds, formed after the merger, stars will be formed at higher rates. From the observational studies in the last ten years, it has been established that the rate of the merger of galaxies increases steadily with redshift up to z ~ 2-3 [1]. Galaxy merger in the local universe is not common to those in the early universe. Therefore, the galaxy merger in the local universe gives an in-depth examination of the role of the merger in the evolution of the galaxy. Due to the limited existing surveys of the merger between dwarf galaxies ($M_* < 10^9 M_\odot$), most of the study of galaxy mergers so far has been concentrated on massive galaxies. It is because, the difficulty in examining the dwarf galaxies is partly due to their low luminosity, low brightness, and swallow potential. The galaxy merger enhances the morphological transformations as well as the star formation and enhances far infra-red emission [2]. The extreme enhancement of star formation can produce a starburst ~1000 $M_\odot$ yr^{-1} [3, 4]. In the starburst regime, the total gas budget is dominated by H_2 gas. Star formation is one of the most important processes in the formation and evolution of the galaxy. In low redshift galaxies, star formation in spiral galaxies occurs mainly in molecular clouds. Starbursts occur in a special class of galaxies called blue compact dwarf galaxies (BCDs). Starburst galaxies are gas-rich and use their gas much faster to form stars. It is anticipated that the gas component in interacting systems is frequently predicted to be more turbulent than an isolated system.

A compact group of galaxies is a dense group of galaxies that undergo into merger after the

interaction. Zwicky [5] reported that the collision of the stars increases frequently when the compactness of a galaxy increases and the matter is ejected in different forms. When two galaxies with compact nuclei collide, an isolated compact galaxy will be formed [6]. Observationally, it is found that the compact galaxies are related to normal galaxies, compact galaxies, or even with both of them. Some galaxies are highly compact, called Ultra Compact Dwarf galaxies (UCDs) [7], the sizes, velocity dispersion, and luminosities of which are similar to the dwarf galaxy cores but they have a higher mass-to-light ratio than even the largest globular clusters [8]. The blue compact dwarf galaxies (BCDs) are the blue colored galaxies having enormous starburst activities and normally higher central surface brightness in comparison to ordinary dwarf irregular galaxies [9], which is explained to be formed by the gas-rich dwarf-dwarf mergers [10, 11]. The BCDs may also be formed by the central starburst supported by the natural gas accretion from the local environment [12, 13].

In this work, the spectroscopic and photometric analysis of a star-forming interacting dwarf galaxy PGC 030133 is performed. The star formation rate (SFR) and line metallicity are calculated by using H_α line flux in spectroscopy while the structural parameters like effective radius, half-light radius, and ellipticity are calculated in photometry.

2. MATERIALS AND METHODS

2.1 Sample Selection

A star-forming class of interacting dwarf galaxies, PGC 030133 is selected from the catalog prepared by Paudel *et al.* [14] based on low redshift (z = 0.0036) and compactness. The galaxy PGC 030133 is located in the sky position R. A. (J2000 = 10:19:01.49) and Dec. (J2000 = +21:17:00.96) at an adopted distance of 24.80 Mpc with a line-of-sight radial velocity of 1080 km/s. Its g and r-band magnitudes are 14.56 mag. and 14.34 mag. respectively, and the total absolute B-band magnitude is -17.11 mag. The logarithmic value of the stellar mass of the galaxy is 8.86 $M_\odot$. The *g-r-i* combined tri-color image of the galaxy PGC 030133 obtained from the Legacy survey is shown in Fig. 1(a). The galaxy has compact morphology with its bright center as compared to the outer part. A reddish, extended tail-like structure can be seen towards the north direction emanated from the galaxy.

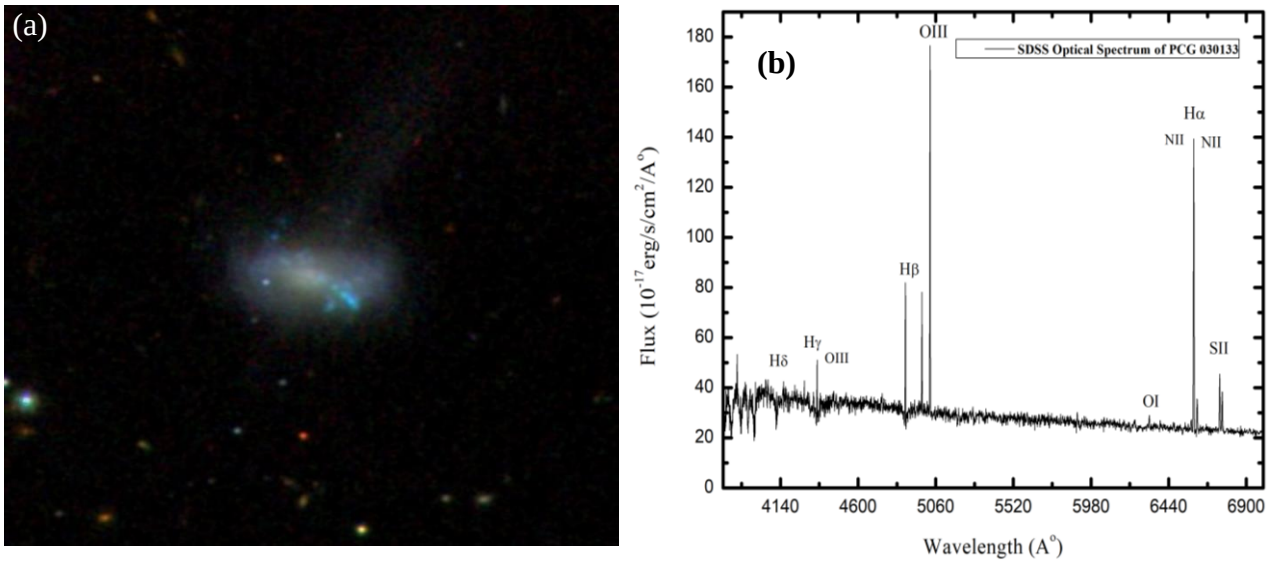

Fig. 1: (a) Optical image of PGC 030133. The image is obtained from the SDSS sky-server. (b) The optical spectrum of the galaxy PGC 030133. Position of the emission lines H_α, H_β, H_γ, H_δ, doublet OIII, OI, SII, and doublet NII are identified and are shown in the spectrum. The X-axis is rest-frame wavelength and Y-axis is flux.

In Fig. 1(b), the SDSS optical spectrum of the galaxy PGC 030133 obtained from the SDSS archival data is shown in the wavelength range of 3800 Å to 7000 Å. Several prominent emission lines such as H_α, H_β, H_γ, H_δ, doublet OIII, OI, SII, and doublet NII in the spectrum can be seen along with some small absorption lines and highlighted some of the prominent emission lines, mainly Balmer lines. The strongest emission line is $OIII_{5007}$, and the second strong line is H_α.

2.2 Data Analysis

(a) Spectroscopic Analysis

In this work, we tend to largely use the Sloan Digital Sky Survey (SDSS) archival data to measure the morphological and chemical parameters of the galaxies. The SDSS Data Archive Server (DAS) is used to get the SDSS g and r-band images and fiber-spectrum which are already well-calibrated. Both images and spectrum data are in fits file format. The SDSS fiber has a diameter of three arc seconds. Therefore, only a tiny fraction of the galaxy area of the central region is covered by the spectroscopic data. The spectral line profile is considered to be gaussian in nature and the Gaussian distribution function is defined by Squires *et al.* [15] as

$$f_G(x) = \frac{1}{\sqrt{2\pi\sigma^2}} e^{\frac{-(x-\mu)2}{2\sigma^2}} \quad (1)$$

Where, x is a normal random variable, μ is the mean deviation and σ is the standard deviation of the distribution.

Some strongest emission lines will be presented in this paper, along with their Gaussian parameters enlisted in a separate table. Then the corresponding elements will be identified. A median of the flux of the spectrum range ±100 from the center of the emission line was taken and subtracted the continuum flux before fitting each of the emission lines. Furthermore, the star formation rate (SFR), the hydrogen line ratio, metallicity, dust extinction will be calculated. The Gaussian area of the H_α emission line will be used to calculate the star formation rate of the galaxy. The SFR will be calculated by adopting the empirical formula proposed by Kennicutt [16] as follows:

$$\text{SFR } (M_\odot \text{year}^{-1}) = 7.9 \times 10^{-42} \sum \text{L } (H_\alpha) \text{ (ergs s}^{-1}) \quad (2)$$

Where $\sum$ L (H_α) is the total luminosity of the H_α line which will be calculated by using the area of the Gaussian fits. The calibration provided by Marino *et al.* [17] will be used to calculate the emission line metallicity by using a line ratio between H_α and NII which is given by

$$12 + \log (O/H) = 8.743 + 0.462 \times \log (NII/ H_\alpha) \quad (3)$$

The line ratio between H_α and H_β fluxes is called Blamer decrement c. The theoretical value of c_0 = 2.86 for an electron temperature of 10^4K and electron density of 10^2 cm^{-3} [18, 19]. Now extinction coefficient E(B − V) = 1.97× log (c/c_0). Total extinction A(H_α) = 2.45 E(B-V) in H_α band. Also, the emitted and observed fluxes of H_α can be related as A(H_α) = -2.5 log [F(H_α)$_{obs}$/F(H_α)$_{em}$]. Then the emitted flux, F(H_α)$_{em}$ can be calculated which will be used to calculate the SFR after extinction correction.

(b) Photometric Analysis

For photometric analysis, we do surface photometry on the r-band optical image of the galaxy because of its higher signal-to-noise ratio as compared to other bands. The major axis light profile of the galaxy is extracted by using the Image Reduction and Analysis Facility (IRAF) task ellipse and the best fitted elliptical isophotes are drawn on the image as described by Jedrzejewski [20], thereby producing several structural parameters of the galaxy such as ellipticity, position angle, effective radius, intensity and so on which are important tools to know the morphology and evolution of the galaxy.

To find the size of a galaxy, we use either a parametric approach or a non-parametric approach. In the former approach, the observed light profile of the galaxy is approximated into parametric functions such as exponential or de Vaucouleur functions which are the special cases of Sersic function [21] defined as

$$I(R) = I_e \exp\left\{-b_n\left[\left(\frac{R}{R_e}\right)^{1/n} - 1\right]\right\} \quad (4)$$

Here, R_e is the effective radius of the galaxy at which the intensity is I_e. n is called Sersic index which defines the 'shape' of the profile. b_n is a function of n which is selected to make sure that the radius R_e encloses half of the profile's total luminosity. The observed light profile is modeled with the Sersic function and the best fitted effective radius R_e and surface brightness μ_e of the galaxy are obtained as free parameters.

Out of many methods in the non-parametric approach, the Petrosian method is used to find the half-light radius R_h. At first, Petrosian radius a_p, [22, 23] is defined, which is the distance from the center of the galaxy at which the surface brightness at a radial distance R is 20 percent of the average surface brightness within that radius. It is assumed that the total flux of the galaxy is covered within the distance of $2a_p$. Once we know the total flux of the galaxy, the galactocentric distance at which total flux is half can be calculated, which is called half-light radius h*r*.

3. RESULTS AND DISCUSSION

3.1 Spectroscopy

Nine main emission lines: H_{δ}, H_{β}, $OIII_{4960}$, $OIII_{5007}$, H_{α}, NII_{6584}, NII_{6551}, $SII_{6717,}$ and SII_{6733} are determined from the spectrum of the galaxy PGC 030133 [Fig. 1(b)] and only six prominent lines of them are shown in Fig. 2 along with their Gaussian fits. The solid line represents the Gaussian distribution and the dots represent the observed data. The error bars are also shown in the Gaussian curves. We can see that there is an excellent agreement of the observed data with the normal distribution. The doublets OIII, NII, and SII have two different emission lines of each. The Balmer lines, H_{α}, $H_{\beta,}$ and H_{δ} are sensitive to the galaxies' gas-mass and star-formation rate. The H_{α}, principally, is a well-known tracer of star-formation and is widely used to calculate the star-formation rate of the gas-rich galaxies. Heavier elements OIII and NII emission fluxes are used to calculate the star-forming galaxies' emission line metallicity.

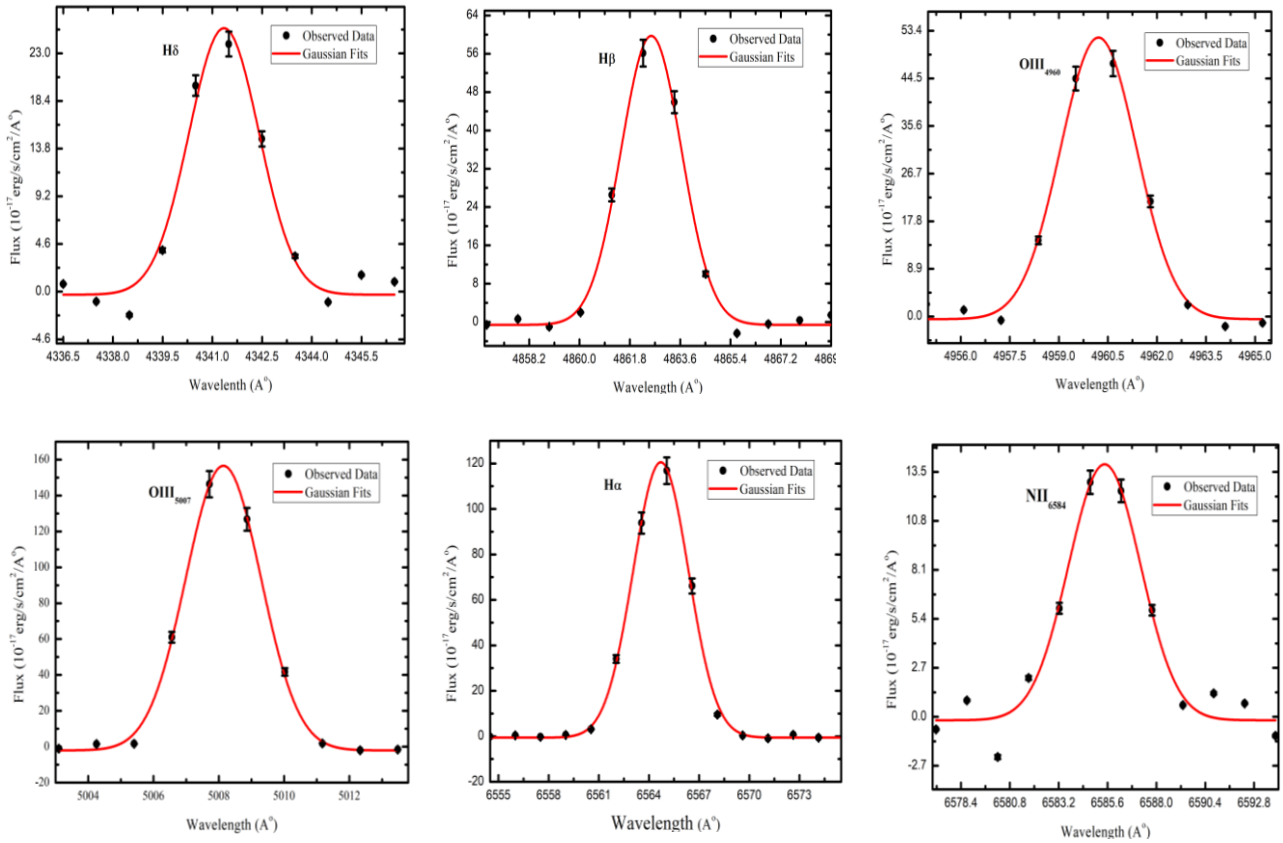

Fig. 2: Six main emission lines ($H_{\delta,}$ $H_{\beta,}$ $OIII_{4960}$, $OIII_{5007}$, $H_{\alpha,}$ and NII_{6584}) of Gaussian fitting procedure for the galaxy PGC 030133 are shown. We show a conservative estimate of the flux error in the plot, i.e., 10 % of the observed flux provided by the SDSS webpage (https://www.sdss.org/dr15/spectro/caveats/). The major cause of the broadening of the characteristic line is the Doppler broadening. The wavelengths given in the X-axis are redshift corrected.

The Gaussian parameters of the nine strongest emission lines of the galaxy PGC 030133 are enlisted in Table 1. The wavelength (λ_p) in angstrom corresponding to the peak intensity, the value of peak intensity (10^{-17} erg/s/cm^2/Å), area of the Gaussian curve (10^{-17} erg/s/cm^2/Å), the height of the Gaussian fits (10^{-17} erg/s/cm^2/Å), the positional difference between Gaussian peak and the observed peak (offset) and coefficient of regression R^2 are recorded corresponding to different elements: H_{δ}, H_{β}, $OIII_{4960}$, $OIII_{5007}$, NII_{6584}, H_{α}, NII_{6551}, SII_{6717} and SII_{6733} responsible for the characteristic lines of the galaxy. We can see from Table 1 that, $OIII_{5007}$ has a maximum intensity of 146.32×10^{-17} erg/s/cm^2/Å, corresponding to the central wavelength 5007 Å. The second strongest intensity is 116.84×10^{-17} erg/s/cm^2/Å corresponding to wavelength 6565 Å, which is due to H_{α} emission. The value of the coefficient of regression is more than 96% suggesting that the fitted curves almost agree with the Gaussian distribution.

Table 1: Preferred Gaussian parameters of the Gaussian fits are listed in this Table.

Elements	H_{δ}	H_{β}	$OIII_{4960}$	$OIII_{5007}$	NII_{6584}	H_{α}	NII_{6551}	SII_{6717}	SII_{6733}
Wavelength	4341	4862	4960	5007	6584	6565	6551	6717	6733
Intensity	23.91	56.13	47.29	146.32	12.93	116.84	4.18	22.43	15.17
Area	68.18	163.25	153.58	457.05	62.57	501.81	19.28	101.20	68.00
Height	25.72	60.32	52.65	158.58	14.11	121.10	4.69	23.49	16.82
Offset	+0.14	-0.29	+0.44	-0.43	-0.70	+0.36	+1.32	-0.47	+0.66
R^2	0.97	0.99	0.99	9.99	0.96	0.99	0.96	0.99	0.97

The negative value of the offset of the Gaussian distribution of H_{β}, $OIII_{5007}$, NII_{6584}, and SII_{6717} shows that the curves have negative skewness and they have a long left-hand tail as compared to right-hand tail. In the same way, the positive value of the offset of the Gaussian distribution of H_{δ}, $OIII_{4960}$, H_{α}, NII_{6551}, and SII_{6733} shows that the curves have positive skewness and they have a long right-hand tail as compared to left-hand tail.

Star Formation Rate

Star Formation Rate (SFR) of the galaxy PGC 030133 calculated by using equation (2) is found to be 0.0029 $M_{\odot}$ $year^{-1}$ before extinction correction and 0.0033 $M_{\odot}$ $year^{-1}$ after extinction correction. We can see that the SFR of the galaxy calculated after extinction correction is more than that before correction indicating that the observed flux of the galaxy is more than the actual flux. The calculated value of SFR of the galaxy is remarkably low (0.0033 $M_{\odot}$ $year^{-1}$) as compared to its catalog value derived by using FUV flux. This is because of the large area coverage of FUV as compared to the SDSS 3" central region. It indicates that just a fraction of star formation occurs in the central part of the galaxy.

The line ratio (c) = 3.07. This shows that the line ratio of the galaxies is slightly greater than its theoretical value (2.8). The higher value of c suggests the presence of dust at the center and the dust absorbs lower wavelength light more efficiently than higher wavelength light. The line ratio NII_{6584}/ H_{α} = 62.57/501.81 = 0.125. Line metallicity calculated by using this line ratio from equation (3) is 12 + log (O/H) = 8.13 dex which suggests that the PGC 030133 overall has metal content nearly three times lower than the sun.

3.2 Photometry

From the photometric calculations, several structural parameters of the galaxy PGC 030133 are obtained which are listed in Table 2. The first, second, third, fourth, fifth, and sixth columns represent the band of filter, mean surface brightness, effective radius, Sersic index, magnitude, and half-light radius respectively of g and z bands.

Table 2: Global structural parameters of PGC 030133.

Band	**M. S. B.Mag/arc sec^2**	**R_e (arcsec)**	**n**	**mg (mag.)**	**h*r* (arcsec)**
g	21.89	9.05	0.98	15.55	3.38
z	21.13	8.00	0.89	14.92	3.05

The angle made by the semi-major axis of the galaxy with the north celestial pole is called position angle and it gives the orientation of the galaxy. The radial profiles of position angle (PA) and ellipticity are shown in Fig. 3. From the figure, it seems that the position angle and ellipticity vary randomly as free parameters around the central region and it is almost constant in outer regions from the center of the galaxy both in g-band [Fig. 3(a)] and z-band [Fig. 3(b)].

From the Sersic modeling of the observed light profile in the parametric method, the effective radius of the galaxy is obtained to be 21.89 arcsec and 21.13 arcsec in g and z-bands respectively. The modeled major axis light profiles at g-band [Fig. 4(a)] and z-band [Fig. (b)] are shown in Fig. 4. It is found that the modeled best-fitted line perfectly coincides with the observed data and hence, the observed light profile can be well modeled with a simple Sersic function with a Sersic index of ~0.9 (near exponential).

The half-life radius (hr) is obtained from the non-parametric approach that better represents the overall size of the galaxy. At first, a Petrosian radius a_p is calculated at n = 0.2; as shown in Fig. 5(a) for g-band. It is assumed that radius $2a_p$ covers most of the galactic light and calculates a half-light radius for that total light as shown in Fig. 5(b). The same is done for the z-band as shown in Fig. 5. The derived Petrosian radius for this galaxy is 17.34 arcsec in g-band and 16.14 arcsec in z-band. Using the Petrosian method in the parametric approach, the half-light radii obtained are 3.38 arcsec and 3.05 arcsec respectively in g and z-bands. Thus, we do not need to know the endpoint of the galaxy to find its size.

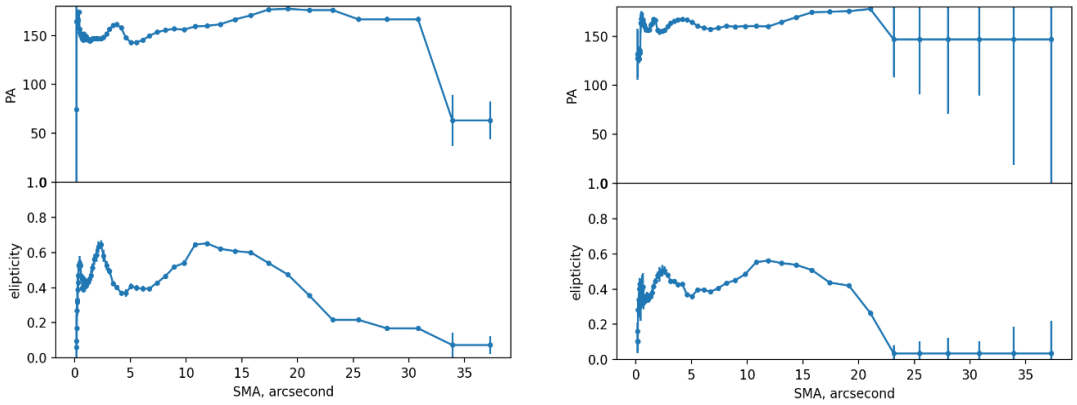

(a) g-band. *(b) z-band.*

Fig. 3: Radial profiles of position angle (PA) and ellipticity

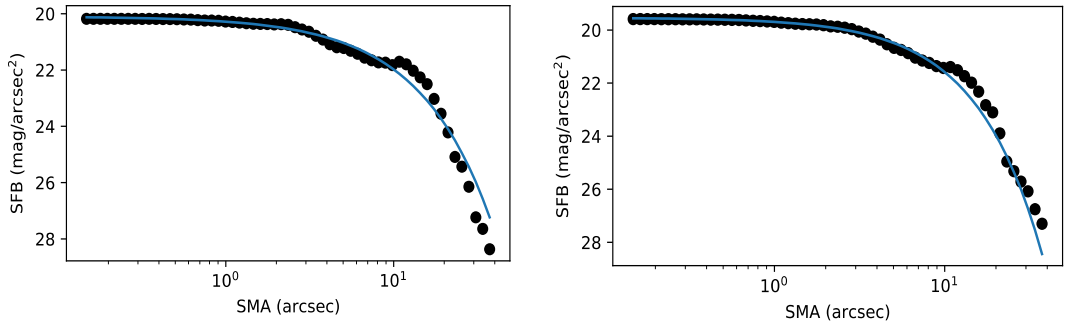

(a) g-band. *(b) z-band.*

Fig. 4: Sersic modeling of the observed light profile of the galaxy PGC 030133

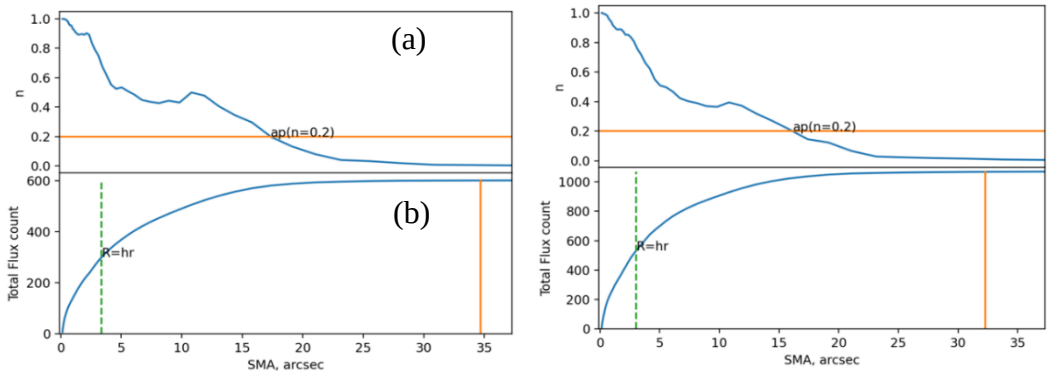

g-band. *z-band.*

Fig. 5: Radial profile of Petrosian index and cumulative intensity at g-band and z-band respectively.

Comparison with previous work

We studied spectroscopic and morphological properties of a merging dwarf galaxy PGC 030133. It is a blue compact dwarf galaxy (BCD). Merging features in BCD-type galaxies are rare. Recent literature shows VCC 848 and UM 448 are the two well-studied BCD galaxies. An optical color of both VCC 848 and UM 448 is shown in Fig. 6. Zhang *et al*. have identified a shell feature BCD (VCC 848) in the Virgo cluster [24, 25]. Compare to VCC 848, PGC 030133 is one magnitude fainter and 0.2 dex bluer in g-r color. The color difference can be well explained by comparing their surrounding environment and gas mass fraction. VCC 848 has 5 times lower gas-mass fraction compared to PGC 030133. Both, VCC 848 and PGC 030133 have a similar half-light radius of ~9". Another study of interacting BCD type galaxy is UM 448, located in a field environment [26]. A resolved spectroscopic study revealed that UM 448 is producing new stars at a staggering pace, i.e., 0.8 $M_{\odot}$year$^{-1,}$ and has overall emission line metallicity 12 + log(O/H) = 8.15 dex.

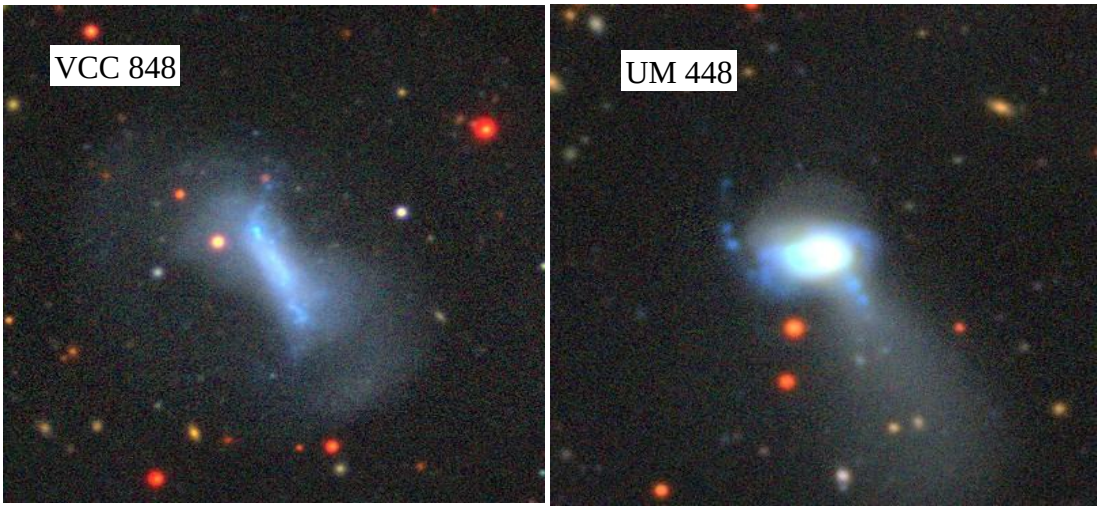

Fig. 6: Example of previously studied merging dwarf galaxies: VCC 848 and UM 448.
The images are obtained from the SDSS sky server.

4. CONCLUSION

From the spectroscopic and photometric analysis of the compact dwarf galaxy, PGC 030133 which is formed just after the merger, different conclusions are drawn based on the observations and calculations. The selected emission lines from the optical spectrum of galaxy PGC 030133 have a coefficient of regression, of more than 96% which indicates almost perfect agreement with Gaussian fits. The star formation rate and line metallicity are calculated by using H_{α} flux. The derived SFR after extinction correction is 0.0033 $M_{\odot}$year^{-1} and its metallicity is 8.13 dex. This shows that the galaxy is a normal star-forming galaxy with total metal content three times lower than the Sun. A detailed morphological study of a compact dwarf galaxy, PGC 030133 is performed by using photometry and found that the major axis light profile can be well modeled with a simple Sersic function with near exponential Sersic index. The effective radius is calculated by modeling the observed light profile in the Sersic function and the half-light radius is calculated by the Petrosian method. The derived values of half-light radius are 3.38 arcsec and 3.05 arcsec in g-band and z-band respectively.

ACKNOWLEDGEMENTS

We acknowledge the University Grants Commission of Nepal, for financial support by providing a Ph.D. Fellowship and Research Support Grant (Award No.: PhD-75/76-S & T-13) to carry out this research. We also acknowledge our anonymous referees for their valuable comments and suggestion. We would like to thank Mr. Rajesh Kumar Bachchan equally, for his remarkable efforts to help us in technical aspects.

This study is based on the archival images and spectra from the Sloan Digital Sky Survey (*http://www:sdss.org/collaboration/credits.html*).

REFERENCES

[1] Lotz, J. M.; Jonsson, P.; Cox, T. J.; Croton, D.; Primack, J. R.; Somerville, R. S. & Stewart, K. The

major and minor galaxy merger rates at z< 1.5. *The Astrophysical Journal*, **742**(2): 103 (2011).

[2] Xu, C. & Sulentic, J. W. Infrared emission in paired galaxies. II-Luminosity functions and far-infrared properties. *The Astrophysical Journal*, **374**: 407-430 (1991).

[3] Sanders, D. B. & Mirabel, I. F. Luminous infrared galaxies. *Annual Review of Astronomy and Astrophysics*, **34**(1): 749-792 (1996).

[4] Dasyra, K. M.; Tacconi, L. J.; Davies, R. I.; Genzel, R.; Lutz, D.; Naab, T.; Burkert, A.; Veilleux, S. & Sanders, D. B. Dynamical properties of ultraluminous infrared galaxies. I. Mass ratio conditions for ULIRG activity in interacting pairs. *The Astrophysical Journal*, **638**(2): 745 (2006).

[5] Zwicky, F. Compact and Dispersed Cosmic Matter, Part II. *Advances in Astronomy and Astrophysics*, **7**: 227-283 (1970). Elsevier.

[6] Zwicky, F. & Zwicky, M. A. Catalogue of selected compact galaxies and post-eruptive galaxies: (1971). Guemligen: Zwicky.

[7] Hilker, M.; Infante, L.; Vieira, G.; Kissler-Patig, M. & Richtler, T. The central region of the Fornax cluster-II. Spectroscopy and radial velocities of member and background galaxies. *Astronomy and Astrophysics Supplement Series*, **134**(1): 75-86 (1999).

[8] Drinkwater, M. J.; Gregg, M. D.; Hilker, M.; Bekki, K.; Couch, W. J.; Ferguson, H. C. et al. A class of compact dwarf galaxies from disruptive processes in galaxy clusters. *Nature*, **423**(6939): 519-521 (2003).

[9] Gil de Paz, A.; Madore, B. F. & Pevunova, O. Palomar/Las Campanas Imaging Atlas of blue compact dwarf galaxies. I. Images and integrated photometry. *Astrophysical journal supplement series*, **147**(1): 29-59 (2003).

[10] Pustilnik, S. A.; Kniazev, A. Y.; Lipovetsky, V. A. & Ugryumov, A. V. Environment status of blue compact galaxies and trigger of star formation. *Astronomy & Astrophysics*, **373**(1): 24-37 (2001).

[11] Bekki, K. Formation of blue compact dwarf galaxies from merging and interacting gas-rich dwarfs. *Monthly Notices of the Royal Astronomical Society: Letters*, **388**(1): L10-L14 (2008).

[12] Johnson, M.; Hunter, D. A.; Oh, S. H.; Zhang, H. X.; Elmegreen, B.; Brinks, E. et al. The stellar and gas kinematics of the LITTLE THINGS dwarf irregular galaxy NGC 1569. *The Astronomical Journal*, **144**(5): 152 (2012).

[13] Ashley, T.; Elmegreen, B. G.; Johnson, M.; Nidever, D. L.; Simpson, C. E. & Pokhrel, N. R. The HI chronicles of little things BCDs II: The origin of IC 10's HI structure. *The Astronomical Journal*, **148**(6): 130 (2014).

[14] Paudel S.; Smith R.; Yoon S. J.; Calderón-Castillo P. & Duc P. A. A Catalog of Merging Dwarf Galaxies in the Local Universe. *The Astrophysical Journal Supplement Series*, **237**(2): 1-20 (2018).

[15] Squires G. L. & Squires, G. L. Practical physics. *Cambridge University Press*: (2001).

[16] Kennicutt Jr, R. C. Star formation in galaxies along the Hubble sequence. *Annual Review of Astronomy and Astrophysics*, **36**(1): 189-231 (1998).

[17] Marino, R. A.; Rosales-Ortega, F. F.; Sánchez, S. F.; De Paz, A. G.; Vílchez, J.; Miralles-Caballero, D. et al. The O3N2 and N2 abundance indicators revisited: improved calibrations based on CALIFA and Te-based literature data. *Astronomy & Astrophysics*, **559:** A114 (2013).

[18] Osterbrock, D. E. Active galactic nuclei, Annals of the New York Academy of Science, **571**: 99-109 (1989).

[19] Calzetti, D.: Armus, L.; Bohlin, R. C.; Kinney, A. L.; Koornneef, J. & Storchi-Bergmann, T., The Dust Content and Opacity of Actively Star-forming Galaxies, *The Astrophysical Journal*, **533**(2): 682–695 (2000).

[20] Jedrzejewski, R. I. CCD surface photometry of elliptical galaxies–I. Observations, reduction, and results. *Monthly Notices of the Royal Astronomical Society*, **226**(4): 747-768 (1987).

[21] Sersic, J. L. Atlas de galaxias australes: (1968).

[22] Blanton, M. R.; Dalcanton, J.; Eisenstein, D.; Loveday, J.; Strauss, M. A.; SubbaRao, M. et al. The Luminosity function of galaxies in SDSS commissioning data. The Astronomical Journal, **121**(5): 2358-2380 (2001).

[23] Petrosian, V. Surface brightness and evolution of galaxies. *The Astrophysical Journal*, **209**: L1-L5 (1976).

[24] Zhang, H. X.; Smith, R.; Oh, S. H.; Paudel, S.; Duc, P. A.; Boselli, A. et al. The Blue Compact Dwarf Galaxy VCC 848 Formed by Dwarf–Dwarf Merging: H I Gas, Star Formation, and Numerical Simulations. *The Astrophysical Journal*, **900**(2): 152 (2020).

[25] Zhang, H. X.; Paudel, S.; Smith, R.; Duc, P. A.; Puzia, T. H.; Peng, E. W. et al. The Blue Compact Dwarf Galaxy VCC 848 Formed by Dwarf–Dwarf Merging. *The Astrophysical Journal Letters*, **891**(1): L23 (2020).

[26] James, B. L.; Tsamis, Y. G.; Barlow, M. J.; Walsh, J. R. & Westmoquette, M. S. The merging dwarf galaxy UM 448: chemodynamics of the ionized gas from VLT integral field spectroscopy. *Monthly Notices of the Royal Astronomical Society*, **428**(1): 86-102 (2013).

JNPS 7 (2): 49-57 (2021)
ISSN: 2392-473X (Print), 2738-9537 (Online)

Research Article *© Nepal Physical Society*
DOI: https://doi.org/10.3126/jnphyssoc.v7i2.38622

SDSS J114818.18-013823.7: Forming Compact Dwarf Galaxy through the Dwarf-Dwarf Merger

D. N. Chhatkuli[1, *], S. Paudel[2], A. K. Gautam[3] and B. Aryal[1]
[1]Central Department of Physics, Tribhuvan University, Nepal
[2]Centre for Galaxy Evolution Research, Department of Astronomy, Yonsei University, Seoul, South Korea
[3]Bhaktapur Multiple Campus, Bhaktapur, Nepal
*Corresponding Email: chhatkulidn@gmail.com

Received: *18 April, 2021;* ***Revised:*** *14 May, 2021;* ***Accepted:*** *26 June, 2021*

ABSTRACT

We studied the spectroscopic properties of the low redshift (z = 0.0130) interacting dwarf galaxy SDSS J114818.18-013823.7. It is a compact galaxy of half-light radius 521 parsec. It's r-band absolute magnitude is -16.71 mag. Using a publicly available optical spectrum from the Sloan Sky Survey data archive, we calculated star-formation rate, emission line metallicity, and dust extinction of the galaxy. Star formation rate (SFR) due to H_α is found to be 0.118 $M_\odot$ $year^{-1}$ after extinction correction. The emission-line metallicity, 12+log(O/H), is 8.13 dex. Placing these values in the scaling relation of normal galaxies, we find that SDSS J114818.18-013823.7 is a significant outlier from both size-magnitude relation and SFR-B-band absolute relation. Although SDSS J114818.18-013823.7 possess enhance rate of star-formation, the current star-formation activity can persist several Giga years in the future at the current place and it remains compact.

Keywords: Dwarf Galaxy, Emission line, Star Formation Rate, Metallicity, Extinction

1. INTRODUCTION

Dwarf galaxies are expected to be dark matter dominated objects. They are the most common galaxies in the universe. They have low surface brightness and metal poor stellar population. Their stellar masses are of the order of 10^6 to 10^9 $M_\odot$. One of the important question in understanding of formation and evolution of dwarf galaxies is how these various morphology dwarf galaxies come to exist and are they transformed from each other during the course of evolution? Dwarf galaxies are low mass objects and therefore, the capacity of binding their contents gravitationally is low as compared to their massive counterparts.

According to □CDM model of cosmology [1], the large-scale structures are formed hierarchically, and the evolution and growth of galaxies are due to merging of other galaxies [2]. Radio 21-cm observation of nearby interacting dwarf galaxies as they evolved through the merging history is yet to be explored in detail, although major mergers of galaxies are known to play an important role, particularly in the formation of the massive elliptical galaxies. In last few years, the observational evidence for mergers between dwarf galaxies has been growing. In recent years, people are working on the evolution of dwarf galaxies by dwarf-dwarf merger along with observational evidences [3, 4, 5, 6, 7, 8, 9]. Early study of dwarf-dwarf interacting pairs established that the star formation rate in gas-rich isolated dwarf-dwarf pair is enhanced by a factor ~ 2 over isolated unpaired dwarfs having similar gas fractions and similar stellar masses alike that has been found in case of huge galaxy pairs [10, 11]. This enhancement of SFR decreases on increasing the separation between two interacting pairs and the lack of enhancement in the SFR in unpaired dwarfs suggests that the star formation is driven by interaction. The star forming activities of the galaxies in the interstellar gas clouds depend up on various factors such as gas, dust, temperature,

gravity, matter-radiation interaction, hydrodynamics, thermodynamics and chemical processes [12].

The galaxies with a smaller half-light radius are called compact galaxies. Many compact galaxies are found to be connected to ordinary massive galaxies [13]. It is, therefore, believed that compact galaxies are formed during the tidal interaction between a giant galaxy and a normal dwarf galaxy where the small galaxy loses its extended outer halo and survived remanent become compact dwarf galaxies. However compact dwarf galaxies are also observed in isolation, where no giant galaxies are found in the vicinity [14]. It is argued that, those isolated compact dwarfs may have formed through the merger, but this hypothesis has not been confirmed by statistically strong evidences. Therefore, a compact galaxy is selected in this work as its study gives the idea of galaxy interactions and merger. Many compact galaxies are found to be connected to ordinary galaxies, other compact galaxies, or even both of them. It is observed that the spectrum and color of the compact galaxies are wider than that of regular galaxies

Metallicity is the abundance of the heavier elements like nitrogen, oxygen, neon, silicon etc. found in a terrestrial object. Metallicity is an important parameter to know the formation and evolution of stars and galaxies. The metallicity is also related with the luminosity, decrease in luminosity of a galaxy means increase in metallicity, at fixed mass and starburst age of the galaxy [15]. In the process of merging of galaxies, the metallicity of interior zones is diluted because of the infill of metal-poor gas driven by gravity from the outskirts of the galactic disc to central region [16].

In this work, a spectroscopic study of a compact interacting dwarf SDSS J114818.18-013823.7 located in an isolated environment will be done and explore its stellar population properties to provide another unequivocal evidence of forming compact dwarf through the merger.

2. SAMPLE SELECTION

A low red shift (z = 0.0130) galaxy, SDSS J114818.18-013823.7 is selected from the catalog of interacting dwarf galaxies [17]. It is a starburst dwarf galaxy located in the sky position R.A. (J2000) = 177.0757°, Dec. (J2000) = -1.6399° with a line-of-sight radial velocity 3902 km/s. It has g and r band magnitude 15.88 mag and 15.66 mag respectively, and total absolute B-band magnitude is -17.21 mag. The *g-r-i* combined tri-color image obtained from the Legacy survey is shown in Figure 1. An extended tail like structure can be seen along the major axis of the galaxy. The bluest star-burst region is misplaced from the center of the galaxy. Interestingly, it can be noticed that outer extended low-surface brightness part is also blue and asymmetric morphology.

The SDSS J114818.18-013823.7 is overall a compact galaxy, the derived half-light radius is 2.1 arcsecond, that corresponds a sky-projected physical radius 530 parsec (pc). It is located in an isolated environment where we find no galaxy within a 500 kpc sky-projected radius.

The SDSS has targeted the central region of SDSS J114818.18-013823.7 to take an optical spectrum. The SDSS fiber has an aperture of 3 arcsecond diameter, which covers a half of the SDSS J114818.18-013823.7 area.

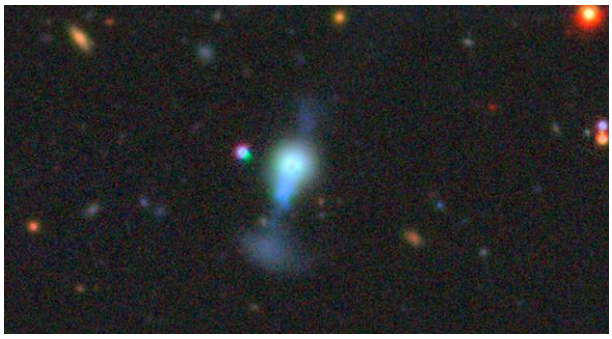

Fig. 1: Optical view of SDSS J114818.18-013823.7. The image is obtained from the SDSS sky-server.

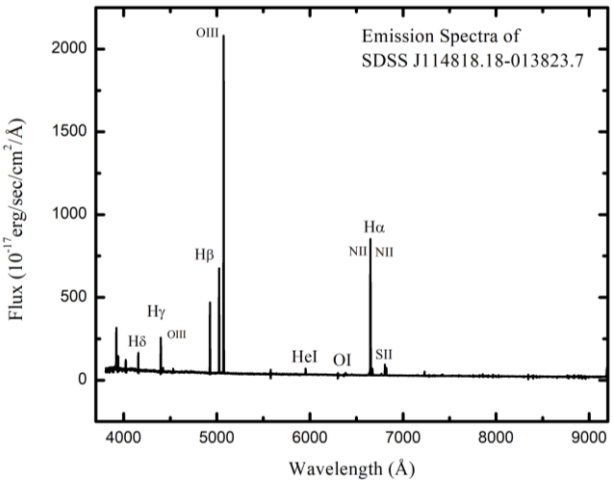

Fig. 2: Optical spectrum of SDSS J114818.18-013823.7 which is plotted by using SDSS archival data. Position of the emission lines H_α, H_β, H_γ, H_δ, OIII doublet, NII doublet, HeI, OI and SII are identified. The X-axis is rest-frame wavelength and Y-axis is flux.

The SDSS optical spectrum of the galaxy SDSS J114818.18-013823.7 in the wavelength range of (3757-9090) Å is shown in the Figure 2. Several characteristic lines can be seen in the spectrum and some of the prominent emission lines, H_α, H_β, H_γ, H_δ, OIII doublet, NII doublet, HeI, OI and SII are highlighted. The strongest emission line is OIII, and H_α is the strongest among the Balmer lines. From this spectrum, it is clear that the galaxy is emission type galaxy.

3. MATERIALS AND METHODS

To measure morphological and chemical parameters of the galaxy, the SDSS archival database (*www.sdss.org/collaboration/credits.html*) is used. The SDSS DR12 data was extracted from the FITS file format by using software ALADIN. The galaxy spectra were obtained by plotting the data using another software ORIGIN. Then the gaussian fits were performed on the prominent emission lines by inspection. The continuum flux is subtracted by taking a median of flux value of spectrum range ± 100 from the center of the emission line and then each line is modelled. The gaussian curves so obtained are explained by a mathematical expression called Gaussian distribution function [18] which is given by

$$f_G(x) = \frac{1}{\sqrt{2\pi\sigma^2}} e^{\frac{-(x-\mu)2}{2\sigma^2}} \quad \text{... (1)}$$

Where, *x* is a normal random variable, μ is the mean and σ is the standard deviation of the distribution. The broadening of the emission lines is due to Doppler's broadening. In this work, 10 prominent emission lines were selected and the gaussian parameters like Full Width Half Maxima (FWHM), area, height, peak intensity, wavelength corresponding to the peak intensity, regression coefficient of each of the gaussian curves were noted in a table and the corresponding responsible element for the emission will be identified. Finally, the emission line due to emission of H_α will be identified and using its area, the star formation rate (SFR) of the galaxy will be calculated before and after extinction correction. In this work, the Hα luminosity is used as the main calculator of the instantaneous Star Formation Rate of the galaxy. The process of recombination of ionized hydrogen in gas clouds and the dust produces Hα line flux. The O and B type stars produce enormous radiation field that ionizes the hydrogen and several emission lines are produced due to recombination of the free electrons with the ionized hydrogen. Hα is one of the most luminous line in visible region and Kennicutt–Schmidt empirical relation can be used to calculate SFR using the Hα emission line flux [19].

$$\text{SFR } (M_\Theta \text{ year}^{-1}) = 7.9\times10^{-42} \sum L\ (H_\alpha)\ (\text{ergs s}^{-1}) \quad \text{... (2)}$$

Where, $\sum L(H_\alpha)$ is the total luminosity of H_α line which will be calculated by using area of the Gaussian fit of H_α line. $\sum L(H_\alpha)$ = Area of Gaussian fit × 10^{-17} × $4\pi R^2$ (ergs s^{-1}). R is the radius of the sphere which is calculated as R = D × 3.08 × 10^{24} cm. Here, D is luminosity distance in Mpc. The Hα emission line is one of the best estimators of SFR because, it depends up on very young stars only, and is independent of recent star formation history. Moreover, Hα traces directly the SFR and has very low dependence on metallicity or on ionization conditions of the gas cloud.

The emission line metallicity of the galaxy can be calculated using ratio of NII and Hα emission line flux [20], using an equation

$$12+\log(O/H) = 8.743 + 0.462 \times \log(NII/H_\alpha) \quad \text{... (3)}$$

The difference in extinction between B band and V band is E (B − V) = 1.97× log (c/c_0). Where, c = H_α/H_β is Blamer decrement. The theoretical value of c_0 is 2.86 [19] for an electron temperature of 10^4 K. Extinction coefficient is now given by

$$A\ (H\alpha) = 2.45\ E\ (B–V) \quad \text{... (4)}$$

4. RESULTS AND DISCUSSION

4.1 Fitted Gaussian Curves

The Gaussian curves representing Gaussian fits of ten selected emission lines HeI, H_δ. H_γ, H_β, $OIII_{4960}$, $OIII_{5008}$, OI, H_α, NII and SII are shown in the Figures 3 and 4 below. The statistical error bars (±1σ) are shown in each curve. From the figure, it can be seen that the observed data agrees almost perfectly with the Gaussian distribution. The Balmer lines i.e., H_δ, H_γ, H_β and H_α that lie in the wavelength range of (4096 to 6574) Å are shown in Figure 3. Balmer lines appear due to abundance of hydrogen in the galaxy which appear relatively stronger as compared to other elements and are often used to identify the unknown objects, to determine the radial velocity, distance, star formation rate and so on. Specially, H_α is used to calculate SFR of the gas-rich galaxies.

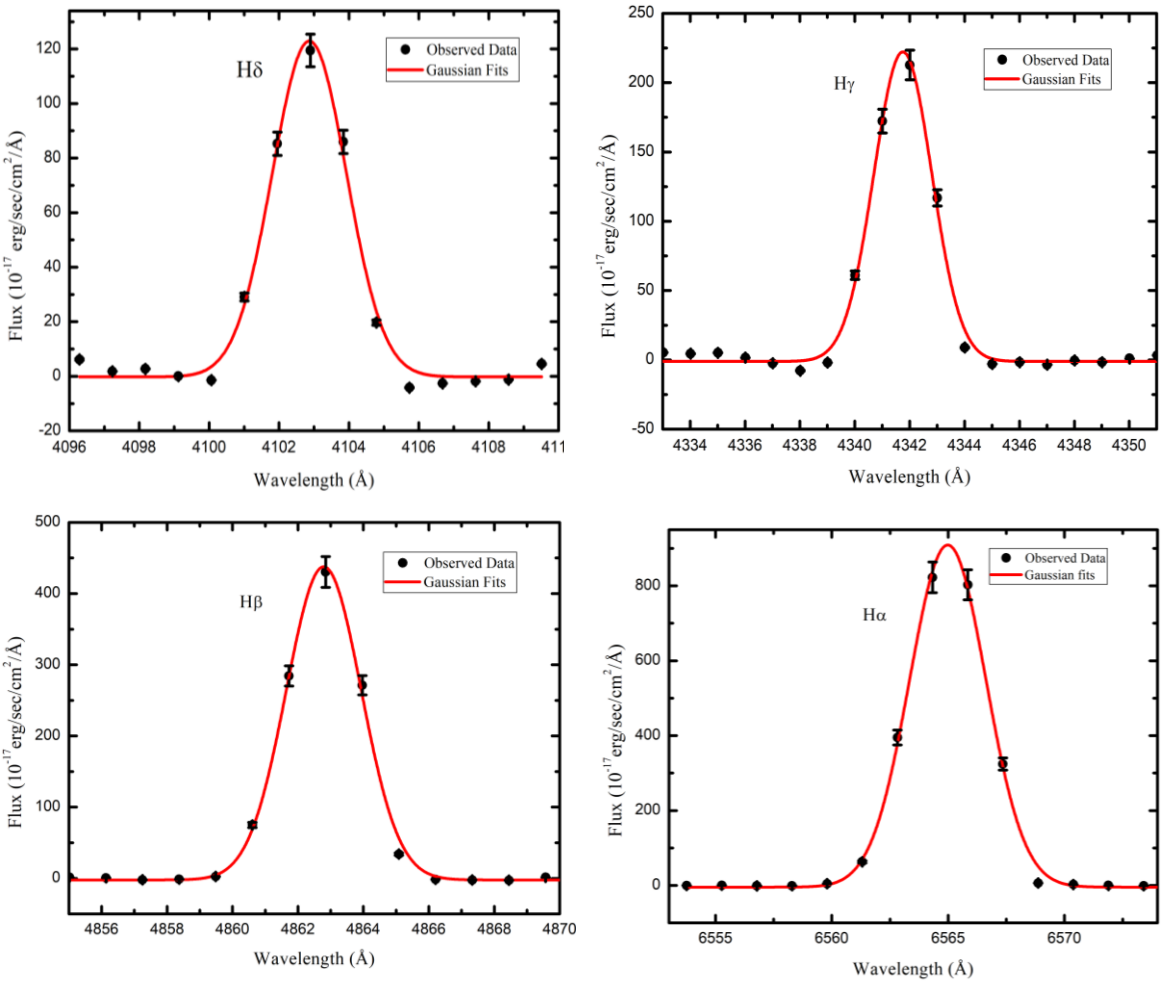

Fig. 3: Gaussian fitting procedure of the prominent emission spectral lines is shown in the figure. Four Balmer lines are: H_δ. H_γ, H_β, and H_α. Solid curves represent Gaussian fits. We show a conservative estimate of the flux error in the plot, i.e., 10 % of the observed flux provided by SDSS webpage (https://www.sdss.org/dr15/spectro/caveats/). Error bars represent the ±1σ statistical errors. The major cause of broadening of characteristic line is due to the Doppler broadening. The wavelengths given in the X-axis are redshift corrected.

Figure 4 shows the emission lines due to HeI, OIII doublet, OI, NII and SII in the wavelength range (3883 to 6729) Å. OIII doublet produces two lines at wavelengths 4960.1 Å and 5008.3 Å respectively. The emission line fluxes of heavier elements OIII and NII are used to calculate the emission line metallicity.

4.2 Observation Table

All the ten emission spectral lines HeI, H_δ. H_γ, H_β, $OIII_{4960,}$ $OIII_{5008}$, OI, H_α. NII and SII of the galaxy SDSS J114818.18-013823.7 are enlisted in the Table 1 along with their Gaussian parameters. The first, second, third and fourth columns represent serial number, the elements responsible for the emission of lines, the wavelength (λ_p) corresponding to the peak intensity, the value of peak intensity (I_p) in erg/s/cm^2/Å respectively. Similarly, fifth, sixth, seventh eighth and nineth columns represent full width half maximum (FWHM), area, height of Gaussian curve, offset and coefficient of regression of the fitted data respectively. We can see that the line due to $OIII_{5008}$ seems to be the most intense (2036.4 erg/s/cm^2/Å) corresponding to the wavelength of 5008.3 Å. H_α is the second strongest line (822.5 erg/s/cm^2/Å) at 6564.3Å. The weakest line is OI (5.3 erg/s/cm^2/Å) at 6366.4 Å. The small values of FWHM (2.30 - 4.01) Å of the Gaussian curves indicate the characteristic peaks. The value of FWHM is maximum (4.01 Å), for NII which indicates that the observed data is in excellent agreement with the Gaussian distribution.

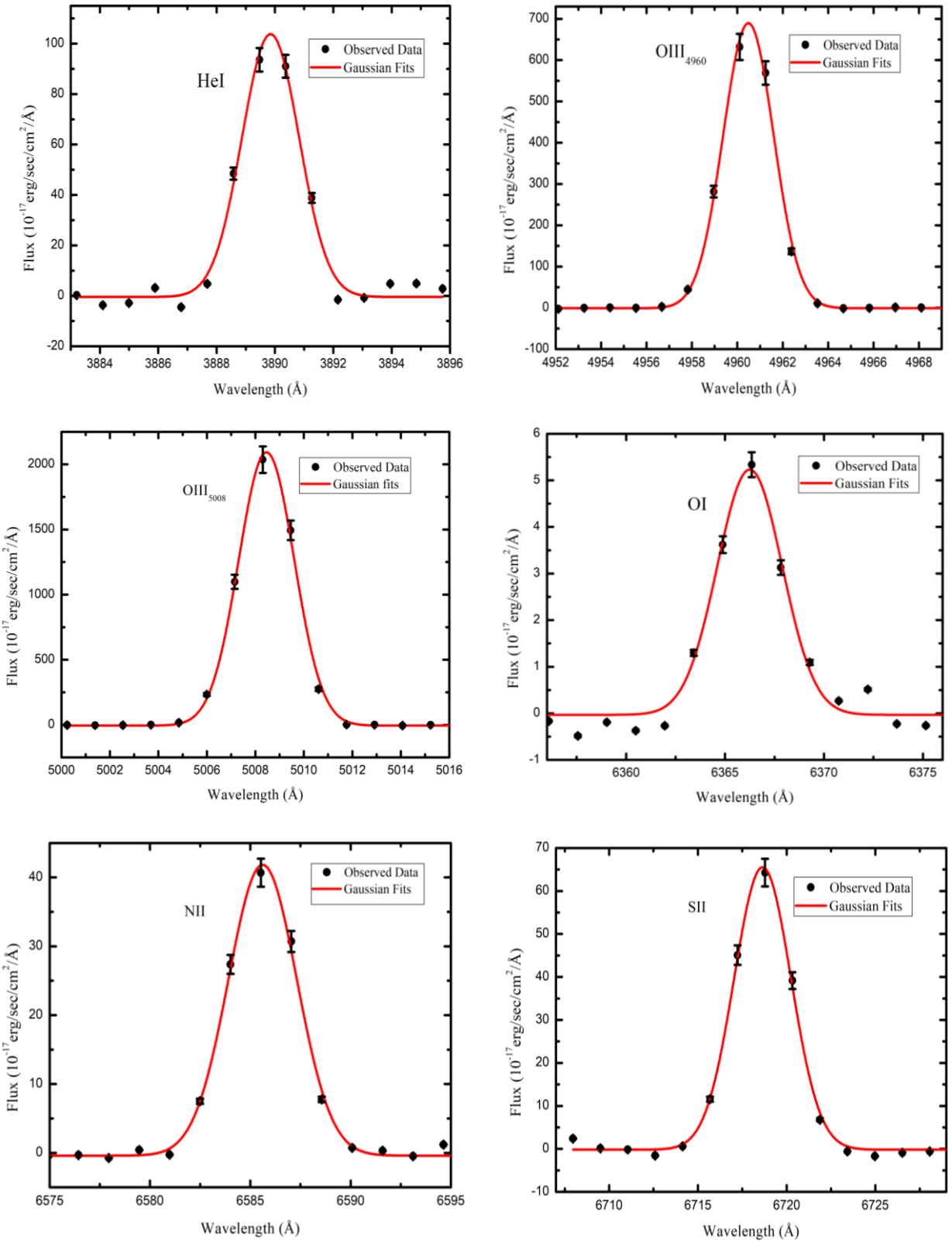

Fig. 4: Second six characteristic peaks of the elements HeI, OIII$_{4960}$, OIII$_{5008}$, OI, NII and SII of the SDSS DR12 spectra of interacting dwarf galaxy SDSS J114818.18-013823. Error bars represent the ±1σ statistical errors. The major cause of broadening of characteristic line is due to the Doppler broadening. The wavelengths given in the X-axis are redshift corrected.

Table 1: This table enlists the Gaussian parameters of the selected characteristic emission lines of spectra of interacting dwarf galaxy SDSS J114818.18-013823.7 shown in Figure 3 and 4.

S.N.	Element	λ_p (Å)	I_p	FWHM (Å)	Area (erg/s/cm^2/Å)	Height (erg/s/cm^2/Å)	Offset	R^2
1.	HeI	3889.5	93.6	2.30	255.85	104.18	– 0.379	0.986
2.	H_δ	4102.9	119.5	2.50	327.61	123.12	+ 0.029	0.990
3.	H_γ	4342.0	212.8	2.49	591.04	223.27	+ 0.256	0.993
4.	H_β	4862.8	430.4	2.70	1261.05	439.90	+ 0.058	0.997
5.	OIII	4960.1	631.9	2.62	1927.93	690.34	– 0.384	0.998
6.	OIII	5008.3	2036.4	2.70	6028.07	2098.08	– 0.156	0.998
7.	OI	6366.4	5.3	3.87	21.65	5.26	+ 0.100	0.949
8.	H_α	6564.3	822.5	3.86	3756.55	913.60	– 0.655	0.998
9.	NII	6585.5	40.7	4.01	180.35	42.23	– 0.090	0.996
10.	SII	6718.8	64.3	3.78	264.10	65.70	+ 0.136	0.995

In the 8th column, we can see both positive and negative values of the Gaussian offset which shows the skewness of the data. The Gaussian distributions of the selected lines of H_δ. H_γ, H_β, OI and SII have positive value of the offset, thereby showing that the curves have a positive skewness. This indicates that the curves are not symmetric and the right-hand tail is longer than the left-hand tail. Likewise, the negative values of Gaussian offset of HeI, OIII doublet, H_α and NII indicate the negative skewness of the curves and the left-hand tail is longer than the right-hand tail. The coefficient of regression is represented by R^2 that measures how close the data are to the fitted curve. From the 9th column of table 1, it can be seen that the value of R^2 is more than 98 % except for OI suggesting that the fitted data agrees almost perfectly with Gaussian distribution.

4.3 Calculation

Star Formation Rate

Area of Gaussian curve for H_α line = 3756.55 × (10^{-17} erg/s/cm^2/Å). Using the adopted distance to the galaxy D = 55.44 Mpc and H_α line flux, Star Formation Rate (SFR) of the galaxy can be calculated by using equation (2). Therefore, SFR = 0.109 $M_\odot$ year $^{-1}$.

Metallicity

Line ratio H_α/H_β = 2.98 indicating that there is internal extinction. The line ratio NII/ H_α = 0.048. Line metallicity can be calculated by using equation 3 as 12 + log (O/H) = 8.13 dex.

SFR after Extinction Correction

From above calculation, Blamer decrement is given by, c = H_α/H_β = 2.98. Now, using equation (4), extinction coefficient is calculated to be, A (Hα) = 0.089408 mag.

Again, we have A (Hα) = – 2.5 log (F(Hα)obs/F(Hα)em). Using the value of observed flux F(Hα)obs = 3756.55 erg/s/cm^2/Å, in this equation the emitted flux is calculated to be F(Hα)em = 4073.80 erg/s/cm^2/Å. Now, the star formation rate after extinction correction is calculated to be, SFR = 0.118 $M_\odot$ year $^{-1}$. It can be seen clearly that the SFR of the Galaxy before extinction is 0.108 $M_\odot$ year $^{-1}$ and that after extinction correction is 0.118 $M_\odot$ year $^{-1}$. i.e.; the SFR after extinction correction is more than its previous value, which means that observed flux of the galaxy is less than the actual value of the flux. Similar work was done by Chhatkuli *et al.* [21] for an interacting dwarf galaxy NGC 2604, and calculated the SFR to be 0.0927 $M_\odot$ year $^{-1}$, that indicates that this galaxy has higher rate of star formation. Blue compact dwarf galaxies are mostly found in isolation but they rarely go through the interaction. Recently, VCC 484 located in the Virgo cluster has been identified as merging blue compact dwarf, but detailed radio and optical imaging study

revealed that VCC 484 no longer become compact dwarf after a few Mega year of evolution time [22]. NGC 4449 is a nearest interacting dwarf which show burst of star-formation with an ongoing star-formation rate of 0.5 $M_\odot$ year $^{-1}$ [23].

4.4 Scaling Relation

Galaxy size-mass relation has been a standard tool to study galaxy formation and evolution mechanism [24]. In Figure 5, two scaling relations between size and r-band magnitude, and SFR and B-band magnitude are shown. It is clear from the left panel plot that SDSS J114818.18-013823.7 is a compact galaxy, where it is located significantly outside of the main locus of size-magnitude relation defined by normal galaxy's points. The right panel plot shows a relation between B-band absolute magnitude and log(SFR) of star-forming galaxies, where our galaxy the SDSS J114818.18-013823.7 is identified with a blue symbol. The comparison sample galaxies, gray symbol data point, are local volume star-forming galaxies [25]. As compared to the normal star-forming galaxies, SDSS J114818.18-013823.7 has enhanced star-formation activity. It has current SFR 0.118 $M_\odot$ year $^{-1}$. The catalog value of neutral hydrogen gas mass is 6.4 x 10^8 $M_\odot$. This implies that current star-formation activity can persist several Giga years in the future at the current pace.

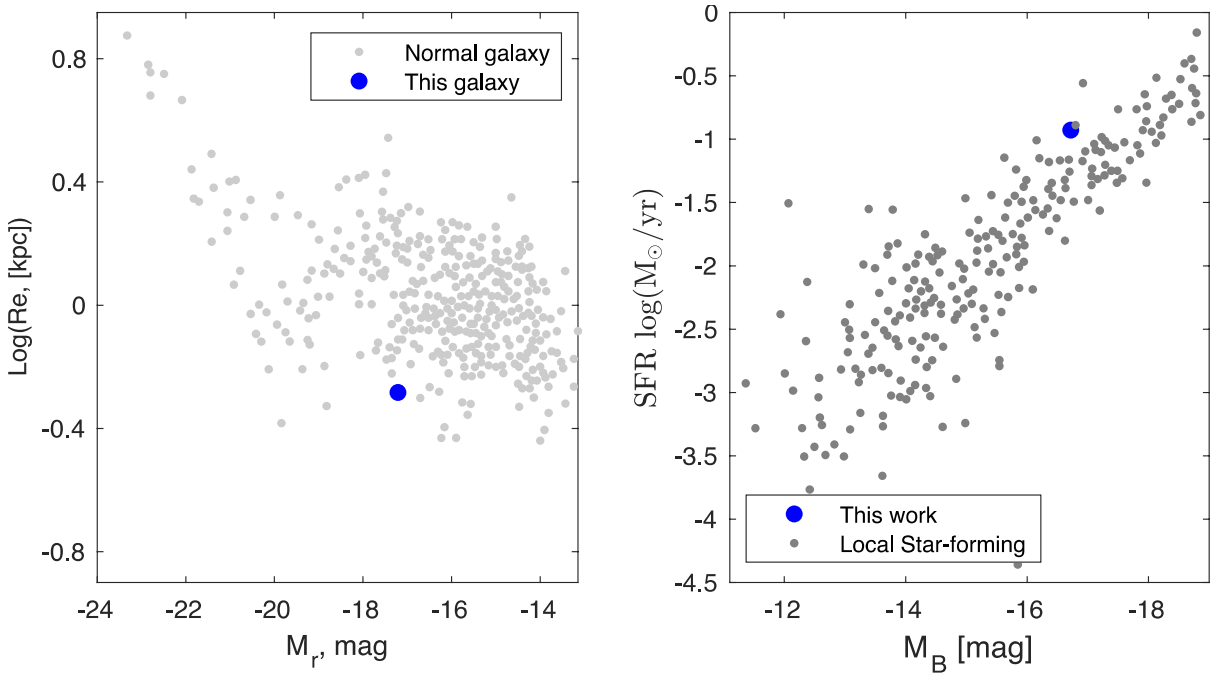

Fig. 5: Size-magnitude relation in Left and SFR-B-band magnitude relation in right. SDSS J114818.18-013823.7 is shown in blue symbol. The gray symbol represents comparison sample taken from Paudel et al., 2011 (left) and Lee et al., (2009) for the right.

5. CONCLUSION

In this work, we studied the spectroscopic properties of the low redshift (z = 0.0130) interacting dwarf galaxy SDSS J114818.18-013823.7 which provides another unequivocal evidence of forming compact dwarf galaxy through the merger. Ten prominent emission lines were noticed from the optical spectra of the galaxy and following conclusions are drawn.

1. The responsible elements for the observed emission lines are HeI, H_δ. H_γ, H_β, $OIII_{4960}$, $OIII_{5008}$, OI, H_α. NII and SII.
2. $OIII_{5008}$ is the most intense (2036.4 erg/s/cm^2/Å) line corresponding to the wavelength of 5008.3 Å, H_α is the second strongest line (822.5 erg/s/cm^2/Å) at 6564.3 Å and the weakest is OI (5.3 erg/s/cm^2/Å) at 6366.4 Å.
3. The emission lines are fitted with gaussian profile and the coefficient of regression of all the emission lines is greater than 98 % except for OI, indicating that the lines are in almost perfect agreement with the Gaussian distribution. The FWHM is found to be less than 5 Å. The broadening of the lines is due to Doppler's broadening.

4. Star formation rate (SFR) calculated from H_{α} emission line is found to be 0.118 $M_{\odot}$ $year^{-1}$ after extinction correction.
5. The galaxy SDSS J114818.18-013823.7 is a compact galaxy having enhanced star formation activities as compared to the normal star forming galaxies and current SFR indicates that current star-formation rate can be prolonged for several Giga year in time and the galaxy remains compact due to central star-formation.

ACKNOWLEDGEMENTS

We are thankful to the anonymous referee for her/his constructive comments to improve the manuscript. D. N. Chhatkuli acknowledges the University Grants Commission of Nepal, for financial support by providing PhD Fellowship and Research Support Grant (Award No.: PhD-75/76-S & T-13) to carry out this research. This study is based on the archival images and spectra from the Sloan Digital Sky Survey (*http://www:sdss.org/collaboration/credits.html*).

REFERENCES

[1] Spergel, D. N.; Bean, R.; Doré, O.; Nolta, M. R.; Bennett, C. L.; Dunkley, J.; ... & Wright, E. L.. Three-year Wilkinson Microwave Anisotropy Probe (WMAP) observations: implications for cosmology. *The Astrophysical Journal Supplement Series*, **170**(2): 377 (2007).

[2] Conselice, C. J.; Yang, C.; & Bluck, A. F. The structures of distant galaxies–III. The merger history of over 20 000 massive galaxies at z< 1.2. *Monthly Notices of the Royal Astronomical Society*, **394**(4): 1956-1972 (2009).

[3] Amorisco, N. C.; Evans, N. W.; & Van De Ven, G. The remnant of a merger between two dwarf galaxies in Andromeda II. *Nature*, **507**(7492): 335-337 (2014).

[4] Crnojević, D.; Sand, D. J.; Caldwell, N.; Guhathakurta, P.; McLeod, B.; Seth, A.; ... & Toloba, E. Discovery of a close pair of faint dwarf galaxies in the halo of Centaurus A. *The Astrophysical Journal Letters*, **795**(2): L35 (2014).

[5] Martinez-Delgado, D.; Romanowsky, A. J.; Gabany, R. J.; Annibali, F.; Arnold, J. A.; Fliri, J.; ... & Merrifield, M. R.. Dwarfs gobbling dwarfs: a stellar tidal stream around NGC 4449 and hierarchical galaxy formation on small scales. *The Astrophysical Journal letters*, **748**(2): L24 (2012).

[6] Johnson, M. Determining the Nature of the Extended HI Structure around LITTLE THINGS Dwarf Galaxy NGC 1569. *The Astronomical Journal*, **145**(6): 146 (2013).

[7] Nidever, D. L.; Ashley, T.; Slater, C. T.; Ott, J.; Johnson, M.; Bell, E. F.; ... & Burton, W. B. Evidence for an interaction in the nearest starbursting dwarf irregular galaxy IC 10. *The Astrophysical Journal Letters*, **779**(2): L15 (2013).

[8] Rich, R. M.; Collins, M. L.; Black, C. M.; Longstaff, F. A.; Koch, A.; Benson, A.; & Reitzel, D. B. A tidally distorted dwarf galaxy near NGC 4449. *Nature*, **482**(7384): 192-194 (2012).

[9] Paudel, S.; & Sengupta, C. UGC 4703 Interacting Pair Near the Isolated Spiral Galaxy NGC 2718: A Milky Way Magellanic Cloud Analog. *The Astrophysical Journal Letters*, **849**(2): L28 (2013).

[10] Stierwalt, S.; Besla, G.; Patton, D.; Johnson, K.; Kallivayalil, N.; Putman, M.; ... & Ross, G. TiNy Titans: The role of dwarf–dwarf interactions in low-mass galaxy evolution. *The Astrophysical Journal*, **805**(1): 2 (2015).

[11] Ellison, S. L.; Mendel, J. T.; Patton, D. R.; & Scudder, J. M. Galaxy pairs in the Sloan Digital Sky Survey–VIII. The observational properties of post-merger galaxies. *Monthly Notices of the Royal Astronomical Society*, **435**(4): 3627-3638 (2013).

[12] Krumholz, M. R.; Klein, R. I.; & McKee, C. F. Radiation-hydrodynamic simulations of the formation of orion-like star clusters. II. The initial mass function from winds, turbulence, and radiation. *The Astrophysical Journal*, **754**(1): 71 (2012).

[13] Labarrere, C. A.; Woods, J. R.; Hardin, J. W.; Campana, G. L.; Ortiz, M. A.; Jaeger, B. R.; ... & Wozniak, T. C.. Early prediction of cardiac allograft vasculopathy and heart transplant failure. *American Journal of Transplantation*, **11**(3): 528-535 (2011).

[14] Paudel, S.; Lisker, T.; Hansson, K. S. A.; & Huxor, A. P. An isolated, compact early-type galaxy with a diffuse stellar component: Merger origin? *Monthly Notices of the Royal Astronomical Society*, **443**(1), 446-453 (2014).

[15] Parnovsky, S. L.; Izotova, I. Y.; & Izotov, Y. I. H α and UV luminosities and star formation rates in a large sample of luminous compact galaxies. *Astrophysics and Space Science*, **343**(1): 361-376 (2013).

[16] Rupke, D. S.; Kewley, L. J.; & Barnes, J. E. Galaxy mergers and the mass-metallicity relation: evidence for nuclear metal dilution and flattened gradients from numerical simulations. *The Astrophysical Journal Letters*, **710**(2): L156 (2010).

[17] Paudel S.; Smith R.; Yoon S. J.; Calderón-Castillo P.; & Duc P. A. A Catalog of Merging Dwarf Galaxies in the Local Universe. *The Astrophysical Journal Supplement Series*, **237**: 1-20 (2018).

[18] Squires G. L. & Squires G. L. Practical physics. *Cambridge University press*. https://www.cambridge.org/np/academic/subjects/physics/general-and-classical physics/practical-physics-4th-edition? (2001).

[19] Kennicutt Jr. and Robert C. Star Formation in Galaxies Along the Hubble Sequence. *Annual Review of Astronomy and Astrophysics*, **36**(1): 189-231 (1998).

[20] Marino, R. A.; Rosales-Ortega, F. F.; Sánchez, S. F.; De Paz, A. G.; Vílchez, J.; Miralles-Caballero, D., ... & Van De Ven, G. The O3N2 and N2 abundance indicators revisited: improved calibrations based on CALIFA and Te-based literature data. *Astronomy & Astrophysics*, **559**: A114 (2013).

[21] Chhatkuli, D.; Paudel, S.; & Aryal, B. Study of Star Formation Rate and Metallicity of an Interacting Dwarf Galaxy NGC 2604. *Journal of Institute of Science and Technology*, **25**(2): 55-60 (2020).

[22] Zhang, H. X.; Paudel, S.; Smith, R.; Duc, P. A.; Puzia, T. H.; Peng, E. W.; ... & Oh, S. H. The Blue Compact Dwarf Galaxy VCC 848 Formed by Dwarf–Dwarf Merging. *The Astrophysical Journal Letters*, **891**(1): L23 (2020).

[23] Cignoni, M.; Sacchi, E.; Aloisi, A.; Tosi, M.; Calzetti, D.; Lee, J. C.; ... & Whitmore, B. C. Star Formation Histories of the LEGUS Dwarf Galaxies. I. Recent History of NGC 1705, NGC 4449, and Holmberg II. *The Astrophysical Journal*, **856**(1): 62 (2018).

[24] Janz, J. & Lisker, T. The Sizes of Early-Type Galaxies. *The Astrophysical Journal*, **689**(1): L25–L28 (2008).

[25] Lee, J. C.; Kennicutt, R.C., Jr.; Funes, S.J.J.G.; Sakai, S.; Akiyama, S. Dwarf Galaxy Starburst Statistics in the Local Volume. *The Astrophysical Journal*, **692**: 1305–1320 (2009).

BIBECHANA
ISSN 2091-0762 (Print), 2382-5340 (Online)
Journal homepage: http://nepjol.info/index.php/BIBECHANA
Publisher: Department of Physics, Mahendra Morang A.M. Campus, TU, Biratnagar, Nepal

A spectroscopic study of the low redshift dwarf galaxy SDSS J134326.99+431118.7 to calculate star formation rate

Daya Nidhi Chhatkuli[1]*, Sanjaya Paudel[2], Binil Aryal[1]**
[1]Central Department of Physics, Tribhuvan University, Nepal.
[2]Centre for Galaxy Evolution Research, Department of Astronomy, Yonsei University, Seoul, South Korea.
*Email: chhatkulidn@gmail.com
**Email: binil.aryal@cdp.tu.edu.np

Article Information:
Received: June 15, 2020
Accepted: July 10, 2020

Keywords:
Dwarf galaxy
Star formation rate
Characteristic peaks
H_α line

ABSTRACT
We present a spectroscopic study of an interacting emission-line dwarf galaxy SDSS J134326.99+431118.7. We analyzed eight-strong emission lines of wavelength in a range of 3902.1Å to 6619.1Å. Among them, the strongest emission line is OIII, with an intensity of 1043.6 x 10^{-17} erg/s/cm^2/Å. These characteristic lines show a perfect Gaussian fit with a coefficient of regression greater than 98%, where the derived full width half maximum (FWHM) is less than 3.8 Å. The line ratio between H_α and H_β, (H_α/H_β), is 2.73. This suggests that the galaxy is a starburst galaxy. Star Formation Rate (SFR) of the galaxy derived from H_α emission line flux is 0.019 $M_\odot year^{-1}$ and emission line metallicity derived from flux ratio between NII and H_α is 7.85 dex. These morphological and physical properties of SDSSJ134326.99+431118.7 are very similar to those of a typical Blue Compact Dwarf (BCD) galaxy. We conclude that we have presented another evidence of forming a BCD-type galaxy through a merger.

DOI: https://doi.org/10.3126/bibechana.v18i1.29466

1. Introduction

A galaxy whose gravitational fields interact with another and produce a disturbance in their morphological and dynamical properties are called interacting galaxies [1]. There are many observational pieces of evidence that link galaxies' morphological and physical evolution with interactions and mergers. Starburst activities are frequent among the interacting galaxies, particularly in low mass cases where a vast amount of gas reservoir is present. The gravitational tidal force of the interacting system destroys the regular

morphology of the participating galaxies and produces bridges and tails between them [2]. This also destabilizes gaseous disk leading to an inflow of star-forming gas toward the central region, which creates a nuclear starburst [3, 4].

According to Lambda Cold Dark Matter (ΛCDM) cosmology, dwarf galaxies are the building blocks of the universe, and all large-scale structures are build up progressively later with the hierarchical coalescence of these building blocks. They dominate the number distribution at any epoch of the universe, and there should be a more frequent merger between dwarf galaxies than between massive galaxies. However, the dwarf-dwarf interactions are not explored in detail, as in the case of massive galaxies' interactions. On the other hand, dwarf galaxies are inherently low-surface brightness in nature, and it is challenging to detect them. Because of this, it is not trivial to detect tidal features in dwarf galaxies, which are even fainter than host galaxies.

There is a great deal of the study of the interacting massive galaxies, but it is less known about the interaction and mergers of the dwarf galaxies to date [5]. It is also true that the merging probability of dwarf galaxies is low at low redshift universe as most of them are bound within the gravity of large scale structures, where dispersion velocities are high [6]. Because of this, dwarf-dwarf interactions are more frequent in the field environment than in the group environment where galaxies are more gas-rich compare to dwarf galaxies located in the group environment [7]. Furthermore, dwarf galaxies merge frequently and assemble due to collision to make bigger galaxies. The growth and evolution of the galaxies is based on the merger of dwarf galaxies [8]. Therefore, it is interesting to study the dwarf-dwarf merger at a low redshift regime and understand the effect of the merger in gas removal and star-formation in these low-mass systems. It is not conclusively understood how important a merger is in dwarf galaxy evolution.

Stierwalt et al. (2015) [9] is the first to perform a statistical study of interacting dwarf galaxy pairs and found that star formation is more intensified in paired dwarfs than that in unpaired galaxies. They found that star-formation rates of interacting dwarf galaxies are anti-correlated with their pair separation. Moreover, a significant fraction of starburst in dwarf galaxies are contributed by the interaction. Lelli et al. (2018) suggest that the activity of the starburst galaxies such as blue compact dwarfs (BCDs) strongly depends on the inner shape of the potential well and the central gas surface density [10].

In this work, we present the spectroscopic study of a star-forming interacting dwarf galaxy SDSS J134326.99+431118.7, a morphologically blue and edge-on dwarf galaxy. This galaxy is located in a nearly isolated environment where we find no massive galaxies within a 500 kpc radius around it.

2. Sample selection

SDSS J134326.99+431118.7 is listed in the catalog of interacting dwarf galaxies by Paudel et al. (2018) [11]. It is located in the sky position RA= 13h 43m 26.9s and Dec = 43d 11m 18.78s with a line-of-sight radial velocity 2511 (Z = 0.00837) km/s. It has g and r band magnitude 16.18 mag and 15.98 mag respectively, and total absolute B-band magnitude is -15.34 mag. In Figure 1, we show the *g-r-i* combined tri-color image obtained from the Legacy survey. We can see a shell feature morphology at the lower side with an extended arc-like feature at the sky projected distance of 5 kpc from the center. The central part is significantly blue compare to the outer extended low-surface brightness region. A red cross mark identifies an off-centered star-burst region, where the SDSS has positioned its fiber to take the optical spectrum.

In Figure 2, we show the SDSS optical spectrum of the wavelength range of 4000 to 6600 A. We can see several characteristic lines in the spectrum and highlighted some of the prominent emission lines, mainly Balmer lines. The strongest emission line is OIII, and H_α is the strongest among the Balmer lines.

Fig. 1: Optical view of SDSS J134326.99+431118.7. The image is obtained from the SDSS sky-server.

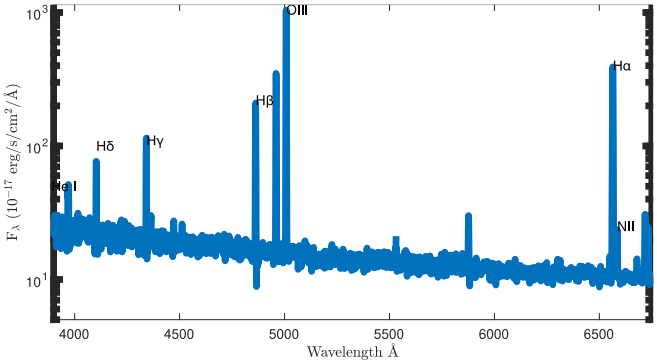

Fig. 2: Optical spectrum of SDSS J134326.99+431118.7. Positon of the emission lines H_α, H_β, H_γ, H_δ, OIII, HeI and NII are identified. The X-axis is rest-frame wavelength and Y-axis is flux.

3. Data analysis

In this work, we extensively use the SDSS archival data to measure morphological and chemical parameters of the galaxy. We obtained the SDSS g and r band images and optical fiber-spectrum from the SDSS Data Archive Server (DAS). The images and spectrum are already well-calibrated, and we further do not perform any operation in this regard. Both images and spectrum data are in the fits file format. The SDSS fiber has a diameter of 3 arc seconds. Hence, the observed spectrum only covers a small portion of the galaxy area. The SDSS optical spectrum has coverage of 3650 to 10,400 Å, which includes primary emission and absorption lines that are frequently used to investigate the chemical properties of stars or galaxies. The spectral resolution of the SDSS spectrum is 1500 at 3800 Å.

The spectrum of the galaxy was analyzed by using the Origin software of the 18th version. We first identified 21 different emission lines in the spectrum as shown in Figure 2. We performed Gaussian fits in each emission line and measured their parameters such as Full Width Half Maximum (FWHM), total flux, and best-fit coefficient. Before modeling each emission line, we subtracted the continuum flux taking a median of flux value of spectrum range ± 100 from the center of the emission line.

Emission line profile of the extragalactic object is dominated by Doppler broadening. The atoms/molecules in a gas, which emits the radiation, will have a distribution of velocities. The photon emitted by transition will be either red or blue-shifted by the Doppler effect, depending on the atom's velocity relative to the observer. Since the spectral line is a combination of all of the emitted radiation, the line profile is considered a Gaussian in nature. The center is zero shift or an average shift of the system. Mathematically Gaussian distribution function is defined as [12]

$$f_G(x) = \frac{1}{\sqrt{2\pi\sigma^2}} e^{\frac{-(x-\mu)^2}{2\sigma^2}} \quad (1)$$

Where, x is a normal random variable, μ is the mean deviation and σ is the standard deviation of the distribution. The FWHM is a width at which maximum amplitude drops to the half. We selected eight emission lines based on a higher intensity, which will be presented in this paper, along with their Gaussian parameters. The Gaussian parameters will be enlisted in a separate table and the corresponding elements will be identified. Moreover, we calculate the star formation rate (SFR) and the hydrogen line ratio. We will use the Gaussian area of $H\alpha$ emission line to calculate the star formation rate of the galaxy. We calculate star

formation rate adopting the empirical formula proposed by Kennicutt (1998) [13] as follows:

$$SFR\ (M_{\odot}year^{-1}) = 7.9\times 10^{-42} \sum L\ (H_{\alpha})\ \ (ergs\ s^{-1}) \qquad (2)$$

where $\sum L(H\alpha)$ is the total luminosity of Hα line which will be calculated by using Gaussian fits. $\sum L(H\alpha)$ = Area of Gaussian fit × 10^{-17} × $4\pi R^2$(ergs s^{-1}). R is the radius of the sphere which is calculated as R = D × 3.08 × 10^{24} cm. Here, D is luminosity distance of the galaxy in Mpc.

We derive emission line metallicity using a line ratio between H_{α} and NII. We use a calibration provided by Marino et al.(2013) [14].

$$12 + \log(O/H) = 8.743 + 0.462 \times \log(NII/\ H_{\alpha}) \quad (3)$$

4. Results

In this work we have analyzed eight main emission lines, i.e., HeI, H_{δ}, H_{γ}, H_{β}, OIII, OIII, H_{α}, and NII which are identified in Figure 2. The OIII is a doublet. Therefore, it has two different emission lines. The H_{δ}, H_{γ}, H_{β}, and H_{α} are Balmer lines and they are sensitive to the galaxies' gas-mass and star-formation rate. The H_{α}, principally, is a well-known tracer of star-formation and widely used to calculate the star-formation rate of the gas-rich galaxies. Heavier elements OIII and NII emission fluxes are used to calculate the star-forming galaxies' emission line metallicity.

In Figure 3, we show a few examples of the Gaussian fitting procedure. Here, we selected four main examples of emission lines of the spectra of interacting dwarf galaxy SDSS J134326.99+431118.7. We list peaks' position and the central wavelength value of all eight emission lines in Table 1. The solid line represents the Gaussian distribution. The error bars are also shown in the Gaussian curves. We can see that there is the almost perfect agreement of the observed data with the Gaussian distribution.

We list all eight strongest emission lines in the spectrum of the galaxy SDSS J134326.99+431118.7 that we have studied in this work in table 1. Their maximum intensity, the wavelength corresponding to maximum intensity, and corresponding elements are also provided. From the table, we can see that the doubly ionized oxygen OIII has a maximum intensity of 1043.6 x 10^{-17} erg/s/cm^2/Å, which has a central wavelength 5050.1 Å. The second strongest intensity (391.8 x 10^{-17} erg/s/cm^2/Å) is found corresponding to the wavelength 6619.1 Å, which is H_{α} line. The weakest intensity (31.34 x 10^{-17} erg/s/cm^2/Å) among the eight emission lines corresponds to the wavelength 6634.23 Å for the NII.

The Gaussian parameters of all eight Gaussian distributions are listed in table 2. The Gaussian height is given in the unit of intensity. Gaussian offset is the positional difference between the Gaussian peak and the observed peak in the spectra. The coefficient of regression represented by R-square is found to be more than 0.980. This suggests a perfect Gaussian fit with the characteristic lines.

Calculation

Star Formation Rate can be calculated by using equation (2). Here, we take D = 35.27 Mpc from the catalogue prepared by Paudel et al. (2018) for this particular galaxy.

Now, R = D × 3.08 × 10^{24} cm

= 35.27 × 3.08 × 10^{24} cm

= 108.63 × 10^{24} cm

Star formation rate due to Hα line is

$SFR(M_{\odot}year^{-1}) = 7.9 \times 10^{-42} \times$ Area of Gaussian fit × 10^{-17} × 4πR

= $7.9 \times 10^{-42} \times 1661.01\times 10^{-17} \times 4\pi \times(108.63 \times 10^{24})^2$ = 0.019 $M_{\odot}year^{-1}$

Line ratio Hα/ H_{β} = 2.73. This is slightly lower than the theoretical value of Hα/ H_{β} = 2.8. We suspect that this discrepancy between the theoretical and observed value is due to the inaccurate subtraction of continuum in the region of

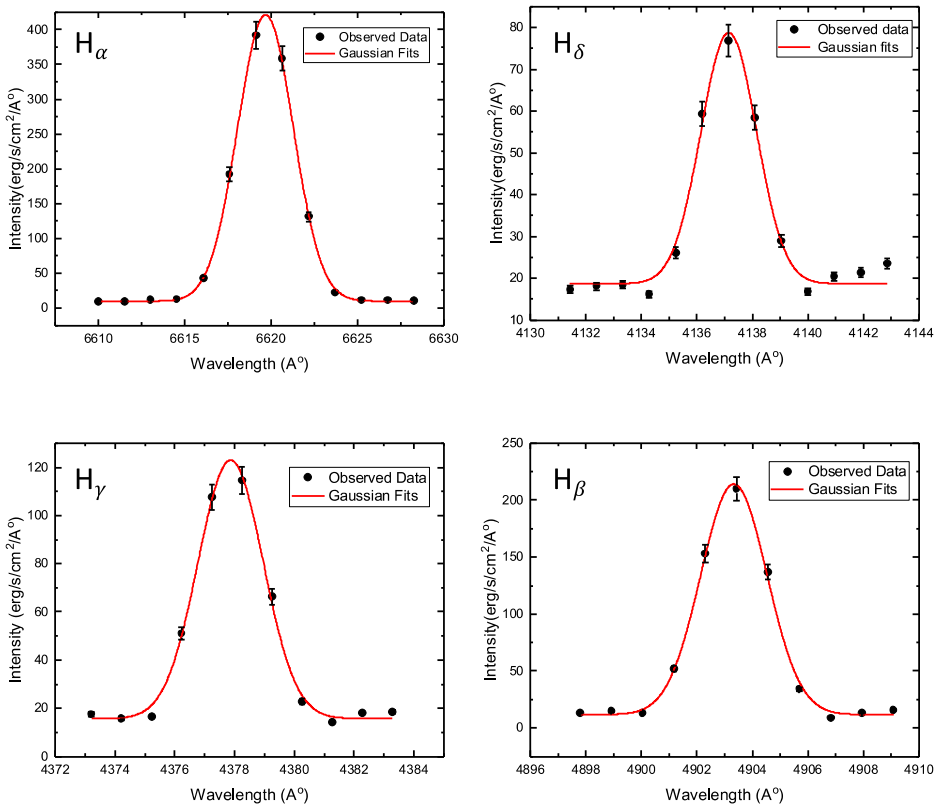

Fig. 3: We show four main examples of Gaussian fitting procedure. They are four Balmer lines: H_α. H_δ, H_γ, and H_β. Solid curves represent Gaussian fits. We show a conservative estimate of the flux error in the plot, i.e., 10 % of the observed flux provided by SDSS webpage (https://www.sdss.org/dr15/spectro/caveats/). The major cause of broadening of characteristic line is due to the Doppler broadening. The wavelengths given in the X-axis are not redshift corrected.

Table 1: The selected characteristic emission lines of spectra of dwarf galaxy SDSS J134326.99+431118.7 shown in Figure 3 are described along with their physical parameters listed in the table. The first column represents the name of the selected emission lines. Second and third columns represent the wavelength ((λ_p) corresponding to the peak intensity, the value of peak intensity (Ip).

Responsible Elements for Emission Lines	**Wavelength Corresponding to Peak Intensity λ_p (Å)**	**Peak Intensity I_p (10^{-17} erg/sec/cm^2/Å)**
HeI	3921.9	64.8
H_δ	4137.1	76.8
H_γ	4378.2	114.6
H_β	4903.4	209.8
OIII	5001.5	349.7
OIII	5050.1	1043.6
H_α	6619.1	391.8
NII	6634.23	31.34

Table 2: Full width half maximum, area of the curve, height of the Gaussian curve, offset and coefficient of regression of the data corresponding to each selected spectral lines are enlisted in the table in second, third, fourth, fifth and sixth column respectively corresponding to the responsible elements.

Element	FWHM (Å)	Area (10^{-17} erg/s/cm^2/Å)	Height (10^{-17} erg/s/cm^2/Å)	Offset	R-square
HeI	2.23	117.49	49.39	-0.253	0.980
H_δ	2.35	150.05	59.92	-0.008	0.984
H_γ	2.57	292.96	107.25	+0.376	0.995
H_β	2.82	606.93	202.38	+0.099	0.997
OIII	2.69	1003.65	350.56	-0.252	0.998
OIII	2.68	2982.67	1045.33	-0.001	0.999
H_α	3.80	1661.01	411.18	-0.558	0.999
NII	3.80	19.30	32.40	+0.023	0.999

H_β, where we can see absorption feature is also present. The ratio between Hα and H_β are also used to check the presence of internal dust reddening in the galaxies. The observed line ratio is near to the theoretical value or less. This imply that SDSSJ134326.99+431118.7 is a nearly dust free galaxy.

Line ratio NII/ H_α = 0.011. We calculate emission line metallicity for this galaxy using equation (3), 12 + log(O/H) = 7.85 dex. Logarithmic value is represented by dex. It is especially suitable while talking about metallicity. Metallicity is measured logarithmically in connection with the plenty of metals in the galaxy.

5. Discussion

Table 2 shows that the selected Gaussian distributions of HeI, H_δ, OIII doublet and Hα have a negative value of the offset. These curves have negative skewness. This means that the left-hand tail is longer than that on the right-hand side, and the mode is more than the mean. Similarly, the distributions of H_γ, H_β and NII have a positive offset. The curves have positive skewness. This means that the right-hand tail is longer than that of the left-hand side, and the mode is less than the mean. The value of FWHM is maximum (3.80 Å), corresponding to the curve of H_α. This indicates that the observed data is in excellent agreement with the Gaussian fit. The Gaussian area is maximum (2982.67 x 10^{-17} erg/s/cm^2/Å) for the line OIII.

Normal galaxies follow scaling relations of B-band absolute magnitude (Mb) versus star-formation rate and Mb versus emission-line metallicity. The position of SDSSJ134326.99+431118.7 in these relations is shown in Figure 4. In this figure, we have taken the SDSS star-forming galaxies as a comparative sample for the magnitude-metallicity relationship and the Local volume star-forming galaxies studied by Lee et al. (2009) [15] for the magnitude-star-formation rate relation. Interestingly, we find that SDSSJ134326.99+431118.7 is a significant outlier. It is significantly metal-poor compare to the normal SDSS star-forming galaxies. Similarly, the star-formation activity in this galaxies is notably higher than that of normal star-forming galaxies of local volume.

The catalog value of the star-formation rate of SDSSJ134326.99+431118.7 is $0.0083 M_\odot\ \mathrm{year}^{-1}$, which is derived by using the Far-Ultraviolet (FUV) flux of the galaxy. This shows that our

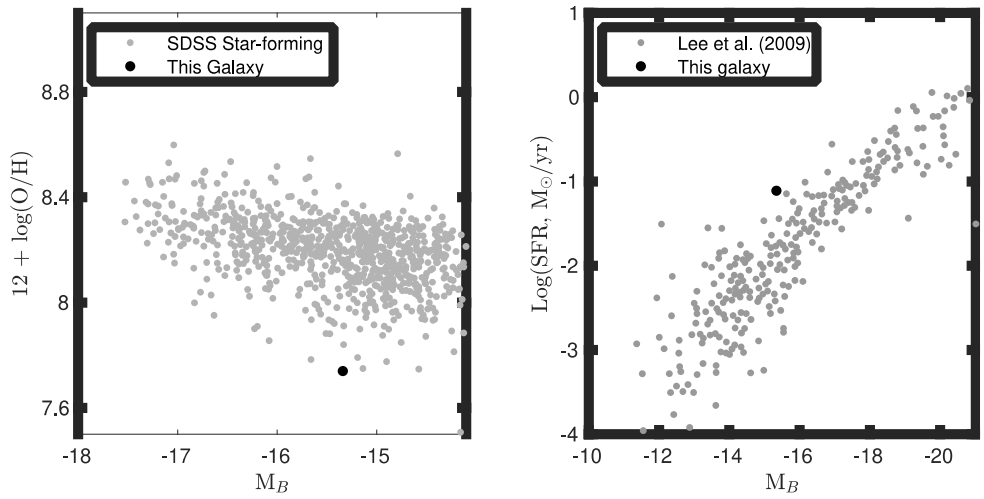

Fig. 4: Magnitude-metallicity relation of star-forming galaxies, left, where the SDSS star-forming galaxies as a comparative sample are shown in gray symbol. The Figure is reproduced from Paudel et al. (2018). In right, we show a relation between star-formation rate and B-band absolute magnitude, where the comparative sample galaxies taken from Lee et al.

derived value of the star-formation rate is significantly lower than the FUV value. This is because, area coverage of FUV is substantially more extensive compared to the SDSS 3" central region. This implies that, only a fraction of star-formation happens in the center of the galaxy.

The emission line metallicity of SDSSJ134326.99+431118.7 is 7.85 dex, which is a typical for metal-poor the vigorously star-forming galaxies, called Blue-Compact Dwarf galaxies (BCDs) [15]. As their name indicates, they are significantly blue and gas-rich compact galaxies, mainly found in a very low-density environment. Comparing morphological and physical properties of SDSSJ134326.99+431118.7 with that of BCDs, it is clear that SDSSJ134326.99+431118.7 is a typical BCDs type galaxy formed by the merger in an isolated environment.

6. Conclusion

The emission-line spectrum of a system of interacting dwarf galaxy SDSS J134326.99+431118.7 is studied. We noticed 21 spectral lines in the spectrum. Among them, only eight most robust emission-lines are analyzed in this work by using Gaussian fits. The following results are concluded from the observations and calculations.

a) We fitted the observed emission lines on the optical spectrum of SDSS J134326.99+431118.7 and found that there is an excellent agreement of all eight characteristic lines with Gaussian fits with more than 98% coefficient of regression.

b) We derived star-formation rate and emission line metallicity of SDSS J134326.99+431118.7, and found that the galaxy does not follow the scaling relation of Mb versus SFR and Mb versus 12 + log(O/H).

c) The morphological and physical properties of SDSSJ134326.99+431118.7 are very similar to those of a typical BCD galaxy. We conclude that we have presented another evidence of forming a BCD-type galaxy through a merger.

Acknowledgements

Daya Nidhi Chhatkuli acknowledge the University Grants Commission of Nepal, for financial support

by providing PhD Fellowship and Research Support Grant (Award No.: PhD-75/76-S & T-13) to carry out this research.

This study is based on the archival images and spectra from the Sloan Digital Sky Survey (*http://www:sdss.org/collaboration/credits.html*).

References

[1] F. Schweizer, Colliding and merging galaxies. Science 231 (1986) 227-234. https://science.sciencemag.org/content/231/4735/227

[2] S. Pearson, G. Besla, M. E. Putman, K. A. Lutz, X. Fernández, S. Stierwalt, ... & E. C. Sung, Local Volume TiNy Titans: gaseous dwarf–dwarf interactions in the Local Universe, Monthly Notices of the Royal Astronomical Society 459 (2016) 1827-1846. https://doi.org/10.1093/mnras/stw757

[3] J. E. Barnes, & L. Hernquist, Transformations of galaxies, II. Gasdynamics in merging disk galaxies. The Astrophysical Journal, 471(1996)(1),(115-142). https://iopscience.iop.org/article/10.1086/177957/meta

[4] K. Bekki, Formation of Blue Compact Dwarf Galaxies From Merging and Interacting gas-rich Dwarfs, Monthly Notices of the Royal Astronomical Society: Letters 388(2008) (1) L10-L14. https://academic.oup.com/mnrasl/article/388/1/L10/977927

[5] S. Paudel, C. Sengupta, & S. J. Yoon, KUG 0200-096: Dwarf Antennae Hosting a Tidal Dwarf Galaxy, The Astronomical Journal 156(2018) (4)(1-7). https://doi.org/10.3847/1538-3881/aadb8d

[6] G. De Lucia, V. Springel, S. D. White, D. Croton, & G. Kauffmann, The Formation History of Elliptical Galaxies, Monthly Notices of the Royal Astronomical Society 366(2006) (2) 499-509. https://doi.org/10.1111/j.1365-2966.2005.09879.x

[7] S. Stierwalt, G. Besla, D. Patton, K. Johnson, N. Kallivayalil, M. Putman, ... & G. Ross, TiNy Titans: The Role of dwarf–dwarf Interactions in low-mass Galaxy Evolution. The Astrophysical Journal 805 (2015) 1-16 http://dx.doi.org/10.1088/0004-637X/805/1/2

[8] C. J. Conselice, C. Yang, & A. F. Bluck, The Structures of Distant Galaxies–III. The Merger History of Over 20 000 Massive Galaxies at z< 1.2, Monthly Notices of the Royal Astronomical Society 394 (2009) 1956-1972. https://doi.org/10.1111/j.1365-2966.2009.14396.x

[9] S. Stierwalt, G. Besla, D. R. Patton, K. E. Johnson, N. Kallivayalil, M. E. Putman,... & G. Ross, The Role of Dwarf-Dwarf Interactions in the Evolution of Low Mass Galaxies, In American Astronomical Society Meeting Abstracts# 225(2015). http://csma31.csm.jmu.edu/physics/courses/391/Speakers/2015Spring/abstract_stierwalt_sabrina.pdf

[10] F. Lelli, F. Fraternali, & M. Verheijen, Evolution of Dwarf Galaxies: a Dynamical Perspective, Astronomy & Astrophysics 563 (2014) 1-27. http://dx.doi.org/10.1051/0004-6361/201322658

[11] S. Paudel, R. Smith, S. J. Yoon, P. Calderón-astillo, & P. A. Duc, A Catalog of Merging Dwarf Galaxies in the Local Universe. The Astrophysical Journal Supplement Series 237 (2018) 1-20. https://doi.org/10.3847/1538-4365/aad555

[12] G. L. Squires & Squires, G. L. Practical physics. Cambridge University press (2001).

[13] Jr. Kennicutt, C. Robert, Star Formation in Galaxies Along the Hubble Sequence, Annual Review of Astronomy and Astrophysics 36 (1998) 189-231.

[14] R. A. Marino et al., "The O3N2 and N2 abundance indicators revisited: improved calibrations based on CALIFA and Te-based literature data," Astronomy and Astrophysics vol. 559 (Nov. 2013) 114. https://doi.org/10.1051/0004-6361/201321956.

[15] Lee, J.C., Kennicutt, R.C., Jr., Funes, S.J.J.G., Sakai, S., Akiyama, S.. Dwarf Galaxy Starburst Statistics in the Local Volume, The Astrophysical Journal 692 (2009) 1305–1320. https://doi.org/10.1088/0004-637X/692/2/1305

Journal of Institute of Science and Technology, 25(2), 55-60 (2020)
ISSN: 2469-9062 (print), 2467-9240 (e)
Doi: https://doi.org/10.3126/jist.v25i2.33736

Research Article

STUDY OF STAR FORMATION RATE AND METALLICITY OF AN INTERACTING DWARF GALAXY NGC 2604

Daya Nidhi Chhatkuli[1*], **Sanjaya Paudel**[2], **Binil Aryal**[1]

[1]*Central Department of Physics, Tribhuvan University, Kirtipur, Kathmandu, Nepal,*
[2]*Centre for Galaxy Evolution Research, Department of Astronomy, Yonsei University, Seoul, South Korea*
[*]*Corresponding author: chhatkulidn@gmail.com*

*(**Received**: June 02, 2020; **Revised**: October 13, 2020; **Accepted**: November 01, 2020)*

ABSTRACT

We present a study of the Sloan Digital all Sky Survey Data Release 12 (SDSS DR12) optical spectra of an interacting dwarf galaxy NGC 2604 that has redshift 0.0069. Thirteen characteristic emission lines were identified in the wavelength range of 3885 Å to 6742 Å, the strongest line was due to H_α emission with a value of emission-line flux 1538.8 erg/s/cm^2/Å. The other twelve emission lines were observed because of OI doublet, H_β, H_γ, H_δ, OIII doublet, HeI, SII doublet and NII doublet transitions. Eleven characteristic lines agreed perfectly with the Gaussian distribution with greater than 99.9 % coefficient of regression. However, full-width half maximum (FWHM) was found to be less than 5 Å. No absorption metallic lines were observed in the spectra which indicates that the galaxy was either newly formed. The line metallicity of the galaxy was found to be 8.4 dex and the extinction coefficient was 0.2134. The star formation rate due to H_α emission after extinction correction was found to be 0.0927 $M_\odot$ year $^{-1}$ which is almost double of the value (0.057 $M_\odot$ year $^{-1}$) before correction.

Keywords: Dwarf galaxy, Characteristic peaks, Extinction, H_α line, Metallicity, Star formation rate.

INTRODUCTION

A small-sized galaxy, having low values of luminosity, surface brightness, and metallicity is known as a dwarf galaxy. According to Lambda Cold Dark Matter (ΛCDM) cosmology, dwarf galaxies are expected to be the first formed dark matter dominated objects and large scale structures are built up by hierarchical merging of these objects. Karachentsev *et al.* (2004), reported that dwarf galaxies occupy more than 70 % of all galaxies in the local Universe. Dwarf galaxies are the most abundant galaxies in the Universe but hard to be detected. The difficulties in detecting dwarf galaxies are mainly due to their low absolute luminosity and low surface brightness. Since only relatively brighter galaxies have been surveyed on large scale, the true number density of dwarf galaxies in the nearby Universe is poorly known. Davies and Morgan (1994) interpreted that the actual number density of dwarf galaxies in the nearby universe is poorly known because of the limited survey of relatively brighter galaxies only. The study of dwarf galaxies provides knowledge on the early process of structure formation and hence we can study the evolution of the Universe.

A dwarf galaxy is composed of as few as several thousand up to as high as a few billion stars. These dwarf galaxies often orbit around larger galaxies. For example, more than 20 dwarf galaxies are orbiting around our Milkyway galaxy (Noyola *et al.*, 2008). Dwarf galaxies in the local universe are mainly classified into three categories. (i) Dwarf elliptical (dEs): The dwarfs that are gas-poor and have elliptical shapes are called dwarf elliptical galaxies. No evidences of recent star formation were found in such galaxies. Comparatively more spherical shaped dwarf galaxies found at the faint end of the dwarf elliptical scale are called spheroid (Sphs) (Web[1]) (ii) dwarf irregulars (Irrs). The galaxies containing a considerable quantity of dust and gas which have clear evidence of star formation are called dwarf irregulars. (iii) star bursting dwarfs: The gas-rich galaxies having a high rate of star formation are called star bursting dwarfs. The starburst activity occurs in the galaxies having steeper gravitational potential. The starburst galaxies are gas-rich dwarf galaxies with high dark matter content, low mass, and low chemical abundance. Most of the dwarf galaxies were formed by the interaction of galaxies. Okazaki and Taniguchi (2000) analyzed that gas-rich galaxies were formed by merger or collision of the galaxies while gas-poor elliptical galaxies was found at the center of galaxy clusters.

The galaxies with low mass, low chemical abundances, high gas, and dark matter content were termed as star-forming dwarf galaxies. Such galaxies mostly reside in the field environment. The star formation rate (SFR) of a galaxy can be obtained in various wavelength regions like X-ray, ultraviolet, optical, far infrared etc. by making use of the experimental/observational calculations obtained from samples of the above-mentioned galaxy types: elliptical, irregulars, or starbursts. The star formation rate of a galaxy depends upon different factors like interstellar gases, temperature, molecular cloud of neutral hydrogen etc. (Thronson & Telesco, 1986). Similarly, metallicity is also one of the factors. The star formation rates in the low metallic dwarf galaxies were found to be overestimated by a factor greater than or equal to 3 (Weilbacher *et al.*, 2001).

In this paper, the spectroscopic analysis was performed on SDSS DR12 spectra of low red-shifted dwarf galaxy NGC 2604. The characteristic peaks of the emission lines were identified along with their responsible elements for the emission. The star formation rate (SFR), extinction coefficient and emission line metallicity were also calculated using Gaussian fits.

Region of interest

We selected a system of interacting dwarf galaxy NGC 2604 having a low redshift of z = 0.0069 from the catalog compiled by Poudel *et al.* (2018). The galaxy NGC 2604 is an interacting galaxy located at R.A. (J2000) = 128.3457^0, Dec. (J2000) = 29.5386^0 (Fig. 1a). The SDSS photometric u, g, r, i, and z color magnitudes are respectively, 14.41 mag, 13.89 mag, 13.36 mag, 13.36 and 13.12 mag. (Web[2]). NGC 2604 is the barred-spiral galaxy that can be observed from Kathmandu, Nepal if viewed from a telescope, in the evening around 19:09 (+0545), 69° above the eastern horizon. It reaches its highest point in the sky at 20:40, 88° above the northern horizon from Kathmandu, and will continue to appear till around 02:00 (Web[3]).

An emerging concept regarding the barred galaxies is that the bars play a controlling role in the comprehensive star formation rate of the disk galaxies. Tubbs (1982) proposed the probability of a decrease in total star-forming rates due to bars in the galaxy. Kim *et al.* (2017) showed that there is a significantly lower star-forming activity of strongly-barred galaxies than their unbarred counterparts. The SDSS optical image of the galaxy UGC 2604 is shown in Fig. 1(a) which is interacting with a nearby companion NGC 2604B. We can see clearly from the image that it is a barred type galaxy. The spectrum of the galaxy is shown in Fig. 1(b). In the spectra, several characteristic lines due to different elements are found. The most prominent line is the H_α line which corresponds to 6564.4 Å. Then the intensity goes on decreasing with H_β, OIII, NII, H_γ lines, and so on. The characteristic lines will be studied in this paper and the reason behind those emissions in the dwarf galaxy will be investigated.

The main objective of this work is the spectroscopic analysis of the galaxy UGC 2604. The specific objective is to calculate the star formation rate of the galaxy from the H_α line, calculate line ratio, metallicity, extinction coefficient and compare the star formation rate.

MATERIALS AND METHODS

This study was based on the Sloan Digital Sky Survey (SDSS) database (*http://www:sdss.org/collaboration/credits.html*). The SDSS DR12 spectral data was extracted from software called ALADIN. The data was plotted using the software ORIGIN 8.0 to obtain spectra of the galaxy. The peaks in emission lines were identified and performed the Gaussian fits on the spectra of emission lines. It was assumed that the characteristic lines get broaden because of Doppler broadening, permitted line cooling, and fine structure cooling. These are natural processes; therefore the Gaussian distribution was expected.

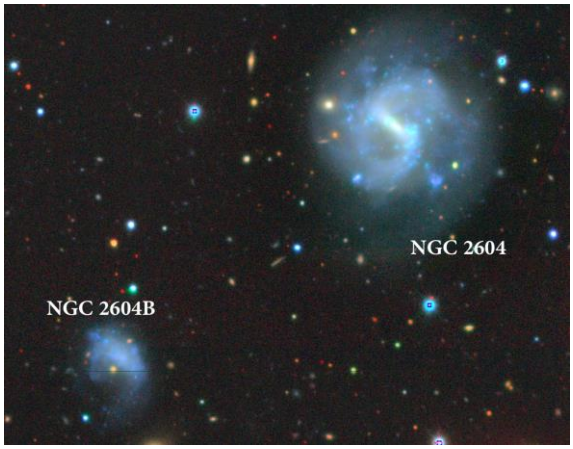

(a)

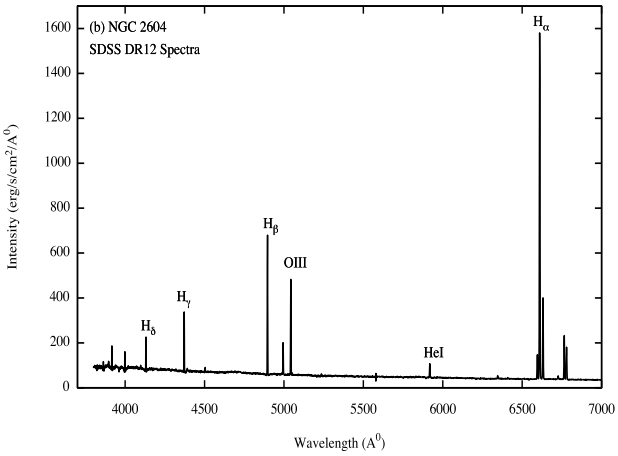

(b)

Fig. 1. (a) SDSS image of dwarf galaxy [Source: SDSS DR12 Science Archive Server], **(b) SDSS DR12 spectra of NGC 2604**

Mathematically Gaussian distribution (Squires, 2001) is defined as;

$$f_G(x) = \frac{1}{\sqrt{2\pi\sigma^2}} e^{\frac{-(x-\mu)2}{2\sigma^2}} \quad (1)$$

Where, *x* is a normal random variable, μ is the mean and σ is the standard deviation of the distribution. If the number of events is very large, then the Gaussian distribution function may be used to describe physical events. The Gaussian distribution is a continuous function that approximates the exact binomial distribution of events. Any deviation from the Gaussian distribution will be analyzed critically. Jha *et al.* (2017) studied the variation of flux density with density of a structure of size 4.46 pc ×

2.36 pc and found a cavity structure at 100 μm images in interstellar medium. From the study of distribution of flux density with distance along major diameter of the structure, they found that the distribution strongly deviated from the Gaussian distribution. This is due to the pulsar wind during the formation of the cavity in interstellar medium.

A table of Gaussian parameters for noticeable characteristic peaks was presented. In the spectra (Fig. 1b), 81 peaks were noticed above the continuum. Out of them, only 13 characteristic peaks having maximum intensity were presented here along with the responsible elements and their Gaussian parameters. Finally, H_α-line was identified, and using the Gaussian area for intensity of the line, star formation rate (SFR) in the dwarf galaxy NGC 2604 was calculated. The star formation rate was calculated by adopting the empirical formula proposed by Kennicutt (1998) as follows;

$$\text{SFR } (M_\odot \text{ year}^{-1}) = 7.9\times10^{-42} \sum L\,(H_\alpha) \quad (\text{ergs s}^{-1}) \qquad (2)$$

Here, $\sum L(H_\alpha)$ is the total luminosity of H_α which was calculated by using Gaussian fits. $\sum L(H_\alpha)$ = Area of Gaussian fit $\times 10^{-17} \times 4\pi R^2$ (ergs s^{-1}). R is the radius of the sphere which was calculated as $R = D \times 3.08 \times 10^{24}$ cm. Here, D is luminosity distance in Mpc. From the calibration provided by Marino *et al.* (2013), the emission line metallicity using a line ratio between NII and H_α was calculated by

$$12 + \log (O/H) = 8.743 + 0.462 \times \log (NII/H_\alpha) \qquad (3)$$

RESULTS AND DISCUSSION

Out of thirteen emission lines selected, only twelve characteristic emission lines are shown in Figs. 2 and 3.The Gaussian fits of the first six emission lines of HeI, $H_{\delta,}$ $H_{\gamma,}$ $H_{\beta,}$ OIII, and OIII are shown in Fig. 2. Solid curves represent Gaussian fits. The statistical error bars (±1σ) were shown. The broadening of the characteristic line was mainly because of the Doppler broadening. The wavelengths given in the X-axis were redshift corrected. A conservative estimate of the flux error is shown in the plot, i.e., 10 % of the observed flux provided by the SDSS webpage (https://www.sdss.org/dr15/spectro/caveats/).

Likewise, the Gaussian fits of the second six emission lines of OI, NII, $H_{\alpha,}$ NII, SII and SII are shown in Fig. 3. Here also, solid curves represented Gaussian fits. The statistical error bars (±1σ) are shown. The broadening of the characteristic line was mainly because of the Doppler broadening.

A very good agreement between the observed distribution and Gaussian fit was found, as shown in Figs. 2 and 3. The lines $H_{\delta,}$ $H_{\gamma,}$ $H_{\beta,}$ and H_α are Balmer lines. The corrected and calibrated Gaussian area was used to find the values of the star formation rate. The Gaussian fits shown in Figs. 2 and 3 ranged from 3885 Å to 6742 Å in the spectra.

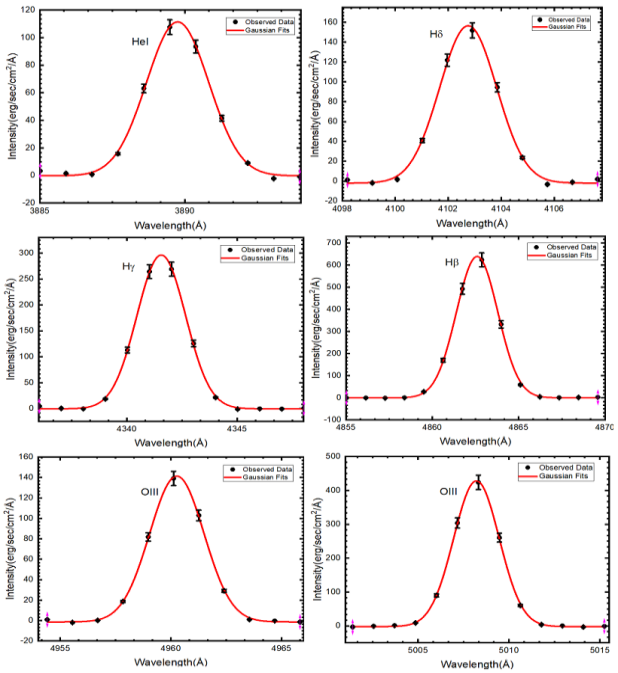

Fig. 2. First six characteristic peaks of the SDSS DR12 spectra of interacting dwarf galaxy NGC 2604 in the range 3885 Å to 5015 Å

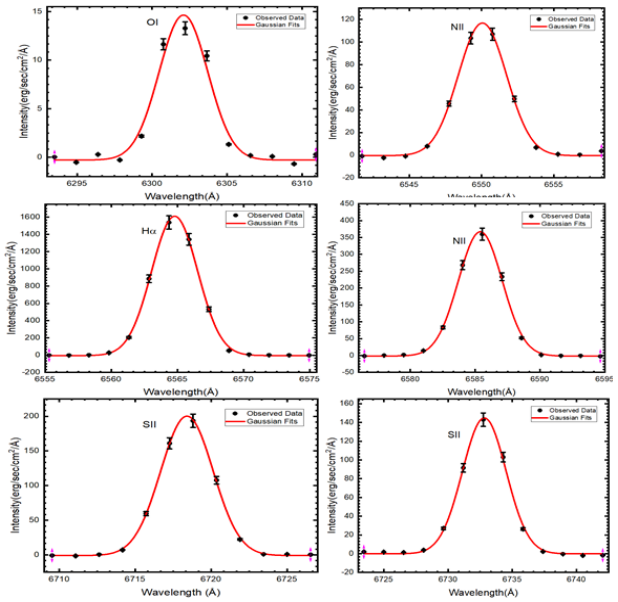

Fig. 3. Second six characteristic peaks of the SDSS DR12 spectra of interacting dwarf galaxy NGC 2604 in the range 6293 Å to 6742 Å. Error bars represent the ±1σ statistical errors

Table 1 shows a list of Gaussian parameters of 13 strongest peaks (shown in Fig. 2 and 3) in the SDSS

spectra of dwarf galaxy NGC 2604. The first, second, third, and fourth columns respectively represent the name of the responsible element for the emission, the peak wavelength (λ_p), the value of peak intensity (I_p) in erg/s/cm^2/Å corresponding to peak wavelength and full width half maximum (FWHM). Similarly, the fifth, sixth, seventh, and eighth columns represent area, height of Gaussian curve, offset, and coefficient of regression of the fitted data, respectively, as summarized in Table 1.

Gaussian offset which showed the skewness of the data is the positional difference between the Gaussian peak and the observed peak in the spectra. The coefficient of regression is represented by R^2 which was found to be more than 0.990 except for OI, suggesting a very good agreement with Gaussian distribution. The small values (2.53 - 4.10) Å of full-width half maxima (FWHM) represent the characteristic peak. Interestingly, the characteristic peaks showed Gaussian nature. The intensity was found to be maximum (1538.8 erg/s/cm^2/A) at the wavelength of 6564.4 Å. This line was because of H_α emission. The second strongest line was due to H_β which was found at the wavelength of 4862.9Å with peak intensity 624.0 erg/s/cm^2/Å. The weakest intensity among the 13 strongest lines was observed at the wavelength of 6364.9Å with peak intensity 5.3 erg/s/cm^2/Å, which was due to neutral oxygen OI.

Table 1. Description of the selected characteristic emission lines of spectra of dwarf galaxy NGC 2604 shown in Fig. 1

Element	λ_p (Å)	I_p	FWHM (Å)	Area (erg/s/cm^2/Å)	Height (erg/s/cm^2/Å)	Offset	R^2
HeI	3889.5	107.5	2.53	300.60	111.53	+0.269	0.998
$H_{\delta,}$	4102.9	151.9	2.54	428.33	158.49	+0.158	0.997
H_γ	4342.0	269.0	2.60	820.17	296.62	+0.465	0.999
H_β	4862.9	624.0	2.82	1920.98	638.95	+0.267	0.999
OIII	4960.1	139.1	2.89	439.30	142.61	–0.149	0.999
OIII	5008.3	423.5	2.95	1349.96	430.02	+0.109	0.999
OI	6302.2	13.3	3.83	60.77	14.91	+0.109	0.973
OI	6364.9	5.3	3.76	23.65	5.91	–0.880	0.925
NII	6550.8	106.9	3.95	492.02	117.16	+0.709	0.998
H_α	6564.4	1538.8	4.10	7048.21	1615.05	–0.431	0.999
NII	6585.6	359.7	3.99	1563.03	368.36	+0.151	0.999
SII	6718.8	193.5	4.07	871.40	201.16	+0.404	0.999
SII	6732.7	142.9	4.01	619.02	144.89	–0.082	0.998

It can be seen from Table 1 that all the selected thirteen spectral Gaussian fits corresponding to the elements HeI, $H_{\delta,}$ $H_{\gamma,}$ $H_{\beta,}$ OIII, OI, NII, NII, and SII have positive values of offset which indicates that they have positive skewness. This means that the tail on the R.H.S. was longer than that on the L.H.S. on the curve and the mode was less than the mean. The rest of the Gaussian fits corresponding to OIII, OI, H_α, and SII lines have negative values of offset, indicating that they have negative skewness. It means that the tail on the L.H.S. of the curve was longer than the tail on the R.H.S. and the mode was more than the mean. The line due to H_α has maximum FWHM (i.e., 4.10 Å), indicating that it was in very good agreement with Gaussian fit.

From Table 1, it can be seen that corresponding to the wavelength 6564.4 Å, maximum intensity of 1538.8 erg/sec/cm^2/Å was observed in the spectral line due to H_α. The wavelength of the H_α spectral line ranged from 6555.29 Å to 6574.94 Å. Therefore, the maximum Gaussian area of the line with 7048.21 erg/s/cm^2/Å in the unit of intensity was detected. This might affect the star formation rate in the Galaxy. Statistically, R^2 measures how close the data are to the fitted curve. The value of R^2 in all the spectral lines was almost 100%. This fact also suggests that the fitted data is Gaussian-like.

Star formation rate

Area of Gaussian curve for H_α line = 7048.21 (10^{-17} erg/s/cm^2/Å). For H_α line, the intensity was maximum. Using the adopted distance to the galaxy D = 29.29 Mpc (Poudel et al., 2018), we calculated $R = D \times 3.08 \times 10^{24}$ cm = $29.29 \times 3.08 \times 10^{24}$ cm = 90.21×10^{24} cm. Star formation rate using H_α line was calculated by using equation (2).

$SFR = 7.9\times10^{-42}\times$area of Gaussian fit $\times 10^{-17}\times4\pi R^2=7.9\times 10^{-42}\times7048.21\times10^{-17}\times4\pi(90.21\times10^{24})^2 =0.057\ M_\odot$ year $^{-1}$

Line ratio H_α/H_β = 7048.21/1920.98 = 3.67. This is slightly greater than the theoretical value (2.8), which is due to internal extinction.

The current star formation rate in our Milky Way galaxy was 2.6, the average star formation rate was about 8.25 $M_\odot$ year^{-1} (Kalberla & Kerp, 2009). GALEX mission revealed that the star formation rate in the early-type galaxies, dwarf galaxies, low surface brightness galaxies, and the extreme outer disks of many normal galaxies was rather low. Although star formation had been detected occasionally in nearby elliptical and S0 galaxies (e.g., Pogge & Eskridge, 1993), most of these galaxies have historically been regarded as "dead" in terms of recent star formation. Kennicutt *et al.* (2008) compiled H_α luminosities for galaxies within the local 11 Mpc, which included ~ 300 dwarf galaxies (M_B > -17). Excluding a handful of dwarf spheroidal galaxies that have no cold gas, only 10 of these (~3 %) were not detected in H_α, meaning that star formation had taken place over the last 3-5 Myr in the other 97 % of the systems. Therefore, our dwarf galaxy meets this criterion.

Metallicity

The line ratio of NII (λ_{peak} = 6585.6 Å) with H_α was calculated as, NII/H_α = 1563.03/7048.21 = 0.2218. Line metallicity was 12 + log (O/H) = 8.743 + 0.462 × log (NII/H_α) = 8.743 + 0.462 × log (0.2218) = 8.44 dex which is slightly lower than solar value.

Extinction correction

The line ratio H_α/H_β which is also called Blamer decrement is given by, c = 3.67. The theoretical value of c_0 = 2.86 for an electron temperature of 10^4 K. Now extinction coefficient E (B − V) = 1.97× log (c/c_0) = 1.97× log (3.67/2.86) = 0.2134. Now, extinction A (Hα) = 2.45 E (B–V) = 2.45 × 0.2134 = 0.5228.

Again, we have A (Hα) = – 2.5 log (F(Hα)obs/F(Hα)em). Using the value of observed flux F(Hα)obs = 7048.21 in this equation, the emitted flux was calculated to be F(Hα)em = 11481.54 erg/s/cm^2/A. Thus, using this value, the star formation rate was calculated as,

Star formation rate due to H_α line = 7.9 ×10^{-42} × Area of Gaussian fit × 10^{-17} × 4πR^2 = 7.9 ×10^{-42}× 11481.54 × 10^{-17} × 4π (90.21 × 10^{24})^2 = 0.0927 $M_\odot$ year $^{-1}$

Thus the SFR of the Galaxy before extinction was 0.057 $M_\odot$ year $^{-1}$ and after extinction correction was 0.0927 $M_\odot$ year $^{-1}$. We can see that the SFR of the galaxy calculated after extinction correction is more (almost double) than that before correction indicating that the actual value of the flux of the galaxy is almost double of the observed value of the flux. This galaxy NGC 2604 has only three low mass galaxies around it which means that the galaxy is almost in the field environment.

CONCLUSION

We studied SDSS DR12 emission spectra of an interacting dwarf galaxy NGC 2604 located at R.A. (J2000) = 128.3457^o, Dec. (J2000) = 29.5386^o, having redshift 0.0069. We noticed thirteen significant peaks from Gaussian fits. Present results conclude as follows:

1. The strongest emission line was found for H_α with intensity 1538.8 erg/s/cm^2/Å. The line ratio H_α/H_β was found to be 3.67
2. Other emission lines were observed because of neutral Oxygen (OI), Balmer lines H_δ, H_γ, H_β, doubly ionized oxygen (OIII) doublet, neutral Helium (HeI), singly ionized Sulpher (SII) doublet, and singly ionized nitrogen (NII) doublet.
3. All the eleven characteristic lines showed a very good agreement with Gaussian fits greater than 99.9 % coefficient of regression. However, full width at half maxima (FWHM) was found to be less than 5 Å. These lines were broadened because of Doppler broadening and permitted line cooling.
4. No metal absorption line was observed in the spectra of interacting dwarf galaxy NGC 2604. This suggests that the galaxy was either newly formed.
5. Star formation rate (SFR) due to H_α emission line was found to be 0.057 $M_\odot$ year^{-1} which is considered as a low star formation rate.

ACKNOWLEDGEMENTS

One of the authors, Daya Nidhi Chhatkuli acknowledges the University Grants Commission of Nepal for financial support by providing a Ph.D. Fellowship (PhD-75/76-S & T-13) to carry out the Ph.D. works.

REFERENCES

Davies, J., & Morgan, I. (1994). Why are dwarf galaxies so difficult to find? *European Southern Observatory Conference and Workshop Proceedings*, *49*, 19-26.

Jha, A. K., & Aryal, B. (2017). A study of a pulsar wind driven structure in far-infrared IRAS map at latitude-10°. *Journal of Institute of Science and Technology*, *22*(1), 1-9.

Kalberla, P. M., & Kerp, J. (2009). The H1 distribution of the milkyway. *Annual Review of Astronomy and Astrophysics*, *47*, 27-61.

Karachentsev, I. D., Karachentseva, V. E., Huchtmeier, W. K., & Makarov, D. I. (2004). A catalog of neighboring galaxies. *The Astronomical Journal*, *127*(4), 2031-2068.

Kennicutt Jr, R. C. (1998). Star formation in galaxies along the hubble sequence. *Annual Review of Astronomy and Astrophysics*, *36*(1), 189-231.

Kennicutt Jr, R. C., Lee, J. C., Funes, J. G., Sakai, S., & Akiyama, S. (2008). A Hα imaging survey of galaxies in the local 11 Mpc volume. *The*

Astrophysical Journal Supplement Series, *178*(2), 247-279.

Kim, E., Hwang, H. S., Chung, H., Lee, G. H., Park, C., Sodi, B. C., & Kim, S. S. (2017). Star formation activity of barred spiral galaxies. *The Astrophysical Journal*, *845*(2), 1-12.

Marino, R. A., Rosales-Ortega, F. F., Sánchez, S. F., De Paz, A. G., Vílchez, J., Miralles-Caballero, D., ... & Díaz, A. I. (2013). The O_3N_2 and N_2 abundance indicators revisited: improved calibrations based on CALIFA and Te-based literature data. *Astronomy & Astrophysics*, *559*, A114. https://doi.org/10.1051/0004-6361/201321956

Noyola, E., Gebhardt, K., & Bergmann, M. (2008). Gemini and hubble space telescope evidence for an intermediate-Mass black hole in ω centauri. *The Astrophysical Journal*, *676*(2), 1008-1015.

Okazaki, T., & Taniguchi, Y. (2000). Dwarf galaxy formation induced by galaxy interactions. *The Astrophysical Journal*, *543*(1), 149-152.

Pogge, R. W., & Eskridge, P. B. (1993). Star formation in the disks of HI-rich S0 galaxies. *The Astronomical Journal*, *106*, 1405-1419.

Poudel, S., Smith, R., Yoon, S. J., Calderón-Castillo, P., & Duc, P. A. (2018). A catalog of merging dwarf galaxies in the local universe. *The Astrophysical Journal Supplement Series*, *237*(2), 1-20.

Squires, G. L., (2001). *Practical physics*. Cambridge University Press.

Thronson Jr, H. A., & Telesco, C. M. (1986). Star formation in active dwarf galaxies. *The Astrophysical Journal*, *311*, 98-112.

Tubbs, A. D. (1982). The inhibition of star formation in barred spiral galaxies. *The Astrophysical Journal*, *255*, 458-466.

Web[1]http://astronomy.swin.edu.au/cosmos/D/Dwarf+Galaxy.

Web[2]http://skyserver.sdss.org/dr9/en/tools/quicklook/quickobj.asp?id=1237660765373988975.

Web[3] https://in-the-sky.org/data/object.php?id=NGC2604.

Weilbacher, P. M. (2001). On star formation rates in dwarf galaxies. *Astronomy & Astrophysics*, *373*(1), L9-L12.

Certificate of Acknowledgement

IS PRESENTED TO

DAYA NIDHI CHHATKULI

for presenting research paper titled

Forming Blue Compact Dwarf Galaxy (BCD) Through the Merger

at ANPA Conference, July 15-17, 2022.

CHANDRA M ADHIKARI, PhD
CONFERENCE CO-CHAIR

PASHUPATI DHAKAL, PhD
CONFERENCE CHAIR

IAUGA 2022

XXXIst General Assembly of the International Astronomical Union

August 2 - 11, 2022 | BEXCO, Busan, Korea

Certificate of Attendance

This is to certify that

Daya Nidhi Chhatkuli

Has attended the XXXIst General Assembly of the International Astronomical Union (IAUGA 2022) which was held in Busan, Korea on August 2 - 11, 2022.

Prof. Hyesung Kang

Chair, IAUGA 2022 National Organizing Committee

Nepal Physical Society

Ghantaghar, Kathmandu, Nepal

International Conference on Frontiers of Physics -2022

(ICFP-2022)

This Certificate of appreciation is awarded to

Daya N. Chhatkuli

from Trichandra M. Campus, TU, Nepal for his oral presentation on the

"Forming Blue Compact Dwarf Galaxy (BCD) through the Merger" in the

International Conference on Frontiers of Physics -2022

held on January 22-24, 2022 via virtual platform.

Prof. Dr. Narayan P. Chapagain

Conference Chair, ICFP-2022

President, Nepal Physical Society

February 1, 2022

Nepal Physical Society

Ghantaghar, Kathmandu

Certificate of Participation

This certificate is awarded to

Mr. Daya Nidhi Chhatkuli **from**

Central Department of Physics, Tribhuvan University, Nepal,

for his presentation entitled

Structural Parameter of a Merging Compact Dwarf Galaxy CG 0315,

On Scientific Session of 37th Annual Convention, February 6, 2021.

Prof. Dr. Narayan Prasad Chapagain
President
Nepal Physical Society

Dr. Sunil Babu Shrestha
Chief Guest
Vice – Chancellor, NAST

Prof. Dr. Leela Pradhan Joshi
Chair, Scientific Committee
37th Annual Convention, NPS

February 6, 2021

Online Interaction on Astronomy & Astrophysics

Organized by

Kurseong College, Darjeeling, West Bengal, India - 734203

30th September, 2020

Certificate of Participant

This is to certify that Mr. Daya Nidhi Chhatkuli
of
Central Department of Physics, Tribhuvan University, Nepal
has participated in the Online Interaction on Astronomy & Astrophysics.

Samir Bal
Principal

Amit Shankar
Convener

Nepal Physical Society

Ghantaghar, Kathmandu

Certificate of Participation

This certificate is awarded to

Mr. Daya Nidhi Chhatkuli from

Tri - Chandra Multiple Campus, TU, Kathmandu for his successful participation in

NPS School of Computing - 2020

Conducted from July 4, 2020 to January 31, 2021.

Prof. Dr. Narayan Prasad Chapagain	**Dr. Sunil Babu Shrestha**	**Dr. Dibakar Sigdel**
President	Chief Guest	Instructor
Nepal Physical Society	Vice – Chancellor, NAST	Data Scientist, UCLA, USA

February 6, 2021

1st International e-Conference on
Recent Advances in Physics & Materials Science-2020
(IC-RAPMS-2020)

Organized by

Kurseong College, Darjeeling, West Bengal, India-734203

In collaboration with

St. Joseph's College, Darjeeling, West Bengal, India-734104

Certificate

This is to certify that **Mr. DAYA NIDHI CHHATKULI**

of

Tribhuvan University

has participated in the 1st International e-Conference on Recent Advances in Physics & Materials Science (IC-RAPMS-2020) held during 9 & 10 July, 2020 and presented a paper entitled

A Spectroscopic study of the Low Redshift Dwarf Galaxy SDSS J134326.99+431118.7 to Calculate Star Formation Rate

Samir Bal

Dr. Samir Bal
Principal
Kurseong College

Amit Shankar

Dr. Amit Shankar
Convener

Fr. Dr. Donatus Kujur S.J.
Principal
St. Joseph's College

1st International e-Conference on
Recent Advances in Physics & Materials Science-2020
(IC-RAPMS-2020)

Organized by

Kurseong College, Darjeeling, West Bengal, India-734203

In Collaboration with

St. Joseph's College, Darjeeling, West Bengal, India-734104

Certificate of Best Oral Presentation

This is to certify that **Mr. Daya Nidhi Chhatkuli**

of

Central Department of Physics, Tribhuvan University, Nepal

is awarded with best oral presentation for his work entitled

A Spectroscopic study of the Low Redshift Dwarf Galaxy SDSS J134326.99+431118.7 to Calculate Star Formation Rate

presented in the 1st International e-Conference on Recent Advances in Physics & Materials Science (IC-RAPMS-2020) held during 9 & 10 July, 2020.

Dr. Samir Bal
Principal,
Kurseong College

Dr. Amit Shankar
Convener

Fr. Dr. Donatus Kujur S.J.
Principal
St. Joseph's College

अंतर-विश्वविद्यालय केंद्र : खगोलविज्ञान और खगोलभौतिकी IUCAA

Inter-University Centre for Astronomy and Astrophysics
An Autonomous Institution of the University Grants Commission

January 16, 2019

CERTIFICATE

This is to certify that **Prof. Daya Nidhi Chhatkuli** from Tribhuvan University, Nepal has attended the ***"Workshop on SITARE- Advanced workshop on Astrophysics"*** held at IUCAA, Pune, during January 10 – 16, 2019.

Professor Ranjeev Misra
Coordinator, IUCAA

INTER-UNIVERSITY CENTRE FOR ASTRONOMY AND ASTROPHYSICS * PUNE *

Mailing Address : IUCAA, Post Bag 4, Ganeshkhind, Pune 411 007, India.
Location : Meghnad Saha Road, Savitribai Phule Pune University Campus, Pune 411 007.
Phone : 020-2569 1414, 2560 4100 | Fax : +91-20-2560 4699
E-mail : root@iucaa.in
Uniform Resource Locator : http://www.iucaa.in